# Nutrient Physiology of Siliceous Phytoplankton Under Warming and Acidification in Arctic and Subtropical Oceans

by

Shea N. Wyatt

B.Ed., University of British Columbia, 2014
B.Sc. (Honours), University of Victoria, 2010

A Dissertation Submitted in Partial Fulfillment
of the Requirements for the Degree of

DOCTOR OF PHILOSOPHY

in the Department of Biology



We acknowledge and respect the Lək̓ʷəŋən (Songhees and Esquimalt) Peoples on whose territory the university stands, and the Lək̓ʷəŋən and W̱SÁNEĆ Peoples whose historical relationships with the land continue to this day.

Nutrient Physiology of Siliceous Phytoplankton Under Warming and Acidification in Arctic and Subtropical Oceans

by

Shea N. Wyatt

B.Ed., University of British Columbia, 2014
B.Sc. (Honours), University of Victoria, 2010

**Supervisory Committee**

Dr. Diana E. Varela, Supervisor
**Department of Biology and School of Earth and Ocean Sciences**

Dr. Rana El-Sabaawi, Departmental Member
**Department of Biology**

Dr. Roberta Hamme, Departmental Member
**School of Earth and Ocean Sciences**

Dr. Paul Covert, Outside Member
**Fisheries and Oceans Canada**

## Abstract

Steadily rising atmospheric $CO_2$ concentrations have the potential to impact marine ecosystems by increasing the temperature and acidity of the world's oceans. In the sunlit upper ocean, phytoplankton affect elemental cycling and contribute to nutrient export to deeper waters by incorporating nutrients into biomass and supporting higher tropic levels. One unique group of phytoplankton, diatoms, are characterized by their typically larger size and heavy silica frustules, and they make considerable contributions to global primary productivity. Diatoms are expected to be impacted by oceanic change in various ways, but the degree of this effect is still uncertain. The overall objective of this thesis is to improve our understanding of how marine diatom physiology, specifically the utilization of silicon (Si), and the contribution by diatoms to the cycles of carbon (C) and nitrogen (N), are affected by climate-induced increases in temperature and acidification.

I investigated the impact of mesoscale physical processes on diatom contributions to utilization rates of C ($\rho$C) and nitrate ($\rho NO_3$) in the Sargasso Sea in the North Atlantic subtropical gyre, an ecosystem impacted by increased stratification due to ocean warming. Diatoms played a minor role in nutrient utilization and biomass during the lowest-productivity time of year, but they dominated nutrient utilization rates in the deeper euphotic zone of the Sargasso Sea when nutrient concentrations were enhanced by eddy-driven upwelling. In the contrasting environment of the Bering and Chukchi Seas, I investigated the effects of a warming ocean on diatom physiology and elemental composition as part of an on-going oceanographic time-series in the Pacific Arctic Region (PAR). I found significant trends in ocean temperature and sea ice breakup dates for different regions of the PAR, and evidence for declining diatom biomass in one area of

the northern Bering Sea. Anomalously low particulate C:N values were observed across the PAR during the 2019 MHW, but otherwise the response of diatom assemblages in the PAR to a sustained warming period and marine heatwave (MHW) in 2019 varied substantially. Estimates of diatom contributions to $\rho C$ and $\rho NO_3$ in the PAR were improved compared to previous studies, demonstrating that diatoms were responsible for most of the nutrient utilization in all regions.

Ocean acidification experiments were conducted with a model diatom species and two natural phytoplankton assemblages to assess the effects of decreased pH on nutrient physiology. Overall, diatom Si utilization and silicification in laboratory and field culture experiments were unaffected by pH. I found that the cell size of a model species of diatom, *Thalassiosira rotula*, decreased under OA, while in subtropical and Arctic phytoplankton assemblages, OA had no conclusive meaningful impacts on other measures of physiology, or assemblage composition.

This dissertation provides valuable insights into how siliceous phytoplankton, particularly diatoms, interact with marine cycles of Si, C, and N across cold and warm marine ecosystems. It also deepens our understanding of how these dynamic systems may respond to oceanic change, and sets the stage for future research on the evolving impacts of climate-driven physical processes.

# Table of Contents

# List of Figures

# List of Tables

## Glossary of terms

| | |
|---|---|
| °C | Degrees Celsius |
| $^{13}C$ | Stable isotope of carbon, mass number of 13. |
| $^{15}N$ | Stable isotope of nitrogen, mass number of 15. |
| $^{32}Si$ | Radioactive isotope of silicon, mass number 32. |
| Ammonium, $NH_4^+$ | A form of nitrogen that exists in aquatic environments, the simplest and most energetically-favourable form of N for phytoplankton to use as a nutrient. |
| BATS | Bermuda-Atlantic Time-series Study – an oceanographic time-series in the subtropical North Atlantic Ocean that has collected data on the physical, biological, and chemical properties of the ocean every month since 1988. |
| Biogenic silica, $bSiO_2$ | A widespread, non-crystalline (amorphous) mineral produced by biological processes. Also referred to as opal or biogenic opal. |
| Carbon, C | A chemical element that occurs in all organic compounds and forms of life. |
| Chlorophyll-*a*, chl-*a* | A pigment used in photosynthesis that absorbs energy from violet-blue and orange-red light. |
| Carbon dioxide, $CO_2$ | A colourless and odourless gas produced by biological respiration and burning carbon containing compounds. An important greenhouse gas for absorbing and radiating heat. |
| Chlorophyta | A phylum that comprises the green algae. |
| CTD | Conductivity, temperature, and depth sensor for water column. Frequently includes additional sensors for the measurement of water column fluorescence, dissolved oxygen concentration, and photosynthetically active radiation. |
| Cryptophyta | A phylum of algae that are usually autotrophic but can also be heterotrphic. |
| $d_s$ | Cohen's $d_s$, an effect size used to indicate the standardized difference between two means. Corrected for small sample size, equivalent to Hedge's *g*. |

| | |
|---|---|
| DBO | Distributed Biological Observatory – a time-series studying biological responses to physical change across a series of station transects in the Pacific Arctic Region. |
| Diatom | Unicellular photosynthetic microalgae that have intricate silica shells, known as frustules. Diatoms are key contributors to marine ecosystems, playing a crucial role in primary production and the global carbon cycle. |
| Dinoflagellata | A phylum of eukaryotic algae that play many important ecological roles. Dinoflagellates are morphologically distinct and are named for the pair of flagella that provide cells with locomotion. |
| DNA | Deoxyribonucleic acid – carrier of genetic information in most living organisms. |
| $\varepsilon^2$ | Epsilon-squared, an effect size used when comparing three or more means. Indicates a relationship between the values and the treatment variables on a scale of 0 – 1. |
| $\eta^2$ | Eta-squared, an effect size used when comparing three or more means. Indicates the percentage of variance in the dependent variable explained by the independent variable. |
| Euphotic zone | Sunlit area of the ocean (typically from surface to 0.1 – 1% incident surface irradiance). |
| Haptophyta | A phylum of mainly freshwater algae, however marine species are the calcium-plated coccolithophores. |
| µm | Micron – one millionth of a metre. |
| µmol | Micromole – the amount of substance equal to a millionth of a mole (standard measure of an amount of a substance, $6.022 \times 10^{23}$ atoms or molecules per mole). |
| Nitrogen, N | A chemical element that is the core component of proteins and genetic material such as DNA. |
| Nanoeukaryote | Eukaryotic microorganisms in the size range of 3 – 15 microns. |
| New productivity | Rate measurement of C biomass supported by $NO_3^-$ generated outside the euphotic zone, rather than regenerated within sunlit waters or from non-$NO_3^-$ sources such as ammonium or urea. |

| | |
|---|---|
| Nitrate, $NO_3^-$ | A form of N found in aquatic ecosystems, used as a nutrient by phytoplankton and naturally produced by biological processes (nitrification) that convert ammonium to nitrate. |
| OA | Ocean acidification – the reduction in pH of the ocean over an extended period time, caused by the uptake of $CO_2$ from the atmosphere. |
| Ochrophyta | A subphylum that includes all brown algae, and the class Bacillariophyceae, an ecologically and biogeochemically important group of phytoplankton known more commonly as diatoms. |
| Ω | Saturation state for calcium carbonate. Values > 1 indicate a saturated condition under which $CaCO_3$ will tend to form a solid. Values < 1 indicate an undersaturated condition under which $CaCO_3$ will tend to dissolve. |
| PAR | Pacific Arctic Region – marine ecosystems extending from the northern Bering Sea into the Chukchi Sea and adjacent Arctic seas and the deep basins of the Arctic Ocean. |
| $pCO_2$ | Partial pressure of $CO_2$, a measure of the amount of $CO_2$ dissolved in water. |
| pH | A value expressing the acidity or alkalinity of a solution. On a logarithmic scale where 7 is neutral, lower values are more acidic, and higher values are more alkaline. |
| Phosphate, $PO_4^{3-}$ | A form of phosphorus found in aquatic ecosystems, used as a nutrient by phytoplankton. |
| Phaeopigment | Non-photosynthetic pigment molecule formed by the degradation of chl-*a* molecules. |
| Picoeukaryote | Eukaryotic organisms in the size range of 0.2 – 3 microns. |
| *Prochlorococcus* | Genus of very small prokaryotic cyanobacteria, globally widespread and an important contributor to marine productivity, approximately 0.5 – 0.7 μm in size . |
| Particulate C, PC | The concentration of C in seawater that can be collected on a filter, including organic and inorganic components. |
| POC | Particulate Organic C, the concentration of C in seawater that can be collected on a filter, excluding carbonate mineral sources. |

| | |
|---|---|
| Particulate N, PN | The concentration of N in seawater that can be collected on a filter, including organic and inorganic components. |
| POC | Particulate Organic N, the concentration of N contained in biological or organic debris that can be collected on a filter. |
| Primary Production | Measurement of C biomass by photosynthesis. |
| Primary Productivity | Rate measurement of C biomass by photosynthesis. |
| $\rho C$ | Utilization rate of C, equivalent to productivity, ($\mu mol\ L^{-1}\ d^{-1}$). |
| $\rho NO_3$ | Utilization rate of $NO_3^-$, ($\mu mol\ L^{-1}\ d^{-1}$). |
| $\rho Si$ | Utilization rate of $Si(OH)_4$, ($\mu mol\ L^{-1}\ d^{-1}$). |
| Sigma-theta, $\sigma_\theta$ | Potential density of seawater minus 1000 kg $m^{-3}$. |
| Silicon, Si | The second most abundant element in the Earth's crust after oxygen, contained in silicate minerals. |
| Silicification | The process of creating biogenic silica from silicic acid by organisms, mostly diatoms in aquatic ecosystems. |
| Silicic acid, $Si(OH)_4$ | Dissolved Si, derived from terrestrial minerals containing Si, or from the degradation of biogenic silica. |
| Stoichiometry | The relationship between relative quantities of substances, typically a ratio. |
| *Synechococcus* | Widespread genus of prokaryotic cyanobacteria commonly found in well-lit surface waters, approximately 0.8 – 1.5 µm in size. |
| *Thalassiosira* | A diverse genus of centric diatoms, comprising over 100 species that are essential to many marine and freshwater ecosystems. Frequently used as model organisms for physiological studies. |
| $V_C$ | Specific uptake rate of C, equivalent to $\rho C$ divided by C biomass concentration, ($d^{-1}$). |
| $V_{NO3}$ | Specific uptake rate of $NO_3^-$, equivalent to $\rho NO_3$ divided by N biomass concentration, ($d^{-1}$). |
| $V_{Si}$ | Specific uptake rate of Si, equivalent to $\rho Si$ divided by $bSiO_2$ biomass concentration, ($d^{-1}$). |

# Acknowledgements

This work would not have been possible without the dedication and support of many people over the past seven years. I am deeply grateful to my supervisor, Diana Varela, for her unwavering mentorship and support, and for providing countless opportunities for professional and personal growth. The students of the Varela lab, past and present – Michael Livingston, Olivia Melville, Rebecca Crawford, Brandon McNabb, Nimrod Rozen, Sile Kafrissen, Luci Marshall, Jennifer Long, and Karina Giesbrecht – made this journey both enjoyable and enriching. To my exceptional field assistants, Annaliese Meyer, Wylee Fitz-Gerald, and Chloe Immonen, thank you for your tireless efforts and dedication. I also appreciate the help of Hannah Dobbs and Emma Coleman with lab work and data analysis that was included in this work.

My committee – Roberta Hamme, Rana El-Sabaawi, and Paul Covert – provided invaluable guidance, manuscript reviews, and learning opportunities. Special thanks to Roberta for her teaching mentorship, and to Paul for his support in my ocean acidification experiments and for allowing use of his lab space to try new methods.

Damian Grundle and the Bermuda Institute of Ocean Sciences (BIOS) made my Sargasso Sea work possible. I thank Jeffrey Krause, Janice Jones, Mark Brzezinski, Mike Lomas, Amy Maas, Nicholas Bates, and Rebecca Garley for their specialized contributions to those experiments and data analyses. I am grateful to the Captain and crew of the RV *Atlantic Explorer* and to Rodney Johnson, Paul Lethaby, Quinn Montgomery, Paloma Lopez, and the rest of the BATS team for their assistance and camaraderie during cruises.

I thank the various Captains and crews of the CCGS *Sir Wilfrid Laurier*, Institute of Ocean Sciences technicians, and collaborators at the University of Maryland and Clark University for their support of my work in the Pacific Arctic Region. Thank you to Sarah Zimmermann for cruise support, data, and technical assistance every year. Many thanks to Jackie Grebmeier, Lee Cooper, Karen Frey, and their students for their support, and collegiality during cruises. I also thank Roger Francois for access to his beta counter and Karen Frey for sea ice data used in Chapter 3.

Funding for this research was provided by the Natural Sciences and Engineering Research Council (NSERC) Discovery Grant Individual to Diana Varela, and NSERC Canada Graduate Scholarship–Masters and Doctoral to Shea Wyatt. The University of Victoria, BIOS, and Canadian Associates of BIOS internship program provided additional funding.

To my family – my daughter, Maya, my parents, Dean and Kathy, and brothers, Devin and Dylan – your love and encouragement have been my foundation. Most importantly, my deepest gratitude goes to my wife, Karen, for her unwavering patience, support, and love throughout this long journey. I could not have done this without you all!

# Dedication

This dissertation is dedicated to the friends, family, teachers, professors, and students who fostered my sense of curiosity and love for the ocean from my earliest days. This dissertation is also dedicated to my daughter, Maya, who has been my constant companion and source of inspiration from the first day of graduate school until the last. The time spent apart required for this work was at times difficult for you to understand, but I hope the opportunities that we enjoyed because of it, and the adventures that lie ahead, are worth it.

– This page intentionally left blank –

# Chapter 1 – General introduction

### 1.1 The marine silicon cycle

Silicon (Si) is vital for the growth of siliceous phytoplankton like diatoms, which are essential to the ocean's nutrient cycles. By consuming Si along with nitrogen (N), phosphorus (P), and carbon (C), the physiology of diatoms and other silicifiers connect major biogeochemical processes. Understanding the ocean's Si cycle is crucial to gain insight into wider issues such as the ocean's biological pump, long-term climate stability, and ecosystem productivity. Modelling and observational studies have refined the inputs and outputs of Si for the world ocean, however understanding the impacts of global change on the modern Si cycle, for example on concentrations of silicic acid ($Si(OH)_4$ and pelagic biogenic silica ($bSiO_2$) production, requires additional field and experimental studies (Tréguer et al., 2021).

Silicon is the second most abundant element in the Earth's crust and is contained in many types of silicate minerals. The process of silicate weathering removes $CO_2$ from the atmosphere, for example in the equation below which represents the weathering of a feldspar mineral:

$$2NaAlSi_3O_8 + 2CO_2 + 11H_2O \rightarrow Al_2Si_2O_5(OH)_4 + 2Na^+ + 4H_4SiO_4 + 2HCO_3^-$$

In a negative feedback cycle on global warming, termed the silicate carbon sink (Zhang et al., 2021), higher $CO_2$ concentrations and warmer temperatures increase the rate of silicate weathering, which in turn reduces $CO_2$ concentrations. Dissolved Si released by silicate weathering in terrestrial environments is released into rivers and groundwater before ultimately entering marine waters, where it becomes available as $Si(OH)_4$ for marine silicifiers, primarily diatoms, during their seasonal cycles of growth (Fig. 1.1) (Tréguer et al., 2021).

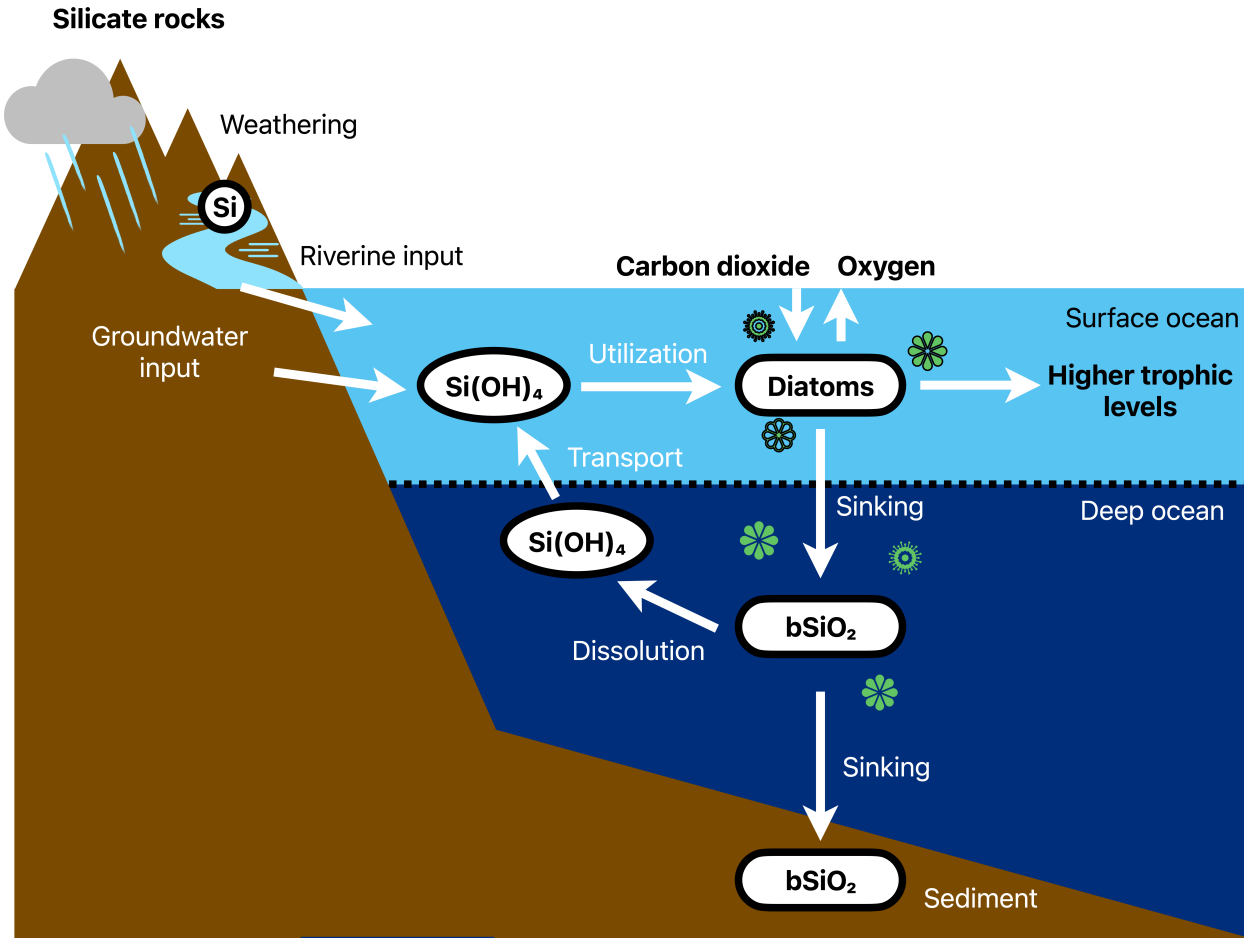


**Figure 1.1.** The marine silicon cycle, simplified to show the main inputs and outputs for the surface layer of the ocean where diatoms utilize $Si(OH)_4$ during their growth. Figure inspired by Tréguer et al. (2021).

On geological time scales, a higher concentration of $Si(OH)_4$ in the ocean has been linked to the relative dominance of diatoms over other phytoplankton (Tréguer and Pondaven, 2000). Diatoms also play an important role in present-day marine cycles of C and N by taking up dissolved nutrients through photosynthesis and growth, and releasing them during decomposition. As such, they can influence atmospheric $CO_2$ concentrations by controlling the C balance in surface waters (Volk and Hoffert, 1985) and the vertical flux of nutrients to the ocean interior, i.e. the biological pump (Alldredge and Silver, 1988).

### 1.2 The role of diatoms in marine ecosystems

Diatoms are a type of unicellular algae that uses $Si(OH)_4$ to form a unique outer cell wall, called a frustule, which is made of amorphous $SiO_2$, known as biogenic $SiO_2$, $bSiO_2$ (Martin-Jezequel et al., 2000). It is hypothesized that the use of Si provides an ecological advantage to diatoms, such as serving as a filter against ultraviolet light (Davidson et al., 1994), protecting against grazing by zooplankton (Smetacek, 1999), and acting as ballast to control water column position (Villareal, 1988). Furthermore, Si is less energetically expensive for cell wall construction instead of organic compounds (Raven, 1983). Diatoms are the largest consumers of this nutrient in the modern ocean, controlling the marine cycle of Si and contributing to vertical fluxes of Si and other nutrients in many ocean regions (Nelson et al., 1995; Treguer et al., 1995).

The vast majority of diatom $bSiO_2$ production is supported by the deep-ocean pool of $Si(OH)_4$, which is recycled from the degradation of sinking particles (Tréguer et al., 2021). The productivity of diatoms is also controlled by N, P, and micronutrient availability (Mongin et al., 2003; Moore et al., 2013), which vary regionally. Globally, diatoms account for ~40% of marine primary productivity (Nelson et al., 1995), contribute to 20% of the total carbon fixed through photosynthesis in the Earth biosphere (Field et al., 1998), support marine food webs, and are intertwined with other major biogeochemical cycles (Tréguer et al., 2021). The various interactions of diatoms with nutrient cycles and their importance in many aspects of marine ecosystems make them highly critical and a useful tool for investigating biogeochemical processes in the ocean.

### 1.3 Ocean warming and acidification

Since the industrial revolution, atmospheric carbon dioxide ($CO_2$) levels have steadily increased from a preindustrial value of 280 ppm to present-day ~420 ppm (SIO, 2024). Projected values range from 750 – 1500 ppm by the year 2100, which will increase global temperatures by up to 4°C (IPCC, 2022) and increase ocean acidity through a decrease in pH of 0.3 – 0.5 units (Caldeira and Wickett, 2003). Warmer temperatures from climate change impact phytoplankton both directly, through their physiology, and indirectly by altering water column stratification, nutrient availability, irradiance exposure levels, and grazing pressure (Winder and Sommer, 2012). These changes influence key processes that lead to shifts in phytoplankton bloom timing and magnitude, as well as phytoplankton assemblage composition and size structures (e.g. Ardyna and Arrigo, 2020; Arrigo et al., 2008; Gaffey et al., 2022). Such shifts likely favour traits best suited to a changing environment and can have important consequences for marine ecosystems. In addition to warming, ocean acidification (OA) is anticipated to affect phytoplankton productivity, nutritional value, and their ability to reproduce and survive in some regions (e.g. Egge et al., 2007; Riebesell et al., 2000; Tatters et al., 2013). Less is known about the direct effects of OA on diatoms compared to other phytoplankton taxa (Kroeker et al., 2013), and many field and laboratory studies been inconclusive or contradictory (Bach and Taucher, 2019).

In high-latitude marine pelagic ecosystems, diatoms are among the most abundant and ecologically important phytoplankton (Armbrust, 2009; Booth and Horner, 1997; Giesbrecht and Varela, 2021; Gradinger, 2009). In contrast, in subtropical oceans, diatoms are less abundant but still play an important role due to their large size and unique physiology (Goldman, 1993; Nelson

and Brzezinski, 1997), and fundamentally because the spatial coverage of such systems accounts for a considerable portion of ocean primary production (Longhurst et al., 1995; Ryther, 1969). Investigating the mechanisms linking climate-driven temperature shifts and OA to diatoms is crucial to comprehending the effects of climate change on distinct marine ecosystems.

### 1.4 Contrasting oceanic regimes: Pacific Arctic and western North Atlantic subtropical regions

The Pacific Arctic Region (PAR) encompasses areas influenced by Pacific Ocean waters flowing into the Arctic Ocean across the shallow shelves of the northern Bering Sea, through the Bering Strait and into the Chukchi Sea. Pelagic primary productivity in the PAR is dominated by diatoms (Booth and Horner, 1997; Crawford et al., 2018; Giesbrecht and Varela, 2021; Gradinger, 2009; Varela et al., 2013; Wyatt et al., 2013) and is closely linked to the benthic ecosystem (Grebmeier et al., 2015; Mathis et al., 2014; Sherr et al., 2013, 2009). Very high autotrophic biomass and rates of primary productivity sustain high benthic macrofaunal biomass (Grebmeier and McRoy, 1989; Highsmith and Coyle, 1990), which in turn supports highly productive and diverse upper trophic levels (Grebmeier et al., 2015).

Climate-induced environmental changes are being observed in the PAR (Jeffries et al., 2013; Lomas et al., 2020; Stabeno et al., 2007; Wood et al., 2015; Woodgate et al., 2012), and there is a growing agreement that the Arctic is approaching a tipping point (Duarte et al., 2012; Mathis et al., 2014). These include a reduction in sea ice extent, earlier seasonal ice melt, and a shift from multi-year ice to thinner, first-year ice (Frey et al., 2015, 2014; Jeffries et al., 2013; Stroeve et al., 2014). However, the changes are not uniform. For example, the Bering Sea has experienced

complex, multi-year variability in sea ice cover due to combinations of wind and temperature (Frey et al., 2015), while the Chukchi Sea has experienced year-round warming and consistent sea ice loss (Cavalieri and Parkinson, 2012). Although research has been ongoing in the PAR since the 1980s (e.g. Grebmeier and McRoy, 1989), to further evaluate the impacts of climate change on pelagic and benthic environments, the Distributed Biological Observatory (DBO) was formally established in 2010. This time-series has already provided valuable insights into the PAR, for example in assessing whether or not the northern Bering and Southern Chukchi Seas are transitioning from a benthic-dominated system to a pelagic system (Grebmeier et al., 2018). Such changes would have critical implications for the highly productive Pacific Arctic ecosystem, and continued shifts in temperature and sea ice dynamics are expected to further affect the timing and magnitude of primary productivity, potentially impacting marine food webs and biogeochemical cycles (Grebmeier, 2012; Mathis et al., 2014).

The Sargasso Sea, located within the western North Atlantic subtropical gyre, is very different from the PAR. Due to the thermal stratification of surface waters (Steinberg et al., 2001), primary production is limited by N throughout most of the year (Lipschultz, 2001). During the winter, nutrients are entrained into surface waters by wind and storms and support a small spring bloom following the onset of seasonal stratification (Steinberg et al., 2001). Phytoplankton assemblages in the Sargasso Sea consist mainly of picocyanobacteria such as *Synechococcus* and *Prochlorococcus*, and small eukaryotic non-silicifiers (Lomas et al., 2013). Despite diatoms being numerically rare in this ecosystem, and having among the lowest reported concentrations of $bSiO_2$, diatoms can still play an important role in seasonal blooms following the entrainment of nutrients into the euphotic zone (Krause et al., 2009). Ocean biology and carbon

biogeochemistry in this region are generally well-understood, due to monthly sampling since 1988 as part of the Bermuda Atlantic Time-series Study (BATS) (Lomas et al., 2013; Steinberg et al., 2001). However, the roles of silicifying organisms such as diatoms and other picoplankton in nutrient utilization are less well-studied (Krause et al., 2017) and only indirect measures of their role in N utilization have been made (Krause et al., 2009). Two of the primary goals of the BATS program are to assess the effects of climate change on ecosystems, and to determine how climatological events drive variability in biogeochemistry (Lomas et al., 2013; Steinberg et al., 2001). Recent studies show that anthropogenic climate change has enhanced stratification in the Sargasso Sea, resulting in reduced vertical supply of nutrient concentrations to surface waters, and causing declines in productivity (Bates and Johnson, 2020; Lomas et al., 2022). Because the supply of nutrients to support phytoplankton is essential for ecosystem functioning, investigating different physical mechanisms of nutrient supply is important for understanding patterns of phytoplankton biomass and productivity in the future.

### 1.5 Elemental composition of diatoms

The uptake and assimilation of nutrients by phytoplankton from the environment dictate their elemental composition. The Redfield ratio (Redfield, 1958) describes the average elemental composition of marine plankton (C:N:P), although since first being proposed, the ratio has been modified to include siliceous plankton such as diatoms (Brzezinski, 1985), resulting in an average Redfield-Brzezinski ratio of 106C:16N:1P:15Si. This relationship between elements is used to understand global and regional biogeochemical cycles, nutrient limitation, and carbon export (Daly et al., 1999; Martiny et al., 2013a) in the world's ocean. Deviations from the average ratio are important for understanding the nutrient status of phytoplankton and their

effects on biogeochemical cycles (Martiny et al., 2013b). Previous studies of elemental ratios in high-latitude seas fall under two categories: those with broad geographic coverage of C:N for only surface waters (Goni et al., 2019), and those with limited geographic scope but better vertical (water column) resolution. However, many previous studies do not include Si (e.g. Bates et al., 2005; Frigstad et al., 2014), resulting in a gap in the current understanding of diatom elemental ratios in both Arctic and subtropical oceans, and especially within the context of changing environmental conditions. Furthermore, many current studies of diatom physiology under OA conditions do not address elemental ratios or physiological indicators such as C and N utilization (Goldman et al., 2017; Hoppe et al., 2015; Riebesell et al., 2013; Sun et al., 2011; Tatters et al., 2012) and there have only been very limited attempts to specifically quantify silicification and $bSiO_2$ production (e.g. Petrou et al., 2019; Wyatt et al., 2024).

### 1.6 Research objectives

The main objective of this dissertation is to enhance the understanding of how diatom physiology responds to climate-induced change in two different regions of the ocean, the Bering and Chukchi Seas in the PAR, and the Sargasso Sea in the subtropical NW Atlantic Ocean. All chapters have a common focus on Si utilization by diatoms and their interactions with other nutrient cycles. Individual chapters have a specific focus on different regions and processes in the changing ocean, such as marine heatwaves, stratification, and the effects of ocean acidification.

*Chapter 2 – Changes in the contributions by differently-sized siliceous phytoplankton to carbon, nitrogen, and silicon utilization after eddy-driven upwelling in the Sargasso Sea*

The objectives of this chapter were to: *i)* quantify the role of siliceous phytoplankton, specifically diatoms, to the utilization of C, nitrate ($NO_3^-$), and $Si(OH)_4$, and *ii)* estimate changes in the contributions of diatoms to pelagic productivity as a response to nutrient upwelling by mesoscale processes throughout the euphotic zone at the main BATS station from September to November, 2018. This study is the first to simultaneously measure size-fractionated phytoplankton utilization rates of C ($\rho$C), $NO_3^-$ ($\rho NO_3$), and $Si(OH)_4$ ($\rho$Si), and standing stocks of biogenic particles (chlorophyll-*a* (chl-*a*), C, N, and $bSiO_2$). By using phytoplankton assemblage composition and cellular quotas, I derived the contribution to nutrient utilization rates by large and small diatoms, and by the cyanobacteria *Synechococcus*. Appendix A presents supplementary material for Chapter 2, and Appendix B contains coupled measurements of size-fractionated primary productivity, nitrate utilization, and silicon dynamics across the North Atlantic subtropical gyre ecosystem.

*Chapter 3 – Elemental composition and nutrient utilization of siliceous phytoplankton assemblages in the Pacific Arctic Region during periods of elevated ocean temperature*

The objectives of this chapter were to: *i)* evaluate changes in long-term records of phytoplankton physiology and elemental composition across the PAR from 2006 to 2022, and *ii)* assess the response of diatom-dominated phytoplankton assemblages in the PAR to the 2019 widespread heatwave event. I evaluated trends in surface temperature, salinity, density, and pH. I calculated ice-breakup dates and ice-free periods prior to

sampling, as well as surface temperature anomalies for all DBO regions. I also measured dissolved nutrient concentrations ($NO_3^-$ and $Si(OH)_4$), size-fractionated chl-*a* concentrations, $bSiO_2$, particulate C, and N concentrations, and $\rho C$, $\rho NO_3$, and $\rho Si$. The data presented builds on previous work in the PAR by the Varela research group at UVic (e.g. Crawford et al., 2018, 2015; Giesbrecht et al., 2019; Giesbrecht and Varela, 2021; Varela et al., 2013; Wyatt et al., 2013), and critically, extends a long time-series of biogeochemical measurements by 5 years in the diverse and climate-affected Pacific Arctic Region. Appendix C contains supplementary materials for Chapter 3.

*Chapter 4 – Morphological and physiological responses of the cosmopolitan marine diatom* Thalassiosira rotula *to acidification*

This chapter addresses whether a model diatom species, *Thalassiosira rotula*, is affected by acclimation to a pH change equivalent to an atmospheric $CO_2$ concentration of 1000 ppm. Measurements include cellular dimensions, cell densities, growth rate, chl-*a* and $bSiO_2$ quotas, particulate C and N quotas, and $\rho C$, $\rho NO_3$, and $\rho Si$. Derived values include cell volumes and surface area to volume ratios, and stoichiometric ratios for particulates and utilization rates. This study is one of the most comprehensive experiments to include different measures of silicification, in particular using the highly-sensitive $^{32}Si$ uptake method. Supplementary material is presented in Appendix D.

Chapter 4 was published in 2024 in *Diatom Research*, but is also included here with correct formatting for the dissertation:

**Wyatt S**, McNabb B, Varela D. (2024). Morphological and physiological responses of the cosmopolitan marine diatom *Thalassiosira rotula* to acidification. *Diatom Research,* 1-14. DOI: 10.1080/0269249X.2024.2369049

*Chapter 5 –Impacts of ocean acidification on phytoplankton from an oligotrophic subtropical ecosystem*

The objective of this chapter was to determine the effect of OA on a phytoplankton assemblage collected from the Sargasso Sea. I conducted an OA experiment in the Sargasso Sea in November 2018, and assessed the biogeochemical response of a phytoplankton assemblage from the main BATS station after acclimation under current (400 ppm) and future (750 ppm) $CO_2$ concentrations. Measurements were the same as for the field study previously conducted in the same region (Chapter 2). This study is one of the few experiments to assess the response of phytoplankton to OA in the Sargasso Sea, and the only to include measurements specifically designed to investigate diatoms, including size-fractionated $bSiO_2$ and $\rho$Si. Supplementary material is presented in Appendix E.

*Chapter 6 – Physiological responses to high $CO_2$ by a summertime diatom assemblage in the northern Bering Sea*

The objective of this chapter was to determine whether the physiology of diatom assemblages in the PAR are affected by OA conditions. I conducted an OA perturbation experiment on a diatom-dominated phytoplankton assemblage from the northern Bering Sea in July 2022. The experimental design was different compared to prior OA

experiments in this dissertation, in that I employed three different $CO_2$ treatments (~400 ppm, ~750 ppm, ~1100 ppm) to manipulate pH, and measurements of productivity, biomass, and elemental composition were collected for every day of the experiment rather than only at the end. In addition, microscopy and novel DNA taxonomic metabarcoding were used to assess changes within the phytoplankton assemblage. Supplementary material is presented in Appendix F.

*Chapter 7 – General conclusions and anticipated significance*

The concluding chapter to this dissertation provides a summary of each data chapter, highlighting the main findings, novelty, and implications of the work. Final thoughts about the significance of my dissertation, and ideas for future directions are described in anticipation of supporting the next student or scientist interested in the impact of climate change on diatom physiology or Si dynamics of marine ecosystems.

– This page intentionally left blank –

# Chapter 2 – Changes in the contributions by differently-sized siliceous phytoplankton to carbon, nitrogen, and silicon utilization after eddy-driven upwelling in the Sargasso Sea

## 2.1 Abstract

The Sargasso Sea, an oligotrophic region of the North Atlantic, is dominated by prokaryotic picophytoplankton. Climate warming has increased stratification, reducing surface nutrient concentrations and phytoplankton productivity. Larger siliceous eukaryotic phytoplankton like diatoms are usually notable only during the spring bloom after winter mixing, but their role during the increasingly stratified summer period is less understood. To better understand the role of diatoms and other silicifiers in nutrient use from summer to fall, we measured size-fractionated nutrient utilization rates and phytoplankton biomass at the Bermuda-Atlantic Time-series Study (BATS) site from September to November 2018. September and October were characterized by low chlorophyll-*a* (chl-*a*) and biogenic silica ($bSiO_2$) biomass, as well as low carbon ($\rho C$), nitrate ($\rho NO_3$), and silicon ($\rho Si$) utilization rates for both small (< 5 μm) and large (> 5 μm) phytoplankton. In November, eddy-driven upwelling increased dissolved nitrate ($NO_3^-$) concentrations, enhancing phytoplankton biomass and productivity in both the mixed layer (ML) and the deep chlorophyll maximum (DCM). Using size-fractionated $bSiO_2$ and $\rho Si$ data, along with their stoichiometric relationship with carbon (C) and nitrogen (N), we estimated the proportion of $\rho C$ and $\rho NO_3$ attributed to the silicifying cyanobacteria *Synechococcus*, and small (< 5 μm) and large (> 5 μm) siliceous eukaryotes, likely diatoms. Depth and $NO_3^-$ availability influenced the contribution of different silicifiers to productivity. In November, contributions from siliceous phytoplankton doubled, with small diatoms increasing nearly five-fold, and large diatoms tripling. Contributions by *Synechococcus* only increased by 40% and were concentrated in the ML. Diatoms, though less abundant than eukaryotes, accounted for 10 – 20% of $\rho NO_3$ at and below the DCM in Sep-Oct, but 80% when $NO_3^-$ increased in November. These results indicate that most $\rho NO_3$ below the DCM is driven by diatoms when new $NO_3^-$ is available, while

utilization rates at shallower depths remain dominated by prokaryotic activity, regenerated nutrients, and non-siliceous phytoplankton. The findings highlight the importance of silicifiers to nutrient utilization during mesoscale processes in an otherwise stratified, oligotrophic time of year.

## 2.2 Introduction

Seasonal variations in the cycling of carbon and other nutrients in the upper ocean affect ecosystem productivity, the air-sea exchange of carbon dioxide, and the export of particulate material to the deep sea. The goal of early studies at the Bermuda-Atlantic Time-series Study (BATS) was to assess temporal and vertical variations in planktonic biomass and production in the Sargasso Sea, an integral part of North Atlantic subtropical gyre ecosystems (Steinberg et al., 2001). More recently, observations encompassing the forty-year history of BATS (Bates and Johnson, 2023, 2020) revealed that time-series studies are critical in identifying physical, chemical, and biological changes over time, due to anthropogenic forcing of oceanic and atmospheric systems. Historically, the BATS ecosystem has been characterized by a phytoplankton community regularly dominated by prokaryotic picoplankton, with blooms of larger phytoplankton such as diatoms only occurring periodically (Lomas et al., 2013; Steinberg et al., 2001). During blooms, the phytoplankton taxa responsible for increases in total chlorophyll biomass vary and the assemblages can be composed of many taxa rather than dominated by a single group (Steinberg et al., 2001). Changes to the size structure, composition, and productivity of Sargasso Sea phytoplankton assemblages during short-term mesoscale processes are lesser known than seasonal cycles, and are important to study for understanding recycling of organic matter and cycling of nutrients in this system. Additionally, anthropogenic climate change has intensified stratification in the Sargasso Sea, reducing vertical nutrient supply to surface waters and leading to declines in surface ocean productivity (Bates and Johnson, 2020; Lomas et al., 2022). Since nutrient availability is crucial for phytoplankton and overall ecosystem function, alternative mechanisms of nutrient delivery may become increasingly important for phytoplankton productivity in the future.

### *2.2.1 The nitrogen cycle and phytoplankton productivity in the Sargasso Sea*

In subtropical regions such as the Sargasso Sea, chlorophyll biomass is regulated by the availability of nutrients (Michaels et al., 1994), rather than by light and mixing depth as observed in the progression of spring blooms in sub-polar regions (Sverdrup, 1953). Nanomolar ammonium ($NH_4^+$) concentrations vary throughout the year, with little depth variation, while detectable concentrations of $NO_3^-$ typically occur only in the surface waters of the Sargasso Sea after vertical mixing in the winter brings deep nutrients into the euphotic zone (Lipschultz, 2001). This supports a short spring-bloom period typically between January and March, when primary production rates, chl-*a* biomass, and concentrations of particulate organic carbon (POC) and nitrogen (PON) are higher than the rest of the year (Lomas et al., 2013; Steinberg et al., 2001). Productivity supported by upwelled or vertically mixed $NO_3^-$ has been termed "new production" (Dugdale and Goering, 1967), and is theoretically equivalent to the biomass exported from the euphotic zone. After phytoplankton growth in the spring and the onset of thermal stratification, N concentrations are undetectable (Lipschultz, 2001), leading to a reduction in overall productivity and the establishment of the DCM layer (Steinberg et al., 2001).

In addition to the main seasonal cycle of productivity, shorter-term processes can impact phytoplankton productivity in the Sargasso Sea. During the winter, prior to the spring phytoplankton bloom, small storms sufficiently mix small amounts of nutrients from deep waters to the euphotic zone. This mechanism produces short-lived blooms that temporarily increase phytoplankton biomass, new production, and export capacity of the ecosystem (Lomas et al., 2009a). Phytoplankton productivity can also increase in the euphotic zone by the upwards shift of isopycnals, caused by formation of cyclonic eddies (McGillicuddy, 2014). This shift brings

higher nutrient concentrations and autotrophic biomass from deeper waters to shallower, higher irradiance depths, stimulating growth and the drawdown of C and other nutrients. In the northern and subtropical regions of the Sargasso Sea, where BATS is located, mesoscale eddies, small winter storms, and deep winter mixing are now understood to be the primary mechanisms for sustaining new production throughout the year (Lipschultz et al., 2002; Lomas et al., 2009a).

### *2.2.2 Autotrophic silicifiers in the Sargasso Sea*

Diatoms, microscopic algae with siliceous cell walls, account for up to 40% of the annual marine biological carbon fixation and for a substantial portion of the carbon exported from the surface to the deep ocean (Nelson et al., 1995), both important processes regulating atmospheric $CO_2$ concentrations. Diatoms are the largest consumers of dissolved Si (silicic acid, $Si(OH)_4$) in the global oceans, forming their external structures from amorphous biogenic silica ($bSiO_2$) (Martin-Jezequel et al., 2000; Moriceau et al., 2019). The utilization of $Si(OH)_4$ by diatoms and other autotrophic silicifiers is coupled with the use of other nutrients such as N, phosphorous (P), and C (Tréguer and De La Rocha, 2013), and in marine coastal and upwelling zones, diatoms are especially important for ecosystem processes and in nutrient cycles.

However, with their vast spatial extent, oligotrophic systems such as midocean gyres are responsible for the majority of marine primary production (Longhurst et al., 1995; Ryther, 1969), and thus play a major role in marine food webs and biogeochemical cycles. In the North Atlantic subtropical gyre, the Sargasso Sea phytoplankton community is comprised mostly of cyanobacteria, with *Prochlorococcus* and *Synechococcus* being both predominant in number and constituting a substantial portion of autotrophic biomass and productivity (Chisholm, 1992;

DuRand et al., 2001; Steinberg et al., 2001). When the BATS program was established it was thought that diatoms were of minor importance in such ecosystems, but notable contributions to nutrient utilization, and both primary and new productivity are now recognized. This change in view came from observations of persistent low concentrations of $Si(OH)_4$ in the Sargasso Sea and elevated $bSiO_2$ flux (Brzezinski and Nelson, 1995; Nelson and Brzezinski, 1997), efforts to determine diatom contributions to new production in deeper waters (Goldman, 1993), and more recently, investigations into short-term processes supporting diatoms (Krause et al., 2009, 2010b; Lomas et al., 2009a, 2009b). In addition to diatoms, one of the most recent studies determined that the abundant cyanobacteria *Synechococcus* makes small but constant contributions to $bSiO_2$ production in the Sargasso Sea (Krause et al., 2017). Despite these recent advances, there is still uncertainty surrounding the significance of oligotrophic oceans in global $bSiO_2$ production and downward export of siliceous material (Tréguer et al., 2021; Tréguer and De La Rocha, 2013). Therefore, the role of silicifiers in primary and new productivity in the Sargasso Sea remains an area of interest.

### *2.2.3 Objectives of this study*

We studied the role of silicifying phytoplankton in nutrient utilization during stratified, late-summer conditions in the Sargasso Sea, with a focus on the DCM and base of the euphotic zone. To improve understanding of how different sizes of phytoplankton interact with cycles of C, N, and Si, we used size-fractionated measurements of nutrient utilization rates ($\rho C$, $\rho NO_3$, $\rho Si$) and particulate biomass (chl-*a*, $bSiO_2$). We supported these measurements using hydrographic, cellular abundance, and algal pigment data. This is the first study that used simultaneous measurements of $\rho C$, $\rho NO_3$, and $\rho Si$ in different size-fractions to estimate the contributions of

differently-sized and siliceous phytoplankton to nutrient utilization and primary productivity throughout the water column in the Sargasso Sea.

## 2.3 Materials and Methods

### *2.3.1 Cruise locations and timing*

Three research cruises were undertaken on the *R/V Atlantic Explorer* from the Bermuda Institute of Ocean Sciences (BIOS) in late summer/early fall 2018. Sampling was conducted at the BATS station (Fig. 2.1) as part of three cruises, BVAL53 (29-September to 07-October), BATS352 (18-October to 21-October), and BATS353 (05-November to 10-November) (Table 2.1).

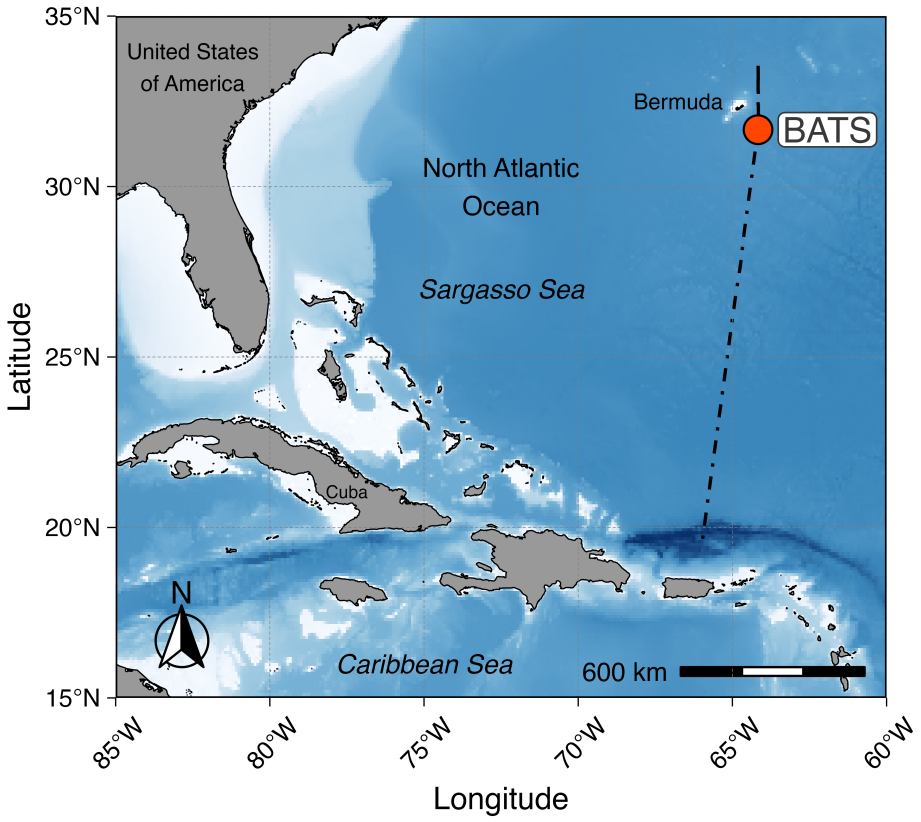


**Figure 2.1.** Location of the Bermuda Atlantic Time-series Study (BATS) station in the subtropical North Atlantic and Sargasso Sea. Hydrographic and productivity measurements were collected at the BATS station during cruises in September, October, and November 2018. Station location is represented by the large red circle. Dashed black line shows cruise track for the BVAL53 cruise (27-Sep to 07-Oct), data from which is presented in Appendix B.

**Table 2.1.** Cruise dates and location for measurements collected at the BATS station in 2018. For the BVAL53 cruise, the BATS station is also referenced as BV2 to preserve consistency with publicly available data from that cruise. Sample dates for two different hydrocasts are shown, "productivity" which focused on nutrient utilization experiments, and "BATS core" which was for the time-series. Measurement abbreviations: CTD – temperature, salinity, dissolved oxygen, and *in vivo* fluorescence; nutrients – dissolved $NO_3^-$, $Si(OH)_4$; biomass – chl-*a*, $bSiO_2$; incubations – $\rho C$, $\rho NO_3$, $\rho Si$; POC/PON – particulate organic C and N; FCM – cell abundances; $C_T$ – total inorganic carbon; pigments – algal chlorophylls and carotenoids.

| Cruise Dates | Cruise Name | Station Name | Latitude (˚N) | Longitude (˚W) | Sample Date | Measurements |
|---|---|---|---|---|---|---|
| 29-Sep to 07-Oct | BVAL53 | BATS (BV2) | 31.667 | 64.168 | 29-Sep *productivity* | CTD, nutrients, biomass, incubations, FCM |
| | | | | | 29-Sep *BATS core* | CTD, nutrients, POC/PON, $C_T$, pigments |
| 18-Oct to 21-Oct | BATS352 | BATS | 31.666 | 64.167 | 18-Oct *productivity* | CTD, nutrients, biomass, incubations, FCM |
| | | | | | 21-Oct *BATS core* | CTD, nutrients, POC/PON, $C_T$, pigments |
| 05-Nov to 10-Nov | BATS353 | BATS | 31.651 | 64.153 | 06-Nov *productivity* | CTD, nutrients, biomass, incubations, FCM |
| | | | | | 07-Nov *BATS core* | CTD, nutrients, POC/PON, $C_T$, pigments |

Additional stations across a latitudinal gradient from the BATS station to 19°N were sampled during the BVAL53 cruise, data from which are included in Appendix B.

### *2.3.2 Hydrography and water sample collection*

For each cruise, two hydrocasts were used to collect the data presented here. The first, the productivity hydrocast, included hydrographic depth profiles as well as discrete samples for dissolved nutrients, particulate biomass, and incubation experiments to determine nutrient utilization rates. The second hydrocast, collected by the BATS program, included hydrographic

depth profiles as well as discrete samples for dissolved nutrients, algal pigment concentrations, total inorganic carbon ($C_T$), and particulate organic C and N (POC & PON) concentrations. Many additional measurements were collected during the second hydrocast but are not used here, however the data is publicly available at https://bats.bios.asu.edu/bats-data/. The second hydrocast is referred to as the BATS core hydrocast throughout the text when needed.

Hydrographic depth profiles included temperature, conductivity, pressure, *in vivo* fluorescence, and dissolved oxygen concentrations, and were collected with a Sea-Bird SBE-09 *plus* CTD instrument package from the ocean surface to 4200 m depth. During the productivity hydrocast, discrete samples were collected with 12-L Niskin bottles placed on the CTD-rosette from seven optical depths ($I_D$) equal to 100, 50, 30, 15, 7, 3, 1, 0.5 and 0.1% of surface irradiance. The 1, 0.5, and 0.1% $I_D$ were sampled on every cruise, and the remaining, shallower depths were chosen based on the structure of the water column to ensure sampling across the ML and around the DCM. $I_D$ was determined using vertical profiles of underwater irradiance measured using the photosynthetically active radiation sensor on the rosette, but the actual sampling depth was rounded to the nearest 20 m to match the BATS core hydrocast that followed. During the BATS core hydrocast on cruise BVAL53, discrete samples were collected similarly from standardized depths at 0, 40, 80, 100, 120, and 150 m. During the BATS core hydrocast on cruises BATS352 and BATS353, discrete samples were collected at 0, 20, 40, 60, 80, 100, 120, 140, and 160 m.

### *2.3.3 Dissolved nutrient concentrations*

Samples for dissolved nutrient concentrations ($NO_3^-$, $PO_4^{3-}$, $Si(OH)_4$) were collected from the BATS core hydrocast by filtering seawater through a 0.8 µm Nuclepore polycarbonate (PC) filter

into an acid-washed HDPE bottle. Samples were collected in duplicate and frozen at -20°C. Later, concentrations were determined using segmented continuous flow analysis on a nutrient autoanalyzer system at BIOS following standard BATS methods, based on JGOFS protocols (Knap et al., 1997). Concentrations of $PO_4^{3-}$ are not presented in this study.

For use in the calculation of $NO_3^-$ utilization rates, additional seawater samples for $NO_3^-$ concentrations were collected in triplicate from the same Niskin bottles from which samples were collected for the rate experiments. Seawater was filtered through disposable 0.45 µm polyether sulfone (PES) filter cartridges. The filtrate was collected in an acid-washed 15 mL centrifuge tube and immediately frozen at -20°C. Concentrations were measured later at the University of Victoria using an Astoria 2 Nutrient Autoanalyzer (Astoria-Pacific Inc., OR, USA) according to Barwell-Clarke and Whitney (1996). Similarly, separate water samples were collected to determine $Si(OH)_4$ concentrations for use in the calculation of Si utilization rates. The $Si(OH)_4$ samples were stored at 4°C to avoid polymerization of $Si(OH)_4$ at freezing temperatures, and analyzed later at the University of Victoria. Concentrations were determined colourimetrically with a Beckman DU 530 UV/Vis spectrophotometer (Beckman Coulter, CA, USA) using a reverse-order reagent blank (Brzezinski and Nelson, 1986) and a 10-cm glass cuvette for the highest analytical precision. Analytical error (coefficient of variation (CV)) for nutrient concentrations was determined using replicated standards in artificial seawater, resulting in CV for $NO_3^-$ = 4.3% and $Si(OH)_4$ = 1.2%. Triplicate values of $NO_3^-$ and $Si(OH)_4$ were averaged before calculating utilization rates.

### *2.3.4 Photosynthetic pigments*

*Size-fractionated and total chlorophyll-a concentrations*

Size-fractionated chlorophyll-*a* (chl-*a*) concentrations were determined by filtering up to 1.0 L of seawater first through a 5.0 µm polycarbonate (PC) filter and then through a 0.7 µm nominal pore-size glass fiber filter (GF-75) (AMD Manufacturing, Ontario, CA). Filters were frozen at -80°C and stored until later analysis. A total chl-*a* sample was collected by filtering 1.0 L of seawater onto a GF-75 filter, but total chl-*a* concentrations are not shown unless noted, as the sum of the size-fractions always matched the total. The chl-*a* samples were promptly analyzed at BIOS following the cruises. Filters were placed in glass centrifuge tubes and submerged in a 90% acetone solution for 24-h at -20°C in the dark. The extracted samples were warmed to room temperature, centrifuged to remove filter particulates, and decanted into borosilicate cuvettes before measurement on a recently calibrated Turner-Designs 10AU fluorometer (Turner Designs, CA, USA). Phaeopigment interference was corrected for by acidifying each sample and measuring again on the fluorometer (Parsons et al., 1984). Chlorophyll-*a* analysis had an average CV of 11.8%, determined from replicated field samples (instead of standards).

*Accessory algal pigment analysis*

Concentrations of algal chlorophyll and carotenoid pigments were determined using samples collected during the BATS core hydrocast. Seawater was collected from Niskin bottles and processed immediately to reduce pigment degradation from sunlight exposure. The water samples were then gently vacuum filtered onto pre-combusted 47 mm glass-fiber filters (0.7 µm porosity), which were quickly frozen in liquid nitrogen and then stored at -80°C until analysis. Chlorophyll and carotenoid pigments were extracted in 90% acetone on ice, and then were

analyzed with an Agilent 1100 series (Agilent Technologies, Germany) liquid chromatograph calibrated with pure pigment standards. Concentrations of phytoplankton pigments were determined by a modified HPLC method (Knap et al., 1997), originally based on Wright et al. (1991). In this study we focused on the following taxonomic groups and pigments: diatoms, fucoxanthin; non-Prochlorophyte cyanobacteria (primarily *Synechococcus*), zeaxanthin; *Prochlorococcus*, chlorophyll-b; Chrysophytes, `19-butanoyloxyfucoxanthin; Prymnesiophytes (haptophytes), `19-hexanoyloxyfucoxanthin; Dinoflagellates, peridinin; Prasinophytes, prasinoxanthin. Chlorophyll-*a*, common to all algal groups, was also measured by HPLC. Here and throughout the rest of the text, *Synechococcus* and *Prochlorococcus* refer to each group of cyanobacteria in general, rather than a specific species or lineage within the genus.

Since all algal taxonomic groups possess some amount and type of chl-*a*, but also other photosynthetic pigments, the amount of measured chl-*a* that can be attributed to different algal groups was calculated using ratios of accessory pigments and corrections following the algorithms of Letelier et al. (1993). For example, diatoms are identified by the presence of fucoxanthin, which must be corrected for the presence of 19'-hexanoyloxyfucoxanthin and 19'-butanoyloxyfucoxanthin. Although developed for the Hawaii Ocean Time-series (HOTS), this approach has shown favourable comparison to taxonomic studies at BATS (Andersen et al., 1996). Since the algorithms were developed for shade-adapted phytoplankton, we did not apply this technique in the upper euphotic zone (< 60 m), focusing instead on the DCM (Steinberg et al., 2001). Algal pigments were compared to chl-*a* measured by HPLC, not chl-*a* collected on the productivity hydrocast.

### *2.3.5 Size-fractionated and total biogenic silica concentrations*

Size-fractionated $bSiO_2$ was collected by filtering 2.0 L of seawater through a 5 µm PC filter (AMD Manufacturing, Ontario, CA), after which the filtrate was filtered onto a 0.6 µm PC filter. Samples for total $bSiO_2$ were collected by filtering 2.0 L of seawater onto a 0.6 µm pore-size PC filter, but total $bSiO_2$ concentrations are not shown unless noted, as the sum of the size-fractions always matched the total. Filters were frozen at -20°C until returned to shore, where they were dried at 60°C for 48-h and stored in a desiccator until further analysis. A 1-h NaOH digestion was used to convert $bSiO_2$ to $Si(OH)_4$ (Brzezinski and Nelson, 1995), using fresh reagents and polymethylpentene centrifuge tubes (Diagenode, Belgium), to ensure low blanks and low limit of detection. Concentration of $Si(OH)_4$ were measured with a Beckman DU 530 UV/Vis spectrophotometer (Beckman Coulter, CA, USA) at the University of Victoria using a reverse-order reagent blank (Brzezinski and Nelson, 1986) and 10-cm glass cuvettes for high precision. The average CV for $bSiO_2$ was 10.3%, based on replicate field samples.

### *2.3.6 Utilization rates of carbon and nitrate*

At each optical light depth, utilization rate of carbon ($\rho C$) and $NO_3^-$ ($\rho NO_3$) were measured using the $^{13}C$-$^{15}NO_3^-$ stable-isotope dual tracer method (Dugdale and Goering, 1967; Slawyk et al., 1977). Seawater was gently subsampled from Niskin bottles into acid-washed 1.0 – 2.4 L PC bottles, leaving enough headspace for isotope additions. For the determination of total $\rho C$, samples were inoculated to a final enrichment target of ~10% of ambient total dissolved inorganic C using a $KH^{13}CO_3$ (99% purity, Cambridge Isotopes Laboratories, MA, USA) isotope tracer stock. For the determination of $\rho NO_3$, the same samples were inoculated using a $Na^{15}NO_3$ (98+% purity, Cambridge Isotopes Laboratories, MA, USA) isotope tracer stock. Since *in situ*

$NO_3^-$ was expected to be depleted or undetectable at most depths, $^{15}NO_3^-$ was added at the detection limit for $NO_3^-$ concentration (0.1 μM) to minimize artificial nutrient enhancement. Inoculated samples were incubated in an on-deck incubator cooled by continuously flowing surface seawater. Each PC bottle corresponding to a specific optical depth was placed in a layered mesh bag that matched the irradiance at depth. After 24-h, half of each bottle was sequentially filtered through 5.0 μm PC filter, and then the filtrates were filtered through combusted GF-75 filters for the measurement of $\rho C$ and $\rho NO_3$ for the < 5 μm size-fraction. The remaining volumes in each bottle were filtered through combusted GF-75 filters only, to determination rates for the total assemblage. All filters were frozen at -20°C until returned to shore and then dried at 60°C for 48-h. The isotopic composition ($^{13}C$:$^{12}C$ and $^{15}N$:$^{14}N$) and total C and N content of each filter were measured at the Stable Isotope Facility at the University of California Davis with a PDZ Europa 20-20 isotope ratio mass spectrometer and a PDZ Europa ANCA-GSL elemental analyzer (Sercon Ltd., Cheshire, UK).

Carbon utilization rates ($\rho C$) were calculated using equation 3 of Hama et al. (1983) and ambient total inorganic carbon ($C_T$) concentrations directly measured during the BATS core hydrocast. Total inorganic C was measured from gastight samples preserved with mercuric chloride, using a SOMMA interfaced with a UIC Model 5011 coulometer (UIC Inc., Joliet, IL) (Knap et al., 1997). Nitrate utilization rates ($\rho NO_3$) were calculated using equation 3 in Dugdale and Wilkerson (1986) and the ambient $NO_3^-$ concentrations for each sample. When ambient $NO_3^-$ concentrations were below the limit of detection (0.1 μM), the value used was 0.1 μM, therefore representing a theoretical maximum utilization rate.

Carbon and N content were measured from the filters collected at the end of each $\rho C/\rho NO_3$ incubation, representing particulate carbon (PC) and particulate nitrogen (PN). To determine PC and PN at the time of sampling, concentrations were back-calculated using $\rho C$ and $\rho NO_3$. The PC and PN content were on average only 2.2% and 1.9% higher at the end of the incubation, respectively, but corrected concentrations were still used. Because filters were not acid-fumed before measurement, PC could also include inorganic C in the water column. The data from size-fractions of PC and PN were used to estimate POC and PON size-fractions, since those samples were not size-fractionated during filtration.

### *2.3.7 Particulate organic carbon and organic nitrogen concentrations*

Discrete samples for POC and PON were collected during BATS core hydrocasts. After filtering seawater through pre-combusted GF/F filters (0.7 µm porosity), samples were frozen (-20°C) until analysis. Samples were thawed and air-dried, and then acidified in a desiccator saturated with hydrochloric acid fumes. Following acidification, filters were again air-dried and then packed in nickel sleeves prior to analysis on an elemental analyzer.

A linear relationship between POC and PON concentrations and the beam-attenuation coefficient (BAC) from the BATS core hydrocast on each cruise was then used to estimate POC and PON on the productivity hydrocast (Appendix A, Fig. A.1 & A.2). This relationship was expected to be highly predictive and statistically significant to allow high-resolution analysis of POC/PON with depth at the BATS station (personal communication, Rebecca May, BATS program).

### *2.3.8 Utilization rate of silicic acid*

The utilization rate of $Si(OH)_4$ ($\rho$Si) was measured using $^{32}Si$ as a tracer in incubation experiments (Brzezinski and Phillips, 1997; Krause et al., 2011). Size-fractionated $\rho$Si was only collected at four or five optical depths, while $\rho$Si for the total assemblage was collected at the same seven depths as for $\rho$C and $\rho NO_3$. Seawater was gently collected from Niskin bottles into either acid-washed 500 mL or 300 mL polycarbonate bottles, leaving enough headspace for isotope additions. 500 mL bottles were used for combined size-fractionated and total $\rho$Si measurements, and 300 mL bottles were used for only total $\rho$Si. Each bottle was inoculated with a 6500 Bq $mL^{-1}$ solution of high specific activity $^{32}Si(OH)_4$ (~25,000 MBq µmol $Si^{-1}$). 970 Bq (58,000 DPM) was added to 300 mL bottles, and 1670 Bq (100,000) DPM to 500 mL bottles. The amount of $^{32}Si(OH)_4$ added was less than $3.8x10^{-8}$ µmol Si, a negligible increase in the total $Si(OH)_4$ available. Inoculated samples were incubated in the same manner as for $\rho$C and $\rho NO_3$ experiments. After ~24-h, the 300 mL bottles for total $\rho$Si were entirely filtered under gentle vacuum pressure onto 0.6 µm PC filters. For larger bottles, half of the bottle volume was filtered directly onto a 0.6 µm PC filter for total $\rho$Si. The remaining volume was filtered under gentle vacuum pressure onto a 5.0 µm PC filter for the determination of $\rho$Si > 5 µm, and the filtrate was then filtered onto a 0.6 µm PC filter for the determination of $\rho$Si < 5 µm. All filters were rinsed with 0.6 µm filtered seawater to remove any excess $^{32}Si$ tracer that may have not been incorporated into siliceous phytoplankton. Each filter was air-dried at room temperature on a 25 mm Nylon disc before being covered with Mylar film and secured with a nylon ring. All samples were stored for at least 5 half-lives (~120 days) of the daughter isotope ($^{32}P$) for any $^{32}P$ that was taken up or otherwise scavenged during the incubation to decay, and for secular equilibrium to occur.

Activity of $^{32}Si$ in the sample was determined by gas-flow proportional counting using a Risø 25-5 low-level beta GM multicounter (DTU Nutech, Denmark) (Krause et al., 2011), and $\rho$Si was calculated using the ambient $Si(OH)_4$ and $bSiO_2$ concentrations for each depth (Brzezinski and Phillips, 1997). Specific uptake rate ($V_{Si}$) was also calculated by normalizing $\rho$Si by $bSiO_2$ biomass.

### *2.3.9 Cell abundance and C quota*

Samples for total cell abundance were collected in 2.0 mL polyethylene cryovials. After preservation with paraformaldehyde (0.5% final concentration) at 4°C for ~1-h, samples were flash frozen in liquid nitrogen, and then stored at -80°C. Samples were analyzed per Casey et al. (2013), using a high-speed jet-in-air Influx™ Cell Sorter (formerly Cytopeia, Inc., Seattle, WA, now Becton Dickenson), modified for small particle detection with a 100X objective magnification. Cells were classified into four classes: *Prochlorococcus*, *Synechococcus*, picoeukaryotes (< 3 μm), and nanoeukaryotes (3 – 15 μm). Cellular quotas of C ($Q_C$) for each class were determined by analyzing natural populations and monocultures of cells by both a flow cytometry and an elemental analyzer, calibrating the forward scatter pulse height output to POC content for each. We used $Q_C$ for *Synechococcus* and *Prochlorococcus* in later calculations.

### *2.3.10 Improved measurements of size-fractionated silicifier biomass and silicon utilization*

We used equation 1 from Krause et al. (2017) (with modifications for a different size-fraction; we used < 5 μm instead of < 3 μm in the original equation) and derived equation 2 to obtain the absolute value of $\int bSiO_2$ attributable to *Synechococcus* ($\int bSiO_{2\,Syn}$).

$$\% \int bSiO_{2\,Syn} = 100 \times \left[ Q_{Si} \times \int Synechococcus \times \int bSiO_{2\,<5\mu m}{}^{-1} \right] \quad (1)$$

$$\int bSiO_{2\,Syn} = Q_{Si} \times \int Synechococcus \quad (2)$$

Euphotic-zone integrated measurements of cell abundance ($\int$*Synechococcus*) and $bSiO_2$ < 5 μm ($\int bSiO_{2\,<5\mu m}$) were collected from this study. Cellular quota of Si ($Q_{Si}$) was obtained from a previous study in the same region. Average $Q_{Si}$ (n = 34) for *Synechococcus* cells in the euphotic zone at the BATS station during September 2013 and October 2012 was 41 amol cell$^{-1}$ (Ohnemus et al., 2016), and was used without a corresponding estimate of uncertainty, similar to Krause et al. (2017). Values of $\int bSiO_{2\,Syn}$ were subtracted from $\int bSiO_{2\,<5\mu m}$ to provide a proxy for non-*Synechococcus* silicifiers < 5 μm, i.e. small diatoms ($\int bSiO_{2\,<5\mu m\ other}$). The large size-fraction of $\int bSiO_2$, > 5 μm, was not affected by *Synechococcus* and was a proxy for large diatoms ($\int bSiO_{2\,>5\mu m}$).

To better understand the contributions by different groups to size-fractionated measurements of $\int \rho Si$, equation 3, from Krause et al. (2017), and equation 4, were used to obtain the absolute value of $\int \rho Si$ attributable to *Synechococcus*.

$$\% \int \rho Si_{Syn} = 100 \times \left[ Q_{Si} \times \int Synechococcus \times \mu_{Syn} \times \int \rho Si_{<5\mu m}{}^{-1} \right] \quad (3)$$

$$\int \rho Si_{Syn} = Q_{Si} \times \int Synechococcus \times \mu_{Syn} \quad (4)$$

Cell abundance ($\int$*Synechococcus*) and $\int\rho Si_{<5\ \mu m}$ were obtained from this study, while cellular quota ($Q_{Si}$) was the same as above. Growth rates ($\mu_{Syn}$) of *Synechococcus* were assumed to be 0.4 $d^{-1}$, a conservative estimate previously used by Krause et al. (2017), also without a measure of uncertainty. Values of $\int\rho Si_{Syn}$ were subtracted from $\int\rho Si_{<5\mu m}$ to provide a proxy for non-*Synechococcus* silicifiers < 5 µm, i.e. small diatoms ($\int\rho Si_{<5\mu m\ other}$). The large size-fraction of $\int\rho Si$, > 5 µm, was not affected by *Synechococcus* and was a proxy for large diatoms ($\int\rho Si_{>5\mu m}$).

### *2.3.11 Silicifier contributions to carbon and nitrate utilization*

Contributions by silicifiers to $\rho C$ and $\rho NO_3$ were determined by converting size-fractionated $\rho Si$ into N and C units (Giesbrecht and Varela, 2021) with the following equations, where the *sf* subscript indicates a rate or ratio for a specific size-fraction. These calculations were done with both depth-integrated values and later in the discussion, at specific depths. For consistency with the previous section the equations use the $\int$ symbol.

$$Silicifier \int \rho C_{sf} = \frac{\int \rho Si_{sf}}{Si{:}\,C_{sf}} \tag{5}$$

$$Silicifier\ \% \int \rho C_{sf} = 100 \times \frac{\int \rho Si_{sf}}{Si{:}\,C_{sf}} \times \int \rho C_{total}^{-1} \tag{6}$$

$$Silicifier \int \rho NO_{3\,sf} = \frac{\int \rho Si_{sf}}{Si{:}\,N_{sf}} \tag{7}$$

$$Silicifier\ \% \int \rho NO_{3\,sf} = 100 \times \frac{\int \rho Si_{sf}}{Si{:}\,N_{sf}} \times \int \rho NO_{3\,total}^{-1} \tag{8}$$

Carbon and $NO_3^-$ utilization for each size-fraction was calculated separately using large diatom ($\int\rho Si_{>5\mu m}$), small diatom ($\int\rho Si_{<5\mu m\ other}$), and *Synechococcus* ($\int\rho Si_{Syn}$) Si utilization rates. Si:C and Si:N ratios depended on the size-fraction being used, described below. To calculate the

percentage attributed to different silicifiers, each size-fraction was divided by the separately measured total rate ($\int\rho_{total}$). A value for C and $NO_3^-$ utilization by all silicifiers was also calculated by adding the large diatom, small diatom, and *Synechococcus* size-fractions.

Under nutrient-limited conditions, depleted N should cause increased Si:N in diatoms. However, at the BATS station, diatom growth is also kinetically limited by low $Si(OH)_4$ concentrations (Brzezinski and Nelson, 1996), which could offset the impact of N limitation and instead decrease cellular Si:C and Si:N. Due to these counteracting effects, for cells > 5 µm, we used average Si:C:N ratios measured for cultured nano-diatoms (< 20 µm) grown under nutrient replete conditions, which were Si:C = 0.09 ± 0.03 and Si:N = 0.80 ± 0.35 (Brzezinski, 1985). To determine the average large diatom (> 5 µm) contribution to $\int\rho C$ and $\int\rho NO_3$, these Si:C and Si:N ratios were used as constants in equations 5 – 8 along with $\int\rho Si_{>5\mu m}$ and total $\int\rho C$ or $\int\rho NO_3$ for each month. For diatom cells < 5 µm, the same Si:C:N ratios were used, as the BATS station is known to export small diatoms of the genera *Minidiscus* and *Minutocellus* (Amacher et al., 2013; Cruz et al., 2021), which can be as small as 2 µm in diameter and have Si:C and Si:N ratios similar to those reported by Brzezinski (1985) (Leblanc et al., 2018). For both size-fractions, if Si:C and Si:N ratios were in fact higher than those used here, the apparent contribution to $\int\rho C$ and $\int\rho NO_3$ would decrease. Conversely, if Si:C and Si:N were lower than the values used, the contributions to either nutrient utilization rate would increase.

*Synechococcus* stoichiometric ratios were a combination of our direct measurements and literature. Average (n = 20) $Q_C$ for *Synechococcus* during productivity hydrocasts was 16±10 fmol $cell^{-1}$, and using a *Synechococcus* C:N ratio of 9.7±3.5 from Baer et al. (2017), $Q_N$ was

1.6±1.2 fmol cell$^{-1}$. Combined with average $Q_{Si}$ (41 amol cell$^{-1}$) from Ohnemus et al. (2016), we derived values of Si:$C_{Syn}$ = 0.0026±0.0016 and Si:$N_{Syn}$ = 0.025±0.016 which compared very closely to the values used by Krause et al. (2017).

### *2.3.12 Data treatment and visualization*

Using CTD vertical profiles, the potential density anomaly ($\sigma_\theta$) of the water column was calculated using the function "swSigma0" from the R package "oce". Surface mixed layer depth (MLD) was defined based on a change in $\sigma_\theta$ by 0.125 kg m$^{-3}$ from surface values.

Euphotic-zone integrated values ($\int$) were calculated by trapezoidal integration from the surface sample to the base of the euphotic zone (140 m, 0.1% $I_D$). For sampling on 18-Oct, the closest sample to the surface during the productivity cast was 18 m instead of 3 m. This resulted in an underestimation for all integrated data presented for 18-Oct compared to other dates.

Sea level gridded data from satellite observations were downloaded from the Copernicus Marine Environment Monitoring Service and Copernicus Climate Change Service. The data product included daily mean estimates of sea level anomaly (SLA) based on satellite altimetry measurements with a 0.25° resolution. The SLA at BATS from September 1, 2018 until November 30, 2018 was extracted in QGIS v. 3.34 (QGIS Association) using the Point Sampling Tool. Contours and trends in SLA were used to determine the presence of an eddy.

All figures were made in RStudio 2023.06 (Posit Software, PBC, Boston, MA) using the package "ggplot2".

## 2.4 Results

### *2.4.1 Hydrography*

In general, hydrographic conditions at the BATS station were consistent with the North Atlantic subtropical gyre ecosystem at this time of year. The water column at BATS was stratified and stable on 29-Sep and 18-Oct (Fig. 2.2A & B), with a MLD of 41 m to 47 m, respectively. These conditions were accompanied by a DCM maintained between approximately 100 – 140 m in both months (Fig. 2.2A & B). Relative *in vivo* fluorescence (rfu) was slightly higher on 29-Sep, but always below 0.2 rfu.

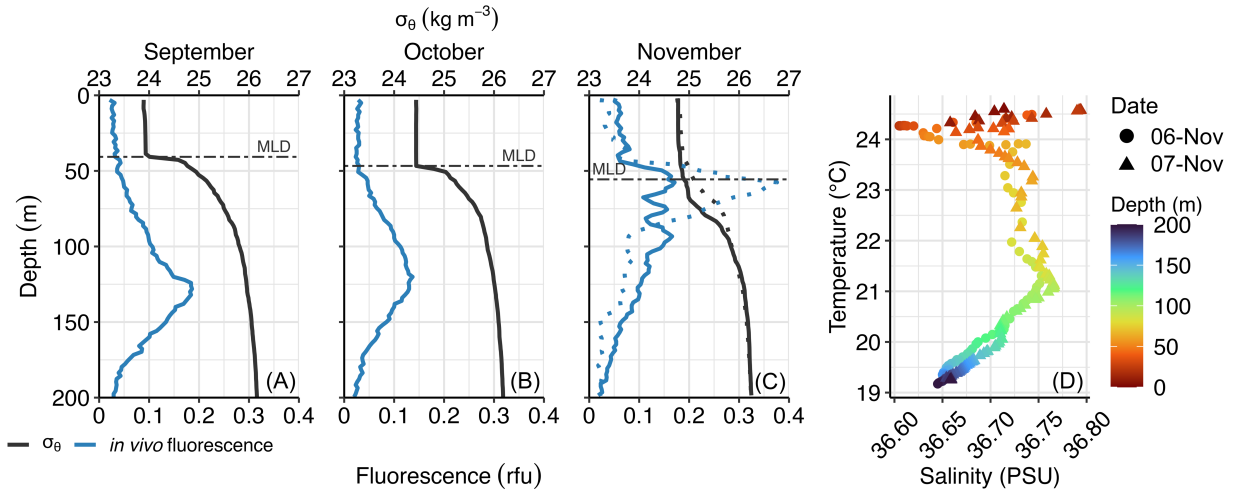


**Figure 2.2.** Potential density anomaly ($\sigma_\theta$) and *in vivo* fluorescence at the BATS station on **(A)** 29-Sep, **(B)** 18-Oct, and **(C)** 06-Nov 2018. Mixed layer depth (MLD) is indicated by the dashed line on each plot. The dotted *in vivo* fluorescence and $\sigma_\theta$ profile in panel C are from just a day later, 07-Nov, showing a rapid increase in fluorescence that was observed during station occupation. Panel **(D)** compares the temperature and salinity characteristics of the upper 200 m of the water column between 06-Nov and 07-Nov, with depth indicated by the colour bar.

In November, the structure of the water column changed, with a greater MLD (56 m) and a pycnocline distributed over a greater range of depths (Fig. 2.2C). This was accompanied by a shallowing of the DCM, ranging between 50 – 100 m, and an increase in biomass (Fig. 2.2C). *In vivo* fluorescence increased up to 2.7x between the productivity cast (06-Nov) and the BATS core hydrocast just a day after on 07-Nov (Fig. 2.2C), and was accompanied by an additional

small shift in the pycnocline. The productivity and BATS core hydrocasts had similar temperature and salinity characteristics (Fig. 2.2D), indicating that the increase in biomass between ~50 – 100 m was primarily due to growth and not because different water masses were sampled on each day.

Changes in the physical structure of the water column in November were due to the influence of an upwelling cyclonic eddy that passed south of the BATS station (Appendix A, Fig. A.3). The effect of the eddy was seen as a rapid decrease in sea level anomaly (Fig. 2.3A), and a shoaling of isopycnals by approximately 40 m (Fig. 2.3B) during occupation of the BATS station.

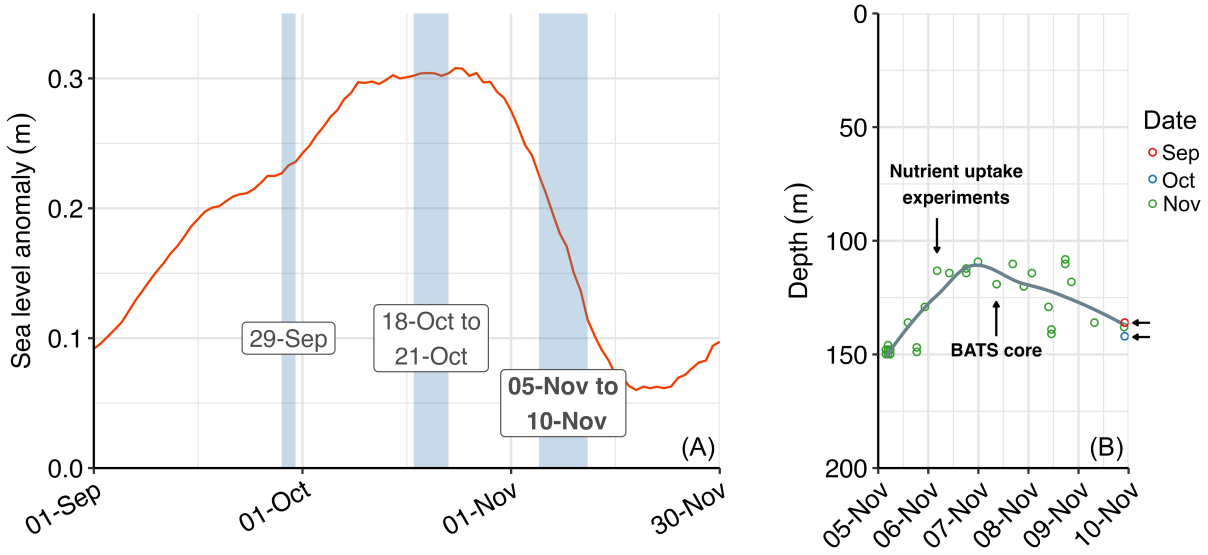


**Figure 2.3.** Changes in sea level anomaly (SLA) and isopycnal depth ($\sigma_\theta = 26$ kg m$^{-3}$) at the BATS station. **(A)** SLA, recorded from 01-Sep to 30-Nov 2018. Days of station occupation are highlighted in blue boxes. **(B)** Isopycnal depth from 05-Nov to 10-Nov, 2018. Green circles indicate the actual depth where $\sigma_\theta = 26.0$ kg m$^{-3}$ for each CTD/rosette cast during station occupation. Grey line is a local regression curve (loess) fitted to show the central tendency of the isopycnal depth during the station occupation. Sampling times for primary productivity and nutrient uptake experiments and the BATS core hydrocast are indicated by arrows and labels. The depth where $\sigma_\theta = 26.0$ kg m$^{-3}$ during previous sampling dates in September and October is indicated by red and blue circles and smaller arrows.

### *2.4.2 Vertical profiles and depth-integrated dissolved nutrient concentrations*

Dissolve nitrate ($NO_3^-$) concentrations remained undetectable in the euphotic zone during September and October, and only increased at depths ≥ 150 m (Fig. 2.4A). Phosphate ($PO_4^{3-}$) was undetectable to 200 m in both months (data not shown). Silicic acid ($Si(OH)_4$) concentrations remained relatively constant with depth, between 0.75 – 1.0 µmol $kg^{-1}$ (Fig. 2.4B). In November, $NO_3^-$ concentrations were detectable as shallow as 60 m, and increased to ≥ 1.0 µmol $kg^{-1}$ at all depths from 100 m and deeper (Fig. 2.4A). This phenomenon increased euphotic-zone integrated $NO_3^-$ by nearly 10x compared to the average of September and October (Fig. 2.4C). There was a measurable increase in $Si(OH)_4$ at depths 100 m or greater, but this did not result in an appreciable increase in integrated $Si(OH)_4$ (Fig. 2.4C).

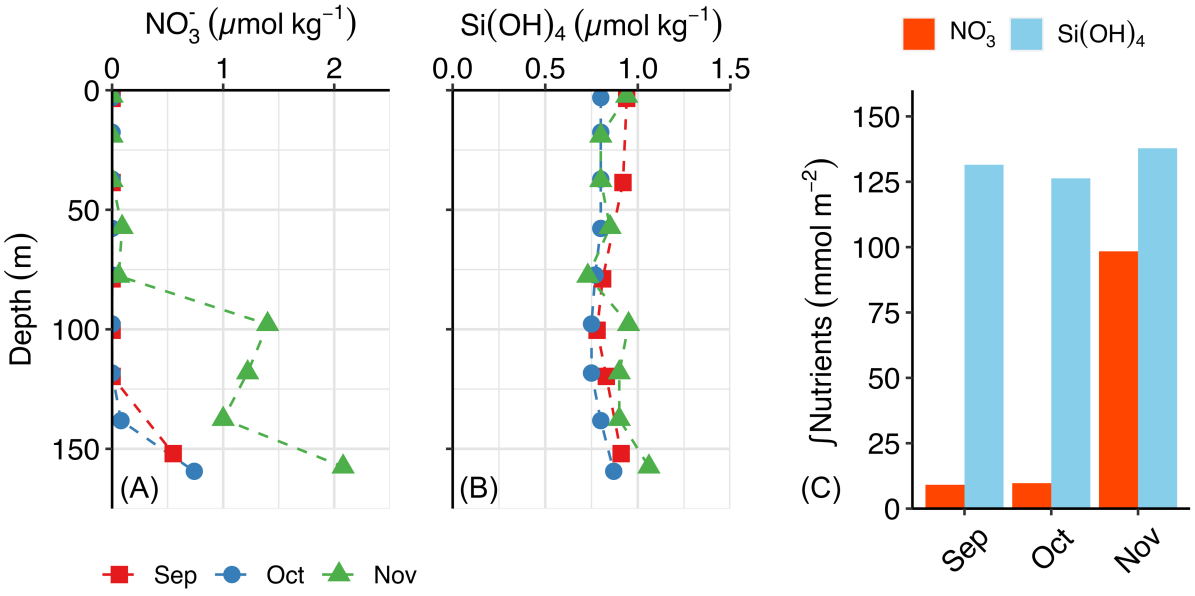


**Figure 2.4**. Nutrient concentrations at the BATS station on 29-Sep, 21-Oct, and 07-Nov 2018. Vertical profiles of **(A)** nitrate, $NO_3^-$, and **(B)** silicic acid, $Si(OH)_4$, were measured from samples collected on the BATS core hydrocast that followed the productivity cast. **(C)** Euphotic zone integrated $NO_3^-$ and $Si(OH)_4$ were calculated to a depth of 150 m in September and 160 m in October and November.

### *2.4.3 Vertical profiles and depth-integrated particulate biomass concentrations*

Chlorophyll-*a* (chl-*a*) biomass mostly followed the same distribution as *in vivo* fluorescence from CTD casts. Unlike *in vivo* fluorescence, particulate chl-*a* biomass showed that the DCM shifted slightly between September (120 – 140 m) and October (100 – 120 m) (Fig. 2.5A), while in November it broadened and shallowed to be between 50 – 100 m. Most chl-*a* biomass was in the < 5 µm size-fraction (Fig. 2.5B), with > 5 µm cells comprising on average 8% of the total in September and October. Despite accounting for less of the total (6%), > 5 µm chl-*a* still notably increased in November throughout the euphotic zone (Fig. 2.5C). Integrated total chl-*a* (∫chl-*a*) (Fig. 2.5D), increased by 54% in November compared to the average of Sep/Oct. Although > 5 µm cells still accounted for a similar proportion of total biomass in November, ∫chl-*a* > 5 µm increased by 65% following nutrient upwelling.

Biogenic silica ($bSiO_2$) biomass was fairly uniform throughout the water column in September and October (Fig. 2.5E), with no noticeable changes in the contribution of small cells (Fig. 2.5F). There was a slight increase in the contribution of > 5 µm cells in the upper 50 m in September (Fig. 2.5G). In November, total $bSiO_2$ throughout the water column increased compared to previous months, up to 4x at some depths in the upper 60 m (Fig. 2.5E). Notably, the November increase in $bSiO_2$ only occurred in the large size-fraction, > 5 µm cells (Fig. 2.5F & G). This increase in large cell $bSiO_2$ in November was particularly noticeable in integrated $bSiO_2$ concentrations ($\int bSiO_2$), accounting for 75% of all $bSiO_2$ biomass (Fig. 2.5H).

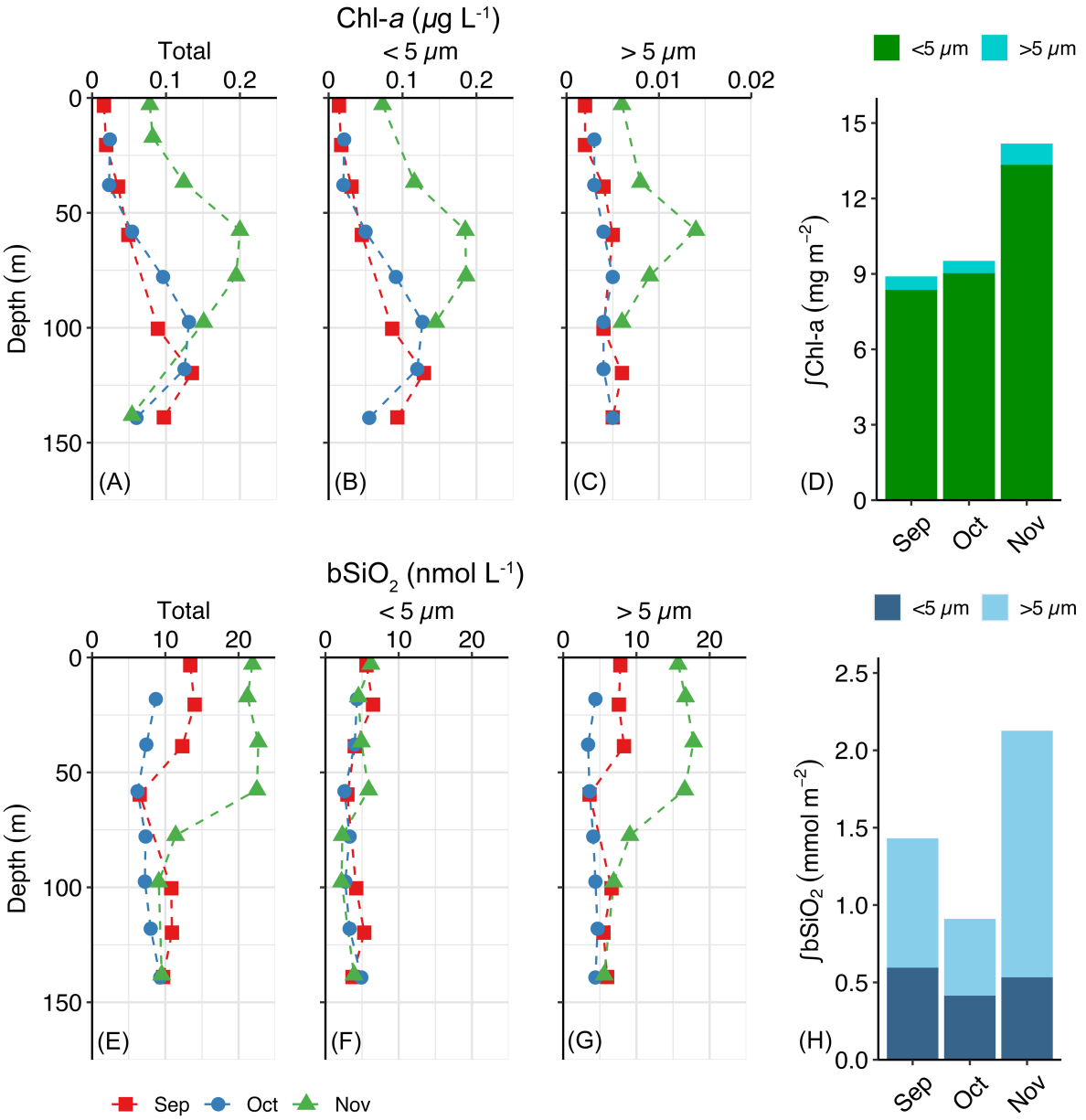


**Figure 2.5.** Chlorophyll-*a* and $bSiO_2$ biomass at the BATS station on 29-Sept, 18-Oct, and 06-Nov 2018. Vertical profiles of **(A)** total chl-*a* as the sum of **(B)** < 5 µm and **(C)** > 5 µm size-fractions. Euphotic-zone (140 m) integrated chlorophyll-*a* (∫Chl-*a*) **(D)** is shown for small (< 5 µm) and large (> 5 µm) size-fractions. Total chl-*a* at 19 m and 137 m in November is from a separate non-size-fractionated sample. Note the 10x difference in scales between panels B and C. Total $bSiO_2$ **(E)** is the sum of **(F)** < 5 µm and **(G)** > 5 µm size-fractions. Euphotic-zone integrated biogenic silica ($\int bSiO_2$) **(H)** is shown for small (< 5 µm) and large (> 5 µm) size-fractions.

### *2.4.4 Phytoplankton assemblage composition based on photosynthetic pigments*

In addition to chl-*a*, other photosynthetic pigments showed distinct subsurface maxima. Specifically, fucoxanthin concentrations (an indicator for diatoms) increased markedly in November slightly below the MLD (56 m), compared to previous months when concentrations were low throughout the water column (Fig. 2.6A). Zeaxanthin (an indicator for *Synechococcus*) had similar profiles on all dates, though maximum values were both higher and shallower in November (Fig. 2.6B), nearer to the MLD (56 m) than before. The indicator pigment for prymnesiophytes (including coccolithophorid haptophytes), `19-hexanoyloxyfucoxanthin, was distributed at depth quite similarly to zeaxanthin (Fig. 2.6C). These pigment profiles showed that while several phytoplankton groups responded to upwelling in November, diatoms had the most distinct response.

Contributions by different taxonomic groups to total chl-*a* biomass at the DCM were calculated on each sampling date (Fig. 2.6D & E). The chl-*a* used in this analysis (from HPLC) is not directly comparable to extracted chl-*a* described in Fig. 2.5. Diatom chl-*a* was calculated to be less than 2 ng $kg^{-1}$ in September and October. In November, diatom chl-*a* increased to 6 ng $kg^{-1}$ at the DCM, and represented 2% of total chl-*a* at the DCM. In addition to diatoms, much of the overall increase in November was accounted for by *Synechococcus* and haptophytes (Fig. 2.6D & E), but the contribution of *Prochlorococcus* to chl-*a* at the DCM decreased. Other taxonomic groups including chrysophytes, dinoflagellates, haptophytes, and prasinophytes increased in biomass in November compared to previous months, but this was not reflected as an increase in overall proportion (Fig. 2.6E).

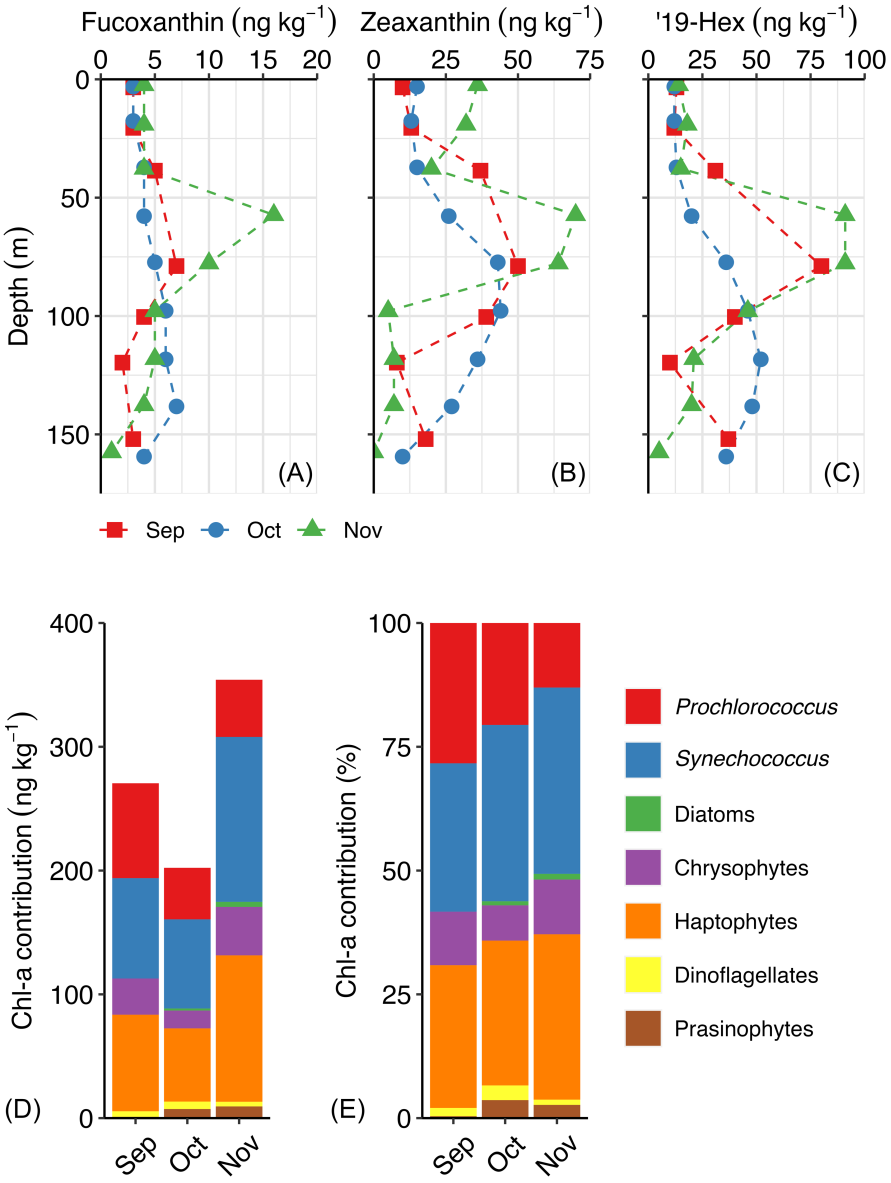


**Figure 2.6.** Photosynthetic pigment concentrations and their contributions to chlorophyll-*a* at the DCM at the BATS station on 29-Sep, 18-Oct, and 06-Nov 2018. Fucoxanthin **(A)** is a proxy for diatoms, **(B)** zeaxanthin is a proxy for non-*Prochlorococcus* cyanobacteria, primarily *Synechococcus*, and **(C)** `19-hexanoyloxyfucoxanthin (`19-hex) is a proxy for haptophytes (coccolithophores). Average contribution at the DCM of **(D)** different taxa to chl-*a* equivalent biomass, and **(E)** of different taxa relative to total chl-*a*. Note different scales in A, B, and C.

### *2.4.5 Phytoplankton assemblage composition based on cell type and size*

The abundance of cyanobacteria (*Prochlorococcus* and *Synechococcus*) was consistent between September and October (Fig 2.7A & B). *Synechococcus* abundance was approximately 10x lower than *Prochlorococcus* overall, and the distributions of these two groups throughout the water column were very different. In September and October, *Prochlorococcus* numerically dominated below 50 m (Fig. 2.7A), and *Synechococcus* was more abundant in surface waters, declining at depths > 80 m (Fig. 2.7B).

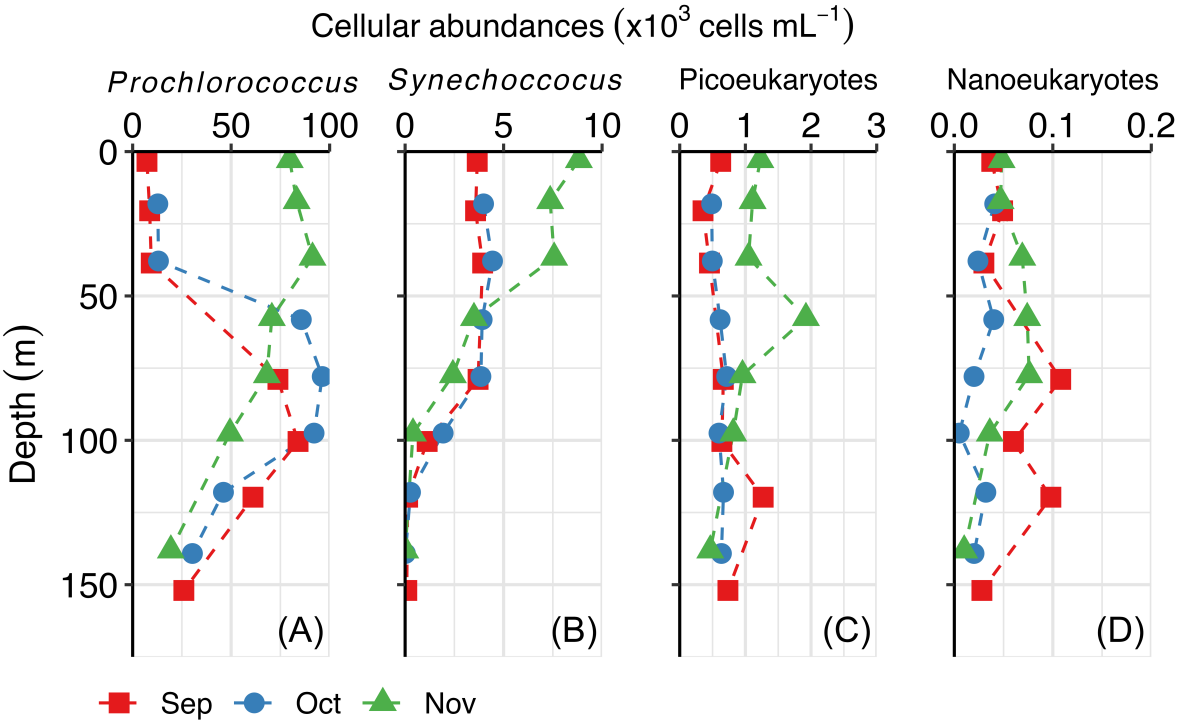


**Figure 2.7.** Vertical profiles of cellular abundance for different size classes at the BATS station on 29-Sep, 18-Oct, and 06-Nov 2018, as determined by flow cytometry. **(A)** *Prochlorococcus*, and **(B)** *Synechoccocus* represent the prokaryotic cyanobacterial community. **(C)** Picoeukaryotes, and **(D)** nanoeukaryotes represent two size classes of the eukaryotic phytoplankton community. Picoeukaryotes are cells < 3 µm, while nanoeukaryotes are cells 3 – 15 µm. Seawater for these measurements and for productivity experiments were collected from the same Niskin bottles. Note different scales from A to D.

In November, the distribution of *Prochlorococcus* changed dramatically, with high abundance in surface waters and declining linearly with depth once below the MLD (56 m). In surface waters,

*Synechococcus* also doubled in numbers in November compared to earlier maximum abundance, but decreased rapidly below 50 m and was less abundant than prior months at depth. Picoeukaryotes were distributed uniformly with depth in September and October (Fig. 2.7C). In November, there was a shift towards greater abundance in surface waters < 60 m, with a distinct maximum around the MLD (56 m). Nanoeukaryotes generally had very low abundance, with maximum values 1 to 3 orders of magnitude lower than all other cell types (Fig. 2.7D). Nanoeukaryotes were more abundant near the MLD in November, compared to a deeper maximum (75 – 125 m) in September.

### *2.4.6 Vertical profiles and depth-integrated primary productivity and nutrient utilization rates*

Primary productivity (PP, $\rho$C) was highest in surface waters and generally decreased with depth on all dates measured (Fig. 2.8). In September and October, there were not any noticeable subsurface maxima for total $\rho$C, and rates were lower than 100 nmol L $d^{-1}$ throughout the upper 60 m (Fig. 2.8A). Carbon utilization rates gradually decreased to approximately zero at the base of the euphotic zone (140 m). Following increased $NO_3^-$ concentrations in November, $\rho$C had a dramatic increase, and throughout the ML rates were ~3 – 5 times higher than in previous months. Most of the increase in $\rho$C was in the < 5 µm size-fraction (Fig. 2.8B), although cells > 5 µm did show a noticeable increase at 58 m (Fig. 2.8C). Euphotic-zone integrated C utilization ($\int\rho$C) was nearly identical in September and October, < 5 mmol C $m^{-2}$ $d^{-1}$, and then increased more than 600% to 31.5 mmol C $m^{-2}$ $d^{-1}$ in November (Fig. 2.8D). On average, cells < 5 µm accounted for 71% of $\int\rho$C in September and October, and 81% in November. The proportion by cells > 5 µm decreased, from an average of 31% in September and October to only 19% on the

last sampling date. However, note that the integrated rate, rather than the proportion, still increased by 350% for large cells under higher nutrient conditions.

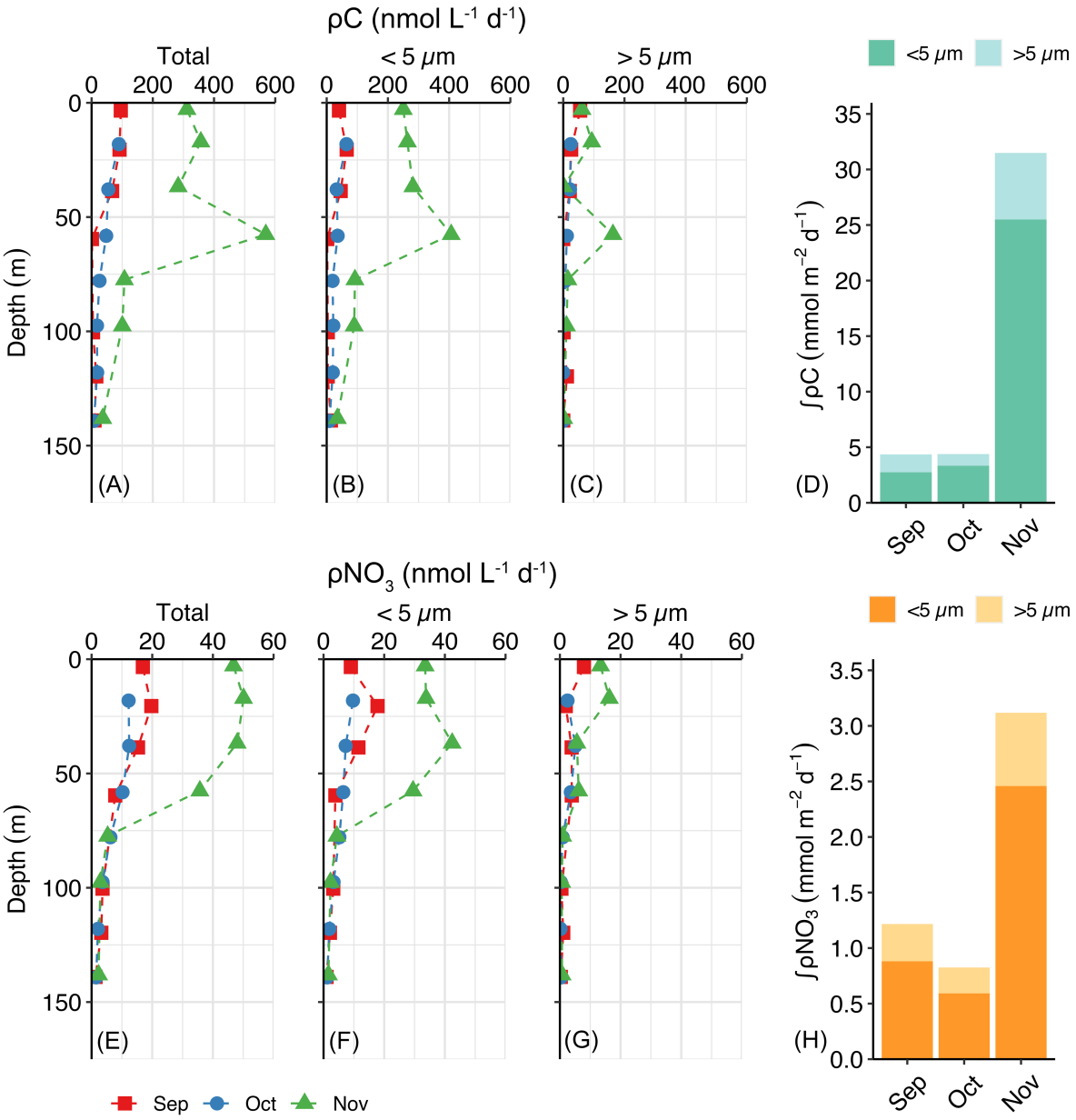


**Figure 2.8.** Primary productivity and nitrate utilization at the BATS station on 29-Sep, 18-Oct, and 06-Nov 2018. Carbon utilization rate, $\rho$C, for **(A)** the whole assemblage (total), **(B)** smaller cells, < 5 µm, **(C)** larger cells, > 5 µm, and **(D)** euphotic zone integrated $\rho$C (primary productivity, $\int\rho$C). $NO_3^-$ utilization rate, $\rho NO_3$ for **(E)** the whole assemblage (total), **(F)** smaller cells, < 5 µm, **(G)** larger cells, > 5 µm, and **(H)** euphotic zone integrated $\rho NO_3$ ($\int\rho NO_3$). Utilization rates were integrated to 140 m in all months.

Similarly to $\rho C$, $\rho NO_3$ was highest in surface waters and decreased with depth throughout the euphotic zone (Fig. 2.8E). Total $\rho NO_3$ was ≤ 20 nmol N $L^{-1}$ $d^{-1}$ in both September and October, but then increased up to ~3 fold in surface waters in November. Small cells < 5 µm were generally responsible for the large increase in $\rho NO_3$ in November (Fig. 2.8F), compared to larger cells which only showed a small increase in surface waters (Fig. 2.8G). Integrated $\rho NO_3$ ($\int \rho NO_3$) followed the same pattern as $\int \rho C$ (Fig. 2.8H). The increase in nutrients in November was reflected as a > 200% increase in $\int \rho NO_3$ to 3.12 mmol N $m^{-2}$ $d^{-1}$ compared to the average of previous months, 1.02 mmol N $m^{-2}$ $d^{-1}$. There was a small change in the proportion of total $\int \rho NO_3$ by cells < 5 µm, from an average of 72% in Sep/Oct to 79% in November. The proportion by larger cells decreased, from 28% to 21%, although it should be emphasized that the integrated rate of $NO_3^-$ utilization by cells > 5 µm was still > 100% higher in November compared to earlier.

Silicic acid utilization ($\rho Si$) for the total assemblage was generally higher than 2 nmol Si $L^{-1}$ $d^{-1}$ throughout the water column in November, and reached nearly 5 nmol Si $L^{-1}$ $d^{-1}$ in the ML. During earlier dates, rates were always < 2 nmol Si $L^{-1}$ $d^{-1}$ (Fig. 2.9A) and there was no clear association with the ML, although rates tended to decrease with depth. Despite being sampled at less depths, size-fractionated $\rho Si$ showed that the two size-fractions were similar in September and October (Fig. 2.9B &C). In November, cells < 5 µm were responsible for nearly double the $\rho Si$ at depths > 75 m, while in surface waters larger cells were more active. Integrated $\rho Si$ ($\int \rho Si$) was 0.29 mmol Si $m^{-2}$ $d^{-1}$ in November, an increase of nearly 300% compared to the average of 0.07 mmol Si $m^{-2}$ $d^{-1}$ for Sep/Oct (Fig. 2.9D). Both larger and smaller cells had large increases in $\int \rho Si$, and cells < 5 µm ultimately accounted for 58% of $\int \rho Si$ compared to 42% for cells > 5 µm.

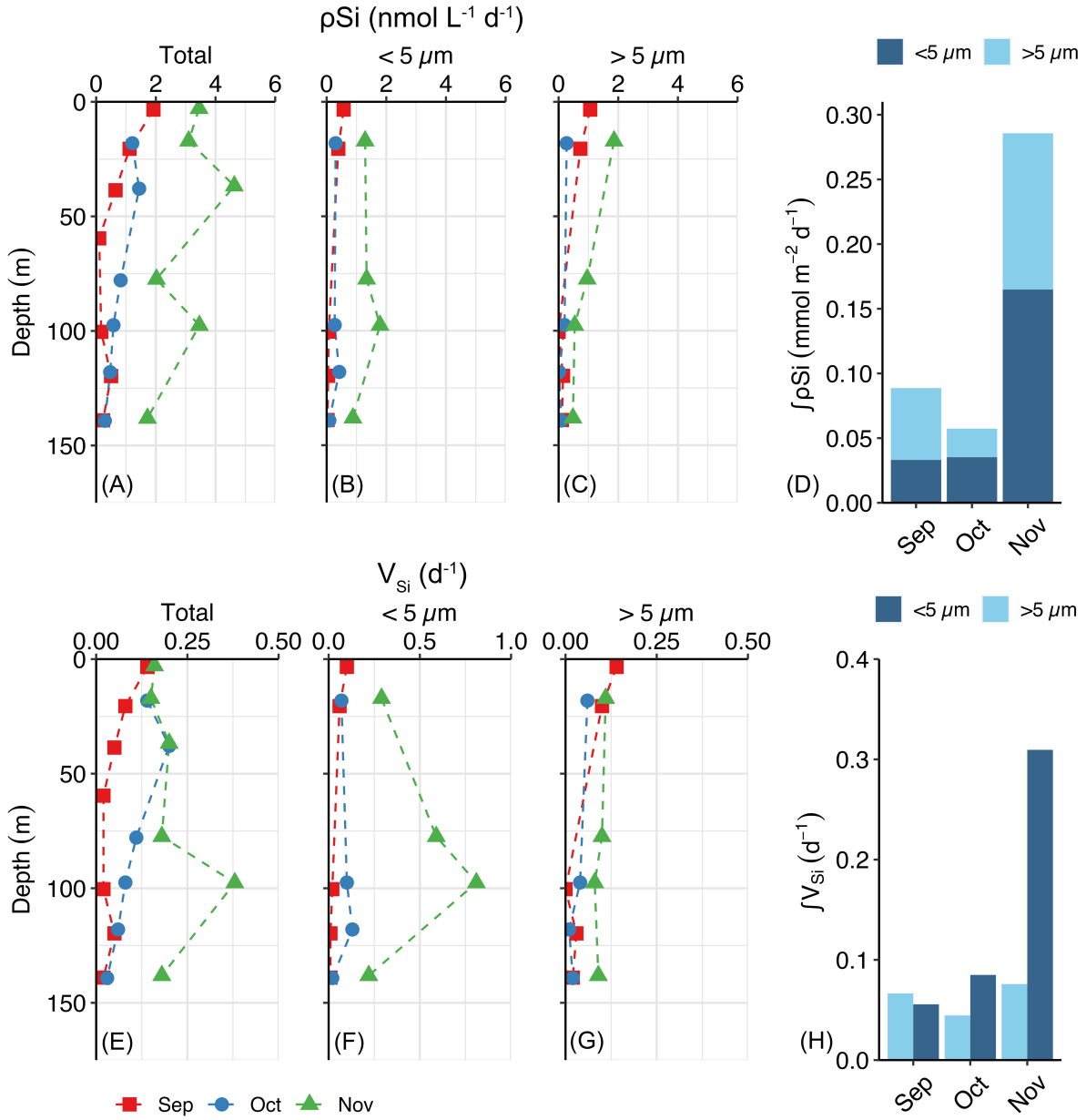


**Figure 2.9.** Silicic acid utilization ($\rho$Si) and specific uptake rate ($V_{Si}$) at the BATS station measured on 29-Sep, 18-Oct, and 06-Nov 2018. $\rho$Si for **(A)** total assemblage, **(B)** smaller cells, < 5 µm, **(C)** larger cells, > 5 µm, and **(D)** euphotic zone integrated $\rho$Si ($\int\rho$Si). Specific uptake rate ($V_{Si}$) of **(E)** all silicifiers (total), **(F)** smaller cells, < 5 µm, **(G)** larger cells, > 5 µm, and **(H)** $\int V_{Si}$ for both size-fractions. Total $\rho$Si was collected at the same time but more depths than size-fractionated samples, and agreed well with the sum of size-fractionated measurements when both were collected at the same depth. Depth of the integration was to 140 m in all months. $V_{Si}$ was calculated as total and size-fractionated $\rho$Si normalized by the corresponding $bSiO_2$ size-fraction. Note the higher scale for $V_{Si}$ < 5 µm. $\int V_{Si}$ was calculated by normalizing $\int\rho$Si for each size-fraction by the corresponding $\int bSiO_2$ size-fraction, and the values are not additive therefore they are not presented as the sum of columns.

Specific uptake rate of Si ($V_{Si}$) for the total assemblage was lowest in September (< 0.01 - 0.14 $d^{-1}$) and decreased from the surface with depth (Fig. 2.9E). It was a similar range of values for both size-fractions (Fig. 2.9F & G). In October, total $V_{Si}$ was up to 0.20 $d^{-1}$ (Fig. 2.9E) and the rate was higher throughout the mixed layer than before. Smaller cells had a higher rate (0.02 – 0.13 $d^{-1}$) at depth than larger cells (0.01 – 0.04 $d^{-1}$) (Fig. 2.9F & G). In November, (Fig. 2.9E), total $V_{Si}$ increased to 0.38 $d^{-1}$ near 100 m, and was > 0.15 $d^{-1}$ at all other depths. This was driven by cells < 5 µm, which reached 0.60 – 0.82 $d^{-1}$ from ~ 75 – 100 m, and was > 0.20 $d^{-1}$ elsewhere. Large cell $V_{Si}$ increased as well, but not to nearly the same degree (Fig. 2.9G), reaching only ~0.10 $d^{-1}$ throughout the water column. Integrated $V_{Si}$ (calculated from $\int\rho Si$ and $\int bSiO_2$) for cells > 5 µm increased slightly in November, from 0.06 to 0.08 $d^{-1}$, while for small cells $\int V_{Si}$ increased 4-fold to 0.31 $d^{-1}$ (Fig. 2.9H).

### *2.4.7 Contributions of Synechococcus to < 5 µm biogenic silica concentrations and silicic acid utilization rates*

To better constrain the potential contribution by small diatoms and other silicifiers, contributions to $\int bSiO_{2\ <5\mu m}$ by *Synechococcus* were calculated. *Synechococcus* cells within the euphotic zone (upper 140 m) made a small contribution to the standing stock of $\int bSiO_{2\ <5\mu m}$, and did not vary much between months, averaging 16±3 µmol $m^{-2}$ (3.1±0.6% of $\int bSiO_{2\ <5\mu m}$) for the entire study period (Table 2.2). By comparison, small non-*Synechococcus* silicifiers (likely small diatoms, $\int bSiO_{2\ <5\mu m\ other}$) averaged 500±90 µmol $m^{-2}$ (97±1% of $bSiO_{2\ <5\mu m}$).

In September and October, *Synechococcus'* proportion of $\int\rho Si_{<5\mu m}$ was 15 – 17% (Table 2.2), and was ~5-fold higher than contribution of *Synechococcus* to $\int bSiO_{2\ <5\mu m}$ for the same months. In

November, the *Synechococcus* proportion of $\int\rho Si_{<5\mu m}$ decreased by nearly 4x to only 4.7%. This was because non-*Synechococcus* small cells, i.e. small diatoms ($\int\rho Si_{<5\mu m\ other}$) increased their Si utilization from < 30 µmol $m^{-2}$ $d^{-1}$ in September and October, to 157 µmol $m^{-2}$ $d^{-1}$ in November, which accounted for over 95% of $\int\rho Si_{<5\mu m}$. Specific uptake rates reflected the increase in small diatom productivity as well, increasing from a Sep/Oct average of 0.06 $d^{-1}$ to 0.31 $d^{-1}$ in November (Table 2.3).

**Table 2.2.** Contributions of *Synechococcus* to euphotic zone integrated $\int bSiO_2$ < 5 µm and $\int\rho Si$ < 5 µm at the BATS station on 29-Sep, 18-Oct, and 06-Nov. $\int bSiO_{2\ Syn}$ and $\int\rho Si_{Syn}$ were calculated as described in equations 1 – 4. Percent $\int bSiO_{2\ Syn}$ and percent $\int\rho Si_{Syn}$ are of the < 5 µm size-fractions only. $\int bSiO_{2\ <5\mu m\ other}$ and $\int\rho Si_{<5\mu m\ other}$ are biomass and utilization rates in the < 5 µm size-fraction after subtracting each contribution by *Synechococcus*, and represent small diatoms. Average $\int\rho Si_{<5\mu m\ other}$ was not calculated (na) due to the high variance between months.

| **Date** | $\int$***Syn*** **(cells $m^{-2}$)** | $\int$**bSiO2** $_{Syn}$ **(µmol $m^{-2}$)** | $\int$**bSiO2** $_{<5\mu m\ other}$ **(µmol $m^{-2}$)** | $\int\rho$**Si**$_{Syn}$ **(µmol $m^{-2}$ $d^{-1}$)** | $\int\rho$**Si**$_{<5\mu m\ other}$ **(µmol $m^{-2}$ $d^{-1}$)** |
|---|---|---|---|---|---|
| 29-Sep | $3.51x10^{11}$ | 14.4 *(2.4%)* | 581 | 5.76 *(17%)* | 27.3 *(83%)* |
| 18-Oct | $3.27x10^{11}$ | 13.4 *(3.2%)* | 401 | 5.36 *(15%)* | 29.8 *(85%)* |
| 06-Nov | $4.72x10^{11}$ | 19.4 (*3.6%)* | 513 | 7.74 *(4.7%)* | 157 *(95%)* |
| | Average | 15.7±3.2 (*3.1±0.6%)* | 500±90 *(97±1%)* | 6.3±1.3 *(15%±9%)* | na *(88±8%)* |

### *2.4.8 Contributions of silicifier groups to depth-integrated nutrient utilization*

During September and October, when the water column was stable and $NO_3^-$ concentrations were undetectable in the euphotic zone, total silicic acid utilization ($\int\rho Si$) by silicifiers was on average 73 µmol Si $m^{-2}$ $d^{-1}$, compared to November when $\int\rho Si$ increased nearly 300% to 290 µmol Si $m^{-2}$ $d^{-1}$ (Table 2.3). *Synechococcus* always contributed less than 10% to $\int\rho Si$ in Sep/Oct, and decreased to only 3% of total $\int\rho Si$ in November. In contrast, small diatoms ($\rho Si_{<5\mu m\ other\ Si}$) and larger diatoms ($\rho Si_{>5\mu m\ Si}$) accounted for 90% of all $\int\rho Si$ prior to nutrient upwelling, and 97% afterwards. This represented a 450% increase in $Si(OH)_4$ utilization for small diatoms, and a 210% increase for larger cells. These patterns in $\int\rho Si$ for each group of silicifier determined their

relative contributions to $\int\rho C$ and $\int\rho NO_3$.

In September and October, on average the majority (> 68%) of $\int\rho C$ was attributed to silicifiers, whether > 5 µm, < 5 µm, or *Synechococcus* (Table 2.3). Between these groups, *Synechococcus* was responsible for the bulk of $\int\rho C$, on average 51%, while small and large diatoms were roughly equal (7 – 10%) to each other. In November, total water column productivity increased more than 7x, however silicifiers did not respond proportionately. *Synechococcus* $\int\rho C$ only increased marginally, but $\int\rho C$ by small diatoms < 5 µm increased by nearly 500%, and > 5 µm diatoms by more than 200%. The overall rate of $\int\rho C$ attributed to silicifiers more than doubled, to 6.1 mmol C $m^{-2}$ $d^{-1}$ compared to 2.9 mmol C $m^{-2}$ $d^{-1}$ on average for Sep/Oct. However, the proportion of the total $\int\rho C$ by silicifiers decreased from 68% in previous months, to just 19%, indicating that other, non-silicifying groups were responsible for the vast majority of $\int\rho C$ in the euphotic zone following upwelling in November.

Nitrate utilization showed a similar pattern, with *Synechococcus* dominating $\int\rho NO_3$ by silicifiers in Sep/Oct, though only accounting for 23% of the total on average (Table 2.3). Both sizes of diatoms were less than 5%, and as a whole all silicifiers accounted for 31% of total $\int\rho NO_3$. In November the pattern of increases for $\int\rho NO_3$ was the same as for $\int\rho C$. Total silicifier contribution to $\int\rho NO_3$ nearly doubled, to 0.7 mmol N $m^{-2}$ $d^{-1}$, with *Synechococcus* $\int\rho NO_3$ staying roughly equivalent to before, and then large increases of over 200% by diatoms > 5 µm and nearly 500% by small diatoms.

**Table 2.3.** Contributions to euphotic zone integrated nutrient utilization rates (total $\int\rho$) by all silicifying groups quantified in this study at the BATS station on 29-Sep, 18-Oct, and 06-Nov 2018. $\int\rho_{Syn}$ is *Synechococcus*, $\int\rho_{<5\mu m\ other}$ is small diatoms, $\int\rho_{>5\mu m}$ is larger diatoms, and total $\int\rho_{Sum}$ is the sum of all silicifier groups. $V_{Si}$ was assumed to be constant for *Synechococcus*, so the increase was *na.*

| **Date** | **Size-fraction** | **$\int\rho$C (µmol C m$^{-2}$ d$^{-1}$) *(% of total $\int\rho$C)*** | **$\int\rho NO_3$ (µmol N m$^{-2}$ d$^{-1}$) *(% of total $\int\rho NO_3$)*** | **$\int\rho$Si (µmol Si m$^{-2}$ d$^{-1}$) *(% of total $\int\rho$Si)*** | **$V_{Si}$ (d$^{-1}$)** |
|---|---|---|---|---|---|
| 29-Sep | Total $\int\rho$ | 4300 | 1220 | 88.4 | |
| | $\int\rho_{Syn}$ | 2240 *(52%)* | 231 *(19 %)* | 5.8 *(6.5 %)* | 0.400 |
| | $\int\rho_{<5\mu m\ other\ Si}$ | 304 *(7.1 %)* | 34.2 *(4.5 %)* | 27.3 *(31 %)* | 0.047 |
| | $\int\rho_{>5\mu m\ Si}$ | 618 *(14%)* | 69.5 *(5.7 %)* | 55.6 *(63 %)* | 0.066 |
| | Total $\int\rho_{Sum}$ | 3160 *(74 %)* | 335 *(28 %)* | 88.4 *(100 %)* | 0.062 |
| 18-Oct | Total $\int\rho$ | 4250 | 825 | 57.3 | |
| | $\int\rho_{Syn}$ | 2080 *(49 %)* | 215 *(26 %)* | 5.4 *(9.3 %)* | 0.400 |
| | $\int\rho_{<5\mu m\ other\ Si}$ | 331 *(7.8 %)* | 37.3 *(4.5 %)* | 29.8 *(52 %)* | 0.074 |
| | $\int\rho_{>5\mu m\ Si}$ | 246 *(5.8 %)* | 27.7 *(3.4 %)* | 22.1 *(39 %)* | 0.045 |
| | Total $\int\rho_{Sum}$ | 2660 *(63 %)* | 280 *(34 %)* | 57.3 *(100 %)* | 0.063 |
| Average contribution by silicifiers *(% of total $\int\rho$)* | Total $\int\rho$ | 4270 | 1020 | 72.9 | |
| | $\int\rho_{Syn}$ | 2160 *(51 %)* | 223 *(22 %)* | 5.6 *(7.7 %)* | 0.400 |
| | $\int\rho_{<5\mu m\ other\ Si}$ | 318 *(7.4 %)* | 35.7 *(3.5 %)* | 28.6 *(39 %)* | 0.061 |
| | $\int\rho_{>5\mu m\ Si}$ | 432 *(10 %)* | 48.6 *(4.8 %)* | 38.9 *(53 %)* | 0.056 |
| | Total $\int\rho_{Sum}$ | 2910 *(68 %)* | 307 *(30 %)* | 72.9 *(100 %)* | 0.063 |
| 06-Nov *(% of total $\int\rho$)* ↑ or ↓ *% change in ρ from Sep/Oct average* | Total $\int\rho$ | 31500 | 3120 | 286 | |
| | $\int\rho_{Syn}$ | 3010 *(9.6 %)* ↑*39 %* | 311 *(10 %)* ↑*39 %* | 7.7 *(2.7 %)* ↑*39 %* | 0.400 *na* |
| | $\int\rho_{<5\mu m\ other\ Si}$ | 1750 *(5.5 %)* ↑*450 %* | 196 *(6.3 %)* ↑*450 %* | 157 *(55 %)* ↑*450 %* | 0.306 ↑*400 %* |
| | $\int\rho_{>5\mu m\ Si}$ | 1340 *(4.3 %)* ↑*210 %* | 151 *(4.8 %)* ↑*210 %* | 121 *(43%)* ↑*210 %* | 0.076 ↑*36 %* |
| | Total $\int\rho_{Sum}$ | 6100 *(19 %)* ↑*110 %* | 658 *(21 %)* ↑*110 %* | 286 *(100%)* ↑*290%* | 0.134 ↑*110 %* |

## 2.5 Discussion

### *2.5.1 Interpretation of biomass proxies and estimates of silicifier contributions to biomass*

Chlorophyll-*a* biomass measured during this study was normal for BATS, comparing closely to maximum ~0.2 µg L$^{-1}$ concentrations that are typical in late fall (Steinberg et al., 2001), while remaining < 0.1 µg L$^{-1}$ throughout most of the water column. Integrated $bSiO_2$ on stratified dates, 29-Sep and 18-Oct (0.9 – 1.4 mmol Si m$^{-2}$), compared well with data in Brzezinski and Nelson (1995), who found $\int bSiO_2$ values between 1 – 2 mmol Si m$^{-2}$ for the same period. The

highest $\int bSiO_2$ we measured in November, 2.1 mmol Si $m^{-2}$, was still much lower than the seasonal maxima of 7.6 – 56.3 mmol $m^{-2}$ that can occur during Jan – April blooms at the BATS station (Brzezinski and Nelson, 1995). Small phytoplankton blooms of both non-siliceous and siliceous phytoplankton frequently occur throughout the fall and winter due to the passage of storms that inject $NO_3^-$ to the base of the euphotic zone (Lomas et al., 2009a). However, based on the upwards shift of isopycnals in November, which increased nutrient concentrations, and patterns in sea level anomaly to the south of the BATS station, in this case the mechanism for the observed bloom was eddy-driven upwelling of $NO_3^-$.

Most autotrophic biomass from Sep – Nov 2018 was comprised of small cells (> 90%) and could be attributed to cyanobacteria or picoeukaryotic organisms such as haptophytes (primarily coccolithophores). Cell abundances were not well-correlated with accessory pigment concentrations, likely because samples for flow cytometry and pigment analysis were taken on separate hydrocasts, separated by up to 72-h. However, if samples for pigments and abundance were obtained from the same casts, pigment concentrations would likely compare better to abundance data.

During our study, large and small cells contributed equally to $bSiO_2$ prior to the November bloom, but as total $bSiO_2$ increased, most growth was by larger cells. Even though $NO_3^-$ concentrations were still at the detection limit from the ocean surface to the base of the ML in November, $bSiO_2$ > 5 µm increased throughout the entire ML, with little variability. Due to diatoms' high intrinsic growth rates and ability to gain dominance during periods of active mixing and nutrient availability (Margalef, 1978; Tang, 1995), the increase in > 5 µm $bSiO_2$

within the ML demonstrated that $NO_3^-$ concentrations were likely being mixed throughout the ML but were not measurable because of rapid drawdown by phytoplankton. Interestingly, fucoxanthin concentrations (a proxy for diatoms) did not compare well with > 5 μm $bSiO_2$ concentrations in the ML. Higher diatom abundances in the Sargasso Sea near the BATS station were previously measured following nutrient increases due to storm mixing (Lomas et al., 2009b), but rapid day-to-day succession within the phytoplankton assemblage followed the increase in diatom abundance, as populations of haptophytes (coccolithophores) and pelagophytes also responded to increased nutrient concentrations. It is therefore likely that the assemblage sampled during our study in November was undergoing rapid composition changes as well. Advective changes in the sampled water masses during the time between the productivity and BATS core hydrocasts could also contribute to uncertainty between proxies. However, since the water masses were comparable between hydrocasts, the mismatch between pigments, cellular abundance, and $bSiO_2$ concentrations therefore suggests that the main driver of differences between the proxies was change within the phytoplankton assemblage during station occupation.

In some high-productivity environments like the Pacific Arctic, almost all $bSiO_2$ can be exclusively attributed to diatoms (Giesbrecht and Varela, 2021), but determining diatom contributions in oligotrophic environments is more complicated. Most historical data for $bSiO_2$ at BATS reflects the total concentration of all silicifiers, but due to their biogeochemical and food-web importance, we were interested in better quantifying the contributions of differently-sized groups. For example, in addition to diatoms, the cyanobacteria *Synechococcus* makes small but consistent contributions to picoplankton $bSiO_2$ biomass and Si utilization (Krause et al., 2017).

Our results indicated that *Synechococcus* was responsible for a very small proportion of $\int bSiO_{2\ <5\mu m}$, and therefore the majority of $\int bSiO_{2\ <5\mu m}$ was associated with other siliceous organisms and/or detrital material. It is unlikely that pico- or nanoplanktonic diatoms contributed much to $bSiO_{2\ <5\mu m}$ in Sep/Oct due to the lack of signal in other diatom proxies (i.e. fucoxanthin profiles). In November, there was more evidence from pigment analysis that pico- or nanoplanktonic diatoms contributed to biomass, and Lomas et al. (2009b) suggest that the common Sargasso Sea diatom *Minidiscus* fits the 3 – 5 µm category. Large diatoms like *Chaetoceros*, *Rhizosolenia*, or chain-forming *Pseudo-nitzschia* may have been present in $\int bSiO_{2\ >5\mu m}$ as well (Krause et al., 2010b). Nanoeukaryote cell abundances in November were higher than in October and more uniform within the ML, further suggesting that diatoms contributed substantially to $\int bSiO_2$ in both size-fractions.

Other organisms that may have contributed to $\int bSiO_{2\ <5\mu m}$ included picoeukaryotes such as non-diatom stramenopiles (chrysophyte algae) (Likhoshway et al., 2006; Marron et al., 2016). However, the pigment used to identify chrysophytes (`19-butanoyloxyfucoxanthin) by Letelier et al. (1993), is now recognized as belonging to the non-silicifying Pelagophyceae (Marron et al., 2016; Steinberg et al., 2001), so the proportion of biomass identified as chrysophytes in our analysis does not contribute much to $\int bSiO_{2\ <5\mu m}$, and chrysophytes remain unquantified. Another group of eukaryotic algae, prymnesiophytes (haptophytes), have been observed in the Sargasso Sea to dominate the eukaryotic algal signal (Treusch et al., 2011). One group of haptophytes, the coccolithophores, includes a species that is covered with silica scales, and other species in which diatom-like Si transporters play an important role in calcification (Durak et al., 2016). Importantly, this requirement for Si is absent from the most common coccolithophore,

*E. huxleyi.* Therefore, while some of the $\int bSiO_{2\ <5\mu m}$ could be accounted for by this group of picoeukaryotic phytoplankton, the contribution to measurable Si utilization and biomass is likely very small. Other eukaryotic autotrophs identified through pigment analysis are not known to utilize Si, so for all further discussion we will only focus on the role of small diatoms when discussing $bSiO_{2\ <5\mu m}$.

### *2.5.2 Novel size-fractionated carbon and nitrate utilization measurements during the oligotrophic period at the BATS station*

Primary productivity ($\rho$C) has been regularly quantified in the Sargasso Sea using isotopic methods since before the inception of the BATS program (Appendix A, Table A.1) (Menzel and Ryther, 1960), although size-fractionated measurements of $\rho$C are rare (Cotti-Rausch et al., 2020; Malone et al., 1993). Isotopic measurements of $\rho NO_3$ have been less frequent (Appendix A, Table A.2) (Lipschultz et al., 2002), and size-fractionated $\rho NO_3$ measurements are seemingly absent from the literature. Most prior studies of $\rho$C and $\rho NO_3$ focused on the winter/spring bloom period (Jan – Apr) following the oligotrophic stratified period (June – Nov). This study added new estimates of size-fractionated $\rho$C and $\rho NO_3$ for two different size-fractions and for an underrepresented period in the seasonal cycle (Sep – Nov). Furthermore, these data were obtained during the transit of an upwelling eddy, which provided additional insights on the role of mesoscale processes on the response of phytoplankton to increased available $NO_3^-$.

Total $\int\rho$C measured during this study in September and October 2018 was about half of the rates observed during stratified summer months in 2011 (Cotti-Rausch et al., 2020), and half of the summer minimums observed during 1989 – 2011 (Lomas et al., 2013; Steinberg et al., 2001).

The proportion of primary productivity attributed to smaller cells (< 5 μm, average 74%) in our study was similar to the picoplankton fraction (< 2 μm) observed in 2011/2012 (average 70%) (Cotti-Rausch et al., 2020), and in 1989/1990 (average 66%) (Malone et al., 1993). Despite their low concentration of biomass (≤8% in all months), larger cells > 5 μm accounted for 27% of $\rho$C during our study, but it was difficult to compare to previous size-fractionated studies due to the overlap of the 2 – 20 μm and 20 – 200 μm ranges used.

Upper ocean productivity is highly dependent on the supply of nutrients brought to the euphotic zone by vertical mixing or overturning of surface waters (Falkowski et al., 1998; Lozier et al., 2011; Sarmiento et al., 2004). Thus stratification, which stabilizes a water column and inhibits the supply of nutrients to surface waters, should be expected to have an inverse relationship to primary productivity. A summer stratification index (density difference between 40 m and 160 m) averaged over 4 months from July – October has been used at the BATS station to indicate the strength of summer stratification. And contrary to above, stratification in this area was previously shown to have a positive relationship with productivity, rather than negative (Steinberg et al., 2001). The summer of 2018 (July – Oct) had a stratification index ($I_S$) of 1.64, which exceeded any stratification index observed in the earlier period used to define the index. This was likely a result of intensified stratification due to a warmer surface ocean (Bates and Johnson, 2020). We do not have $\rho$C measurements for July and August BATS cruises, however our average daily $\int\rho$C for Sep/Oct (51.3 mg C $m^{-2}$ $d^{-1}$) was lower than values observed during the first decade of the BATS program (~100 – 1500 mg C $m^{-2}$ $d^{-1}$), and therefore it appears that greater stratification and lower productivity are connected. As noted by Lozier et al. (2011) though, the relationship between stratification and productivity at BATS has more recently been

shown to only be strong on seasonal time scales, and not at an interannual time scales. They suggest instead that biomass and primary productivity depend on many different variables that are not as easily predicted as the stratification index, such as timing of stratification, strength of wind, and advective supply of nutrients. Indeed, more recent analysis of the BATS time-series shows significant reductions in nutrient inventories associated with reductions in net primary production (Lomas et al., 2022). The response of $\int\rho C$ that we observed with increased $NO_3^-$ in November clearly emphasized the importance of nutrient supply by mesoscale processes in supporting productivity.

Nitrate utilization during our study compared well with previous isotopic studies (Appendix A, Table A.2). In our study we chose to use the limit of detection of $NO_3^-$ in calculating $\rho NO_3$ instead of zero [$NO_3^-$], and therefore our total $\int\rho NO_3$ for September and October of 1.22 and 0.82 mmol $m^{-2}$ $d^{-1}$, respectively, likely reflect the maximum potential utilization. If adjusted to use zero ambient $NO_3^-$, $\rho NO_3$ were approximately half (~1.9x decrease), while the true *in situ* rate likely lies in between both values. In either case, $\int\rho NO_3$ in September and October (0.8 – 1.2 mmol $m^{-2}$ $d^{-1}$, Fig. 2.8H) agreed well with the range of average values (0.4 – 2.4 mmol $m^{-2}$ $d^{-1}$) reported for summer oligotrophic periods in the 1990s (Lipschultz, 2001). Higher $\int\rho NO_3$ in November (3.12 mmol $m^{-2}$ $d^{-1}$), was within the ranges observed during spring blooms in 2004 (0.9 – 4.3 mmol $m^{-2}$ $d^{-1}$) and 2005 (0.7 – 3.5 mmol $m^{-2}$ $d^{-1}$) (Lomas et al., 2009a). Proportions of $\int\rho NO_3$ accounted for by different size-fractions were the same as $\int\rho C$ (Fig. 2.8), indicating that smaller cells (< 5 μm) were utilizing $NO_3^-$ much more (74%) than large cells. This made sense given the much greater abundance of picoeukaryotes and especially in surface waters, the

cyanobacteria *Synechococcus,* which can potentially utilize $NO_3^-$ in addition to other sources of N like $NH_4^+$ (Glover et al., 1988).

### *2.5.3 Contributions of different siliceous phytoplankton to silicic acid utilization*

Total integrated $\rho$Si in September and October 2018 was, to our knowledge, the lowest ever recorded for this region of the ocean. Previous low rates recorded in October 2012 and September 2013 were 7-fold and 4-fold higher, respectively (Krause et al., 2017). Specific uptake rates ($V_{Si}$) were comparable between studies, indicating that while the intrinsic ability of the cells to use Si was similar between 2012/2013 and 2018, there was more Si being used in the water column in 2012/2013 due to higher biomass of siliceous organisms. The $\int\rho$Si measured in November 2018, although nearly a 300% increase from the rates from the previous months, was still on the lower end of previous estimates at the BATS station (Appendix A, Table A.3). The highest values of $\int\rho$Si measured during spring bloom periods at BATS were 4-fold higher (Krause et al., 2009, 2010b; Nelson and Brzezinski, 1997) than our most productive measurement. During another mesoscale eddy in the Sargasso Sea in July 2012, $\int\rho$Si increased to nearly 6.0 mmol $m^{-2}$ $d^{-1}$, 20 times higher than our highest $\int\rho$Si (Krause et al., 2017). Peak $bSiO_2$ biomass in 2012 was 152 nmol $L^{-1}$ compared to our 2018 eddy $bSiO_2$ concentrations that were between 21 – 23 nmol $L^{-1}$ in the ML. This higher accumulation of biomass at the time of sampling in 2012 accounted for the much higher $\int\rho$Si. Another study of $bSiO_2$ production at the BATS station followed an April 2007 mode-water eddy, which induced similar vertical movement of nutrients and water to the surface. This phenomenon also greatly enhanced $bSiO_2$ production in the euphotic zone and was accompanied by an order of magnitude increase in diatom abundances, specifically larger forms like *Chaetoceros* sp. (Krause et al., 2010b). Results

from these previous studies, in particular from the 2007 and 2012 eddy events, corroborate our observations that suggest most of the enhanced $\int\rho$Si observed in November 2018 was due to the growth and accumulation of diatoms in the euphotic zone. The biomass and utilization rates during 2018 were likely less enhanced by eddy-driven upwelling than in the previous studies, as the BATS station was only influenced by the periphery of the cyclonic eddy (Appendix A, Fig. A.3), and did not capture the full effect or duration of the mesoscale feature.

Similar to our measurements of $bSiO_2$, we also calculated the contribution of *Synechococcus* to size-fractionated estimates of $\int\rho$Si to better understand contributions by different groups. The Sep/Oct percent contributions to $\int\rho Si_{<5\mu m}$ by *Synechococcus* (15 – 17%) were in the lower range of values previously reported for the region, 22 – 108 %, average 55±35% (Krause et al., 2017), but the November value (4.7%) was far lower. This is explained by the different size cut-off for our small size-fraction, which included $\int\rho$Si from 3 – 5 µm, a size range that included additional living nanoplanktonic diatoms. This reduced the proportion of $\int\rho Si_{<5\mu m}$ accounted for by *Synechoccocus*, but not the actual amount of $\int\rho$Si by *Synechococcus*. On the other end of the size-fraction, our methods only captured particles > 0.6 µm, while Krause et al. (2017) extended the particle range to include 0.4 µm. Despite this difference, they suggest that doing so did not significantly change $\int bSiO_2$ or $\int\rho$Si estimates compared to previous studies that used the more common 0.6 µm pore size cut-off.

*Synechococcus* accounted for a larger proportion of $\int\rho Si_{<5\mu m}$ than $\int bSiO_{2\ <5\mu m}$ (Table 2.2). This apparently surprising result can be explained by the presence of multiple sources of $\int bSiO_{2\ <5\mu m}$, such as living pico- or nanoplanktonic diatoms, *Synechococcus,* and considerable detrital

material (e.g. from diatoms, or zooplankton (e.g. Rhizaria)) (Krause et al., 2010a). On the other hand, $\int\rho Si_{<5\mu m}$ would only come from living sources. In November, 95% of $\int\rho Si_{<5\mu m}$ was attributed to organisms other than *Synechococcus*. Given our evidence for diatoms increasing their growth in November, we suggest that the vast majority of $\int\rho Si_{<5\mu m}$ was attributable to pico- and nanoplanktonic diatoms in the 3 – 5 µm range. The remainder of total $\int\rho Si$, from cells > 5 µm, was most likely attributed to larger diatoms, which although numerically scarce, still accounted for over 40% of total $\int\rho Si$ in November. Comparison to the only other size-fractionated Si utilization study by Krause et al. (2017) is not easily done because of the difference in size-fractions used. Krause et al. (2017) found that 92 – 99% of total $\int\rho Si$ was due to cells > 3 µm in size, while our > 5 µm cells accounted for 39 – 64% of $\int\rho Si$. The difference is likely due to activity by the 3 – 5 µm cells that were contributing to the smaller size-fraction in our study. When removing *Synechococcus* contribution from $\int\rho Si_{<5\mu m}$, the remaining $\int\rho Si_{<5\mu m\ other}$ (picoeukaryote and small nanoeukaryote diatoms) and $\int\rho Si_{>5\mu m}$ together contributed a proportion of total $\int\rho Si$ across all months of our study, 91 – 97%, that compared very well with Krause et al. (2017).

### *2.5.4 Contributions of differently-sized silicifiers to carbon and nitrate utilization*

In this study, the measurement of size-fractionated $\rho Si$ allowed for the first time a direct comparison of Si to C and $NO_3^-$ utilization across different groups of silicifiers. Based on $\int\rho Si$ and subsequent conversion to estimate $\int\rho C$ and $\int\rho NO_3$, we showed that silicifiers as a group made notable contributions to C and $NO_3^-$ utilization. *Synechococcus* accounted for more productivity than diatoms of any size when looking at the whole euphotic zone because *Synechococcus* was much more abundant and active in the ML. At the BATS station specifically, much of the $NO_3^-$

in surface stratified waters has been shown to be recycled in the ML, suggesting that assimilation of $NO_3^-$ by phytoplankton during periods of low $NO_3^-$ concentration should be considered regenerated productivity, rather than "new" (Lipschultz, 2001; Martin and Pondaven, 2006; Yool et al., 2007). This means that using $\int\rho NO_3$ as a proxy for new productivity and C export in subtropical gyre regions is an overestimate. In September and October, $\int\rho NO_3$ attributed to *Synechococcus* was therefore likely from locally regenerated sources, as no detectable amounts of $NO_3^-$ were observed throughout the ML, and *Synechococcus* abundance declined rapidly at depths below the ML. Given the increase in upwelled $NO_3^-$ concentrations at depth in November, and increased pico- and nanoeukaryote abundance near the MLD, it was not surprising that the amount of $\int\rho NO_3$ attributed to both small and large diatoms increased considerably compared to September and October.

The ratio of new productivity to primary productivity (f-ratio), was traditionally expected to be very low (0.06) in oligotrophic regions (Eppley and Peterson, 1979), indicating that most productivity would be derived from regenerated nutrient sources such as $NH_4^+$. Although we did not correct for any potential contribution by $NH_4^+$, urea, or other organic nitrogen sources, the minimum f-ratios that we observed at the BATS station (Table 2.4) were > 1 in September and ≥ 0.89 in October. These values are clearly much higher than what was expected, and suggest that all or most $\rho C$ was supported by $NO_3^-$, which is unlikely given the lack of $NO_3^-$ throughout the water column at the time of sampling. One possible explanation was that the $^{15}NO_3^-$ used in the incubation experiments artificially enhanced both $\rho C$ and $\rho NO_3$. This is supported by the highest $\rho C$ and $\rho NO_3$ occurring at the highest irradiance despite having the lowest biomass, although we did take care to add only the lowest detectable amount of $^{15}NO_3^-$. Ambient temperature can also

affect incubation conditions, and the on-deck incubator temperature was maintained by surface seawater, which could affect samples collected from below the ML. The rates at those depths were low however, so this likely did not affect the f-ratios.

**Table 2.4.** Integrated $\rho NO_3$ converted to C units and resulting f-ratio (new productivity divided by total primary productivity) at the BATS station on 29-Sep, 18-Oct, and 06-Nov 2018. The range of values given for $\int\rho NO_3$ are the values calculated when using zero (min) or detection-limit (max) for ambient $NO_3^-$ concentrations. POC:PON were derived using the beam-attenuation coefficient (BAC) from the productivity hydrocast. An asterisk (*) indicates a POC:PON ratio derived using a linear relationship that was not statistically significant (p = 0.08), however the ratio was similar to POC:PON from the BATS hydrocast (7.56).

| **Date** | **$\int\rho NO_3$ (mmol N $m^{-2}$ $d^{-1}$)** | **POC:PON** | **$\int\rho NO_3$ (mmol C $m^{-2}$ $d^{-1}$)** | **$\int\rho C$ (mmol C $m^{-2}$ $d^{-1}$)** | **f-ratio** |
|---|---|---|---|---|---|
| 29-Sep | 0.63 – 1.22 | 7.80* | 4.89 – 9.49 | 4.30 | 1.14 – 2.21 |
| 18-Oct | 0.43 – 0.82 | 8.74 | 3.77 – 7.21 | 4.25 | 0.89 – 1.70 |
| 06-Nov | 1.63 – 3.12 | 7.96 | 12.9 – 24.8 | 31.5 | 0.41 – 0.79 |

In November we observed an f-ratio that ranged between 0.41 – 0.79, which although lower, was more in line with previous observations at BATS. The lower f-ratio that we observed in November compared to September and October was surprising, because $NO_3^-$ was much higher throughout the water column, and should have been utilized if the phytoplankton were "primed" to take up $NO_3^-$ as has been shown for phytoplankton that experience intermittent $NO_3^-$ limitation (Twomey et al., 2007). However, it has also been noted that $^{15}NO_3^-$ utilization experiments can underestimate $NO_3^-$ drawdown due to the release of dissolved organic $^{15}N$ during incubations at higher ambient $NO_3^-$ concentrations (Lomas et al., 2009a). This, in addition to the potential uncertainties discussed above that may increase f-ratio values, could explain the decrease in f-ratio that we observed in November.

Despite the uncertainties surrounding the f-ratios calculated in this study, high f-ratios have been previously observed in the Sargasso Sea, ranging from 0 – 0.8 in the 1990s (Lipschultz, 2001) and 0.2 – 0.5 and 0.15 – 0.33 in 2004 and 2005, respectively (Lomas et al., 2009a). In other

oligotrophic regions such as the coastal waters of Western Australia, high f-ratios have been observed as well, ~0.5, indicating equal use of $NO_3^-$ and $NH_4^+$ (Twomey et al., 2007). In these other studies, growth enhancement by $^{15}NO_3^-$ was not expected to influence the results as great care was taken to minimize the concentration added, and temperature effects were also ruled out. Therefore, higher $\rho NO_3$ than expected was concluded to be an accurate measurement, explained by high nighttime $\rho NO_3$ due to high N-stress, and "cryptic upwelling" that prevents phytoplankton from exhibiting signs of $NO_3^-$ limitation (Lomas et al., 2009a). Our measurements of $\rho NO_3$ were likely to be influenced by the same mechanisms, and when combined with the potential for some degree of artificial enhancement from $^{15}NO_3^-$, could explain the unexpectedly high f-ratio values in all months.

In addition to the use of f-ratios, there is more recent evidence in the Sargasso Sea (Fawcett et al., 2014, 2011; Oostende et al., 2017) that prokaryotic picophytoplankton, i.e. cyanobacteria, rely on recycled sources of N almost exclusively during the oligotrophic period, while larger eukaryotes obtain the majority of their N from upwelled $NO_3^-$. Those studies used isotopic methods to determine the origin of the N utilized by different groups. Here we can also approximate the relative importance of $NO_3^-$ to growth by comparing ratios of $\rho Si:\rho NO_3$ to $bSiO_2$:PON for different size classes. A higher $\rho Si:\rho NO_3$ than $bSiO_2$:PON would imply that Si productivity is being supported by regenerated N instead of $NO_3^-$. In this study, the ratio of $\rho Si:\rho NO_3$ to $bSiO_2$:PON for large cells averaged 1.0 for Sept/Oct, and was 0.9 in November, indicating that $\rho NO_3$ accounted for essentially all of the particulate N present in larger diatoms. The same comparison for small cells was on average 3.3 for Sep/Oct and 4.0 in November, suggesting that much of the N used for growth of small cells was from regenerated sources.

Estimates of PON in these ratios were based on the size-fractions of PN, applied to the discrete PON samples that were not size-fractionated. We also did not correct small cell estimates of $\rho Si{:}\rho NO_3$ to $bSiO_2$:PON for *Synechococcus* because $\rho Si_{Syn}{:}\rho NO_{3\ Syn}$ were already derived from our assumed $bSiO_{2\ Syn}$:$PON_{Syn}$ ($Q_{Si}$:$Q_N$), leading to a circular calculation.

Based on our comparison of f-ratios, utilization and particulate ratios, and evidence from the literature, our interpretation that *Synechococcus* likely used regenerated $NO_3^-$ or $NH_4^+$ throughout this study period is reinforced. As such, we believe the use of depth-integrated values for the entire euphotic zone (as is common in the literature) obfuscates the actual contribution of diatoms to primary and new productivity because of the overwhelming abundance and productivity of *Synechococcus* in surface waters. Therefore, we suggest that it is more appropriate to only look at the autotrophic, eukaryotic biomass below surface stratified waters as being relevant for new productivity during the stratified, oligotrophic time of year. This is because most of the N used in the ML was regenerated, and eukaryotic cells are heavily favoured during export from Sargasso Sea euphotic zone (Fawcett et al., 2011). While we do not speculate directly on export rates, we hypothesize that diatoms, rather than *Synechococcus*, will dominate primary and new productivity below the mixed layer and at the depth of the DCM. In particular after $NO_3^-$ concentrations increased due to upwelling, our measurements of diatom $\rho NO_3$ may be a better representation of new $NO_3^-$ productivity, serving as a proxy for the amount of export from the euphotic zone by diatoms.

### *2.5.5 Nutrient utilization at the deep chlorophyll maximum and base of the euphotic zone*

By applying the same conversions of $\rho$Si to $\rho$C and $\rho NO_3$ to specific depths rather than the entire euphotic zone, we found distinct differences in silicifier contributions to $\rho$C and $\rho NO_3$ between the ML, DCM, and base of the euphotic zone (Fig. 2.10). During September and October, within the ML silicifiers made up less than 50% of $\rho$C (Fig. 2.10A & B), and around 25% of $\rho NO_3$ (Fig. 2.10D & E). Unlike the depth-integrated utilization rates where *Synechococcus* contributions to $\int\rho$C were more than twice the contributions to $\int\rho NO_3$, in the ML about 25% of both measures of productivity were attributed to *Synechococcus*. Small and large diatoms usually accounted for less than 10% of $\rho$C and $\rho NO_3$. Around the DCM, *Synechococcus* dominated $\rho$C for the entire assemblage, but became far less important towards the base of the euphotic zone because cyanobacteria abundance declined dramatically. For $\rho NO_3$, all silicifiers contributed less than 50%, with smaller diatoms < 5 µm being somewhat favoured over larger ones. Following the upwelling of $NO_3^-$ in November, both total $\rho$C and $\rho NO_3$ increased throughout the water column and the contributions of different silicifiers changed dramatically compared to previous sampling dates (Fig. 2.10C & F).

When compared to the average contribution by each silicifier size for Sep/Oct, the largest increase in $\rho$C and $\rho NO_3$ by diatoms > 5 µm was through the DCM (450 – 730%) (Table 2.5), and at the base of the euphotic zone (380%). While not as much of an increase, productivity by large diatoms still more than doubled within the ML. The largest increase in $\rho$C and $\rho NO_3$ by diatoms < 5 µm was at the base of the euphotic zone (1300%), but rates also increased substantially within the DCM (700 – 800% increase) (Table 2.5).

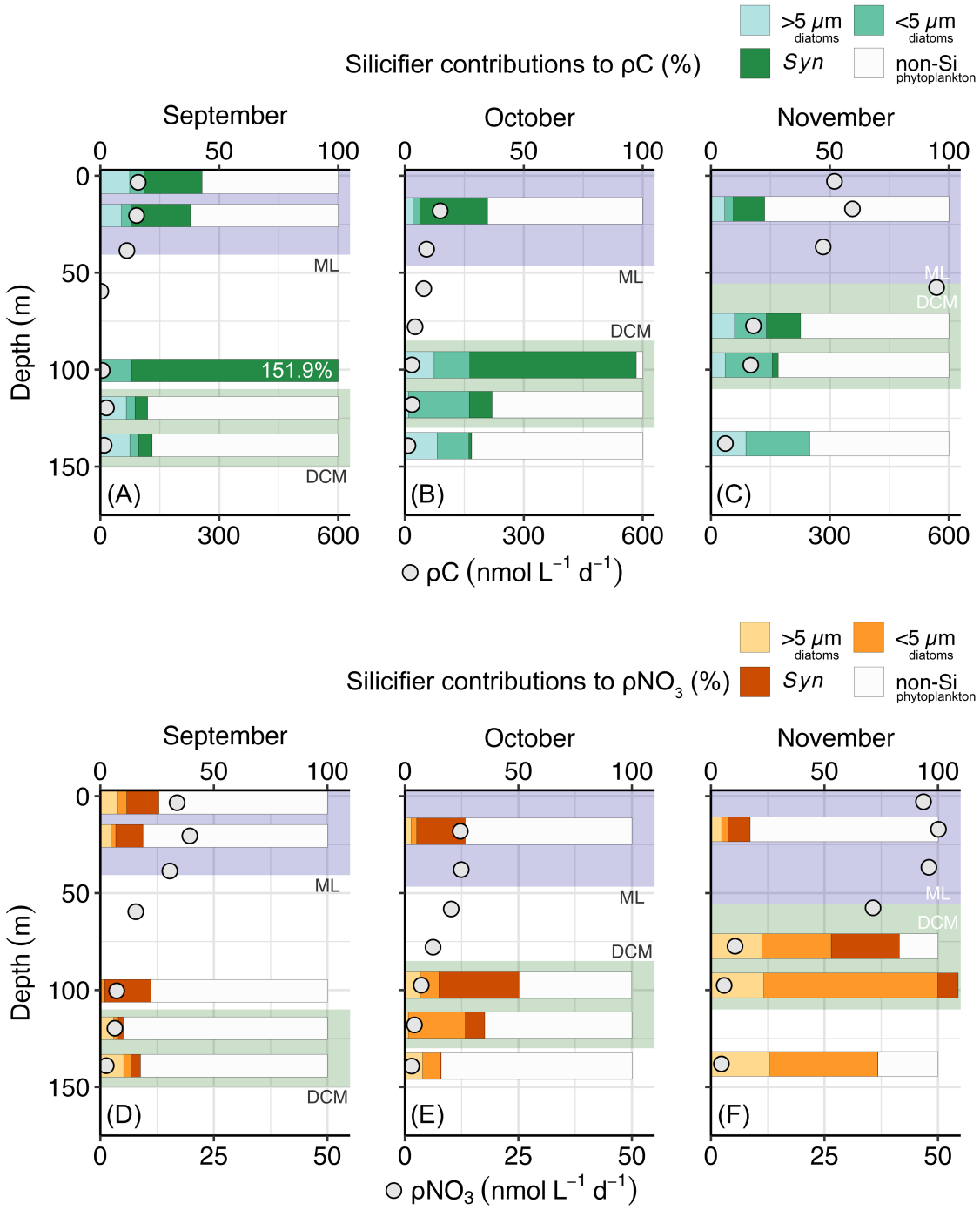


**Figure 2.10.** Contributions by different silicifier groups to carbon and nitrate utilization rates throughout the water column at the BATS station on 29-Sep, 18-Oct, and 06-Nov. Utilization rates of carbon ($\rho$C) and the % contribution of different silicifiers to $\rho$C in **(A)** September, **(B)** October, and **(C)** November. Contribution by silicifiers (green bars, top axis), total $\rho$C shown by grey circles, bottom axis. Utilization rates of nitrate ($\rho NO_3$) and the % contribution of different silicifiers to $\rho NO_3$ in **(D)** September, **(E)** October, and **(F)** November. Contribution by silicifiers (orange bars, top axis), total $\rho NO_3$ shown by grey circles, bottom axis. Mixed layer (ML) and deep chlorophyll maximum (DCM) are highlighted as shaded areas and labelled for each month.

**Table 2.5.** Changes in the contribution of silicifiers to $\rho$C and $\rho NO_3$ at the BATS station on 06-Nov compared to 29-Sep and 18-Oct for the mixed layer (ML), the DCM peak (DCM), the base of the deep chlorophyll max ($DCM_Z$), and base of the euphotic zone ($Z_{Eu}$). Values are the percent change in November compared to the average of Sep/Oct. There are two values for $\rho_{total}$, for each rate measured, but only one value for each silicifier column since the relative changes were the same. $\int\rho_{Syn}$ is *Synechococcus*, $\int\rho_{<5\mu m\ other}$ is small diatoms, and $\int\rho_{>5\mu m}$ is larger diatoms. Specific values used to calculate the % change are in Appendix A, Table A.4 & A.5.

| | | Silicifier contributions | | | |
|---|---|---|---|---|---|
| **Depth Range** | **$\rho_{total}$ ($\rho$C / $\rho NO_3$)** | **$\rho_{>5\mu m\ Si}$ (diatoms)** | **$\rho_{<5\mu m\ other\ Si}$ (small diatoms)** | **$\rho_{Syn}$ (*Synechococcus)*** | **Total $\rho_{Si}$ (all silicifiers)** |
| | **(% change in Nov from average of Sep/Oct)** | | | | |
| ML | 288% / 208% | 171% | 226% | 97% | 127% |
| DCM | 552% / 56% | 452% | 800% | 136% | 301% |
| $DCM_Z$ | 625% / 73% | 729% | 693% | 124% | 550% |
| $Z_{Eu}$ | 324% / 64% | 379% | 1316% | -90% | 613% |

As hypothesized, *Synechococcus* was the only group of silicifier that did not increase their productivity consistently in November. This group only slightly more than doubled its contributions to $\rho$C and $\rho NO_3$ in the DCM, but exhibited a marked decrease (-90%, Table 2.5) in relative productivity at the base of the euphotic zone compared to Sep/Oct. Contrasted with depth-integrated values for *Synechococcus*, which previously showed that *Synechococcus* accounted for more $\int\rho$C and $\int\rho NO_3$ following $NO_3^-$ upwelling, this depth analysis showed that such an increase was limited to shallower waters only.

Overall, when looking at specific depths instead of with an integrated perspective, it is clear that the relative contribution to productivity, $\rho NO_3$ in particular, is heavily favoured by diatoms below the ML when eddy-driven upwelling occurs. Since the majority of silicifier $\rho NO_3$ within the ML was carried out by *Synechococcus,* and based on regenerated N already, this confirms that the role of *Synechococcus* in primary and new productivity is overestimated when looking from a depth-integrated perspective only. This finding is shared by Fawcett et al. (2011), who found that small eukaryotes acquire the majority of their N from upwelled $NO_3^-$, and that

exported material from the euphotic zone is primarily eukaryotic biomass. Thus, by excluding $\rho NO_3$ within the ML and any prokaryote contributions in November, $\rho NO_3$ from the DCM to the base of the euphotic zone was a better estimate of genuine new productivity by diatoms. Since diatoms are favourable for exporting biogenic matter from surface waters, this has implications for the efficiency and magnitude of the biological pump during mesoscale processes such as eddies.

Following periodic storm-driven injections of $NO_3^-$ into the euphotic zone at the BATS station, Lomas et al. (2009a) measured $\rho NO_3$ that varied from ~1 – 3 nmol $L^{-1}$ $h^{-1}$ in the upper 60 m of the water column, and consistently < 0.5 nmol $L^{-1}$ $h^{-1}$ at and below 80 m. In the same study, primary productivity was shown to range from ~0.2 – 1.2 mmol C $m^{-3}$ $d^{-1}$ in the upper euphotic zone (above 60 m) and decreased with depth. In our study, we observed similar ranges and patterns of $\rho C$ and $\rho NO_3$ with depth, and we similarly observed biogeochemical evidence of a rapid response by diatoms to increased $NO_3^-$ supply. While we did not directly measure N and C export, Lomas et al. (2009a) found that export increased by 2 – 5 times following the bloom of diatoms and coccolithophores, compared to the following year when new productivity measurements were similar but not attributed to those specific groups. Therefore, we suggest that the increase in silicifier productivity observed in November 2018, although supported by a different physical mechanism (eddy-driven vs. storm-driven) would have likely resulted in a similar increase in exported material following the bloom.

Our values for $\rho NO_3$ determined from the DCM to the base of the euphotic zone may more accurately reflect the magnitude of export than whole water column estimates, which should not

include prokaryotic or surface productivity based on locally regenerated $NO_3^-$. When we integrate the amount of $\rho NO_3$ across the DCM to the base of the euphotic zone (Appendix A, Table A.5), we see that silicifiers accounted for nearly 93% of all new productivity in November, of which 80% was eukaryotic pico- and nanoplankton. Therefore, diatoms potentially exported 0.15 mmol N $m^{-2}$ $d^{-1}$ compared to < 0.02 mmol N $m^{-2}$ $d^{-1}$ during earlier conditions in Sep/Oct. Since we did not have multiple days of deployments during which new productivity was estimated, we are unable to confidently estimate new production for the duration of the increase in productivity caused by the eddy. After a conservative 50 – 75 % correction for differences between the $\rho NO_3$ method and direct export measures like sediment traps (Lomas et al., 2009b), 0.38 – 0.57 mmol N $m^{-2}$ could have been produced by diatoms during our 5-day station occupation (Fig. 2.3). Previous estimates of total new production in the Sargasso Sea from July to November, at 60.8 mmol N $m^{-2}$ (Lipschultz, 2001) were not considered truly "new" production due to nutrient regeneration and low productivity. Our estimate, though small, may more accurately represent diatom new production from truly "new" $NO_3^-$, and serve as a proxy for export during eddy-driven upwelling in an otherwise oligotrophic period.

## 2.6 Conclusions

This study provided the first simultaneous size-fractionated estimates of contributions by silicifiers such as diatoms and *Synechococcus* to $\rho C$, $\rho NO_3$, and $\rho Si$ during an under-studied time of year in the Sargasso Sea. Using depth-integrated and depth-specific measurements, we concluded that during oligotrophic, stratified conditions, the primary contributors to $\rho C$ and $\rho NO_3$ were either small, non-siliceous phytoplankton, or cyanobacteria such as *Synechococcus*. In contrast, during an eddy-driven nutrient injection, there was a strong response from all

autotrophic biomass and productivity, but specifically, there was a shift in the type and size of phytoplankton responsible for the most nutrient utilization. Eukaryotic silicifiers such as pico- and nanoeukaryotic diatoms increased their contributions to biomass and productivity at the DCM and base of the euphotic zone, and accounted for 80% of all $\rho NO_3$, or new productivity. While the contribution to the annual budget of new productivity in the Sargasso Sea was small, these findings highlight the important role of diatoms during transient mesoscale phenomena not frequently reported in the literature. Furthermore, as surface stratification in subtropical ecosystems continues to intensify, mechanisms such as eddies may play an increasingly important role in driving the downward flux of organic matter from surface waters.

– This page intentionally left blank –

# Chapter 3 – Elemental composition and nutrient utilization of siliceous phytoplankton assemblages in the Pacific Arctic Region during periods of elevated ocean temperature

## 3.1 Abstract

The Pacific Arctic Region (PAR) is undergoing rapid environmental change due to climatic shifts, and has experienced periods of warming as well as extreme temperature events over the past two decades. Marine ecosystems in the high-latitude region of the Bering and Chukchi seas are already experiencing changes in species distributions and physical processes. It is expected that additional changes will occur as the rate of climatic change is high compared to temperate marine environments. As part of a long-running time-series from July 2006 to 2022, we assessed whether phytoplankton productivity and elemental composition in the PAR have changed noticeably over time, and whether a marine heat wave (MHW) in 2019 had a noticeable effect on different physiological measures within diatom-dominated phytoplankton assemblages. A strong warming trend observed from 2011 – 2019 resulted in early sea ice retreat in all Bering and Chukchi Seas regions, and the Arctic MHW of 2019 enhanced this effect. Significant declines in diatom biomass, possibly due to changes in bloom timing, were observed in one area of the northern Bering Sea during the same time period, but other regions did not show consistent impacts of a warming ocean. Effects of the 2019 MHW alone on phytoplankton biomass, nutrient utilization rates, and elemental composition throughout the PAR varied. There was evidence of increased diatom productivity ($\rho$Si) in the low-nutrient southern Chukchi Sea, and we observed an unusual open-water bloom of diatoms in the northern Chukchi Sea, which produced the highest biogenic silica ($bSiO_2$) concentrations and rates of silicic acid utilization ($\rho$Si) ever recorded for the region. Anomalously low C:N ratios were observed throughout much of the PAR in 2019, although specific drivers of this phenomenon were not apparent. Throughout the entire study period, temperature was not directly correlated with any one measure of phytoplankton physiology. Many of the observed differences during the 2019 MHW were likely

due to changes in assemblage composition, bloom distributions, or bloom timing relative to sea ice melt and retreat, rather than the direct effect of warming. This study is the longest time-series of diatom productivity measurements in the PAR and provides valuable long-term insights into the impacts of climate change on phytoplankton productivity and elemental composition in the PAR. By capturing changes over a 16-year period, it offers a resource for understanding how rapidly warming Arctic ecosystems may adapt under climate stress.

## 3.2 Introduction

### *3.2.1 The Pacific Arctic Region and climate change*

The Pacific Arctic Region (PAR) is comprised of the areas influenced by Pacific Ocean waters that flow into the Arctic Ocean across the shallow shelves of the northern Bering Sea, through Bering Strait and into the Chukchi Sea (Fig. 3.1). With a shallow water column and low zooplankton grazing pressure (Campbell et al., 2009), diatom-dominated pelagic primary productivity (Booth and Horner, 1997; Crawford et al., 2018; Giesbrecht and Varela, 2021; Gradinger, 2009) in the PAR is tightly coupled to the benthos (Grebmeier et al., 2015; Mathis et al., 2014; Sherr et al., 2013, 2009). Very high rates of primary productivity in the PAR (Varela et al., 2013) result in some of the highest benthic macrofaunal biomass in the world's oceans (Grebmeier and McRoy, 1989; Highsmith and Coyle, 1990), and support diverse and abundant higher trophic levels (Grebmeier et al., 2006).

There is a growing consensus that the Arctic is approaching a tipping point (Duarte et al., 2012; Mathis et al., 2014), evident from observations of major climate-induced environmental changes in the PAR (Jeffries et al., 2013; Lomas et al., 2020; Stabeno et al., 2007; Wood et al., 2015; Woodgate et al., 2012). The most notable physical changes in the PAR are a reduction in sea ice extent, earlier seasonal ice melt, and a shift from multi-year ice to thinner, first-year ice (Frey et al., 2015, 2014; Jeffries et al., 2013; Stroeve et al., 2014). These shifts in ice extent and timing are not uniform across the PAR. The northern Bering Sea has experienced complex, multi-year variability in the timing of sea ice cover due to a combination of warming and wind-driven processes (Frey et al., 2015), while the Chukchi Sea has seen rapid declines in sea ice cover due to year-round warming (Cavalieri and Parkinson, 2012). Sea ice variability and declines could

have a substantial impact on both the timing and magnitude of primary productivity, potentially causing cascading effects throughout the benthic environment, higher trophic levels within marine food webs, and influencing biogeochemical cycles (Grebmeier, 2012; Mathis et al., 2014).

Further compounding the general trends of warming and sea ice loss that the PAR has been subject to for the past several decades, there have been unprecedented marine heatwave (MHW) events over the Arctic Ocean since 2007 (Barkhordarian et al., 2024; Walsh et al., 2020). Marine heatwaves, characterized by their prolonged and anomalously high sea surface temperature, could have important impacts on Arctic ecosystems by disrupting marine food webs, harming fish stocks, and causing loss of biodiversity (Smale et al., 2019; Smith et al., 2022). In general, extreme climate and weather events often have greater impacts on ecosystems than gradual changes in climate (Ummenhofer and Meehl, 2017), and yet there have been surprisingly few attempts to directly assess the impact of extreme events in northern high latitudes on phytoplankton eco-physiology and nutrient dynamics.

Studies on the direct effect of temperature on Arctic phytoplankton found some consistent patterns in the response of productivity and biomass to increased temperature. A possible thermal threshold around 5 – 6°C may exist for Arctic phytoplankton assemblages, above which growth rate and biomass decrease (Coello-Camba et al., 2015) and community production switches to net heterotrophy (Holding et al., 2013). Rehder et al. (2014) suggested that Arctic phytoplankton may benefit from moderate warming as individual species exhibit wide thermal windows with temperature optima that have not yet been exceeded by current environmental conditions.

However, Coello-Camba and Agustí (2017) found that the optimum temperature for some Arctic phytoplankton communities had already been exceeded as early as 2013. Species of phytoplankton and benthic macrofauna that may be better suited to predicted future environmental conditions have moved into Arctic regions by advection of Atlantic (Neukermans et al., 2018; Oziel et al., 2020) and Pacific Ocean water (Carmack and Wassmann, 2006; Grebmeier, 2012; Waga et al., 2020; Woodgate et al., 2010). This poleward shift of temperate species further complicates attempts to investigate questions about temperature tolerance in high-latitude regions.

### *3.2.2 Nutrient cycling by siliceous phytoplankton and the composition of biogenic particulates*

Photoautotrophs link the marine cycles of dissolved and particulate elements through biological processes such as phytoplankton growth, food web interactions, and organic matter export of biogenic particles. Diatoms, a phytoplankton group with an obligate requirement for dissolved silicon (Si, as $Si(OH)_4$) to build their external frustule and internal structures (Martin-Jezequel et al., 2000), also utilize considerable amounts of inorganic carbon (C) and nitrogen (N) (Tréguer and De La Rocha, 2013). Their uptake of these nutrients connects the biogeochemical cycles of Si, C, and N, and eventually biogenic material is exported from surface waters through the biological pump (Tréguer and Pondaven, 2000). Changes in light and nutrient availability, biological forcing through assemblage composition, and net differences in physiological processes such as nutrient utilization, respiration, biomass production, and cell division may affect the ratios of different elements in particulates and during uptake (Moreno and Martiny, 2018; Rehder et al., 2024; Sterner et al., 2008; Sterner and Elser, 2002). Across the pan-Arctic, large regional variations in primary productivity exist due to the heterogeneous nature of the

marine environment (Carmack and Wassmann, 2006; Giesbrecht et al., 2019; Giesbrecht and Varela, 2021; Varela et al., 2013), and the nutrient concentrations and elemental composition of biogenic particulates vary widely (Wyatt et al., 2013). Within the PAR specifically, diatoms dominate productivity and phytoplankton assemblage composition, but there are notable differences between different areas of the Bering and Chukchi Seas (Giesbrecht et al., 2019; Giesbrecht and Varela, 2021). It is therefore particularly important to investigate how phytoplankton productivity and physiology will respond to higher temperatures and other climate-induced environmental changes in the PAR.

### *3.2.3 Study area and objectives*

The Distributed Biological Observatory (DBO) (http://pmel.noaa.gov/dbo), established in 2010, aims to evaluate the impacts of climate change on the physical and biological conditions of the pelagic and benthic environment of the PAR. Sampling for the DBO is conducted along a series of stations located within "biological hotspots" that have historically shown high productivity, biodiversity, and rates of biological change (DBO1 to 5) within the northern Bering Sea and Chukchi Sea (Fig. 3.1).

The northern Bering Sea is a shallow shelf influenced by nutrient-rich Pacific water, supplied by advection from the Bering Sea basin (Grebmeier et al., 2006). Seasonally covered by ice, DBO1 is located near the St. Lawrence Island Polyna, and DBO2 is located in the Chirikov Basin between St. Lawrence Island and Bering Strait. From the Bering Sea, northward flowing waters are carried through the narrow, shallow Bering Strait and are comprised of a combination of cold

nutrient-rich Anadyr Water (AW) from the west, Bering Shelf (BS) water in the centre, and warmer nutrient-poor Alaska Coastal Current (ACC) from the east (Mathis et al., 2014).

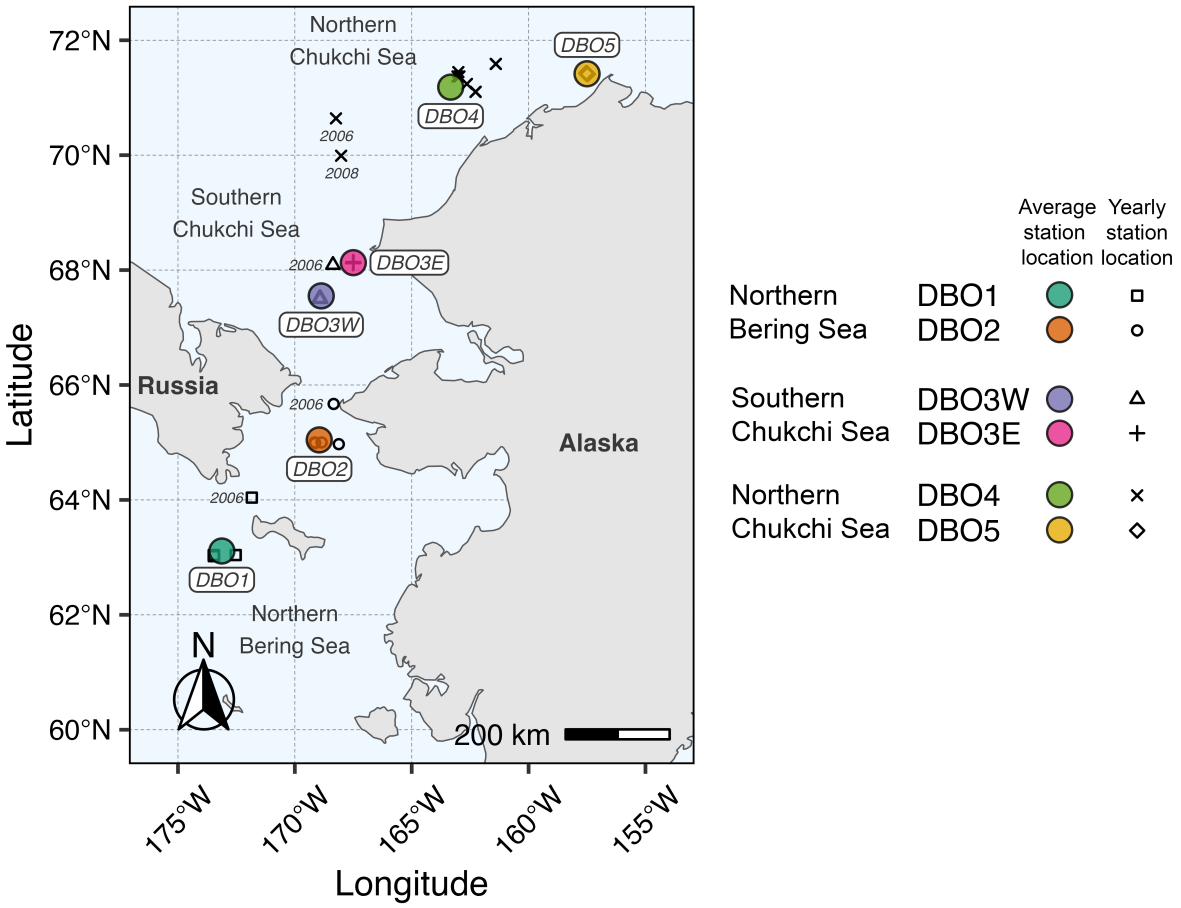


**Figure 3.1.** Station locations in the Distributed Biological Observatory (DBO) sampled between 2006 – 2022. Enlarged circles indicate the average station location within each region for the study period. Station locations for individual years are indicated by smaller symbols. Outlier stations from cruises in 2006 and 2008 are labelled when they are not located near the average station location.

The southeastern Chukchi Sea (DBO3) is divided into two regions, western (DBO3W) influenced by Bering Strait Water (BSW), itself comprised of mixed AW and BS water masses, and eastern (DBO3E), which is within the ACC (Giesbrecht et al., 2019). Further north, the northeastern Chukchi Sea (DBO4) is supplied by BSW offshore and the ACC closer to the coast (Wood et al., 2015), both of which eventually channel through Barrow Canyon (DBO5) and into

the Canada Basin. Since 2010, stations within these regions have been revisited seasonally and annually by various international collaborators under the DBO framework, as well as by other programs such as Canada's Three Oceans (C3O) prior to 2010, to investigate seasonal and interannual variability within the PAR.

Here we present long-term records from 2006 – 2022 of the distribution and variability of phytoplankton assemblage biomass, elemental composition, and nutrient utilization rates, along with environmental data including temperature, salinity, pH, and sea ice breakup dates. The objectives of this study were to identify potential changes in phytoplankton productivity over the course of the entire time-series or during a sustained warming period from 2011 – 2019, and to identify biogeochemical impacts caused by a widespread Arctic MHW in 2019.

## 3.3 Materials and Methods

### *3.3.1 Cruise locations and timing*

Thirteen research cruises from 2006 to 2022 were undertaken annually in July onboard the *CCGS Sir Wilfrid Laurier*, typically departing from Victoria, BC, and ending in Utqiavik (Barrow), AK. Each year, water and CTD sampling were conducted at up to six distinct DBO regions (DBO1, DBO2, DBO3W, DBO3E, DBO4, and DBO5) within the northern Bering Sea and Chukchi Sea (Fig 3.1). Within each region, rates of primary productivity and nutrient utilization were measured at one major station. There was an effort to sample the same stations each year, however there were often minor variations in the station locations due to ice-cover and weather events (Table 3.1).

**Table 3.1.** Locations and names of stations sampled between 2006 and 2022 in the DBO region. Data from years highlighted in grey are included in previous publications by Giesbrecht et al. (2019) and Giesbrecht and Varela (2021). Years during which utilization rates of C ($\rho$C), $NO_3^-$ ($\rho NO_3$), and $Si(OH)_4$ ($\rho$Si) were measured are marked with an "x".

| Year | DBO1 | DBO2 | DBO3W | DBO3E | DBO4 | DBO5 | $\rho C/\rho NO_3$ | $\rho$Si |
|---|---|---|---|---|---|---|---|---|
| 2006 | BCS-6 | BRS-4a | PH-2 | – | MOS-04 | – | X | |
| 2008 | SLIP-4 | UTBS-1 | UTN-4 | – | CCL-4 | BarC-2 | X | |
| 2011 | SLIP-4 | UTBS-1 | UTN-4 | – | – | – | X | |
| 2012 | SLIP-4 | UTBS-4 | – | SEC-5 | – | – | X | |
| 2013 | SLIP-4 | UTBS-1 | UTN-4 | – | DBO4.4 | BarC-5* | X | X |
| 2014 | SLIP-4 | UTBS-1 | UTN-4 | SEC-5 | DBO4.3 | – | X | X |
| 2015 | SLIP-4 | UTBS-1 | UTN-4 | – | DBO4.4 | BarC-5 | X | X |
| 2016 | SLIP-4 | UTBS-1 | UTN-4 | – | DBO4.2 | – | X | X |
| 2017 | SLIP-4 | UTBS-1 | UTN-4 | SEC-5 | DBO4.4 | BarC-5 | X | |
| 2018 | SLIP-4 | UTBS-1 | UTN-4 | SEC-5 | DBO4.4n** | – | X | X |
| 2019 | SLIP-4 | UTBS-1 | UTN-4 | SEC-5 | DBO4.4n | BarC-5 | X | X |
| 2021 | SLIP-4 | UTBS-1 | UTN-4 | SEC-5 | DBO4.2 | BarC-5a*** | X | X |
| 2022 | SLIP-4 | UTBS-1 | UTN-4 | SEC-5**** | DBO4.4n | BarC-5a | X | X |

* $\rho C/\rho NO_3$ experiments not done
2020 cruise was not conducted due to COVID-19 pandemic restrictions on ship access.
** DBO4.4n – Starting in 2018 a new DBO4 line "n" was sampled to account for shifting benthic community, except for 2021 when the old line was used due to ice coverage.
*** BarC-5a was a new station offset by ~1 nautical mile from previous BarC-5 due to installation of an undersea cable.
**** Only near-surface (55% $I_D$, 5 m) and chlorophyll max (1% $I_D$, 18 m) samples were collected so depth-integration was not possible.

### *3.3.2 Hydrography and water sample collection*

Hydrographic measurements were collected with a Sea-Bird SBE-09 *plus* CTD instrument package from the surface to ~5 m above the sea floor. Seawater samples were carefully collected from 12-L Niskin bottles mounted on the CTD-rosette at depths that typically corresponded to optical depths ($I_D$) equal to 100, 55, 30, 15, 1, and 0.1% of surface irradiance. $I_D$ was determined using vertical profiles of underwater irradiance measured with the photosynthetically active radiation sensor on the rosette.

### *3.3.3 Dissolved nutrient concentrations*

Seawater samples for dissolved nutrient concentrations ($NO_3^-$, $PO_4^{3-}$, $Si(OH)_4$) were collected in triplicate from each depth from the same Niskin bottles sampled for nutrient utilization experiments (see 3.3.6 and 3.3.7). Seawater was filtered through disposable 0.45 µm polyether sulfone (PES) filter cartridges. The filtrate was collected in an acid-washed 15 mL centrifuge tube and immediately frozen at -20°C. Samples collected for the measurement of $Si(OH)_4$ concentrations were stored at 4°C to avoid polymerization of $Si(OH)_4$ at freezing temperatures. Nutrient concentrations were measured later using continuous segmented flow analysis on an Astoria 2 Nutrient Autoanalyzer (Astoria-Pacific, OR, USA) according to Barwell-Clarke and Whitney (1996). The coefficient of variation (CV) for nutrient concentrations analyzed from 2018 – 2022 was determined using replicated samples: $NO_3^-$ = 14.1%, $PO_4^{3-}$ = 7.2%, $Si(OH)_4$ = 7.0%. Estimated error for data prior to 2018 was not available.

### *3.3.4 Total and size-fractionated chlorophyll-a concentrations*

Size-fractionated chlorophyll-*a* (chl-*a*) concentrations were determined by gently filtering up to 0.5 L of seawater first through a 5.0 µm nominal pore size PC filter and then through a 0.7 µm nominal pore size glass fiber filter (GF-75, AMD Manufacturing, Ontario, CA). The total chl-*a* concentrations presented are the sum of the two size-fractions. The filters were frozen at -20°C until later analysis when they were submerged in a 90% acetone solution inside glass scintillation vials for 24-h at -20°C in the dark. Prior to measurement, samples were left to warm to room temperature and decanted into borosilicate cuvettes. Fluorescence was measured on a recently calibrated Turner-Designs 10AU fluorometer (Turner Designs, CA, USA), and phaeopigment interference was corrected for by acidifying each sample and measuring again on the fluorometer

(Parsons et al., 1984). Chlorophyll-*a* analysis from 2018 to 2022 had an average CV of 13.6%, determined from triplicate field samples instead of standards.

### *3.3.5 Biogenic silica concentrations*

Samples for the determination of biogenic silica ($bSiO_2$) concentrations (a proxy for diatom biomass) were collected by filtering up to 2.0 L of seawater through a 0.6 µm PC filter (AMD Manufacturing, Ontario, CA). Filters were immediately dried at 60°C for 48-h and stored in a desiccator until further analysis. The conversion of $bSiO_2$ to $Si(OH)_4$ was achieved by digesting the filter with NaOH for 1-h (Brzezinski and Nelson, 1995), using fresh reagents and polypropylene centrifuge tubes. From 2019 onwards, reusable polymethylpentene centrifuge tubes (Diagenode, Belgium) were used to improve the limit of detection. The concentration of $Si(OH)_4$ was measured with a Beckman DU 530 UV/Vis spectrophotometer (Beckman Coulter, CA, USA) using a reverse-order reagent blank (Brzezinski and Nelson, 1986). The 2018 – 2022 average CV for $bSiO_2$ was 17.8%, based on triplicate field samples.

### *3.3.6 Carbon and nitrate utilization rate, and particulate C and N concentrations*

At each $I_D$, the utilization rate of carbon ($\rho C$) and $NO_3^-$ ($\rho NO_3$) were measured using the $^{13}C$-$^{15}NO_3^-$ dual tracer method (Dugdale and Goering, 1967; Slawyk et al., 1977). Seawater was gently subsampled from Niskin bottles into acid-washed 1.0 L PC bottles, leaving enough headspace for isotope additions. For the determination of $\rho C$, samples were inoculated to a final enrichment target of ~10% ambient total inorganic C ($C_T$) using a $KH^{13}CO_3$ (99% purity, Cambridge Isotopes Laboratories, MA, USA) isotope tracer stock. For the determination of $\rho NO_3$, the same samples were inoculated using a $Na^{15}NO_3$ (98+% purity, Cambridge Isotopes

Laboratories, MA, USA) isotope tracer stock with the final $^{15}N$ enrichment target being ~10% of ambient $NO_3^-$. Since *in situ* $NO_3^-$ measurements were not available at the time of sampling, average concentrations of ambient $NO_3^-$ from previous years were used to determine the isotope addition. In cases where $NO_3^-$ concentrations were expected to be below the limit of detection, $^{15}NO_3^-$ was added at the detection limit of 0.1 µM $^{15}NO_3^-$ to reduce artificial enhancement of growth. Inoculated samples were incubated in a deck incubator cooled by continuously flowing surface seawater. Samples were placed in transparent tubes covered with neutral density and blue light filters that simulated the amount ($I_D$) and wavelengths of irradiance at the depth of collection. After ~24-h, each sample was gently filtered through a combusted GF-75 filter under low light. All filters were immediately dried at 60°C for 48 hours and then stored in a desiccator until further analysis. The isotopic composition ($^{13}C$:$^{12}C$ and $^{15}N$:$^{14}N$) and total C and N content were measured at the Stable Isotope Facility at the University of California Davis with a PDZ Europa ANCA-GSL elemental analyzer and a PDZ Europa 20-20 isotope ratio mass spectrometer (Sercon Ltd., Cheshire, UK). Samples were not acid-fumigated to remove inorganic material, therefore the C and N content measured corresponds to total particulate carbon (PC) and particulate nitrogen (PN). Carbon utilization rate ($\rho C$) was calculated using equation 3 in Hama et al. (1983) and average dissolved inorganic C ($C_T$) concentrations from previous years' cruises. Nitrate utilization ($\rho NO_3$) was calculated using equation 3 in Dugdale and Wilkerson (1986) and the ambient $NO_3^-$ concentrations at the time of sampling. When ambient $NO_3^-$ concentrations were below the limit of detection (0.1 µM), the value used in the calculation was 0.1 µM, therefore the $\rho NO_3$ represents a theoretical maximum rate. For consistency with prior published data (Giesbrecht et al., 2019), PC and PN were the total C and N content measured at

the end the incubation for each sample. Average CV for triplicate field samples from 2018 – 2022 were: $\rho C$ = 11.8%, PC = 8.3%, $\rho NO_3$ = 8.8%, PN = 13.2%.

### *3.3.7 Silicic acid utilization rates*

At each $I_D$, the utilization rate of $Si(OH)_4$ ($\rho Si$, a proxy for diatom productivity) was measured using $^{32}Si$ incubation experiments (Brzezinski and Phillips, 1997; Krause et al., 2011). Seawater was collected from Niskin bottles into acid-washed 250 mL PC bottles and inoculated with 370 Bq (22,000 DPM) of a 3700 Bq $mL^{-1}$ solution of high specific activity $^{32}Si(OH)_4$ (~25,000 MBq µmol $Si^{-1}$). The amount of $^{32}Si(OH)_4$ added was less than $1.4x10^{-8}$ µmol Si, a negligible increase in the total $Si(OH)_4$ available. Inoculated samples were incubated in the same manner as for $\rho C$ and $\rho NO_3$. After ~24-h each bottle was filtered onto 0.6 µm PC filters. Filters were rinsed with 0.6 µm filtered seawater to remove any excess $^{32}Si$ tracer that may have adsorbed onto diatom frustules or other particles. Each filter was air-dried at room temperature on a 25mm Nylon disc before being covered with Mylar film and secured with a nylon ring. All samples were stored for at least 5 half-lives of $^{32}P$ (~120 days) to reach secular equilibrium between $^{32}Si$ and the daughter isotope.

The activity of $^{32}Si$ in each sample was determined by gas-flow proportional counting using a Risø 25-5 low-level beta GM multicounter (DTU Nutech, Denmark) (Krause et al., 2011), and $\rho Si$ was calculated using the ambient $Si(OH)_4$ and $bSiO_2$ concentrations at the time of sampling (Brzezinski and Phillips, 1997). The average CV for triplicate field samples from 2018 – 2022 was 21.1%. The specific uptake rate ($V_{Si}$) was calculated by normalizing $\rho Si$ by the $bSiO_2$ biomass for each depth.

### *3.3.8 Contributions by diatoms to carbon and nitrate utilization rates*

The contribution of diatoms to $\rho$C and $\rho NO_3$ was determined by converting Si utilization into C and N units with the following equations:

$$Diatom \int \rho C = \frac{\int \rho Si}{\int Si{:}\,C} \tag{1}$$

$$Diatom\,\% \int \rho C = 100 \times \frac{\int \rho Si}{\int Si{:}\,C} \times \int \rho C_{total}{}^{-1} \tag{2}$$

$$Diatom \int \rho NO_3 = \frac{\int \rho Si}{\int Si{:}\,N} \tag{3}$$

$$Diatom\,\% \int \rho NO_3 = 100 \times \frac{\int \rho Si}{\int Si{:}\,N} \times \int \rho NO_{3_{total}}{}^{-1} \tag{4}$$

Utilization rates of Si, C, and $NO_3^-$ were measured directly, and ∫Si:C and ∫Si:N were calculated from integrated $bSiO_2$, PC, and PN concentrations. A similar analysis of 2013 – 2016 data by Giesbrecht and Varela (2021) used ratios that were averaged for the entire study region (Appendix C, Table C.1). Integrated Si:C was similar between that study and ours, but ∫Si:N was quite different, 1.27±0.54 mol $mol^{-1}$ for 2013 – 2016, and 0.88±0.41 for 2018 – 2022. Because of this difference, as well as variability within each region between stations and years, we used stoichiometric ratios that were specific to each station for each year. If diatom Si:C and Si:N ratios were in fact higher than the measured ratios used here, the contribution of diatoms to ∫$\rho$C and ∫$\rho NO_3$ would decrease, while if diatom Si:C and Si:N were lower, the apparent contributions to either nutrient utilization rate would increase. We used the *in situ* stoichiometry for consistency with the earlier publication, and because on average, ∫Si:C and ∫Si:N within each region still compared very favourably with those measured for cultured diatoms grown under nutrient replete conditions (Si:C = 0.13 ± 0.04 and Si:N = 1.12 ± 0.33) (Brzezinski, 1985).

### *3.3.9 Surface pH values*

To determine surface ocean pH values, $C_T$ and total alkalinity (TA) were measured from seawater collected from Niskin bottles by carefully filling 500 mL gastight glass bottles with a silicone draw tube. Bottles were generously overflowed to remove bubbles from the draw tube and sample bottle, a small headspace (~1%) was left to allow for water expansion, and water samples were then preserved with saturated mercuric chloride. Analysis for $C_T$ took place at the Institute of Ocean Sciences (Fisheries and Oceans Canada) using a SOMMA interfaced with a UIC Model 5011 coulometer (UIC Inc., Joliet, IL) controlled by VINDTA 3D software (Marianda, Kiel, Germany). TA was measured using the open cell titration method with a Metrohm dosimat (Metrohm, Herisau, Switzerland) (Dickson et al., 2007). Values of total pH ($pH_T$) were calculated in Microscoft Excel (Microsoft, Richmond, WA) using CO2SYS version 25 (Pelletier et al., 2007) with K1 and K2 constants from Mehrbach et al. (1973) refit by Lueker et al. (2000), and the $KHSO_4$ dissociation constant from Dickson (1990). All nutrient concentrations in CO2SYS were set to zero for pH calculations due to inconsistent data availability in earlier cruises, which reduced pH values by < 0.01 units. Since only surface (typically < 5 m) samples were used, which often had very low to undetectable nutrient concentrations, this assumption had very little impact on the calculated $pH_T$ values.

### *3.3.10 Sea ice cover and breakup timing*

Sea ice cover was calculated using data collected by the Advanced Microwave Scanning Radiometer for the Earth Observing System of the Earth-observing satellite platform Aqua (NASA). Timing of sea ice breakup was determined based on the commonly used sea ice cover threshold of 15% (e.g. Neeley et al., 2018), and the ice-free period prior to sampling was

determined by subtracting the sea ice breakup date from the sample collection date.

### *3.3.11 Time-series analysis of sea surface temperature anomalies*

Marine heat wave (MHW) years were identified by using the observed temperature anomaly at every station for every year and literature information. The sea surface temperature anomaly (STA) was determined by averaging the sea surface temperature for a specific region over the entire data set (2006 – 2022), and then calculating the difference between the temperature for each year and the average. The 2019 MHW is focused on in additional data analysis methods, and cruise metadata for that year are presented in Table 3.2.

**Table 3.2.** Sampling dates and locations of major productivity stations during the 2019 DBO cruise. Dates and locations for every year are available in the accompanying dataset.

| DBO Region | Ocean | Description | Station Name | Date (UTC) | Latitude (°N) | Longitude (°W) |
|---|---|---|---|---|---|---|
| 1 | Northern Bering Sea | South of St. Lawrence Island | SLIP-4 (DBO1.8) | 14-Jul-19 | 63.030° | 173.460° |
| 2 | | Chirikov Basin, North of St. Lawrence Island | UTBS-1 (DBO2.5) | 16-Jul-19 | 64.990° | 169.136° |
| 3W | Southern Chukchi Sea | Southern Chukchi Sea | UTN-4 | 17-Jul-19 | 67.500° | 168.909° |
| 3E | | Alaskan Coastal Current | SEC-5 (DBO3.4) | 18-Jul-19 | 68.130° | 167.498° |
| 4 | Northern Chukchi Sea | Wainwright, Alaska | DBO4.4n | 20-Jul-19 | 71.588° | 161.406° |
| 5 | | Barrow Canyon | BarC-5 (DBO5.5) | 21-Jul-19 | 71.410° | 157.487° |

### *3.3.12 Data treatment and visualization*

A stratification index for each station and year was calculated as the difference in seawater density between the surface and 1% surface irradiance. Seawater density was calculated as sigma-θ ($\sigma_\theta$), the potential seawater density anomaly (potential density minus 1000 kg $m^{-3}$) using the function swSigma0 from R package “oce”.

Particulate concentrations and rate measurements were integrated from the surface to the base of the euphotic zone using a trapezoidal integration technique. Ratios of particulates and utilization rates were calculated from the integrated values. These integrated values were plotted as boxplots to show the range of data, as well as the median and mean.

All figures were made in RStudio v.2023.06 (Posit Software, PBC, Boston, MA) using the package "ggplot2".

### *3.3.13 Data analysis and statistics*

To initially evaluate the variability of the entire data set, principal component analysis (PCA) was conducted using physical and biological variables. Measures of the physical environment (latitude, temperature), nutrients ($NO_3^-$), phytoplankton biomass (chl-*a*), and diatom productivity ($\rho$Si) were selected as they were individual measures of a distinct attribute at each station and did not tend to correlate positively with each other. Since measurements of $\rho$Si did not take place prior to 2013, this analysis was limited to 2013 – 2022. PCA was conducted using the function "prcomp" in the base R package.

For boxplots of regional integrated data, outliers were defined as values above the third quartile + 1.5*interquartile range. Data from the 2019 MHW were highlighted, and the 95% confidence intervals were shown as well to approximate whether or not the 2019 MHW value fell outside the typical range of values for a particular region. As a secondary analysis, discrete data from the 2019 MHW was compared to vertical profiles of 2011 – 2022 data and the individual vertical

profiles are presented in the appendix for this chapter. Both comparison methods were summarized in the results as a table.

Changes in depth-integrated concentrations of nutrients and particulates, utilization rates, and elemental ratios were assessed against time using linear regressions. The potential for false-positive results exists when making many different statistical comparisons, however because oceanographic studies do not typically apply specific family-wise error rate correction factors to p-values, the regressions were instead interpreted conservatively. When significant trends for only one or two indicators of phytoplankton productivity were observed, the results were presented but not necessarily discussed. When multiple, consistent significant trends were observed within a region, the results were discussed with more certainty.

## 3.4 Results

### *3.4.1 Characterization of regional variability*

In the PAR, we analyzed the variability within and between DBO regions to assess whether each region should be studied individually, or grouped based on their broader geographic context. Sea surface temperature decreased significantly as latitude increased ($p < 0.001$, $R^2 = 0.31$, Fig. 3.2A), while ice breakup date significantly increased ($p < 0.001$, $R^2 = 0.62$) with latitude (Fig. 3.2B). Temperature and ice breakup within each region also appeared to be correlated with year (see section 3.4.2 & 3.4.3). Other measurements did not show clear relationships with latitude. For example, surface pH and depth-integrated chl-*a* (data not shown) did not have any particular trends and covered similar ranges at all latitudes. Because of this complexity, rather than looking for linear relationships with latitude, principal component analysis was used to evaluate the variability of the entire data set and look for patterns that would be useful in interpreting the data.

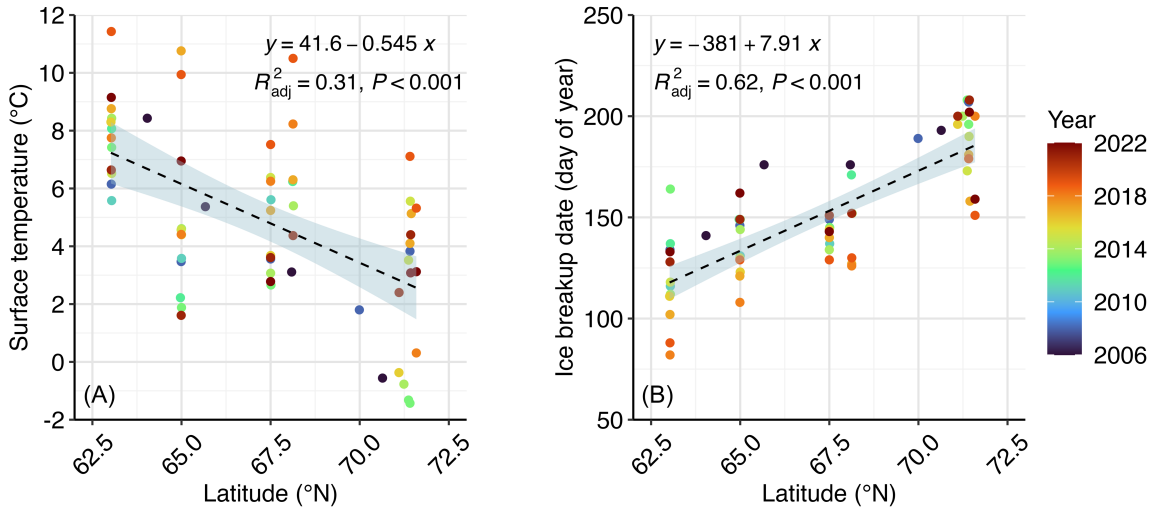


**Figure 3.2.** Changes in **(A)** surface temperature, and **(B)** date of ice break-up with latitude in the Pacific Arctic Region from 2006 – 2022. Year is represented by the colour bar, the dashed line is the linear regression with time, and the shaded area around the line is the confidence interval.

When using discrete data to have the highest possible sample size, PCA captured over 60.0% of variance between the first two principal components. However, discrete data was affected by differences between surface and deeper values, adding variability that dominated many variables, seen as clustering in one direction of the biplot (Fig. 3.3A). Even with skewed data, both regions in the northern Bering Sea, DBO1 & 2, completely overlapped, and similarly the northern Chukchi Sea, DBO4 & 5, fully coincided as well. The southern Chukchi Sea (DBO3W and E) remained mostly separate, especially the nutrient-poor ACC influenced DBO3E (Fig 3.3A).

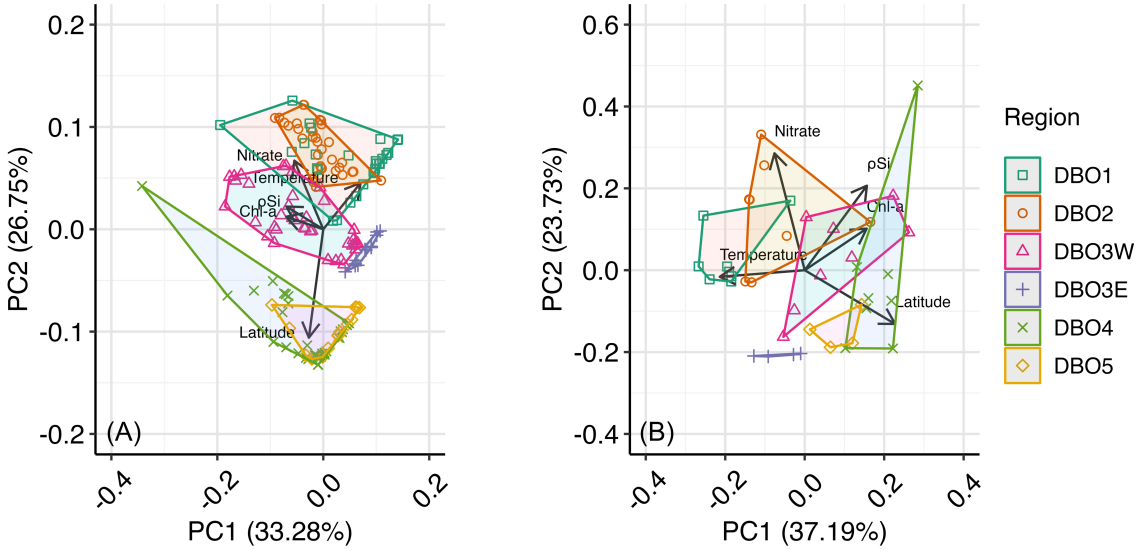


**Figure 3.3.** Principle component biplot of the DBO time-series dataset from 2013 – 2022. Each plot includes characteristics of the physical environment (latitude, surface temperature) and **(A)** discrete or **(B)** depth-integrated nutrients (nitrate), phytoplankton biomass (chl-*a*), and diatom productivity ($\rho$Si). Physical characteristics and biological measures were selected as they were measures of distinct attributes for each station. Years prior to 2013 were not included because $\rho$Si was not collected. Clustering of data points indicates similarity between regions. Angles between vectors show how characteristics correlate with one another.

Depth-integrated data better captured the variability of each station during each year by minimizing the influence of individual surface samples, and was therefore expected to be more useful to draw conclusions from. Using this approach, the first two principal components (PC1 and PC2) captured slightly more variance than before, 60.9% (Fig. 3.3B). There was less

intersection between regional clusters of data points, which suggested that there were underlying patterns or similarities within each region that were distinct from those in other regions, i.e. the variance explained by the principle components was influenced by region-specific characteristics. Where regional clusters overlapped, it was usually due to only one or two data points, and it was with a region that was geographically adjacent. This suggested that while each DBO region is distinct from each other, in some years there have been similarities between their characteristics. Therefore, all further results are presented on a regional basis (from DBO1 to DBO5) because of these observed differences, as well as the historical context which originally defined the DBO sampling program. When interpreting results, larger geographic domains such as the northern Bering Sea, southern Chukchi Sea, or northern Chukchi Sea are still sometimes used to encompass the DBO regions that fall within them.

### *3.4.2 Trends in sea-surface temperature anomalies and identification of a 2019 marine heatwave*

During the study period from 2006 – 2022, STAs varied widely across all regions (Fig. 3.4). A general trend of warming was identified between 2011 – 2019, followed by a return to STAs more similar to early years in the time-series. Notably, in 2019 all STAs were positive and exceeded 3°C for each region. The highest STA in 2019 occurred in the northern Bering Sea, DBO2, with a STA of 5.0°C.

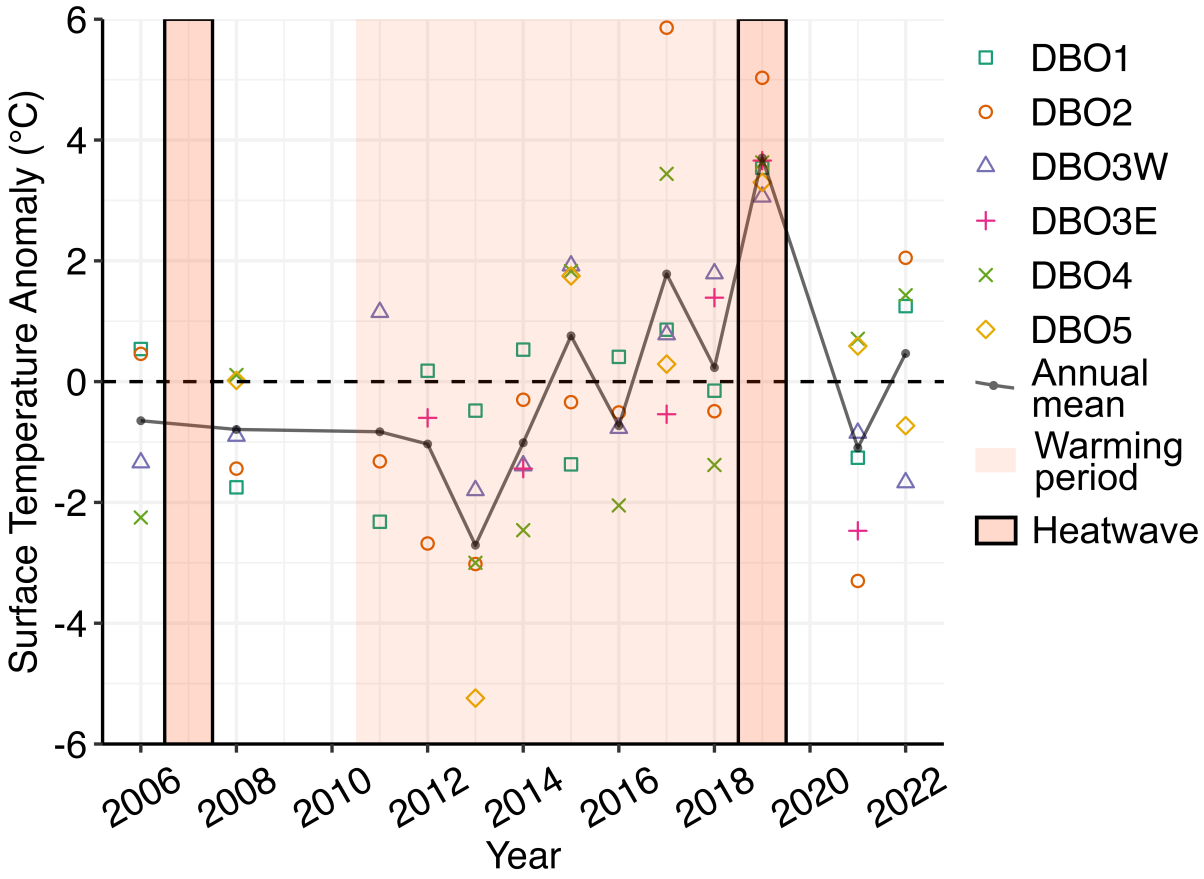


**Figure 3.4** Surface temperature anomalies of DBO regions during the study period, 2006 – 2022. Outlined years indicate when marine heatwaves were identified in the Pacific Arctic Region according to literature (Barkhordarian et al. (2024)). Sampling did not occur in 2007. Temperature anomalies are fitted with the mean value for each year. Highlighted years (2011 – 2019) emphasize the warming trend observed during that period.

There were high positive STAs observed in some regions in other years as well, in particular DBO2 and DBO4 in 2017 (Fig. 3.4; Appendix C, Table C.2), but other regions were not as affected. A literature comparison (Barkhordarian et al., 2024) identified 2007 and 2019 as years in which widespread MHWs occurred in the PAR. Our time-series did not collect samples in 2007, therefore, all subsequent comparisons consider 2019 to be the MHW year during the study period.

### *3.4.3 Trends in physical characteristics and measurements of phytoplankton productivity over time*

As seen in Fig. 3.4, there was a positive trend in sea surface temperature anomalies from 2011 – 2019, followed by a return to more normal temperatures in 2021 and 2022. To discern if this interrupted warming trend impacted other measures, linear trends with time for all other measurements were compared between the periods 2011 – 2019 and 2006 – 2022.

In the northern Bering Sea at DBO1, sea surface temperature increased significantly (Fig. 3.5A) during the warming period from 2011 – 2019 (0.42°C $yr^{-1}$, $p = 0.035$, $R^2 = 0.42$). Both surface salinity (0.11 PSU $yr^{-1}$, $p = 0.006$, $R^2 = 0.64$) and ice-free period (6.7 days $yr^{-1}$, $p = 0.023$, $R^2 = 0.48$) increased significantly during the 2011 – 2019 period, but not from 2006 – 2022 (Fig. 3.5B & C). Surface pH was sampled at more stations within the region during each year of the time-series (Fig. 3.5D), and a significant negative trend was observed for the entire study period (-0.01 $yr^{-1}$, $p = 0.015$, $R^2 = 0.16$). Several productivity measures in DBO1 had significant trends from 2006 – 2022, but not during 2011 – 2019. Integrated $NO_3^-$ ($\int NO_3$) (Fig. 3.5E) declined by 18.1 mmol $m^{-2}$ $yr^{-1}$ ($p = 0.036$, $R^2 = 0.28$), as did integrated $bSiO_2$ ($\int bSiO_2$) (Fig. 3.5.F), by 13.8 mmol $m^{-2}$ $yr^{-1}$ ($p = <0.001$, $R^2 = 0.71$). As a result of decreasing $\int bSiO_2$, ratios of both integrated $bSiO_2$:PC ($\int$Si:C) (Fig. 3.5G) and $bSiO_2$:PN ($\int$Si:N) (Fig. 3.5H) decreased ($\int$Si:C -0.03 mol $mol^{-1}$ $yr^{-1}$, $p = 0.003$, $R^2 = 0.57$; $\int$Si:N -0.17 mol $mol^{-1}$ $yr^{-1}$, $p = 0.005$, $R^2 = 0.51$). No other physical characteristics or measures of phytoplankton productivity at DBO1 had significant relationships with either time period (Appendix C, Table C.3 – C.5).

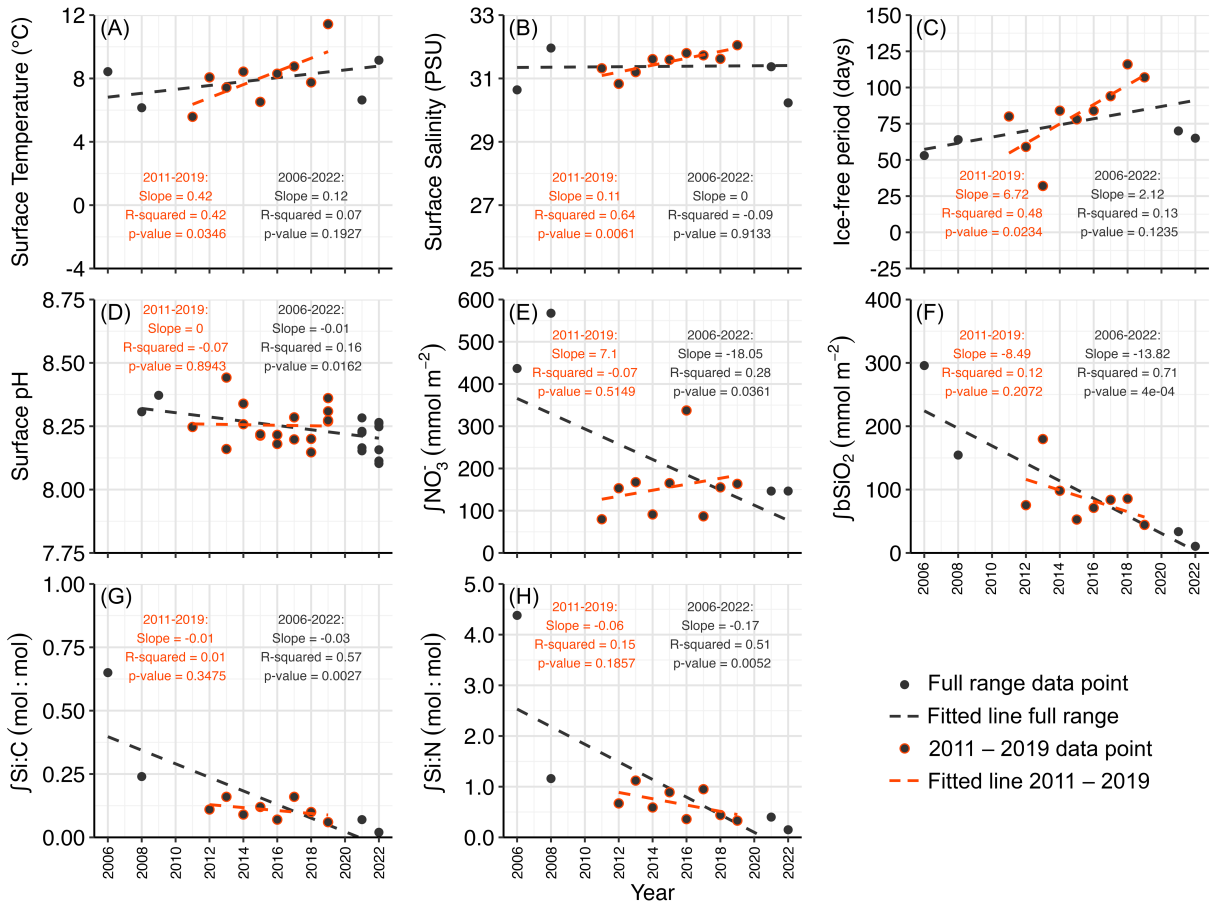


**Figure 3.5.** Trends in physical characteristics and phytoplankton productivity in the DBO1 region of the northern Bering Sea from 2006 – 2022. Temperature trends, and other data with a statistically significant linear relationship versus time for at least one time period are presented (black points, 2006 – 2022; red circled points, 2011 – 2019). **(A)** Surface temperature, **(B)** surface salinity, **(C)** ice-free period prior to sampling, **(D)** surface pH, **(E)** integrated nitrate, $\int NO_3^-$, **(F)** integrated biogenic silica, $\int bSiO_2$, **(G)** integrated $bSiO_2$:PC, ∫Si:C, and **(H)** integrated $bSiO_2$:PN, ∫Si:N. Fitted lines and statistical summaries are provided for each period in the corresponding colour.

In the northern Bering Sea's DBO2 region, fewer significant trends were observed over time than at DBO1, however a stronger warming signal was observed (Fig. 3.6A) from 2011 – 2019, 0.83°C $yr^{-1}$ ($p = 0.027$, $R^2 = 0.46$). The warming trend was not significant from 2006 – 2022. Ice-free period before sampling (Fig. 3.6B) also increased with time from 2011 – 2019, by 3.6 days $yr^{-1}$ ($p = 0.041$, $R^2 = 0.40$), but not during the full study period. In contrast to DBO1, surface pH values increased at DBO2 (Fig. 3.6C). The change was slower during the full time-series (0.02 $yr^{-1}$, $p = 0.037$, $R^2 = 0.12$) than from 2011 – 2019 (0.04 $yr^{-1}$, $p = 0.03$, $R^2 = 0.23$). Specific uptake

of Si ($V_{Si}$) increased at DBO2 since measurements began in 2013 (Fig. 3.6D). The trend was consistently positive, but only significant for 2013 – 2022 (0.03 $d^{-1}$ $yr^{-1}$, p = 0.033, $R^2$ = 0.49). The ratio of integrated $\rho C$ to integrated $\rho NO_3$ decreased from 2006 – 2022, by -1.16 mol $mol^{-1}$ $yr^{-1}$ (p = 0.028, $R^2$ = 0.31). All other physical characteristics or measures of phytoplankton productivity at DBO2 did not have a significant relationship with time (Appendix C, Table C.3 – C.5).

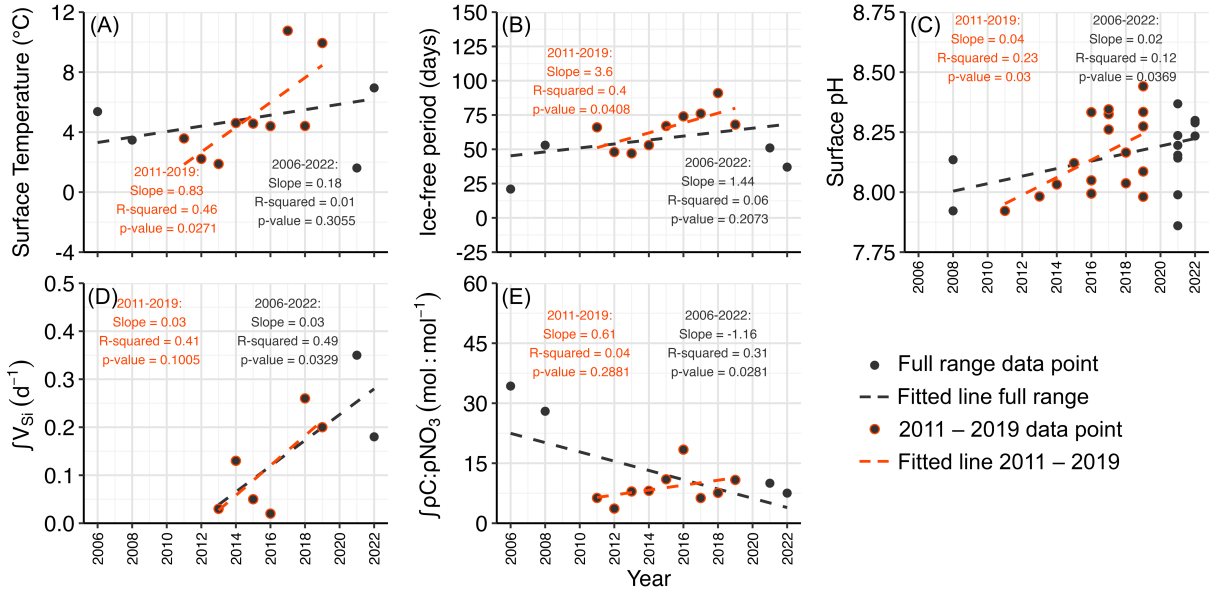


**Figure 3.6.** Trends in physical characteristics and phytoplankton productivity in the DBO2 region of the northern Bering Sea from 2006 – 2022. Temperature trends, and other data with a statistically significant linear relationship versus time for at least one time period are presented (black points, 2006 – 2022; red circled points, 2011 – 2019). **(A)** Surface temperature, **(B)** ice-free period prior to sampling, **(C)** surface pH, **(D)** specific uptake of Si, $V_{Si}$, and **(E)** ratio of integrated C utilization rate and $NO_3^-$ utilization rate, $\int \rho C:\rho NO_3$. Fitted lines and statistical summaries are provided for each period in the corresponding colour.

The southern Chukchi Sea had far fewer significant trends with time than lower latitudes. At DBO3W, temperature trends were not significant for either time period (Fig. 3.7A). The only significant trend was for the ratio of integrated $\rho Si$ to integrated $\rho C$ (Fig. 3.7B), which increased by 0.05 mol $mol^{-1}$ $yr^{-1}$ from 2013 – 2019 (p = 0.018, $R^2$ = 0.73) and by 0.03 mol $mol^{-1}$ $yr^{-1}$ when

all available years were included (2013 – 2022, p = 0.049, $R^2$ = 0.42). All other trends with time were not significant (Appendix C, Table C.3 – C.5).

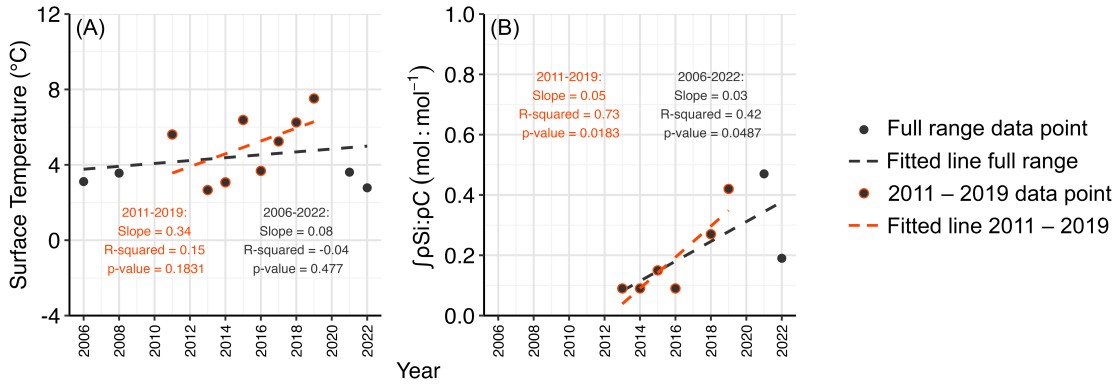


**Figure 3.7.** Trends in physical characteristics and phytoplankton productivity in the DBO3W region of the southern Chukchi Sea from 2006 – 2022. Temperature trends, and other data with a statistically significant linear relationship versus time for at least one time period are presented (black points, 2006 – 2022; red circled points, 2011 – 2019). **(A)** Surface temperature, **(B)** ratio of integrated $Si(OH)_4$ utilization rate and C utilization rate, $\int\rho Si{:}\rho C$. Fitted lines and statistical summaries are provided for each period in the corresponding colour.

Sampling in the southern Chukchi Sea's DBO3E region started in 2012. Surface temperatures showed no significant trend during either time period (Fig. 3.8A). However, despite a non-significant trend in temperature, the ice-free period prior to sampling increased significantly from 2012 – 2019 (Fig. 3.8B) by 6.5 days $yr^{-1}$ (p = 0.015, $R^2$ = 0.86). Two measures of phytoplankton productivity were affected over time as well, both ∫Si:C and ∫Si:N (Fig. 3.8C &D). Integrated Si:C decreased by 0.02 mol $mol^{-1}$ $yr^{-1}$ from 2012 – 2021 (p = 0.046, $R^2$ = 0.59) and ∫Si:N decreased by 0.15 mol $mol^{-1}$ $yr^{-1}$ (p = 0.008, $R^2$ = 0.82) for the same period, or 0.18 mol $mol^{-1}$ $yr^{-1}$ (p = 0.009, $R^2$ = 0.90) from 2012 – 2019. There was an increase in $\int\rho NO_3$ during the warming phase (0.38 mmol $m^{-2}$ $d^{-1}$ $yr^{-1}$, p = 0.008, $R^2$ = 0.91) but not over the entire time series (Fig. 3.8E), and this caused the ratio of $\int\rho C{:}\rho NO_3$ to decrease with from 2012 –2019 (-7.76 mol $mol^{-1}$ $yr^{-1}$, p = 0.031, $R^2$ = 0.77) (Fig. 3.8F). All other trends with time were not significant (Appendix C, Table C.3 – C.5).

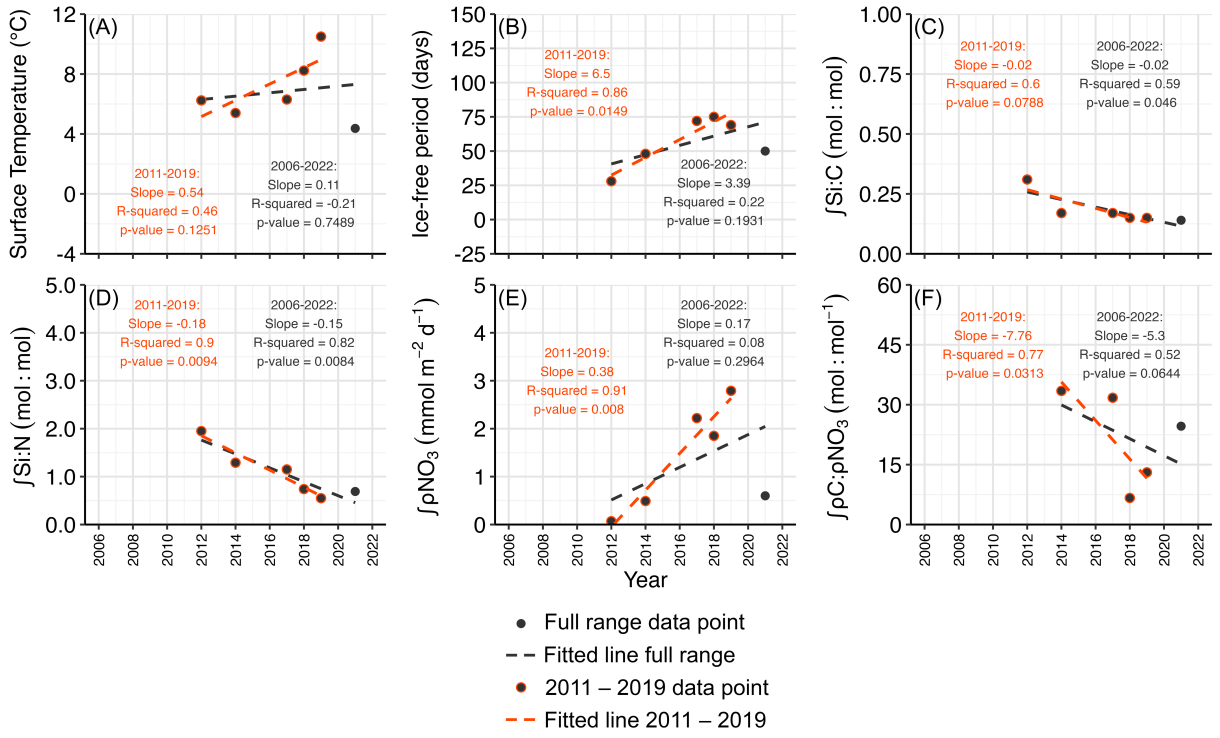


**Figure 3.8.** Trends in physical characteristics and phytoplankton productivity in the DBO3E region of the southern Chukchi Sea from 2006 – 2022. Temperature trends, and other data with a statistically significant linear relationship versus time for at least one time period are presented (black points, 2006 – 2022; red circled points, 2011 – 2019). **(A)** Surface temperature, **(B)** ice-free period prior to sampling, **(C)** integrated $bSiO_2$:PC, ∫Si:C, **(D)** integrated $bSiO_2$:PN, ∫Si:N, **(E)** integrated $NO_3^-$ utilization rate, $\int\rho NO_3$, and **(F)** ratio of integrated C utilization rate and $NO_3^-$ utilization rate, $\int\rho C{:}\rho NO_3$. Fitted lines and statistical summaries are provided for each period in the corresponding colour.

In the northern Chukchi Sea, DBO4, sea surface temperatures did not change significantly over time (Fig. 3.9A). Ratios of integrated PC to integrated PN (∫C:N, Fig. 3.9B) decreased from 2011 – 2019, by 0.82 mol $mol^{-1}$ $yr^{-1}$ ($p = 0.020$, $R^2 = 0.63$), and the rate of $NO_3^-$ utilization by diatoms (diatom $\int\rho NO_3$, Fig. 3.9C) increased by 16.4 mmol $m^{-2}$ $d^{-1}$ $yr^{-1}$ during the warming period ($p = 0.038$, $R^2 = 0.62$).

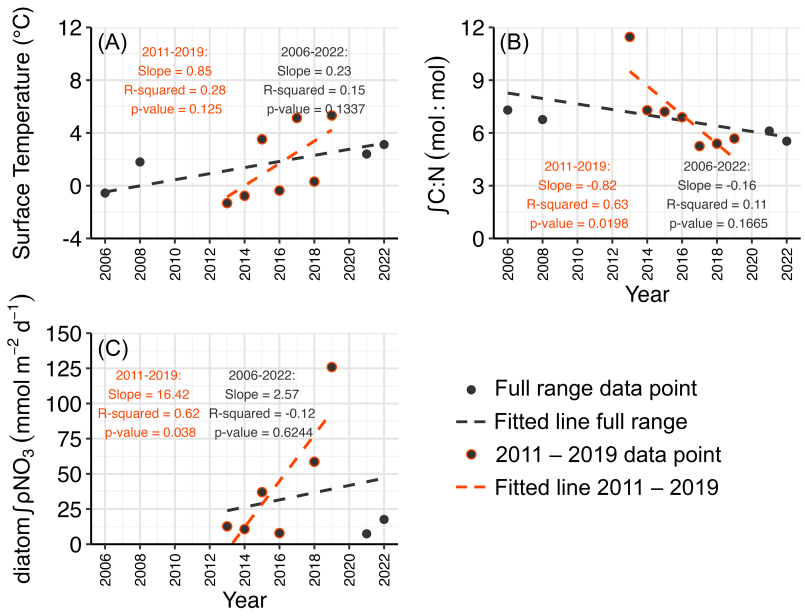


**Figure 3.9.** Trends in physical characteristics and phytoplankton productivity in the DBO4 region of the northern Chukchi Sea from 2006 – 2022. Temperature trends, and other data with a statistically significant linear relationship versus time for at least one time period are presented (black points, 2006 – 2022; red circled points, 2011 – 2019). **(A)** Surface temperature, **(B)** integrated PC:PN, ∫C:N, and **(C)** integrated $NO_3^-$ utilization rate by diatoms, diatom $\int\rho NO_3$. Fitted lines and statistical summaries are provided for each period in the corresponding colour.

The DBO5 region of the northern Chukchi Sea also had few significant trends. Sea surface temperature did not have a significant relationship with time (Fig. 3.10A). Surface salinity (Fig. 3.10B) increased by 0.08 PSU $yr^{-1}$ from 2006 – 2022 ($p = 0.015$, $R^2 = 0.67$), and surface pH (Fig. 3.10C) decreased by 0.01 $yr^{-1}$ since 2006 ($p = 0.017$, $R^2 = 0.07$). Only one measure of phytoplankton productivity changed over time. Integrated utilization rate of C, $\int\rho C$ (Fig. 3.10D) decreased by 8.1 mmol $m^{-2}$ $d^{-1}$ $yr^{-1}$ ($p = 0.028$, $R^2 = 0.68$), although the trend was likely driven by a single high value from 2008 compared to otherwise low values over the rest of the data set. All other trends were not significant (Appendix C, Table C.3 – C.5).

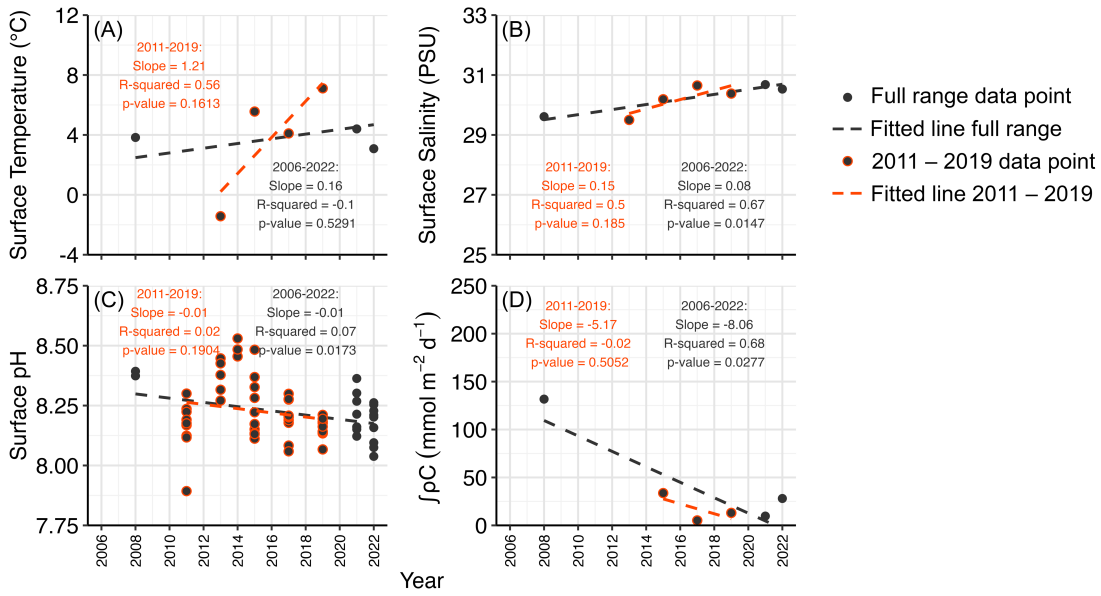


**Figure 3.10.** Trends in physical characteristics and phytoplankton productivity in the DBO5 region of the northern Chukchi Sea from 2006 – 2022. Temperature trends, and other data with a statistically significant linear relationship versus time for at least one time period are presented (black points, 2006 – 2022; red circled points, 2011 – 2019). **(A)** Surface temperature, **(B)** surface salinity, **(C)** surface pH, and **(D)** integrated utilization rate of C, $\int \rho C$. Fitted lines and statistical summaries are provided for each period in the corresponding colour.

### *3.4.4 Regional variability of physical characteristics and comparison to 2019*

In general, sea surface temperatures were highest in the northern Bering Sea, averaging 7.9±1.5°C in DBO1 and 4.9±2.8°C in DBO2 (Fig. 3.11A), compared to the coldest region, DBO4 in the northern Chukchi Sea, which averaged 1.7±2.4°C. Variability within all regions was high from 2006 – 2022, spanning at least 6°C, but 2019 had the highest sea surface temperatures of the entire time-series (large white circles in Fig 3.11A, Table 3.3), except for DBO2, which was even warmer in 2017. In 2019, the entire water column was warmer than normal in both regions of the northern Bering Sea (Appendix C, Fig. C.1A). In all other areas, warming was restricted to the upper water column, and temperatures remained similar to previous years at depth (Table 3.3).

Surface salinity was highest in the northern Bering Sea and southern Chukchi Sea, where medians ranged from 31.6 to 32.4 PSU (Fig. 3.11B). In the northern Chukchi Sea regions of DBO4 & 5, median salinity was 29.6 and 30.4 PSU, respectively. In 2019, the highest value (large white circles in Fig 3.11B) of surface salinity was recorded at DBO1, 32.1 PSU, but otherwise there weren't any noteworthy values associated with the 2019 MHW (Table 3.3). In 2019, salinity values were elevated at the surface (DBO1) and throughout the water column (DBO2) (Appendix C, Fig. C.1B). At all other regions salinity was not noticeably different from previous ranges (Table 3.3).

Lower-latitude regions tended to be less-stratified (Fig. 3.11C), with stratification index medians ranging from 1.2 kg $m^{-3}$ at DBO1 to 0.30 kg $m^{-3}$ at DBO3E. The northern Chukchi Sea (DBO4 & 5) was more stratified, with median index values of 2.5 and 1.6 kg $m^{-3}$, respectively. The only region that had clearly anomalous stratification in 2019 was DBO3E (Table 3.3), which although high (large white circle in DBO3E, Fig 3.11C) at 0.97 kg $m^{-3}$ relative to the median for DBO3E, was not particularly high compared to other DBO regions.

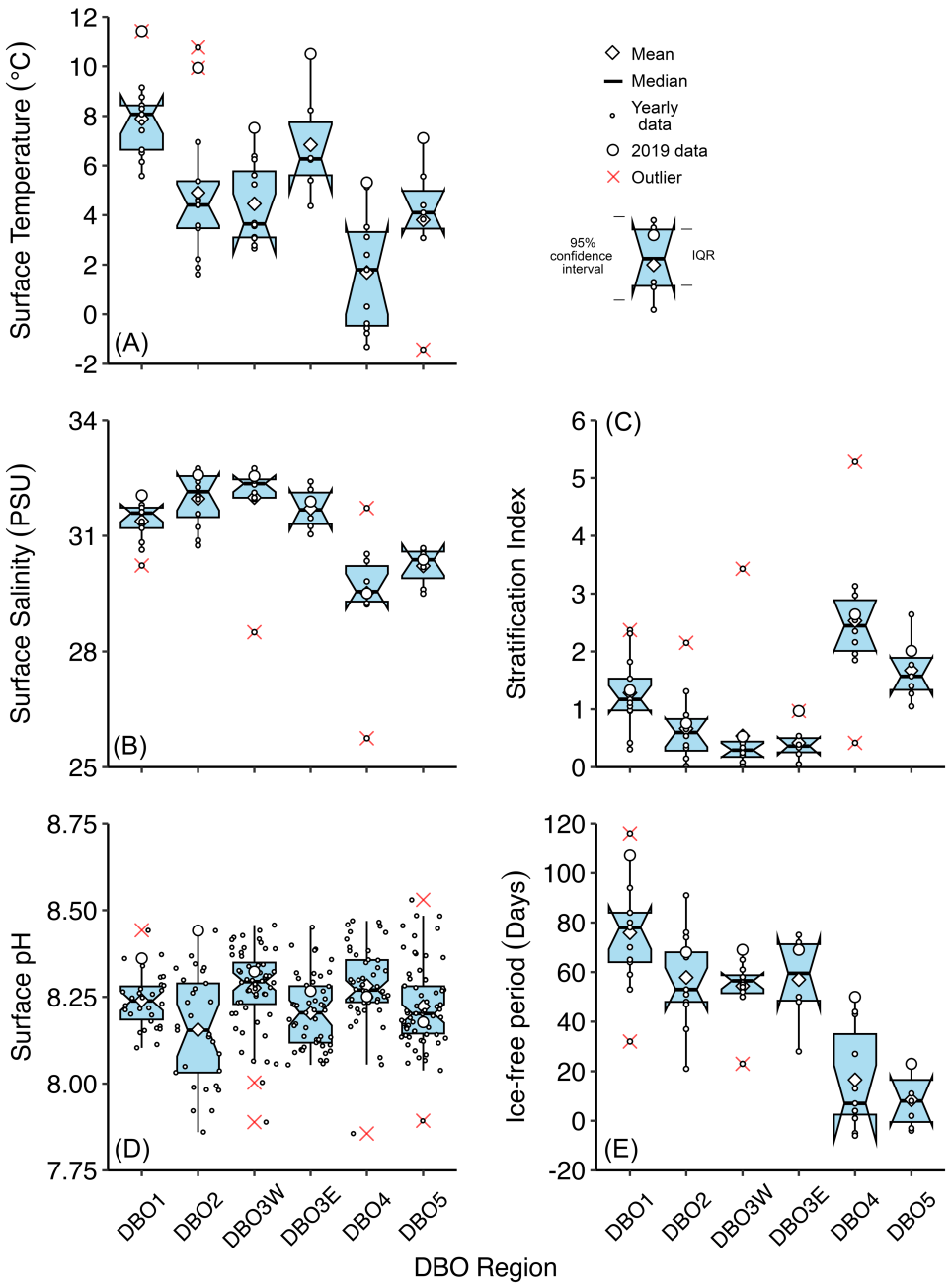


**Figure 3.11.** Physical characteristics of DBO regions during the study period from 2006 – 2022. **(A)** Surface temperatures, **(B)** surface salinity, **(C)** stratification index, **(D)** surface pH, and **(E)** ice-free period. Regions are arranged by DBO region increasing in latitude. Additional pH data was available for all of the regions, so all available data is presented. The horizontal line in the middle of each box represents the median, and the box area represents the interquartile range (IQR), the 25$^{th}$ and 75$^{th}$ percentiles of the data. Maximum and minimum values are included in the whiskers extending above and below each box. Outliers are indicated with a red 'x'. Each data point represents a single station during a specific year and are shown as a small circle. Data from the 2019 MHW are indicated with a larger white circle. Mean values for the entire study period are represented as the diamond symbol. The 95% confidence intervals are represented by the upper and lower notch around the median.

**Table 3.3.** Summary of 2019 MHW characteristics relative to the mean/median of depth-integrated and discrete values for the 2006 – 2022 period. Columns headed with "∫" are for the depth-integrated regional values. Columns headed with "D" are for the discrete data. Max = highest value; Min = lowest value; High = > upper 95% confidence interval (CI); Low = < lower 95% CI; No text = neutral, within 95% CI; *NA* = no comparison available. When the 2019 value was near the 95% CI boundary, the value was conservatively assumed to be within CI. An asterisk (*) indicates where a Min or Max value was within or near the CI. Surf = restricted to shallower depths; Mid = restricted to middle depths; Deep = restricted to deeper depths. Darker green = Max; light green = High; light blue = Low; dark blue = Min.

| | Northern Bering Sea | | | | Southern Chukchi Sea | | | | Northern Chukchi Sea | | | |
|---|---|---|---|---|---|---|---|---|---|---|---|---|
| | DBO1 | | DBO2 | | DBO3W | | DBO3E | | DBO4 | | DBO5 | |
| **PHYSICAL CONDITIONS** | | | | | | | | | | | | |
| | ∫ | D | ∫ | D | ∫ | D | ∫ | D | ∫ | D | ∫ | D |
| **Temp.** | Max | Max Surf | High | High | Max | High Surf | Max | Max Surf | Max | High Surf | Max | Max Surf |
| **Salinity** | Max | Max Surf | | High | | | | | | | | |
| **$\sigma_\theta$ index** | | *NA* | | *NA* | High | *NA* | Max | *NA* | | *NA* | High | *NA* |
| **Surface pH** | High | *NA* | Max | *NA* | | *NA* | High | *NA* | | *NA* | | *NA* |
| **Ice-free period** | High | *NA* | High | *NA* | Max | *NA* | | *NA* | Max | *NA* | Max | *NA* |
| **NUTRIENT CONCENTRATIONS** | | | | | | | | | | | | |
| **$NO_3^-$** | | | Low | Min | Low | Low | | | Max | High Deep | | |
| **$Si(OH)_4$** | Min | High Surf | Low | Min | Min* | Low | | Low Surf | | High Deep | | |
| **PARTICULATE CONCENTRATIONS** | | | | | | | | | | | | |
| **Chl-*a*** | High | | | | | Low Surf | | | | | | |
| **% Chl-*a* > 5 µm** | | *NA* | | *NA* | | *NA* | Max | *NA* | | *NA* | | *NA* |
| **$bSiO_2$** | Low | | | High Mid | Low | Low Surf | Low | | Max | Max Deep | | |
| **PC** | | High Deep | High | High Mid | Low | Low Surf | | | High | High Deep | | |
| **PN** | | High Deep | High | High Mid | | Low Surf | | High Surf | Max | High Deep | Max | High Surf |
| **ELEMENTAL RATIOS** | | | | | | | | | | | | |
| **C:N** | | Low Surf | | High Surf | Min | Low | Min | Min | Low | | Min | Min |
| **Si:C** | | Low | Low | Low Mid | | High Surf | | | Max | High Surf | | |
| **Si:N** | | Low | Low | Low Deep | | | Min* | | Max | | Min | |
| **NUTRIENT UTILIZATION RATES** | | | | | | | | | | | | |
| **$\rho$C** | | | High | High Mid | Low | Low Surf | High | | | | | |
| **$\rho NO_3$** | | | | High Mid | | | Max* | | | | | |
| **$\rho$Si** | | | | | | | Max | Max | Max | Max Mid | | |
| **$V_{Si}$** | | | | | | | Max | Max | Max | Max Mid | | |
| **NUTRIENT UTILIZATION RATIOS** | | | | | | | | | | | | |
| **$\rho C:\rho NO_3$** | | *NA* | | *NA* | | *NA* | Low | *NA* | | *NA* | | *NA* |
| **$\rho Si:\rho C$** | | *NA* | | *NA* | High | *NA* | Max | *NA* | Max | *NA* | | *NA* |
| **$\rho Si:\rho NO_3$** | | *NA* | High | *NA* | | *NA* | Max* | *NA* | Max | *NA* | Max | *NA* |
| **DIATOM CONTRIBUTIONS TO UTILIZATION RATES** | | | | | | | | | | | | |
| **diatom $\rho$C** | | *NA* | High | *NA* | | *NA* | Max | *NA* | Max | *NA* | | *NA* |
| **diatom $\rho NO_3$** | | *NA* | High | *NA* | | *NA* | Max | *NA* | Max | *NA* | | *NA* |

There was high variability in surface pH across DBO regions, ranging from 7.86 to 8.53 (Fig. 3.11D). In 2019 pH was the highest ever recorded at DBO2 (Fig. 3.11D, Table 3.3), and both DBO1 and DBO3E were higher than typical. pH values at discrete depths were not included in this study.

Since sea ice breakup occurred later in the year at higher-latitudes, the ice-free period prior to sampling ranged from a maximum median of 78 days in the southernmost DBO1 region, to 7 days prior to sampling at DBO4 (Fig. 3.11E). The 2019 ice-free period was among the longest for the northern Bering and southern Chukchi Seas, and was the longest ever observed in the northern Chukchi Sea (Table 3.3). The station sampled at DBO4 was ice-free 50 days prior to sampling in 2019 compared to a median of just 7 days, and at DBO5, the station was ice-free 23 days prior to sampling in 2019, compared to a median of 8 days (Fig 3.11E).

### *3.4.5 Regional variability of nutrient and particulate concentrations and comparison to 2019*

Depth-integrated $NO_3^-$ ($\int NO_3^-$) and $Si(OH)_4$ ($\int Si(OH)_4$) were highly variable within most regions (Fig. 3.12A & B). Excluding DBO3E, median concentrations ranged between 108 – 403 mmol $NO_3^-$ $m^{-2}$ and 173 – 636 mmol $Si(OH)_4$ $m^{-2}$ across the PAR. In the coastal southern Chukchi Sea (DBO3E), nutrients were low, just 8.2 mmol $NO_3^-$ $m^{-2}$ and 99.8 mmol $Si(OH)_4$ $m^{-2}$. In 2019, $\int NO_3^-$ at DBO4 was 317 mmol $m^{-2}$, the maximum recorded for the region, and $\int NO_3^-$ was noticeably low at both DBO2 and DBO3W, 87.0 mmol $m^{-2}$ and 37.2 mmol $m^{-2}$, respectively (Table 3.3). During the MHW, $\int Si(OH)_4$ was much lower than usual in the northern Bering Sea, only 123 mmol $m^{-2}$ at DBO1, and somewhat low at DBO2, 161 mmol $m^{-2}$ (Fig. 3.12B). At the productive area of the southern Chukchi Sea, DBO3W, $\int Si(OH)_4$ was also low, 54.5 mmol $m^{-2}$

(Table 3.3). Throughout the rest of the southern and northern Chukchi Sea, $\int Si(OH)_4$ was unremarkable in 2019 compared to previous years. Discrete nutrient concentrations in 2019 (Appendix C, Fig. C.1C & D) were generally similar to prior years (Table 3.3). The only clear deviation from typical values was that both $NO_3^-$ and $Si(OH)_4$ were very depleted throughout the water column in the northernmost Bering Sea (DBO2), and also quite low at all depths in the productive southern Chukchi Sea (DBO3W). Concentrations of $PO_4^{3-}$ (data not shown) did not vary much between regions, with lowest $\int PO_4^{3-}$ at DBO3E (19.2 mmol $m^{-2}$) and highest $\int PO_4^{3-}$ at DBO5 (39.2 mmol $m^{-2}$). Other than two surface samples that were below the detection limit, $PO_4^{3-}$ was replete at all depths and locations throughout the entire study period.

Integrated chlorophyll-*a* (∫chl-*a*) varied widely between regions, from median lows of 10.9 mg $m^{-2}$ at DBO3E to the highest at DBO3W, 103 mg $m^{-2}$. During 2019, ∫chl-*a* was not notably different in most regions (Fig. 3.12C), other than being higher than normal in DBO1, 58.9 mg $m^{-2}$ (Table 3.3). Integrated $bSiO_2$ ($\int bSiO_2$) was also highly variable (Fig. 3.12D), and was typically highest in DBO3W, 210 mmol $m^{-2}$, compared to other regions where the range of median $\int bSiO_2$ was from 79.6 to 144 mmol $m^{-2}$. During the 2019 MHW, $\int bSiO_2$ was somewhat low in DBO1, DBO3W, and DBO3E compared to the median at each region, and a notable maximum occurred at DBO4, 384 mmol $m^{-2}$, where $\int bSiO_2$ was over three-fold higher than the median (Table 3.3). Integrated Particulate C and PN concentrations (∫PC & ∫PN) did not vary much between regions (Fig. 3.12E & F), and the pattern was very similar to ∫chl-*a* and $\int bSiO_2$. In 2019, ∫PC was low at DBO3W compared to the regional median, while ∫PC was relatively high at DBO2 and DBO 4 (Table 3.3). ∫PN was similarly higher at DBO2, and reached new maximum concentrations at DBO4, 230 mmol $m^{-2}$, and in DBO5, 187 mmol $m^{-2}$ (Table 3.3).

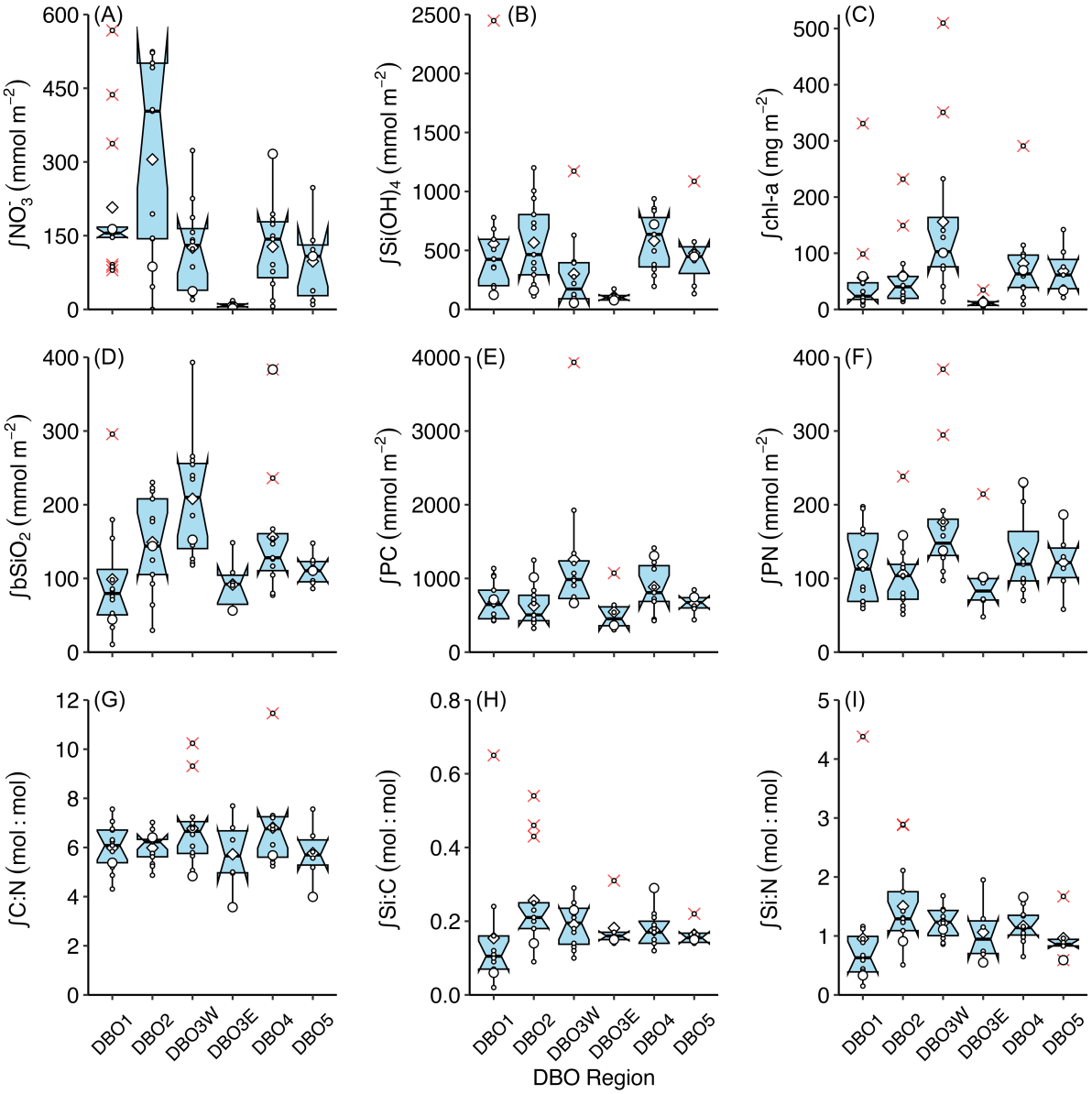


**Figure 3.12.** Dissolved nutrient and particulate concentrations, and elemental ratios for DBO regions from 2006 – 2022. Depth-integrated **(A)** nitrate, $\int NO_3^-$, **(B)** silicic acid, $\int Si(OH)_4$, **(C)** chlorophyll-*a*, ∫chl-*a*, **(D)** biogenic silica, $\int bSiO_2$, **(E)** particulate C, ∫PC, and **(F)** particulate N, ∫PN. Measurements were depth-integrated from the surface to the bottom of the euphotic zone (0.1% $I_D$). Ratios of **(G)** ∫C:N, **(H)** ∫Si:C, and **(I)** ∫Si:N were calculated from the depth-integrated values from each year. Description of box plot parameters as in Fig. 3.11.

Concentrations of $bSiO_2$, PC, and PN were notably high in 2019 for much of the water column in DBO2, although chl-*a* concentrations were well within the range of values typical to the region

(Appendix C, Fig. C.2A – D). The other region of the northern Bering Sea, DBO1, did not have any clear or consistent deviations from normal biogenic particulate concentrations. In 2019, all biogenic particulates had low concentrations in the surface waters of DBO3W, and $bSiO_2$ concentrations were high at the base of the euphotic zone in DBO4. Otherwise, only occasional deviations from the usual patterns occurred throughout the rest of the PAR (Table 3.3).

Throughout all regions, integrated C:N ratios (∫C:N) generally varied around the expected Redfield ratio of 6.6 mol C to mol N (Fig. 3.12G), but relative changes in ∫PC and ∫PN during the 2019 MHW resulted in the lowest ever recorded ∫C:N for some regions for that year (Table 3.3). At DBO3W, ∫C:N was 4.8 mol $mol^{-1}$, and ∫C:N was at or below 4 for the first time at DBO3E and DBO5, with 3.6, and 4.0 mol $mol^{-1}$, respectively. Patterns in ∫C:N across the PAR were reflected in discrete data as well (Table 3.3 & Appendix C, Fig. C.3A). Most notably, in 2019, the lowest recorded value for the surface ocean (55% $I_D$) in the entire DBO time-series and across all regions occurred, 2.8 mol $mol^{-1}$ at DBO5.

Ratios of ∫Si:C (Fig. 3.12H) and ∫Si:N (Fig. 3.12I) were low at DBO2, 0.14 and 0.91 mol $mol^{-1}$, compared to median values for this study of 0.21 mol $mol^{-1}$ for ∫Si:C and 1.3 mol $mol^{-1}$ for ∫Si:N. The highest ratios for both ∫Si:C and ∫Si:N at DBO4 occurred in 2019, 0.29 and 1.7 mol $mol^{-1}$ respectively. Due to high ∫PN values at DBO3E & 5, ∫Si:N was anomalously low in both regions in 2019, 0.55 and 0.59 mol $mol^{-1}$, although the minimum value recorded in DBO3E was not clearly removed from the confidence interval. Discrete ratios of Si:C and Si:N were low in the northern Bering Sea in 2019, though only near the base of the euphotic zone in DBO2 (Table 3.3 & Appendix C, Fig. C.3B & C). The ratios of Si:C were somewhat high for Si:C in DBO3W &

4, but there were otherwise no observations of unusual Si relationships to PC and PN in other regions.

### *3.4.6 Regional variability of nutrient utilization rates and comparison to 2019*

Integrated nutrient utilization rates of C ($\int\rho C$) and $NO_3$ ($\int\rho NO_3$) varied widely (Fig. 3.13A & B). The highest median values of $\int\rho C$ and $\int\rho NO_3$ occurred at DBO3W, 187 mmol C $m^{-2}$ $d^{-1}$ and 17.9 mmol $NO_3^-$ $m^{-2}$ $d^{-1}$, and the lowest rates in DBO3E, 15.5 mmol C $m^{-2}$ $d^{-1}$ and 1.2 mmol $NO_3^-$ $m^{-2}$ $d^{-1}$. General patterns between regions were very similar for both measures of productivity, and followed the trends for all particulate concentrations. In 2019, $\int\rho C$ was low at DBO3W, only 55.6 mmol C $m^{-2}$ $d^{-1}$, and was relatively high at both DBO2, 152 mmol C $m^{-2}$ $d^{-1}$, and at DBO3E, 36.5 mmol C $m^{-2}$ $d^{-1}$ (Fig. 3.13A). The only notable observation for $\int\rho NO_3$ in 2019 was a maximum at DBO3E, 2.8 mmol $NO_3^-$ $m^{-2}$ $d^{-1}$, although in general, rates of $\int\rho NO_3$ in that region were very low already (median 1.2 mmol $m^{-2}$ $d^{-1}$) (Fig. 3.13B). Discrete $\rho C$ and $\rho NO_3$ in 2019 were mostly similar to other years (Table 3.3 & Appendix C, Fig. C.4A & B). Higher rates of $\rho C$ were observed at middle depths at DBO2, and $\rho C$ was low in surface waters in the southern Chukchi Sea (DBO3W).

Integrated $Si(OH)_4$ utilization ($\int\rho Si$) followed a similar pattern between regions as $\int\rho C$ and $\int\rho NO_3$ (Fig. 3.13C). Compared to median $\int\rho Si$, in 2019 maximum values of $\int\rho Si$ were observed at DBO3E, 5.7 mmol Si $m^{-2}$ $d^{-1}$, and DBO4 reached a very high value of 210 mmol Si $m^{-2}$ $d^{-1}$ (Fig. 3.13C, Table 3.3). Specific uptake rates ($V_{Si}$) mirrored this pattern, reaching regional maximums of 0.55 $d^{-1}$ at DBO4 and 0.10 $d^{-1}$ at DBO3E in 2019 (Fig. 3.13D). Discrete $\rho Si$ and $V_{Si}$ were typical in 2019 compared to other years throughout the northern Bering Sea and productive

southern Chukchi Sea (Table 3.3 & Appendix C, Fig. C.4C & D). The highest rates of $\rho$Si and $V_{Si}$ for DBO3E in this time-series were observed throughout the water column in 2019. Maximum rates were also observed further north in DBO4 in the middle of the water column and near the base of the euphotic zone.

Ratios of $\int\rho C:\rho NO_3$ were typically higher than the particulate ratios, with medians that ranged from 3.4 mol mol$^{-1}$ at DBO1 to 28.2 mol mol$^{-1}$ at nutrient-poor DBO3E (Fig. 3.13E). Other than the very high median at DBO3E, $\int\rho C:\rho NO_3$ were otherwise similar across all regions, and the 2019 MHW had no obvious effect on $\int\rho C:\rho NO_3$ in any region. The northernmost regions, DBO4 & 5, had higher ratios of $\int\rho Si:\rho C$ and $\int\rho Si:\rho NO_3$ compared to the northern Bering Sea and southern Chukchi Sea (Fig. 3.13F & G). In 2019, $\int\rho Si:\rho C$ was relatively high in the productive southern Chukchi Sea, 0.42 mol mol$^{-1}$ at DBO3W, and was the highest recorded value for DBO3E, 0.16 mol mol$^{-1}$. At DBO4 $\int\rho Si:\rho C$ was nearly 4-fold higher than previously observed, 7.96 mol mol$^{-1}$ compared to the median of 0.45 mol mol$^{-1}$. $\int\rho Si:\rho NO_3$ followed a similar pattern to $\int\rho Si:\rho C$ overall, but was notable in 2019 where maximum values were recorded at DBO3E, DBO4, and DBO5 (Fig. 3.13G). At DBO3E, $\int\rho Si:\rho NO_3$ was 2.1 mol mol$^{-1}$ in 2019 compared to a median of 1.0 mol mol$^{-1}$ and at DBO4 in the northern Chukchi Sea, $\int\rho Si:\rho NO_3$ was 40.4 mol mol$^{-1}$ versus the median of 4.1 mol mol$^{-1}$. Ratios of utilization rates were not presented by depth due to very high variability making the results difficult to decipher.

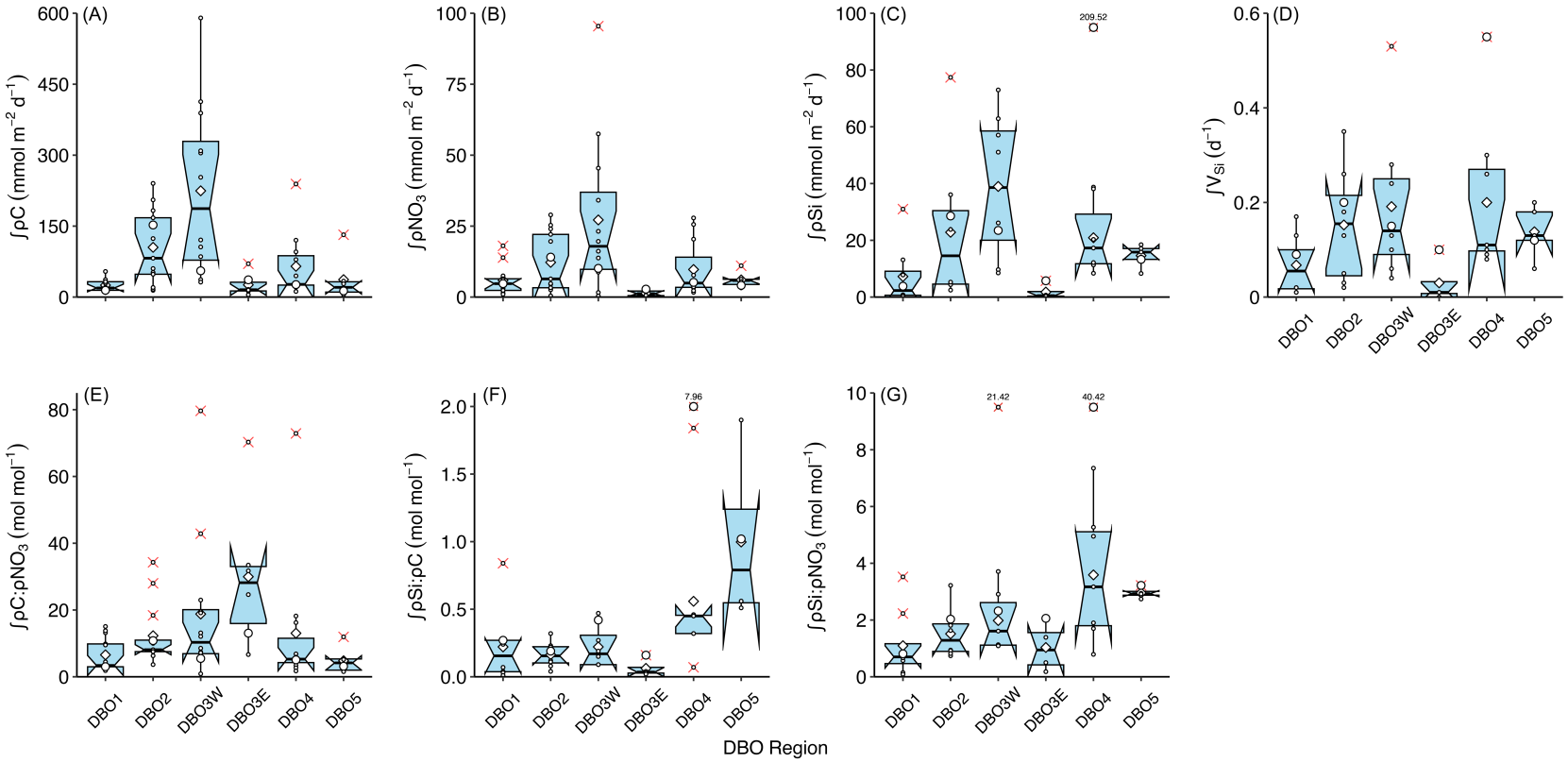


**Figure 3.13.** Nutrient utilization rates and ratios in the DBO regions from 2006 – 2022. **(A)** Carbon utilization, $\int\rho C$, **(B)** $NO_3^-$ utilization, $\int\rho NO_3$, **(C)** $Si(OH)_4$ utilization, $\int\rho Si$, and **(D)** specific uptake rate of Si, $V_{Si}$. Depth-integrated values for A – C were integrated through the euphotic zone from the surface to 0.1% light depth. Specific uptake rate of Si was calculated from $\int\rho Si$ and $\int bSiO_2$. Ratios of **(E)** $\int\rho C{:}\rho NO_3$, **(F)** $\int\rho Si{:}\rho C$, and **(G)** $\int\rho Si{:}\rho NO_3$. Silicon utilization rates ($\rho Si$ and $V_{Si}$) were only collected from 2013 – 2022. Description of box plot parameters as in Fig. 3.11.

### *3.4.7 Changes in contributions by diatoms to carbon and nitrate utilization and long-term averages for the PAR*

In addition to calculating the amount of $\rho C$ and $\rho NO_3$ attributable to diatoms, we also compared the proportion of chl-*a* by large cells > 5 µm to estimate diatom contributions to biomass. Chlorophyll-*a* biomass > 5 µm was typically 75% or higher in most regions (Fig. 3.14A), except for DBO3E where most years saw large cells account for < 40% of chl-*a*. In 2019, % chl-*a* > 5 µm was consistently similar to previous values in each region, except for at DBO3E where nearly 80% of cells were > 5 µm, compared to the median of 37% (Fig. 3.14A). At both DBO3E and DBO4, the highest rates of $\int \rho Si$ and $V_{Si}$ ever measured for each region were in 2019. This translated into very high values of diatom $\int \rho C$ (Fig. 3.14B) and diatom $\int \rho NO_3$ (Fig. 3.14C). DBO2 also saw higher than typical diatom productivity, and the anomalously low $\int$Si:N ratio at DBO5 resulted in a high diatom $\int \rho NO_3$ for 2019. However, since the typical range of diatom $\int \rho NO_3$ values was very small at DBO5, the 2019 maximum was not particularly high overall.

Compared to the total rates of $\int \rho C$, on average diatoms contributed more as latitude increased (Fig. 3.15A). Diatoms accounted for ~70% of $\int \rho C$ in the northern Bering Sea, and increased to 100% at DBO5 in the northern Chukchi Sea. The only exception was DBO3E, where average diatom contributions (39%) were very similar to the median large-celled chl-*a* biomass (37%). A similar pattern existed for diatom contributions to $\int \rho NO_3$ (Fig. 3.15B). Diatoms accounted for increasingly more $\int \rho NO_3$ with latitude, although there was less variability as on average all regions in the northern Bering Sea and southern Chukchi Sea ranged between 74 – 93%, and DBO4 and 5 were 96% and 100% on average, respectively.

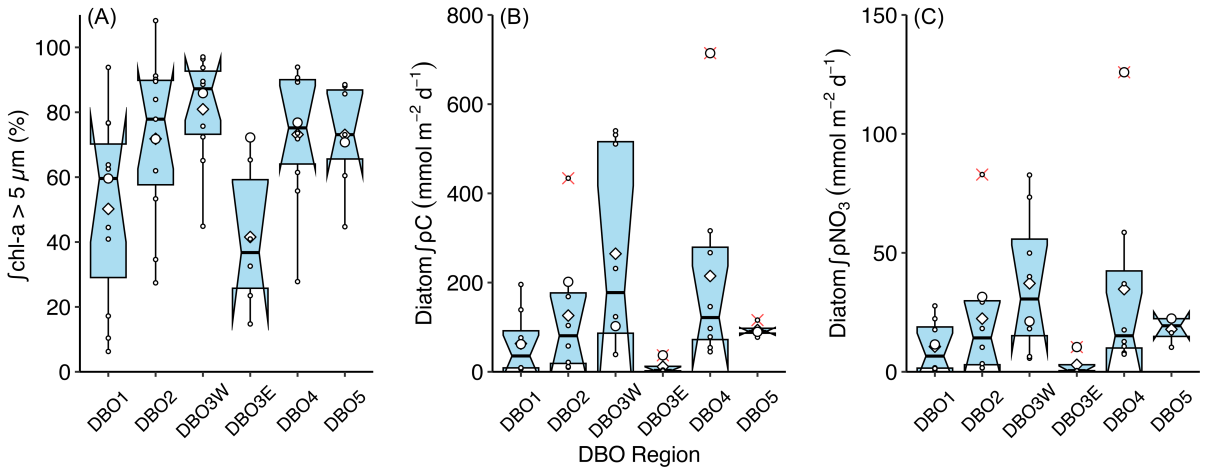


**Figure 3.14.** Large-celled (>5 µm) chl-*a* biomass in the DBO regions from 2006 – 2022, and diatom contributions to C and $NO_3^-$ utilization rates in the DBO regions from 2013 – 2022. **(A)** Large-celled chl-*a* biomass, ∫chl-*a* > 5 µm, **(B)** C utilization by diatoms, diatom ∫*ρ*C, and **(C)** $NO_3^-$ utilization by diatoms, diatom ∫*ρ*$NO_3$. Calculation of % chl-*a* > 5 µm used depth-integrated 5 µm chl-*a* and total chl-*a* (sum of two size-fractions). Description of box plot parameters as in Fig. 3.11.

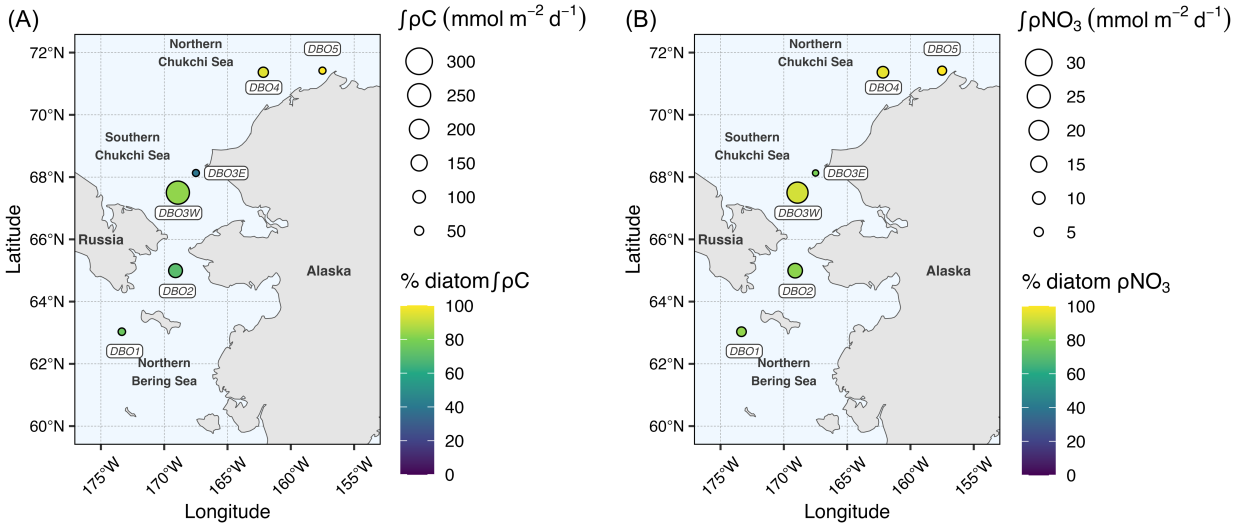


**Figure 3.15.** Diatom contributions to C and nitrate utilization in the DBO regions from 2013 – 2022. **(A)** Average ∫*ρ*C and the % contribution by diatoms to ∫*ρ*C. **(B)** Average ∫*ρ*$NO_3$ and the % contribution by diatoms to ∫*ρ*$NO_3$. Diatom contributions, average ∫*ρ*C, and average ∫*ρ*$NO_3$ were only calculated for years when *ρ*Si measurements were collected, 2013 – 2022.

## 3.5 Discussion

The Arctic MHW of 2019 enhanced the ocean warming period observed in the PAR from 2011 – 2019, which contributed to early sea ice retreat across most DBO regions, and enhanced stratification in some areas of the Chukchi Sea. Effects of the warming period and MHW on phytoplankton biomass and nutrient utilization rates were regionally inconsistent. From the beginning of this time-series, diatom biomass ($bSiO_2$) has declined south of St. Lawrence Island (DBO1) at the time of sampling in mid-July, while C and $NO_3^-$ utilization ($\rho C$ and $\rho NO_3$) by all phytoplankton has been highly variable but not followed any specific trends. Particulate C:N ratios were anomalously low for much of the PAR in 2019, and diatom productivity ($\rho Si$) was enhanced in the low-nutrient southern Chukchi (DBO3E) and the northern Chukchi Sea at DBO4 in 2019. Other regions however, showed little impact on diatom productivity from the MHW.

### *3.5.1 Physical drivers of phytoplankton dynamics*

*Temperature trends in the PAR during a warming period and marine heatwave*

During this time-series, a warming period was identified between 2011 – 2019. Temperature trends during the warming period were significant in the northern Bering Sea (DBO1 & 2), but not elsewhere. Despite some regions not having significant temperature trends, a marine heatwave was clearly identified in every region across the PAR in 2019 by surface temperature anomalies that were higher than any other year sampled (with one exception). In the following years (2021 & 2022), temperatures returned to values more similar to earlier in the time-series.

Since sampling occurred on approximately the same day every year in July, this meant that while sea ice broke up on average ~55 – 75 days prior to sampling in the northern Bering Sea at DBO1

and DBO2, in the Chukchi Sea sampling sometimes occurred while ice cover was still present. In some cases, the position of the station was even slightly modified to allow sampling while intact sea ice covered the typical location, or prevented sampling from occurring at all. This was reflected by the lack of data in certain years at northern locations, most notably DBO5. Regardless, the earliest breakup date for all DBO regions was generally in 2019 and correspondingly, it had the longest ice-free period.

The Bering Sea has been subject to increased MHW characteristics over past decades, including greater frequencies, durations, and intensities of temperature anomalies (Carvalho et al., 2021). Due to their proximity, the Bering and Chukchi Seas are known to be influenced by ocean currents and the meteorology of the Northeastern Pacific Ocean (Carvalho and Wang, 2020). Specifically, they are affected by the North Pacific Oscillation more than the Pacific Decadal Oscillation or El-Niño (Yeo et al., 2014). During our study period, we would thus expect the Bering Sea to have been influenced by the unprecedented North Pacific "blob" warming event in 2014 (Bond et al., 2015), in addition to the other Arctic MHW described by Barkhordarian et al. (2024). The connection between the North Pacific Ocean climatology and PAR was found to expose the Bering Sea to a relatively warmer temperature regime during 2014 – 2016 (Lomas et al., 2020). Although we did not observe consistently higher temperature anomalies from 2014 – 2016 at DBO1, surface temperatures were higher further north at DBO2. However, what was considered to be anomalously warm less than a decade ago is now not particularly extreme compared to more recent temperature observations. Warming has continued to such an extent in the Bering Sea that the 2014 – 2016 temperatures are now just part of the overall warming period that we observed from 2011 – 2019.

*Sea ice dynamics and control of seasonal phytoplankton blooms*

Biological processes, due to their complex relationship with the physical environment, were not expected to vary linearly with latitude, instead being controlled by a combination of timing of sea ice breakup, wind-driven mixing, and nutrient availability (Waga and Hirawake, 2020). The breakup and formation of sea ice are tied to primary productivity by limiting light and restricting water mixing and nutrient access (Grebmeier, 2012). Arrigo et al. (2008) estimated that primary production would increase across the Arctic Ocean as sea ice extent decreases, depending on regional nutrient concentrations. As predicted, fall phytoplankton blooms have begun to occur in the PAR due to the extended growing season, caused by delayed sea ice formation which increases light availability and allows storm-induced replenishment of nutrients (Cooper and Grebmeier, 2022; Waga and Hirawake, 2020). Ardyna and Arrigo (2020) recently proposed that phytoplankton productivity, phenology, and assemblage composition will continue to change with climate-affected environmental drivers, and eventually become a novel Arctic biogeochemical environment. Our sampling typically occurred between calendar day 199 – 205, which is close to the beginning of fall blooms in the northern Bering Sea and southern Chukchi Sea at 214±14 days (Waga and Hirawake, 2020). Therefore, our observations could eventually capture the onset of a secondary bloom rather than the tail-end of the first bloom, as is the current scenario.

The rapid pace of change being observed in environmental drivers make it very unlikely that our observations from a single point in time on an annual basis are suitable to understand the complex response of phytoplankton phenology and productivity from multiple environmental drivers. Other studies that focus on bottom-up or top-down controls of phytoplankton blooms in

the PAR are better suited for that purpose. Therefore, we aim to describe any observed changes potentially linked to the warming period from 2011 – 2019, or to the 2019 MHW, without necessarily providing a specific mechanistic explanation based on our own data.

### *3.5.2 Contributions by diatoms to carbon and nitrate utilization during the 2019 MHW*

The most notable observation in 2019 was record high contributions by diatoms at DBO3E and DBO4 compared to their contributions during the rest of the time series. This suggests that these two very different marine regimes presented more favourable conditions for diatom productivity in 2019, or that the timing of sampling coincided with a more active or diatom-rich assemblage during that year. Large-celled chl-*a* > 5 µm supported this idea, although other large-celled phytoplankton may have been present as well, e.g. dinoflagellates (Crawford et al., 2018).

In addition to diatom productivity being high in some regions during the 2019 MHW, our long-term averages were generally higher compared to the values previously determined for 2013 – 2016 (Giesbrecht and Varela, 2021) (Table 3.4). Variability remained very high within most regions, and the longer-term time-series (2013 – 2022) demonstrated that diatoms play an important biogeochemical role in $\rho$C and $\rho NO_3$ across the PAR. Several studies from across that Arctic suggest that as warming continues, diatom-dominated phytoplankton assemblages are shifting to those dominated by the haptophyte *Phaeocystis* (Nöthig et al., 2015; Orkney et al., 2020; Soltwedel et al., 2016). The only region where we clearly observed a significant change in diatom biomass was DBO1, where $\int bSiO_2$, $\int$Si:C, and $\int$Si:N declined over the entire time-series, while overall phytoplankton productivity, e.g. $\rho$C, remained consistent albeit variable over time. In DBO4, only diatom $\int \rho NO_3$ increased during the 2011–2019 warming period, and because

other measures of diatom productivity such as diatom $\int\rho C$, total $\int\rho Si$, and particulate concentrations did not change, the significant change in $\int\rho NO_3$ was likely a false-positive due to the many statistical comparisons made. While not showing many clear signs of changes with time, our dataset now captures a wide range of natural variability within different regions of the PAR, and may serve as a baseline for future observations of changes in diatom productivity.

**Table 3.4.** Depth-integrated rates of carbon and nitrate utilization by diatoms, and percent diatom contribution to total carbon and nitrate utilization in the DBO regions from 2013 – 2022. Values and percentages are the mean±standard deviation for all years in a particular region. Values without standard deviation indicate only one sampling year during the period.

| | 2013-2016 | | 2013-2022 | | 2013-2016 | | 2013-2022 | |
|---|---|---|---|---|---|---|---|---|
| **Region** | **Diatom $\int\rho C$ (mmol $m^{-2}$ $d^{-1}$)** | ***%*** | **Diatom $\int\rho C$ (mmol $m^{-2}$ $d^{-1}$)** | ***%*** | **Diatom $\int\rho NO_3$ (mmol $m^{-2}$ $d^{-1}$)** | ***%*** | **Diatom $\int\rho NO_3$ (mmol $m^{-2}$ $d^{-1}$)** | ***%*** |
| **DBO1** | 87.4±95.2 | *70±35* | 63.2±71.3 | *75±33* | 13.1±13.9 | *76±29* | 10.6±10.8 | *83±24* |
| **DBO2** | 36.7±45.0 | *40±15* | 126±144 | *70±33* | 6.2±8.0 | *65±9* | 22.3±27.2 | *82±20* |
| **DBO3W** | 301±257 | *66±32* | 265±226 | *83±28* | 36.8±30.7 | *86±17* | 37.2±29.5 | *93±14* |
| **DBO3E** | 4.0 | *25* | 11.4±17.1 | *39±41* | 0.5 | *100* | 2.9±4.9 | *74±36* |
| **DBO4** | 136±95.4 | *90±19* | 215±225 | *95±14* | 17.1±13.4 | *100±0* | 34.7±40.9 | *96±11* |
| **DBO5** | 77.5 | *100* | 93.6±16.1 | *100±0* | 10.3 | *100* | 17.9±5.8 | *100±0* |

### *3.5.3 Regional differences in physical, chemical, and biological characteristics across the PAR*

*Northern Bering Sea phytoplankton bloom magnitude and phenology*

The seasonal bloom had likely already passed in both DBO1 and DBO2 when sampled (Fujiwara et al., 2015), as it typically occurs when the sea ice retreats earlier in the year (Brown et al., 2011). It was hypothesized that Bering Sea primary productivity would likely rise under conditions of future warming and sea ice loss (Brown et al., 2011). More recent analysis however, has shown that warm conditions from 2017 – 2019 in the Bering and Chukchi Sea resulted in early loss of sea ice and weaker stratification, which reduced the strength of the biological pump, shown by interannual chl-*a* and diatom flux measurements (Lalande et al., 2021). In contrast, analysis of relatively cold (2007 – 2012) and warm (2014 – 2016) periods by Lomas et al. (2020), suggested a more complex seasonal mechanism where warmer spring temperatures were associated with more frequent subsurface chl-*a*, but colder fall periods were associated with greater chl-*a* biomass throughout the water column. Therefore, it is not clear

whether or not productivity is changing in a specific direction in the northern Bering Sea. It appears instead that the system is becoming more complex regarding when and where productivity occurs.

Interconnected patterns of trophic interactions in the Bering Sea have also been explained by the revised oscillating control hypothesis (OCH) (Hunt et al., 2011). The OCH doesn't specifically include primary producers, but it does describe the alternation between warm and cold periods and subsequent variation in the timing and distribution of phytoplankton biomass and productivity to support higher trophic levels. For example, cold years see an association between primary production and the timing of sea ice melt. If the water column is stratified by ice-melt at the same time as adequate irradiance, an ice-associated phytoplankton bloom occurs in surface waters. During warmer periods, it is hypothesized that early sea ice melt delays phytoplankton biomass and productivity due to insufficient irradiance until later in the spring, when stratification has broken down. The latter leads to open-water blooms of different phytoplankton species that does not support as much large crustacean zooplankton, which negatively impacts higher trophic levels due to lower-quality nutrition.

Since our sampling in the northern Bering Sea began in 2006, a long ice-free period prior to sampling has corresponded to warmer surface water temperatures and a low stratification index. Because we always sampled well after sea ice breakup, chl-*a* biomass and other particulates have been more concentrated at depth because the spring bloom depleted nutrients in surface waters. Rates of C and $NO_3^-$ utilization were typically low in DBO1 as expected, but still elevated in DBO2, perhaps signifying that the bloom had not progressed as far in DBO2 or culminated more

recently than in DBO1. While our observations generally aligned with the OCH expectations, over the study period we did not observe a strong relationship between physical characteristics (ice-free period, temperature, salinity, or stratification index) and measures of productivity, e.g. chl-*a*, $bSiO_2$, $\rho C$, $\rho Si$, or C:N (Appendix C, Fig. C.5 – 9). These results perhaps reflect a limitation of the once-a-year sampling program compared to more frequent ship-based or mooring studies that can measure the phenology of different events in much higher resolution (Brown et al., 2011; Lomas et al., 2020; Stabeno et al., 2012a, 2012b, 2007; Stabeno and Bell, 2019).

Due to the already strong warming trend in DBO1 and DBO2 (2011 – 2019 warm period), the effect of the 2019 MHW was less likely to stand out from prior observations. A decrease in $bSiO_2$ over time in DBO1 was previously attributed to the timing of the spring bloom by Giesbrecht et al. (2021) and our observations continue to support the hypothesis that warmer temperatures and earlier sea ice breakup are leading to earlier blooms. While other warming events were documented during our study period in the Bering Sea, this was not evident in our data set, suggesting that the various physical impacts of MHWs may not consistently affect bloom physiology at the current degree of warming.

*Impacts of marine heatwaves and higher temperatures on Bering Sea ecosystems*

Although our work showed limited evidence of direct impacts of higher temperatures on diatom productivity and phytoplankton assemblages in the Bering Sea, ecosystem effects of warm periods in the Bering Sea have been observed. Mooring observations on the Bering Sea shelf and in the northern Bering Sea showed that phytoplankton blooms are occurring earlier in nearshore

areas and the northern Bering Sea, and that open-water blooms have become more widespread (Nielsen et al., 2024). In 2018 and 2019 in particular, open-water blooms dominated the northern Bering Sea for the first time, signalling the potential for a continued shift towards a pelagic instead of benthic ecosystem (Nielsen et al., 2024). Because ice-associated algae are more effective at exporting to the benthos (Riebesell et al., 1991; Stabeno et al., 2020), and early ice breakup without sufficient light for growth may delay open-water blooms, these changes in bloom type and timing are reducing the quantity and quality of sinking particulates to the seafloor and potentially impacting benthic fauna and higher trophic levels (Grebmeier et al., 2018).

Accordingly, die-offs and limited reproductive success of sea birds, as well as low forage fish catches and low abundances of large crustacean zooplankton were observed in the northern Bering Sea following very low sea ice extent in 2018, which was due to a combination of warming and wind-driven processes (Duffy-Anderson et al., 2019). Types and abundance of zooplankton differed strongly between prolonged warm and cold periods before 2010, notably a lack of large copepods and euphausiids during warms years (Stabeno et al., 2012b). Differences up to the highest trophic levels were also evident, as a decrease in the number of fin whales present on the southeastern Bering shelf during warm years (Stabeno et al., 2012b).

*Southern Chukchi Sea productivity contrasted between high and low nutrient regimes*

A combination of bloom phenology and mixing are likely the factors that determined productivity in the DBO3W region – nutrient concentrations are typically high, and the time of sampling was closer to the start of seasonal blooms here (e.g. Frey et al., 2015; Fujiwara et al.,

2016). In 2019, high temperatures in surface waters and early sea ice retreat led to relatively high stratification (but still low compared to elsewhere), and lower-than-normal nutrient and biomass concentrations were observed in surface waters. This is unlike in the northern Bering Sea where earlier sea ice melt leads to open-water blooms following a breakdown in stratification. It has also been proposed that higher biomass and nutrient utilization rates in DBO3W compared to the northern Bering Sea are not explained by bottom-up controls such as stratification. Rather, low zooplankton grazing, a top-down control typically limiting biomass only in later stages of phytoplankton blooms (Sherr et al., 2013), may explain why productivity is usually high in DBO3W when sampled in mid-July.

A comparison of 2019 with another fairly warm year by Park et al. (2021), attributed the timing of open water blooms in the western Chukchi Sea to sea ice retreat, but higher biomass to warmer water temperatures. Their study described summer bloom timing and biomass to be both anomalously late and large, respectively, in 2019. However, our sampling dates aligned with the middle of their defined summer period and only showed bloom characteristics that were well within the range of values previously determined for that time of year, and did not show any clear association with temperature. The explanation for this is likely due to the spatial distribution of the bloom, because although the summer bloom observed by Park et al. (2021) was widespread and generally covered much of the southern Chukchi Sea, our long-term station used for sampling DBO3W appeared to be just beyond the northernmost limit of their remotely observed chl-*a* anomalies in 2019.

In the southeastern Chukchi Sea (DBO3E), biomass and productivity of all phytoplankton and

especially diatoms are historically much lower compared to the western region (Giesbrecht et al., 2019; Giesbrecht and Varela, 2021). This phytoplankton assemblage has been known to contain certain diatoms species, e.g. *Chaetoceros* and *Cylindrotheca*, while species found abundantly throughout DBO3W e.g. *Fragilariopsis* and *Thalassiosira*, are typically absent in favour of groups like coccolithophores and flagellates (Giesbrecht et al., 2019). This difference is driven by availability of $NO_3^-$, which is depleted throughout the water column rather than $Si(OH)_4$, which remains available at depth. The 2019 MHW increased diatom productivity ($\rho$Si) substantially compared to the normal amount in this region, but not $bSiO_2$ biomass. Although there weren't appreciable differences in the nutrients available compared to other years, the ice-free period prior to our sampling date was not unusual, despite record high temperatures. Thus, it is possible that our sampling time coincided with the beginning of a small diatom bloom but before any biomass had begun to accumulate. The utilization rates obtained were still among the lowest in the entire DBO for that year or during the entire study.

*Evidence of an open-water diatom bloom in the northern Chukchi Sea*

The Chukchi Sea is the last shallow shelf that separates the Pacific and Arctic oceans, and its characteristics influence waters as they flow from north from the Pacific. Typically, nutrients are consumed in surface waters of the Chukchi Sea through primary productivity that begins as sea ice retreats (Hill and Cota, 2005; Palmer et al., 2014). During our occupation of the northern Chukchi Sea in 2019, surface concentrations of $NO_3^-$ at DBO4 were depleted, but anomalously high $NO_3^-$ concentrations were measured at depth. Later in the summer, nutrients can be replenished by upwelling of nutrient-rich waters from the Canada Basin and distributed throughout the Chukchi Sea (Beaird et al., 2020). In this case it was likely that high $NO_3^-$

concentrations were simply the remaining $NO_3^-$ still to be used from original concentrations that were present earlier in the season. In a previous study on Si dynamics in this region (Giesbrecht and Varela, 2021), DBO4 was typically sampled prior to the onset of the seasonal bloom. In 2019 though, because of an unremarkable stratification index and also a long ice-free period, we may have observed an open-water bloom rather than an ice-associated bloom, something that has not been regularly documented at this location (Palmer et al., 2014; Sakshaug, 2004). Increased diatom biomass at 1% and 0.1% $I_D$ were supported by anomalously high $NO_3^-$ and sufficient $Si(OH)_4$ to drive very large increases in $\int\rho Si$ and $V_{Si}$. Sampling was likely near the end of the bloom as biogenic particulate concentrations were high at depth while there weren't concurrent increases in $\rho C$ or $\rho NO_3$ with the enhanced Si utilization. This suggests a decoupling of C and N cycling from Si at the end of the bloom, resulting in anomalously high Si:C and Si:N ratios which could indicate an assemblage that was more diatom-rich and therefore likely to be more efficient for export to the seafloor.

At DBO5 by comparison, other than low $NO_3^-$ concentrations limiting $\rho NO_3$ which led to very high $\rho Si:\rho NO_3$, most of the regional characteristics were not particularly affected by the MHW. Multivariate statistical studies suggest that phytoplankton groups other than diatoms will thrive in a future Chukchi Sea characterised by warmer sea surface temperatures, less ice, and nutrient depletion (e.g. Neeley et al., 2018). Our snapshot of MHW conditions in the northern Chukchi showed that diatoms still thrived and dominated phytoplankton assemblage composition and physiology during an anomalously warm period.

### *3.5.4 Elemental composition of phytoplankton assemblages in the PAR*

*Relationship of C:N ratios to indicators of diatom biomass*

Ratios of particulate C:N were anomalously low throughout much of the PAR during the 2019 MHW, however interpretation of this fairly plastic phytoplankton trait should be done carefully given that temperature differentially impacts biomass accumulation and growth rates (and cell division) (Rehder et al., 2024). Average integrated ratios of C:N for the PAR over the entire study period (2006 – 2022) agreed well with the Redfield ratio of C:N (6.6 mol $mol^{-1}$) and the average C:N (6 mol $mol^{-1}$) for cold, nutrient-rich waters at high latitudes (Martiny et al., 2013). It is not unheard of for marine organic matter to have C:N ratios as low as 3.8 (Geider and Roche, 2002), but values for 2019, especially in DBO3E and DBO5, were considerably lower, falling below 4 for depth-integrated values, and discrete values were as low as 3.3 (DBO3E) and 2.8 (DBO5). Physical characteristics such as temperature, salinity, stratification index, and ice-free period did not have meaningful direct correlations with C:N (Appendix C, Fig. C.9).

Low C:N ratios have been previously documented in other areas of the Arctic, including the PAR. In the Beaufort Sea and Canada Basin, anomalously low C:N below the Redfield ratio were attributed to the prevalence of small, eukaryotic phytoplankton and heterotrophic prokaryotes (Crawford et al., 2015) instead of larger eukaryotes such as diatoms. Low C:N can have implications for the biological carbon pump, which is more efficient when phytoplankton assemblages have elevated C:N, and especially when high C:N is associated with relatively dense, silica-ballasted diatoms (Armstrong et al., 2001). In a multi-dimensional comparison, (Crawford et al., 2015) associated low C:N with chl-*a* biomass < 5 μm in size, low concentrations of $bSiO_2$, and a relatively large contribution of small flagellate phytoplankton to

the total phytoplankton assemblage. Replicating the same analysis with discrete data (Fig. 3.16), we found that over the entire study period there was no clear relationship between $bSiO_2$ and chl-*a* > 5 µm with C:N. In 2019, however, the highest values of C:N were associated with higher concentrations of $bSiO_2$ and chl-*a* > 5 µm, while low C:N were not. Our study does not currently include taxonomic information, but observations of very high $\rho$Si in some regions and general patterns of $bSiO_2$ and chl-*a* >5 µm concentrations throughout the PAR in 2019 showed that diatoms were still driving productivity during the MHW. While this may simply be a new observation that extends the range of natural variability in the PAR, the low C:N ratios observed in 2019 could indicate a decoupling of Si utilization and diatom biomass from C:N in mid-July.

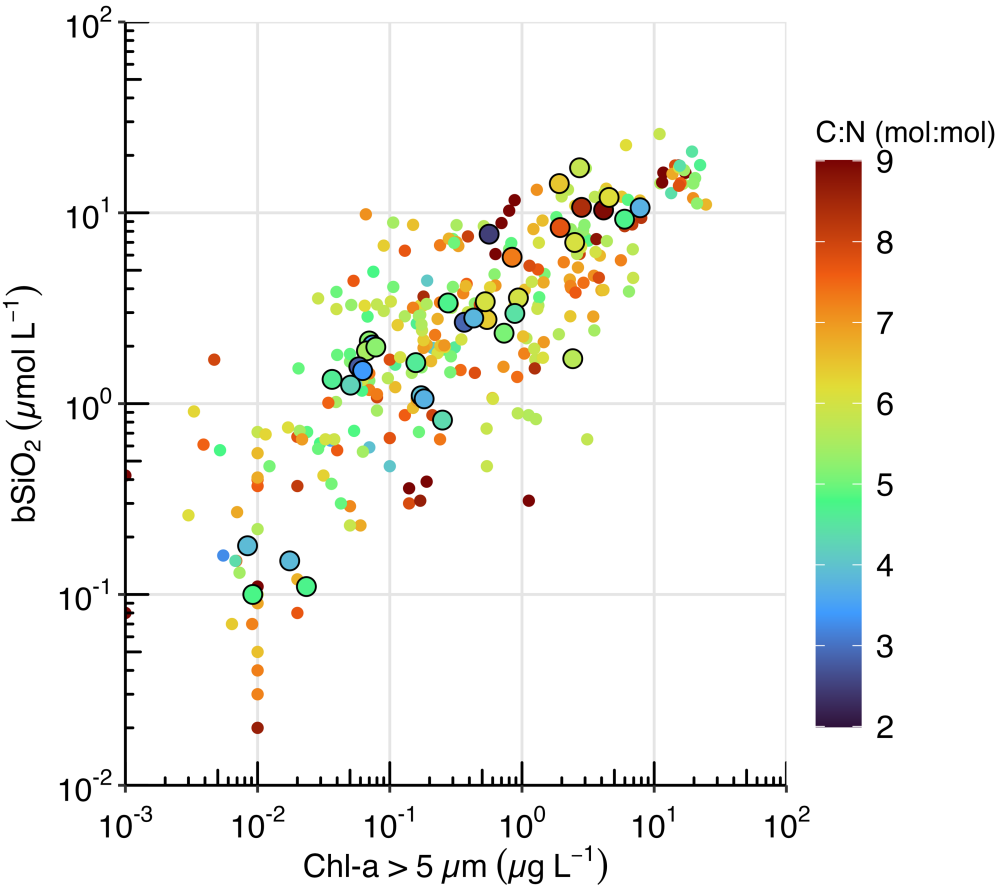


**Figure 3.16.** Biogenic silica ($bSiO_2$) concentration versus large size-fraction (>5 µm) chl-*a* concentration at all depths for stations in the DBO study regions from 2006 – 2022. Particulate C to PN ratio represented by the colour contours on the vertical scale. Size-fractioned chl-*a* biomass samples were not collected in 2006 and 2011. The 2019 MHW data is indicated by larger points outlined in black.

*Elemental composition of biogenic particles at different ambient temperatures*

When compared to temperature, particulate concentrations of C, N and $bSiO_2$ had maximum biomass at temperatures between 2 – 4 °C (Fig. 3.17A-C). The association of colder temperatures with higher $bSiO_2$, PC, or PN concentrations was unsurprising because warmer surface waters are often nutrient-depleted with low particulate biomass, while colder water decreases the rate of particulate remineralization, and in particular, enhances preservation of $bSiO_2$ (Nelson et al., 1995). Notably, higher particulate concentrations were observed in 2019 at DBO2 at warmer temperatures than any other year. These anomalously high $bSiO_2$ concentrations at DBO2 were likely the result of bloom timing, as nutrient concentrations were very low throughout the water column, indicating that high concentrations of diatoms were present at the time of sampling. In addition, temperature can control the elemental density of sub-polar and polar diatoms, increasing density at lower temperatures (Lomas et al., 2019). As such, because water temperatures were high at DBO2 in 2019, it is likely that the observation was due to a higher concentration of cells rather than any change in density.

Particulate ratios of C:N had no relationship with temperature, but most of the 2019 discrete data, which still covered the full range of temperatures normally seen in the PAR, were below the Redfield value of 6.6 (Fig. 3.17D). Ratios of Si:C and Si:N were highest at temperatures at or below ~4°C (Fig. 3.17E & F). This was mostly driven by concentrations of $bSiO_2$, which were lower at high temperatures, potentially reflecting low diatom abundance in phytoplankton assemblages at warmer temperatures, or a reduction in $bSiO_2$ quota for diatoms growing under warmer conditions. In general, the range of values observed for Si:C across all DBO regions and years (0.00 – 1.07 mol $mol^{-1}$ by depth; 0.02 – 0.65 mol $mol^{-1}$ depth-integrated) encompassed the

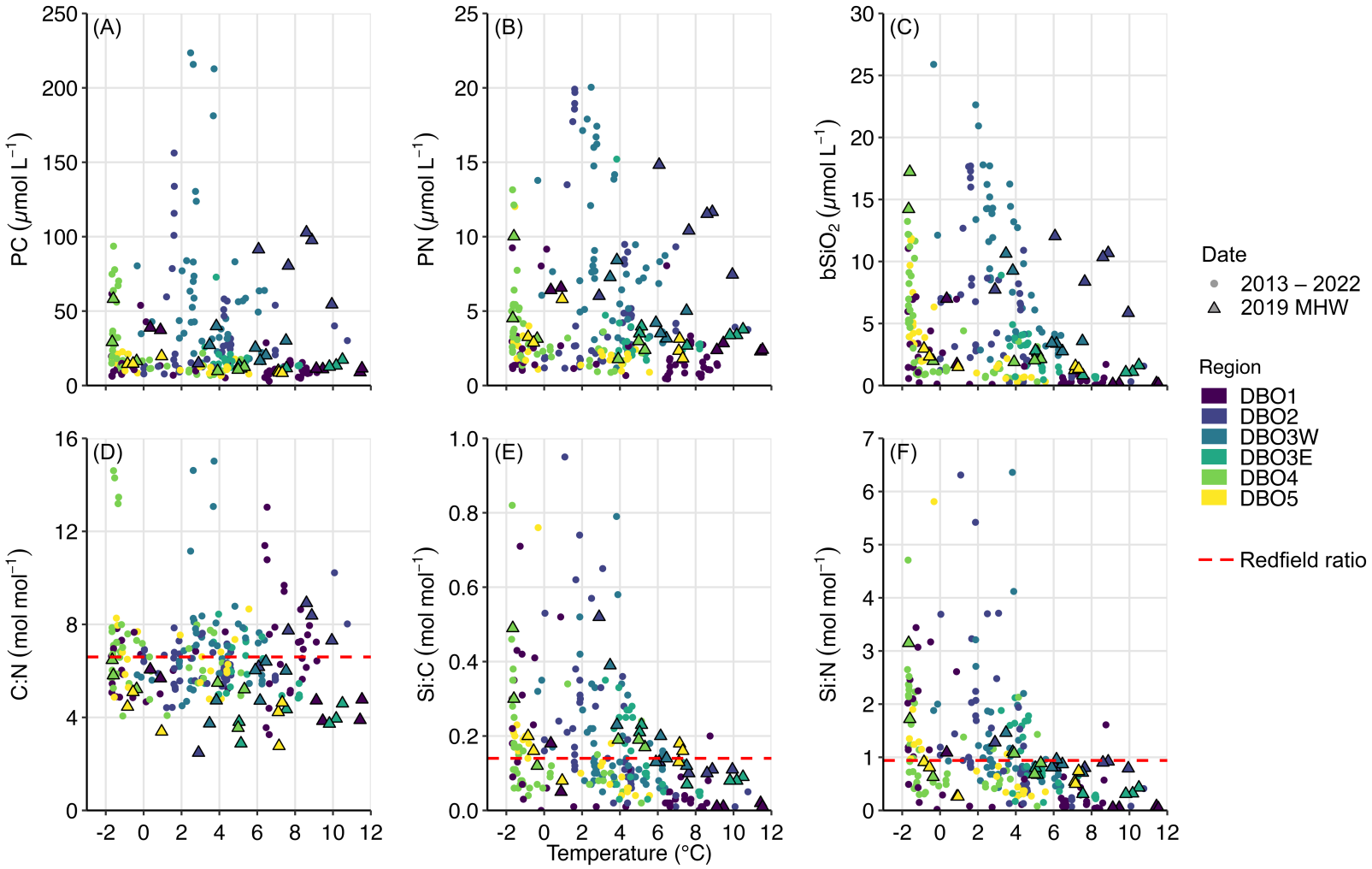


**Figure 3.17.** Relationship between biogenic particulate concentrations and particulate ratios and temperature for all DBO regions from 2013 – 2022. Particulate concentrations of **(A)** PC, **(B)** PN, and **(C)** $bSiO_2$. Ratios of **(D)** PC:PN, **(E)** $bSiO_2$:PC, and **(F)** $bSiO_2$:PN, with the Redfield ratio shown for each. Data are constrained to 2013 – 2022 to make sampling effort for all measurements and regions as similar as possible. Colours correspond to different DBO regions and each data point represents data from a single depth.

range of values (0.09 – 0.87 mol $mol^{-1}$) for a wide diversity of polar diatoms cultured by Lomas et al. (2019) at varying growth phases, ambient nutrient concentrations, and light levels. The relationship between nutrient utilization rates and temperature showed similar but less clear patterns as those seen for corresponding particulate concentrations (Appendix C, Fig. C.10), and may warrant additional analysis.

### *3.5.5 Relationships between nutrient utilization rates and particulate ratios*

Ratios of $\rho C:\rho NO_3$ were often higher than particulate C:N, which could be ascribed to the production and release of dissolved organic matter with a high C:N ratio, or the utilization of nitrogen sources other than $NO_3^-$, such as dissolved organic nitrogen, urea, or ammonium (Geider and Roche, 2002). In our study, this was highlighted at the nitrate-poor DBO3E, which consistently had high $\rho C:\rho NO_3$, and phytoplankton were therefore most likely using alternative N sources to fuel productivity. In a study comparing C productivity (as net primary productivity, NPP) to $\rho NO_3$, Lomas et al. (2020), observed higher values of NPP:$\rho NO_3$ during warm periods in the Bering Sea, implying recycled N is important in warm seasons. In our dataset, surface samples were the warmest and more frequently low in $NO_3^-$ in any given year.

In the DBO regions of the Chukchi Sea, some of the highest ratios of $\rho Si:\rho C$ and $\rho Si:\rho NO_3$ ever observed were recorded in 2019 during the MHW, but there were different reasons for each. At DBO3E and DBO4, record-high $\rho Si$ and $V_{Si}$ were observed while $\rho C$ and $\rho NO_3$ were not noticeably high. At DBO3W, low $\rho C$ accounted for high $\rho Si:\rho C$, and at DBO5, low $\rho NO_3$ explained the high $\rho Si:\rho NO_3$. In all of these examples, a higher utilization of Si relative to other nutrients indicated that diatoms were accumulating Si, though whether luxury uptake or being

put towards growth was uncertain. It is difficult to draw comparisons between different regions within the PAR that have varying assemblage compositions, as cellular stoichiometry, in particular $bSiO_2$ quotas of diatoms, vary substantially among diatom morphological types (Baines et al., 2010). Therefore, conclusive assessment of the processes underlying varying stoichiometry is not possible without taxonomic data, as regional and temporal differences in stoichiometry are largely determined by assemblage composition.

When compared to particulate ratios (Fig. 3.18A & B), other than the extreme outlier values at DBO4, the ratios of $\rho Si:\rho C$ and $\rho Si:\rho NO_3$ to their equivalent particulate ratios during the 2019 MHW (outlined circles) were within the previously observed range of variability. The temperature anomaly of a particular region didn't influence the relationship between utilization rates and particulates. 2019 was not the only year to experience utilization ratios in excess of the particulate ratios, and the greater degree of variability in $\rho Si:\rho NO_3$ compared to Si:N (Fig. 3.18B) reinforced the notion that N sources other than $NO_3^-$ played a role in supporting diatom productivity for several regions during many years.

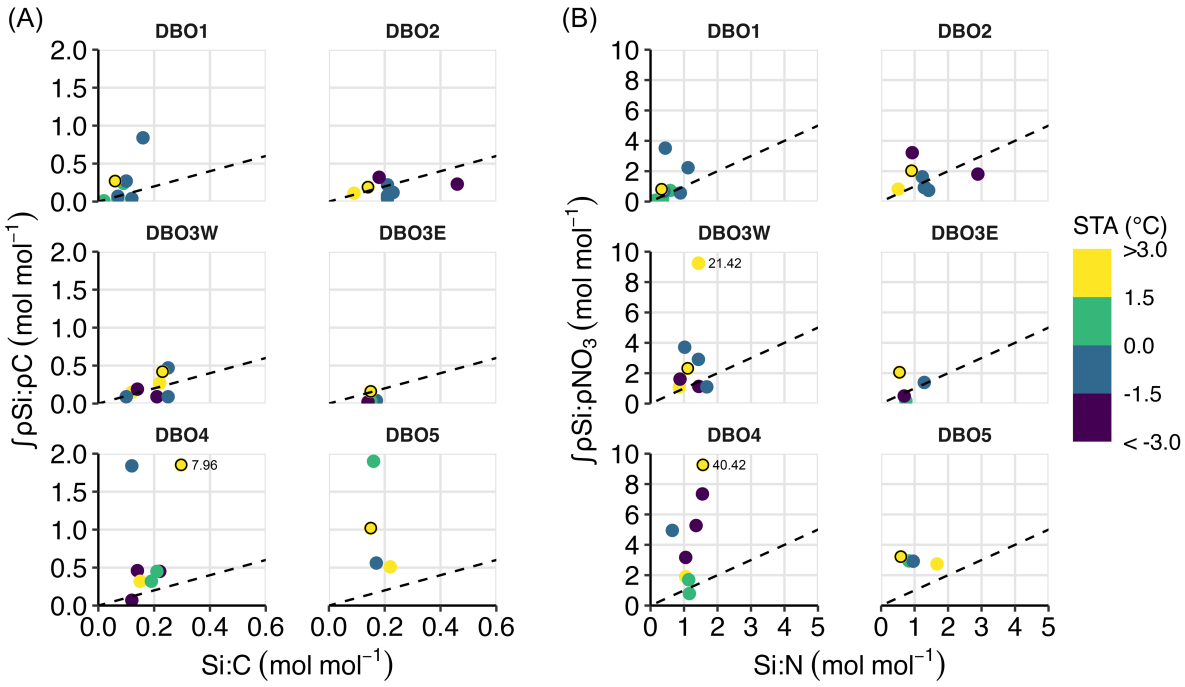


**Figure 3.18.** Relationship between utilization rate ratios and particulate element ratios across DBO regions from 2013 – 2022. Comparisons of **(A)** ∫$\rho$Si:$\rho$C to ∫Si:C, and **(B)** ∫$\rho$Si:$\rho NO_3$ to ∫Si:N. Surface temperature anomaly (STA) for a particular year is represented as a binned colour value. Each data point is a depth-integrated values for the euphotic-zone for a particular year. Data for 2019 are shown as the outlined point. Extreme outliers are annotated with the utilization rate ratio value directly beside the point. The 1:1 relationship between utilization rate ratio and particulate ratio is shown as a dashed line.

### 3.6 Conclusions

In this study we presented evidence that the 2019 MHW observed across the PAR had a significant impact on some measures of phytoplankton biomass, productivity, or elemental composition. The impact was not consistent across the biogeochemically distinct DBO regions, and our observations were not consistent enough to draw strong conclusions about the potential impact of warming on any particular region. An unusual bloom of diatoms may have occurred in the typically nutrient-poor southern Chukchi Sea, and a rare, late open-water bloom of diatoms in the northern Chukchi Sea was observed as well. Low C:N ratios across most of the PAR during the 2019 MHW may have been a physiological response to higher temperatures, or driven by a change in phytoplankton assemblage composition, but evidence for either scenario was mixed.

Over the course of the time-series from 2006 – 2022, diatom biomass has declined in the northern Bering Sea south of St. Lawrence Island, but trends in other regions are uncertain. There was an association of higher particulate concentrations as well as high Si:C and Si:N with colder temperatures throughout the PAR, although this was likely the effect of bottom-up controls on biomass such as nutrient concentrations rather than a direct effect of temperature. After nearly 15 years of time-series work in the PAR, and during a warming period from 2011 – 2019, it is still uncertain if any of the trends observed, significant or not, are a reflection of natural variability, or truly an anthropogenic alteration due to climate change. Lastly, estimates of diatom contributions to total C and $NO_3^-$ utilization rates in all DBO regions were improved by this study, and indicated that diatoms are equally or more important in their contributions than the previous estimate from 2013 – 2016. Although conclusions to this study are limited by the temporal aspects of the sampling program, it is clear that comprehensive measurements on an annual basis still show important patterns between regions as well as have potential for identifying anomalous phytoplankton dynamics in a sensitive and rapidly changing marine ecosystem.

– This page intentionally left blank –

# Chapter 4 – Morphological and physiological responses of the cosmopolitan marine diatom *Thalassiosira rotula* to acidification

Wyatt S, McNabb B, Varela D. (2024). Morphological and physiological responses of the cosmopolitan marine diatom *Thalassiosira rotula* to acidification. *Diatom Research,* 1-14. DOI: 10.1080/0269249X.2024.2369049

## 4.1 Abstract

We investigated the effect of decreased pH on the morphology and nutrient physiology of the cosmopolitan marine diatom *Thalassiosira rotula* (CCMP3362) by acclimating unialgal cultures to two different $CO_2$ gas concentrations under optimal light, temperature and nutrient conditions. At lower pH (higher $CO_2$), *T. rotula* exhibited a reduction in cell diameter (7%), surface area (13%), and volume (20%), and an increase in surface area-to-volume ratio (7%). All measures of silicification in *T. rotula*, i.e. silica ($SiO_2$) quota, rate of silicic acid ($Si(OH)_4$) utilization, and elemental ratios of $SiO_2$:C and $SiO_2$:N, remained unchanged. Similarly, carbon (C) and nitrogen (N) quotas, ratios and utilization rates were mostly unaffected by pH. In contrast, the utilization rate of nitrate ($\rho NO_3$) was significantly lower at decreased pH when the rate was normalized by cell number instead of by cell volume. The changes in cell morphology found in this study under low pH were likely not large enough to significantly impact physiological processes and the role of this species in marine food webs and biogeochemical cycles. It is possible that the interactive effects of pH, temperature, light, and nutrient availability characteristic of different regions of the world ocean could result in stronger physiological and morphological responses in this widespread diatom. However, under constant optimal growth conditions, *T. rotula* was only mildly affected by changes in pH, and in particular the physiology and elemental stoichiometry of C, N and Si were not sensitive to acidification.

## 4.2 Introduction

Diatoms account for ~40% of marine primary productivity (Nelson et al., 1995), contribute to 20% of the total carbon (C) fixed through photosynthesis in the Earth biosphere (Field et al., 1998), support marine food webs, and are intertwined with other major biogeochemical cycles (Tréguer et al., 2021). This group of phytoplankton assimilates silicic acid ($Si(OH)_4$) to produce their rigid outer skeleton (*i.e.* frustule) made of amorphous hydrated silica ($SiO_2 \cdot nH_2O$) (Martin-Jezequel et al., 2000), making them the largest consumer of $Si(OH)_4$ in the ocean. Due to this requirement, diatoms control oceanic Si cycling and contribute to vertical Si fluxes in many oceanic regions (Nelson et al., 1995; Tréguer et al., 2021). Silicification, photosynthesis, and growth by diatoms couple the Si cycle to the carbon (C) and nitrogen (N) cycles (Brzezinski et al., 2003; Marchetti et al., 2010) and they therefore play an important role in marine biogeochemical cycling. As such, diatoms can influence atmospheric carbon dioxide ($CO_2$) concentrations by controlling the C balance in surface waters (Volk and Hoffert, 1985) and the vertical flux of nutrients to the ocean interior, *i.e.,* the biological carbon pump (Alldredge and Silver, 1988).

Ocean acidification (OA) is expected to have varying effects on diatoms and on phytoplankton in general. The marine pool of dissolved inorganic carbon ($C_T$) is the result of an equilibrium between aqueous $CO_2$, carbonic acid ($H_2CO_3$), bicarbonate ($HCO_3^-$), and carbonate ($CO_3^{2-}$) ions, with the majority of dissolved C existing as $HCO_3^-$. Phytoplankton have evolved C-concentrating mechanisms (CCMs) to overcome the low concentration of $CO_2$ at surface ocean pH, and the slow rate of $CO_2$ diffusion in water (Reinfelder, 2011; Spalding, 2008) by preferentially using the higher concentrations of $HCO_3^-$. Their physiology is thus intimately connected to the

equilibria of dissolved $C_T$. Increased anthropogenic $CO_2$ emissions are elevating the concentration of aqueous $CO_2$ and shifting the C equilibrium, resulting in a pH decrease of slightly more than 0.1 units that translates into an acidity increase of ~26% in the surface ocean since the Industrial Revolution (Fabry et al., 2008). Despite the biogeochemical and ecological importance of diatoms, studies that investigate the effects of OA on diatom morphology, elemental composition, and productivity remain under-represented compared to those on other groups of organisms such as corals, certain types of zooplankton, and fishes.

A great deal is understood about the elemental composition and stoichiometry of diatom species growing optimally (Brzezinski, 1985; Lomas et al., 2019), under nutrient-limited (Baines et al., 2011; Meyerink et al., 2017), or under variable light (Spilling et al., 2015) conditions. In contrast, there are only a few studies on the effects of OA on diatom stoichiometry and nutrient uptake, and they do not consistently include Si along with C and N (Riebesell et al., 2007). In fact, the effects of OA on diatom Si:C:N utilization rates and elemental ratios are generally absent from the literature, with most studies focusing on abundance, biomass, and photosynthetic rates of natural phytoplankton assemblages (Bach et al., 2017; Hoppe et al., 2015). Hoppe et al. (2018) showed that the elemental stoichiometry in several subarctic diatom assemblages was unaffected by $CO_2$ manipulation under different light intensities. Hoppe et al. (2017b) observed shifts in diatom taxa at low pH despite the experimental assemblage maintaining similar primary production and elemental composition compared to ambient pH levels. In a methodologically unique study, Petrou et al. (2019) reported that Si incorporation by several different diatom species in the Southern Ocean decreased under low pH, however the effect of OA on stochiometric responses were not investigated.

Using OA as a single-stressor or together with other environmental variables results in varying responses or resilience in marine diatoms. A meta-analysis of field studies demonstrated that OA often selected in favour of larger species and had a greater negative effect on oceanic diatoms, but could also increase diatom biomass or abundance in coastal, estuarine, and benthic environments (Bach and Taucher, 2019). Valenzuela et al. (2018) showed increased tolerance of *Thalassiosira pseudonana* to ultra-violet A and B under elevated $CO_2$, suggesting enhanced diatom resilience in an acidified ocean. Additionally, a constant ambient pH was more important for diatom C:N:P stoichiometry and biomass than a specific pH value (Clark et al., 2014). Other investigations also documented some interactive effects of OA, temperature, light, and nutrient concentration on phytoplankton responses (Gao et al. 2012a). For example, transparent exopolymer particle (TEP) production by *Thalassiosira weissflogii* increased under warmer temperatures, but the combination of lower pH and elevated temperature decreased TEP aggregation and sinking rates, potentially decreasing C and Si flux out of the euphotic zone from diatom blooms (Seebah et al., 2014). The negative effects of UV radiation on the photosynthetic rate of *Phaeodactylum tricornutum* were enhanced under a combination of OA and nitrate-limited conditions (Li et al., 2015). Growth rate increased at low light and low pH compared to high light at any pH (Qu et al., 2021), and was also enhanced at high temperature, long day length, and low pH in *Skeletonema costatum* (Li et al., 2021). In general, the conclusions of these studies agree that the impacts of OA on diatoms are likely dependent on synergistic effects with other environmental factors, and the species of diatom as well.

While diatom OA research is advancing, there are still significant gaps in the understanding of nutrient stoichiometry, silicon utilization rates, and frustule $SiO_2$ content in diatoms exposed to

high $CO_2$ conditions. The experiment presented here investigated the effects of decreased pH ($pH_T$ = 7.75) on the morphology, specific growth rate (μ), cellular quotas and ratios of C, N, $SiO_2$ and chlorophyll-*a (*Chl-*a*), and utilization rates and ratios of C, nitrate ($NO_3^-$), and $Si(OH)_4$ in *Thalassiosira rotula.* The genus *Thalassiosira* is one of the most globally abundant (Leblanc et al., 2012) and successfully grows under broad ranges of temperature, light, and salinity conditions (Schone, 1974, 1972). The species *Thalassiosira rotula* (Meunier) is a pelagic diatom found across a wide latitudinal range from subarctic to subtropical oceanic and coastal waters (Hasle, 1976). Therefore, the experimental findings presented here on the effects of OA on a cosmopolitan diatom species could potentially apply to many parts of the ocean.

## 4.3 Materials and Methods

### *4.3.1 Culture conditions*

While *T. rotula* has recently been considered the same species as *Thalassiosira gravida* due to their morphological similarities (Sar et al., 2011), the clone used here is identified as *T. rotula* in the NCMA culture collection (CCMP3362, National Center for Marine Algae and Microbiota, East Boothbay, Maine, U.S.) and throughout this paper.

Culture experiments with *T. rotula* were conducted with ESAW media (Berges et al., 2001). Initial macronutrient concentrations were typical of ESAW with 550 μM $NO_3^-$, 21 μM phosphate ($PO_4^{3-}$) and 105 μM $Si(OH)_4$. The media was bubbled with sterile air for 24 hours to adjust the pH to ambient values and sterilized by filtration (0.2 μm VacuCap, Cytiva, MA), before the diatom inoculum was introduced.

A photoperiod of 13:11h light:dark and a temperature of 14˚C were chosen to mimic conditions typical of temperate surface waters where *T. rotula* tends to be most commonly found (Hasle, 1976). An optimal irradiance of 150 µmol photons $m^{-2}$ $s^{-1}$ was experimentally determined prior to the start of the OA experiments, and utilized for such experiments to ensure optimal growth rate at the two pH treatments. For the determination of optimal irradiance, *T. rotula* was grown in 50 mL semi-continuous cultures and maintained in exponential phase at irradiance levels of 10, 19, 38, 75, 150 and 300 µmol photons $m^{-2}$ $s^{-1}$ for 10 generations to ensure acclimation of diatoms to culture conditions. After the acclimation period, growth rates were calculated at each irradiance, and plotted against irradiance level (Appendix D, Figure D.1). The growth rate did not increase above 150 µmol photons $m^{-2}$ $s^{-1}$, and therefore, a two-litre parent culture was established at this irradiance under the 13:11 h photoperiod and 14˚C temperature conditions. From this point forward, cells were maintained in exponential growth phase by semi-continuous batch culturing. All dilutions with new media were carefully performed using sterile technique in a HEPA-filtered laminar flow hood. The parent culture was acclimated to the effects of air bubbling for two weeks before the beginning of the OA experiment using sterile-filtered (0.2 µm) air drawn from outside the laboratory (ambient $CO_2$ concentration) and continuously bubbled at ~125 mL $min^{-1}$ through a polycarbonate (PC) air bubbler.

### *4.3.2 Experimental design*

For the OA experiments, two sets of triplicate cultures (two litres each) were prepared in sterile, 2.8 L PC flasks from the homogenously mixed parent culture. One set of three cultures was grown and acclimated under the same ambient $CO_2$ concentration treatment as the parent culture, low $CO_2$ (LC) of 500 ppm, and the other set of three cultures was simultaneously grown and

acclimated under high $CO_2$ (HC) conditions of 1000 ppm using a pre-mixed $CO_2$/air standard (Praxair, ON, Canada). Since semi-continuous culturing technique requires experimental cultures to be diluted with new media to maintain the cells in mid-logarithmic growth phase, the pH of the media was maintained by pre-acclimating this media for 24 hours with the LC or HC gas level before diluting the cultures.

During the experimental period, the growth rate of every culture was monitored daily using *in vivo* fluorescence and cell numbers, and the pH of the cultures were also monitored daily using a glass pH electrode. Based on preliminary OA experiments that our laboratory carried out with the same diatom species, cell densities were kept lower than ~6,000 cells $mL^{-1}$ at all times to prevent diatom activity from substantially altering the pH of the media. Cultures were run for 10 generations of growth or ~8 days to ensure acclimation of diatoms to the LC and HC culture conditions, at which time the experimental cultures were sampled for all the measurements of interest.

### *4.3.3 Experimental measurements*

After the acclimation period, the following measurements were conducted for each culture in the exponential phase: carbonate system parameters (total pH ($pH_T$), total inorganic carbon ($C_T$), total alkalinity (TA)), *in vivo* fluorescence, cellular density and morphology, Chl-*a* biomass, C, N, and Si cellular quotas, dissolved nutrient concentrations, and nutrient utilization rates.

### *4.3.4 Carbonate system parameters*

Triplicate samples for $pH_T$ were taken daily to ensure constant pH in all cultures. $pH_T$ was monitored by subsampling the cultures into a light-proof, airtight container. The samples were then kept in a 14˚C water bath along with a TRIS/HCl seawater buffer matching the ESAW media salinity (Dickson et al., 2007). A Milwaukee MA911 glass electrode (Milwaukee Instruments, NC, USA) connected to a LabQuest 2 data logger (Vernier, OR, USA) was used to take sequential voltage measurements of pH samples and buffer, after which the $pH_T$ was calculated from the difference in voltage as per SOP6A of Dickson et al. (2007). Throughout the manuscript, $pH_T$ denotes the specific pH value on the total scale, and pH is used when discussing a general change in acidity.

To constrain the carbonate system, $C_T$ and TA were also measured from the experimental cultures. Samples of 500 mL were carefully drawn from 2 of the replicate cultures per treatment (since 1 replicate did not have enough volume remaining) using a silicon tube. The sample was generously overflowed to remove bubbles from the draw tube and sample bottle, and then preserved with 200 µL of saturated mercuric chloride in a gastight glass bottle. Analysis for $C_T$ took place at the Institute of Ocean Sciences (Fisheries and Oceans Canada) using a SOMMA interfaced with a UIC Model 5011 coulometer (UIC Inc., Joliet, IL) controlled by VINDTA 3D software (Marianda, Kiel, Germany), and TA was measured using the open cell titration method with a Metrohm dosimat (Metrohm, Herisau, Switzerland) (Dickson et al., 2007). Values of $pH_T$ and $pCO_2$ were calculated in Microscoft Excel (Microsoft, Richmond, WA) using CO2SYS version 25 (Pelletier et al., 2007) with K1 and K2 constants from Mehrbach et al. (1973) refit by Lueker et al. (2000), and the $KHSO_4$ dissociation constant from Dickson (1990).

### *4.3.5 Growth rate and cell morphology*

*In vivo* fluorescence was measured daily, three hours into the light period, using a Turner-Designs 10AU fluorometer (Turner Designs, CA, USA). Growth rate (μ) was calculated as the slope of the natural log of *in vivo* fluorescence (exponential phase) over time for each replicate culture. In addition, 30-mL samples were preserved with Lugol's Solution (Parsons et al., 1984) in amber glass jars for measurements of cell density and morphology. Cell density was determined from a 1-mL subsample by counting ≥400 cells in random fields of a 50x20 Sedgewick-Rafter Counting Chamber (Graticules Ltd., Tonbridge, UK) with a 100x objective on an Olympus IX71 epifluorescence inverted microscope (Olympus Corporation, Tokyo, Japan). Cell counts were performed in triplicate for each replicate within treatment, and then averaged for each treatment. Cell dimensions (length and diameter) were determined by taking photos of individual cells with a Q-Imaging Retiga 2000r camera (Burnaby, BC, Canada) and using calibrated measurement tools in image analysis software ImageJ 1.52a (NIH & LOCI, University of Wisconsin). To account for intercellular variability in morphology, 30 cells in girdle view from each triplicate culture were measured and averaged for length and diameter, for a total of 90 cells per treatment. Cell volume (V) and surface area (SA) were calculated with the formula for a cylinder using the length and diameter of individual cells. Although *T. rotula* is typically a chain-forming diatom, the clone used in this experiment is documented to occur only as short chains and single cells. In our experiments, chains were not consistently seen, and only rarely did two-cell chains occur. Therefore, chain length and the distance between cells on a chain were not included as morphological measurements.

### *4.3.6 Chlorophyll-a quota*

Chlorophyll-*a* (Chl-*a*) quota for each culture was determined by filtering a 25 mL sample on a GF75 glass fiber filter (0.7 µm nominal porosity) and freezing it at -20˚C until analysis. Filters were submerged in a 90% acetone solution and sonicated for 10 minutes in an ice bath, after which the extraction was carried out for 24 hrs at -20˚C in the dark. Extracted samples were left to reach room temperature for two hours and decanted into borosilicate cuvettes before measurement on a Turner-Designs 10AU fluorometer (Turner Designs, CA, USA) pre-calibrated at room temperature with pure chlorophyll standards. Concentration of Chl-*a* was determined after correction for phaeopigment interference by acidification (Parsons et al., 1984). Additional triplicate Chl-*a* samples were taken from each treatment replicate to determine sampling and analytical error. The resulting error (calculated as the coefficient of variation, CV) was 13.7%.

### *4.3.7 Dissolved nutrients*

Nutrient concentrations were measured in triplicate from each culture and then averaged. Samples for the measurement of $NO_3^-$ concentrations were collected from each culture by filtration through pre-combusted GF75 glass fiber filters (0.7 µm nominal porosity) loaded into acid-washed Swinnex filter holders. The filtrate was collected in an acid-washed 15 mL centrifuge tube, immediately frozen at -20˚C and $NO_3^-$ concentrations were later measured using an Astoria 2 Nutrient Autoanalyzer according to Barwell-Clarke and Whitney (1996). The concentration of $Si(OH)_4$ was determined from samples drawn from each culture by filtration through 0.6 µm PC filters to avoid Si contamination from glass fiber filters. The $Si(OH)_4$ samples were stored at 4˚C to avoid polymerization of $Si(OH)_4$ at freezing temperatures, and analyzed colourimetrically with a Beckman DU 530 UV/Vis spectrophotometer (Beckman

Coulter, CA, USA) using a reverse-order reagent blank (Brzezinski and Nelson, 1986). The coefficient of variation was calculated from the triplicate samples from each replicate; average CV for $NO_3^-$ = 2.9%, and $Si(OH)_4$ = 1.9%.

### *4.3.8 Carbon and nitrogen utilization rates and cellular quotas*

Utilization rate of carbon ($\rho$C) and $NO_3^-$ ($\rho NO_3$) were measured using a $^{13}C$-$^{15}NO_3^-$ dual tracer method (Dugdale and Goering, 1967; Slawyk et al., 1977). Each culture was subsampled into acid-washed 250 mL PC bottles, leaving only enough headspace for isotope additions. Samples for the determination of total $\rho$C were inoculated using a $KH^{13}CO_3$ (99% purity, Cambridge Isotopes Laboratories, MA, USA) isotope tracer stock with the target $^{13}C$ enrichment being ~10% of the total $C_T$ in the experimental culture. Samples for $\rho NO_3$ were inoculated using a $Na^{15}NO_3$ (98+% purity, Cambridge Isotopes Laboratories, MA, USA) with the final $^{15}N$ enrichment target being ~10% of the estimated $NO_3^-$ in the experimental culture. Inoculated samples were incubated under the same temperature and light conditions as the experimental cultures for only 4 hours, to minimize changes in pH, and terminated by filtration through pre-combusted 0.7 µm glass fiber filters. Filters were dried at 60˚C for 48 hours and the isotopic composition ($^{13}C$:$^{12}C$ and $^{15}N$:$^{14}N$) and total C and N content were measured at the Stable Isotope Facility at the University of California Davis with a PDZ Europa 20-20 isotope ratio mass spectrometer and a PDZ Europa ANCA-GSL elemental analyzer, respectively (Sercon Ltd., Cheshire, UK). Carbon utilization ($\rho$C) was calculated using the particulate C concentration and isotope balance of $^{13}C$ and $^{12}C$ at the end of the incubation, and the length of incubation (equation 3, Hama et al., 1983). Nitrate utilization ($\rho NO_3$) was calculated using the particulate N concentration and isotope balance of $^{15}N$ and $^{14}N$ at the end of the incubation, and the length of

incubation (equation 3, Dugdale and Wilkerson, 1986). Estimates of CV for C and N content (quotas) and utilization rates from triplicate measurements of the same incubation bottle are not available for this study. Our typical CV for triplicates (n = 51) for the same measurements from incubation experiments done previously in our lab were $\rho C$ = 12.5%, $\rho NO_3$ = 6.7%, C quota = 9.3%, N quota = 14.2%.

### *4.3.9 Silicon utilization rates and silica cellular quota*

The utilization rate of Si ($\rho Si$) was measured using the radioisotope $^{32}Si$ (Brzezinski and Phillips, 1997; Krause et al., 2011). Cultures were subsampled into acid-washed 250 mL polycarbonate bottles, leaving only enough headspace for the addition of 50 µL of a 3700 Bq $mL^{-1}$ $^{32}Si(OH)_4$ solution of high specific activity (~25,000 MBq µmol $Si^{-1}$). Inoculated samples were incubated for only 4 hours, to minimize changes in pH, under the same temperature and light conditions as the experimental cultures, and then terminated by gentle vacuum filtration on 0.6 µm PC filters. Excess $^{32}Si$ tracer that may have been adsorbed on diatom surfaces was removed by rinsing the filters with 0.6 µm filtered seawater. Filters were mounted on nylon discs, dried at room temperature for 24 hours and covered with Mylar film. Samples were stored until the rate of decay and production of the daughter isotope $^{32}P$ reached equilibrium (~120 days). This delay maximizes accuracy and sensitivity of the beta-counting analysis (Krause et al., 2011).

The $^{32}Si$ activity in the samples was determined by gas-flow proportional counting using a Risø 25-5 low-level beta GM multicounter (DTU Nutech, Denmark) (Krause et al., 2011). Production of new Si (or utilization rate of Si, $\rho Si$) during the incubation was calculated using the measured $^{32}Si$ in particulates at the end of the incubation, the activity of $^{32}Si$ added to the incubation, the

total $Si(OH)_4$ concentration (ambient plus tracer), and the length of the incubation (equation 21 & 22, Brzezinski & Phillips 1997). Estimates of CV for $\rho$Si from triplicate measurements of the same incubation bottle are not available for this study. Our average CV (n = 39) for triplicate measures of $\rho$Si using the same method previously in our lab was 7.5%.

Samples for $SiO_2$ quotas were collected by filtering a 25 mL sample from each culture on a 0.6 μm pore-size PC filter. Filters were dried at 60˚C for 48 hours and then stored in a desiccator at room temperature until further analysis. A 1-hr NaOH digestion was used to convert $SiO_2$ to $Si(OH)_4$ (Brzezinski and Nelson, 1995), the concentration of which was measured with a Beckman DU 530 UV/Vis spectrophotometer (Beckman Coulter, CA, USA) using a reverse-order reagent blank (Brzezinski and Nelson, 1986). The CV for $SiO_2$ quota was 10.3%.

### *4.3.10 Data analysis and statistics*

Values for quotas and utilization rates were normalized by cell volume, except for the $SiO_2$ quota that was normalized by surface area (fmol $\mu m^{-2}$) since Si is deposited on the surface of the diatom cells. For each treatment, triplicate culture data were then averaged (mean of three replicates ± 1 standard deviation). Assumptions of normality and equal variance were validated using the Shapiro-Wilks and Levene's tests, and then two-sample t-tests were used to determine differences between the LC and HC treatments. A sample size of 3 replicates per treatment was used for practicality and because it is common in studies of this nature (Alcaraz-Rocha et al., 2023; Berges et al., 2002; Gao et al., 2012; Hoppe et al., 2017a; Li et al., 2012). Due to the exploratory nature of this study and small sample size, an alpha level of 0.10 (instead of the more typical $\alpha = 0.05$) was used in interpreting the statistical results. To facilitate the comparison of

our results with other studies, the effect size Cohen's $d_s$ was calculated, with a correction for small sample size to reduce overinflation of the result (Appendix D, Table D.1) (Lakens, 2013; Nakagawa and Cuthill, 2007; Rosenberg et al., 2013).

All statistical analyses were performed in Python 3.7 (van Rossum and Drake 2009) and RStudio 1.3.1093 (RStudio, PBC, Boston, MA). Formal Shapiro-Wilks and Levene's tests were run in Python using the native 'scipy' package. Cohen's $d_s$ effect sizes were calculated in Microsoft Excel.

## 4.4 Results

### *4.4.1 General culture conditions*

Final LC and HC cell densities ranged from ~450-1800 cells $mL^{-1}$ and ~1050-2600 cells $mL^{-1}$, respectively, and were not significantly different from each other ($p = 0.21$). Small changes in cell density throughout the experiment were typical of cultures grown under a semi-continuous batch culture regime, and did not affect growth rate throughout the experimental period. The average $pH_T$ of the treatments were different from each other ($p = 0.0003$) and remained overall constant (±0.03 units) over the course of the experiment.

Calculations of $pH_T$ calculated from $C_T$ and TA showed some discrepancy compared to electrode $pH_T$, however the difference between treatments was consistent, with calculated $pH_T$ averaging 0.08-0.09 units lower than the directly measured electrode $pH_T$ (Table 4.1). The LC treatment was designed to simulate current atmospheric concentrations of $CO_2$ of ~410 ppm, whereas the results of the carbonate measurements revealed that the available supply of ambient air was

higher in $CO_2$ than anticipated, 597 ppm (Table 4.1). The HC treatment also resulted in higher $pCO_2$ than expected, 1045 ppm. For OA culture experiments with small volume and high biomass, Hoppe et al. (2012) recommend calculating $pCO_2$ using only TA and measured electrode $pH_T$, which in this case produced a LC $pCO_2$ of 500 ppm, and HC $pCO_2$ of 821 ppm (Table 4.1).

**Table 4.1** Measurements of the carbonate system for low carbon (LC) and high carbon (HC) treatments of the OA experiment with *Thalassiosira rotula*. Electrode $pH_T$ is the mean (n = 3) ± standard deviation of replicate culture measurements from each treatment. Total carbon (C*T*) and total alkalinity (TA) are reported as the mean of two replicates from the end of the experiments. Calculated $pH_T$ is the average pH on the total scale, and $pCO_2$ is the average calculated $pCO_2$ in the exponentially growing cultures after bubbling ambient and 1000 ppm $CO_2$ air at ~0.125 mL min-1. Both $pH_T$ and $pCO_2$ were calculated with CO2SYS using $C_T$, TA, nutrient concentrations, and salinity of the culture media as inputs.

| Treatment | $pH_T$ (electrode) | $C_T$ (µmol $kg^{-1}$) | TA (µmol $kg^{-1}$) | $pH_T$ (calculated) | $pCO_2$ (µatm) | |
|---|---|---|---|---|---|---|
| LC | 7.96±0.01 | 2035.9 | 2174.5 | 7.88 | 597* | 500** |
| HC | 7.75±0.00 | 2110.0 | 2177.5 | 7.66 | 1045* | 821** |

* $pCO_2$ calculated using $C_T$ and TA measurements.
** $pCO_2$ calculated using only the TA and measured electrode $pH_T$, as recommended in Hoppe et al. (2012).

### *4.4.2 Growth rate and cellular morphology*

*T. rotula* grew at the same rate under both pH conditions (Fig. 4.1A). While cell length was unchanged by pH (Fig. 4.1B), other morphological characteristics were affected. Diameter decreased by 7% under HC conditions (Fig. 4.1C) and as a result, both the surface area (-13%) and the volume (-20%) also decreased (Fig. 4.1D and E). The larger decrease in volume relative to surface area at LC resulted in an increased SA:V ratio in the HC treatment of 7% (Fig. 4.1F).

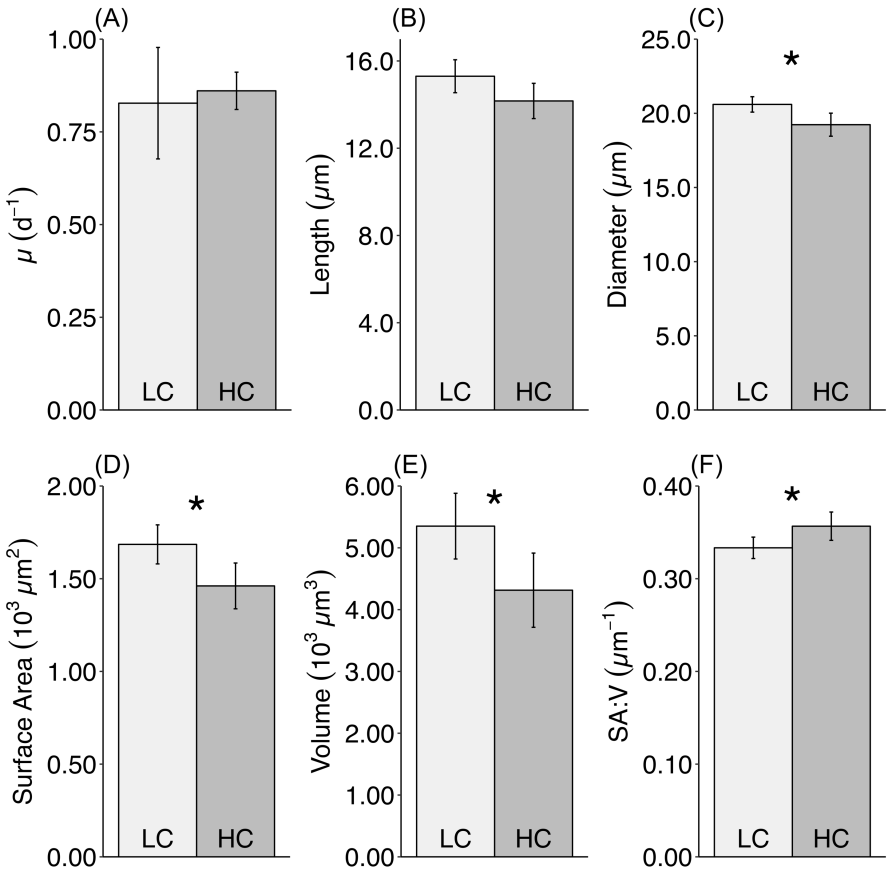


**Figure 4.1.** Cellular characteristics for *Thalassiosira rotula* growing exponentially and acclimated under LC ($pH_T$ 7.96) and HC ($pH_T$ 7.75) conditions. **(A)** Growth rate, μ, **(B)** length, **(C)** diameter, **(D)** surface area, **(E)** volume, and **(F)** surface area-to-volume (SA:V) ratio. All values (bars) are the mean ± standard deviation of the 3 replicate cultures. Differences between treatments with a p-value < 0.10 are indicated by *.

### *4.4.3 Cellular quotas of carbon, nitrogen, silica, and chlorophyll-a*

Lower pH had no effect on cellular quotas of C or N when normalized by cell volume (Fig. 4.2A and B) or by cell number (Appendix D, Table D.1). The $SiO_2$ quota was also unaffected by pH (Fig. 4.2C), whether it was normalized per unit surface area or cell number (Appendix D, Table D.1). Chl-*a* quota did not change with pH, but because a sample was lost from the LC treatment, statistics could not be performed on a sample size (n) equal to 2 (Fig. 4.2D, Appendix D Table D.1).

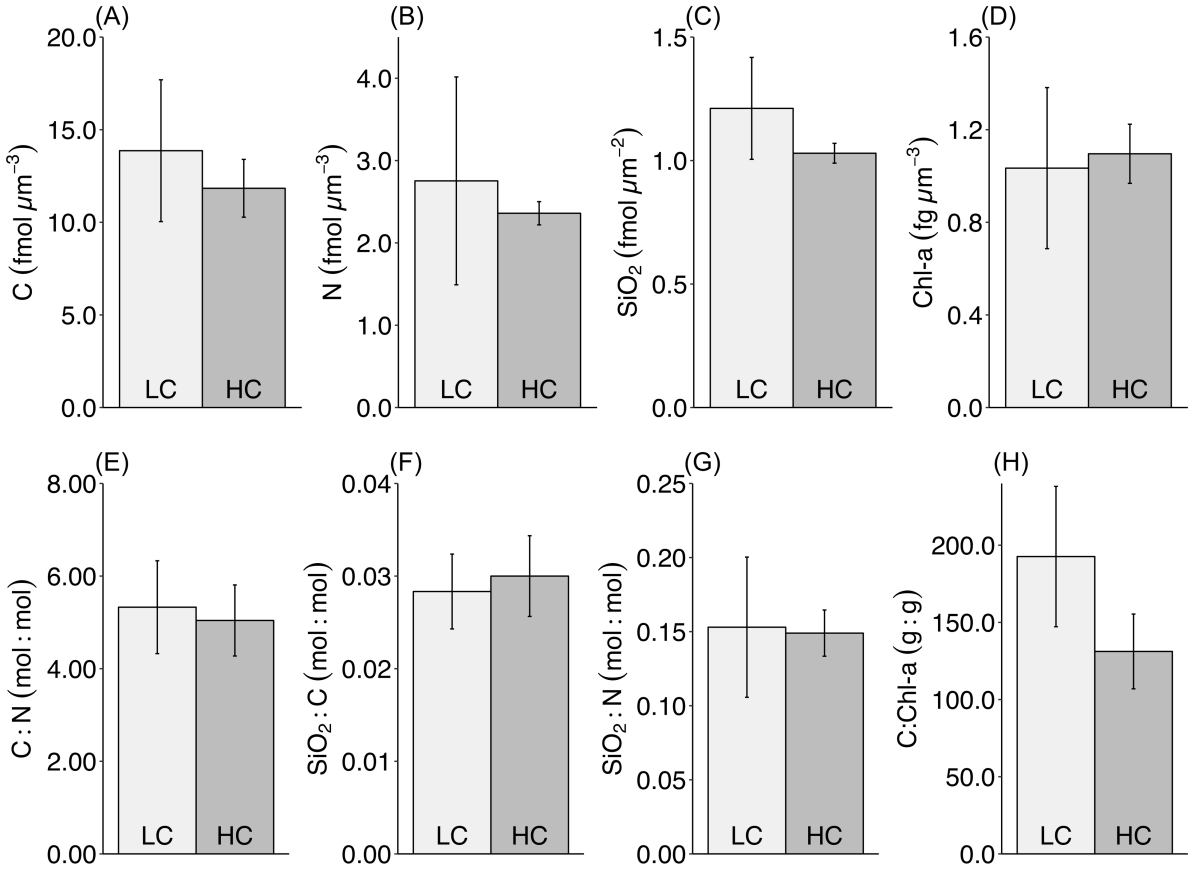


**Figure 4.2.** Cellular quotas and ratios for *Thalassiosira rotula* growing exponentially and acclimated under LC (pHT 7.96) and HC (pHT 7.75) conditions. **(A)** Carbon quota, C, **(B)** nitrogen quota, N, (**C)** silica quota, SiO2, **(D)** chlorophyll-a quota, Chl-a, and quota ratios of **(E)** C:N, **(F)** SiO2:C, **(G)** SiO2:N, and **(H)** C:Chl-a. Quotas are normalized by the average cell volume of each culture, except for SiO2 that is normalized by surface area. All ratios were calculated for individual cultures and averaged (n = 3) for each treatment. Ratios using SiO2 were calculated with the volume normalized quota instead of the surface area normalized quota. All values (bars) are the mean (n = 3) ± standard deviation per treatment. In the LC treatment, n = 2 for the Chl-a quota (D) and C:Chl-a (H) due to a lost Chl-a sample. No differences between treatments were found, all p-values > 0.10.

### *4.4.4 Ratios of cellular quotas*

A decrease in pH did not affect the C:N, $SiO_2$:C and $SiO_2$:N ratios (Fig. 4.2E-G). While there were no changes in the quotas of C and Chl-*a* due to pH, the ratio of C:Chl-*a* had a non-significant but numerically substantial decrease by 32% from 192.7±45.5 g $g^{-1}$ under LC to 131.2±24.2 g $g^{-1}$ under the HC condition (Fig. 4.2H). However, the lost Chl-*a* sample in the LC treatment prevented valid statistical testing of this change.

### *4.4.5 Nutrient utilization rates*

Low pH (HC) had no effect on $\rho$C or $\rho NO_3$ when normalized by cell volume (Fig. 4.3A and B), but when normalized by cell number (Appendix D, Table D.1), $\rho NO_3$ decreased by 20% at lower pH ($p = 0.04$, $d_s = 2.01$). Unlike the $SiO_2$ quota, $\rho$Si was normalized by cellular volume, rather than SA, to better reflect that utilization measurements represent net Si deposition balanced by intracellular processes of Si efflux and incorporation from intracellular reserves. At HC, $\rho$Si did not change when either normalized by volume (Fig. 4.3C) or cell number (Appendix D, Table D.1).

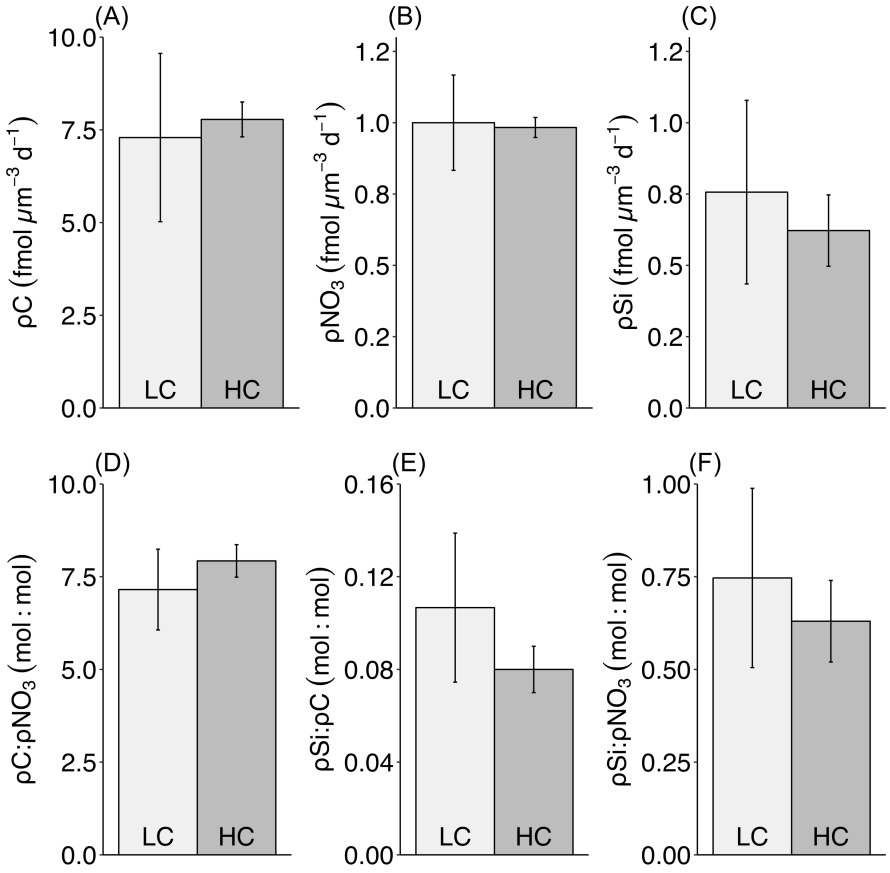


**Figure 4.3.** Nutrient utilization rates and ratios for *Thalassiosira rotula* growing exponentially and acclimated under LC ($pH_T$ 7.96) and HC ($pH_T$ 7.75) conditions. **(A)** Carbon, $\rho$C, **(B)** nitrate, $\rho NO_3$, and **(C)** silicic acid, $\rho$Si, utilization rates, and **(D)** $\rho$C:$\rho NO_3$, **(E)** $\rho$Si:$\rho$C, and **(F)** $\rho$Si:$\rho NO_3$. Ratios were calculated for individual cultures and averaged (n = 3) for each treatment. Utilization rates are normalized by the average cell volume of each culture. Values (bars) are the mean (n = 3) ± standard deviation per treatment. No differences between treatments were found, all p-values > 0.10

### *4.4.6 Ratios of nutrient utilization rates*

There were no significant differences between LC and HC ratios of utilization rates for C, $NO_3^-$, or Si (Fig. 4.3D-F).

## 4.5 Discussion

Under optimal light, temperature and nutrient conditions, *T. rotula* exhibited significant 7% reduction in diameter, 13% reduction in surface area, 20% reduction in volume, and a 7%

increase in SA:V at low pH. A decrease in size was the only significant effect of acidification on this diatom, and there was also evidence of a decrease in $\rho NO_3$ at low pH, although only on a per-cell basis. The growth rate, C, N, and $SiO_2$ quotas, elemental ratios, and utilization rates of C and Si otherwise did not vary between the two pH treatments, demonstrating that under the experimental conditions used in this study, cellular processes in *T. rotula* are generally unaffected by ocean acidification. Although there was deviation from the targeted pH treatments, the difference in pH (~0.2) was still larger than between pre-industrial and current pH levels in the ocean (~0.1 units) and our results therefore demonstrate differences due to a shift in pH rather than a comparison of a specific future high $CO_2$ concentration to the present condition. It is important to note that cells were acclimated for 8 days under the pH treatments, and a longer exposure to low pH conditions may have potentially resulted in additional or larger responses to OA. Furthermore, some of the numerically interesting but not statistically significant results could have been due to low power from sample size equal to 3, rather than no treatment effect.

### *4.5.1 Effect of acidification on growth rate*

A variety of responses of growth rate to decreased pH have been observed in previous studies. An increase in growth rate in the HC treatment would have not been expected as the result of increased $C_T$, since the growth rate of diatoms is not considered to be C limited because of the presence of CCMs (Roberts et al., 2007). However, responses to OA on growth rate and metabolic or photo-chemical processes have been observed under constant light regimes and under the interactions of light with other factors. For example, under constant light and HC, *Phaeodactylum tricornutum* showed increases in growth rate, C fixation and respiration (Wu et al., 2010), and in Wu et al. (2014), OA conditions alone enhanced the growth rate of larger

centric diatom species by up to ~30%, compared to ~5% for smaller centric species. In experiments with multiple irradiance levels and N sources, the growth rate of *Thalassiosira pseudonana* increased under HC only when exposed to high irradiance and with ammonium as the N source instead of $NO_3^-$ (Shi et al., 2015). Contrary to these results, pH has also been observed to have no effects on growth rate in several species of diatoms. *Thalassiosira pseudonana* grown under 400 and 1000 ppm $CO_2$, with either constant or variable light conditions, showed no differences in growth rate due to pH (Li et al., 2020). *Phaeodactylum tricornutum*, *T. pseudonana*, and *Skeletonema costatum* grown under irradiance levels ranging from 5% - 100% of incident natural light decreased their growth rate only at low pH under the highest irradiance levels (Gao et al., 2012). In our study, if *T. rotula* growth rate was affected by an interaction of high irradiance with pH as in Gao et al. (2012b), then there could have been a decrease in growth rate at low pH since we used an optimum irradiance similar to the high irradiance levels used in other studies. However, a difference in growth rate was not observed between pH treatments, and we conclude that the growth rate of *T. rotula* appears to be unaffected by acidification.

### *4.5.2 Morphological changes due to acidification and their impact on physiology*

One of the key traits for phytoplankton biology is cell size, which may affect element quotas and uptake rates (Edwards et al., 2011; Marañón, 2015), and growth rates (Chen and Liu, 2010). Therefore, the observed change in size for *T. rotula* may have biological and ecological implications. While smaller-sized phytoplankton generally have an advantage in low-light and low-nutrient environments, due to more efficient light absorption and more favourable nutrient diffusion characteristics, large cells are more effective at taking up nutrients under high-nutrient

conditions (Marañón, 2015). Intermediate-sized phytoplankton are best able to exploit-high nutrient concentrations and maximize biomass production and growth rate, and typically dominate biomass during blooms (Marañón, 2015). Because cells become less biomass-dense as they increase in size, due to unequal scaling of cellular contents with cell volume (Marañón, 2015), lower cellular quotas per unit volume would be expected for the larger cells in the LC treatment. However, there were no differences between quotas for the differently sized cells between the treatments, suggesting that the size difference was not large enough to cause this effect. Cell size reduction can occur in diatoms as a result of repeated cell division or the onset of environmental stress (Jewson, 1992). However, due to the optimum growth conditions used in our experiment and the lack of effect of pH on the growth rate of *T. rotula,* it is unlikely that a difference in cell size would have been the result of factors other than the $CO_2$ treatment.

A decrease in diameter, SA, and V, as well as a subsequent increase in SA:V were observed under low pH, but the differences between low and high pH may not have been large enough to change the ecological niche or the biogeochemical role of *T. rotula*. Contrary to Wu et al. (2014), who suggested that OA may favour larger phytoplankton species by enhancing their growth without affecting cell size, we found that OA affected the cell size without affecting the growth rate. Their study and ours used *Thalassiosira* species and semi-continuous culturing techniques, differing mostly in how the pH was adjusted and maintained throughout the experiment.

The growth rate, cell size, and $SiO_2$ content of a frustule are significant factors in determining diatom buoyancy and sinking velocity (Miklasz and Denny, 2010), which can affect ocean biogeochemistry (Smetacek, 1999; Tréguer et al., 2018). According to Stokes' law predictions,

the 7% decrease in cell diameter under HC would not result in significant changes in sinking velocity when compared to other *T. rotula* cells (Miklasz and Denny, 2010). Therefore, this change in size due to OA would have minimal effect on sinking from or retention of diatom cells within the euphotic zone, and on nutrient export from surface to deeper waters.

### *4.5.3 Diatom silicification proxies under acidification*

The balance among the processes of influx or uptake of Si, deposition of $SiO_2$, and efflux of Si from the cell determines the $SiO_2$ quota in diatoms (Milligan et al., 2004). Furthermore, the coupling between the processes of Si and C incorporation into diatom cells has an impact on the $SiO_2$:C quotas, which can ultimately affect cell sinking from or retention in the surface ocean. A low $SiO_2$:C content can potentially decrease nutrient export to deep waters through a reduction in ballasting capacity, which results in reduced sinking and increased remineralization throughout the mesopelagic (Ragueneau et al., 2006). However, the effect of OA on diatom sinking and aggregation is complicated by factors such as TEP production (Seebah et al., 2014).

Another function of the $SiO_2$ frustule is as a potential deterrent to grazing (Pondaven et al., 2007), and while the role of $SiO_2$ in preventing grazing is under debate (Bach and Taucher, 2019), preferential grazing could magnify potential pH-induced taxonomic shifts within diatom assemblages, and change the composition of detritus and zooplankton faecal pellets. This effect would alter the role of diatoms in food webs and biogeochemical cycles upon which many ecosystems depend. Petrou et al. (2019) found that OA reduced Si incorporation in a Southern Ocean diatom assemblage but also had varying effects within different taxa, which could potentially lead to different levels of grazing resistance, ballasting, and survival by individual

species. Additionally, Baines et al. (2010) found that diatom $SiO_2$ content varied mostly due to long-term ecological and physical conditions rather than short-term physiological responses to ambient conditions in phytoplankton assemblages from the Southern Ocean and Equatorial Pacific. Milligan et al. (2004) showed that while the influx of Si into *Thalassiosira weissflogii* slightly increased at high $pCO_2$, the Si was not retained as efficiently as under low $pCO_2$. This was reflected in greatly increased efflux of Si from the cell and a correspondingly lower rate of incorporation, decreasing the $SiO_2$ quota by ~20% at high $pCO_2$. Therefore, it is most likely that OA affects assemblage silicification through a combination of effects, with some species having reduced $SiO_2$ content, enhanced grazing on less-silicified taxa, and species shifts as a result of changing pH conditions. Thus, despite the evidence in the literature and the critical impact that reduced Si utilization rates and $SiO_2$ content in diatoms could have on marine biogeochemistry, we did not observe any effects of OA on the utilization of Si or $SiO_2$ quota in *T. rotula.*

Larger cells are typically more heavily silicified due to more $SiO_2$ per cell required to support a greater surface area (Mejía et al., 2013). In our study the larger-celled *T. rotula* under LC treatment had no differences in silicification ($SiO_2$:C and $SiO_2$:N) compared to the smaller cells grown under HC. It is most likely that the $SiO_2$:C and $SiO_2$:N ratios remained constant because modest (although not significant) decreases in the $SiO_2$ quotas were comparable to similar non-significant decreases in the C and N quotas. Therefore, these ratios cannot be used as a true indicator of the degree of cell silicification in this species. Interestingly, there was a large difference between the ratios of $\rho$Si:$\rho$C and $SiO_2$:C, and between $\rho$Si:$\rho NO_3$ and $SiO_2$:N. This indicated either an imbalance between the influx of nutrients into cells and the incorporation of Si, C, and N into cellular materials, or a potential artifact due to the relatively-instantaneously

derived utilization rates while the quotas reflect biomass accumulated over time. An extension of this study would be to expose the cultures to decreased pH for a longer time period to assess whether or not the $SiO_2$:C and $SiO_2$:N particulate ratios eventually reflect the utilization rates.

*Thalassiosira rotula* has been described as having varied valve structure within monocultures, with weakly silicified valves, irregularly formed patterns, and unevenly thickened band structures (Hasle, 1976). The magnitude of $SiO_2$:C and $SiO_2$:N in this study for both LC and HC treatments was much lower than previously reported for *T. rotula* by Brzezinski (1985), where a *T. rotula* isolate (clone 411) was cultured (19˚C, 180-200 µmol photons $m^{-2}$ $s^{-1}$, modified F media) under ambient $pCO_2$ and two different light cycles (18:6h L:D and continuous light). Our stoichiometric measurements demonstrate that the *T. rotula* used in our study (CCMP3362) was generally a more weakly-silicified strain than clone 411 used by Brzezinski (1985). Our $SiO_2$:C and $SiO_2$:N ratios were lower by a factor of ~3 for $SiO_2$:C and ~5 for $SiO_2$:N (Brzezinski 1985) (Appendix D, Table D.2), mostly due to higher C and N quotas and a slightly lower $SiO_2$ quota in both treatments of our study. Ratios of $SiO_2$:C and $SiO_2$:N have also been shown to fluctuate throughout the cell cycle by a factor of up to 2 for *T. pseudonana* (Brzezinski, 1985). Assuming similar variability for our strain of *T. rotula*, the lower $SiO_2$:C and $SiO_2$:N ratios in our experiment could be further explained by the phase of the cell cycle at which they were sampled. Brzezinski (1985) observed increases of 22% in $SiO_2$:C and 4% in $SiO_2$:N for *T. rotula* when changing from a L:D cycle to continuous light. These changes in ratios were several times larger than the non-significant differences in our study, indicating that seasonal environmental variables such as light regime can have a greater effect than pH. Overall, the lower $SiO_2$:C and $SiO_2$:N

ratios of *T. rotula* observed here are likely the result of a combination of culture conditions and the use of a weakly-silicified strain.

### *4.5.4 Carbon and nitrogen cellular processes under acidification*

The lack of significant changes in C and N quotas between treatments in our study was surprising, since smaller cell size should have resulted in higher cellular quotas per unit volume (Marañón, 2015; Marañón et al., 2013; Montagnes and Franklin, 2001). When compared to a different strain of *T. rotula* cultured by Brzezinski (1985) (Appendix D, Table D.2), our C and N quotas of *T. rotula* under both LC and HC were noticeably higher. This was likely due to the cells in our study being much smaller overall regardless of LC and HC treatments, leading to higher quotas than the strain used in Brzezinski (1985). However, compared to other *Thalassiosira* species, the C and N quotas in this study fall within the range of values for species grown under varying temperature, light, and ambient $pCO_2$ (Brzezinski, 1985; Conley et al., 1989), suggesting that our measurements are reasonable for the genus as a whole.

A higher SA:V is known to enhance nutrient utilization rates in smaller cells in comparison to larger cells (Irwin et al., 2006). In diatoms, a more silicified frustule can also act as a more effective pH buffer for increased CCM activity at lower $pCO_2$ (Milligan et al., 2004), which may lead to changes in C fixation. While *T. rotula* cells in our HC treatment were smaller in size and had higher SA:V, $\rho$C was not enhanced. Only cell-normalized $\rho NO_3$ changed at low pH, decreasing by 20%, which did not support the assumption that smaller cells are more effective at utilizing nutrients. This was potentially due to decreased need for N and other nutrients in producing small cells, although there were no observed differences in N quota to support this.

Since the other measures of $NO_3^-$ utilization and N incorporation were not significantly different between pH treatments, it is uncertain how meaningful this observation is. We conclude that under the experimental conditions used in this study, the uptake rates of C and $NO_3^-$ in *T. rotula* were generally unaffected by lower pH.

### *4.5.5 Chlorophyll-a and C:Chl-a ratios under acidification*

The lack of significant change in Chl-*a* quota between pH levels was consistent with studies on other diatom species (Wu et al., 2010; Yang and Gao, 2012). Nevertheless, decreased Chl-*a* under low pH conditions can result after long-term acclimation over a period much longer than commonly used in OA experiments (Alcaraz-Rocha et al., 2023). This may suggest that the practice of acclimating diatoms for 10 generations at exponential growth phase is not sufficient to observe the more subtle effects of pH on Chl-*a* content. Changes in Chl-*a* concentration are particularly important, as the Chl-*a* content of cells has implications for the photosynthetic capabilities of a phytoplankton assemblage. The use of bulk Chl-*a* content as a proxy for phytoplankton biomass and even for photosynthetic rates and production estimates is widespread (Hofmann et al., 2019), and the ratio of C:Chl-*a* is fundamental to remote sensing data outputs and ecosystem modeling (Lomas et al., 2019). Therefore, a change in Chl-*a* under OA would be important for ocean productivity studies and models that investigate current and future climate scenarios.

The C:Chl-*a* ratios in this study were in the high range of values for cultured diatoms, which are typically lower than 200 g $g^{-1}$ (Taylor et al., 1997), and there was no evidence of changes in C:Chl-*a* for *T. rotula* due to OA. In natural assemblages, C:Chl-*a* ratios can vary from ~10 to >

160 (Spilling et al., 2015; Taylor et al., 1997) and it is known that C:Chl-*a* can respond to changes in nutrient availability, temperature, and irradiance (Taylor et al., 1997). Specific C:Chl-*a* ratios can then be constrained to oceanographic regions of interest (Lomas et al., 2019). Carbon:Chl-*a* ratios are thus useful and critical in converting easily-measured Chl-*a* to phytoplankton C biomass that are difficult to obtain in the field (Taylor et al. 1997).

### 4.6 Conclusions

As one of the key members of phytoplankton assemblages, diatoms play a key role in linking Si to C and N biogeochemical cycles. Fully constraining these cycles and quantifying the processes of the biological C pump remain difficult due to uncertainties about how phytoplankton species and assemblages will respond as climate change continues to affect the physical and chemical properties of the ocean. This study adds to the body of work addressing the effect of pH on the morphology, elemental composition, and nutrient physiology in diatoms.

Under the experimental conditions of this study, we provide evidence that low pH can result in decreased cell size in the cosmopolitan *T. rotula*, which may affect the role of this and similar diatoms in biogeochemical processes. In contrast, OA may not affect Si utilization, $SiO_2$ content, or the stoichiometric relationships between Si, C, and N in diatom assemblages dominated by *T. rotula, T. gravida,* or related species. Therefore, based on our results, impacts of OA on diatoms may be small or nil, but natural phytoplankton assemblages and ocean processes are inherently more complex than the conditions imposed in the experiment presented here. Since *Thalassiosira* species are common in northern environments such as the Pacific-Arctic region, which is highly vulnerable to enhanced OA effects (Mathis et al., 2015; Wassmann et al., 2010), further studies

using more diatom species, larger pH differences, and longer acclimation periods may provide better insights of climatic effects on natural diatom assemblages.

# Chapter 5 – Impacts of ocean acidification on phytoplankton from an oligotrophic subtropical ecosystem

## 5.1 Abstract

The Sargasso Sea, located in the western North Atlantic subtropical gyre, is the location of the longest time-series of ocean acidification (OA) observations in the world. However, experimental studies about the direct impact of OA on phytoplankton assemblages in this region are limited. Here, we assessed the effect of decreased pH on a phytoplankton assemblage collected from the deep chlorophyll maximum (DCM) at the Bermuda-Atlantic Time-series Study (BATS) station in November 2018. By exposing replicated treatments to different concentrations of $CO_2$-enriched air at *in situ* temperature and irradiance, we simulated current (~410 ppm) and future (~750 ppm) $CO_2$ conditions. After a seven-day incubation period, we found that rates of carbon ($\rho$C), nitrate ($\rho NO_3$), and silicic acid ($\rho$Si) utilization were unchanged for the entire assemblage, and for < 5 µm and > 5 µm size-fractions. Total and size-fractionated biomass of chlorophyll-*a* (chl-*a*), biogenic silica ($bSiO_2$), and particulate C and N were unaffected as well. Ratios of Si:C, Si:N, C:N, and C:chl-*a* were different for each size-fraction, but unaffected by pH. The abundance of cells and C quotas of *Prochlorococcus*, pico- (< 3 µm), and nano- (3-15 µm) eukaryote phytoplankton were unaffected, but the C-quota of *Synechococcus* decreased significantly under low pH conditions, by 16%. However, because *Synechococcus* abundance was not affected by pH, and the group only makes a very small contribution to DCM assemblage biomass, < 0.2 % of POC, this difference was unlikely to have any impact on biogeochemical cycles and C export. These results highlight the potential for Sargasso Sea phytoplankton assemblages to remain unchanged by OA, and could be used as a baseline for further investigation into the effect of pH when combined with synergistic changes in temperature, irradiance, or nutrient availability.

## 5.2 Introduction

### *5.2.1 Ocean acidification and the Sargasso Sea*

Emissions of anthropogenic $CO_2$ to the atmosphere from a variety of sources (e.g. fossil fuel use, terrestrial and ecological land-use changes, cement and lime manufacturing) continue to increase (Friedlingstein et al., 2020). These emissions not only warm the atmosphere, but also lead to substantial uptake of $CO_2$ by the ocean (Gruber et al., 2019; Khatiwala et al., 2013). This uptake alters seawater chemistry through shifting $CO_2$-carbonate chemical equilibria and lowering seawater pH (Caldeira and Wickett, 2003). This is of global significance for ocean chemistry and marine ecosystems, and understanding the implications of such fundamental changes to the ocean requires both long-term data and rigorous experimental work to assess the response of ecosystems and organisms.

The Bermuda Atlantic Time-series Study (BATS) is located in the Sargasso Sea, in the western North Atlantic subtropical gyre. Measurements of warming, salinification, deoxygenation, and ocean acidification (OA) span more than 40 years from 1983 – present, and is one of the longest global ocean time-series records (Bates and Johnson, 2023). During this period, the surface ocean has warmed by ~1°C, salinity has increased by 0.136, dissolved oxygen has decreased by 6%, and pH has decreased by ~0.1 units, which represents an increase in acidity of more than 30%. The rate of change during the past four decades has not be constant, with most of the changes in temperature, salinity, and deoxygenation taking place since the 2010s, while pH decrease was faster between 1990 – 2010 (Bates and Johnson, 2020). In its present state, ocean chemistry in the Sargasso Sea has been altered beyond the range of seasonal changes that were first observed in the 1980s. For example, winter pH values, which were typically around 8.2 in

past decades, are now similar to the lower summer values from that time, ranging between ~8.08 to 8.10 (Bates and Johnson, 2020). Assuming rates of change do not abate because emissions of anthropogenic $CO_2$ remain high, pH will further decrease to 8.01 (2050) and 7.91 (2100). This high-resolution and long-term dataset is crucial for monitoring OA in the Sargasso Sea and for gaining insight into variability and trends of ocean change. However, experimental work assessing the potential impact of OA on individual species or at a community/assemblage level is scarce in this ocean region.

### *5.2.2 Phytoplankton in the Sargasso Sea*

In midocean subtropical gyres such as the Sargasso Sea, the phytoplankton community is comprised mostly of cyanobacteria, with *Prochlorococcus and Synechococcus* being both predominant in number and constituting a substantial portion of autotrophic biomass (Chisholm, 1992; DuRand et al., 2001; Steinberg et al., 2001). While siliceous eukaryotic phytoplankton such as diatoms can be present in oligotrophic oceans throughout the year, they typically do not represent a substantial portion of phytoplankton assemblages in the Sargasso Sea, except during the relatively small spring bloom and occasional periods of heightened productivity (Hulburt, 1990; Lomas et al., 2013; Nelson and Brzezinski, 1997; Steinberg et al., 2001). Other eukaryotic phytoplankton such as pelagophytes and prymnesiophytes (predominantly coccolithophores) are consistently abundant at the BATS station, with varied contributions by different species depending on season and depth (Steinberg et al., 2001).

Due to their dominance in oligotrophic oceans, prior OA research in the Sargasso Sea has focused on cyanobacteria (e.g. Bao and Gao, 2021; Fu et al., 2007; Lomas et al., 2012; Lu et al.,

2006). Results of these studies show varying direct or interactive effects of OA. For example, higher temperature combined with low pH increased chl-*a* normalized photosynthesis rates of *Synechococcus*, while *Prochlorococcus* photosynthesis was unchanged (Fu et al., 2007). As a result, C and N quotas of *Synechococcus* increased while *Prochlorococcus* maintained constant stoichiometry. Lu et al. (2006) found that the response of *Synechococcus* depended on the strain, with phycocyanin-rich strains benefiting through increased growth rates at low pH. Bao and Gao (2021) showed that low pH significantly increased growth rate and electron transport of *Synechococcus* at both limiting and inhibiting irradiance levels, but those effects were not detected under optimal irradiance. The combination of these results suggests that OA could influence the dominance of different ecotypes of *Synechococcus* compared to *Prochlorococcus*, both geographically and throughout the water column. *Trichodesmium*, another cyanobacteria found in surface waters of the Sargasso Sea, increased $N_2$-use and C-fixation under nutrient replete conditions and elevated $CO_2$ (Lomas et al., 2012). This could increase the input of fixed N into marine ecosystems as $CO_2$ levels in surface waters rise. A caveat to the Lomas et al. (2012) study is that nutrient replete conditions are not representative of surface conditions in oligotrophic oceans such as the Sargasso Sea.

From a eukaryotic phytoplankton perspective, the most studied impact of OA globally is on calcifying phytoplankton, specifically coccolithophores. The physiology of these ubiquitous phytoplankton is likely sensitive to pH because $CaCO_3$ formation depends on $CO_2$ concentrations in seawater. As a result, pH negatively affects the role of coccolithophores in biogeochemical C cycling and food web dynamics (Engel et al., 2005; Peng et al., 2024). Other eukaryotes that are present at the BATS station include diatoms, which can be important for C export during short-

lived blooms both in the Sargasso Sea and in many other parts of the ocean. The response of diatoms to OA has been highly variable. Culture studies have shown little to no direct effects (e.g. Clark et al., 2014; Wyatt et al., 2024), or strong interactive effects between pH and irradiance, temperature, or nutrients (Li et al., 2015; Qu et al., 2021; Seebah et al., 2014). Field studies of oceanic diatom assemblages report a range of responses to OA – positive, negative, or neutral – regarding diatom physiology or assemblage composition (Bach and Taucher, 2019).

### *5.2.3 Study objective*

Due to their vast area, oligotrophic systems such as the Sargasso Sea are important for oceanic primary production (Longhurst et al., 1995; Ryther, 1969), and thus play an essential role in marine food webs and biogeochemical cycles. To better understand how OA affects C, N, and Si nutrient cycles, as well as the biomass and elemental composition of different size-fractions of prokaryotic and eukaryotic phytoplankton, we conducted an OA experiment in November 2018. A phytoplankton assemblage from near the deep chlorophyll maximum (DCM) at the BATS station was exposed to projected late-century pH levels, and we measured the short-term physiological response after seven days of acclimation.

## 5.3 Materials and Methods

### *5.3.1 Experimental design and implementation*

The phytoplankton assemblage used for this OA experiment was collected at the DCM, 96 m deep (~0.5% surface irradiance) at the BATS station (31.668˚N, 64.175˚W) during the BATS353 cruise on 09-November 2018. *In situ* hydrographic measurements were collected with a Sea-Bird SBE-09 *plus* CTD instrument package, and seawater samples were collected using 12 L Niskin

bottles on a CTD-rosette. Sampling was targeted to be at or just below the DCM to maximize biomass and ambient nutrients available for phytoplankton. Acid-washed and pre-rinsed 20-L low-density polyethylene cubitainers were filled with seawater from two 12-L Niskin bottles and amended with a small amount of additional nutrients (1.5 µM $NO_3^-$, 0.8 µM $Si(OH)_4$, and 0.3 µM $PO_4^{3-}$). The cubitainers were then maintained at the in-situ temperature (~23.0°C) and kept in the dark during transport to environmental chambers at the Bermuda Institute of Ocean Sciences (BIOS).

The cultures were incubated in an environmental chamber under conditions equivalent to the irradiance and temperature at which the phytoplankton assemblage was collected. Temperature was monitored with a HOBO Pendant (Onset, MA, USA) and averaged 22.4±0.15°C. Irradiance was checked periodically throughout the experiment with a LI-190R Quantum sensor (LI-COR Environmental, NB, USA) and averaged 15.1±1.4 µmol photons $m^{-2}$ $s^{-1}$. A light:dark cycle of 11-h:13-h was used to simulate the natural diurnal cycle at that time of year. The cultures were continuously bubbled with 0.2 µm filtered sterile air mixtures at ~350 mL $min^{-1}$. Triplicate cultures were exposed to two treatment levels for seven days. For a control treatment, outdoor air (target 410 ppm, LC) was used, while an elevated $pCO_2$ treatment (target 750 ppm, HC) was created by mixing outdoor air with a pure $CO_2$ standard using Aalborg GFC17 mass flow controllers (Aalborg Instruments, Orangeburg, New York, USA). Additional nutrients were added to each culture on the fourth day to ensure limitation by macronutrients did not occur.

Initial (ambient) values for all parameters described below were measured from samples collected from an additional cubitainer that was amended with nutrients and handled identically

as all experimental replicates. Final (end of incubation) values for phytoplankton biomass, elemental composition, flow cytometry, and nutrient utilization rates were obtained from samples collected at day seven, to allow phytoplankton time to acclimate to culture conditions.

### *5.3.2 Carbonate system parameters – pH, total inorganic carbon, and total alkalinity*

To ensure pH changes did not occur during the experiment, the pH was monitored daily. pH was measured by collecting subsamples from each cubitainer into light-proof, airtight containers. A Milwaukee MA911 glass electrode (Milwaukee Instruments, NC, USA) connected to a LabQuest 2 data logger (Vernier, OR, USA) was used to take sequential voltage measurements of pH samples and a TRIS/HCl buffer that matched seawater salinity (Dickson et al., 2007). The pH was calculated on the total scale ($pH_T$) from the difference in voltage as per SOP6A of Dickson et al. (2007).

Total inorganic C ($C_T$) and total alkalinity (TA) were used to constrain the entire carbonate system for ambient conditions and at the end of the OA experiment. Total inorganic C was also used in the calculation of $\rho$C. Ambient samples prior to the experiment were taken directly from the Niskin bottle before filling the cubitainer to avoid contamination. At the end of the experiment, samples were collected from the cultures. 500 mL of sample was withdrawn using a silicon tube and generously overflowed to remove bubbles, a small headspace (~1%) was left to allow for water expansion, and then samples were preserved in a gastight glass bottle with 200 µL of mercuric chloride. Total inorganic C was analyzed using a SOMMA interfaced with a UIC Model 5011 coulometer (UIC Inc., Joliet, IL) (Knap et al., 1997). Total alkalinity was measured using the open cell titration method with a Metrohm dosimat (Metrohm, Herisau, Switzerland)

(Dickson et al., 2007). Calculations of $pH_T$ and $pCO_2$ were done in RStudio v.2023.06.0+421 (Posit Software, Boston, MA) using the package "seacarb" v.3.3.3 with constants for K1 and K2 from Mehrbach et al. (1973) refit by Lueker et al. (2000), and the $KHSO_4$ dissociation constant from Dickson (1990). Uncertainties in the computed carbonate system were estimated by propagating input uncertainties of each parameter ($C_T$, TA, temperature, salinity, nutrient concentrations, and thermodynamic constants) (Orr et al., 2018).

### *5.3.3 Chemical and biological measurements*

The methods used to determine dissolved nutrient concentrations, particulate biomass of chlorophyll-*a*, biogenic silica, particulate C and N, assemblage composition, and nutrient utilization rates are described in detail in Chapter 2. A summary is provided here.

### *5.3.4 Dissolved nutrient concentrations*

Dissolved nutrient concentrations ($NO_3^-$, $PO_4^{3-}$) were determined using continuous segmented flow analysis on an Astoria 2 Nutrient Autoanalyzer according to Barwell-Clarke and Whitney (1996). Separate water samples were collected to determine the ambient concentration of $Si(OH)_4$. These samples were stored at 4°C to avoid polymerization of $Si(OH)_4$, and analyzed colourimetrically with a Beckman DU 530 UV/Vis spectrophotometer (Beckman Coulter, CA, USA) using a reverse-order reagent blank (Brzezinski and Nelson, 1986) and a 10-cm glass cuvette for high analytical precision.

### *5.3.5 Chlorophyll-a concentrations*

Size-fractionated chlorophyll-*a* (chl-*a*) concentrations were determined by sequentially filtering 1.0 L of seawater through a 5.0 µm nominal pore size PC filter and then through a 0.7 µm nominal pore size glass fiber filter (GF-75) (AMD Manufacturing, Ontario, CA). Filtered samples were frozen at -80°C before being extracted in a 90% acetone solution for 24-h at -20°C in the dark. The fluorescence of the extracted samples was read on a recently calibrated Turner-Designs 10AU fluorometer (Turner Designs, CA, USA), and phaeopigment interference was corrected by acidifying each sampling and measuring again on the fluorometer (Parsons et al., 1984). Concentrations of chl-*a* for the total assemblage were determined by adding the two size-fractions together.

### *5.3.6 Biogenic silica concentrations*

Size-fractionated biogenic silica ($bSiO_2$) was collected by sequentially filtering up to 2.0 L of seawater through a 5 µm and 0.6 µm PC filter. Filters were dried at 60°C for 48 hours and then a 1-h NaOH digestion was used to convert $bSiO_2$ to $Si(OH)_4$ (Brzezinski and Nelson, 1995), using fresh reagents and polymethylpentene centrifuge tubes (Diagenode, Belgium) to ensure low blanks and limit of detection. The concentration of $Si(OH)_4$ was measured with a Beckman DU 530 UV/Vis spectrophotometer (Beckman Coulter, CA, USA) using a reverse-order reagent blank (Brzezinski and Nelson, 1986) and 10-cm glass cuvettes for high precision. Concentrations of $bSiO_2$ for the total assemblage were determined by adding the two size-fractions together.

### *5.3.7 Utilization rates of carbon and nitrate*

The utilization rates of carbon ($\rho$C) and $NO_3^-$ ($\rho NO_3$) were measured using the $^{13}C$-$^{15}NO_3^-$ dual tracer method (Dugdale and Goering, 1967; Slawyk et al., 1977). Seawater was gently subsampled from each replicate cubitainer into acid-washed 1.2 L PC bottles, leaving only enough headspace for isotope additions. Samples were inoculated to a final enrichment target of ~10% ambient $C_T$ using $KH^{13}CO_3$ (99% purity, Cambridge Isotopes Laboratories, MA, USA). For the determination of $\rho NO_3$, the same samples were inoculated using $Na^{15}NO_3$ (98+% purity, Cambridge Isotopes Laboratories, MA, USA). Since *in situ* $NO_3^-$ was expected to be initially low, i.e. ~1 µM, and our amendments were only 1.5 µM, $^{15}NO_3^-$ was added at the detection limit for $NO_3^-$ concentration (0.1 µM) to minimize artificial nutrient enhancement. Inoculated samples were incubated alongside each original replicate cubitainer in the environmental chamber to maintain the same temperature and irradiance. Each incubation was run for 24-h before being ended by vacuum filtration. To collect the < 5 µm size-fraction, half of the volume in the culture was pre-filtered through a 5.0 µm PC filter (which was discarded) and then through a combusted GF-75 filter. The remaining half of each sample was filtered through a combusted GF-75 filter to collect the total fraction. All filters were dried at 60°C for 48-h. The isotopic composition ($^{13}C$:$^{12}C$ and $^{15}N$:$^{14}N$) and total C and N content were measured at the Stable Isotope Facility at the University of California Davis with a PDZ Europa ANCA-GSL elemental analyzer and a PDZ Europa 20-20 isotope ratio mass spectrometer (Sercon Ltd., Cheshire, UK). Carbon utilization rate was calculated using equation 3 of Hama et al. (1983) and the $C_T$ concentration for each replicate. $\rho NO_3$ was calculated using equation 3 in Dugdale and Wilkerson (1986). Filtered samples were not acidified, therefore the C and N content represent total particulate C (PC) and nitrogen (PN). Since PC and PN were determined from samples obtained at the end of a

24-h incubation, values were back-calculated using $\rho C$ and $\rho NO_3$ to determine the C and N content at the time of sampling.

### *5.3.8 Utilization rate of silicic acid*

The utilization rate of $Si(OH)_4$ ($\rho Si$) was measured using $^{32}Si$ incubation experiments (Brzezinski and Phillips, 1997; Krause et al., 2011). Seawater was collected from each cubitainer into acid-washed 500 mL polycarbonate bottles and inoculated with 1670 Bq (100,000 DPM) of a 6500 Bq $mL^{-1}$ solution of high specific activity $^{32}Si(OH)_4$ (~25,000 MBq µmol $Si^{-1}$). The amount of $^{32}Si(OH)_4$ added was less than $3.8x10^{-8}$ µmol Si, a negligible increase in the total $Si(OH)_4$ available. Inoculated samples were incubated in the same manner as for $\rho C$ and $\rho NO_3$. After the 24-h incubation, each sample was sequentially filtered under gentle vacuum pressure onto 5.0 µm and 0.6 µm PC filters, and rinsed with 0.6 µm filtered seawater to remove any excess $^{32}Si$ tracer that may have not been incorporated. Each filter was air-dried at room temperature on a nylon disk before being covered with Mylar film. Samples were stored for at least 5 half-lives (~120 days) to reach secular equilibrium before measurement.

$^{32}Si$ activity in the sample was determined by gas-flow proportional counting using a Risø 25-5 low-level beta GM multicounter (DTU Nutech, Denmark) (Krause et al., 2011), and $\rho Si$ was calculated using the ambient $Si(OH)_4$ and $bSiO_2$ concentrations at the time of sampling (Brzezinski and Phillips, 1997). The $\rho Si$ for the total fraction was obtained by addition of the data collected from the 5 µm and 0.6 µm filters. Specific uptake rate ($V_{Si}$) was also calculated for each size-fraction by normalizing $\rho Si$ by $bSiO_2$ biomass.

### *5.3.9 Cell abundance and particulate organic carbon quota*

Flow cytometry samples for cell abundance were collected in 2.0 mL polyethylene cryovials. After preservation with paraformaldehyde (0.5% final concentration) at 4°C for ~1-h, the samples were flash frozen in liquid nitrogen, and then stored at -80°C. Samples were analyzed per Casey et al. (2013), using a high-speed jet-in-air Influx™ Cell Sorter (formerly Cytopeia, Inc., Seattle, WA, now Becton Dickenson), modified for small particle detection with a 100X objective magnification. Cellular quotas of C (POC) for all taxa were determined by analyzing natural populations and monocultures of cells by flow cytometry and an elemental analyzer, calibrating the forward scatter pulse height output to POC content for each (Casey et al., 2013).

### *5.3.10 Silicifier contributions to carbon and nitrate utilization*

Contributions by silicifiers to $\rho$C and $\rho NO_3$ were determined by converting size-fractionated $\rho$Si into N and C units (Giesbrecht and Varela, 2021) with the following equations, where the *sf* subscript indicates a rate or ratio for a specific size-fraction.

$$Silicifier\ \rho C_{sf} = \frac{\rho Si_{sf}}{Si{:}\,C_{sf}} \tag{1}$$

$$Silicifier\ \%\ \rho C_{sf} = 100 \times \frac{\rho Si_{sf}}{Si{:}\,C_{sf}} \times \rho C_{total}{}^{-1} \tag{2}$$

$$Silicifier\ \rho NO_{3\,sf} = \frac{\rho Si_{sf}}{Si{:}\,N_{sf}} \tag{3}$$

$$Silicifier\ \%\ \rho NO_{3\,sf} = 100 \times \frac{\rho Si_{sf}}{Si{:}\,N_{sf}} \times \rho NO_{3\,total}{}^{-1} \tag{4}$$

Carbon and $NO_3^-$ utilization for each size-fraction was calculated separately using large (> 5 μm), and small (< 5 μm) Si utilization rates. Si:C and Si:N ratios depended on the size-fraction

being used, described below. A total value for C and $NO_3^-$ utilization by all silicifiers was calculated by adding the large and small size-fractions.

For cells > 5 μm, we used average Si:C:N ratios measured for cultured nano-diatoms (< 20 μm) grown under nutrient replete conditions, which were Si:C = 0.09 ± 0.03 and Si:N = 0.80 ± 0.35 (Brzezinski, 1985). To determine the average large diatom (> 5 μm) contribution to $\rho$C and $\rho NO_3$, these Si:C and Si:N ratios were used as constants in equations 1 – 4 along with $\rho$Si > 5 μm and total $\rho$C or $\rho NO_3$. For cells < 5 μm, the same Si:C:N ratios were used, as the BATS station is known to export small diatoms of the genera *Minidiscus* and *Minutocellus* (Amacher et al., 2013; Cruz et al., 2021), which can be as small as 2 μm in diameter and have Si:C and Si:N ratios similar to those reported by Brzezinski (1985) (Leblanc et al., 2018).

The cyanobacteria *Synechococcus* had very low abundance (< 100 cells $mL^{-1}$) at the depth sampled for this experiment, compared to abundance of nearly 10,000 cells $mL^{-1}$ in surface waters. Therefore, unlike in Chapter 2, contributions by silicifiers to $\rho$C and $\rho NO_3$ did not include estimates for amounts attributed to *Synechococcus*.

### *5.3.11 Data treatment and visualization*

Culture data were averaged for each treatment and presented as the mean of three replicates ± 1 standard deviation. Figures were made in RStudio using the package “ggplot2”.

### *5.3.12 Data analysis and statistics*

Assumptions of normality and equal variance were validated, and then two-sample t-tests were used to determine differences between the LC and HC treatments. Data that did not meet the assumptions of normality and equal variance were compared using non-parametric two-sample t-tests. The effect size Cohen's $d_s$ was calculated to facilitate comparison with other studies, and was corrected for small sample size to reduce overinflation of the result (Lakens, 2013; Rosenberg et al., 2013). All statistical tests and effect sizes were calculated in Excel (Microsoft, Redmond, WA).

The potential for false-positive results exists when making many statistical comparisons, however a specific family-wise error rate correction factor (e.g. Bonferroni) was not applied to the p-values in this study. Instead, statistically significant results were interpreted cautiously, to avoid missing true effects but to also prevent assigning too much importance to them.

## 5.4 Results

### *5.4.1 Ambient conditions*

The phytoplankton assemblage collected from 96 m on 09-Nov 2018 was very similar to measurements made three days prior, on 06-Nov, which are reported in Chapter 2. Concentrations of total and size-fractionated particulates and nutrient utilization rates indicated that most of the biomass and productivity was in the < 5 µm size-fraction (Table 5.1). Larger cells had higher Si:C ratios than smaller cells, and large cells had more C per unit chl-*a* as well. The assemblage was numerically dominated by *Prochlorococcus*, 36700±1500 cells $mL^{-1}$, followed by picoeukaryotes (810±50 cells $mL^{-1}$) and much lower abundance of *Synechococcus* (200±30 cells $mL^{-1}$) and nanoeukaryotes (25±6 cells $mL^{-1}$).

### *5.4.2 General culture conditions*

Carbonate system measurements indicated that the control treatment was equal to 405 µatm $pCO_2$ and the experimental treatment was equal to 794 µatm $pCO_2$ (Table 5.2). This resulted in a difference of 0.25 pH units between the LC ($pH_T$ = 8.06±0.01) and HC ($pH_T$ = 7.81±0.00) treatments. These final $pCO_2$ values were reasonably consistent with the recommended levels for a two-treatment experiment (control and 750 ppm) in the guide to best practices for OA research (Riebesell et al., 2011), and the control compared very well with ambient conditions. Throughout the experiment, macronutrient concentrations ($NO_3^-$, $PO_4^{3-}$, $Si(OH)_4$) were replete in all replicates of both treatments, and there were no significant differences between any nutrient concentrations by the end of the acclimation period (Appendix E, Table E.2).

**Table 5.1.** Hydrographic and physiological measurements of a phytoplankton assemblage collected at the BATS station on 09-Nov, prior to the start of the acidification experiment. Values reported as the mean±sd of triplicate measurements, ‡ indicates n = 2. Carbonate system uncertainties as described in Table 5.2. NA indicates a value that could not be calculated due a zero denominator in a ratio.

| **Ambient values prior to OA experiment** | | | |
|---|---|---|---|
| *Hydrographic* | | *Dissolved nutrients (amended)* | |
| Temperature (°C) | 22.8 | $NO_3^-$ (µmol $L^{-1}$) | 1.27 *(2.65)* |
| Salinity (PSU) | 36.78 | $PO_4^{3-}$ (µmol $L^{-1}$) | 0.13 *(0.39)* |
| Irradiance (µmol photons $m^{-2}$ $s^{-1}$) | 18.45 | $Si(OH)_4$ (µmol $L^{-1}$) | 0.71 *(1.28)* |
| *Carbonate system* | | | |
| Total inorganic C (µmol $kg^{-1}$) | 2102±2‡ | | |
| Total alkalinity (µmol $kg^{-1}$) | 2409±4‡ | | |
| $pH_T$ | 8.02±0.01‡ | | |
| *Particulate biomass* | | | |
| Chlorophyll-a | | Particulate carbon | |
| Total chl-a (ng $L^{-1}$) | 109±16 | Total PC (µmol $L^{-1}$) | 2.6±0.17 |
| > 5 µm chl-a (ng $L^{-1}$) | 8±3 | > 5 µm PC (µmol $L^{-1}$) | 0.4±0.2‡ |
| < 5 µm chl-a (ng $L^{-1}$) | 102±16 | < 5 µm PC (µmol $L^{-1}$) | 2.2±0.02‡ |
| % chl-a > 5 µm (%) | 7±3 | % PC > 5 µm (%) | 15±7‡ |
| Biogenic silica | | Particulate nitrogen | |
| Total $bSiO_2$ (nmol $L^{-1}$) | 11±0.4 | Total PN (µmol $L^{-1}$) | 0.5±0.03 |
| > 5 µm $bSiO_2$ (nmol $L^{-1}$) | 7.2±0.8 | > 5 µm PN (µmol $L^{-1}$) | 0.0±0.0‡ |
| < 5 µm $bSiO_2$ (nmol $L^{-1}$) | 3.7±0.5 | < 5 µm PN (µmol $L^{-1}$) | 0.6±0.1‡ |
| % $bSiO_2$ > 5 µm (%) | 66±5 | % PN > 5 µm (%) | 0.0±0.0‡ |
| *Particulate ratios* | | | |
| Total C:N (mol $mol^{-1}$) | 5.3±0.6 | Total Si:N (mol $mol^{-1}$) | 0.022±0.002 |
| > 5 µm C:N (mol $mol^{-1}$) | NA | > 5 µm Si:N (mol $mol^{-1}$) | NA |
| < 5 µm C:N (mol $mol^{-1}$) | 3.9±0.7‡ | < 5 µm Si:N (mol $mol^{-1}$) | 0.006±0.002‡ |
| Total Si:C (mol $mol^{-1}$) | 0.004±0.0001 | Total C:chl-a (g $g^{-1}$) | 291±25 |
| > 5 µm Si:C (mol $mol^{-1}$) | 0.021±0.009‡ | > 5 µm C:chl-a (g $g^{-1}$) | 600±500‡ |
| < 5 µm Si:C (mol $mol^{-1}$) | 0.002±0.0002‡ | < 5 µm C:chl-a (g $g^{-1}$) | 260±50‡ |
| *Nutrient uptake rates* | | | |
| Carbon utilization rate | | Silicon utilization rate | |
| Total $\rho C$ (nmol $L^{-1}$ $d^{-1}$) | 154±5 | Total $\rho Si$ (nmol $L^{-1}$ $d^{-1}$) | 8±2 |
| > 5 µm $\rho C$ (nmol $L^{-1}$ $d^{-1}$) | 27±11 | > 5 µm $\rho Si$ (nmol $L^{-1}$ $d^{-1}$) | 4±2 |
| < 5 µm $\rho C$ (nmol $L^{-1}$ $d^{-1}$) | 129±8 | < 5 µm $\rho Si$ (nmol $L^{-1}$ $d^{-1}$) | 5±0.4 |
| % $\rho C$ > 5 µm (%) | 17±7 | % $\rho Si$ > 5 µm (%) | 40±9 |
| Nitrate utilization rate | | Specific uptake rate of Si | |
| Total $\rho NO_3$ (nmol $L^{-1}$ $d^{-1}$) | 17±0.7 | Total $V_{Si}$ ($d^{-1}$) | 0.76±0.18 |
| > 5 µm $\rho NO_3$ (nmol $L^{-1}$ $d^{-1}$) | 5±2 | > 5 µm $V_{Si}$ ($d^{-1}$) | 0.49±0.24 |
| < 5 µm $\rho NO_3$ (nmol $L^{-1}$ $d^{-1}$) | 12±1 | < 5 µm $V_{Si}$ ($d^{-1}$) | 1.33±0.3 |
| % $\rho NO_3$ > 5 µm (%) | 27±11 | | |
| *Cell abundances and C quotas* | | | |
| *Prochlorococcus* (cells $mL^{-1}$) | 36700±1500‡ | *Prochlorococcus* (fg POC $cell^{-1}$) | 105±1.1‡ |
| *Synechococcus* (cells $mL^{-1}$) | 200±30‡ | *Synechococcus* (fg POC $cell^{-1}$) | 170±40‡ |
| Picoeukaryotes (cells $mL^{-1}$) | 810±50‡ | Picoeukaryotes (fg POC $cell^{-1}$) | 1530±60‡ |
| Nanoeukaryotes (cells $mL^{-1}$) | 25±6‡ | Nanoeukaryotes (fg POC $cell^{-1}$) | 4900±600‡ |

**Table 5.2.** Calculated $pH_T$ and $pCO_2$ for low carbon (LC) and high carbon (HC) treatments of the OA experiment conducted on a phytoplankton assemblage collected from the BATS station on 09-Nov 2018. Calculated $pH_T$ is the average pH on the total scale, and $pCO_2$ is the average calculated $pCO_2$ after bubbling ambient and enriched $CO_2$ air at ~350 mL/min. Uncertainties are the geometric mean of the average propagated analytical uncertainty and the treatment standard deviation. Full carbonate system parameters including individual replicates and estimates of uncertainty are presented in Appendix E, Table E.1.

| ***Treatment*** | **$pH_T$ (calculated)** | **$pCO_2$ (µatm)** |
|---|---|---|
| LC | 8.06±0.01 | 405±10 |
| HC | 7.81±0.00 | 794±11 |

### *5.4.3 Biomass and elemental composition*

There were no significant differences in phytoplankton biomass or elemental composition between LC and HC treatments at the end of the experimental period (Fig. 5.1A–D). Size-fractionated measurements did not show differences either (Table 5.3). High variance between replicates within each treatment resulted in particulate ratios with high variance as well. Therefore, ratios of C:N, Si:C and Si:N were unchanged, for the whole assemblage (Fig. 5.1E–G) and size-fractions (Table 5.3). Due to undetectable PN > 5 µm under HC, ratios of C:N and Si:N could not be calculated or compared to the LC treatment for larger cells.

Particulate C:chl-*a* ratios for LC and HC were not different from each other either (Fig. 5.1H), however the values for both treatments were exceptionally high, 1630±110 g $g^{-1}$ for LC and 1500±300 g $g^{-1}$ for HC. This was particularly high compared to ambient C:chl-*a*, which was 291±25 g $g^{-1}$ (Table 5.1)

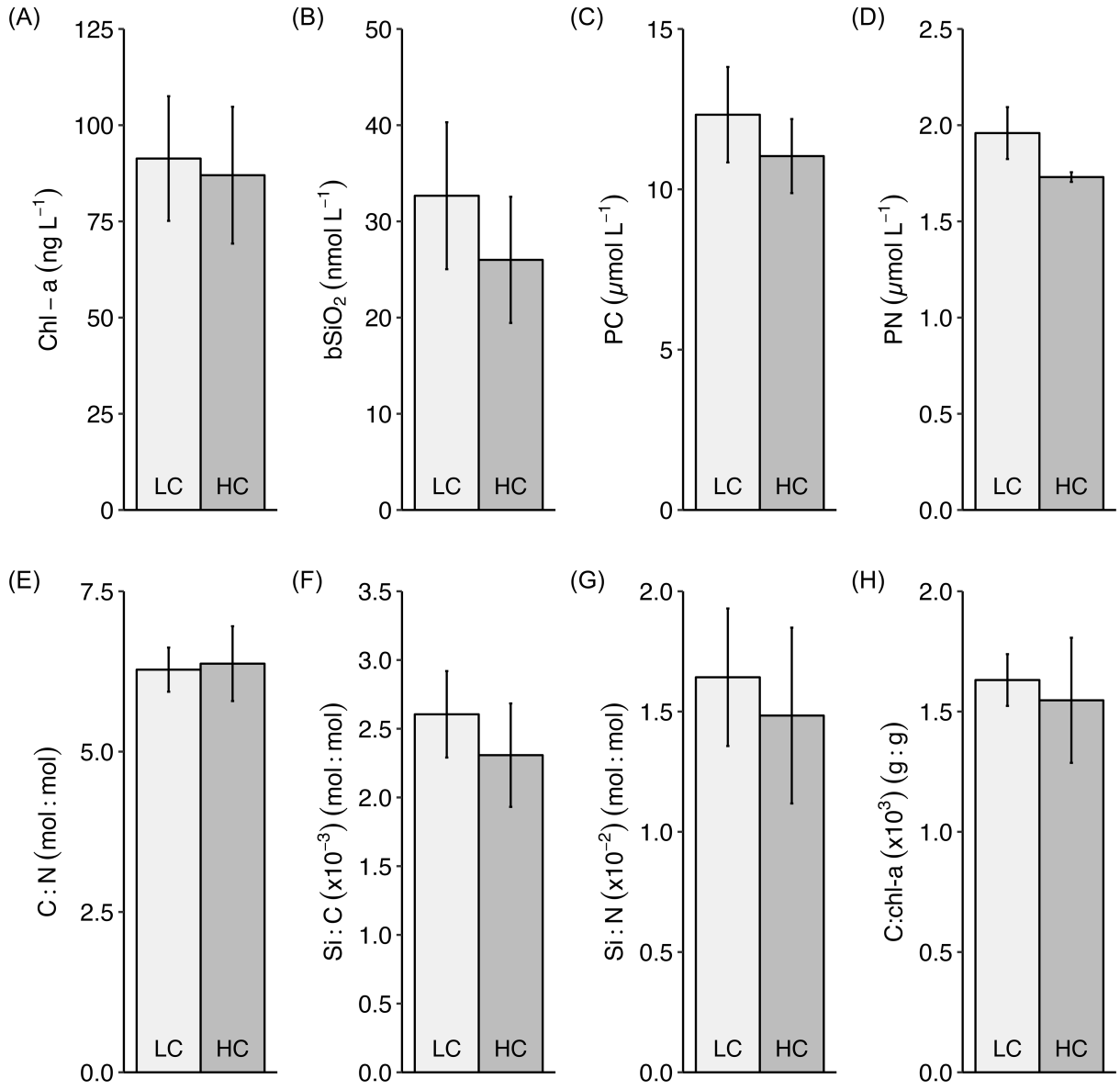


**Figure 5.1.** Differences in total biomass and elemental composition for the entire phytoplankton assemblage after exposure to low carbon (LC, ambient pH) and high carbon (HC, acidification) treatments. Phytoplankton were collected from the BATS station on 09-Nov 2018 and measurements were made at the end of the incubation period (7 days). **(A)** Chlorophyll-*a*, chl-*a*, **(B)** biogenic silica, $bSiO_2$, **(C)** particulate C, PC, and **(D)** particulate N, PN, are the mean (n = 3) of replicates for each treatment ± standard deviation. Elemental ratios, **(E)** C:N, **(F)** Si:C, **(G)** Si:N, and **(H)** C:chl-*a.* Panels marked with an asterisk (*) indicate a significant result ($p < 0.05$) between the LC and HC treatments. Differences in PN (panel D) were tested using a non-parametric t-test due to unequal variance in each treatment. Summary of statistical tests in Appendix E, Table E.2.

**Table 5.3.** Size-fractionated particulate concentrations under low carbon (LC, ambient pH) and high carbon (HC, acidification) treatments of the OA experiment, conducted on a phytoplankton assemblage collected from the BATS station on 09-Nov 2018. ‡ indicates when sample size < 3. P-values marked with # were calculated with a non-parametric two-sample t-test due to unequal variances. All other p-values were calculated using a parametric two-sample t-test. P-values marked with an asterisk (*) indicate a significant result. NA indicates a value that could not be calculated due to insufficient sample size or a zero denominator in a ratio.

| **Parameter** | **LC (pH = 8.06)** | **HC (pH = 7.81)** | **p-value ($\alpha$ = 0.05)** | **Cohen's $d_s$** |
|---|---|---|---|---|
| *Particulate biomass* | | | | |
| Chlorophyll-a | | | | |
| > 5 µm chl-a (ng $L^{-1}$) | 4±1 | 4±1 | 0.67 | 0.30 |
| < 5 µm chl-a (ng $L^{-1}$) | 88±17 | 83±17 | 0.76 | 0.21 |
| % chl-a > 5 µm (%) | 4±2 | 5±1 | 0.61 | 0.36 |
| Biogenic silica | | | | |
| > 5 µm $bSiO_2$ (nmol $L^{-1}$) | 19±6 | 12±5 | 0.21 | 0.98 |
| < 5 µm $bSiO_2$ (nmol $L^{-1}$) | 13±2 | 13±2 | 0.95 | 0.04 |
| % $bSiO_2$ > 5 µm (%) | 58±5 | 47±7 | 0.08 | 1.51 |
| Particulate carbon | | | | |
| > 5 µm PC (µmol $L^{-1}$) | 0.7±0.5 | 0.1±0.2 | 0.16 | 1.13 |
| < 5 µm PC (µmol $L^{-1}$) | 11.6±1.4 | 11.3±1.7 | 0.82 | 0.16 |
| % PC > 5 µm (%) | 6±4 | 1±2 | 0.19 | 1.03 |
| Particulate nitrogen | | | | |
| > 5 µm PN (µmol $L^{-1}$) | 0.1±0.1 | 0.0±0.0 | 0.23# | 1.10 |
| < 5 µm PN (µmol $L^{-1}$) | 2.0±0.3 | 2.3±0.4 | 0.35 | 0.69 |
| % PN > 5 µm (%) | 5±5 | 0±0 | 0.25# | 1.06 |
| *Particulate ratios* | | | | |
| > 5 µm C:N (mol $mol^{-1}$) | 8.2±5.0‡ | NA | NA | NA |
| < 5 µm C:N (mol $mol^{-1}$) | 5.9±0.7 | 5.0±1.3 | 0.35 | 0.69 |
| > 5 µm Si:C (mol $mol^{-1}$) | 0.073±0.09 | 0.020‡ | NA | NA |
| < 5 µm Si:C (mol $mol^{-1}$) | 0.001±0.000 | 0.001±0.000 | 0.79 | 0.18 |
| > 5 µm Si:N (mol $mol^{-1}$) | 0.166±0.14‡ | NA | NA | NA |
| < 5 µm Si:N (mol $mol^{-1}$) | 0.007±0.002 | 0.006±0.002 | 0.54 | 0.44 |
| > 5 µm C:chl-a (g $g^{-1}$) | 2900±2300 | 1600‡ | NA | NA |
| < 5 µm C:chl-a (g $g^{-1}$) | 1600±200 | 1700±400 | 0.82 | 0.16 |

### *5.4.4 Nutrient utilization rates*

Nutrient utilization rates were unaffected by OA, for both the total assemblage (Fig. 5.2A–D) as well as > 5 µm and < 5 µm size-fractions (Table 5.4). Rates were still much higher in small cells than the > 5 µm size-fraction, accounting for > 90% of both $\rho$C and $\rho NO_3$ in either treatment. Ratios of nutrient utilization rates are not shown or compared because high variability in $\rho$C, $\rho NO_3$, and $\rho$Si resulted in extreme variance in ratios.

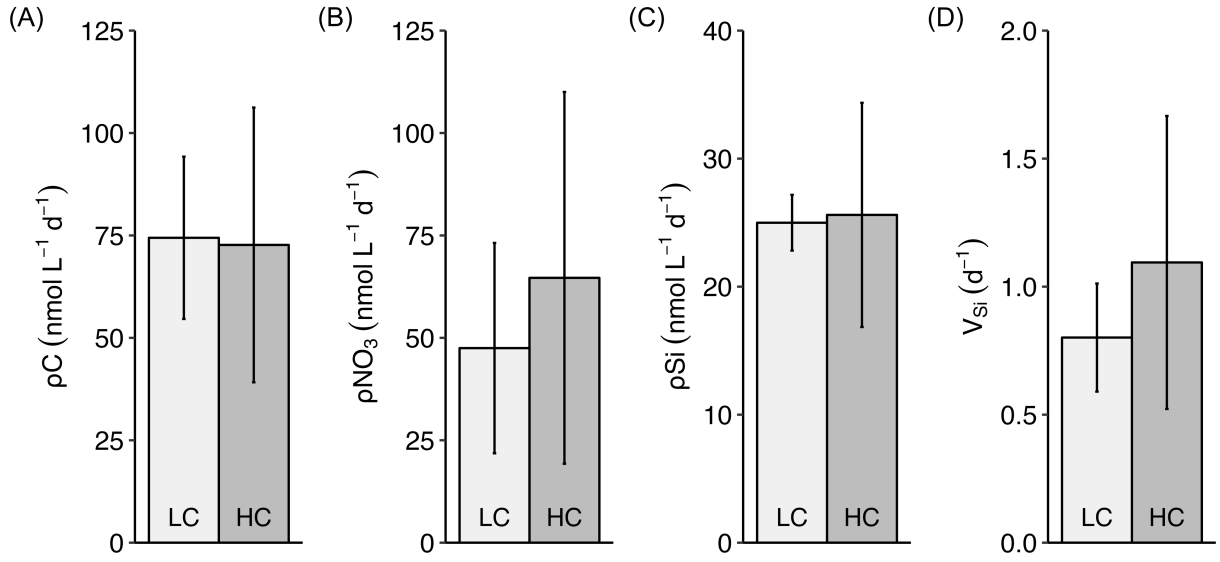


**Figure 5.2.** Differences in nutrient utilization rates for the entire phytoplankton assemblage after exposure to low carbon (LC, ambient pH) and high carbon (HC, acidification) treatments. Phytoplankton were collected from the BATS station on 09-Nov 2018 and measurements were made at the end of the incubation period (7 days). **(A)** Utilization rate of C, $\rho$C, **(B)** utilization rate of $NO_3^-$, $\rho NO_3$, **(C)** utilization rate of Si, $\rho$Si, and **(D)** specific uptake rate of Si, $V_{Si}$, are the mean (n = 3) of replicates for each treatment ± standard deviation. Panels marked with an asterisk (*) indicate a significant result ($p < 0.05$) between the LC and HC treatments. Summary of statistical tests in Appendix E, Table E.2.

**Table 5.4.** Size-fractionated nutrient utilization rates under low carbon (LC, ambient pH) and high carbon (HC, acidification) treatments of the OA experiment, conducted on a phytoplankton assemblage collected from the BATS station on 09-Nov 2018. P-values marked with # were calculated with a non-parametric two-sample t-test due to unequal variances. All other p-values were calculated using a parametric two-sample t-test. P-values marked with an asterisk (*) indicate a significant result.

| **Parameter** | **LC (pH = 8.06)** | **HC (pH = 7.81)** | **p-value ($\alpha$ = 0.05)** | **Cohen's $d_s$** |
|---|---|---|---|---|
| *Nutrient uptake rates* | | | | |
| Carbon utilization rate | | | | |
| > 5 µm $\rho$C (nmol $L^{-1}$ $d^{-1}$) | 5±4 | 3±4 | 0.59 | 0.38 |
| < 5 µm $\rho$C (nmol $L^{-1}$ $d^{-1}$) | 71±25 | 71±30 | 1.00 | 0.00 |
| % $\rho$C > 5 µm (%) | 7±6 | 5±7 | 0.65 | 0.32 |
| Nitrate utilization rate | | | | |
| > 5 µm $\rho NO_3$ (nmol $L^{-1}$ $d^{-1}$) | 5±9 | 7±9 | 0.84 | 0.14 |
| < 5 µm $\rho NO_3$ (nmol $L^{-1}$ $d^{-1}$) | 43±21 | 59±40 | 0.54 | 0.43 |
| % $\rho NO_3$ > 5 µm (%) | 8±14 | 7±7 | 0.96 | 0.04 |
| Silicon utilization rates | | | | |
| > 5 µm $\rho$Si (nmol $L^{-1}$ $d^{-1}$) | 7±2 | 7±2 | 0.85 | 0.13 |
| < 5 µm $\rho$Si (nmol $L^{-1}$ $d^{-1}$) | 18±2 | 19±7 | 0.84# | 0.15 |
| % $\rho$Si > 5 µm (%) | 29±7 | 28±5 | 0.85 | 0.13 |
| > 5 µm $V_{Si}$ ($d^{-1}$) | 0.4±0.3 | 0.6±0.3 | 0.43 | 0.57 |
| < 5 µm $V_{Si}$ ($d^{-1}$) | 1.33±0.11 | 1.5±0.7 | 0.76# | 0.21 |

### *5.4.5 Community composition and particulate organic carbon quotas*

In addition to size-fractionated measurements of biomass and productivity, cell abundance was determined using four different classes: *Prochlorococcus*, *Synechococcus*, picoeukaryotes (< 3 μm), and nanoeukaryotes (3 – 15 μm). Relative to other groups, *Prochlorococcus* was by far the most abundant, approximately $8.0 \times 10^4$ cells $mL^{-1}$ (Fig. 5.3A) in both treatments on average. By comparison, *Synechococcus* abundance was less than 100 cells $mL^{-1}$ (Fig. 5.3B) in all replicates, and picoeukaryotes were less than 500 cells $mL^{-1}$ in all replicates of both treatments (Fig. 5.3C). Nanoeukaryotes were 7±3 cells $mL^{-1}$ under HC conditions, and undetectable in all replicates of the LC treatment (Fig. 5.3D). There were no statistically significant differences between LC and HC treatments for the abundance of *Prochlorococcus, Synechococcus,* picoeukaryotes, or nanoeukaryotes (Appendix E, Table E.2). Even though nanoeukaryote abundance was undetectable under LC conditions, high variance under HC conditions meant the difference was still not significant when compared using a non-parametric test ($p > 0.05$).

The only significant difference observed in this study was a 16% decrease in POC per cell for *Synechococcus* under HC conditions ($p = 0.02$, $d_s = 0.66$) (Fig 5.3F, Appendix E, Table E.2). Quotas of POC for *Prochlorococcus* and picoeukaryotes remained unchanged (Fig. 5.3E & F), and for nanoeukaryotes, POC quota was unable to be statistically tested due to the disappearance of that size-class in the LC treatment (Fig. 5.3H).

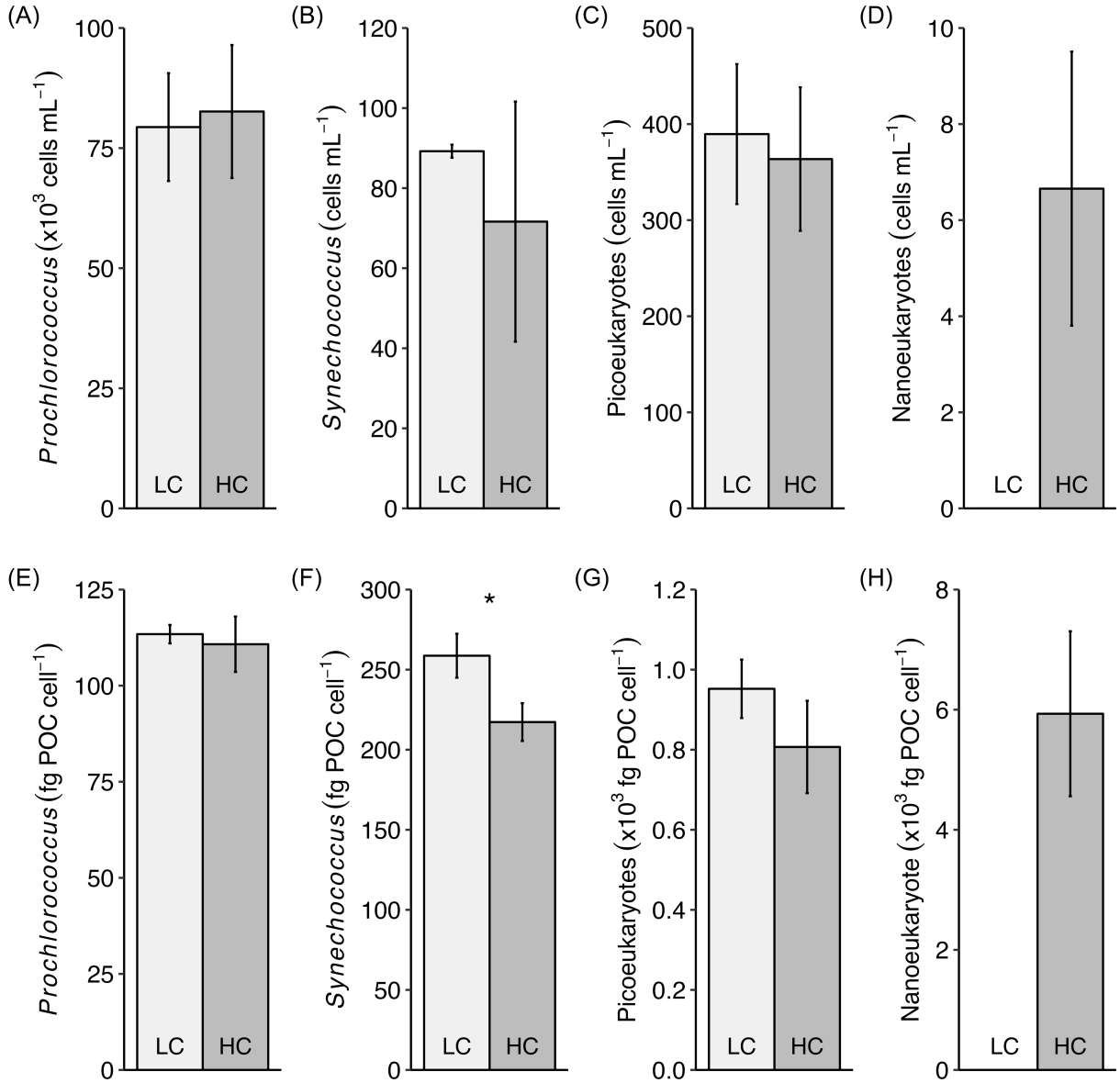


**Figure 5.3.** Differences in cellular abundance and POC quotas for different prokaryotic and eukaryotic groups in the entire phytoplankton assemblage after exposure to low carbon (LC, ambient pH) and high carbon (HC, acidification) treatments. Phytoplankton were collected from the BATS station on 09-Nov 2018 and measurements were made at the end of the incubation period (7 days). **(A)** *Prochlorococcus*, **(B)** *Synechococcus*, **(C)** picoeukaryotes (< 3 µm), and **(D)** nanoeukaryotes (3 – 15 µm). POC quotas for **(E)** *Prochlorococcus*, **(F)** *Synechococcus*, **(G)** picoeukaryotes, and **(H)** nanoeukaryotes. All values are the mean (n = 3) of replicates for each treatment ± standard deviation. Panels marked with an asterisk (*) indicate a significant result ($p < 0.05$) between the LC and HC treatments. Differences in *Synechococcus* and nanoeukaryote abundance (panels B and D) were tested using a non-parametric t-test due to unequal variance in each treatment. Nanoeukaryote POC quota was not calculated for LC in panel H. Summary of statistical tests in Appendix E, Table E.2.

### *5.4.6 Silicifier contributions to carbon and nitrate utilization*

There were no significant differences between treatments for the total or size-fractionated contribution of silicifiers to either $\rho$C or $\rho NO_3$ (Table 5.5). Similar to results from Chapter 2, small cells < 5 µm contributed the most to both estimates. Total contributions by silicifiers to $\rho$C exceeded the total $\rho$C, which was separately measured. Therefore, these calculations were clearly an overestimate, because $\rho$Si was much higher than could be expected relative to total $\rho$C for even a pure diatom culture, which this phytoplankton assemblage was not. Total contributions by silicifiers to $\rho NO_3$ were more reasonable, accounting for between 50 – 66% of separately measured total $\rho NO_3$ but were still likely overestimates.

**Table 5.5.** Silicifier contributions to $\rho$C and $\rho NO_3$ under low carbon (LC, ambient pH) and high carbon (HC, acidification) treatments of the OA experiment, conducted on a phytoplankton assemblage collected from the BATS station on 09-Nov 2018. P-values marked with $^{\#}$ were calculated with a non-parametric two-sample t-test due to unequal variances. All other p-values were calculated using a parametric two-sample t-test. P-values marked with an asterisk (*) indicate a significant result.

| **Silicifier contributions to $\rho$C and $\rho NO_3$** | **LC (pH = 8.06)** | **HC (pH = 7.81)** | **p-value ($\alpha$ = 0.05)** | **Cohen's $d_s$** |
|---|---|---|---|---|
| Total $\rho C_{Si}$ (nmol $L^{-1}$ $d^{-1}$) | 278±24 | 300±100 | 0.91 | 0.08 |
| > 5 µm $\rho C_{Si}$ (nmol $L^{-1}$ $d^{-1}$) | 80±30 | 77+24 | 0.85 | 0.13 |
| < 5 µm $\rho C_{Si}$ (nmol $L^{-1}$ $d^{-1}$) | 197±18 | 210±80 | 0.83$^{\#}$ | 0.15 |
| | | | | |
| Total $\rho NO_{3\text{-}Si}$ (nmol $L^{-1}$ $d^{-1}$) | 31±3 | 32±11 | 0.91 | 0.08 |
| > 5 µm $\rho NO_{3\text{-}Si}$ (nmol $L^{-1}$ $d^{-1}$) | 9±3 | 9±3 | 0.85 | 0.13 |
| < 5 µm $\rho NO_{3\text{-}Si}$ (nmol $L^{-1}$ $d^{-1}$) | 22±2 | 23±9 | 0.83$^{\#}$ | 0.15 |

## 5.5 Discussion

The present study examined short-term (7 days) acclimation to OA of a DCM phytoplankton assemblage occurring at the BATS station in November. Concentrations of particulates and nutrient utilization rates were generally highly variable among replicates, which may have obfuscated direct pH-related effects, but there were some interesting observations within the data.

### *5.5.1 Size-fractionated biomass concentrations and nutrient utilization rates*

Our size-fractionated measurements of biomass and utilization rates used slightly different size ranges compared to assemblage composition data. The < 5 μm size-fraction contained both prokaryotic groups as well as picoeukaryotes. Cells > 5 μm generally corresponded to nanoeukaryotes, although it is known that some species of eukaryotic phytoplankton occupy a size range that would also include them in the < 5 μm cells. For example, the BATS station is known to export diatoms as small as 2 μm (Amacher et al., 2013; Cruz et al., 2021), and coccolithophores can be near the 5 μm cutoff as well, though they typically average 5 – 6 μm at the BATS station (DuRand et al., 2001). Because of this, and the absence of statistically significant differences in our size-fractionated data, when our discussion focuses on pico- and nanoeukaryotic groups or a specific size-fraction, we cannot necessarily draw conclusions related to the other size-fractionated measures, although some inferences are possible.

Larger cells consistently made up a small proportion of cell abundances, total biomass, and nutrient utilization rates at the beginning of the experiment. As a group, nanoeukaryotes did not thrive during the acclimation period under either treatment condition. Nanoeukaryote cell

abundance was more than 70% lower in the HC treatment compared to starting concentrations, and nanoeukaryotic cells were completely absent from all replicates of the LC treatment. Large (> 5 μm) size-fractionated biomass decreased similarly when compared to the start of the experiment, with some measures (e.g. PC & PN under HC) having very low or even undetectable concentrations. It was contradictory that there were undetectable concentrations of > 5 μm PC and PN under HC conditions at the end of the experiment but nanoeukaryotes were present, while under LC conditions nanoeukaryotes disappeared entirely but > 5 μm biomass was still measured. Because the > 5 μm size-fraction was still present under LC conditions, but particle concentrations of $bSiO_2$, PC, and PN were very low or undetectable under HC, it appeared that numerically interesting (though not statistically significant) decreases occurred for several >5 μm measurements. The only explanation for the presence of > 5 μm biomass but an absence of nanoeukaryotes is that cells larger than 15 μm, the cutoff for nanoeukaryote classification in this study, were present. Phytoplankton larger than 15 μm do occur in the Sargasso Sea (Cotti-Rausch et al., 2020; Goldman, 1993), and may have therefore accounted for the > 5 μm chl-a biomass, other particulates, and nutrient utilization rates.

A past study demonstrated that on average, microphytoplankton (20 – 200 μm) comprised 9±6% of integrated chl-*a* biomass and 15±12% of integrated C utilization (Cotti-Rausch et al., 2020). At a depth similar to that sampled for this experiment (~100 m) though, microphytoplankton typically contributed more to biomass than productivity (Cotti-Rausch et al., 2020). In our measurements, cells > 5 μm accounted for around 5% of chl-*a* biomass and on average 5 – 7% of $\rho$C, which are on the low end of the range of values reported by Cotti-Rausch et al. (2020). Looking at silicifiers specifically, in this study large cells accounted for about half of $bSiO_2$, 30%

of $\rho$Si, and $V_{Si}$ was between 0.4±0.3 – 0.6±0.3 $d^{-1}$, indicating that diatoms were present and actively growing. Particulate ratios of Si:C and Si:N for the > 5 μm size-fraction were notably higher compared to the < 5 μm size-fraction. As such, we have evidence that a portion of the phytoplankton assemblage was large-celled and actively growing, with contributions by both large and small diatoms, but it was uncertain how the large eukaryotic cells responded to pH treatment compared with their response to incubation conditions. Therefore, we were unable to draw any conclusions about the impact of OA in the Sargasso Sea on diatoms or other large eukaryotic species that were present.

### *5.5.2 Assemblage composition, and anomalous carbon to chlorophyll-a ratios*

In addition to the declines observed in nanoeukaryotes, all other classes of cells, which were part of the < 5 μm size-fraction, experienced shifts in their relative proportions during the experiment. Compared to the start of the experiment, *Prochlorococcus* approximately doubled in abundance in both pH treatments, with no difference between treatments, while *Synechococcus* and picoeukaryotes decreased by a factor of approximately 2 or more. Because *Prochlorococcus* overwhelmingly dominated the entire assemblage both before and at the end of the experiment, measurements from < 5 μm cells are likely a reflection of the physiology and biomass of *Prochlorococcus* rather than *Synechococcus* or picoeukaryotes. This was reflected in a particularly unusual result, exceptionally high C:chl-*a*. Both treatments had values > 1500 g $g^{-1}$ at the end of the experiment, which was dramatically higher than ambient C:chl-*a*, 291±25 g $g^{-1}$. Even ambient C:chl-*a* was fairly high, given that most oceanic ratios range between ~10 – 160 g $g^{-1}$ (Taylor et al., 1997). This anomalous ratio suggests that either chl-*a* content was uncharacteristically low for the entire assemblage, or PC was unusually high. *Prochlorococcus*,

specifically *Prochlorococcus marinus*, is known to be widespread in the Sargasso Sea and to make substantial contributions to autotrophic biomass and productivity (Goericke and Welschmeyer, 1993). Since this species lacks chl-*a* (Goericke and Repeta, 1992), and accounted for such a large portion of biomass in this experiment, it explains the low chl-*a* content in the whole assemblage. In addition, picocyanobacteria increase their production of C-rich transparent exopolymers (TEPs) when growth rates are reduced (Deng et al., 2016). Therefore, exceptionally high C:chl-*a* is explained by the combined effects of *Prochlorococcus* abundance and low chl-*a* pigment concentrations, as well as very high PC concentrations that resulted from the experimental conditions.

### *5.5.3 Cyanobacteria particulate organic carbon at low pH*

The only significant difference between pH treatments was a reduced POC quota for *Synechococcus* under HC conditions. While this may be a false-positive result due to the number of statistical comparisons that were made in this study, there is precedent in the literature that the C physiology of *Synechoccocus* may be affected by pH. A previous OA study in the Sargasso Sea demonstrated that elevated $pCO_2$ increased *Synechococcus* growth at low and high light, but not optimal light (Bao and Gao, 2021), suggesting *Synechococcus* may respond differently at various depths. The irradiance used in our experiment was similar to the optimal irradiance defined by Bao and Gao (2021), perhaps explaining why we did not see an effect of pH on *Synechococcus* growth. Unlike a different previous study where higher $pCO_2$ boosted C incorporation in certain strains of *Synechococcus* (Lu et al., 2006), we observed a decrease in C content for *Synechococcus*, possibly due to energy allocation being redirected towards maintaining growth rather than carbohydrate storage. For the entire < 5 μm size-fraction,

decreased C content was not observed, likely because *Prochlorococcus* dominated through abundance and C content was unchanged for those cells. In fact, *Synechococcus* only made up < 0.2% of total POC content under the HC treatment, compared to 96% by *Prochlorococcus.* Since *Prochlorococcus* showed no changes in C content, similar to findings of Fu et al. (2007), any potential impact of OA due to changes in C quota of *Synechococcus* or other groups was minimal. However, nearly 20% of total POC within the surface mixed layer can be attributed to *Synechococcus* at the BATS station in late summer (Chapter 2), so if lower pH caused a reduction in POC quota in surface waters as well, this could have a meaningful impact on the C cycle.

### *5.5.4 Ocean acidification research in oligotrophic regions*

In addition to the studies discussed above, the impact of OA on low-nutrient phytoplankton assemblages has been investigated in different oligotrophic regions of the ocean using *in situ* mesocosm experiments, which are more realistic and ecologically relevant. Results have been mixed. During a mesocosm-based study that maintained oligotrophic conditions for the duration of the experiment, OA was found to have no effect on any of the tested parameters, including growth rates, primary productivity, particulate concentrations, or respiration rates (Gazeau et al., 2017; Maugendre et al., 2017). In a different mesocosm experiment in the eastern subtropical North Atlantic, phytoplankton assemblages experienced considerable shifts in species composition in response to both lower pH, and after the addition of nutrients to simulate upwelling (Taucher et al., 2018). Lastly, Bach et al. (2016) suggested that communities in nutrient-limited regions may be more sensitive to changes in carbonate chemistry than those in areas with abundant inorganic nutrients. While mesocosm conditions are much more

representative of real-world conditions than small incubation experiments, these authors noted that it became increasingly difficult to detect $CO_2$-induced effects over time due to variability within replicates of treatments. Our results agree more closely with Maugendre et al. (2017), where OA has no impact on the assemblage productivity, but conflicting results between these larger and likely more-realistic mesocosm experiments demonstrate that research into OA in oligotrophic regions is still in its infancy.

Overall productivity in the Sargasso Sea has decreased significantly in the past decade (Lomas et al., 2022), potentially driven by increases in sea surface temperature and reduced nutrient inventories. The ecosystem has compensated for reduced eukaryotic biomass by increasing export efficiency of POC through more efficient nutrient use by cyanobacteria, preventing observed changes in carbon export (Lomas et al., 2022). This ongoing adaptation to climate change with respect to productivity and carbon export demonstrates that the Sargasso Sea is more resilient to change due to its diverse phytoplankton community. While our study did not find any indications of physiological compensation by phytoplankton to OA, it did demonstrate that the DCM assemblage was unaffected by OA with regards to productivity, composition, and biomass.

### 5.6 Conclusions

Oligotrophic regions like the Sargasso Sea are expected to expand due to ocean warming (Polovina et al., 2008), potentially affecting global biogeochemistry and primary production. Cyanobacteria and eukaryotic phytoplankton play key roles in oligotrophic marine ecosystems, but their response to OA remains uncertain. Experimental studies are essential to understand how

OA might affect the biological carbon pump and other biogeochemical cycles. This study added to the small pool of literature on the response of phytoplankton physiology and composition to OA in the Sargasso Sea. Very limited significant differences between pH treatments were observed, only a reduction in POC quota for *Synechococcus*, a group which contributed very little to overall biomass or productivity. All other measures of community composition, biomass, and physiology were unaffected both for the entire assemblage and in different size-fractions. These findings highlight how phytoplankton assemblages in this oligotrophic region may remain unchanged as future conditions continue to shift due to anthropogenic activity.

# Chapter 6 – Physiological responses to high $CO_2$ by a summertime diatom assemblage in the northern Bering Sea

## 6.1 Abstract

Ocean acidification (OA) resulting from rising anthropogenic $CO_2$ concentrations has been identified as a stressor affecting marine ecosystems. This effect combined with earlier sea ice retreat and warming of waters in the Pacific Arctic can potentially have deleterious impacts on marine biota. We present the results of an experiment that assessed the effect of OA on the nutrient utilization rates, elemental composition, and taxonomy of a summertime diatom-dominated Arctic phytoplankton assemblage. Seawater samples were collected from the chlorophyll-*a* (chl-*a*) maximum at a station in the Chirikov Basin, in the northern Bering Sea. Three $CO_2$ treatments (~400, 750, and 1100 ppm) were continuously bubbled through triplicate replicates, adjusting pH to 8.26, 7.90, and 7.70. To prevent nutrient limitation, incubated samples were amended with nitrate ($NO_3^-$), phosphate ($PO_4^{3-}$) and silicic acid ($Si(OH)_4$). Under controlled temperature and light conditions, a bloom resulted, with distinct pre-bloom, exponential growth, and post-bloom phases at all pH levels throughout the six-day long experiment. Daily measurements of dissolved nutrient concentrations, particulate concentrations of chl-*a*, biogenic silica ($bSiO_2$), carbon (PC), and nitrogen (PN), and nutrient utilization rates ($\rho$) of C ($\rho$C), $NO_3^-$ ($\rho NO_3$), and $Si(OH)_4$ ($\rho$Si) showed that there were no statistically significant differences between pH treatments for any measurements. Lugol's samples and DNA metabarcoding revealed that diatoms made up approximately 90% of total cells throughout the experiment, and there were no statistically conclusive differences in taxonomy between pH treatments. Overall, our results demonstrate that at OA levels exceeding present-day natural variability, diatom assemblages in the northern Bering Sea are unaffected by OA, but further investigation into the interactive effects of OA with other changing environmental characteristics is necessary.

## 6.2 Introduction

Located in the Pacific Arctic Region (PAR), the northern Bering Sea is one of the most productive marine ecosystems in the world (Grebmeier, 2012; Grebmeier et al., 2006). Due to notable warming trends and marine heatwave events (Barkhordarian et al., 2024; Walsh et al., 2020), the area has experienced complex multi-year variability in sea ice cover (Frey et al., 2015). In addition to dramatic changes in sea ice dynamics and temperature caused by climate change, Arctic marine ecosystems are susceptible to ocean acidification (OA), the process by which the pH of seawater is reduced by uptake of anthropogenic $CO_2$ (Feely et al., 2004). The PAR is particularly vulnerable to OA due to mixing processes and low temperatures that naturally precondition the water column to have a more acidified state compared to more temperate environments (Mathis et al., 2015). Other mechanisms that reduce seawater pH in high-latitude environments include high respiration rates following seasonal production (Bates et al., 2009; Cross et al., 2012; Mathis et al., 2011) or contributions of freshwater from sea ice melt and terrestrial runoff (Bates et al., 2014; Mathis et al., 2011). Globally, observations from open-ocean time-series show that the uptake of higher levels of $CO_2$ has already decreased surface water pH by 0.1 units (Bates and Johnson, 2023) compared to pre-industrial times. In high-latitude surface marine waters, the potential rate of OA is particularly concerning (Fabry et al., 2009), and the overall decrease in pH is projected to be larger than elsewhere, with modelled declines exceeding 0.45 pH units by the year 2100, compared to 1995–2014 (Kwiatkowski et al., 2020).

Most prior research on OA has focused on the effects of a reduced saturation state ($\Omega$) for calcite and aragonite as pH declines (e.g. Feely et al. 2004; Hoegh-Guldberg et al. 2007; Fabry et al.

2008; Goethel et al. 2017). These two minerals are the most common forms of calcium carbonate ($CaCO_3$) used by marine calcifying organisms such as bivalves, corals, zooplankton and some phytoplankton groups. Calcifying phytoplankton, specifically coccolithophores, have been subject to extensive research (Engel et al., 2005; Langer et al., 2009; Riebesell et al., 2000; Seifert et al., 2020). In general, OA is considered to be detrimental to marine calcifiers, especially during larval stages of invertebrate species, and for calcifying algae and corals. However, a recent systematic review of nearly 1000 papers and across all calcifying taxa suggests that while certain life-stages and taxa are certainly sensitive to OA, the majority of observations (70%) indicate that many species may have the potential to acclimate (Leung et al., 2022). As a result, future hypotheses should not be constrained by the expectation of negative impacts.

Non-calcifying organisms are under-represented in the OA literature. In particular, diatoms, a globally ubiquitous and very important member of phytoplankton assemblages, have only been rigorously studied for approximately the past 15 years. Diatoms account for nearly half of marine primary production (Nelson et al., 1995), and contribute one-fifth of total C fixed through photosynthesis on a global scale (Field et al., 1998). They are also key players in biogeochemical cycles of C, N, and Si (Tréguer et al., 2021), in which they control the fluxes of nutrients from surface waters to the ocean interior (Alldredge and Silver, 1988; Ragueneau et al., 2006; Tréguer et al., 2018). Because diatoms consume silicic acid, $(Si(OH)_4$, to build their rigid frustule out of amorphous biogenic silica, ($bSiO_2$) (Martin-Jezequel et al., 2000), they control the balances of Si in the surface ocean (Nelson et al., 1995; Tréguer et al., 2021). Due to the crucial roles of diatoms for Earth's primary production and in nutrient cycling, any shift in their physiology or

abundance compared to other phytoplankton could have major impacts on marine food webs, affect ecosystem services like fisheries and oxygen production, and change deep-ocean $CO_2$ sequestration (Armbrust, 2009; Tréguer et al., 2018). For natural diatom assemblages, most studies show that decreased pH increases diatom abundance and biomass, and assemblage composition shifts towards larger species (Bach and Taucher, 2019). Despite recent increases in diatom OA research, it remains poorly understood how OA will influence phytoplankton assemblages in the PAR, which are almost entirely comprised of diatoms during the summer bloom period (Giesbrecht et al., 2019; Giesbrecht and Varela, 2021). Changes in the contributions of diatoms to phytoplankton assemblages, or their utilization of Si, could have far-reaching effects on biogeochemical fluxes in the Arctic because the northern Bering Sea and Bering Strait act as the main import gateway for silicic acid ($Si(OH)_4$) to the Arctic (Torres-Valdés et al., 2013), which in turn exports nutrients to the global ocean. Therefore, understanding the impact of anthropogenic change on Si-related processes in the Bering Sea is critical to refine uncertainties about the future of the marine biogeochemical cycle of Si (Tréguer et al., 2021).

There are few experimental studies that directly assessed the effects of enhanced $pCO_2$ (typically 750 – 1000 µatm $CO_2$) on Arctic phytoplankton in general, or diatoms specifically. The results of those studies frequently showed mixed impacts. For example, primary production and phytoplankton growth increased with OA in the Arctic (Coello-Camba et al., 2014; Engel et al., 2013; Holding et al., 2015), but some of the potential benefits may have been offset by negative impacts due to increased temperatures that accompany climate-driven $CO_2$ increases in the atmosphere (Holding et al., 2015). On the other hand, other experiments showed that Arctic

phytoplankton may be capable of compensating for environmental variability and resisting OA under enhanced irradiance levels (Hoppe et al., 2017a) and temperatures (Hoppe et al., 2018). Under OA, Arctic phytoplankton assemblages can shift towards smaller-celled species (Brussaard et al., 2013), or the dominant diatom species can change (Hoppe et al., 2017b), but some studies have also shown that community composition is not affected by pH (Hoppe et al., 2018; Newbold et al., 2012). Clearly, evidence is mixed about the resilience of Arctic phytoplankton to OA. Regardless of whether OA increases or decreases different measures of productivity or assemblage composition, changes in phytoplankton physiology could cause substantial changes within Arctic ecosystems, impacting food webs and biogeochemical cycles. It is uncertain to what extent existing studies can be applied to different times of year or regions in the PAR, so with this study we seek to address biogeochemical impacts of OA during the summertime bloom period in the northern Bering Sea.

## 6.3 Materials and Methods

### *6.3.1 Water sampling and experiment setup*

During the 2022 Distributed Biological Observatory (DBO) cruise onboard the *CCGS Sir Wilfrid Laurier*, a phytoplankton assemblage was sampled on July 18 at station DBO2.5 (UTBS-1, DBO2 region), located at 64°59.545 N 169°8.286 W in the Chirikov Basin, north of St. Lawrence Island.

Using a CTD rosette, seawater was collected from the depth of maximum chlorophyll-*a* (chl-*a*) at 15 m, equal to 1% surface irradiance. To determine if large zooplankton might potentially affect the incubations, one 12 L Niskin bottle was initially filtered through a 250 μm Nitex mesh

and examined under a dissecting microscope. Large chains of diatoms were present on the mesh, however, no obvious large zooplankton were visible. Therefore, water was not pre-filtered when setting up the incubations to retain the complete diatom assemblage. Seawater was collected from the Niskin bottles into nine separate acid-washed 11-L low-density polyethylene cubitainers, for a total of three cubitainers per experimental treatment, and then incubated under different pH levels for six days.

*Incubation conditions*

Cubitainers were placed in an on-deck incubator covered with mesh to reduce irradiance by 50%, equivalent to a water depth of approximately 5 m. Flowing seawater maintained the temperature of the deck incubator at 7.4±1.2°C, which was 4.0°C warmer than *in situ* conditions. Surface irradiance varied depending on cloud-cover, but based on irradiance measured using the CTD package during hydrocasts for the rest of the cruise, mean surface irradiance during daytime was 565 µE $m^{-2}$ $s^{-1}$. Macronutrients were added to each cubitainer, which increased the concentrations to approximately 25 µM $NO_3^-$, 2 µM $PO_4^{3-}$, and 35 µM $Si(OH)_4$. Following nutrient additions, each container was gently mixed and fitted with custom silicone tubing and sampling fittings.

*pH manipulation and monitoring*

In order to manipulate pH in the three experimental treatments, three different air-$CO_2$ concentrations were prepared by mixing industrial grade $CO_2$ (99.5% purity) (Linde Canada Inc., ON, CA) into compressed zero-$CO_2$ air. Flow rates were controlled using Bronkhorst EL-FLOW Select mass flow controllers (Bronkhorst High-Tech B.V., NL). Gases were mixed at a rate of

0.27 – 0.74 mL $CO_2$ $min^{-1}$ into 0.67 L zero-air $min^{-1}$ using FlowView v.1.23 software (Bronkhorst High-Tech B.V., NL). The $CO_2$ concentrations were regularly monitored with a LI-850 $CO_2/H_2O$ gas analyzer (LI-COR Environmental, NE, USA) to ensure consistency throughout the experiment. $CO_2$ concentrations on average were 398±2 ppm, 763±5 ppm, and 1122±6 ppm.

Each cubitainer in the deck incubator was connected to the gas mixing setup using aquarium air tubing, with the flow rate for each cubitainer being ~220 mL $min^{-1}$. One set of three cubitainers was grown under the ~400 ppm $CO_2$ concentration, representing an ambient control group (low $CO_2$, LC), and the other two sets of three cubitainers were grown under the ~750 ppm (medium $CO_2$, MC) and ~1100 ppm (high $CO_2$, HC) $CO_2$ concentrations.

### *6.3.2 Experimental measurements*

During the course of the experiment, all treatment replicates were subsampled daily for particulate concentrations and rate measurements (Table 6.1). Temperature and pH were monitored daily, but measurements of carbonate system parameters (total carbon, $C_T$, and total alkalinity, TA) were only taken on the first and last days of the experiment due to large volume requirements. Lugol's preserved samples for taxonomic identification and cell counts were collected midway through the experiment, and due to the very large volume required, DNA metabarcoding samples were only collected at the end of the experiment using the remaining water in each cubitainer.

**Table 6.1.** Measurements collected over the course of the OA experiment conducted with a diatom assemblage collected from the northern Bering Sea in July 2022. Ambient is the ambient measurement taken directly from a Niskin bottle. Day 1 is the measurement from cubitainers after nutrients were added, approximately three hours after the initial collection of water from the station. All following samples were collected at the same time each day. Blank spaces indicate where no sample was taken, ND indicates no data from a sample that was collected.

| | | Day of experiment | | | | | |
|---|---|---|---|---|---|---|---|
| **Measurement** | **Ambient** | **1** | **2** | **3** | **4** | **5** | **6** |
| *Biomass proxies* | | | | | | | |
| Total chlorophyll-*a* (chl-*a*) | x | x | x | x | x | x | x |
| Chl-*a* > 5 µm | x | x | x | x | x | x | x |
| Total biogenic silica ($bSiO_2$) | x | x | x | x | x | x | x |
| $bSiO_2$ > 5 µm | x | x | x | x | x | x | x |
| Particulate carbon (PC) | x | x | x | x | x | x | x |
| Particulate nitrogen (PN) | x | x | x | x | x | x | x |
| *Dissolved nutrients* | | | | | | | |
| Nitrate ($NO_3^-$) | x | x | x | x | x | x | x |
| Phosphate ($PO_4^{3-}$) | x | x | x | x | x | x | x |
| Silicic acid ($Si(OH)_4^-$) | x | x | x | x | x | x | x |
| *Taxonomy* | | | | | | | |
| Lugol's | x | | | | x | | ND |
| Phytoplankton DNA | ND | | | | | | x |
| *Nutrient utilization rates* | | | | | | | |
| Carbon utilization ($\rho C$, $V_C$) | x | x | x | x | x | x | x |
| Nitrate utilization ($\rho NO_3$, $V_{NO3}$) | x | x | x | x | x | x | x |
| Silicic acid utilization ($\rho Si$, $V_{Si}$) | x | x | x | x | x | x | x |
| *Physical* | | | | | | | |
| Temperature | x | x | x | x | x | x | x |
| Salinity | x | | | | | | |
| Total carbon ($C_T$) | x | | | | | | x |
| Total alkalinity (TA) | x | | | | | | x |
| Electrode pH ($pH_T$) | | x | x | x | x | x | x |

### *6.3.3 pH, total carbon, and total alkalinity measurements*

The pH of every treatment replicate was monitored daily throughout the experiment. Water was subsampled from each cubitainer into a light-proof, airtight container. All pH samples were then kept in a water bath fed from the same seawater loop as the incubator, alongside an identical container filled with a TRIS/HCl seawater buffer made to approximately match the seawater

salinity (Dickson et al., 2007). A Milwaukee MA911 glass electrode (Milwaukee Instruments, NC, USA) and LabQuest 2 data logger (Vernier, OR, USA) were used to take sequential voltage measurements of the pH sample and TRIS/HCl buffer. The pH using the total scale ($pH_T$) was calculated from the difference in voltage following SOP6A in Dickson et al. (2007). For the rest of this paper, pH is used when discussing general changes in acidity, and $pH_T$ is used when referencing a specific pH value. These measurements showed that differences in pH remained constant during the experiment (Appendix F, Table F.1). However, phytoplankton biomass increased dramatically after the first three days of the experiment, and based on prior experiments that showed pH shifts due to high biomass, the overall gas flow rate was increased to 333 mL $min^{-1}$ per cubitainer to offset a potential pH increase caused by enhanced C uptake. $CO_2$ mixing rates were adjusted to produce the same final concentrations at the higher flow rate.

At the beginning and end of the experiment, total carbon ($C_T$) and total alkalinity (TA) were measured to constrain the carbonate system and calculate the $pH_T$ and $pCO_2$ of every cubitainer. A 500 mL sample was carefully drawn from each cubitainer using a silicone tube, a headspace (~1%) was left to allow for water expansion, and then each sample was preserved with 200 µL of mercuric chloride in gastight glass bottles. The temperature of each cubitainer was recorded at the same time. Analysis for $C_T$ took place at the Institute of Ocean Sciences (Fisheries and Oceans Canada) using a SOMMA interfaced with a UIC Model 5011 coulometer (UIC Inc., Joliet, IL) controlled by VINDTA 3D software (Marianda, Kiel, Germany), and TA was measured using the open cell titration method with a Metrohm dosimat (Metrohm, Herisau, Switzerland) (Dickson et al., 2007). Calculations of $pH_T$ and $pCO_2$ were done in RStudio v.2023.06.0+421 (Posit Software, Boston, MA) using the package “seacarb” v.3.3.3 with

constants for K1 and K2 from Mehrbach et al. (1973) refit by Lueker et al. (2000), and the $KHSO_4$ dissociation constant from Dickson (1990). Uncertainties in the computed carbonate system were estimated by propagating input uncertainties of each parameter ($C_T$, TA, temperature, salinity, and nutrient concentrations, and thermodynamic constants) (Orr et al., 2018).

Surface pH values for the entire 2006 – 2022 DBO time-series were calculated to quantify the natural variability that exists across the PAR in mid-July. Samples for $C_T$ and TA were collected from Niskin bottles as described above, and analyzed with the same methodology as well. For these samples only, all nutrient concentrations were assumed to be zero for pH calculations due to inconsistent data availability in earlier cruises. Since only surface (typically < 5 m) samples were used, which often had very low to undetectable nutrient concentrations, this assumption had very little impact on the calculated $pH_T$ values.

### *6.3.4 Phytoplankton taxonomy*

Taxonomy samples were preserved with Lugol's solution (Parsons et al., 1984) in 125 mL dark HDPE bottles, and then refrigerated at 4°C until analysis. Bottles were thoroughly but gently mixed, and then a subsample (between 5 – 25 mL) was settled in an Utermöhl settling chamber (KC Denmark A/S, Denmark) for 24 hours. Cells from randomly selected fields were counted with a 100x objective on an Olympus IX71 epifluorescence inverted microscope (Olympus Corporation, Tokyo, Japan). Cell numbers were recorded until at least 400 cells of the most abundant cell type were counted (typically 10 – 20 fields). Photos of each microscope field were taken with a Q-Imaging Retiga 2000r camera (Burnaby, BC, Canada) to confirm taxonomic

identifications. Cells in the Lugol's preserved samples from the end of the experiment (day 6) were degraded and fragmented, so counts of different taxa were unreliable.

Samples for DNA extraction and sequencing were collected by filtering between 0.50 – 1.02 L of seawater from each replicate onto 0.2 µm pore size Sterivex filter cartridges (Millipore Sigma, MA, USA). The cartridges were immediately frozen at -80°C until analysis. DNA was extracted from the filters using the Sterivex Power Water kit (Qiagen, Germany), and analysed by the Dalhousie University Integrated Microbiome Resource (IMR) for 18S rRNA. Full details on amplification and sequencing are available in Crawford (2024). Sequences were filtered to remove metazoan and fungal taxa. Sequence reads were not corrected for library size, therefore a statistical analysis was not conducted on the results. The sample collected to assess the starting assemblage composition did not sequence successfully.

### *6.3.5 Chlorophyll-a concentrations and growth rate*

Size-fractionated chl-*a* concentrations were determined by gently filtering 150 mL of seawater through a 0.7 µm nominal porosity GF-75 glass fiber filter (AMD Manufacturing, Ontario, CA) and another 150 mL through a 5.0 µm polycarbonate (PC) filter. Filters were frozen at -20°C until analysis. To extract the pigment, filters were submerged in a 90% acetone solution, sonicated for 10 minutes, and then left in the dark for 24 hrs at -20°C. Following the extraction, samples were warmed to room temperature and decanted into borosilicate cuvettes in the dark. Fluorescence was measured with a Turner-Designs 10AU fluorometer (Turner Designs, CA, USA) pre-calibrated with pure chlorophyll standards. The concentration of chl-*a* was determined

after correction for phaeopigment interference by acidification (Parsons et al., 1984). Growth rate (μ) was calculated as the slope of the natural log of chl-*a* over time, for each replicate.

### *6.3.6 Dissolved nutrient concentrations*

Samples for the concentration of dissolved nutrients ($NO_3^-$, $PO_4^{3-}$, and $Si(OH)_4$) were collected by filtering seawater through disposable filter cartridges (PES, 0.45 μm nominal porosity) into acid-washed 15 mL centrifuge tubes. Samples for $NO_3^-$ and $PO_4^{3-}$ were immediately frozen at -20°C, while separate samples for $Si(OH)_4$ were stored at 4°C to avoid polymerization of $Si(OH)_4$. All nutrient concentrations were measured by continuous segmented flow analysis on an Astoria 2 Nutrient Autoanalyzer (Astoria, OR, USA) according to Barwell-Clarke and Whitney (1996).

### *6.3.7 Carbon and nitrate utilization rates and particulate C and N*

Utilization rate of carbon ($\rho C$) and $NO_3^-$ ($\rho NO_3$) were measured using a $^{13}C$-$^{15}NO_3^-$ dual tracer method (Dugdale and Goering, 1967; Slawyk et al., 1977). All treatment replicates were subsampled into acid-washed 250 mL PC bottles, leaving only enough headspace for isotope additions. Samples for the determination of total $\rho C$ were inoculated using $KH^{13}CO_3$ (99% purity, Cambridge Isotopes Laboratories, MA, USA) isotope tracer stock with the target $^{13}C$ enrichment of each sample being ~10% of the total ambient $C_T$. Samples for $\rho NO_3$ were inoculated using $Na^{15}NO_3$ (98+% purity, Cambridge Isotopes Laboratories, MA, USA) with the final $^{15}N$ enrichment target being ~10% of the amended $NO_3^-$ concentrations. Inoculated samples were incubated alongside the original cubitainers for 24 hours, and then terminated by filtration through combusted 0.7 μm GF-75 filters. Filtered samples were dried at 60°C for 48 hours and

stored until further analysis. The isotopic composition ($^{13}C$:$^{12}C$ and $^{15}N$:$^{14}N$) and total C and N content were measured at the Stable Isotope Facility at the University of California Davis with a PDZ Europa 20-20 isotope ratio mass spectrometer and a PDZ Europa ANCA-GSL elemental analyzer, respectively (Sercon Ltd., Cheshire, UK). Carbon utilization rate was calculated using equation 3 in Hama et al. (1983) and average $C_T$ concentrations for each treatment. Nitrate utilization rate was calculated using equation 3 in Dugdale and Wilkerson (1986) and the $NO_3^-$ concentrations at the time of sampling for each replicate. When ambient $NO_3^-$ concentrations were the below the limit of detection (0.1 µM), the value used in the calculation was 0.1 µM, therefore $\rho NO_3$ represents a theoretical maximum rate. Specific uptake rates ($V_C$, $V_{NO3}$) were calculated by dividing $\rho C$ and $\rho NO_3$ by total C and N content. Because the total C and N content were measured at the end of the incubation, particulate C (PC) and particulate N (PN) concentrations from the start of the incubation were back-calculated using the rates of $\rho C$ and $\rho NO_3$. The relationship between PC and PN (C:N) and $\rho C$ to $\rho NO_3$ ($\rho C$:$\rho NO_3$) were calculated on a molar basis (mol $mol^{-1}$), while PC to chl-*a* (C:chl-*a*) was calculated based on mass (g $g^{-1}$).

### *6.3.8 Silicic acid utilization rates and biogenic silica concentrations*

The utilization rate of $Si(OH)_4$ ($\rho Si$) was measured using the radioisotope $^{32}Si$ (Brzezinski and Phillips, 1997; Krause et al., 2011). All treatment replicates were subsampled into acid-washed 250 mL polycarbonate bottles and inoculated with 65 µL of a 3700 Bq $mL^{-1}$ solution of high specific activity $^{32}Si(OH)_4$ (~25,000 MBq µmol $Si^{-1}$). The amount of $^{32}Si(OH)_4$ added was $9.6x10^{-9}$ µmol Si, a negligible increase in the total $Si(OH)_4$ available. Inoculated samples were incubated for 24 hours alongside the original cubitainers, and then terminated by vacuum filtration on 0.6 µm PC filters. Excess $^{32}Si$ tracer that may have adsorbed onto particulates was

removed by rinsing filters with 0.6 µm filtered seawater. Filters were mounted on nylon discs, dried at room temperature for 24 hours, covered with Mylar film, and stored until $^{32}Si$ and its daughter isotope $^{32}P$ were at secular equilibrium (~120 days).

The $^{32}Si$ activity in the samples was determined by gas-flow proportional counting using a Risø 25-5 low-level beta GM multicounter (DTU Nutech, Denmark) (Krause et al., 2011), and $\rho Si$ was calculated using the ambient $Si(OH)_4$ and $bSiO_2$ concentrations at the time of sampling (Brzezinski and Phillips, 1997). Specific uptake rate ($V_{Si}$) was calculated by normalizing $\rho Si$ by $bSiO_2$ concentrations at the time of sampling.

Size-fractionated biogenic silica concentrations were collected by filtering 150 mL of each replicate through a 0.6 µm pore-size PC filter, and another 150 mL through a 5.0 µm PC filter. Filters were dried at 60°C for 48 hours and then stored in a desiccator at room temperature until further analysis. A 1-hr NaOH digestion was used to convert $bSiO_2$ to $Si(OH)_4$ (Brzezinski and Nelson, 1995), the concentration of which was measured with a Beckman DU 530 UV/Vis spectrophotometer (Beckman Coulter, CA, USA) using a reverse-order reagent blank (Brzezinski and Nelson, 1986).

Ratios for nutrient utilization rates, $\rho Si:\rho C$, and $\rho Si:\rho NO_3$, and their equivalent particulate ratios, $bSiO_2$ to PC (Si:C) and $bSiO_2$ to PN (Si:N) were calculated on a molar basis (mol $mol^{-1}$).

### *6.3.9 Data treatment and visualization*

Data from the post-bloom phase of the experiment, day 6, had a reduced sample size for several measurements. Carbon and $NO_3^-$ utilization, as well as PC and PN, were affected by high-biomass samples that exceeded the calibration range of the elemental analyzer, and in some cases even fully saturated the detectors. This resulted in underestimation of isotope enrichment and uncertainty in the final calculated values at day 6, therefore those samples were excluded from averages. One sample for chl-*a* and two samples for $bSiO_2$ were affected by damaged filters. While only affecting individual measures by one or two samples, this reduced the available sample size for ratios of particulates noticeably, and as such statistical comparisons on day 6 should be taken with caution.

All figures were made in RStudio using the package "ggplot2".

### *6.3.10 Data analysis and statistics*

Differences in pH due to the experimental treatments were tested using a one-way ANOVA, followed by a Tukey post-hoc comparison of means. However, many of the different measures of particulate concentrations, elemental ratios, and nutrient utilization rates did not meet the assumptions of normality or equal variance between treatment groups that are required for an ANOVA test. Therefore, for consistency, all comparisons between experimental treatments were done using a Kruskal-Wallis rank-sum test. If the hypothesis of no-difference between medians of treatments was rejected by the Kruskal-Wallis rank-sum test, Dunn's post-hoc comparison was computed to determine pair-wise differences between the treatment levels. Since there were only three experimental treatments, the likelihood of family-wise error rates was low. As such,

p-values for the post-hoc comparison were not adjusted using a Bonferroni or other correction method. All statistical analyses were performed in RStudio.

To compute the relative impact of observed differences of different measurements between treatments, an effect size was calculated. Unfortunately, there is no single agreed upon method for calculating effect size for Kruskal-Wallis tests, however, epsilon-squared ($\varepsilon^2$) and eta-squared ($\eta^2$) are commonly used (Tomczak and Tomczak, 2014). While not directly comparable to the other OA studies in this dissertation, which use Cohen's $d_s$ effect sizes (Nakagawa and Cuthill, 2007; Rosenberg et al., 2013) to normalize differences between means, $\varepsilon^2$ and $\eta^2$ still provide additional information about the difference between treatments beyond the significance value itself. For $\varepsilon^2$, a value of 0 indicates no relationship between the measurement and the treatment, a value of 1 indicates a "perfect" (i.e. very strong) relationship, and there are varying levels in between (e.g. 0.00 < 0.01 – negligible, 0.01 < 0.04 – weak, 0.04 < 0.16 – moderate, 0.16 < 0.36 - relatively strong, 0.36 < 0.64 – strong, 0.64 < 1.00 – very strong). For $\eta^2$, the value from 0 to 1 and multiplied by 100% indicates the percentage of variance in the dependent variable explained by the independent variable. Effect sizes were calculated in Microsoft Excel.

Statistical results were typically interpretated at an alpha level of 0.05. However, although not statistically conclusive, when paired with a strong effect size, an alpha level close to 0.10 was also considered to be numerically interesting and worth discussing without drawing any conclusions. In addition, the potential for false-positive results exists when making many statistical comparisons, however a specific family-wise error rate correction factor (e.g. Bonferroni) was not applied to the p-values in this study. Instead, statistically significant results

were interpreted cautiously, to avoid missing true effects but to also avoid assigning too much importance to them.

## 6.4 Results

### *6.4.1 Experiment conditions due to carbonate system manipulation*

Over the course of the experiment, the average pH difference between the low carbon control (LC) and medium carbon (MC) treatment was 0.30±0.04, and the average difference between MC and the high carbon (HC) treatment was 0.17±0.05 (Appendix F, Table F.1). Electrode $pH_T$ values at the end of the experiment were slightly different than those determined by carbonate system measurements, likely due to greater uncertainty associated with electrode measurements, and variability between treatment replicates (Appendix F, Table F.1 & F.2). Differences between electrode pH and calculated pH may have also been due to high concentrations of organic material present in the measured water samples. Using $pH_T$ values derived from $C_T$ and TA collected on the final day of the experiment (Table 6.2), a one-way ANOVA test showed that experimental treatment had a significant effect, $F_{(2, N = 9)} = 201.8$, $p < 0.001$. A Tukey post-hoc test showed significant differences between LC and MC, $p < 0.001$, between LC and HC, $p < 0.001$, and between MC and HC, $p = 0.001$. Compared to the ambient $pH_T$ of the seawater when initially collected, 8.27±0.01 (Table 6.2), the LC treatment in our experiment was representative as a control ($pH_T$ = 8.26±0.02). Compared to the natural variability of pH in the DBO2 region of the northern Bering Sea and the broader PAR (Fig. 6.1), the pH treatment for LC was representative of typical values, the MC treatment was near the low end of values previously observed, and the HC treatment was at least 0.1 units lower than even the most extreme values observed in the prior 16 years.

**Table 6.2.** Calculated $pH_T$ and $pCO_2$ for ambient and experimental treatments of a pH manipulation experiment conducted on a diatom assemblage collected from the Bering Sea in July 2022 and acclimated to different levels of $pCO_2$. Ambient values are *in situ* and collected prior to the beginning of the experiment, while the low carbon (LC), medium carbon (MC), and high carbon (HC) treatments are for the end of the experiment after six days of acclimation. Calculated $pH_T$ is the average pH on the total scale, and $pCO_2$ is the average calculated $pCO_2$ after bubbling ambient and enriched $CO_2$ air. Uncertainties are the geometric mean of the average propagated analytical uncertainty and the treatment standard deviation. Full carbonate system parameters including individual replicates and estimates of uncertainty are presented in Appendix F, Table F.2.

| **Treatment** | **$pH_T$ (calculated)** | **$pCO_2$ (µatm)** |
|---|---|---|
| Ambient | 8.27±0.01 | 219±7 |
| LC | 8.26±0.02 | 233±10 |
| MC | 7.90±0.03 | 590±40 |
| HC | 7.70±0.03 | 950±60 |

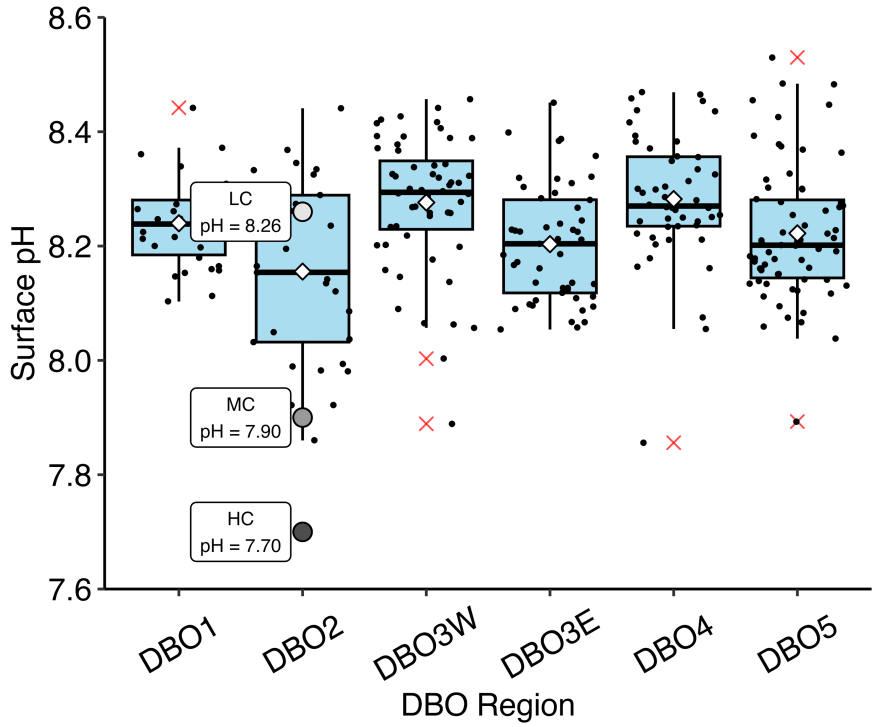


**Figure 6.1.** Regional distribution of surface pH values in the Distributed Biological Observatory from 2006 – 2022. Individual points correspond to a different year and location within a particular region. Regional means represented by the diamond symbol, and outliers are shown as red "x" symbols. Calculated $pH_T$ values for LC, MC, and HC treatments of the OA experiment conducted in 2022 are overlaid with the region sampled in the same year in the northern Bering Sea (DBO2). Regions are arranged by increasing latitude.

### *6.4.2 Progression of chlorophyll-a biomass, growth rates, and nutrient concentrations*

Chlorophyll-*a* concentrations (Fig. 6.2) and nutrient concentrations (Fig 6.3) indicated that phytoplankton in every replicate of the experiment experienced bloom conditions that could be divided into three phases. The pre-bloom phase was characterized by chl-*a* concentrations < 5 µg $L^{-1}$ (Fig 6.2) and replete nutrients, averaging > 25 µmol $NO_3^-$ $L^{-1}$, > 2.0 µmol $PO_4^{3-}$ $L^{-1}$, and > 30 µmol $Si(OH)_4$ $L^{-1}$ (Fig. 6.3A – C). This phase was followed by exponential growth, characterized by a rapid increase in chl-*a* biomass and the drawdown of all nutrients from day 2 to 4.

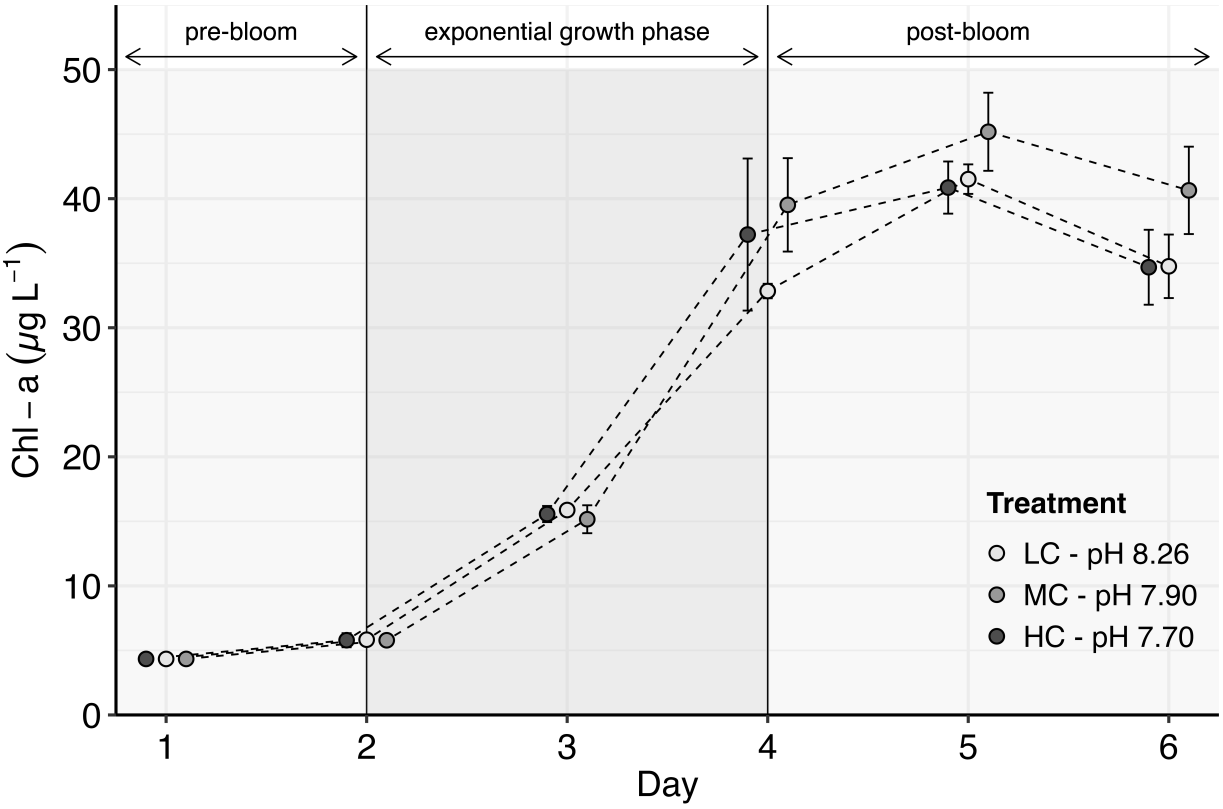


**Figure 6.2.** Progression of chl-*a* concentrations in a diatom assemblage collected from the northern Bering Sea in July 2022 during acclimation to different pH levels. Three bloom phases are indicated: a pre-bloom phase from days 0 to 2, exponential growth from days 2 to 4, when nutrient concentrations were replete, and a post-bloom phase after day 4, when all macronutrients ($NO_3^-$, $Si(OH)_4$, $PO_4^{3-}$) were below detection limits. The mean (n = 3) of each $CO_2$ treatment is represented by different shaded circles, and the standard deviation is represented by error bars from each circle. When no error bars are present, the size of the symbol is larger than the standard deviation.

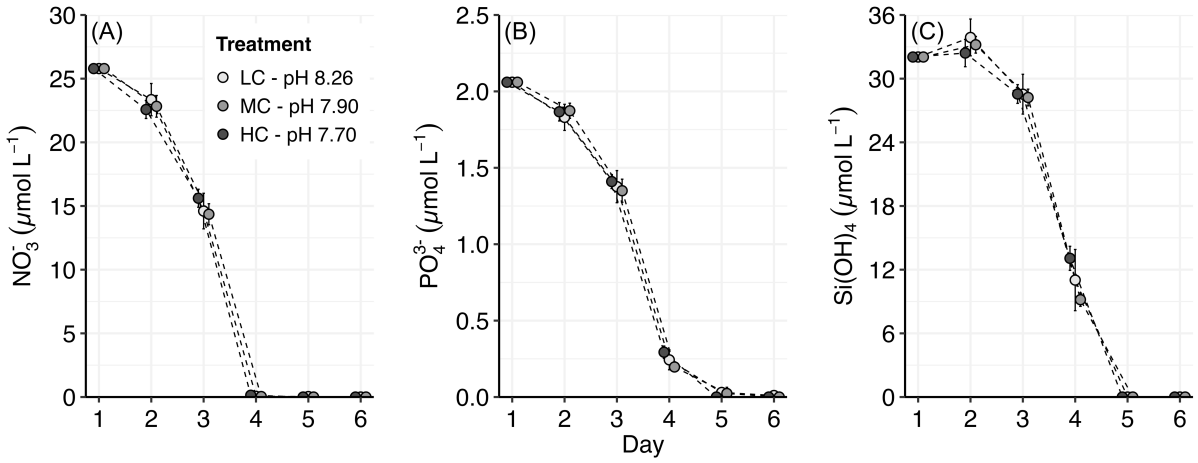


**Figure 6.3.** Progression of nutrient concentrations in a diatom assemblage collected from the northern Bering Sea in July 2022 during acclimation to different pH levels. Concentrations of **(A)** nitrate, $NO_3^-$, **(B)** phosphate, $PO_4^{3-}$, and **(C)** silicic acid, $Si(OH)_4$. Symbols and errors bars as in Fig. 6.2.

Growth rates (μ) were highest in all treatments between day 2 and day 3, LC = 1.00±0.05 $d^{-1}$, MC = 0.96±0.11 $d^{-1}$ and HC = 0.99±0.08 $d^{-1}$ (Table 6.3, Appendix F, Fig. F.1). By the end of the exponential growth phase on day 4, chl-*a* biomass was 32.8±0.6 μg $L^{-1}$ for the LC treatment, 39.5±3.6 μg $L^{-1}$ for the MC treatment, and 37.2±5.9 μg $L^{-1}$ for the HC treatment. Macronutrient concentrations fell below their respective detection limits at different times. Nitrate was below the detection limit (0.1 μmol $L^{-1}$) on day 4, phosphate (limit 0.03 μmol $L^{-1}$) on day 6, and silicic acid (limit 0.2 μmol $L^{-1}$) was undetectable on day 5. During the post-bloom phase, following the exhaustion of all macronutrients and end of biomass accumulation on day 5, growth rates became negative (LC = -0.19±0.09 $d^{-1}$, MC = -0.11±0.03 $d^{-1}$, and HC = -0.17±0.04 $d^{-1}$) (Table 6.3, Appendix F, Fig. F.1). Based on a Kruskal-Wallis rank-sum test, there were no significant differences in chl-*a*, growth rates, or nutrient concentrations between the treatments at any point throughout the experiment.

**Table 6.3.** Maximum and minimum growth rate (μ) of a diatom assemblage collected from the northern Bering Sea in July 2022 during acclimation to different levels of $pCO_2$. H ($\chi^2$) is the chi-squared test statistic, n is the sample size, p-value is interpreted with $\alpha = 0.05$. Effect sizes $\varepsilon^2$ and $\eta^2$ are interpreted as described in the methods. Growth rates for other days are presented in Appendix F, Figure F.1.

| Day | LC ($pH_T$ 8.26) | MC ($pH_T$ 7.90) | HC ($pH_T$ 7.70) | H ($\chi^2$) | n | p-value | $\varepsilon^2$ | $\eta^2$ |
|---|---|---|---|---|---|---|---|---|
| Day 2-3 (exponential growth phase) | 1.00±0.05 $d^{-1}$ | 0.96±0.11 $d^{-1}$ | 0.99±0.08 $d^{-1}$ | 0.27 | 9 | 0.88 | 0.03 | 0% |
| Day 5-6 (post-bloom phase) | -0.19±0.09 $d^{-1}$ | -0.11±0.03 $d^{-1}$ | -0.17±0.04 $d^{-1}$ | 5.00 | 9 | 0.08 | 0.63 | 50% |

### *6.4.3 Progression of total and size-fractionated particulate C, N and $bSiO_2$ concentrations*

Other measures of phytoplankton biomass followed similar patterns to chl-*a*, and there were no consistent differences between pH treatments (Fig. 6.4). Particulate C and N increased similarly for all treatments until day 4 (Fig. 6.4A & B), after which PC continued to increase to a maximum that ranged between 470±50 μmol $L^{-1}$ and 490±80 μmol $L^{-1}$. Particulate N remained constant after day 4, plateauing for all treatments around 25 – 27 μmol $L^{-1}$. Biogenic silica increased throughout the experiment, and contrary to chl-*a* and PN, it plateaued on day 5 but did not show a decline on day 6 (Fig. 6.4C). The maximum concentrations of $bSiO_2$ were 33.8±0.6 μmol $L^{-1}$ for the HC treatment, 34.2±0.7 for the MC treatment, and 34.2±1.9 μmol $L^{-1}$ for the LC treatment. The proportion of chl-*a* biomass > 5 μm started at 81% and remained fairly constant in the LC and MC treatments until day 5, when the proportion declined to 54±4% and 56±5%, respectively (Fig. 6.4D). Chl-*a* > 5 μm in the HC treatment declined rapidly to 64±12% by day 3, after which it remained mostly constant, with 61±2% at the end of the experiment. Large-celled $bSiO_2$ made up 90% of the total biomass at the beginning of the experiment and increased to 100% in all treatments by day 3, which was maintained for the rest of the experiment.

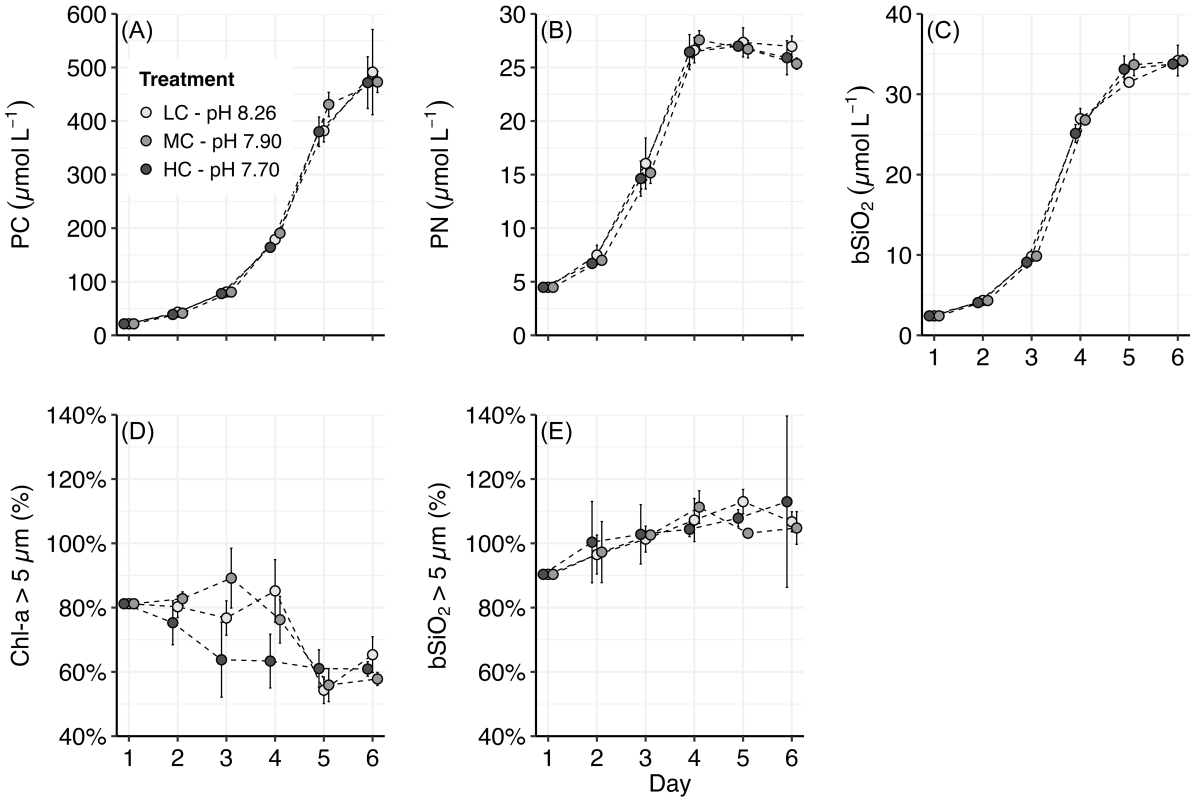


**Figure 6.4.** Biomass concentrations of a diatom assemblage collected from the northern Bering Sea in July 2022 during acclimation to different pH levels. Concentrations of **(A)** particulate C, **(B)** particulate N, **(C)** biogenic silica, $bSiO_2$, **(D)** % chl-*a* > 5 µm, and **(E)** % $bSiO_2$ > 5 µm. Symbols and errors bars as in Fig. 6.2.

### *6.4.4 Elemental composition of biogenic particles*

For all pH treatments, the relative proportions of C:N were slightly lower than the Redfield ratio of 6.6 mol $mol^{-1}$ throughout the pre-bloom and exponential growth phase of the experiment (Fig. 6.5A). Once PN stopped increasing on day 4, the C:N ratio dramatically increased, reaching slightly more than 18 mol $mol^{-1}$ for all treatments. Both the Si:C and Si:N ratios began the experiment at values less than the reference Redfield-Brzezinski values of 0.14 mol $mol^{-1}$ (Si:C) and 0.94 mol $mol^{-1}$ (Si:N) (Fig. 6.5B & C). As $bSiO_2$ increased during the exponential growth phase, Si:C and Si:N increased to be approximately equal to the reference values on day 4. The ratio of Si:C decreased on day 5 and 6 as PC continued to accumulate and $bSiO_2$ concentrations

began to plateau. The ratio of Si:N continued to increase on day 5 and 6 due to continued slow increase in $bSiO_2$ but constant PN concentrations during the post-bloom phase. Carbon to chl-*a* ratios varied between 54 – 89 g $g^{-1}$ during the pre-bloom and exponential growth phases, and all treatments varied similarly with time. Once chl-*a* biomass accumulation slowed on day 4 and PC continued to increase, C:chl-*a* increased rapidly, reaching a range between 135±3 g $g^{-1}$ for the MC treatment and 165±30 g $g^{-1}$ for the HC treatment. There were no statistical differences between treatments for any of the particulate ratios throughout the experiment.

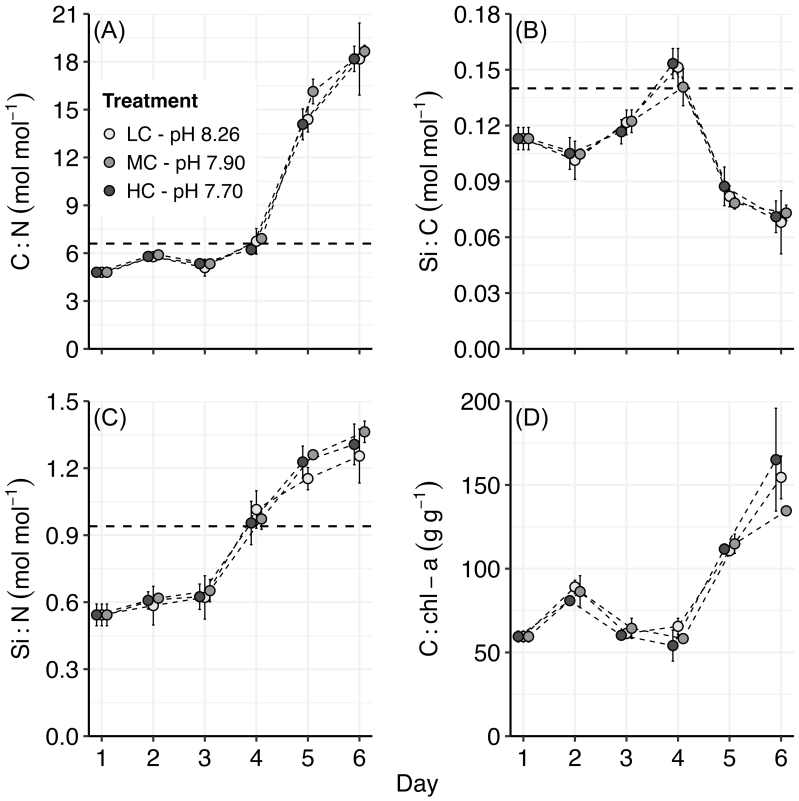


**Figure 6.5.** Particulate ratios of a diatom assemblage collected from the northern Bering Sea in July 2022 during acclimation to different pH levels. Ratios of **(A)** C:N, **(B)** Si:C, **(C)** Si:N, and **(D)** C:chl-*a*. The Redfield value is indicated with a dashed horizontal line. Symbols and errors bars as in Fig. 6.2.

### *6.4.5 Nutrient utilization rates and ratios*

Nutrient utilization rates clearly drove the accumulation of particulate biomass. Carbon utilization, $\rho C$, increased rapidly in all three treatments until reaching a maximum rate on day 4, after which the rate declined (Fig. 6.6A). From day 4 onwards, when nutrient concentrations began to be limiting, the variability of $\rho C$ was much higher than under nutrient-replete conditions. Nitrate utilization, $\rho NO_3$, initially followed a similar pattern as $\rho C$ (Fig. 6.6B). Once $NO_3^-$ concentrations were depleted on day 4, $\rho NO_3$ decreased dramatically but did not go to zero, due to enhancement by $^{15}NO_3^-$ during daily rate measurement incubations. Silicic acid utilization, $\rho Si$, was similar to $\rho NO_3$, however the utilization rate remained high for an additional day due to $Si(OH)_4$ not being depleted until one day later than $NO_3^-$ (Fig. 6.6C). As in $\rho C$, the variability of $\rho NO_3$ and $\rho Si$ increased as nutrients were depleted. There were no statistical differences between pH treatments for the nutrient utilization rates.

Ratios of $\rho C$:$\rho NO_3$ started near to the Redfield value (6.6 mol mol$^{-1}$) during the pre-bloom phase (Fig. 6.6D). Once $\rho NO_3$ declined on day 4, $\rho C$:$\rho NO_3$ rapidly increased to over 60 mol mol$^{-1}$ for all treatments, indicating a strong decoupling of C from $NO_3^-$ utilization. The ratio decreased as the post-bloom phase began, but remained higher than the Redfield value. Silicic acid utilization relative to $\rho C$ and $\rho NO_3$ both started near their Redfield-Brzezinski ratios, at 0.14±0.01 mol mol$^{-1}$ and 0.98±0.09 mol mol$^{-1}$, respectively (Fig. 6.6E & F). Both ratios increased as exponential growth continued and $\rho Si$ increased more relative to $\rho$ for other nutrients. Once $Si(OH)_4$ was depleted on day 5 and $\rho Si$ went to undetectable values, both $\rho Si$:$\rho C$ and $\rho Si$:$\rho NO_3$ dropped to zero. Throughout the experiment, there were no statistical differences in nutrient utilization ratios related to pH treatment.

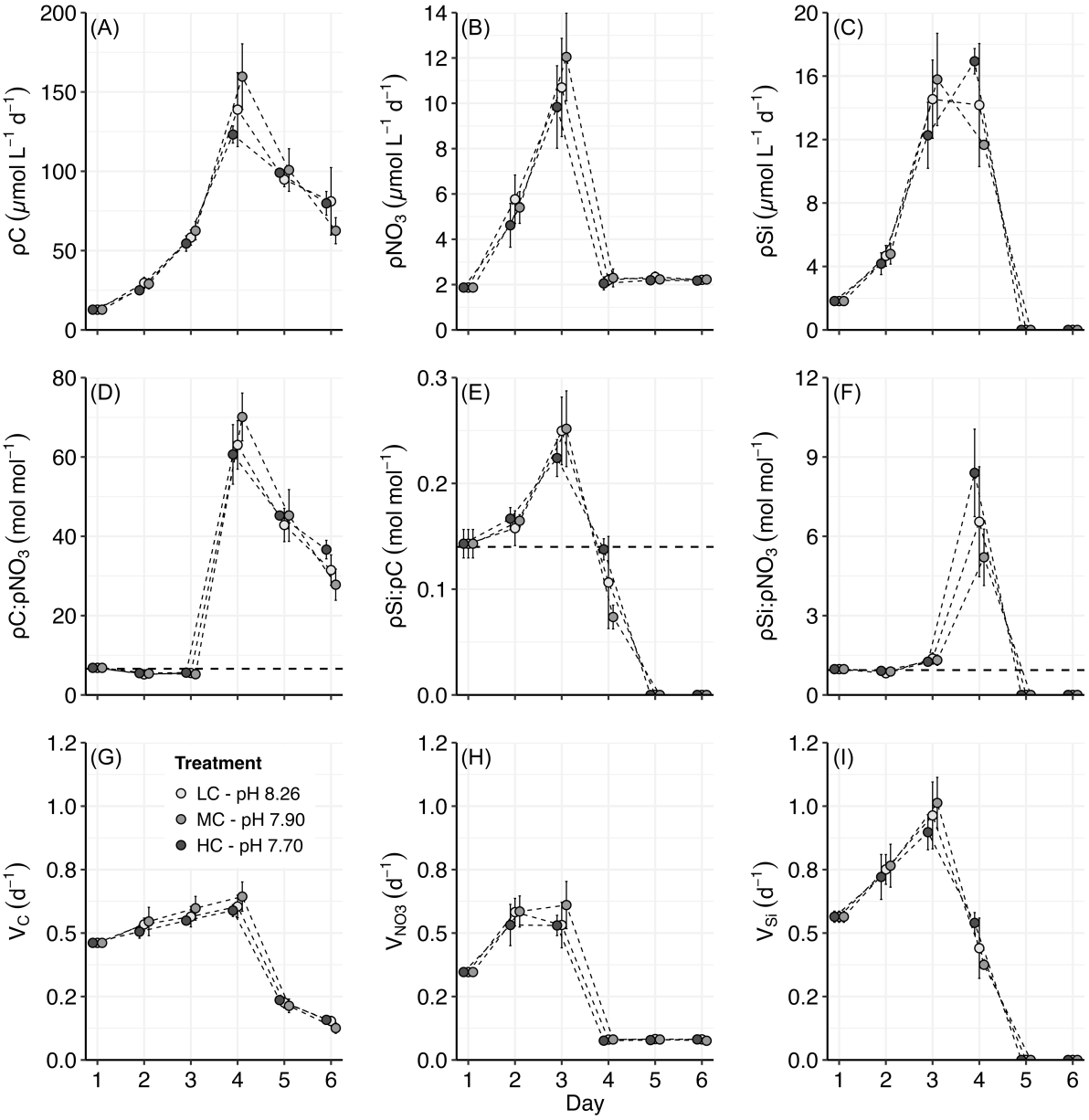


**Figure 6.6.** Nutrient utilization rates of a diatom assemblage collected from the northern Bering Sea in July 2022 during acclimation to different pH levels. Rates of **(A)** carbon utilization, $\rho$C, **(B)** nitrate utilization, $\rho$NO3, and **(C)** silicic acid utilization, $\rho$Si. Ratios of utilization rates, **(D)** $\rho$C:$\rho$NO3, **(E)** $\rho$Si:$\rho$C, and **(F)** $\rho$Si:$\rho$*NO3*. Specific uptake rates for **(G)** carbon, $V_C$, **(H)** nitrate, $V_{NO3}$, and **(I)** silicic acid, $V_{Si}$. Ratios are referenced against Redfield ratios for C:N:Si, indicated by the dashed horizontal line. Symbols and errors bars as in Fig. 6.2.

Specific uptake rates, which indicate the intrinsic capacity of phytoplankton to utilize a nutrient, generally reflected the same patterns as values of $\rho$ (Fig. 6.6G – I). Specific uptake rates were highest during the exponential phase of the experiment, and $V_{NO3}$ and $V_{Si}$ both decreased strongly as nutrient limitation began on day 4. Specific uptake of C reached a maximum on day 4 and then declined to the point where almost no C utilization was occurring. All pH treatments responded similarly throughout the experiment, and no significant differences were observed.

### *6.4.6 Summary of physiology during exponential growth and post-bloom phases*

Although there were no statistically significant differences between treatments for any measured variables, we combined the data from two specific days to summarize the overall phytoplankton assemblage response to OA during different phases of growth. Day 3, during which all nutrient concentrations were still replete, biomass was accumulating, and nutrient utilization rates were high, represents the exponential growth phase. Day 6 represents the post-bloom phase when all nutrient concentrations were depleted, and biomass accumulation had ceased. For more context during the exponential growth phase, day 4 is included in the appendix (Appendix F, Fig. F.2 & Table F.3). However, since $NO_3^-$ concentrations were already depleted at this point, phytoplankton may have been affected by N limitation in addition to the pH treatment effects, and the results are not presented or discussed at any length.

During the exponential growth phase (on day 3), the MC treatment showed a neutral response or modest degree of enhancement for nearly all assessed measures compared to the LC control

treatment (Fig. 6.7A). This was contrasted by the opposite trend under the most acidic treatment (HC), where there was an apparent decrease across nearly all measures relative to the control.

It is important to emphasize that the changes in MC and HC treatments at day 3 were not statistically significant – results of Kruskal-Wallis tests showed that pH treatment had no significant effect on the different measures of biomass, stoichiometry, or nutrient utilization (Appendix F, Table F.4). Despite a lack of statistical significance when interpreted at $\alpha = 0.05$, some measures during the exponential phase had much lower p-values than other variables (i.e. $p < 0.20$), and strong effect sizes (i.e. $\varepsilon^2 > 0.36$), potentially indicative of a meaningful relationship between variables. Based on the p-values and effect sizes, indicators of large-cells and diatom biomass including chl-*a* > 5 µm ($\chi^2_{(2, N = 9)} = 3.82$, $p = 0.15$, $\varepsilon^2 = 0.48$, $\eta^2 = 30\%$), $bSiO_2$ ($\chi^2_{(2, N = 9)} = 3.29$, $p = 0.19$, $\varepsilon^2 = 0.41$, $\eta^2 = 21\%$), and $bSiO_2$ > 5 µm ($\chi^2_{(2, N = 9)} = 4.36$, $p = 0.11$, $\varepsilon^2 = 0.54$, $\eta^2 = 39\%$) were all potentially affected by pH. Since these statistical results were in related measures of biomass (e.g. independently sampled proxies of diatom biomass), it is unlikely that they were false-positives caused by the number of statistical comparisons performed. However, no individual Kruskal-Wallis tests were significant, so post-hoc Dunn's comparisons were not carried out to avoid over-interpreting the non-significant results.

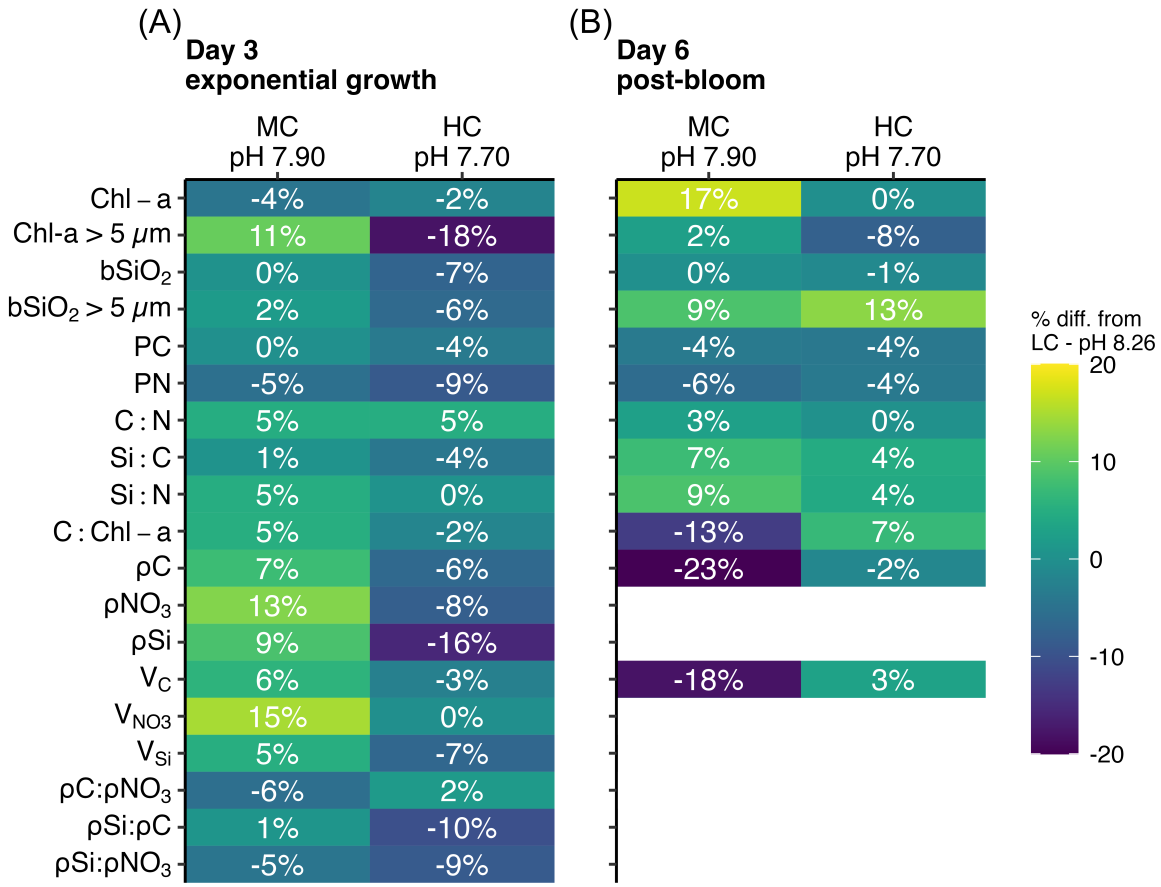


**Figure 6.7.** Relative changes in measures of biomass, stoichiometry, and nutrient utilization rates for a diatom assemblage collected from the northern Bering Sea in July 2022 after acclimation to different pH levels for **(A)** three days and **(B)** six days. Values are the percent differences between the means of the control (LC) and MC or HC experimental treatments. Colour corresponds to the percentage. A statistical summary of p-values and effect sizes are reported in Appendix F, Table F.4 & F.5.

In the post-bloom phase (day 6), the response of both the MC and HC treatments was mixed and highly variable (Fig. 6.7B). The MC treatment caused some changes in chl-*a* and C:chl-*a*, which changed by 17% and -13%, respectively. P-values were close to 0.10, and effect sizes for those measurements were strong, potentially indicative of meaningful differences (chl-*a* $\chi^2_{(2,\,N=8)} = 5.00$, $p = 0.08$, $\varepsilon^2 = 0.71$, $\eta^2 = 60\%$; C:chl-*a* ($\chi^2_{(2,\,N=7)} = 3.93$, $p = 0.14$, $\varepsilon^2 = 0.65$, $\eta^2 = 48\%$) (Appendix F, Table F.5). Inconsistent changes and weak statistical evidence across other measures and treatments on day 6 made even qualitative patterns difficult to identify.

### *6.4.7 Taxonomic profiles of different bloom phases*

Lugol's preserved samples were collected only on day 4, when $NO_3^-$ was limited. While not directly linked to day 3's particulate concentrations or utilization rates, they still represent the assemblage composition during the experiment's exponential growth phase. During day 4, diatoms made up nearly 90% of cellular abundance under all pH treatments (Fig. 6.8A). This was an increase of ~15% from ambient *in situ* conditions (Appendix F, Table F.6), indicating that all incubation conditions used for the experiment favoured diatom growth.

Although not statistically conclusive, OA may have induced a shift in the diatom assemblage. At a genus level, there was evidence that the abundance of *Thalassiosira* sp. was different between treatments ($\chi^2_{(2, N = 9)} = 5.60$, $p = 0.061$, $\varepsilon^2 = 0.70$, $\eta^2 = 60\%$; Table 6.4). Concentrations of *Thalassiosira* declined from 150±100 x$10^4$ cells $L^{-1}$ under LC conditions or 130±22 x$10^4$ cells $L^{-1}$ under MC, to 76±3 x$10^4$ cells $L^{-1}$ under HC. However, this change was not significant when viewed as relative abundance (Fig. 6.8A; Appendix F, Table F.6). Total diatom abundance was the same between treatments as well. Although relative abundances suggested that *Chaetoceros* sp. may have increased under HC and replaced *Thalassiosira* sp., high variability among HC replicates made it difficult to determine any clear effect of pH.

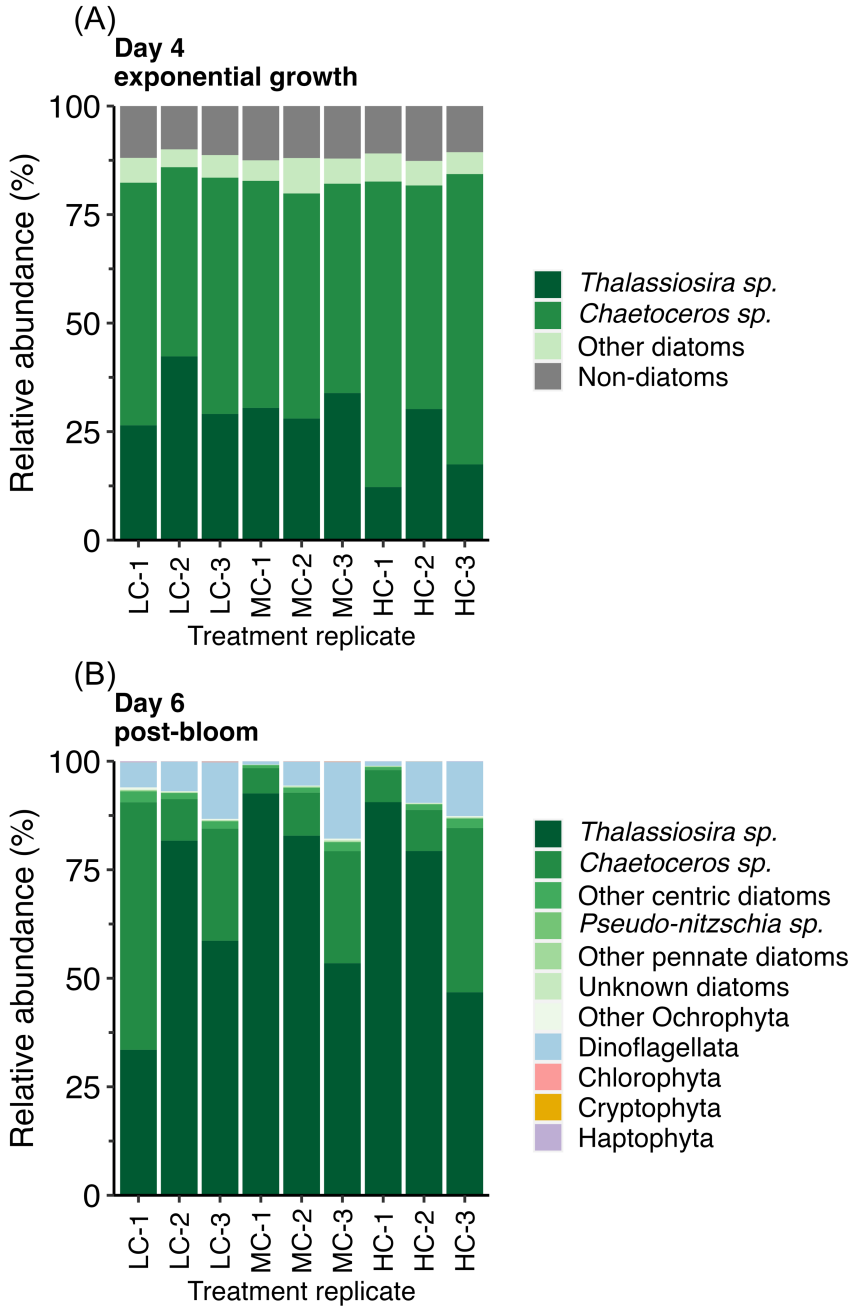


**Figure 6.8.** Taxonomy of a Bering Sea diatom and other phytoplankton assemblage during acclimation to different $pCO_2$ treatments. Relative abundance **(A)** during the exponential growth phase (day 4), based on Lugol's preserved samples, and **(B)** during the post-bloom phase (day 6), based on DNA metabarcoding analysis. All non-diatom taxa are grouped for Lugol's preserved samples. For DNA metabarcoding analysis (B), taxa are grouped at the phylum level other than Ochrophyta, which is shown as different centric and pennate diatom genera as well as unknowns. Other centric diatoms not abundant enough to plot in (B): *Rhizosolenia, Leptocylindrus, Proboscia, Porosira, Minidiscus, Actinocyclus, Attheya, Minutocellus, Eucampia, Guinardia, Melosira,* and unknown *Mediophyceae spp.* Other pennate diatoms not abundant enough to plot in (B): *Navicula, Nitzschia,* and *Cylindrotheca*.

**Table 6.4.** Cell abundances for initial (ambient *in situ*) and exponential growth phases (day 4) of a northern Bering Sea phytoplankton assemblage acclimated to different pH levels. Cell counts come from Lugol's preserved samples. Comparisons among LC, MC, and HC treatments were made with a Kruskal-Wallis rank sum test. H ($\chi^2$) is the chi-squared test statistic, n is the sample size, p-value is interpreted with $\alpha = 0.05$. Effect sizes $\varepsilon^2$ and $\eta^2$ are interpreted as described in the methods for Chapter 6.

| | **Ambient** | **LC ($pH_T$ 8.26)** | **MC ($pH_T$ 7.90)** | **HC ($pH_T$ 7.70)** | **H ($\chi^2$)** | **n** | **p-value** | **$\varepsilon^2$** | **$\eta^2$** |
|---|---|---|---|---|---|---|---|---|---|
| Cell counts (x$10^4$ cells $L^{-1}$) | | | | | | | | | |
| Total | 25±5 | 430±160 | 410±50 | 440±200 | 0.36 | 9 | 0.837 | 0.04 | 0% |
| Diatoms | 19±6 | 390±150 | 360±40 | 390±180 | 0.36 | 9 | 0.837 | 0.04 | 0% |
| Non-diatom | 6.3±1.2 | 47±13 | 49±5 | 49±20 | 0.36 | 9 | 0.837 | 0.19 | 0% |
| Diatom counts (x$10^4$ cells $L^{-1}$) | | | | | | | | | |
| *Thalassiosira* sp. | 5±3 | 150±100 | 130±22 | 76±3 | 5.60 | 9 | 0.061 | 0.70 | 60% |
| *Chaetoceros* sp. | 12±3 | 220±50 | 210±19 | 290±160 | 0.62 | 9 | 0.733 | 0.08 | 0% |
| Other diatoms | 2.2±0.2 | 21±4 | 26±9 | 26±14 | 0.36 | 9 | 0.837 | 0.04 | 0% |

DNA metabarcoding revealed that on average over 90% of phytoplankton taxa were still diatoms at day 6 in all treatments (Fig. 6.8B, Table 6.5). Of the other species of phytoplankton, dinoflagellates were present in noticeable amounts in individual replicates, up to 18% of relative abundance. However, on average, dinoflagellate abundance for all pH treatments was less than 10%. Unlike during exponential growth, the diatom genus *Thalassiosira* was more than 50% of the taxa in most treatment replicates, and was not less abundant under HC. *Chaetoceros* sp. typically made up between ~9 – 25% of relative abundance. Other species of centric diatoms were less than 3% in all samples, and pennate diatoms such as *Pseudo-nitzschia* were less than 0.1% of the relative abundance. Statistical comparisons between replicates using metabarcoding data were not possible, and because of different methodologies, metabarcoding-derived relative abundance cannot be directly compared to the cell counts from day 4. Therefore, it is not possible to infer whether any change in assemblage composition between the exponential growth and post-bloom phases occurred.

**Table 6.5.** Average relative abundance during the post-bloom phase (day 6) of a northern Bering Sea phytoplankton assemblage following acclimation to different pH levels. Relative abundance from DNA metabarcoding data. Values for each treatment are presented in percentage as the mean (n = 3) ± standard deviation of the percent abundance relative to the total for each replicate within each treatment.

| | Relative abundance (%) | | |
|---|---|---|---|
| | **LC** ($pH_T$ 8.26) | **MC** ($pH_T$ 7.90) | **HC** ($pH_T$ 7.70) |
| **Diatoms (Bacillariophyceae)** | | | |
| *Thalassiosira* | 58±24 | 76±20 | 72±23 |
| *Chaetoceros* | 31±24 | 14±11 | 18±17 |
| Other centric | 1.9±0.6 | 1.3±0.7 | 1.4±0.8 |
| *Pseudo-nitzschia* | 0.08±0.04 | 0.03±0.02 | 0.05±0.04 |
| Other pennate | 0.16±0.12 | 0.11±0.08 | 0.13±0.09 |
| Unknown diatom | 0.08±0.09 | 0.19±0.12 | 0.07±0.06 |
| Other Ochrophyta | 0.33±0.22 | 0.15±0.17 | 0.15±0.16 |
| *Average diatoms* | *91±4* | *92±9* | *92±6* |
| **Other phyla** | | | |
| Dinoflagellata | 8.6±4 | 8.0±9 | 7.7±6 |
| Chlorophyta | 0.06±0.04 | 0.04±0.03 | 0.01±0.01 |
| Cryptophyta | 0.02±0.01 | 0.02±0.02 | 0.01±0.01 |
| Haptophyta | 0.11±0.07 | 0.05±0.05 | 0.05±0.03 |

## 6.5 Discussion

Testing the direct effect of $CO_2$ concentration on natural diatom assemblages is challenging, and in the PAR these experiments have been rarely conducted. Most knowledge comes from controlled lab experiments that did not always simulate natural conditions, and often overlooked studying the impact of pH on the development and decline of diatom blooms. To address these shortcomings, a diatom-rich phytoplankton assemblage was collected from the northern Bering Sea and subjected to three pH treatments, simulating modern and future OA scenarios. Following the addition of nutrients, a phytoplankton bloom occurred simultaneously in all experimental replicates over the course of six days. After a short pre-bloom period, exponential growth began, characterized by exponential increases in growth rate, particulate biomass and nutrient utilization rates. A post-bloom period of 2 days followed nutrient depletion, and the experiment ended on day 6.

We identified potential indicators of an OA impact on diatoms, specifically a positive effect on large-celled phytoplankton biomass (chl-*a* > 5 μm) during exponential growth at $pH_T$ 7.90, and a negative effect on chl-*a* > 5 μm and $bSiO_2$ under HC ($pH_T$ 7.70). The diatom genus *Thalassiosira* sp. may have decreased in abundance under HC conditions as well, although evidence for this impact was statistically inconclusive. Overall though, bloom dynamics in all pH treatments were similar, and there were no definitive statistical differences for any measured variable among pH levels on any day of the experiment. This indicated that natural diatom assemblages in the PAR may be well-adapted to the pH levels used in this experiment, and tolerant of one of the anticipated climate change impacts in this region.

### *6.5.1 $CO_2$ impacts on diatom biomass and carbon utilization*

A positive effect of OA on large diatoms was demonstrated by Wu et al. (2014), who found a positive relationship between cell volume and a $CO_2$ fertilization effect on diatom growth rates, i.e. larger cells benefit from higher concentrations of $CO_2$. This effect could be expected based on the consideration that high $CO_2$ concentrations are more beneficial for C acquisition by large species that are diffusion limited by their lower surface-to-volume ratios that smaller cells (Wolf-Gladrow and Riebesell, 1997). Diatoms have evolved C concentrating mechanisms (CCMs) to overcome the slow rate of $CO_2$ diffusion in water (Reinfelder, 2011; Spalding, 2008), and there is experimental evidence to suggest that increased $CO_2$ reduces the energy requirements for CCM activity (Taucher et al., 2015). Therefore, more resources could be allocated for growth instead of CCM activity under OA scenarios. However, in our experiment, indications of increased > 5 µm phytoplankton biomass at pH 7.90 compared to ambient (pH 8.26) were statistically inconclusive about whether or not a $CO_2$ fertilization effect occurred.

### *6.5.2 Taxonomic shifts due to changes in pH*

In a synthesis of diatom OA studies, Bach and Taucher (2019) reported that nearly all diatom assemblage studies investigating changes in size distribution under different $CO_2$ levels have reported either no shift at all, or a shift to larger diatoms under more acidified conditions. Cell counts from day 4 of our experiment showed that *Thalassiosira* diatoms may have decreased under HC conditions – these diatoms were present as long chains in the assemblages across all treatments, as opposed to *Chaetoceros* cells which were present as single cells (data not shown). However, the total proportion of diatoms in the assemblage was similar across all pH treatments, and since both *Thalassiosira* and *Chaetoceros* generally exceed the 5 µm cutoff for size-

fractionated biomass, there was no supporting biomass evidence for an assemblage shift. There was also no evidence that any diatom species other than *Thalassiosira* changed their total or relative abundance under any pH treatment, so it is most likely that OA did not have an impact on assemblage composition.

Although there were no statistically conclusive changes during our experiment, other studies have found impacts of OA on the same or similar species. In a laboratory study, *Thalassiosira weissflogii* achieved higher population densities under elevated $CO_2$ concentrations when nutrients were depleted (Taucher et al., 2015). The most abundant *Chaetoceros* species in our experiment, *Chaetoceros gelidus* (previously known as *C. socialis*), was physiologically resilient to OA in culture (Biswas, 2022), and the other most abundant species, *C. neogracilis*, grew more quickly under $CO_2$ enhanced conditions, though only at temperatures that are not representative of the Arctic (Nagao et al., 2020). A species of common Arctic diatom, *T. hyalina*, demonstrated increased sensitivity to photophysiological stress under OA conditions compared to sea ice associated pennate diatoms (Kvernvik et al., 2020), but not a strong response to OA alone. As a more realistic field study, compared to the conditions imposed in laboratory settings, our results demonstrated that Arctic assemblages dominated by *Thalassiosira* sp. and *Chaetoceros* sp. are not likely to be affected when OA is the only impact.

### *6.5.3 pH dependence of silicon biomineralization*

During exponential growth, there was statistically inconclusive evidence of a small negative impact on $bSiO_2$ concentrations at $pH_T$ 7.70, a level which exceeds present-day natural variability in surface waters of the northern Bering Sea. Silicon biomineralization is thought to

be dependent on ocean pH, as biogenic opal precipitation occurs in low-pH conditions within cells (Martin-Jezequel et al., 2000; Vrieling et al., 1999), and dissolution rates of $bSiO_2$ frustules decrease at lower pH (Loucaides et al., 2012). Experimental evidence on living diatoms is somewhat contradictory though. For example, Hervé et al. (2012) demonstrated that several high-level processes including frustule morphogenesis and silica polymerization are sensitive to acid-base balance, which leads to increased $bSiO_2$ quotas of diatoms under conditions that are both more-acidic and more-basic than current ambient ocean values (~7.8 – 8.2). Their experiments however, relied upon an extreme range of pH values that far exceed natural variability of the ocean. In contrast, Petrou et al. (2019) clearly demonstrated that realistic low pH treatments in fact reduced Si incorporation in different diatom species in the Southern Ocean. Biogenic silica quotas of an Antarctic *Chaetoceros* species decreased under higher $CO_2$ concentrations, under both constant and dynamic light (Hoppe et al., 2015), but Hoppe et al. (2017a) also demonstrated that OA had no effect on silicification and the Si:C ratios of diatom assemblages from Baffin Bay. They postulated that the non-responsiveness was due to physiological resilience, or a shift between differentially silicified *Chaetoceros* strains. Wyatt et al. (2024) did not observe any clear impacts of OA on silicification in *Thalassiosira rotula* either, while Milligan et al. (2004) found that high $pCO_2$ favoured low Si:C ratios in *T. weissflogii*. Thus, evidence for an impact of pH on $bSiO_2$ is contradictory and effects of pH on Si dynamics in diatoms are likely the result of many interacting factors. It is uncertain if the potential decrease in $bSiO_2$ in this experiment was due to an underlying physiological change, or a shift to a less-silicified diatom species. In either case, there would be cascading impacts to the fluxes of $Si(OH)_4$ in surface waters of the Arctic, ballasting of particulate material, and the coupling between Si and other biogeochemical cycles.

### *6.5.4 Potential impacts of multiple environmental factors*

The response of diatoms to rising $CO_2$ levels is influenced by other environmental factors changing simultaneously due to climate change. The main global impact, increased ocean temperatures, will affect nutrient supply and the exposure of phytoplankton to irradiance through changes in water-column stratification (Behrenfeld et al., 2006). In the northern Bering Sea, an extended growing season and freshening of surface waters in response to sea ice melt and increased terrestrial runoff will also occur (Bates et al., 2014; Mathis et al., 2011). Taken together with OA, these factors will likely lead to shifts in diatom physiology, assemblage composition, and size structure. Negative impacts of OA are typically associated with multi-driver interactions, or extreme pH levels below 7.6 (Hoppe et al., 2015; Wolf et al., 2018), which are more severe than what is expected in the next century. Positive interactive effects have been observed too; for example, elevated $CO_2$ may benefit diatoms under low and moderate irradiance levels but could cause harm under high light due to photoinhibition (Gao et al., 2012). Similarly, warming could affect species differently, depending on their thermal preferences (Boyd et al., 2018). Overall, there will likely be complex and region-specific shifts in diatom physiology and phytoplankton assemblages, affecting their roles in marine ecosystems.

## 6.6 Conclusions

In this study, we demonstrated that the Pacific Arctic's naturally high $pCO_2$ variability, driven by low temperatures, low alkalinity, and seasonal primary production, promotes the occurrence of diatom species with the ability to tolerate a wide range of pH levels. There was statistically inconclusive evidence of small changes in diatom biomass and assemblage composition during exponential growth, but otherwise, the elemental composition and nutrient physiology of a

northern Bering Sea diatom assemblage was unaffected by pH. These results indicated that OA likely has only a small or nil impact on diatoms and their contributions to biomass and nutrient utilization during the summer. However, interpreting the pH-related effects on phytoplankton blooms requires caution, as other environmental factors will also vary as atmospheric $CO_2$ concentrations continue to rise. While the diatoms present in this study appeared to be well-suited to continue to thrive in these waters, future ocean acidification experiments will need to address multiple environmental factors to provide a more complete picture of change in this region.

– This page intentionally left blank –

# Chapter 7 – General conclusions and anticipated significance

This dissertation provides new insights on the interactions of siliceous phytoplankton with marine cycles of Si, C, and N across different ecosystems, over time, and during changes in some of the underlying physical processes that control phytoplankton productivity. In two contrasting oceanic regimes, the western North Atlantic subtropical gyre (Sargasso Sea) and the Pacific Arctic Region (PAR, Bering and Chukchi Seas), I investigated the biomass and elemental composition of phytoplankton assemblages, as well as rates of silicic acid utilization ($\rho$Si) by diatoms, and diatom contributions to rates of C ($\rho$C) and nitrate ($\rho NO_3$) utilization. These physiological processes were investigated in the context of physical changes occurring as a result of climate change. In the Sargasso Sea, increased surface warming results in enhanced stratification, which reduces the mixing of nutrients into surface waters. This process can inhibit the supply of nutrients to pelagic primary producers, and therefore, other means of nutrient replenishment, such as upwelling from eddies, may be essential to support productivity in the surface ocean. In the PAR, sustained ocean warming and widespread marine heatwaves have increased surface ocean temperatures and affected sea ice dynamics, thereby impacting timing and magnitude of phytoplankton blooms through changes in the availability of irradiance and nutrients to phytoplankton. In addition, I investigated the impact of ocean acidification (OA) on a model diatom species and phytoplankton assemblages from both the PAR and Sargasso Sea, focusing on the physiological effects of future pH levels on siliceous species. Throughout this dissertation, I used a highly-sensitive and novel method for measuring Si utilization in regions of the ocean that are under-studied with respect to both Si dynamics and the interactions of siliceous phytoplankton with other marine biogeochemical cycles. $^{32}$Si uptake incubations highlighted the value in using specialized techniques to better understand biogeochemical and physiological changes. The main findings, novelty, and implications of this work are summarized below.

## 7.1 Chapter conclusions and implications

***Chapter 2 – Changes in the contributions by differently-sized siliceous phytoplankton to carbon, nitrogen, and silicon utilization after eddy-driven upwelling in the Sargasso Sea***

This chapter assessed size-fractionated estimates of contributions by siliceous phytoplankton to nutrient utilization rates in the Sargasso Sea during late-summer (September to November), and during an eddy-driven upwelling event.

The main findings are:

- Under stratified, oligotrophic conditions in September and October 2018, small prokaryotic and eukaryotic phytoplankton contributed more to $\rho C$ and $\rho NO_3$ than silicifying phytoplankton throughout the water column and at the deep-chlorophyll maximum.
- During an eddy-driven nutrient injection to the euphotic zone in November 2018, there was a strong response from all autotrophic biomass with a concomitant increase in nutrient utilization rates.
    - Eukaryotic silicifiers, such as pico- and nanoeukaryotic diatoms, contributed more to the biomass and productivity at the deep-chlorophyll maximum and base of the euphotic zone in comparison to non-silicifiers. Diatoms specifically accounted for 80% of all $\rho NO_3$ below the mixed layer during the passing of the eddy.
    - Within the surface mixed layer, the main contributors to $\rho C$ and $\rho NO_3$ were either small, non-siliceous phytoplankton, or cyanobacteria such as *Synechococcus.*

Novelty and implications: I performed the first study of size-fractionated nutrient utilization ($\rho C$,

$\rho NO_3$, and $\rho Si$) by phytoplankton during the late-summer in the Sargasso Sea. I also captured the effect of a mesoscale eddy on the relative contribution of different silicifying phytoplankton to particulate biomass and nutrient utilization rates. While other studies have assessed $\rho C$, $\rho NO_3$, or $\rho Si$ separately and at different times of year, I measured all three simultaneously for $> 5$ µm and $< 5$ µm phytoplankton size classes, and determined the contributions to these rates by the cyanobacteria *Synechoccoccus* before and after the eddy upwelling event. These results provide a novel perspective on phytoplankton productivity throughout the water column, in particular around the base of the euphotic zone where nutrients are injected from deeper waters, even during low-productivity times of year. The findings highlight the important role of diatoms during eddy-driven upwelling, which is not frequently reported in the literature. As surface stratification in subtropical ecosystems continues to intensify, mechanisms such as eddies may play an increasingly important role in supplying nutrients in the euphotic zone and supporting the downward flux of organic matter from surface waters.

***Appendix B – Coupled measurements of primary productivity, nitrate utilization, and silicon dynamics across the North Atlantic subtropical gyre ecosystem***

This appendix included size-fractionated measurements of phytoplankton biomass and nutrient utilization rates across a latitudinal transect (33°N to 19°N) of the North Atlantic subtropical gyre ecosystem, from 27-Sep to 07-Oct, 2018.

The main findings are:

- Phytoplankton biomass (chl-*a*) was consistent across the North Atlantic subtropical gyre, and concentrated at a deep-chlorophyll maximum.

- Cells < 5 µm dominated chl-*a* (> 90%) throughout the water column at all stations.
- Biogenic silica concentrations were low at all depths and stations, and cells > 5 µm accounted for between 57 – 64% of total $bSiO_2$.
- Nutrient utilization rates were low, and did not follow the same patterns as biomass. Carbon utilization rates increased towards southern stations, while $\rho NO_3$ did not vary between latitudes. Small cells < 5 µm accounted for 66% of $\rho C$ and $\rho NO_3$.
- Silicic acid utilization rates were low but spatially variable across latitudes, and were ~3-fold higher at the southernmost station. Cells < 5 µm accounted for 73% of $\rho Si$ at the southernmost station, compared to other stations where cells > 5 µm accounted for 61%.

Novelty and implications: In this appendix, I offer new insights into phytoplankton productivity across a subtropical ecosystem and additional context to Chapter 2. These results are the first size-fractionated measurements of phytoplankton biomass coupled to simultaneous measures of size-fractionated $\rho C$, $\rho NO_3$, and $\rho Si$ in this region. I also provide biogenic and lithogenic silica concentrations, which are rarely reported across the North Atlantic subtropical gyre.

***Chapter 3 – Elemental composition and nutrient utilization of siliceous phytoplankton assemblages in the Pacific Arctic Region during periods of elevated ocean temperature***

This chapter is the longest time-series of productivity measurements by siliceous phytoplankton in the PAR, and investigates the effects of ocean warming on diatom productivity and elemental composition at different biological hotspots throughout the Distributed Biological Observatory (DBO).

The main findings are:

- The PAR was subject to a distinct warming period between 2011 – 2019, with positive trends in sea-surface temperatures from the northern Bering Sea to the northern Chukchi Sea. A widespread marine heatwave (MHW) in 2019 resulted in exceptionally high temperature anomalies and early ice breakup in all regions of the DBO.
- Diatom biomass and other indicators of silicon dynamics declined significantly over the entire time-series in the DBO1 region of the northern Bering Sea. Other regions did not show consistent impacts during either the warming period or the longer time-series.
- During the 2019 MHW, in the nutrient-poor southern Chukchi Sea and northern Chukchi Sea there was evidence of higher diatom productivity ($\rho$Si) than at any other point in the time-series in the same locations.
- Anomalously low ratios of particulate C:N were observed throughout much of the PAR during the 2019 MHW. Higher ratios of particulate Si:C and Si:N were frequently associated with lower temperatures, although no clear mechanism for either set of observations was seen.

Novelty and implications: I contributed an additional 5 years of data to the existing DBO time-series, including 4 more years of $\rho$Si measurements and capturing a period of unprecedented warming throughout the region. Using the full length of the phytoplankton productivity time-series (2006 – 2022), I assessed the impact of a warming period from 2011 – 2019, and the 2019 marine heatwave on its own, to a comprehensive suite of measurements across 6 different biological hotspots. The dataset presented in this dissertation represents, to my knowledge, the longest running account of Si dynamics in the Arctic, and makes a noteworthy contribution to the

ongoing assessment of rapidly changing high-latitude marine ecosystems. This chapter showed that the ecosystem of the northern Bering Sea may be shifting to become more pelagic, but diatoms are still highly dominant in most phytoplankton assemblages across the PAR in mid-July. Spanning 16 years (2006 – 2022), this time-series serves as a crucial resource for understanding how rapidly warming Arctic ecosystems may adapt to climate stress.

***Chapter 4 – Morphological and physiological responses of the cosmopolitan marine diatom* Thalassiosira rotula *to acidification***

This chapter added to the body of work addressing the effect of pH on the morphology, elemental composition, and nutrient physiology of diatoms growing under optimal conditions.

The main findings are:

- Low pH (7.75) can result in decreased cell size in the cosmopolitan diatom *Thalassiosira rotula*, which may affect the role of this and similar diatoms in biogeochemical processes.
- Silicification, i.e. $bSiO_2$ quotas, $\rho$Si, and ratios of Si:C and Si:N remained unchanged under OA conditions.
- Particulate quotas of C, N, and chl-*a* were unaffected by OA, and $\rho$C and $\rho NO_3$ were generally unaffected as well.

Novelty and implications: In addition to OA experiments on diatoms being less common than for other phytoplankton, this study is one of few diatom culturing experiments that specifically focuses on silicification. The species used, *T. rotula*, has also not been used in any prior OA study. Based on my results, the changes in cell size found were likely not ecologically or

biogeochemically important. Impacts of OA alone on $\rho$Si, $bSiO_2$ quotas, or the relationships between Si, C, and N in diatom assemblages dominated by *T. rotula, T. gravida,* or related species may be small or nil.

***Chapter 5 – Impacts of ocean acidification on phytoplankton from an oligotrophic subtropical ecosystem***

This chapter assessed the impact of a future OA scenario on the nutrient physiology and elemental composition of a phytoplankton assemblage from the deep-chlorophyll maximum in the Sargasso Sea.

The main findings are:

- The POC quota of *Synechococcus* decreased by 16% under low pH conditions.
- Large cells > 5 μm accounted for approximately half of $bSiO_2$ concentrations and 30% of $Si(OH)_4$ utilization, but there were no significant differences between pH treatments.
- Silicifiers were responsible for between 50 – 66% of $\rho NO_3$ utilization, and pH treatment had no effect on their contribution to any nutrient utilization rates.
- All other indicators of phytoplankton physiology were unaffected by OA at pH levels simulating turn of the century projections (~7.9).

Novelty and implications: This is one of the only studies to conduct an OA experiment on phytoplankton in the Sargasso Sea. A focus on Si dynamics and assessing the contributions of siliceous phytoplankton to $\rho$C and $\rho NO_3$ was especially unique. Diatoms in this region are likely well-suited to future pH conditions in the Sargasso Sea. My observation of decreased

*Synechococcus* POC quotas due to pH are unlikely to affect overall C export or nutrient cycling because *Synechococcus* accounts for a very small proportion of deep-chlorophyll maximum biomass. Although phytoplankton assemblages in the Sargasso Sea may remain unchanged under future OA scenarios, interactive effects with nutrient concentrations were unresolved by this study.

***Chapter 6 – Physiological responses to high $CO_2$ by a summertime diatom assemblage in the northern Bering Sea***

For this chapter, I exposed a natural phytoplankton assemblage collected from the northern Bering Sea to simulated ocean acidification conditions representing two future pH scenarios.

The main findings are:

- There were no statistically conclusive impacts of pH on the physiology or assemblage composition during either the exponential or nutrient-limited phases of growth.

Novelty and implications – This chapter is one of only a handful of OA studies that investigate Si dynamics in phytoplankton assemblages in the Arctic. The data are the most comprehensive assessment of elemental composition and nutrient utilization rate measurements for diatoms under multiple OA treatments in the PAR. Use of daily measurements for all parameters, instead of only at the end of the acclimation period, provide unique insight into the development of phytoplankton blooms under different pH conditions. Overall, results indicated that diatom assemblages in the northern Bering Sea seem well adapted to pH variability and may be tolerant of future OA conditions. However, further investigation is needed into some of the statistically

inconclusive results, and to improve understanding about interactive effects of pH with other environmental factors.

### 7.2 Final thoughts and future directions

Nutrient cycling in the ocean will be affected by climate change due to impacts on ocean circulation, stratification, and upwelling (Aumont et al., 2003; Bopp et al., 2013, 2005). This will lead to less siliceous phytoplankton production in surface oceans at lower latitudes due to decreased $Si(OH)_4$ supply from upwelling (Tréguer et al., 2018), and although the impact of climate change on phytoplankton in polar seas is debated, melting sea ice should decrease light limitation, and nutrient supply may increase, potentially increasing diatom productivity (Tréguer et al., 2021). It is also possible that pelagic $bSiO_2$ production will be altered by ocean pH and temperature, leading to complex interactions between the different impacts of climate change in various ecosystems. Predictions about ocean productivity under climate change vary widely (Laufkötter et al., 2015), and refinement of our understanding of the magnitude of Si fluxes in the marine environment is necessary to anticipate changes in the Si cycle, and the ecological and biogeochemical impacts that accompany such change (Tréguer et al., 2021).

This dissertation advances understanding about the complex interactions between phytoplankton, with a special focus on siliceous phytoplankton, and the marine cycles of Si, C, and N across different ecosystems and under varying environmental conditions. By contrasting oceanic regions – the Pacific Arctic Region and the North Atlantic subtropical gyre – this work highlighted how diatoms and other phytoplankton respond to climate-driven changes such as warming, stratification, and ocean acidification in drastically different environments. Key

findings include the critical role of eddy-driven nutrient upwelling in sustaining diatom productivity in the Sargasso Sea, the variability of diatom productivity in response to marine heatwaves in the PAR, and the minimal impacts of ocean acidification on phytoplankton and diatom physiology across both ecosystems. This work provides new insights into the response of siliceous phytoplankton and biogeochemical cycles to oceanic change, and lays the groundwork for future research to deepen our understanding of these dynamic systems.

Additional research is warranted on several of the conclusions from this dissertation, both to refine uncertainties, and improve our understanding of how marine ecosystems will adapt to future climate scenarios. Some suggestions for future studies include:

- Continued refinement of how silicifying organisms contribute to nutrient utilization in the Sargasso Sea during mesoscale phenomena that interrupt an otherwise oligotrophic system. For example, a field study can incorporate size-fractionated measures of C, N, and Si utilization while following the progression of a bloom during the process of nutrient upwelling rather than at a single sampling point. Use of $^{15}NH_4^+$ or $^{15}$N-urea isotopic tracers in addition to $^{15}NO_3^-$ would refine uncertainty around the source of N used by different size-fractions.
- Ongoing assessment of productivity and both elemental and taxonomic composition of phytoplankton across the PAR. Mechanistic studies to investigate the interaction between bloom timing and observations from ship-based sampling could involve remote-sensing or higher-resolution seasonal data from moorings or glider programs in the areas of interest. Ship-based nutrient utilization experiments conducted across multiple stations within each DBO region would assess spatial variability of productivity. Improved

taxonomic sampling through the use of techniques like DNA metabarcoding and microscopy could improve understanding about differences in assemblage composition and the relative contributions of different taxa in each region.

- Additional assessment of Si dynamics in the PAR, specifically the nutrient physiology of sea ice diatom assemblages, which have not been directly sampled. Collection of under-ice algae and measurement of $\rho$Si and elemental composition prior to ice breakup would provide insight about the timing and magnitude of diatom productivity at a time that is presently unknown. This would require early access to lower latitudes of the PAR, or in the northern Chukchi Sea, opportunistic sampling of sea ice in years when sea ice breakup has not yet occurred by mid-July.
- Modelling studies to look at the direct effect of temperature on elemental composition of phytoplankton assemblages in the PAR. Incorporation of models of diatom C or N metabolism could help elucidate the patterns of Si:C:N observed in our study, and potentially explain the observations of anomalously low C:N during a marine heatwave.
- Continue the investigation of the impact of ocean acidification on diatom physiology, particularly silicification.
    - *Thalassiosira* species are common in northern environments such as the Pacific Arctic Region, but other genera are also common. Further studies using more diatom species in unialgal studies, with larger pH differences, and longer acclimation periods, may provide better insights of OA effects on natural diatom assemblages.
    - Collect and isolate individual species from the PAR for use in unialgal studies.

- Use natural diatom assemblages and individual diatom species to investigate interactions of pH with temperature, irradiance, and/or nutrient limitation during acclimation-type experiments under controlled conditions.
- Although logistically difficult and prohibitively costly, for better comparison to natural cycles, conduct large-scale OA mesocosm studies similar to those that have been previously organized (e.g. in the eastern North Atlantic, Norwegian fjords, and the Mediterranean Sea), but emphasize Si dynamics. If implemented in the Bering or Sargasso Sea, such an experiment could capture longer-term acclimation of phytoplankton and variability under extended OA. This would reveal physiological and assemblage changes through different periods of seasonal change (e.g. irradiance, mixing, nutrient availability), allow the direct measurement of export, and potentially, impacts on higher trophic levels (e.g. grazing zooplankton) if not excluded from the experiments.

– This page intentionally left blank –

# Appendix A – Supplementary material for Chapter 2

This appendix contains supplementary materials to support *Chapter 2 – Changes in the contributions by differently-sized siliceous phytoplankton to carbon, nitrogen, and silicon utilization after eddy-driven upwelling in the Sargasso Sea.* These include:

1. Figures of the linear relationship between beam-attenuation coefficient (BAC) and particulate organic C (POC) and nitrogen (PON). Linear regression coefficients and r-squared values were calculated in RStudio 2023.06 (Posit Software, PBC, Boston, MA) using the package "ggpmisc".
2. Vertical profiles of discrete POC and PON concentrations compared to POC and PON concentrations derived from the linear relationship with BAC. Derived values are presented for the hydrocast used to determine the relationship between BAC and POC/PON, and also for the hydrocast during which productivity experiments were conducted.
3. Figures of the sea level anomaly around the BATS station on 06-Nov and 07-Nov, 2018, to confirm the presence of a cyclonic eddy that transited to the south of the study area.
4. Tables containing summarized data and references for comparison to prior studies on C, nitrate, and silicic acid utilization rates in the Sargasso Sea, at the BATS station.
5. Tables summarizing the contributions of different size-classes of silicifiers (diatoms > 5 μm, diatoms < 5 μm, *Synechococcus*) to total C utilization and nitrate utilization rates for three cruises completed during the study.

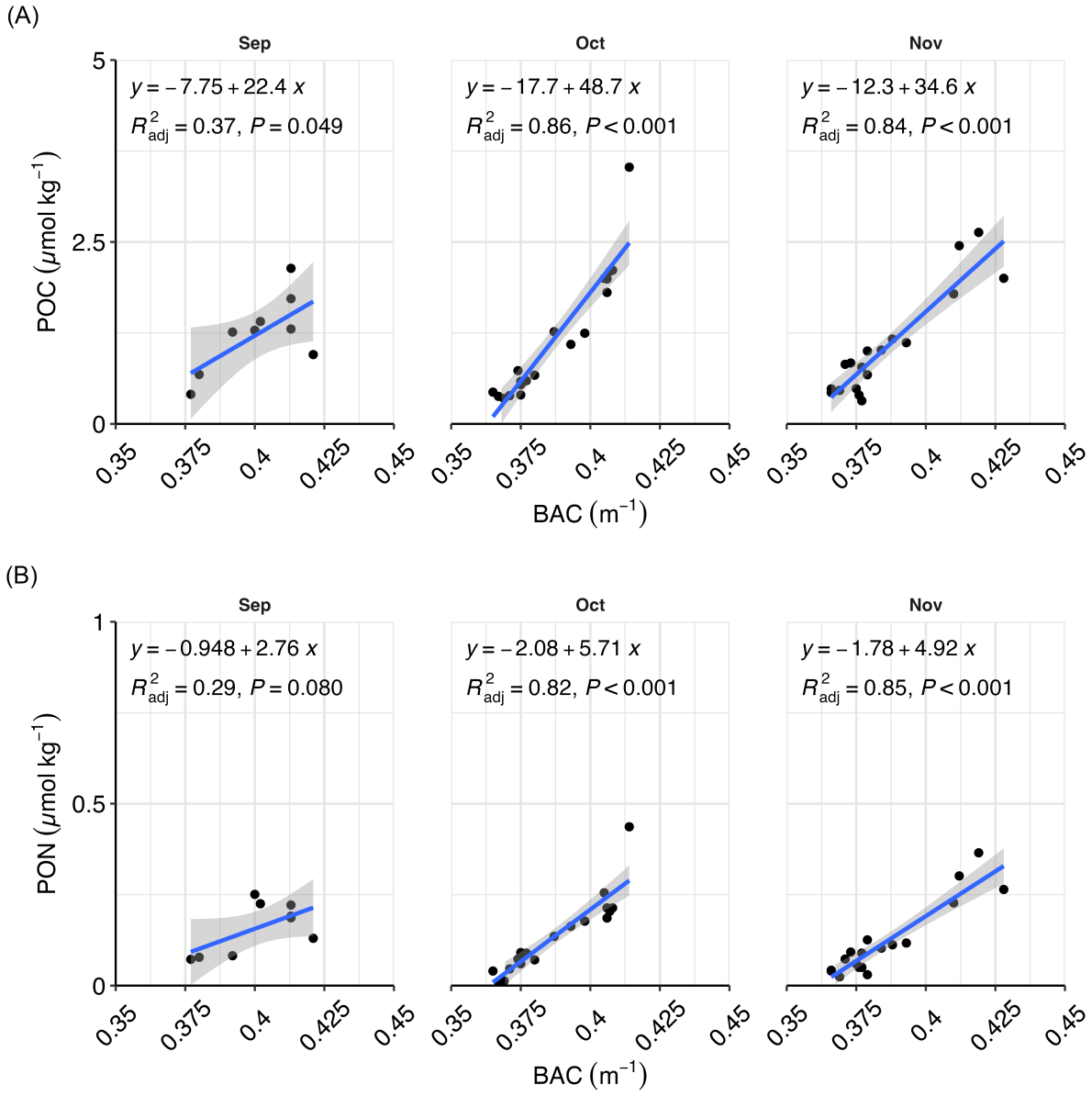


**Figure A.1.** Relationship between CTD beam attenuation coefficient (BAC) and particulate concentrations at the BATS station on 29-Sep, 21-Oct, and 07-Nov. Linear regressions of **(A)** particulate organic carbon (POC) and **(B)** particulate organic nitrogen (PON) are shown as the blue line, and the grey shaded area represents the 95% confidence interval for the fitted line.

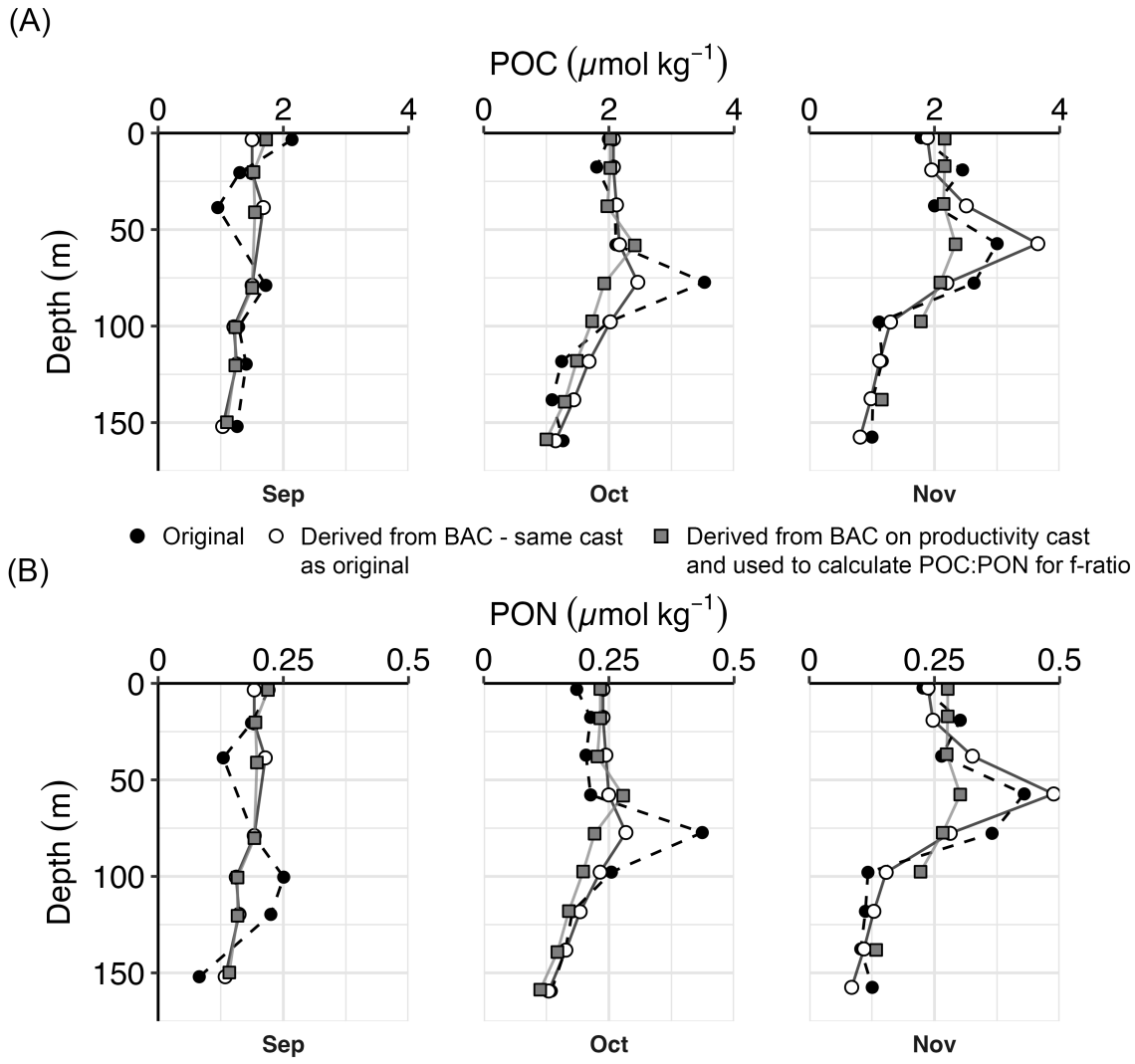


**Figure A.2.** Comparison of measured and derived values of **(A)** POC and **(B)** PON in the euphotic zone at the BATS station on 29-Sep, 18/21-Oct, and 06/07-Nov 2018. Black circles are values from the BATS core hydrocast, and white circles are derived values for comparison on the same hydrocast. Grey squares are values of POC or PON derived from BAC during the cast that was used for nutrient utilization incubations. Derived values were calculated using the relationship between BAC and POC or PON (Appendix A, Fig. A.1).

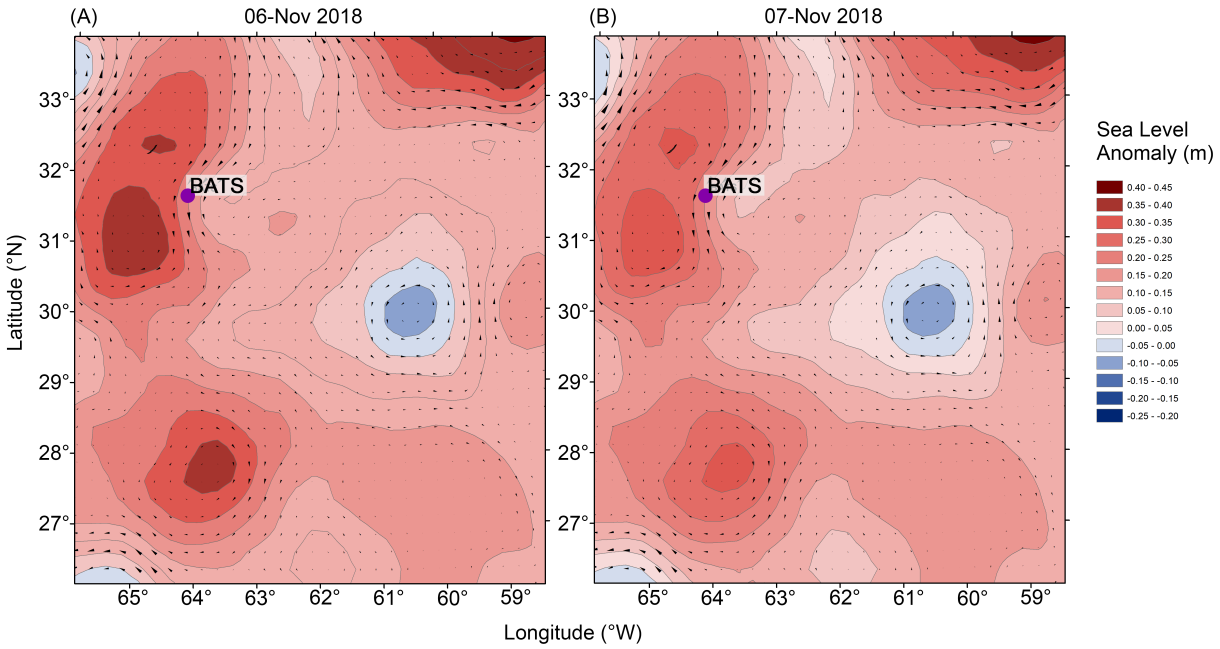


**Figure A.3.** Contour plot of sea level anomalies (SLA) around the BATS station on **(A)** 06-Nov, 2018 and **(B)** 07-Nov, 2018. Colours indicate the SLA, size and direction of arrows indicate geostrophic flow.

**Table A.1.** Average integrated primary productivity (PP) rates ($\int\rho C$) at the BATS station from a selection of previous studies during different years or seasons. All previous studies referenced used the radioisotope $^{14}C$ incubation method, whereas our study used the stable isotope $^{13}C$.

| **Date** | **Pico PP (0.7-2 µm)** | **Nano PP (2-20 µm)** | **Micro PP (20-200 µm)** | **Total PP** | **Reference** | **Comments** |
|---|---|---|---|---|---|---|
| | | (mg C $m^{-2}$ $d^{-1}$) | | | | |
| Jan – Dec 1958 | | | | 200 – 2000 | Menzel and Ryther (1960) | |
| August 1989 | 89 (63%) | 39 (28%) | 14 (10%) *53 (38%)* | 141 | Malone et al. (1993) | |
| March/April 1990 | 226 (68%) | 87 (26%) | 20 (6%) *107 (32%)* | 333 | | |
| 1989 – 1997 | | | | ~100 – 1500 | Steinberg et al. (2001) | *Review of BATS* |
| 1989 – 2011 | | | | 429.8±0.08 | Lomas et al. (2013) | *Updated review of BATS, dark-corrected NPP* |
| Feb/March 2004 | | | | 390 – 751 | Lomas et al. (2009a) | |
| Feb/March 2005 | | | | 516 – 652 | | |
| Spring 2011 | 123 (76%) | 13 (6%) | 25 (17%) *38 (23%)* | 161 | Cotti-Rausch et al. (2020) | *Merged nano (2-20 µm) and micro (20-200 µm) productivity.* 100 m integration. |
| Summer 2011 | 72±32 (77%) | 7±3 (8%) | 12±10 (15%) *19±10 (23%)* | 91±19 | | |
| Spring 2012 | 119±12 (81%) | 6±5 (5%) | 21±7 (15%) *27±9 (19%)* | 146±0 | | |
| Summer 2012 | 90±76 (46%) | 57±7 (34%) | 32±12 (20%) *89±14 (54%)* | 178±71 | | |
| | **Pico/nano PP (0.7 – 5 µm)** | **Nano/micro PP (> 5 µm)** | | **Total PP** | | |
| Sept 2018 | 33.0 (64%) | 19.3 (37%) | | 51.6 | This study | *Integrated to 140 m* |
| Oct 2018 | 40.0 (78%) | 12.6 (25%) | | 51.1 | | |
| Nov 2018 | 306.2 (81%) | 72.0 (19%) | | 378.2 | | |

**Table A.2.** Average integrated nitrate utilization rates ($\int \rho NO_3$) at BATS from previous studies that use the stable isotope $^{15}NO_3$ tracer technique. Values presented in other studies were originally shown as an average over a year, but were converted to daily rates for comparison here. When available, the range of values was also included.

| **Date** | **Pico $\int \rho NO_3$ (0.7-2 µm)** | **Nano $\int \rho NO_3$ (2-20 µm)** | **Micro $\int \rho NO_3$ (20-200 µm)** | **Total $\int \rho NO_3$** | **Reference** | **Comments** |
|---|---|---|---|---|---|---|
| | | | (mmol N $m^{-2}$ $d^{-1}$) | | | |
| Feb – Dec 1992 | | | | 2.6 | Lipschultz et al. (2001) | |
| July – Nov 1993 | | | | 0.4 | | |
| Feb/Mar 2004 | | | | 0.9 – 4.3 | Lomas et al. (2009a) | *Integrated to 140 m* |
| Feb/Mar 2005 | | | | 0.7 – 3.5 | | |
| | **Pico/nano $\int \rho NO_3$ (0.7 – 5 µm)** | **Nano/micro $\int \rho NO_3$ (> 5 µm)** | | **Total $\int \rho NO_3$** | | |
| Sept 2018 | 0.88 (72%) | 0.34 (28%) | | 1.22 | This study | *Integrated to 140 m* |
| Oct 2018 | 0.59 (72%) | 0.23 (28%) | | 0.82 | | |
| Nov 2018 | 2.46 (79%) | 0.66 (21%) | | 3.12 | | |

**Table A.3.** Average integrated silicon utilization rates ($\int\rho$Si) at the BATS station from previous studies during different years or seasons. All methods utilized $^{32}$Si tracer techniques, except for Nelson and Brzezinski (1997), which used $^{30}$Si stable isotopes. Yearly averages from previous studies were converted to daily rates for comparison. When available, the range of values was also included.

| **Date** | **Pico $\rho$Si (0.4-3 µm)** | **Nano $\rho$Si (>3 µm)** | **Total $\rho$Si** | **Reference** | **Comments** |
|---|---|---|---|---|---|
| | | (mmol Si $m^{-2}$ $d^{-1}$) | | | |
| August 1991 – May 1994 | | | 0.100–0.913 (0.42±0.22) | Nelson and Brzezinski (1997 | |
| Feb/Mar 2004 | | | 1.03±0.82 | Krause et al. (2009) | |
| Feb/Mar 2005 | | | 0.97±1.45 | | Integration to 220 m, but 85% within upper 140 m |
| April 2007 | | | 0.8 – 1.1 | Krause et al. (2010b) | |
| July 2012 | 0.07 (1.2%) | 5.92 (98.8%) | 5.99 | Krause et al. (2017) | *$V_{>3}$ = 0.82; $V_{<3}$ = 0.05* |
| October 2012 | 0.012 (3.1%) | 0.39 (96.9%) | 0.40 | | *$V_{>3}$ = 0.38; $V_{<3}$ = 0.07* |
| September 2013 | 0.03 (8.3%) | 0.32 (91.7%) | 0.35 | | *$V_{>3}$ = 0.22; $V_{<3}$ = 0.17* |
| | **Pico/nano $\rho$Si (0.7 – 5 µm)** | **Nano/micro $\rho$Si (> 5 µm)** | **Total $\rho$Si** | | |
| Sept 2018 | 0.033 (38%) | 0.056 (64%) | 0.088 | This study | *Integrated to 140 m; main text Table 2.3 for V values* |
| Oct 2018 | 0.035 (61%) | 0.022 (39%) | 0.057 | | |
| Nov 2018 | 0.165 (58%) | 0.121 (42%) | 0.286 | | |

**Table A.4.** Contributions of silicifiers to total primary productivity ($\rho$C) according to depth at the BATS station on 29-Sep, 18-Oct, and 06-Nov 2018. Columns show the overall amount of $\rho$C measured (total $\rho$C), amount attributable to large-celled silicifiers ($\rho C_{>5\mu m\ Si}$), small-celled silicifiers ($\rho C_{<5\mu m\ other\ Si}$), *Synechococcus* ($\rho C_{Syn}$) and total amount of $\rho$C for all silicifiers combined (total $\rho C_{Si}$). The % of total $\rho$C for each group of silicifier is indicated in italics. Depth ranges are ML = within mixed layer, DCM = peak of the deep chlorophyll max, $DCM_Z$ = base of the range of depths for the deep chlorophyll max, $Z_{Eu}$ = base of the euphotic zone (0.1% $I_D$). Depths in metres are rounded to the nearest 10 m. $\int\rho C_{DCM\text{-}ZEu}$ is the integrated productivity inclusive of the DCM to the base of the euphotic zone.

| **Date** | **Depth (m)** | **Depth range** | **Total $\rho$C** | **$\rho C_{>5\mu m\ Si}$** | **$\rho C_{<5\mu m\ other\ Si}$** (nmol C $L^{-1}$ $d^{-1}$) | **$\rho C_{Syn}$** *(% of $\rho$C)* | **Total $\rho C_{Si}$** |
|---|---|---|---|---|---|---|---|
| 29-Sep | < 5 | ML | 95.4 | 11.7 *(12%)* | 5.7 *(6.0%)* | 23.4 *(25%)* | 40.8 *(43%)* |
| | 20 | ML | 91.3 | 8.1 *(8.9%)* | 3.6 *(4.0%)* | 22.8 *(25%)* | 34.6 *(38%)* |
| | 120 | DCM | 15.4 | 1.7 *(11%)* | 0.6 *(4%)* | 0.8 *(5%)* | 3.1 *(20%)* |
| | 140 | $DCM_Z/Z_{Eu}$ | 9.5 | 1.2 *(12%)* | 0.4 *(4%)* | 0.5 *(6%)* | 2.1 *(22%)* |
| | | *$\int\rho C_{DCM\text{-}ZEu}$ ($\mu$mol $m^{-2}$ $d^{-1}$)* | *240.0* | *27.6 (12%)* | *8.9 (3.7%)* | *13.1 (5.4%)* | *49.6 (21%)* |
| 18-Oct | 20 | ML | 89.1 | 3.0 *(3.4%)* | 2.6 *(2.9%)* | 25.4 *(29%)* | 31.1 *(35%)* |
| | 100 | DCM | 17.6 | 2.2 *(12%)* | 2.6 *(15%)* | 12.3 *(70%)* | 17.1 *(97%)* |
| | 120 | $DCM_Z$ | 18.2 | 0.3 *(2%)* | 4.7 *(26%)* | 1.7 *(9.6%)* | 6.7 *(37%)* |
| | 140 | $Z_{Eu}$ | 7.7 | 1.0 *(14%)* | 1.0 *(13%)* | 0.1 *(1%)* | 2.2 *(28%)* |
| | | *$\int\rho C_{DCM\text{-}ZEu}$ ($\mu$mol $m^{-2}$ $d^{-1}$)* | *641.0* | *39.0 (6.1%)* | *134.7 (21%)* | *163.5 (26%)* | *337.2 (53%)* |
| 06-Nov | 20 | ML | 356.9 | 20.7 *(5.8%)* | 13.0 *(3.6%)* | 47.0 *(13%)* | 80.7 *(23%)* |
| | 80 | DCM | 107.3 | 10.6 *(9.9%)* | 14.4 *(13%)* | 15.5 *(14%)* | 40.5 *(38%)* |
| | 100 | $DCM_Z$ | 100.4 | 6.0 *(6.0%)* | 19.8 *(20%)* | 2.6 *(2.5%)* | 28.4 *(28%)* |
| | 140 | $Z_{Eu}$ | 36.4 | 5.3 *(15%)* | 9.7 *(27%)* | 0.0 *(0%)* | 15.1 *(42%)* |
| | | *$\int\rho C_{DCM\text{-}ZEu}$ ($\mu$mol $m^{-2}$ $d^{-1}$)* | *4867.6* | *398.4 (8.2%)* | *944.7 (19%)* | *234.3 (4.8%)* | *1577.3 (32%)* |

**Table A.5.** Contributions of silicifiers to total nitrate utilization ($\rho NO_3$) according to depth at the BATS station on 29-Sep, 18-Oct, and 06-Nov 2018. Columns show the overall amount of $\rho NO_3$ measured (total $\rho NO_3$), amount attributable to large-celled silicifiers ($\rho NO_{3\ >5\mu m\ Si}$), small-celled silicifiers ($\rho NO_{3\ <5\mu m\ other\ Si}$), *Synechococcus* ($\rho NO_{3\ Syn}$) and total amount of $\rho C$ for all silicifiers combined (total $\rho NO_{3\ Si}$). Depth ranges are ML = within mixed layer, DCM = peak of the deep chlorophyll max, $DCM_Z$ = base of the range of depths for the deep chlorophyll max, $Z_{Eu}$ = base of the euphotic zone. Depths in metres are rounded to the nearest 10 m. $\int \rho NO_{3DCM\text{-}ZEu}$ is the integrated productivity inclusive of the DCM to the base of the euphotic zone.

| Date | Depth (m) | Depth range | Total $\rho NO_3$ | $\rho NO_{3\ >5\mu m\ Si}$ | $\rho NO_{3\ <5\mu m\ other\ Si}$ | $\rho NO_{3\ Syn}$ | Total $\rho NO_{3\ Si}$ |
|---|---|---|---|---|---|---|---|
| | | | (nmol N $L^{-1}$ $d^{-1}$) *(% of total $\rho NO_3$)* | | | | |
| 29-Sep | < 5 | ML | 16.9 | 1.3 *(7.8%)* | 0.6 *(4%)* | 2.4 *(14%)* | 4.4 *(26%)* |
| | 20 | ML | 19.7 | 0.9 *(5%)* | 0.4 *(2%)* | 2.4 *(12%)* | 3.7 *(19%)* |
| | 120 | DCM | 3.2 | 0.2 *(6%)* | 0.1 *(2%)* | 0.1 *(3%)* | 0.3 *(11%)* |
| | 140 | $DCM_Z/Z_{Eu}$ | 1.3 | 0.1 *(10%)* | 0.0 *(3%)* | 0.1 *(4%)* | 0.2 *(18%)* |
| | | *$\int \rho NO_{3\text{-}DCM\text{-}ZEu}$ ($\mu mol\ m^{-2}\ d^{-1}$)* | *43.4* | *3.1 (7.2%)* | *1.0 (2%)* | *1.4 (3.1%)* | *5.5 (13%)* |
| 18-Oct | 20 | ML | 12.2 | 0.3 *(3%)* | 0.3 *(2%)* | 2.6 *(21%)* | 3.3 *(27%)* |
| | 100 | DCM | 3.6 | 0.2 *(7%)* | 0.3 *(8%)* | 1.3 *(35%)* | 1.8 *(50%)* |
| | 120 | $DCM_Z$ | 2.1 | 0.0 *(2%)* | 0.5 *(25%)* | 0.2 *(9%)* | 0.7 *(35%)* |
| | 140 | $Z_{Eu}$ | 1.5 | 0.1 *(8%)* | 0.1 *(8%)* | 0.0 *(1%)* | 0.2 *(16%)* |
| | | *$\int \rho NO_{3\text{-}DCM\text{-}ZEu}$ ($\mu mol\ m^{-2}\ d^{-1}$)* | *96.3* | *4.4 (4.6%)* | *15.2 (16%)* | *16.9 (18%)* | *36.4 (38%)* |
| 06-Nov | 20 | ML | 50.1 | 2.3 *(4.7%)* | 1.5 *(2.9%)* | 4.8 *(9.7%)* | 8.6 *(17%)* |
| | 80 | DCM | 5.3 | 1.2 *(23%)* | 1.6 *(31%)* | 1.6 *(30%)* | 4.4 *(83%)* |
| | 100 | $DCM_Z$ | 2.9 | 0.7 *(23%)* | 2.2 *(77%)* | 0.3 *(9%)* | 3.2 *(109%)* |
| | 140 | $Z_{Eu}$ | 2.3 | 0.6 *(26%)* | 1.1 *(47%)* | 0.0 *(0%)* | 1.7 *(74%)* |
| | | *$\int \rho NO_{3\text{-}DCM\text{-}ZEu}$ ($\mu mol\ m^{-2}\ d^{-1}$)* | *188.8* | *44.8 (23.7%)* | *106.3 (56.3%)* | *24.2 (12.8%)* | *175.3 (93%)* |

– This page intentionally left blank –

# Appendix B – Coupled measurements of primary productivity, nitrate utilization, and silicon dynamics across the North Atlantic subtropical gyre ecosystem

## B.1 Abstract

In subtropical regions of the ocean such as the Sargasso Sea, located in the western North Atlantic subtropical gyre, phytoplankton biomass and productivity are regulated by the availability of nutrients. This ecosystem relies on seasonal and mesoscale phenomena to resupply nutrients to sunlit surface waters to support growth. During the oligotrophic late-summer across the Sargasso Sea, ocean conditions are typically highly stratified by warm surface waters, leading to undetectable nutrient concentrations throughout the water column from the surface to near the base of the euphotic zone. Phytoplankton biomass is typically concentrated around a deep chlorophyll maximum (DCM) and consists mostly of cyanobacteria and small eukaryotic algal taxa. To assess the distribution and magnitude of productivity by different phytoplankton in this ecosystem, we collected measurements of dissolved nitrate ($NO_3^-$) and silicic acid ($Si(OH)_4$), size-fractionated (> 5 µm, < 5 µm) chlorophyll-*a* (chl-*a*) and biogenic silica ($bSiO_2$) biomass, and size-fractionated utilization rates of carbon ($\rho C$), $NO_3^-$ ($\rho NO_3$), and $Si(OH)_4$ ($\rho Si$). Sampling locations covered a latitudinal gradient starting north of the Bermuda Atlantic Time-series Study (BATS) station (31.67 °N) and ending near Puerto Rico (19.67 °N). We found that the surface ocean was highly stratified and nutrient-depleted across all latitudes, with injections of $NO_3^-$ from deeper water around 150 m at most stations. Chlorophyll-*a* biomass was always < 0.15 µg $L^{-1}$ and heavily favoured cells < 5 µm, forming a DCM between approximately 100 – 140 m at all stations. Biogenic silica was also low at all stations and depths (< 15 nmol $L^{-1}$) and had little pattern with depth. Utilization rates of C consistently increased along the north to south transect, and cells > 5 µm accounted for more $\rho C$ at southern latitudes. In contrast, $\rho NO_3$ did not vary much with latitude, and was only ~1 mmol $m^{-2}$ $d^{-1}$ at all stations. Interestingly, $\rho Si$ was much higher at the southernmost station than elsewhere, although a mechanism for this was not clear

based on our data. These results provide additional context for an accompanying study at the BATS station that occurred from Sep-Nov 2018 (Chapter 2). They also provide the first size-fractionated measurements of biomass along with simultaneous measures of $\rho C$, $\rho NO_3$, and $\rho Si$ in this region, offering new insights into how different size-fractions of phytoplankton vary in their composition, biomass, and productivity across a subtropical ecosystem.

## B.2 Introduction

The Bermuda-Atlantic Time-series Study (BATS) is one of the longest records of oceanic hydrographic, chemical, and biological measurements (Bates and Johnson, 2020). The BATS station is located in the Sargasso Sea, in the western North Atlantic subtropical gyre, and is bordered by the Gulf Stream on the west and northwest, and by the North Atlantic equatorial current to the south. The region is characterized by a southwest net flow, driving by weak geostrophic recirculation (Siegel and Deuser, 1997) and net downwelling (McClain and Firestone, 1993). Examples of mesoscale processes include high energy eddies such as cold core rings, and smaller cyclonic and anticyclonic eddies, which can provide spatially and temporally intermittent fluxes of nutrients into the euphotic zone (McGillicuddy and Robinson, 1997; Siegel et al., 1999; Steinberg et al., 2001). With a high-pressure atmospheric system that prevents seasonal weather fronts from passing, the summertime ocean has a warm, shallow mixed layer (Steinberg et al., 2001). Storm activity in the fall and winter erodes the seasonal thermocline, changing the physical structure with much deeper mixing depths of up to 150 – 300 m, causing ecosystem dynamics to shift dramatically (Bates et al., 1998; Krause et al., 2009; Lomas et al., 2009; Nelson, 1998). This time-series plays a crucial role in studying ocean biogeochemistry and its impact on carbon and other nutrient cycling in a large oligotrophic region.

This data chapter provides broader ecosystem context and background for Chapter 2, which examines the role of silicifying phytoplankton in C, $NO_3^-$, and Si utilization at the BATS station during eddy-driven upwelling. This study however, was conducted during stratified, oligotrophic late-summer conditions at four stations along a transect from the BATS station to the southernmost region of the Sargasso Sea (Fig. B.1). The measurements described here include

dissolved nutrient concentrations, size-fractionated (< 5 µm, > 5 µm) chlorophyll-*a* (chl-*a*), biogenic silica ($bSiO_2$) biomass, and size-fractionated nutrient utilization rates. Of interest to those who study the marine silicon cycle, lithogenic silica ($LSiO_2$) concentrations are described as well. No prior studies have used these measurements simultaneously in different size-fractions to estimate the contributions of differently-sized phytoplankton to biomass and nutrient utilization throughout the water column across the North Atlantic subtropical gyre ecosystem.

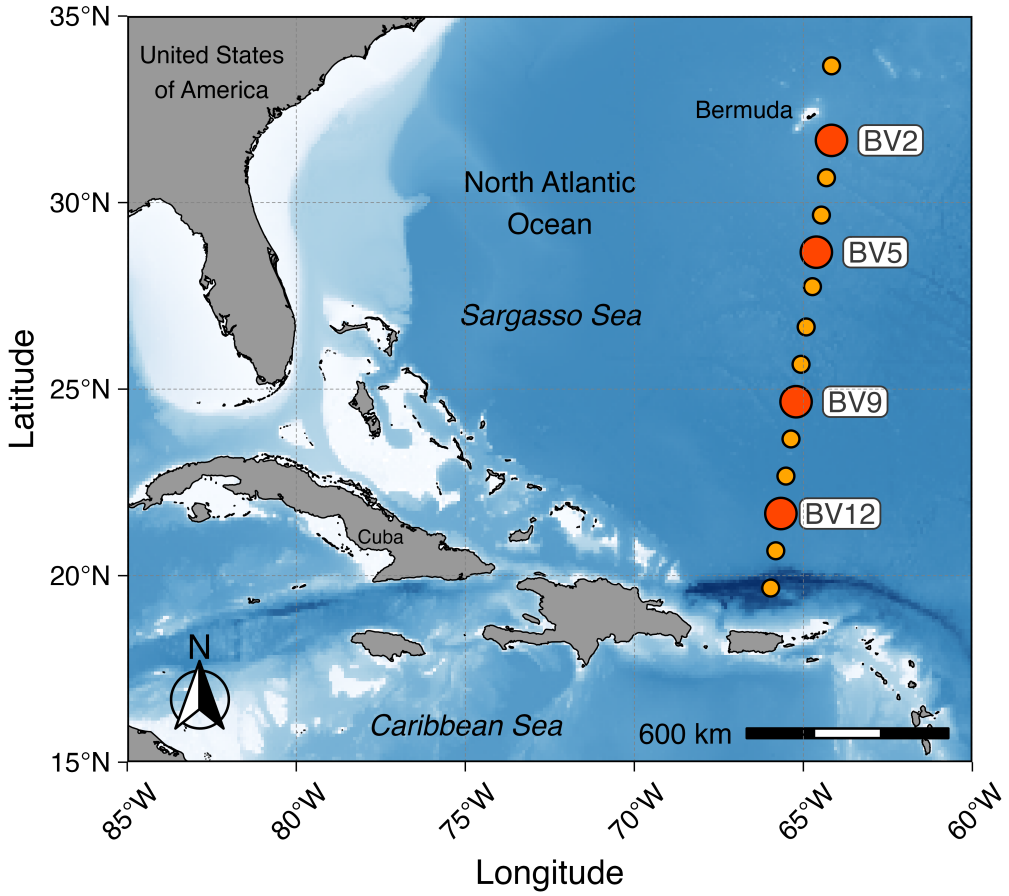


**Figure B.1.** Stations sampled across the Sargasso Sea in the North Atlantic during the BVAL53 cruise from September 27 – October 4, 2018. Larger circles indicate stations where nutrient utilization experiments and size-fractionated biomass measurements were conducted in addition to core measurements made by the BATS program. BV12 was sampled for nutrient utilization experiments during the return leg of the cruise, on October 7, 2018.

## B.3 Materials and Methods

### *B.3.1 Cruise locations and timing*

A research cruise (BVAL53) was undertaken on the *R/V Atlantic Explorer* from the Bermuda Institute of Ocean Sciences (BIOS) from 27-Sep to 07-Oct, 2018. We conducted incubation experiments for primary productivity and nutrient utilization at four of those stations, BV2 (the BATS station), BV5, BV9, and BV12 (Fig B.1, Table B.1). These four stations are designated as "productivity" stations throughout the manuscript. Additional stations were sampled along the transect, but their data is not used extensively in this study.

**Table B.1.** Sampling dates and locations for the BVAL53 cruise in 2018 in the Sargasso Sea. Stations at which size-fractionated biomass and incubation experiments for C, $NO_3^-$, and Si utilization rates were conducted are highlighted in bold. Hydrographic measurements and dissolved nutrients were collected at all stations. *Note productivity measurements for BV12 were sampled on the return leg of the cruise.

| Station Name | Date Sampled | Latitude (˚N) | Longitude (˚W) |
|---|---|---|---|
| BV1 | 27-Sep | 33.665 | 64.166 |
| **BV2 (BATS)** | **29-Sep** | **31.667** | **64.168** |
| BV3 | 29-Sep | 30.666 | 64.317 |
| BV4 | 29-Sep | 29.665 | 64.467 |
| **BV5** | **30-Sep** | **28.670** | **64.616** |
| BV6 | 01-Oct | 27.746 | 64.731 |
| BV7 | 01-Oct | 26.666 | 64.917 |
| BV8 | 02-Oct | 25.665 | 65.069 |
| **BV9** | **02-Oct** | **24.662** | **65.216** |
| BV10 | 03-Oct | 23.664 | 65.366 |
| BV11 | 03-Oct | 22.669 | 65.516 |
| BV12 | 03-Oct | 21.666 | 65.667 |
| **BV12*** | **07-Oct** | **21.665** | **65.665** |
| BV13 | 04-Oct | 20.667 | 65.816 |
| BV14 | 04-Oct | 19.668 | 65.966 |

### *B.3.2 Hydrography and water sample collection*

For each cruise, two hydrocasts were used to collect the data presented here. The first, the productivity hydrocast, included hydrographic depth profiles as well as discrete samples for dissolved nutrients, particulate biomass, and incubation experiments to determine nutrient utilization rates. The second hydrocast, collected by the BATS program, included many

additional measurements, but we only used hydrographic depth profiles as well as discrete samples for dissolved nutrients and total inorganic carbon ($C_T$). The remaining data is publicly available at https://bats.bios.asu.edu/bats-data/. The second hydrocast is referred to as the BATS core hydrocast throughout the text when needed.

Hydrographic measurements, including temperature, conductivity, pressure, *in vivo* fluorescence, and dissolved oxygen concentrations, were collected along the transect with a Sea-Bird SBE-09 *plus* CTD instrument package during hydrocasts from surface to >4200 m depth. Water samples for nutrient utilization experiments and biomass measurements were collected from 12-L Niskin bottles on the CTD-rosette at depths that corresponded to optical depths ($I_D$) of 100, 50, 30, 15, 7, 3, 1, 0.5 or 0.1% of surface irradiance. $I_D$ was determined using vertical profiles of underwater irradiance measured using the photosynthetically active radiation (PAR) sensor on the instrument package mounted on the rosette. Optical depths were chosen so as to include the surface mixed layer, and the DCM, and also rounded to match the nearest standardized depth used on the BATS core hydrocast. During the BATS core hydrocast, discrete samples were collected at standardized depths at 0, 40, 80, 100, 120, and 150 m.

### *B.3.3 Dissolved nutrient concentrations*

Samples for dissolved nutrient concentrations ($NO_3^-$, $PO_4^{3-}$, $Si(OH)_4$) were collected at every station on the cruise by filtering seawater through a 0.8 µm Nuclepore polycarbonate (PC) filter into an acid-washed HDPE bottle. Samples were collected in duplicate and frozen at sea at -20°C. Later, concentrations were determined using segmented continuous flow analysis on a

nutrient autoanalyzer system at BIOS following standard BATS methods, based on JGOFS protocols (Knap et al., 1997).

For use in the calculation of $NO_3^-$ utilization rates, additional seawater samples for $NO_3^-$ concentrations were collected in triplicate from the same Niskin bottles from which samples were collected for the rate experiments. Seawater was filtered through disposable 0.45 µm polyether sulfone (PES) filter cartridges. The filtrate was collected in an acid-washed 15 mL centrifuge tube and immediately frozen at -20°C. Concentrations were measured later at the University of Victoria using an Astoria 2 Nutrient Autoanalyzer (Astoria-Pacific Inc., OR, USA) according to Barwell-Clarke and Whitney (1996). Similarly, separate water samples were collected to determine $Si(OH)_4$ concentrations for use in the calculation of Si utilization rates. The $Si(OH)_4$ samples were stored at 4°C to avoid polymerization of $Si(OH)_4$ at freezing temperatures, and analyzed later at the University of Victoria. Concentrations were determined colourimetrically with a Beckman DU 530 UV/Vis spectrophotometer (Beckman Coulter, CA, USA) using a reverse-order reagent blank (Brzezinski and Nelson, 1986) and a 10-cm glass cuvette for the highest analytical precision. Analytical error (coefficient of variation (CV)) for nutrient concentrations was determined using replicated standards in artificial seawater, resulting in CV for $NO_3^-$ = 4.3% and $Si(OH)_4$ = 1.2%. Triplicate values of $NO_3^-$ and $Si(OH)_4$ were averaged before calculating utilization rates.

### *B.3.4 Chlorophyll-a concentrations*

Size-fractionated chlorophyll-*a* (chl-*a*) concentrations were determined by gently filtering up to 1.0 L of seawater first through a 5.0 µm polycarbonate (PC) filter and then through a 0.7 µm nominal pore-size glass fiber filter (GF-75) (AMD Manufacturing, Ontario, CA). Filters were

frozen at -80°C and stored until later analysis. A total chl-*a* sample was collected by filtering 1.0 L of seawater onto a GF-75 filter, but total chl-*a* concentrations are not shown unless noted, as the sum of the size-fractions always matched the total. The chl-*a* samples were promptly analyzed at BIOS following the cruises. Filters were placed in glass centrifuge tubes and submerged in a 90% acetone solution for 24-h at -20°C in the dark. The extracted samples were warmed to room temperature, centrifuged to remove filter particulates, and decanted into borosilicate cuvettes before measurement on a recently calibrated Turner-Designs 10AU fluorometer (Turner Designs, CA, USA). Phaeopigment interference was corrected for by acidifying each sample and measuring again on the fluorometer (Parsons et al., 1984). Chlorophyll-*a* analysis had an average CV of 11.8%, determined from replicated field samples (instead of standards).

### *B.3.5 Biogenic and lithogenic silica concentrations*

Size-fractionated $bSiO_2$ was collected by gently filtering 2.0 L of seawater through a 5 µm PC filter (AMD Manufacturing, Ontario, CA), after which the filtrate was filtered onto a 0.6 µm PC filter. Samples for total $bSiO_2$ were collected by filtering 2.0 L of seawater onto a 0.6 µm pore-size PC filter, but total $bSiO_2$ concentrations are not shown unless noted, as the sum of the size-fractions always matched the total. Filters were frozen at -20°C until returned to shore, where they were dried at 60°C for 48-h and stored in a desiccator until further analysis. A 1-h NaOH digestion was used to convert $bSiO_2$ to $Si(OH)_4$ (Brzezinski and Nelson, 1995), using fresh reagents and polymethylpentene centrifuge tubes (Diagenode, Belgium), to ensure low blanks and low limit of detection. Concentration of $Si(OH)_4$ were measured with a Beckman DU 530 UV/Vis spectrophotometer (Beckman Coulter, CA, USA) at the University of Victoria using a

reverse-order reagent blank (Brzezinski and Nelson, 1986) and 10-cm glass cuvettes for high precision. The average CV for $bSiO_2$ was 10.3%, based on triplicate field samples.

Lithogenic silica ($LSiO_2$) concentrations were determined by digesting the remaining filter and particles in 2.5M hydrofluoric acid (HF) for 48-h. After digestion, saturated boric acid was used to dilute the resulting solution and the concentration of $Si(OH)_4$ was determined as described above. CV for $LSiO_2$ was not quantified but differences due to sampling were expected to be similar to $bSiO_2$ as they were analyzed from the same filters.

### *B.3.6 Utilization rates of carbon and nitrate*

At each optical light depth, utilization rate of carbon ($\rho C$) and $NO_3^-$ ($\rho NO_3$) were measured using the $^{13}C$-$^{15}NO_3^-$ stable-isotope dual tracer method (Dugdale and Goering, 1967; Slawyk et al., 1977). Seawater was gently subsampled from Niskin bottles into acid-washed 1.0 – 2.4 L PC bottles, leaving enough headspace for isotope additions. For the determination of total $\rho C$, samples were inoculated to a final enrichment target of ~10% of ambient total dissolved inorganic C using a $KH^{13}CO_3$ (99% purity, Cambridge Isotopes Laboratories, MA, USA) isotope tracer stock. For the determination of $\rho NO_3$, the same samples were inoculated using a $Na^{15}NO_3$ (98+% purity, Cambridge Isotopes Laboratories, MA, USA) isotope tracer stock. Since *in situ* $NO_3^-$ was expected to be depleted or undetectable at most depths, $^{15}NO_3^-$ was added at the detection limit for $NO_3^-$ concentration (0.1 μM) to minimize an artificial nutrient enhancement. Inoculated samples were incubated in an on-deck incubator cooled by continuously flowing surface seawater. Each PC bottle corresponding to a specific optical depth was placed in a layered mesh bag that matched the irradiance at depth. After 24-h, half of each bottle was

sequentially filtered through a 5.0 μm PC filter, and then the filtrates were gently filtered through combusted GF-75 filters for the measurement of $\rho C$ and $\rho NO_3$ for the < 5 μm size-fraction. The remaining volumes in each bottle were filtered through combusted GF-75 filters only, to determination rates for the total assemblage. All filters were frozen at -20°C until returned to shore and then dried at 60°C for 48-h. The isotopic composition ($^{13}C$:$^{12}C$ and $^{15}N$:$^{14}N$) and total C and N content of each filter were measured at the Stable Isotope Facility at the University of California Davis with a PDZ Europa 20-20 isotope ratio mass spectrometer and a PDZ Europa ANCA-GSL elemental analyzer (Sercon Ltd., Cheshire, UK). Carbon utilization rates ($\rho C$) were calculated using equation 3 of Hama et al. (1983) and ambient $C_T$ concentrations directly measured during the BATS core hydrocast. Total inorganic C was measured from gastight samples preserved with mercuric chloride, using a SOMMA interfaced with a UIC Model 5011 coulometer (UIC Inc., Joliet, IL) (Knap et al., 1997). Nitrate utilization rates ($\rho NO_3$) were calculated using equation 3 in Dugdale and Wilkerson (1986) and the ambient $NO_3^-$ concentrations for each sample. When ambient $NO_3^-$ concentrations were below the limit of detection (0.1 μM), the value used was 0.1 μM, therefore representing a theoretical maximum utilization rate.

### *B.3.7 Utilization rate of silicic acid*

The utilization rate of $Si(OH)_4$ ($\rho Si$) was measured using $^{32}Si$ as a tracer in incubation experiments (Brzezinski and Phillips, 1997; Krause et al., 2011). Size-fractionated $\rho Si$ was only collected at four or five optical depths, while $\rho Si$ for the total assemblage was collected at the same seven depths as for $\rho C$ and $\rho NO_3$. Seawater was gently collected from Niskin bottles into either acid-washed 500 mL or 300 mL polycarbonate bottles, leaving enough headspace for

isotope additions. 500 mL bottles were used for combined size-fractionated and total $\rho$Si measurements, and 300 mL bottles were used for only total $\rho$Si. Each bottle was inoculated with a 6500 Bq $mL^{-1}$ solution of high specific activity $^{32}Si(OH)_4$ (~25,000 MBq µmol $Si^{-1}$). 970 Bq (58,000 DPM) was added to 300 mL bottles, and 1670 Bq (100,000) DPM to 500 mL bottles. The amount of $^{32}Si(OH)_4$ added was less than $3.8x10^{-8}$ µmol Si, a negligible increase in the total $Si(OH)_4$ available. Inoculated samples were incubated in the same manner as for $\rho$C and $\rho NO_3$ experiments. After ~24-h, the 300 mL bottles for total $\rho$Si were entirely filtered under gentle vacuum pressure onto 0.6 µm PC filters. For larger bottles, half of the bottle volume was filtered directly onto a 0.6 µm PC filter for total $\rho$Si. The remaining volume was filtered under gentle vacuum pressure onto a 5.0 µm PC filter for the determination of $\rho$Si > 5 µm, and the filtrate was then filtered onto 0.6 µm PC filter for the determination of $\rho$Si < 5 µm. All filters were rinsed with 0.6 µm filtered seawater to remove any excess $^{32}$Si tracer that may have not been incorporated into siliceous phytoplankton. Each filter was air-dried at room temperature on a 25 mm Nylon disc before being covered with Mylar film and secured with a nylon ring. All samples were stored for at least 5 half-lives (~120 days) of the daughter isotope ($^{32}$P) for any $^{32}$P that was taken up or otherwise scavenged during the incubation to decay, and for secular equilibrium to occur.

Activity of $^{32}$Si in the sample was determined by gas-flow proportional counting using a Risø 25-5 low-level beta GM multicounter (DTU Nutech, Denmark) (Krause et al., 2011), and $\rho$Si was calculated using the ambient $Si(OH)_4$ and $bSiO_2$ concentrations for each depth (Brzezinski and Phillips, 1997). Specific uptake rate ($V_{Si}$) was also calculated by normalizing $\rho$Si by the $bSiO_2$ biomass.

### *B.3.8 Data treatment and visualization*

Using CTD vertical profiles, the potential density anomaly ($\sigma_\theta$) of the water column was calculated using the function "swSigma0" from the R package "oce".

Euphotic zone concentrations and rate measurements were depth-integrated ($\int$) using trapezoidal integration between data points from the surface (~3 m) to the deepest sample (~140 – 160 m). Surface samples were not collected for BV5 and BV9, therefore, the integrated values for BV5 and BV9 were an underestimate. The data presented in this manuscript are the uncorrected values, however the amount of underestimation was approximated by duplicating the shallowest sample (~40 m) at BV5 and BV9, and applying it to the surface. This showed that chl-*a* and $bSiO_2$ were underestimated by 3% and 13%, respectively. Nutrient utilization rates had a bigger difference due to the maximum values for each profile generally occurring in the shallowest waters. The uncorrected rates were 24%, 24%, and 23% lower for $\rho C$, $\rho NO_3$, and $\rho Si$.

All figures were made in RStudio 2023.06 (Posit Software, PBC, Boston, MA) using the package "ggplot2".

## B.4 Results and Discussion

### *B.4.1 Hydrography and nutrient concentration profiles*

Surface water temperatures across the North Atlantic subtropical gyre increased towards the southernmost station, reaching nearly 30°C (Fig. B.2A). Salinity had little variability up to ~21°N, where the upper 50 m of the water column freshened considerably (Fig. B.2B). A stratified surface layer was ~ 50 m deep at 33°N and gradually deepened along the transect to 22°N, before shallowing somewhat at the southernmost station (Fig. B.2C).

Due to strong stratification and low surface nutrients, a deep chlorophyll maximum (DCM) between 100 – 150 m was established along the entire transect (Fig. B.3A). The depth at which oxygen concentrations were highest was consistently shallower than the DCM (Fig. B.3B). Oxygen concentrations and *in vivo* fluorescence were somewhat higher at the more northern latitudes.

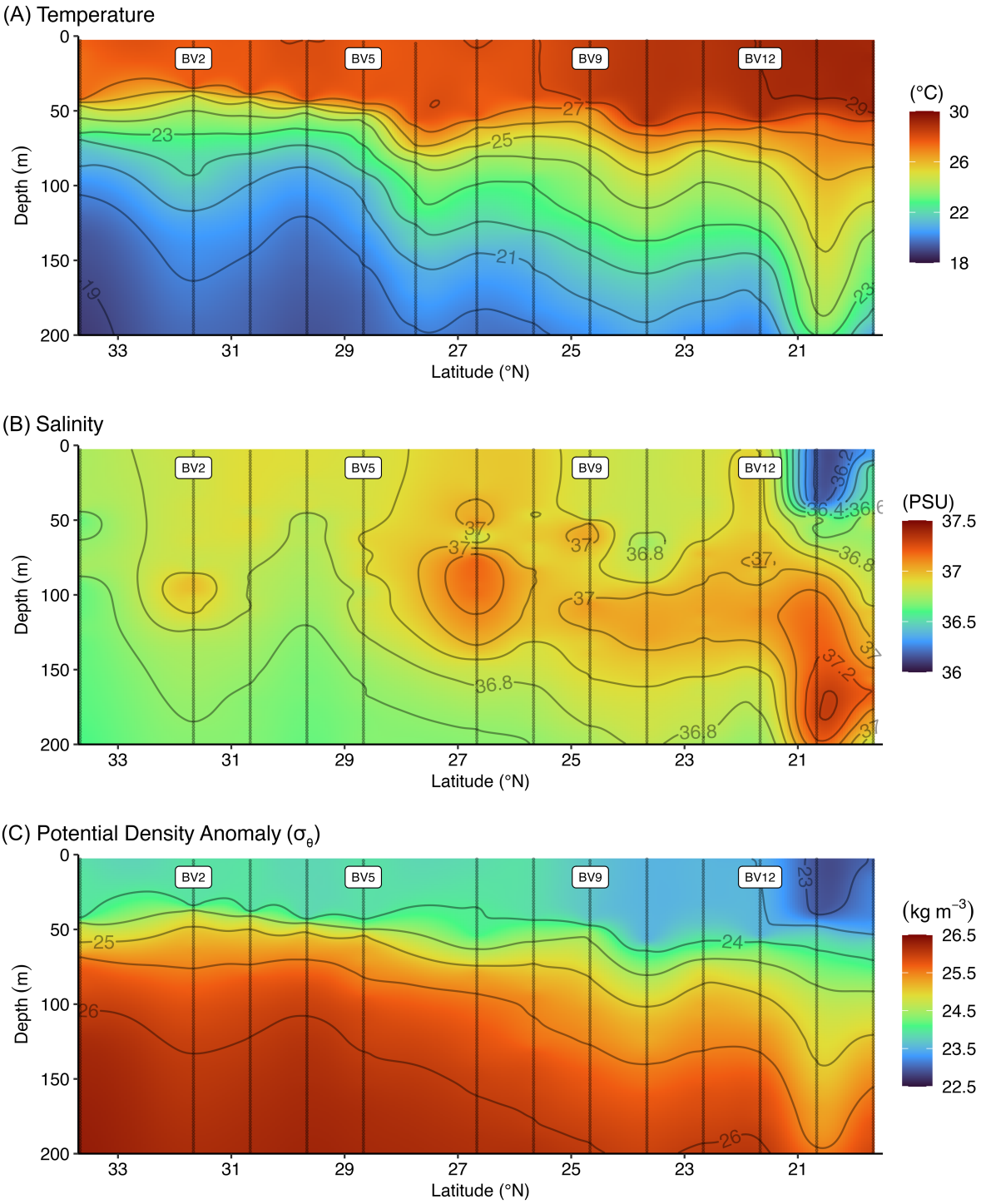


**Figure B.2.** Physical characteristics of the upper 200 m from 33.665°N to 19.668°N during BVAL53 in September/October 2018. **(A)** Temperature, **(B)** salinity, and **(C)** potential density anomaly ($\sigma_\theta$). Vertical grey lines indicate sampling station locations. Salinity values were not available for station BV6, 27.746°N, and therefore $\sigma_\theta$ was not calculated for that station. Note the "bowed" contours for temperature and $\sigma_\theta$ along shallow isopycnals between ~33 – 29°N are an artefact of the interpolation method.

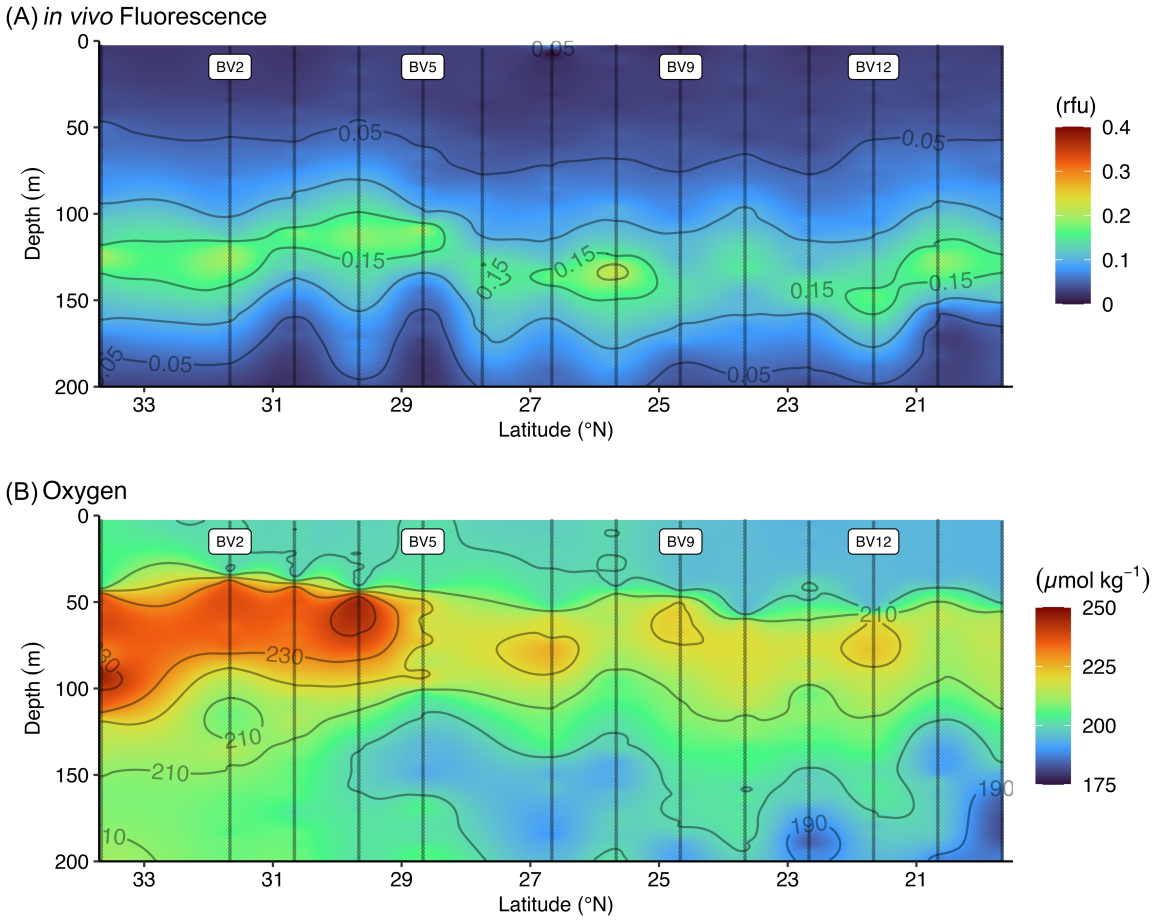


**Figure B.3. (A)** *In vivo* fluorescence, and **(B)** oxygen concentrations of the upper 200 m from 33.665°N to 19.668°N, sampled during BVAL53 in September/October 2018. Oxygen concentrations were not available for station BV6, 27.746°N.

Concentrations of $NO_3^-$ were undetectable along much of the transect at depths shallower than 120 m, although there was a small injection at BV5 where 1.13 µmol $kg^{-1}$ was observed at 100 m. The nutricline deepened at southern latitudes (Fig. B.4A). Silicic acid concentrations were higher than 0.71 µmol $kg^{-1}$ at any depth or latitude (Fig. B.4B), and had some small subsurface maxima > 2 µmol $kg^{-1}$ at stations north of 27°N. Phosphate was generally undetectable in the upper 200 m (Fig. B.4C) at all latitudes.

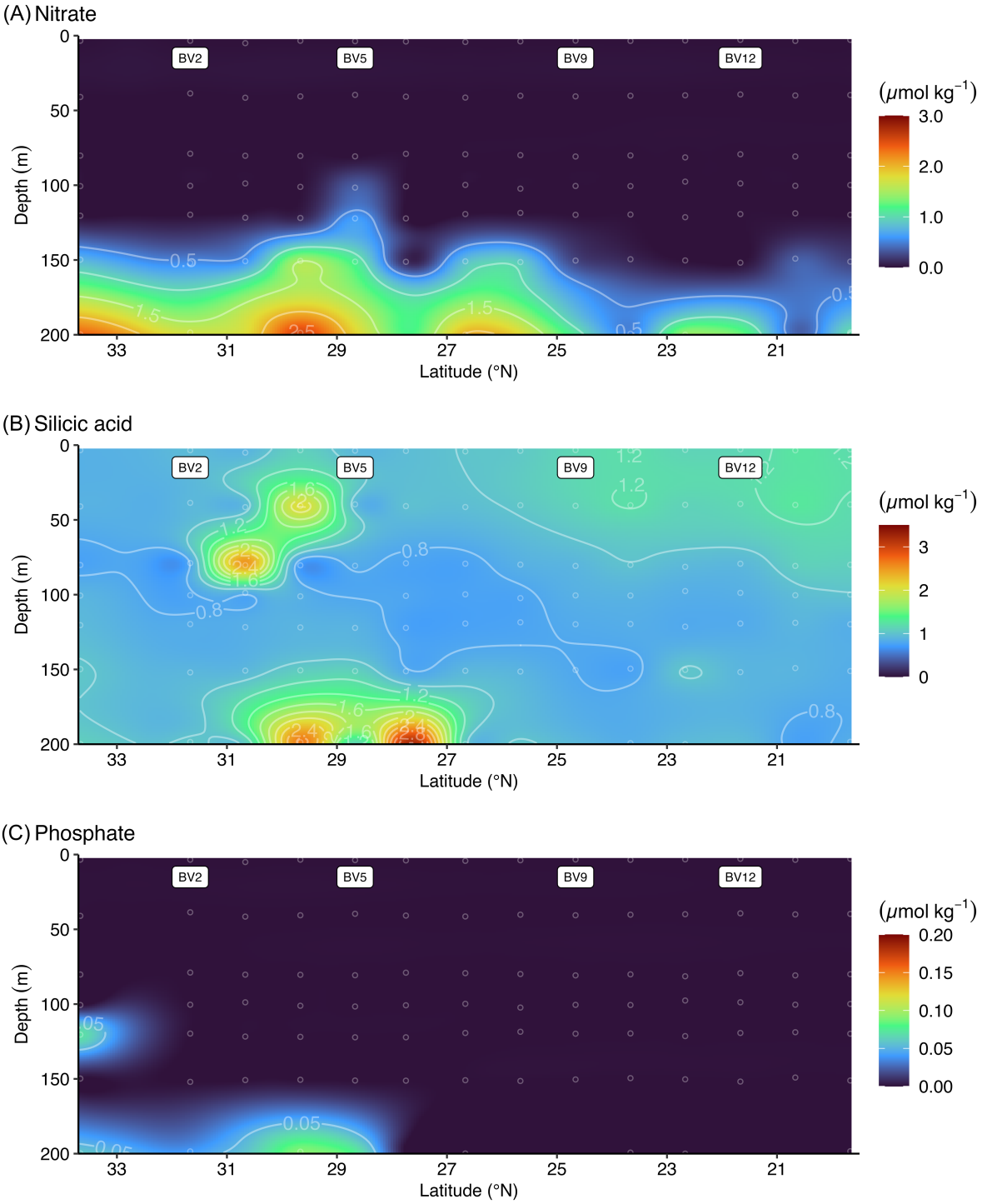


**Figure B.4.** Nutrient characteristics of the upper 200 m from 33.665°N to 19.668°N, sampled during BVAL53 in September/October 2018. **(A)** Nitrate, $NO_3^-$, **(B)** silicic acid, $Si(OH)_4$, and **(C)** phosphate, $PO_4^{3-}$. A $Si(OH)_4$ outlier was removed from BV5 at 100 m after comparison with separate samples taken for nutrient utilization experiments. Separate (not shown) samples for $NO_3^-$ and $Si(OH)_4$ were collected at the 4 indicated stations (in white boxes) for use in calculating nutrient utilization rates.

The late-summer hydrographic and nutrient characteristics that we observed were consistent with time-series measurements for the BATS station and surrounding region (Lomas et al., 2013; Steinberg et al., 2001). Although mixed layer depths (~50 m) did not approach the upper boundary of 18°C water (> 200 m), which is known to be nutrient-rich (Lomas et al., 2013), cooler water temperatures at depth were associated with a shallower nutricline, and $NO_3^-$ injections at < 120 m in northern latitudes. Higher $NO_3^-$ therefore supported the slightly higher biomass concentrations and subsurface maxima of oxygen observed. At the southernmost station, low surface salinity depressed isopycnals throughout the euphotic zone but did not noticeably impact nutrient or biomass concentrations. This surface signal was potentially the Antilles Current, a poorly documented, weak western boundary current that separates the Caribbean Sea from the Atlantic Ocean (Costin, 1968; Meinen et al., 2019).

### *B.4.2 Nutrient concentrations at productivity stations*

At the four productivity stations, $NO_3^-$ concentrations were undetectable shallower than 100 m, although BV2 and BV5 had concentrations above 0.5 μmol $kg^{-1}$ at 150 m depth (Fig. B.5A). Silicic acid was nearly identical between profiles, and varied between 0.75 – 1.25 μmol $kg^{-1}$ with a subtle sub-surface minimum between 75 – 125 m at all stations (Fig. B.5B). Depth-integrated concentrations of $NO_3^-$ ($\int NO_3$) were lowest at the two southernmost stations, while one station to the north (BV5) had noticeably higher $\int NO_3^-$, 38.7 mmol $m^{-2}$ (Fig. B.5C). Concentrations of $\int Si(OH)_4$ were between 125 – 150 mmol $m^{-2}$ at all stations.

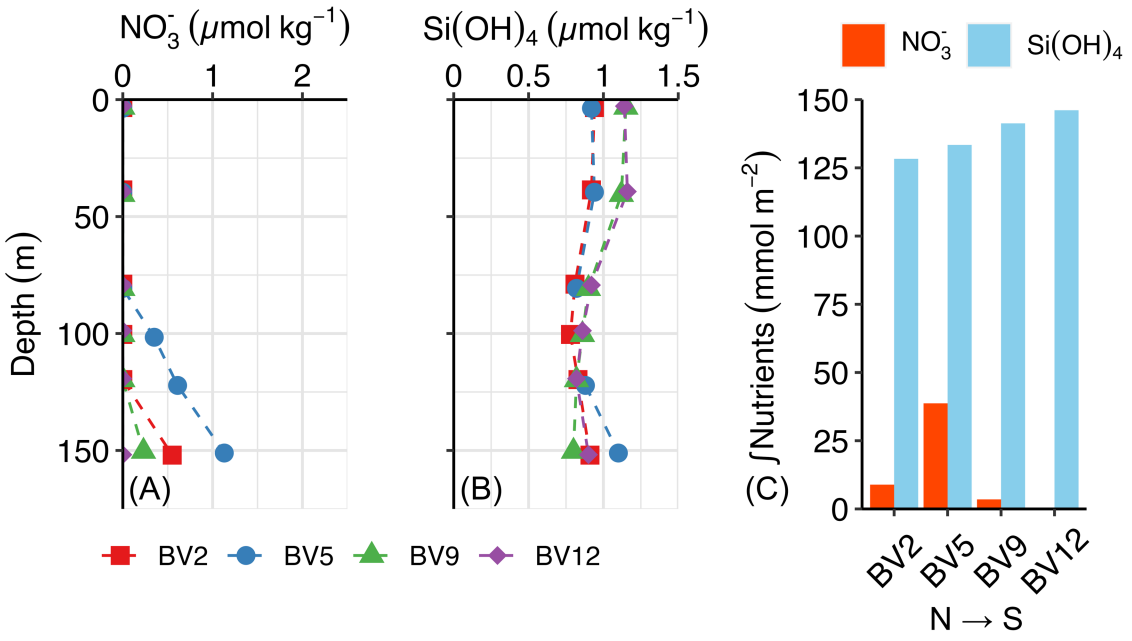


**Figure B.5.** Dissolved nutrient concentrations along the BVAL53 transect N → S at the 4 major stations in Sep/Oct 2018. **(A)** Nitrate, $NO_3^-$ **(B)** silicic acid, $Si(OH)_4$, and **(C)** depth-integrated $NO_3^-$ ($\int NO_3$) and $Si(OH)_4$ ($\int Si(OH)_4$) were calculated to 150 m. Profiles and depth-integrated concentrations of $PO_4^{3-}$ not shown because $PO_4^{3-}$ was below the detection limit at all depths to 150 m.

### *B.4.3 Profiles and depth-integrated chlorophyll-a and biogenic silica concentrations*

Extracted chlorophyll-*a* biomass at the four productivity stations followed a similar distribution with depth, having very low concentrations in surface waters < 0.02 µg $L^{-1}$, and ~0.15 µg $L^{-1}$ between 100-150 m (Fig. B.6A). Size-fractionated concentrations were similar at the 4 stations, with the small size-fraction (< 5 µm) closely mirroring the profile for the total concentrations (Fig. B.6B). Larger cells (> 5 µm) did not show as much variability with depth, with the exception of BV5 which had a small subsurface maximum around 80 m (Fig. B.6C). Euphotic zone depth-integrated chl-*a* ($\int$chl-*a*) showed roughly the same proportions and total concentrations across the N-S gradient, ranging from 7.5 – 8.9 mg $m^{-2}$ at BV2, BV5, and BV9, and increasing by ~44% at BV12 compared to the average of the three more northern stations

(Fig. B.6D). Chlorophyll-*a* > 5 µm made up a maximum of 9% of total ∫chl-*a* at BV5, and was the lowest (5%) at BV12.

Biogenic silica had little variability with depth, ranging between 5 – 14 nmol $L^{-1}$, and only reaching concentrations > 10 nmol $L^{-1}$ in the upper 50 m at BV2 (Fig. B.6E). There was almost no vertical variability for the two size-fractions at any station (Fig. B.6F & G), and only BV2 showed > 5 µm cells comprising more biomass in the upper 50 m (Fig. B.6G). Depth-integrated $bSiO_2$ ($\int bSiO_2$) and the proportions of the different fractions were also somewhat uniform latitudinally, ranging between 1.0 – 1.4 mmol $m^{-2}$ and > 5 cells comprised 57 – 64%, respectively (Fig. B.6H).

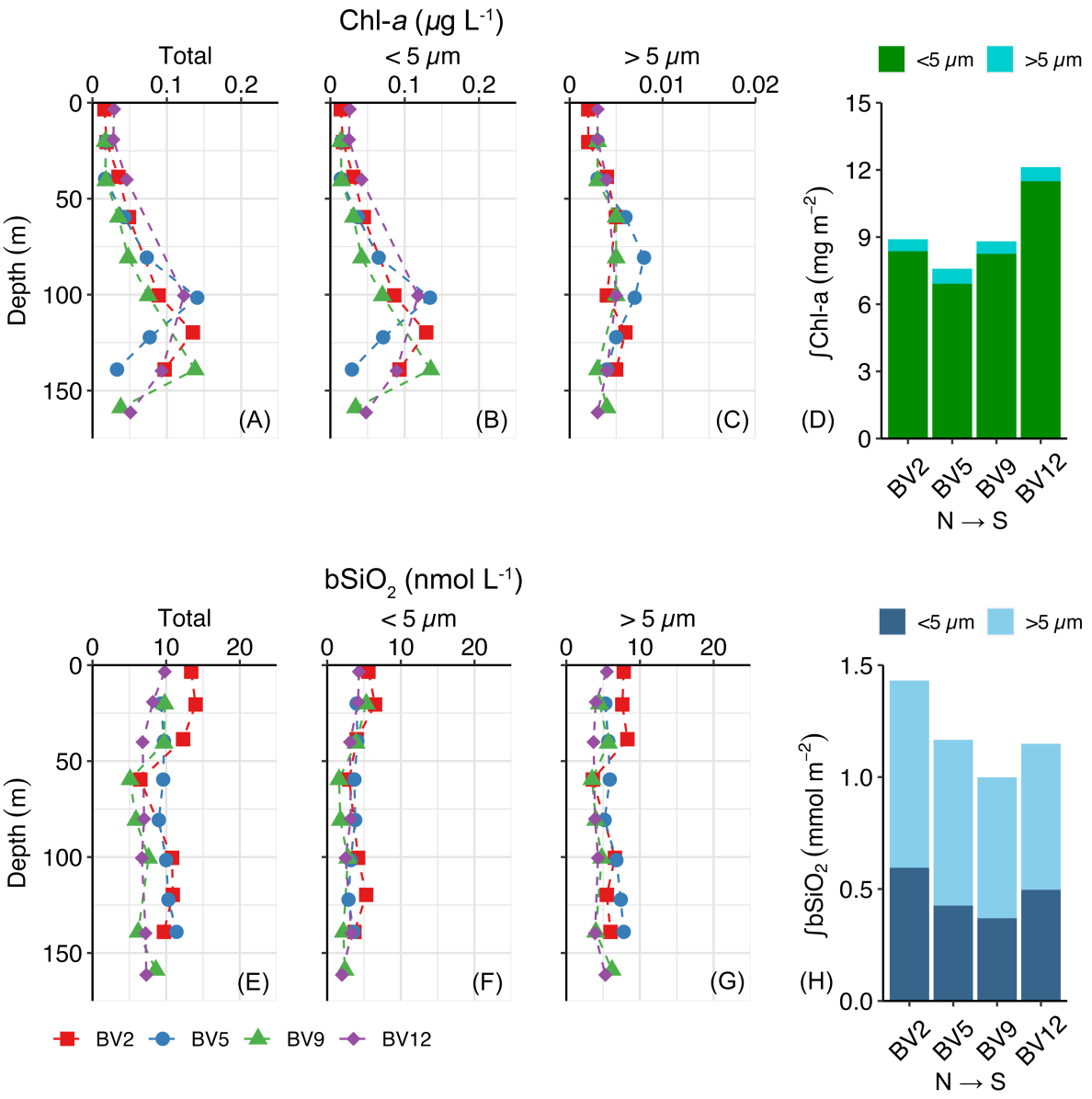


**Figure B.6.** Chlorophyll-*a* (chl-*a*) and biogenic silica ($bSiO_2$) concentrations along the BVAL53 transect N → S at the 4 productivity stations in Sep/Oct 2018. **(A)** Total chl-*a* is the sum of **(B)** chl-*a* < 5 µm, and **(C)** chl-*a* > 5 µm. **(D)** Depth-integrated chl-*a*, ∫Chl-*a*, was calculated from the shallowest depth to the base of the euphotic zone, 140 – 160 m. Note different scale for panel C. **(E)** Total $bSiO_2$ is the sum of **(F)** $bSiO_2$ < 5 µm, and **(G)** $bSiO_2$ > 5 µm. **(H)** Depth-integrated $bSiO_2$, ∫$bSiO_2$, was calculated from the shallowest sample to the base of the euphotic zone, 140 – 160 m. BV12 was sampled on the return leg of the transect.

### *B.4.4 Profiles and depth-integrated nutrient utilization rates*

Utilization of carbon ($\rho$C) was highest in waters < 50 m at all 4 stations, and the two southernmost stations, BV9 and BV12, had noticeably higher rates than northern stations (Fig. B.7A). There was no clear difference between $\rho$C size-fractions at each station when looking at individual depths (Fig. B.7B & C). On average, integrated $\rho$C ($\int\rho$C) averaged 8.1±3.9 mmol $m^{-2}$ $d^{-1}$, and small cells accounted for the majority, 66±11%. However, $\int\rho$C and the contribution of larger cells to total $\rho$C increased at lower latitudes (Fig. B.7D).

Nitrate utilization ($\rho NO_3$) followed a similar pattern to $\rho$C with depth, although differences between northern and southern latitudes were not observed (Fig. B.7E – G). Small cells accounted again for the majority (66±5%) of total $\int\rho NO_3$, which averaged 1.0±0.2 mmol $m^{-2}$ $d^{-1}$ (Fig. B.7H). There was no pattern for $\int\rho NO_3$ along the N-S transect.

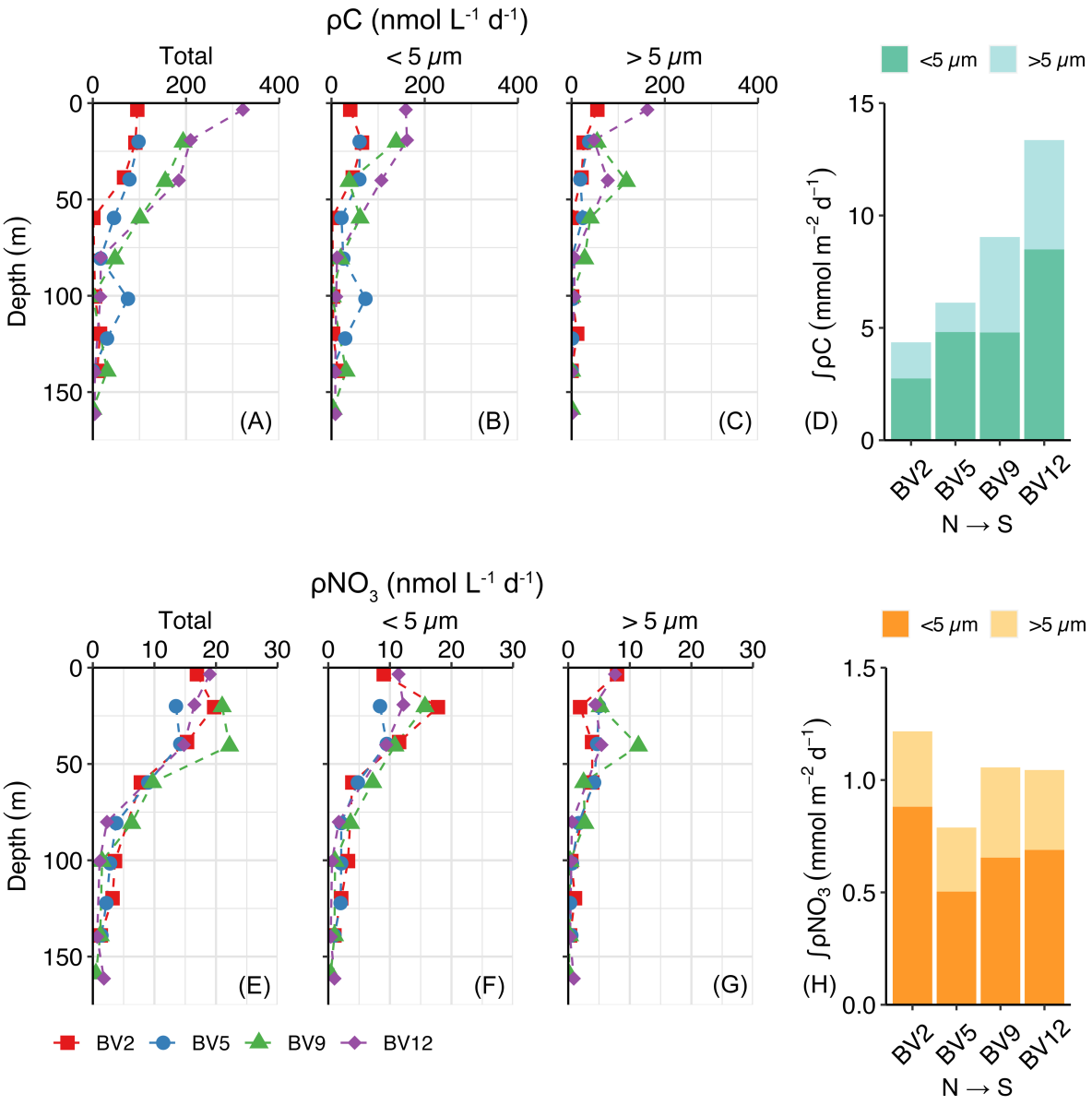


**Figure B.7.** Nutrient utilization rates along the BVAL53 transect N → S at the 4 productivity stations in Sep/Oct 2018. Carbon utilization, $\rho$C, for **(A)** total , **(B)** < 5 µm, and **(C)** > 5 µm size-fractions. **(D)** Depth-integrated $\rho$C, $\int\rho$C, was calculated from the shallowest depth to the base of the euphotic zone, 140 – 160 m. Nitrate utilization, $\rho NO_3$, for **(E)** total, **(F)** < 5 µm, and **(G)** > 5 µm size-fractions. **(H)** Depth-integrated $\rho NO_3$, $\int\rho NO_3$, was calculated from the shallowest sample to the base of the euphotic zone, 140 – 160 m. BV12 was sampled on the return leg of the transect.

Silicon utilization ($\rho$Si) had roughly the same pattern as other utilization rates, with higher $\rho$Si in surface waters and decreasing with depth (Fig. B.8A). At BV12, however, there were much higher rates than in the previous stations at the surface and at 100 m. This was corroborated by measurements of total $\rho$Si, which were not the sum of size-fractions, as well as separate size-fractionated measurements (Fig. B.8B & C). These two maxima greatly increased $\int\rho$Si for the water column, although because the increase was mostly in cells < 5 µm, the proportion of $\int\rho$Si contributed by large cells declined from an average of 61% at BV2, BV5 and BV9, to 27% at BV12 (Fig. B.8D).

Specific uptake rates ($V_{Si}$) were similar at BV2, BV5, and BV9, but much higher at BV12 (Fig. B.8E – G), indicating that while siliceous phytoplankton biomass ($bSiO_2$) was consistent, cells at BV12 had a greater ability to use Si at the time of sampling. This suggests high $\rho$Si observed at BV12 was due to increased utilization per unit biomass, and not biomass accumulation. Small cells at BV12 had much higher $V_{Si}$ compared to larger cells at two depths, unlike other stations. Normalizing $\int\rho$Si by $\int bSiO_2$ for each size-fraction further highlighted this (Fig. B.8H), with $\int V_{Si}$ < 5 µm reaching 0.38 $d^{-1}$ compared to 0.11 $d^{-1}$ for cells > 5 µm. Unfortunately, since incubation experiments were conducted at BV12 on the return leg of the BVAL53 cruise, additional measurements from the BATS core hydrocast such as flow cytometry and accessory pigment concentrations are not available to further interpret this result.

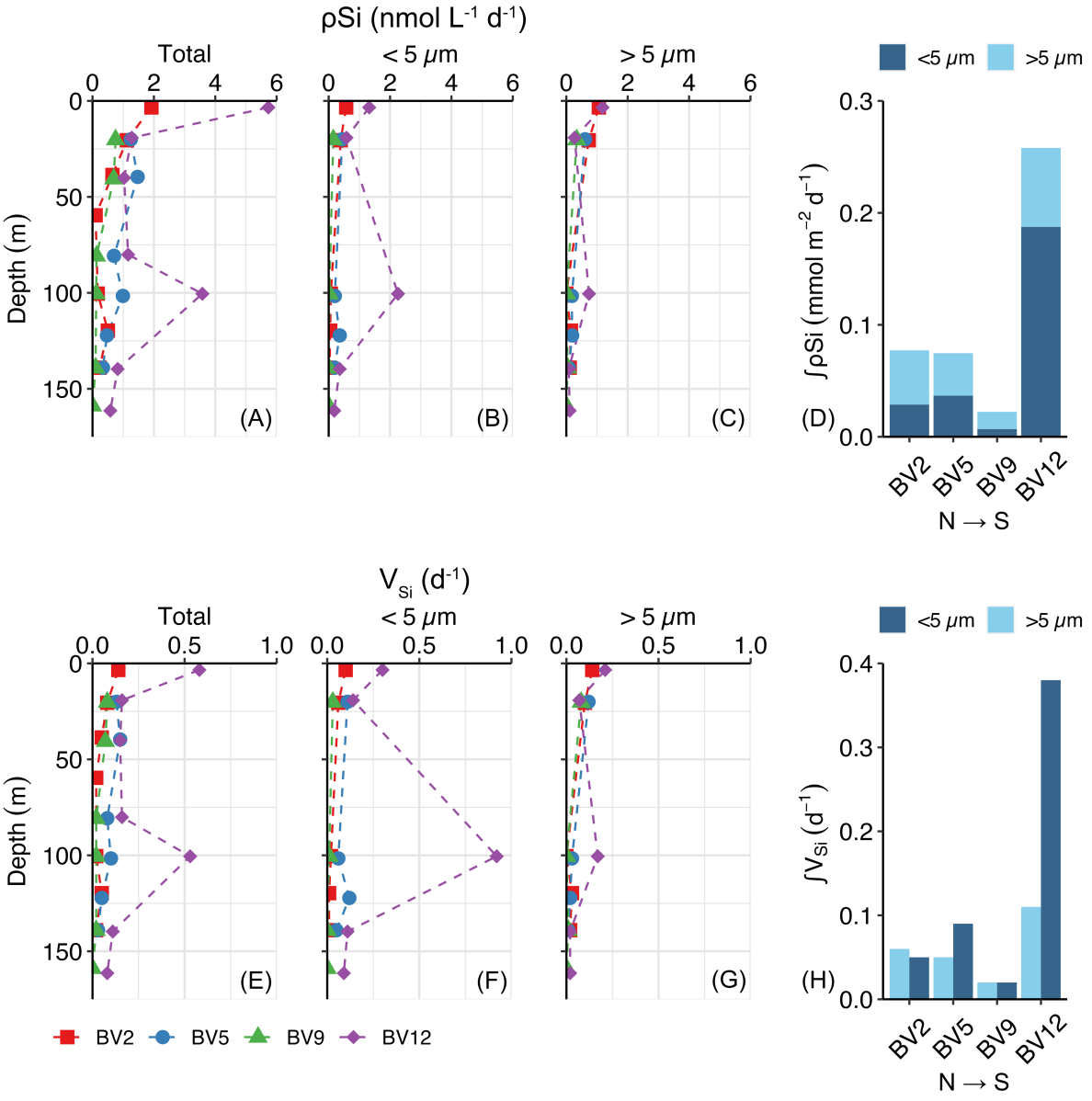


**Figure B.8.** Nutrient utilization rates along BVAL53 transect in Sep/Oct 2018. Silicon utilization, $\rho$Si, for **(A)** total, **(B)** < 5 µm, and **(C)** > 5 µm size-fractions. **(D)** Depth-integrated $\rho$Si, $\int\rho$Si, was calculated from the shallowest depth to the base of the euphotic zone, 140 – 160 m. Specific uptake rate of silicon ($V_{Si}$) for the **(E)** total assemblage, **(F)** < 5 µm, and **(G)** > 5 µm size-fractions. Specific uptake was calculated for each size-fraction separately, therefore total $V_{Si}$ is not the sum of the size-fractions. **(H)** Integrated specific uptake rate, $\int V_{Si}$ was calculated by normalizing $\int\rho$Si for each size-fraction by the corresponding $\int bSiO_2$ size-fraction, and the values are not additive therefore they are not presented as the sum of columns. Total values of $\rho$Si and $V_{Si}$ were collected separately to provide additional vertical resolution since size-fractioned measurements were not possible at all depths. BV12 was sampled on the return leg of the transect.

### *B.4.5 Profiles and depth-integrated lithogenic silica concentrations*

Lithogenic silica concentrations followed a similar distribution at all four productivity stations (Fig. B.9A). Concentrations were highest in surface waters, between ~5 – 20 nmol $L^{-1}$, and declining to < 5 nmol $L^{-1}$ below 50 m. Depth-integrated $LSiO_2$ ($\int LSiO_2$) averaged 0.8±0.3 mmol $m^{-2}$ along the sampling transect (Fig. B.9B).

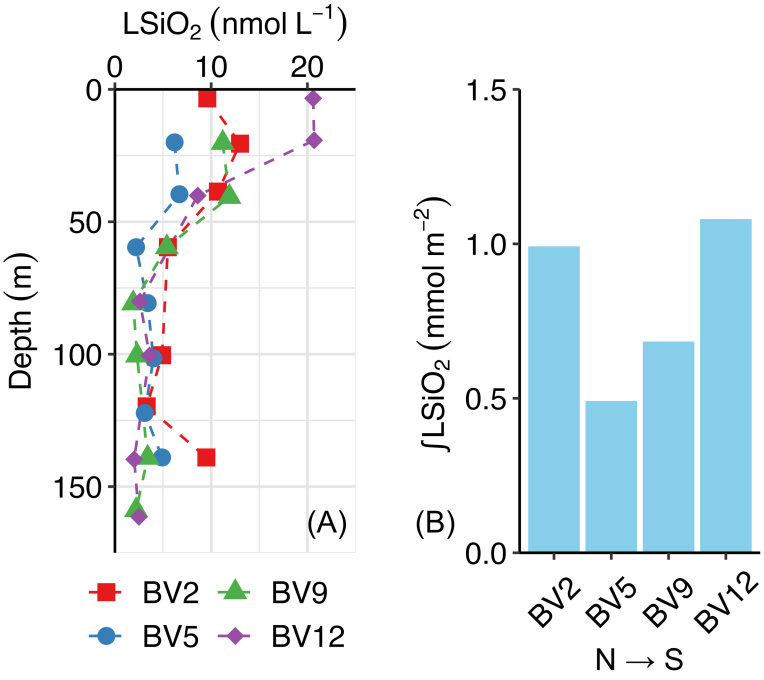


**Figure B.9.** Lithogenic silica ($LSiO_2$) concentrations along the BVAL53 transect N → S at the 4 major stations in Sep/Oct 2018. **(A)** Lithogenic $SiO_2$ concentrations in the euphotic zone. **(B)** Depth-integrated $LSiO_2$, $\int LSiO_2$, was calculated from the shallowest sample to the base of the euphotic zone, 140 – 160 m. BV12 was sampled on the return leg of the transect.

## B.5 Conclusions

Between 27-Sep and 07-Oct, the sampling transect was characterized by a stratified water column, and nutrient concentrations that were generally undetectable except at the base of the euphotic zone. At all stations sampled, phytoplankton biomass (chl-*a*) was concentrated at the deep-chlorophyll maximum and small cells < 5 µm comprised more than 90% of chl-*a*. Biogenic

silica concentrations were low at all depths and stations, and unlike chl-*a*, cells > 5 μm accounted for between 57 – 64% of total $bSiO_2$. Nutrient utilization rates did not follow the same patterns as biomass, other than small cells being more productive than large cells. Although low overall, $\rho C$ and $\rho NO_3$ were highest in surface waters and declined with depth. Along the N to S transect, $\rho C$ consistently increased, but $\rho NO_3$ was spatially variable. At the three stations north of 24°N, $\rho Si$ was low at all depths, while at the southernmost station, BV12, $\rho Si$ was ~3-fold higher than elsewhere and there was a distinct subsurface maximum at 100 m. To our knowledge, these results are the first simultaneous measurements of size-fractionated phytoplankton biomass and nutrient utilization rates in this region. Biogenic and lithogenic silica concentrations, and $\rho Si$ measurements are rarely reported across the Sargasso Sea, therefore this appendix offers new data about Si dynamics and phytoplankton productivity across a subtropical gyre ecosystem.

– This page intentionally left blank –

# Appendix C – Supplementary material for Chapter 3

This appendix contains supplementary materials to support *Chapter 3 – Elemental composition and nutrient utilization of siliceous phytoplankton assemblages in the Pacific Arctic Region during periods of elevated ocean temperature.* These include:

- A table comparing ratios of Si:C and Si:N from a previous study (2013 – 2016) to more recently collected ratios (2018 – 2022), and the average for the whole time period (2013 – 2022) during which $\rho$Si was measured.
- A table of average sea surface temperature from 2006 – 2022, as well as the 2019 surface temperature anomaly (STA) and year of maximum positive STA.
- Tables of summary statistics for linear regressions of the relationship between different physical and biological measurements with time. Two time periods, 2011 – 2019, and 2006 – 2022, are used.
- Vertical profiles of physical and biogeochemical measures from 2011 – 2022 including temperature and salinity, nutrient concentrations, particulate biomass, and nutrient utilization rates. Using 95% confidence intervals and the mean of 2011 – 2022 (excluding 2019), at every depth for each region it was estimated whether the 2019 MHW data was outside the typical range of values. Data from 2006 and 2008 were not included in vertical profiles due to inconsistencies in the $I_D$ used, and different locations of stations.
- Multiplots of the relationship between different biomass or nutrient utilization rates with temperature, salinity, stratification index, and ice-free period. These data are presented by region.
- A multiplot of the relationship between nutrient utilization rates or ratios of utilization rates with temperature, as well as discussion of the figure.

**Table C.1.** Comparison of depth-integrated Si:C and Si:N ratios averaged across all DBO regions for different time periods when $\rho$Si was measured. Ratios were calculated using the euphotic zone integrated values of $bSiO_2$, PC, and PN.

| Ratio | 2013-2016 | 2018-2022 | 2013-2022 |
|---|---|---|---|
| ∫Si:C | 0.18±0.09 | 0.16±0.07 | 0.17±0.08 |
| ∫Si:N | 1.27±0.54 | 0.88±0.41 | 1.04±0.50 |

**Table C.2.** Surface temperature anomalies (STA) in 2019 compared to the average surface temperature for each DBO region from 2006 – 2022. For all regions other than DBO2, 2019 was also the maximum positive STA.

| Region | Average surface temperature, 2006 – 2022 (°C) | 2019 STA (°C) | Maximum positive STA (°C, year) |
|---|---|---|---|
| DBO1 | 7.89±1.52 | 3.54 | 3.54, 2019 |
| DBO2 | 4.91±2.82 | 5.03 | 5.86, 2017 |
| DBO3W | 4.46±1.66 | 3.06 | 3.06, 2019 |
| DBO3E | 6.84±2.20 | 3.66 | 3.66, 2019 |
| DBO4 | 1.69±2.40 | 3.63 | 3.63, 2019 |
| DBO5 | 3.81±2.66 | 3.30 | 3.30, 2019 |

**Table C.3.** Summary statistics for linear regressions between different observations of physical characteristics and nutrient inventories with time during the DBO time-series from 2011 – 2019 and 2006 – 2022. "Ice-free" is the number of days between the breakup of sea ice and when sampling occurred. Slope and $R^2_{adj}$ are shown. Relationships with a p-value ≤ 0.05 are shown in **bold**, and p-values ≤ 0.01 are ***bold italic.***

| | DBO1 | | DBO2 | | DBO3W | | DBO3E | | DBO4 | | DBO5 | |
|---|---|---|---|---|---|---|---|---|---|---|---|---|
| | Slope | $R^2$ | Slope | $R^2$ | Slope | $R^2$ | Slope | $R^2$ | Slope | $R^2$ | Slope | $R^2$ |
| **PHYSICAL CONDITIONS** | | | | | | | | | | | | |
| **2011-2019 warming period** | | | | | | | | | | | | |
| **Surf T** | **0.42** | **0.42** | **0.83** | **0.46** | 0.34 | 0.15 | 0.54 | 0.46 | 0.85 | 0.28 | 1.21 | 0.56 |
| **Surf S** | ***0.11*** | ***0.64*** | 0.04 | <0.01 | 0.05 | 0.21 | -0.06 | <0.01 | 0.12 | <0.01 | 0.16 | 0.50 |
| **$\sigma_\theta$ index** | -0.02 | <0.01 | 0.07 | <0.01 | -0.01 | <0.01 | 0.04 | <0.01 | -0.09 | <0.01 | 0.07 | <0.01 |
| **Surf pH** | -0.001 | <0.01 | **0.037** | **0.23** | 0.013 | 0.05 | -0.010 | 0.03 | -0.005 | <0.01 | -0.009 | 0.02 |
| **Ice-free** | **6.72** | **0.48** | **3.60** | **0.40** | 0.02 | <0.01 | **6.50** | **0.86** | 6.68 | 0.31 | 2.80 | 0.85 |
| **2006-2022** | | | | | | | | | | | | |
| **Surf T** | 0.12 | 0.07 | 0.18 | 0.01 | 0.08 | <0.01 | 0.11 | <0.01 | 0.23 | 0.15 | 0.16 | <0.01 |
| **Surf S** | 0.00 | <0.01 | -0.00 | <0.01 | -0.06 | <0.01 | -0.10 | 0.22 | 0.03 | <0.01 | ***0.08*** | ***0.67*** |
| **$\sigma_\theta$ index** | -0.01 | <0.01 | 0.04 | <0.01 | 0.06 | 0.01 | -0.01 | <0.01 | -0.02 | <0.01 | -0.07 | 0.36 |
| **Surf pH** | **-0.008** | **0.16** | **0.016** | **0.12** | 0.008 | 0.05 | -0.007 | 0.03 | -0.004 | <0.01 | **-0.009** | **0.07** |
| **Ice-free** | 2.12 | 0.13 | 1.44 | 0.06 | 1.17 | 0.18 | 3.39 | 0.22 | 1.46 | 0.03 | 0.42 | <0.01 |
| **NUTRIENT CONCENTRATIONS** | | | | | | | | | | | | |
| **2011-2019 warming period** | | | | | | | | | | | | |
| **∫$NO_3^-$** | 7.10 | <0.01 | -22.5 | <0.01 | -16.9 | 0.29 | 0.41 | <0.01 | 20.4 | <0.01 | 19.9 | 0.58 |
| **∫$Si(OH)_4$** | 2.25 | <0.01 | -8.27 | <0.01 | -18.1 | <0.01 | 1.69 | <0.01 | -18.8 | <0.01 | 43.0 | <0.01 |
| **2006-2022** | | | | | | | | | | | | |
| **∫$NO_3^-$** | **-18.1** | **0.28** | -9.68 | <0.01 | -4.03 | <0.01 | 0.37 | <0.01 | 1.71 | <0.01 | -7.36 | 0.02 |
| **∫$Si(OH)_4$** | -58.4 | 0.14 | -12.9 | <0.01 | -23.2 | 0.03 | 1.55 | <0.01 | 2.39 | <0.01 | -40.3 | 0.28 |

**Table C.4.** Summary statistics for linear regressions between different observations of integrated particulate concentrations and elemental ratios with time during the DBO time-series from 2011 – 2019 and 2006 – 2022. Slope and $R^2_{adj}$ are shown. Relationships with a p-value ≤ 0.05 are shown in **bold**, and p-values ≤ 0.01 are ***bold italic.***

| | **DBO1** | | **DBO2** | | **DBO3W** | | **DBO3E** | | **DBO4** | | **DBO5** | |
|---|---|---|---|---|---|---|---|---|---|---|---|---|
| | Slope | $R^2$ | Slope | $R^2$ | Slope | $R^2$ | Slope | $R^2$ | Slope | $R^2$ | Slope | $R^2$ |
| **PARTICULATE CONCENTRATIONS** | | | | | | | | | | | | |
| **2011-2019 warming period** | | | | | | | | | | | | |
| **∫bSiO$_2$** | -8.49 | 0.12 | -3.48 | <0.01 | 0.32 | <0.01 | -5.08 | 0.17 | 24.4 | 0.13 | -6.14 | 0.02 |
| **∫chl-*a*** | -11.9 | <0.01 | -5.06 | <0.01 | -9.65 | <0.01 | 1.07 | <0.01 | 1.44 | <0.01 | -7.20 | 0.45 |
| **∫PC** | 6.14 | <0.01 | 42.2 | 0.19 | 2.4 | <0.01 | 4.43 | <0.01 | 8.42 | <0.01 | 76.5 | 0.96 |
| **∫PN** | 6.84 | <0.01 | 5.56 | 0.10 | 4.51 | <0.01 | 6.19 | 0.63 | 19.2 | 0.35 | 32.1 | 0.90 |
| **2006-2022** | | | | | | | | | | | | |
| **∫bSiO$_2$** | ***-13.8*** | ***0.71*** | -1.18 | <0.01 | 5.53 | 0.02 | 2.01 | <0.01 | 5.62 | <0.01 | -1.45 | <0.01 |
| **∫chl-*a*** | -3.1 | <0.01 | 4.51 | 0.04 | 7.83 | <0.01 | 0.28 | <0.01 | 3.4 | <0.01 | 3.65 | 0.01 |
| **∫PC** | -1.52 | <0.01 | 28.2 | 0.16 | 45.8 | <0.01 | 50.7 | 0.18 | 8.07 | <0.01 | -7.95 | <0.01 |
| **∫PN** | 0.77 | <0.01 | 4.73 | 0.12 | 6.50 | 0.06 | 14.30 | 0.55 | 4.64 | 0.07 | 0.40 | <0.01 |
| **ELEMENTAL RATIOS** | | | | | | | | | | | | |
| **2011-2019 warming period** | | | | | | | | | | | | |
| **∫C:N** | -0.24 | 0.34 | 0.07 | 0.02 | -0.36 | 0.19 | -0.39 | 0.32 | **-0.83** | **0.63** | -0.89 | 0.90 |
| **∫Si:C** | -0.01 | <0.01 | -0.03 | 0.19 | 0.01 | <0.01 | -0.02 | 0.60 | 0.02 | 0.24 | -0.02 | 0.29 |
| **∫Si:N** | -0.06 | 0.15 | -0.13 | 0.12 | -0.03 | <0.01 | ***-0.18*** | ***0.90*** | 0.00 | <0.01 | -0.27 | 0.88 |
| **2006-2022** | | | | | | | | | | | | |
| **∫C:N** | -0.05 | <0.01 | 0.01 | <0.01 | -0.01 | <0.01 | -0.31 | 0.33 | -0.16 | 0.11 | -0.08 | <0.01 |
| **∫Si:C** | ***-0.03*** | ***0.57*** | -0.01 | 0.19 | 0.00 | <0.01 | **-0.02** | **0.59** | 0.00 | 0.06 | 0.00 | <0.01 |
| **∫Si:N** | ***-0.17*** | ***0.51*** | -0.07 | 0.16 | -0.01 | <0.01 | ***-0.15*** | ***0.82*** | 0.00 | <0.01 | -0.01 | <0.01 |

**Table C.5.** Summary statistics for linear regressions between different observations of integrated nutrient utilization rates with time during the DBO time-series from 2011 – 2019 and 2006 –2022. Slope and $R^2_{adj}$ are shown. Relationships with a p-value ≤ 0.05 are shown in **bold**, and p-values ≤ 0.01 are ***bold italic.*** Si utilization ($\rho$Si and $V_{Si}$) only began in 2013. NA values with an asterisk (*) are due to insufficient sample size to calculate a slope and regression statistics.

| | **DBO1** | | **DBO2** | | **DBO3W** | | **DBO3E** | | **DBO4** | | **DBO5** | |
|---|---|---|---|---|---|---|---|---|---|---|---|---|
| | Slope | $R^2$ | Slope | $R^2$ | Slope | $R^2$ | Slope | $R^2$ | Slope | $R^2$ | Slope | $R^2$ |
| **NUTRIENT UTILIZATION RATES** | | | | | | | | | | | | |
| **2011-2019 warming period** | | | | | | | | | | | | |
| **$\int\rho C$** | -0.36 | <0.01 | 6.55 | <0.01 | -19.6 | <0.01 | 4.48 | <0.01 | -26.9 | 0.37 | -5.17 | <0.01 |
| **$\int\rho NO_3$** | -0.65 | <0.01 | 0.09 | <0.01 | -3.32 | 0.11 | ***0.38*** | ***0.91*** | -0.15 | <0.01 | -0.53 | <0.01 |
| **$\int\rho Si$** | -3.11 | 0.24 | 4.05 | 0.27 | -1.60 | <0.01 | 0.70 | <0.01 | 24.1 | 0.41 | 0.57 | <0.01 |
| **$\int V_{Si}$** | -0.01 | <0.01 | 0.03 | 0.41 | -0.01 | <0.01 | 0.01 | <0.01 | 0.06 | 0.47 | 0.01 | <0.01 |
| **2006-2022** | | | | | | | | | | | | |
| **$\int\rho C$** | -0.89 | <0.01 | 6.51 | 0.08 | 8.70 | <0.01 | 1.77 | <0.01 | -5.86 | 0.10 | **-8.06** | **0.68** |
| **$\int\rho NO_3$** | -0.37 | 0.04 | 0.75 | 0.04 | -1.32 | <0.01 | 0.17 | 0.08 | -0.10 | <0.01 | -0.39 | 0.43 |
| **$\int\rho Si$** | -2.13 | 0.34 | 3.74 | 0.10 | 3.45 | 0.07 | 0.15 | <0.01 | 4.11 | <0.01 | 0.65 | 0.20 |
| **$\int V_{Si}$** | -0.01 | 0.19 | **0.03** | **0.49** | 0.01 | <0.01 | 0.00 | <0.01 | 0.01 | <0.01 | 0.01 | <0.01 |
| **NUTRIENT UTILIZATION RATIOS** | | | | | | | | | | | | |
| **2011-2019 warming period** | | | | | | | | | | | | |
| **$\int\rho C$:$\rho NO_3$** | 0.57 | <0.01 | 0.61 | 0.04 | 4.09 | 0.04 | **-7.76** | **0.77** | -7.58 | 0.30 | -0.56 | <0.01 |
| **$\int\rho Si$:$\rho C$** | -0.05 | <0.01 | 0.01 | <0.01 | **0.05** | **0.73** | 0.02 | <0.01 | 1.04 | 0.53 | *NA** | *NA** |
| **$\int\rho Si$:$\rho NO_3$** | 0.08 | <0.01 | 0.09 | <0.01 | 1.80 | 0.08 | 0.01 | <0.01 | 4.38 | 0.34 | *NA** | *NA** |
| **2006-2022** | | | | | | | | | | | | |
| **$\int\rho C$:$\rho NO_3$** | 0.39 | 0.06 | **-1.16** | **0.31** | 0.59 | <0.01 | -5.30 | 0.52 | -1.18 | <0.01 | -0.62 | 0.57 |
| **$\int\rho Si$:$\rho C$** | -0.05 | 0.19 | 0.01 | <0.01 | **0.03** | **0.42** | 0.00 | <0.01 | 0.21 | <0.01 | 0.09 | <0.01 |
| **$\int\rho Si$:$\rho NO_3$** | -0.08 | <0.01 | 0.09 | <0.01 | 0.31 | <0.01 | -0.08 | <0.01 | 0.51 | <0.01 | 0.03 | <0.01 |
| **DIATOM CONTRIBUTIONS TO UTILIZATION RATES** | | | | | | | | | | | | |
| **2011-2019 warming period** | | | | | | | | | | | | |
| **diatom $\int\rho C$** | -16.9 | 0.09 | 28.7 | 0.52 | -13.8 | <0.01 | 4.59 | <0.01 | 81.1 | 0.49 | *NA** | *NA** |
| **diatom $\int\rho NO_3$** | -1.68 | <0.01 | 4.58 | 0.47 | -1.25 | <0.01 | 1.41 | <0.01 | **16.4** | **0.62** | *NA** | *NA** |
| **2006-2022** | | | | | | | | | | | | |
| **diatom $\int\rho C$** | -14.1 | 0.33 | 25.7 | 0.23 | 15.3 | <0.01 | 1.06 | <0.01 | 7.59 | <0.01 | 3.57 | 0.21 |
| **diatom $\int\rho NO_3$** | -1.96 | 0.25 | 4.78 | 0.22 | 3.47 | <0.01 | 0.37 | <0.01 | 2.57 | <0.01 | 1.21 | 0.13 |

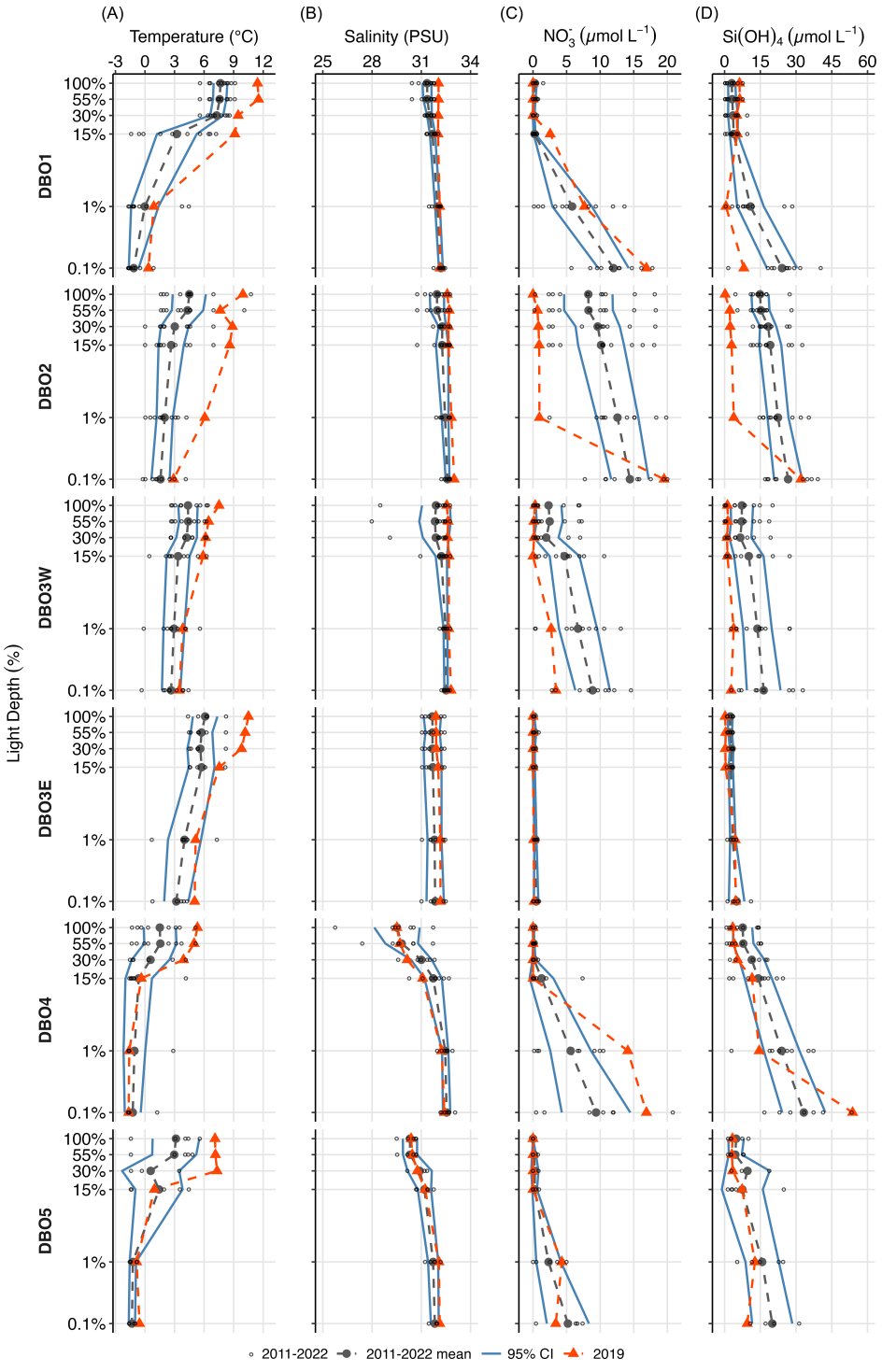


**Figure C.1.** Vertical profiles of physical properties and nutrient concentrations across DBO regions from 2011 – 2022. **(A)** Temperature, **(B)** salinity, **(C)** nitrate, $NO_3^-$, and **(D)** silicic acid, $Si(OH)_4$, plotted against light depth (%). Data points for a specific year are represented as small grey circles (○), the mean of 2011-2022 excluding 2019 as black circles (●), and values during the heat wave year (2019) as red triangle symbols (▲). Confidence intervals (95%) calculated from the yearly values are shown as solid grey-blue lines. Data from 2006 and 2008 were excluded because samples were collected at different light depths during those cruises.

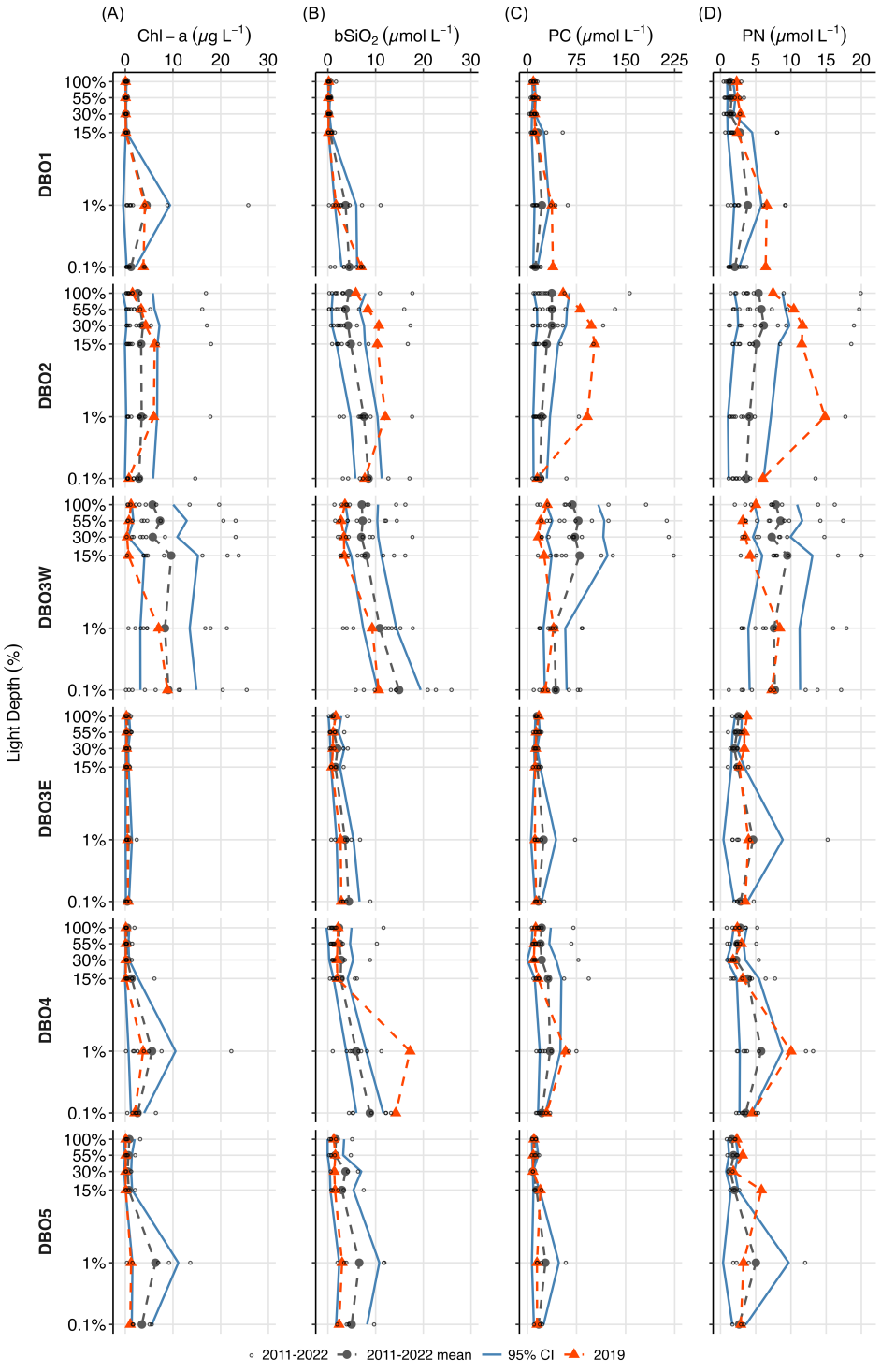


**Figure C.2.** Vertical profiles of particulate concentrations across DBO regions from 2011 – 2022. **(A)** Chlorophyll-*a*, chl-*a*, **(B)** biogenic silica, $bSiO_2$, **(C)** particulate C, PC, and **(D)** particulate N, PN, plotted against light depth (%). Data points for a specific year are represented as small grey circles (○), the mean of 2011-2022 excluding 2019 as black circles (●), and values during the heat wave year (2019) as red triangle symbols (▲). Confidence intervals (95%) calculated from the yearly values are shown as solid grey-blue lines. Data from 2006 and 2008 were excluded because samples were collected at different light depths during those cruises.

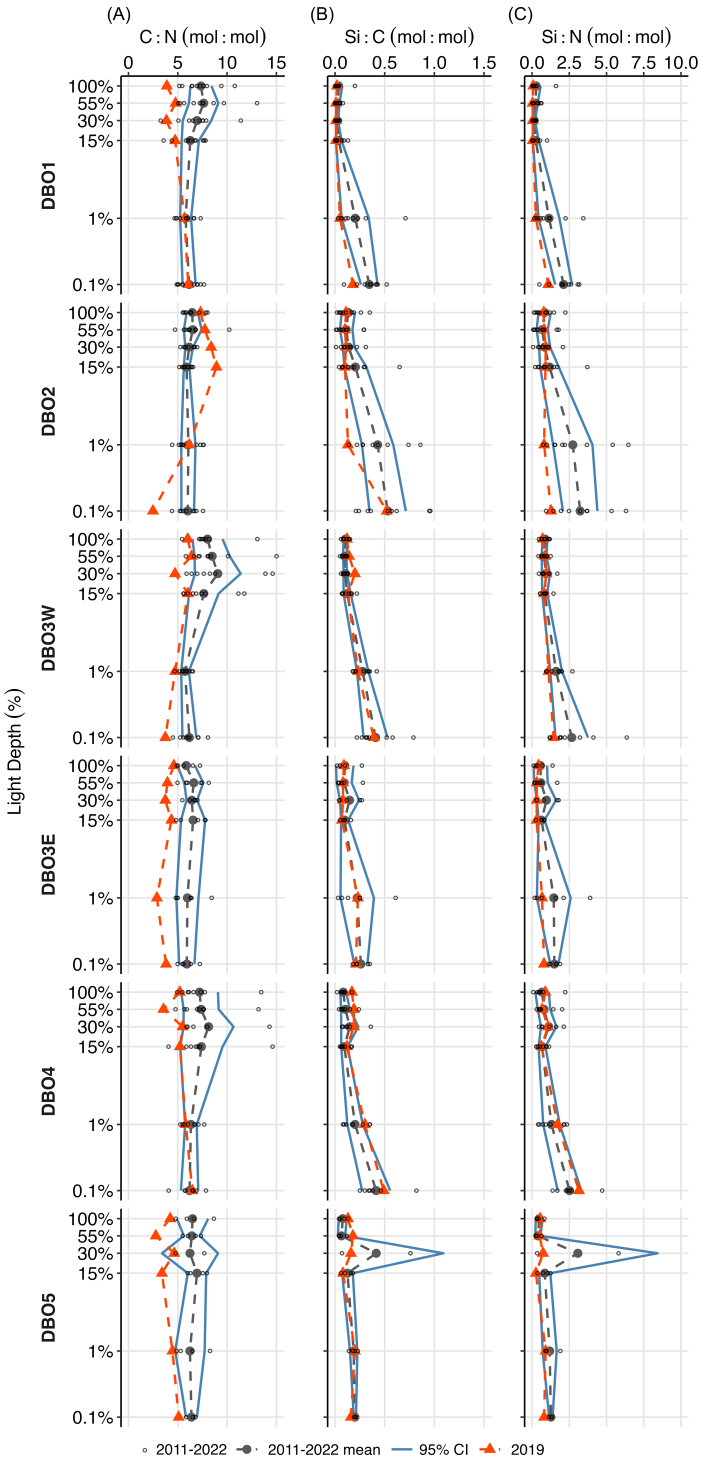


**Figure C.3.** Vertical profiles of elemental ratios across DBO regions from 2011 – 2022, calculated from particulate concentrations. **(A)** C:N, **(B)** Si:C, and **(C)** Si:N, are plotted against light depth (%). Data points for a specific year are represented as small grey circles (○), the mean of 2011-2022 excluding 2019 as black circles (●), and values during the heat wave year (2019) as red triangle symbols (▲). Confidence intervals (95%) calculated from the yearly values are shown as solid grey-blue lines. Data from 2006 and 2008 were excluded because samples were collected at different light depths during those cruises.

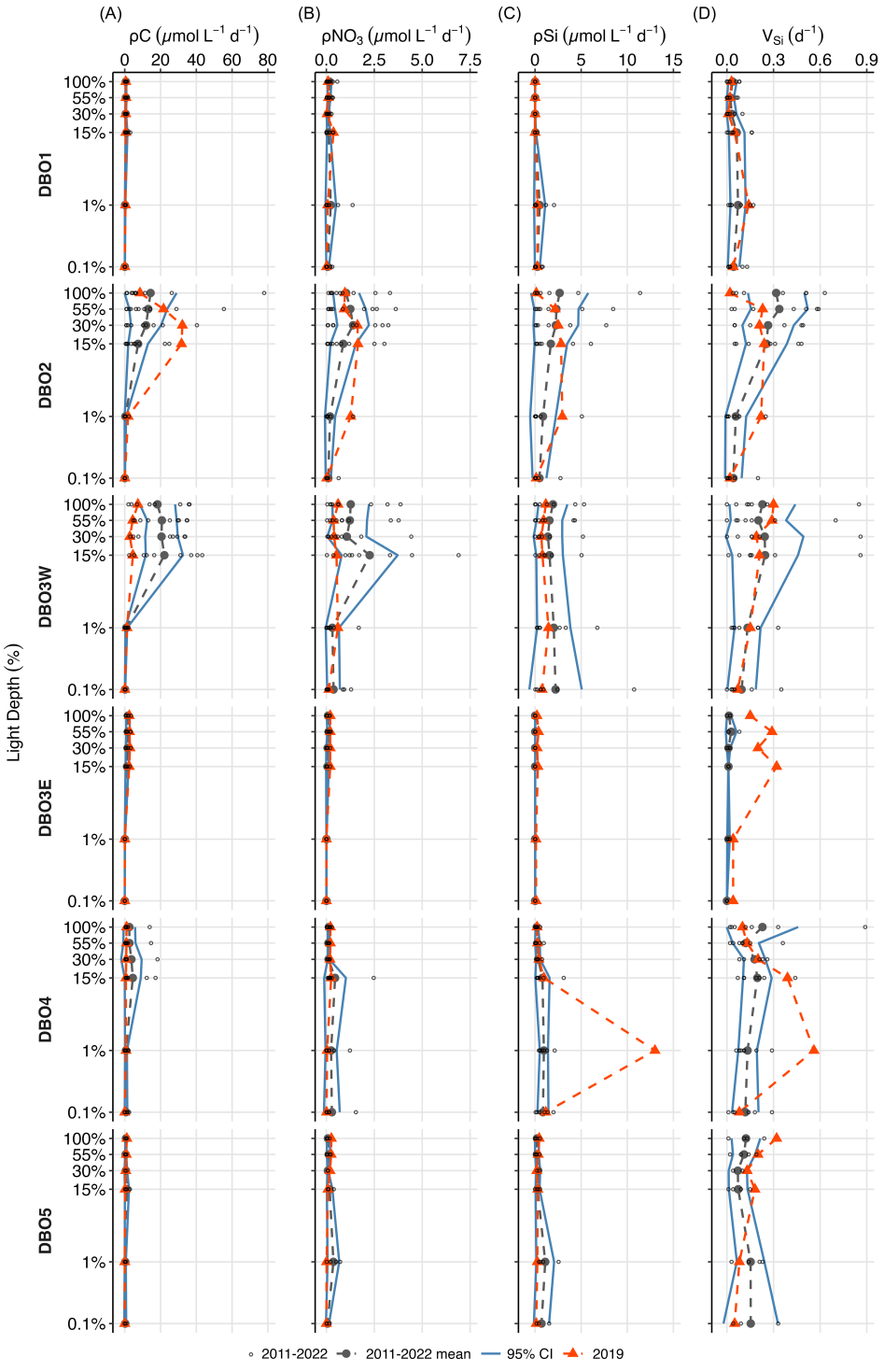


**Figure C.4.** Vertical profiles of nutrient utilization rates across DBO regions from 2011 – 2022. **(A)** Carbon utilization, $\rho C$, **(B)** $NO_3^-$ utilization, $\rho NO_3$, **(C)** $Si(OH)_4$ utilization, $\rho Si$, and **(D)** specific uptake of $Si(OH)_4$, $V_{Si}$, plotted against light depth (%). Data points for a specific year are represented as small grey circles (○), the mean of 2011-2022 excluding 2019 as black circles (●), and values during the heat wave year (2019) as red triangle symbols (▲). Confidence intervals (95%) calculated from the yearly values are shown as solid grey-blue lines. Data from 2006 and 2008 were excluded because samples were collected at different light depths during those cruises.

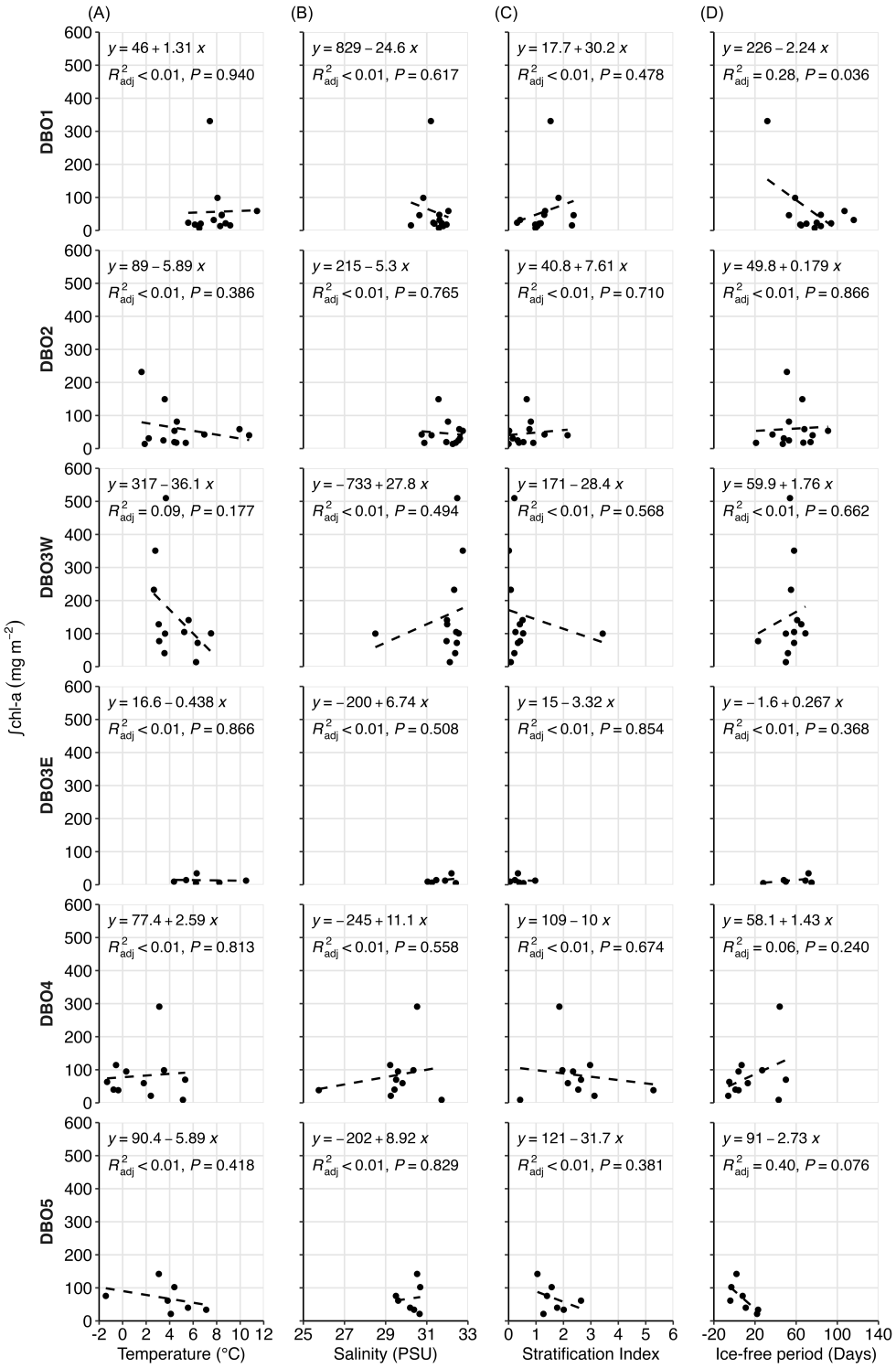


**Figure C.5.** Relationships between chlorophyll-*a* inventory (∫chl-*a*) and physical characteristics across DBO regions from 2006 – 2022. **(A)** Temperature, **(B)** salinity, **(C)** stratification index, $\sigma_\theta$, and **(D)** ice-free period were plotted against ∫chl-*a* and fitted with a linear model (dashed line). Regression statistics and p-values are shown on each panel.

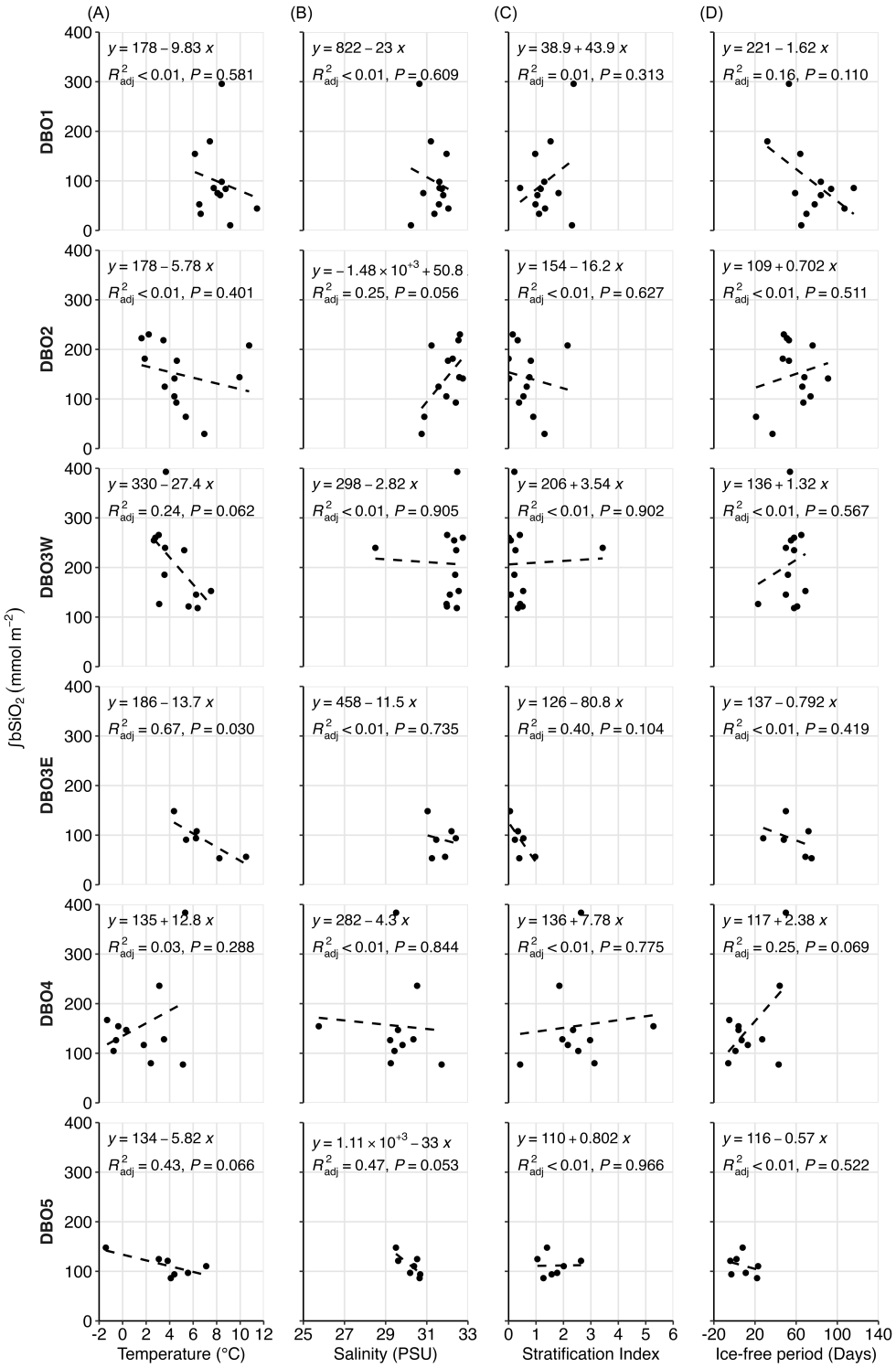


**Figure C.6.** Relationships between $bSiO_2$ inventory ($\int bSiO_2$) and physical variables across DBO regions from 2006 – 2022. **(A)** Temperature, **(B)** salinity, **(C)** stratification index, $\sigma_\theta$, and **(D)** ice-free period were plotted against $\int bSiO_2$ and fitted with a linear model (dashed line). Regression statistics and p-values are shown on each subplot.

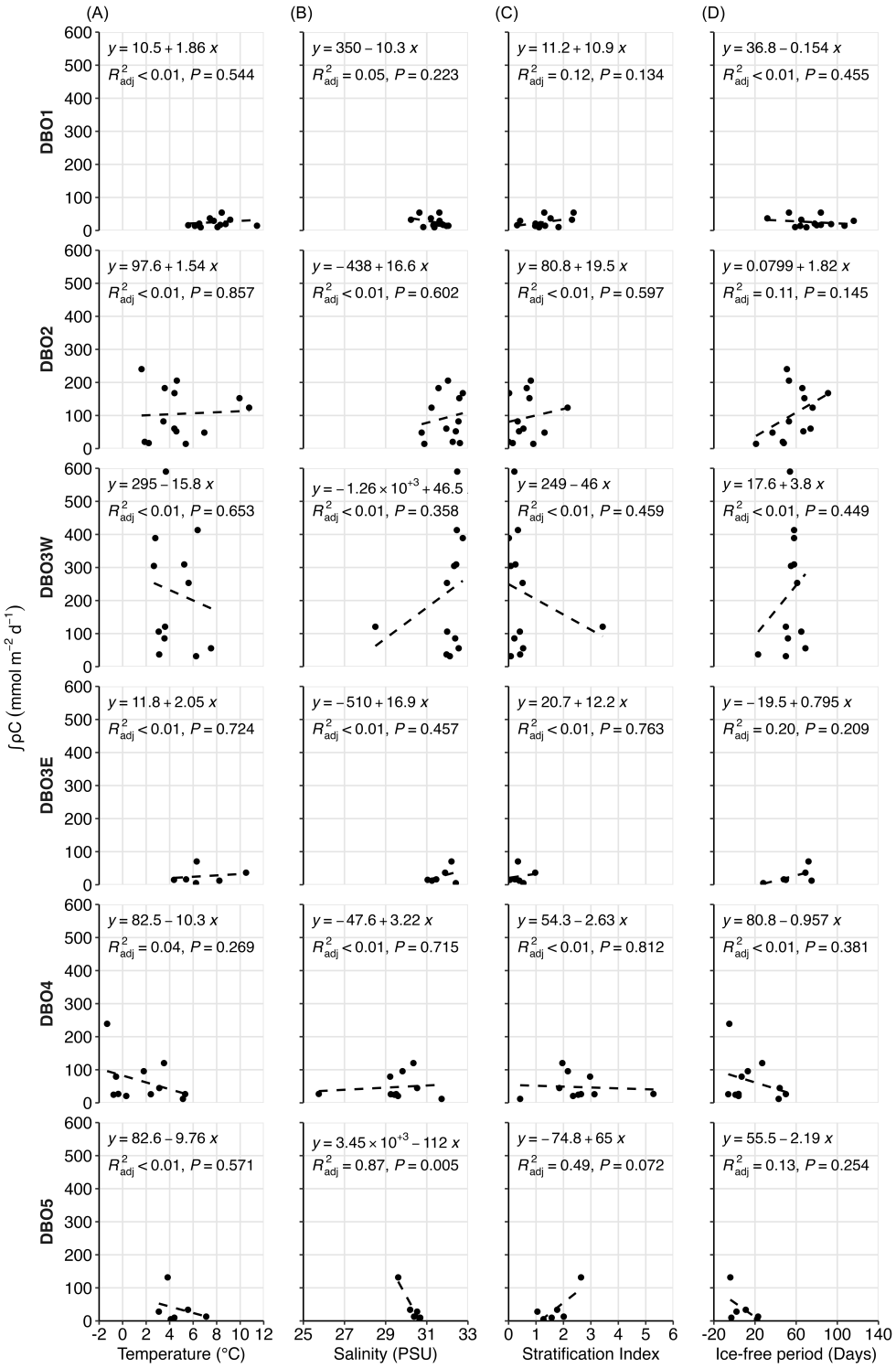


**Figure C.7.** Relationships between C utilization rate ($\int\rho C$) and physical variables across DBO regions from 2006 – 2022. **(A)** Temperature, **(B)** salinity, **(C)** stratification index, $\sigma_\theta$, and **(D)** ice-free period were plotted against $\int\rho C$ and fitted with a linear model (dashed line). Regression statistics and p-values are shown on each subplot.

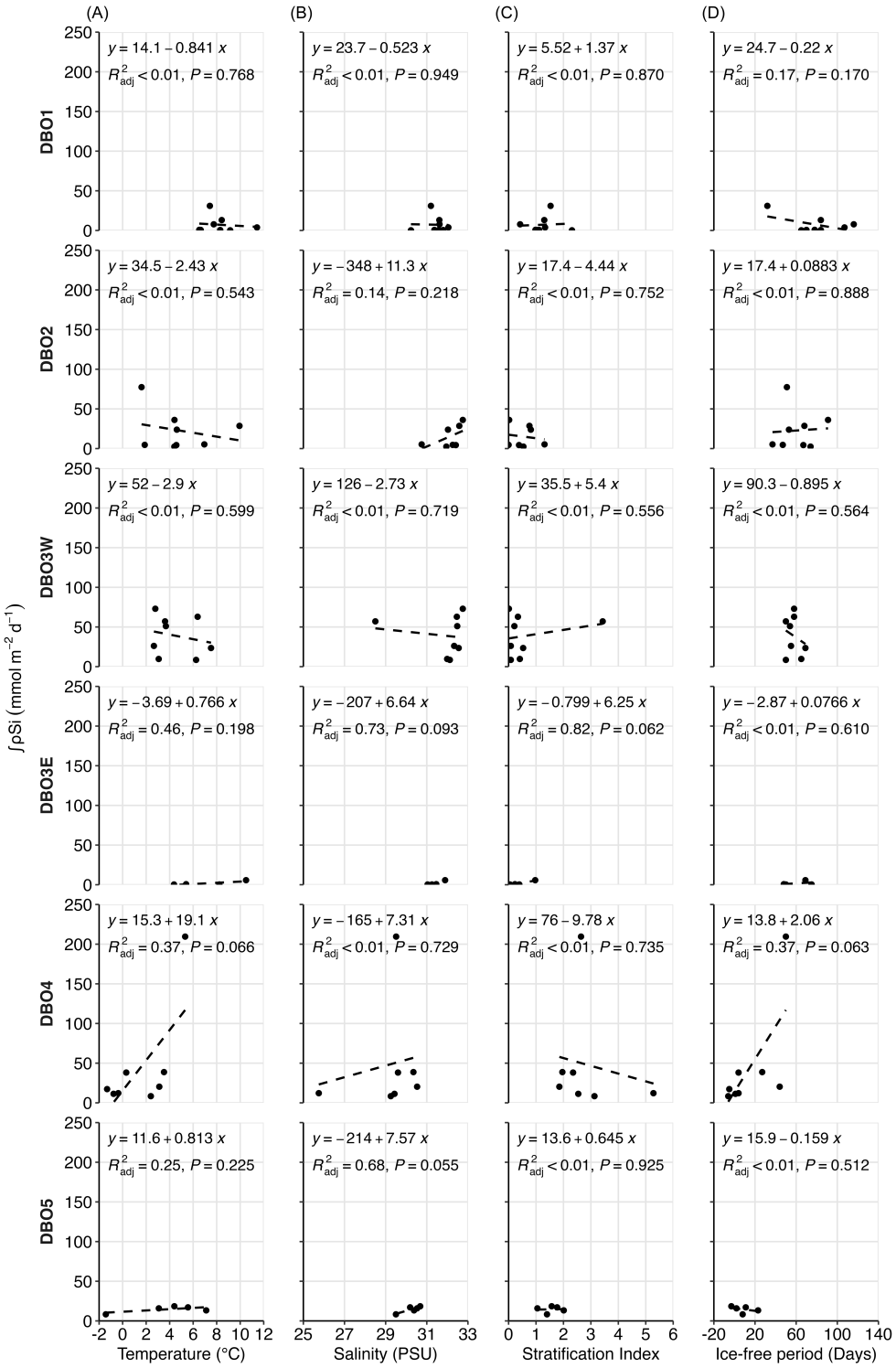


**Figure C.8.** Relationships between Si utilization rate ($\int\rho$Si) and physical variables across DBO regions from 2006 – 2022. **(A)** Temperature, **(B)** salinity, **(C)** stratification index, $\sigma_\theta$, and **(D)** ice-free period were plotted against $\int\rho$Si and fitted with a linear model (dashed line). Regression statistics and p-values are shown on each subplot.

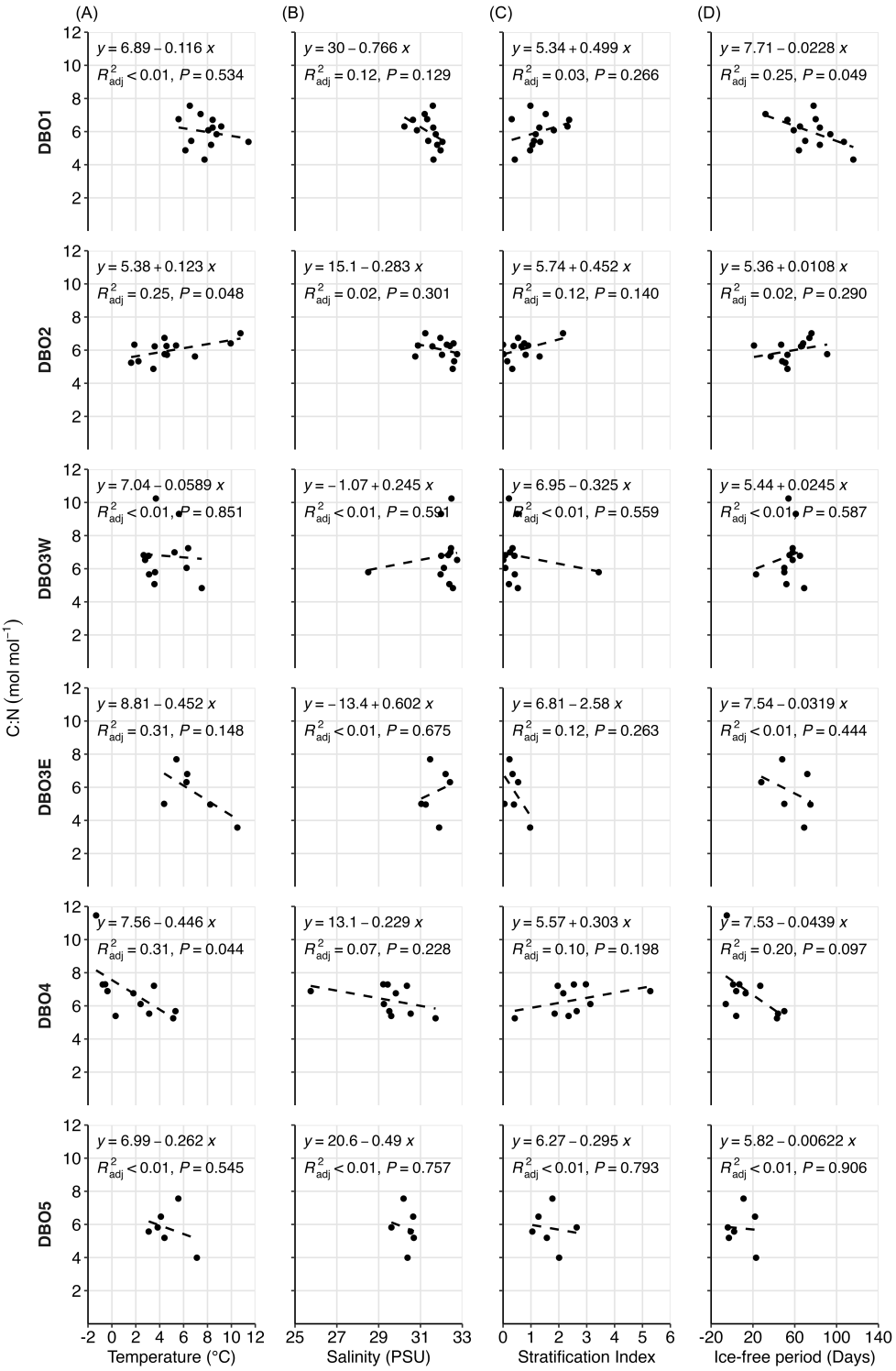


**Figure C.9.** Relationships between C:N and physical variables across DBO regions from 2006 – 2022. **(A)** Temperature, **(B)** salinity, **(C)** stratification index, $\sigma_\theta$, and **(D)** ice-free period were plotted against C:N and fitted with a linear model (dashed line). Regression statistics and p-values are shown on each subplot. C:N was calculated from ∫PC and ∫PN for each year and region.

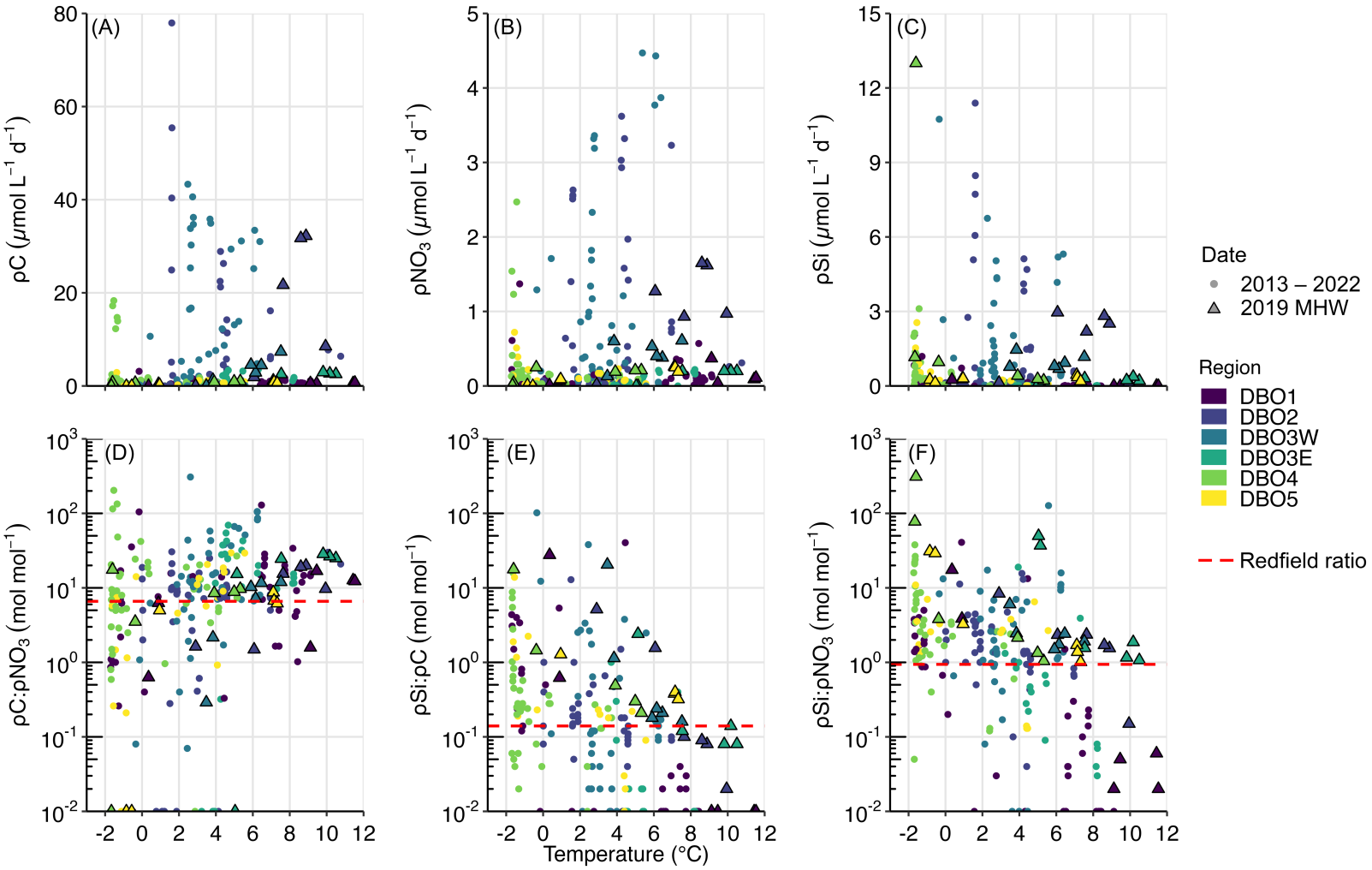


**Figure C.10.** Relationship between nutrient utilization rates and ratios and temperature for all DBO regions from 2013 – 2022. Utilization rates of **(A)** C, $\rho$C, **(B)** $NO_3^-$, $\rho NO_3$, and **(C)** $Si(OH)_4$, $\rho$Si. Ratios of **(D)** $\rho$C:$\rho NO_3$, **(E)** $\rho$Si:$\rho$C, and **(F)** $\rho$Si:$\rho NO_3$, with the Redfield ratio shown for each. Note that the y-axis is log transformed for panels D – F. Data are constrained to 2013 – 2022 to make sampling effort for all measurements and regions as similar as possible. Colours correspond to different DBO regions and each data point represents data from a single depth.

The relationship between nutrient utilization rates and temperature (Fig. C.10A – C) showed similar but less clear patterns as those seen for corresponding particulate concentrations (Chapter 3, Fig. 3.17A – C). Extremely high ratios of utilization rates resulted (Fig. C.10D – F) when C, $NO_3^-$ or Si utilization were decoupled, which complicates interpretation. Ratios of $\rho C:\rho NO_3$ were different than Redfield at most temperatures, but there was a tendency for $\rho C:\rho NO_3$ to be higher than 6.6 mol $mol^{-1}$ at temperatures above ~4°C. This indicated that $\rho C$ at warmer temperatures was supported by non-$NO_3^-$ utilization. At colder temperatures, lower $\rho C:\rho NO_3$ indicated that $\rho C$ was more closely tied to $NO_3^-$ utilization, although there was high variability in this relationship.

Similarly to $bSiO_2$ concentrations, $\rho Si$ was clearly favoured at temperatures less than 6°C (Fig. C.10C), resulting in $\rho Si:\rho C$ and $\rho Si:\rho NO_3$ that were often much higher at or below ~6°C (Fig. C.10E & F). This suggested that diatom productivity was closely tied to $\rho NO_3$ in colder, likely deeper waters across the PAR, which was also demonstrated in the separate calculations of diatom contributions to $\rho NO_3$ in Chapter 3.

– This page intentionally left blank –

# Appendix D – Supplementary material for Chapter 4

This appendix contains the supplementary material accompanying *Chapter 4 – Morphological and physiological responses of the cosmopolitan marine diatom* Thalassiosira rotula *to acidification*. These include:

- A figure showing the results of a preliminary experiment used to determine the optimum irradiance for growth of *T. rotula*. The optimum irradiance (150 µmol photons $m^{-2}$ $s^{-1}$) was then used for the OA acclimation experiment in Chapter 4.
- Two supplementary tables. The first contains the mean±sd of all measurements presented in figures of the main chapter, as well as the statistical summary and effect sizes calculated for each. The second table is a comparison of morphological measurements and elemental composition for *T. rotula*, between the strains used in this experiment and a prior study.

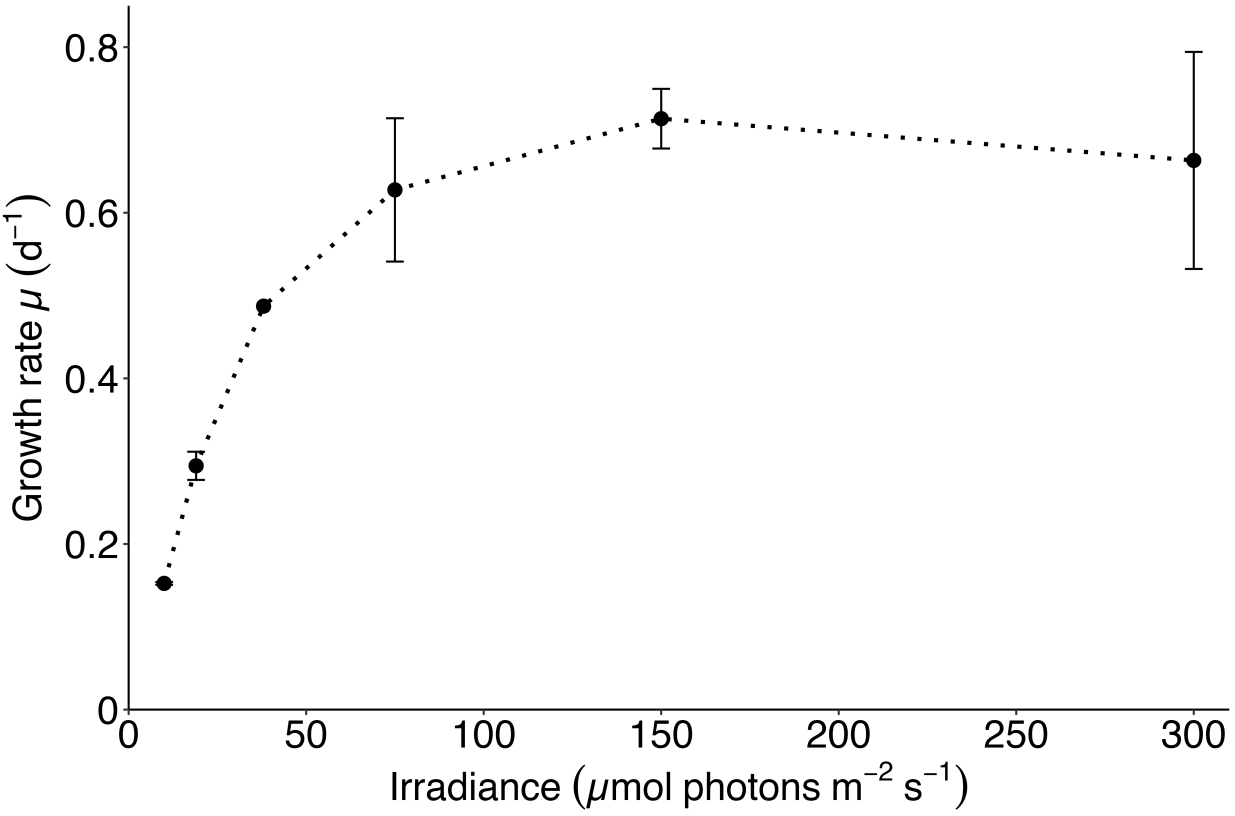


**Figure D.1.** Growth rate of *Thalassiosira rotula* in ESAW media at different irradiance levels during the preliminary experiment to determine optimum irradiance for growth. Data points are the mean (n=3) ± standard deviation. At 10 and 75 µmol photons $m^{-2}$ $s^{-1}$ one culture crashed prior to acclimation and therefore n = 2. At 38 µmol photons $m^{-2}$ $s^{-1}$ two cultures crashed prior to acclimation and therefore n = 1 (and no error bar). At the lowest irradiance level (10 µmol photons $m^{-2}$ $s^{-1}$), error bars are smaller than the symbol.

**Table D.1.** Growth rate (μ), cellular morphology, cellular quotas, cellular quota ratios, nutrient utilization rates, and nutrient utilization ratios for *Thalassiosira rotula* grown exponentially and acclimated under low carbon (LC, $pH_T$ 7.96) and high carbon (HC, $pH_T$ 7.75) conditions. All quotas and rates were normalized by the average cell volume (with the exception of $SiO_2$ that was normalized by the average cell surface area) or cell number in each treatment. Ratios using $SiO_2$ were calculated with the volume normalized quota instead of the surface area normalized quota. All values are the mean (n = 3) ± standard deviation, with the exception of Chl-*a* quota and C:Chl-*a* for LC (marked by ‡) that are the mean of two replicates. Test statistic and p-value are the result of a two-sample t-test, and differences were determined with alpha = 0.10. Significant results are indicated with an asterisk (*). A Cohen's $d_s$ effect size equal to 0.5 can be interpreted as the means of two groups differing by 0.5 standard deviations (Lakens, 2013; Rosenberg et al., 2013).

| **Cellular measurement** | **LC** | **HC** | **Test statistic** | **p-value (α = 0.10)** | **Effect size (Cohen's $d_s$)** |
|---|---|---|---|---|---|
| Growth rate, μ ($d^{-1}$) | 0.83±0.15 | 0.86±0.05 | -0.37 | 0.73 | 0.24 |
| Length ($\mu m$) | 15.3±0.8 | 14.2±0.8 | 1.73 | 0.16 | 1.13 |
| Diameter ($\mu m$) | 20.6±0.5 | 19.2±0.7 | 2.64 | 0.06* | 1.72 |
| Surface area ($\mu m^2$) | 1690±105 | 1460±124 | 2.39 | 0.08* | 1.56 |
| Volume ($\mu m^3$) | 5350±532 | 4310±601 | 2.24 | 0.09* | 1.46 |
| SA:V | 0.334±0.011 | 0.357±0.013 | -2.37 | 0.08* | 1.55 |
| *Cellular quotas* | | | | | |
| C *(fmol $\mu m^{-3}$)* | 13.9±3.83 | 11.8±1.56 | 0.85 | 0.44 | 0.55 |
| C *(pmol $cell^{-1}$)* | 74.0±20.1 | 51.7±14.1 | 1.57 | 0.19 | 1.03 |
| N *(fmol $\mu m^{-3}$)* | 2.75±1.26 | 2.36±0.14 | 0.54 | 0.62 | 0.35 |
| N *(pmol $cell^{-1}$)* | 14.5±5.76 | 10.2±1.55 | 1.26 | 0.28 | 0.82 |
| $SiO_2$ *(fmol $\mu m^{-2}$)* | 1.21±0.21 | 1.03±0.04 | 1.49 | 0.21 | 0.97 |
| $SiO_2$ *(pmol $cell^{-1}$)* | 2.05±0.44 | 1.51±0.15 | 2.03 | 0.11 | 1.33 |
| Chl-*a* *(fg $\mu m^{-3}$)* | 1.03±0.35‡ | 1.10±0.13 | n/a | n/a | 0.07 |
| Chl-*a* *(pg $cell^{-1}$)* | 5.46±1.12‡ | 4.73±0.87 | n/a | n/a | 0.55 |
| *Cellular quota ratios* | | | | | |
| C:N *(mol:mol)* | 5.33±1.00 | 5.04±0.77 | 0.39 | 0.71 | 0.26 |
| $SiO_2$:C *(mol:mol)* | 0.028±0.004 | 0.030±0.005 | -0.48 | 0.66 | 0.31 |
| $SiO_2$:N *(mol:mol)* | 0.153±0.047 | 0.149±0.016 | 0.14 | 0.90 | 0.09 |
| C:Chl-*a* (g:g) | 192.7±45.5‡ | 131.2±24.2 | n/a | n/a | 1.36 |
| *Nutrient utilization rates* | | | | | |
| $\rho$C *(fmol $\mu m^{-3}$ $d^{-1}$)* | 7.29±2.27 | 7.78±0.47 | -0.37 | 0.73 | 0.24 |
| $\rho$C *(pmol $cell^{-1}$ $d^{-1}$)* | 38.2±8.38 | 33.6±5.36 | 0.80 | 0.47 | 0.53 |
| $\rho NO_3$ *(fmol $\mu m^{-3}$ $d^{-1}$)* | 1.00±0.17 | 0.98±0.04 | 0.21 | 0.84 | 0.14 |
| $\rho NO_3$ *(pmol $cell^{-1}$ $d^{-1}$)* | 5.31±0.39 | 4.23±0.47 | 3.08 | 0.04* | 2.01 |
| $\rho$Si *(fmol $\mu m^{-3}$ $d^{-1}$)* | 0.76±0.32 | 0.62±0.13 | 0.68 | 0.54 | 0.44 |
| $\rho$Si *(pmol $cell^{-1}$ $d^{-1}$)* | 3.97±1.40 | 2.68±0.60 | 1.47 | 0.21 | 0.96 |
| *Nutrient utilization ratios (mol:mol)* | | | | | |
| $\rho$C:$\rho NO_3$ | 7.15±1.09 | 7.93±0.44 | -1.14 | 0.32 | 0.74 |
| $\rho$Si:$\rho$C | 0.11±0.03 | 0.08±0.01 | 1.39 | 0.24 | 0.91 |
| $\rho$Si:$\rho NO_3$ | 0.75±0.24 | 0.63±0.11 | 0.75 | 0.49 | 0.49 |

**Table D.2.** Comparison of cellular measurements (mean ± SD) between this work and Brzezinski (1985) that exposed *Thalassiosira rotula* to different light:dark (L:D) regimes. During our OA experiment, *T. rotula* (CCMP3362) was exposed to LC = $pH_T$ 7.96 and HC = $pH_T$ 7.75 under 13:11h L:D. In Brzezinski (1985), *T. rotula* clone 411 was exposed to ambient pH but under both an 18:6h L:D regime and continuous light.

| **Cellular measurement** | **CCMP3362 LC (13:11 L:D)** | **CCMP3362 HC (13:11 L:D)** | **Clone 411 Ambient pH (18:6 L:D)** | **Clone 411 Ambient pH (continuous light)** |
|---|---|---|---|---|
| Density (*cells* $mL^{-1}$) | 964±737 | 1893±775 | 897 | 3400 |
| Surface area ($\mu m^2$) | 1690±105 | 1460±124 | 2630 | 3010 |
| Volume ($\mu m^3$) | 5350±532 | 4310±601 | 10400 | 11500 |
| SA:V | 0.334±0.011 | 0.357±0.013 | 0.25 | 0.26 |
| *Cellular quotas* | | | | |
| C (*fmol* $\mu m^{-3}$) | 13.9±3.83 | 11.8±1.56 | 5.4 | 2.2 |
| N (*fmol* $\mu m^{-3}$) | 2.75±1.26 | 2.36±0.14 | 0.64 | 0.30 |
| $SiO_2$ (*fmol* $\mu m^{-2}$) | 1.21±0.21 | 1.03±0.04 | 2.0 | 0.93 |
| *Quota ratios (mol:mol)* | | | | |
| C:N | 5.33±1.00 | 5.04±0.77 | 8.4 | 7.4 |
| $SiO_2$:C | 0.028±0.004 | 0.030±0.005 | 0.09 | 0.11 |
| $SiO_2$:N | 0.153±0.047 | 0.149±0.016 | 0.79 | 0.82 |

# Appendix E – Supplementary material for Chapter 5

This appendix contains the supplementary material accompanying *Chapter 5 – Impacts of ocean acidification on phytoplankton from an oligotrophic subtropical ecosystem.* These include:

- A table showing replicate measurements of the carbonate system, used to calculate the averages in Table 5.2.
- A statistical summary table to accompany Figures 5.1, 5.2, and 5.3 in Chapter 5.

**Table E.1.** Measurements of the carbonate system for low carbon (LC) and high carbon (HC) treatments of the OA experiment conducted on a phytoplankton assemblage collected from the BATS station on 09-Nov 2018. Total carbon ($C_T$) and total alkalinity (TA) are reported as individual replicates collected on the last day (day 7) of the experiment. Calculated $pH_T$ is on the total scale, and $pCO_2$ is after bubbling ambient and enriched $CO_2$ air at ~350 mL/min. Uncertainty for $C_T$ and TA are the typical analytical uncertainty for each. Uncertainty for each treatment replicate $pH_T$ and $pCO_2$ is the propagated analytical uncertainty. Mean $pH_T$ and $pCO_2$ are the mean of each treatment ± the geometric mean of the average propagated analytical uncertainty and the treatment standard deviation. Duplicate $C_T$/TA samples were collected from experimental replicates that had enough remaining volume, and are shown to present uncertainty due to sampling.

| ***Treatment*** | **$C_T$ (µmol kg$^{-1}$)** | **TA (µmol kg$^{-1}$)** | **$pH_T$ (calculated)** | **$pCO_2$ (µatm)** |
|---|---|---|---|---|
| LC-1 | 2153±2 | 2467±5 | 8.07±0.01 | 401±14 |
| LC-2 | 2126±2 | 2432±5 | 8.05±0.01 | 412±15 |
| LC-3 | 2144±2 | 2459±5 | 8.06±0.01 | 401±14 |
| *LC mean* | | | *8.06±0.01* | *405±10* |
| | | | | |
| HC-1 | 2259±2 | 2435±5 | 7.81±0.02 | 790±30 |
| HC-2 | 2272±2 | 2450±5 | 7.81±0.01 | 790±30 |
| HC-3 | 2269±2 | 2446±5 | 7.81±0.01 | 800±30 |
| *HC mean* | | | *7.81±0.00* | *794±11* |
| | | | | |
| *Sampling uncertainty* | | | | |
| Ambient-1a | 2103±2 | 2407±5 | 8.01±0.01 | 409±15 |
| Ambient-1b | 2101±2 | 2411±5 | 8.02±0.01 | 399±14 |
| | | | | |
| LC-2a | 2126±2 | 2432±5 | 8.05±0.01 | 412±15 |
| LC-2b | 2118±2 | 2420±5 | 8.04±0.01 | 416±15 |
| | | | | |
| HC-1a | 2259±2 | 2435±5 | 7.81±0.02 | 790±30 |
| HC-1b | 2247±2 | 2417±5 | 7.79±0.02 | 820±30 |
| | | | | |
| HC-3a | 2269±2 | 2446±5 | 7.81±0.01 | 800±30 |
| HC-3b | 2249±2 | 2419±5 | 7.79±0.02 | 830±30 |

**Table E.2.** Phytoplankton physiological measurements under low carbon (LC) and high carbon (HC) treatments of the OA experiment, conducted on a phytoplankton assemblage collected from the BATS station on 09-Nov 2018. P-values marked with $^{\#}$ were calculated with a two-sample t-test assuming unequal variances. All other p-values were calculated using t-tests that assumed equal variance. P-values marked with an asterisk (*) indicate a significant result.

| **Parameter** | **LC (pH = 8.06)** | **HC (pH = 7.81)** | **p-value ($\alpha$ = 0.05)** | **Cohen's $d_s$** |
|---|---|---|---|---|
| *Dissolved nutrients* | | | | |
| $NO_3^-$ (μmol $L^{-1}$) | 2.7±0.4 | 3.07±0.18 | 0.21 | 0.97 |
| $PO_4^{3-}$ (μmol $L^{-1}$) | 0.24±0.05 | 0.21±0.00 | 0.41$^{\#}$ | 0.65 |
| $Si(OH)_4$ (μmol $L^{-1}$) | 2.84±0.06 | 2.80±0.01 | 0.36 | 0.68 |
| *Particulate biomass* | | | | |
| Total chl-a (ng $L^{-1}$) | 91±16 | 87±18 | 0.79 | 0.19 |
| Total $bSiO_2$ (nmol $L^{-1}$) | 32±8 | 26±7 | 0.33 | 0.73 |
| Total PC (μmol $L^{-1}$) | 12.3±1.5 | 11.0±1.2 | 0.30 | 0.77 |
| Total PN (μmol $L^{-1}$) | 2.0±0.1 | 1.7±0.03 | 0.10$^{\#}$ | 1.89 |
| *Particulate ratios* | | | | |
| C:N (mol $mol^{-1}$) | 6.3±0.3 | 6.4±0.6 | 0.82 | 0.16 |
| Si:C (mol $mol^{-1}$) | 0.0026±0.0003 | 0.0023±0.0004 | 0.35 | 0.69 |
| Si:N (mol $mol^{-1}$) | 0.016±0.003 | 0.015±0.004 | 0.58 | 0.39 |
| C:Chl-a (g $g^{-1}$) | 1630±100 | 1550±300 | 0.63 | 0.34 |
| *Nutrient uptake rates* | | | | |
| Total $\rho$C (nmol $L^{-1}$ $d^{-1}$) | 74±20 | 73±30 | 0.94 | 0.05 |
| Total $\rho NO_3$ (nmol $L^{-1}$ $d^{-1}$) | 48±26 | 65±50 | 0.60 | 0.37 |
| Total $\rho$Si (nmol $L^{-1}$ $d^{-1}$) | 25±2 | 26±9 | 0.91 | 0.08 |
| Total $V_{Si}$ ($d^{-1}$) | 0.80±0.2 | 1.10±0.6 | 0.45 | 0.54 |
| *Cell abundances and C quotas* | | | | |
| *Prochlorococcus* (cells $mL^{-1}$) | 79000±11000 | 83000±14000 | 0.77 | 0.21 |
| *Synechococcus* (cells $mL^{-1}$) | 89±2 | 70±30 | 0.42$^{\#}$ | 0.66 |
| Picoeukaryotes (cells $mL^{-1}$) | 390±70 | 360±80 | 0.69 | 0.28 |
| Nanoeukaryotes (cells $mL^{-1}$) | 0±0 | 7±3 | 0.06$^{\#}$ | 2.64 |
| Total cell density | 80000±11000 | 83000±14000 | 0.77 | 0.20 |
| *Prochlorococcus* (fg POC $cell^{-1}$) | 113±2 | 111±7 | 0.58 | 0.39 |
| *Synechococcus* (fg POC $cell^{-1}$) | 259±14 | 217±12 | 0.02$^{*}$ | 2.59 |
| Picoeukaryotes (fg POC $cell^{-1}$) | 950±70 | 810±120 | 0.14 | 1.20 |
| Nanoeukaryotes (fg POC $cell^{-1}$) | NA | 5900±1300 | NA | NA |

# Appendix F – Supplementary material for Chapter 6

This appendix contains the following supplementary material to accompany *Chapter 6 – Physiological responses to high $CO_2$ by a summertime diatom assemblage in the northern Bering Sea.* These include:

- Two tables with additional electrode pH and carbonate system measurements, including estimates of analytical uncertainty.
- A figure showing growth rate (μ), calculated from chl-*a* concentrations, for all three $CO_2$ treatments over the duration of the acclimation experiment described in Chapter 6.
- A heatmap figure comparing phytoplankton physiology measurements under two different pH levels to a control, on the fourth day of the acclimation experiment described in Chapter 6.
- A statistical summary for Kruskal-Wallis rank-sum tests used to assess differences between the measurements presented in Fig. F.2.
- Statistical summary tables for Kruskal-Wallis rank-sum tests used to assess differences between the measurements on both day 3 and day 6, presented in Fig. 6.7.
- A table summarizing the relative abundances of diatoms from Lugol's preserved samples collected during the exponential growth phase of the experiment (day 4), with a statistical summary comparing between experimental treatments.

**Table F.1.** Daily electrode $pH_T$ measurements for the OA experiment conducted on a diatom assemblage collected from the Bering Sea in July 2022. Values are reported as the mean of three replicates ± standard deviation. Uncertainty for the mean differences between treatments were propagated from daily measurements. Day 1 values are the same for all treatments because pH measurements were made prior to the start of bubbling.

| Treatment | Day 1 | Day 2 | Day 3 | Day 4 | Day 5 | Day 6 | |
|---|---|---|---|---|---|---|---|
| LC | 8.15±0.01 | 8.14±0.01 | 8.16±0.04 | 8.26±0.08 | 8.42±0.08 | 8.26±0.01 | |
| MC | 8.15±0.01 | 7.93±0.11 | 7.92±0.01 | 8.02±0.10 | 7.96±0.03 | 7.89±0.04 | |
| HC | 8.15±0.01 | 7.79±0.21 | 7.74±0.03 | 7.85±0.00 | 7.75±0.05 | 7.73±0.03 | *Mean* |
| ΔLC-MC | *Na* | 0.21±0.11 | 0.24±0.04 | 0.24±0.13 | 0.46±0.09 | 0.37±0.04 | 0.30±0.04 |
| ΔMC-HC | *Na* | 0.14±0.24 | 0.18±0.03 | 0.17±0.10 | 0.21±0.06 | 0.16±0.05 | 0.17±0.05 |

**Table F.2.** Measurements of the carbonate system for ambient and experimental treatments of a pH manipulation experiment conducted on a diatom assemblage collected from the Bering Sea in July 2022 and acclimated to different levels of $pCO_2$. Total carbon ($C_T$) and total alkalinity (TA) are reported as individual replicates collected on the last day (day 7) of the experiment. Calculated $pH_T$ is on the total scale, and $pCO_2$ is after bubbling ambient and enriched $CO_2$ air. Uncertainty for $C_T$ and TA are the typical analytical uncertainty for each. Uncertainty for each treatment replicate $pH_T$ and $pCO_2$ is the propagated analytical uncertainty. Mean $pH_T$ and $pCO_2$ are the mean of each treatment ± the geometric mean of the average propagated analytical uncertainty and the treatment standard deviation.

| ***Treatment*** | **$C_T$ (µmol kg$^{-1}$)** | **TA (µmol kg$^{-1}$)** | **$pH_T$ (calculated)** | **$pCO_2$ (µatm)** |
|---|---|---|---|---|
| LC-1 | 2017±2 | 2233±5 | 8.25±0.02 | 235±10 |
| LC-2 | 2024±2 | 2235±5 | 8.24±0.02 | 243±10 |
| LC-3 | 2011±2 | 2239±5 | 8.28±0.02 | 221±9 |
| *LC mean* | | | *8.26±0.02* | *233±10* |
| MC-1 | 2171±2 | 2242±5 | 7.86±0.02 | 650±30 |
| MC-2 | 2150±2 | 2229±5 | 7.88±0.02 | 610±30 |
| MC-3 | 2133±2 | 2233±5 | 7.95±0.02 | 520±20 |
| *MC mean* | | | *7.90±0.03* | *590±40* |
| HC-1 | 2192±2 | 2229±5 | 7.74±0.02 | 870±40 |
| HC-2 | 2205±2 | 2225±5 | 7.67±0.02 | 1010±50 |
| HC-3 | 2216±2 | 2243±5 | 7.70±0.02 | 970±50 |
| *HC mean* | | | *7.70±0.03* | *950±60* |
| *Sampling uncertainty* | | | | |
| Ambient-1a | 2014±2 | 2214±5 | 8.27±0.02 | 215±9 |
| Ambient-1b | 2014±2 | 2207±5 | 8.25±0.02 | 223±9 |

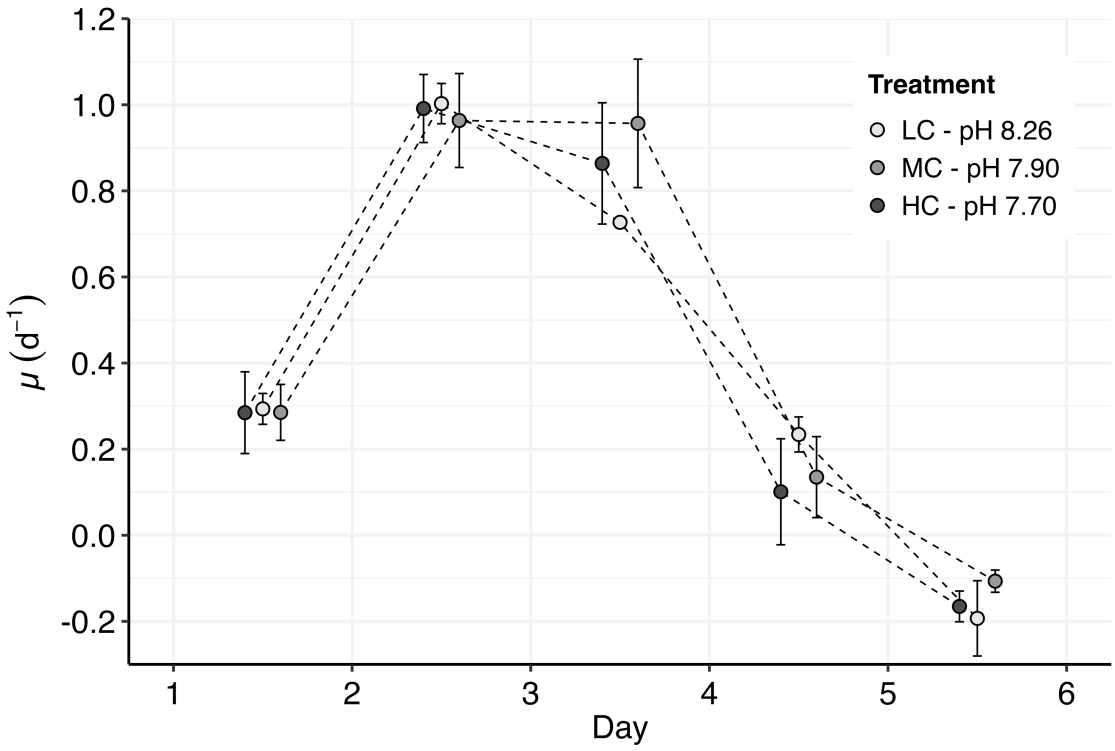


**Figure F.1.** Growth rate (μ) of a diatom assemblage collected from the northern Bering Sea in July 2022 during acclimation to different pH levels. The mean (n = 3) of each $CO_2$ treatment is represented by different shaded circles, and the standard deviation is represented by error bars from each circle. When no error bars are present, the size of the symbol is larger than the standard deviation.

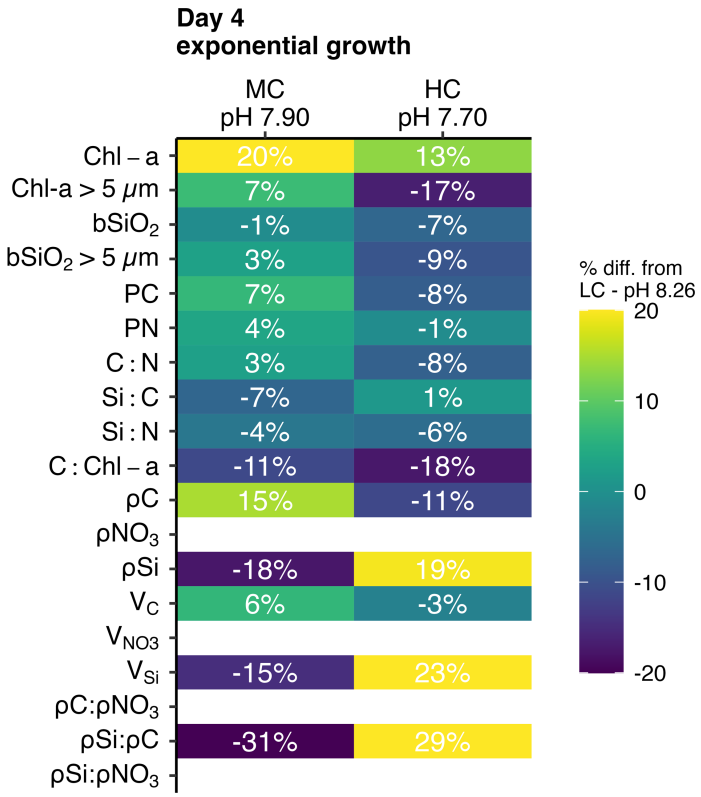


**Figure F.2.** Relative changes in measures of biomass, stoichiometry, and nutrient utilization rates for a diatom assemblage collected from the northern Bering Sea in July 2022, after four days of acclimation to different pH levels. Values are the percent differences from the means of a control (LC) and the MC or HC experimental treatments. Colour corresponds to the percentage. A statistical summary of p-values and effect sizes for day 4 are reported in Table F.3.

**Table F.3.** Statistical summary of Kruskal-Wallis rank-sum tests between variables under different pH treatments for the exponential growth phase (day 4). Variables tested are listed in the same order as heatmap Fig. F.2. H ($\chi^2$) is the chi-squared test statistic, n is the sample size, p-value is interpreted with $\alpha = 0.05$. Effect sizes $\varepsilon^2$ and $\eta^2$ are interpreted as described in the methods. "na" indicates where data were excluded due to the phase of the experiment, e.g. $NO_3^-$ was depleted so any $\rho NO_3$ measured was not useful and a statistical test was not completed.

| **Variable** | **H ($\chi^2$)** | **n** | **p-value** | **$\varepsilon^2$** | **$\eta^2$** |
|---|---|---|---|---|---|
| *Particulate biomass* | | | | | |
| Chl-*a* | 3.20 | 9 | 0.202 | 0.40 | 20% |
| Chl-*a* > 5 µm | 4.62 | 9 | 0.099 | 0.58 | 44% |
| $bSiO_2$ | 3.29 | 9 | 0.193 | 0.19 | 21% |
| $bSiO_2$ > 5 µm | 3.47 | 9 | 0.177 | 0.43 | 24% |
| PC | 5.96 | 9 | 0.051 | 0.74 | 66% |
| PN | 1.69 | 9 | 0.430 | 0.21 | 0% |
| *Particulate ratios* | | | | | |
| C:N | 3.20 | 9 | 0.202 | 0.40 | 20% |
| Si:C | 2.51 | 9 | 0.285 | 0.31 | 8% |
| Si:N | 1.10 | 9 | 0.578 | 0.14 | 0% |
| C:chl-*a* | 4.36 | 9 | 0.113 | 0.54 | 39% |
| *Nutrient utilization rates* | | | | | |
| $\rho C$ | 5.07 | 9 | 0.079 | 0.63 | 51% |
| $\rho NO_3$ | *na* | *na* | *na* | *na* | *na* |
| $\rho Si$ | 3.20 | 9 | 0.202 | 0.40 | 20% |
| $V_C$ | 2.49 | 9 | 0.288 | 0.31 | 8% |
| $V_{NO3}$ | *na* | *na* | *na* | *na* | *na* |
| $V_{Si}$ | 3.82 | 9 | 0.148 | 0.48 | 30% |
| *Nutrient utilization ratios* | | | | | |
| $\rho C:\rho NO_3$ | *na* | *na* | *na* | *na* | *na* |
| $\rho Si:\rho C$ | 3.52 | 9 | 0.172 | 0.44 | 25% |
| $\rho Si:\rho NO_3$ | *na* | *na* | *na* | *na* | *na* |

**Table F.4.** Statistical summary of Kruskal-Wallis rank sum tests between variables under different pH treatments for the exponential growth phase (day 3). Variables tested are listed in the same order as heatmap Fig. 6.7. H ($\chi^2$) is the chi-squared test statistic, n is the sample size, p-value is interpreted with $\alpha = 0.05$. Effect sizes $\varepsilon^2$ and $\eta^2$ are interpreted as described in the methods.

| **Variable** | **H ($\chi^2$)** | **n** | **p-value** | **$\varepsilon^2$** | **$\eta^2$** |
|---|---|---|---|---|---|
| *Particulate biomass* | | | | | |
| Chl-*a* | 0.57 | 9 | 0.752 | 0.07 | 0% |
| Chl-*a* > 5 μm | 3.82 | 9 | 0.148 | 0.48 | 30% |
| $bSiO_2$ | 3.29 | 9 | 0.193 | 0.41 | 21% |
| $bSiO_2$ > 5 μm | 4.36 | 9 | 0.113 | 0.54 | 39% |
| PC | 1.16 | 9 | 0.561 | 0.14 | 0% |
| PN | 0.62 | 9 | 0.733 | 0.08 | 0% |
| *Particulate ratios* | | | | | |
| C:N | 0.09 | 9 | 0.957 | 0.01 | 0% |
| Si:C | 0.97 | 9 | 0.615 | 0.12 | 0% |
| Si:N | 1.16 | 9 | 0.561 | 0.14 | 0% |
| C:chl-*a* | 1.16 | 9 | 0.561 | 0.14 | 0% |
| *Nutrient utilization rates* | | | | | |
| $\rho C$ | 3.20 | 9 | 0.202 | 0.40 | 20% |
| $\rho NO_3$ | 2.22 | 9 | 0.329 | 0.28 | 4% |
| $\rho Si$ | 2.49 | 9 | 0.288 | 0.31 | 8% |
| $V_C$ | 2.49 | 9 | 0.288 | 0.31 | 8% |
| $V_{NO3}$ | 1.69 | 9 | 0.430 | 0.21 | 0% |
| $V_{Si}$ | 2.22 | 9 | 0.329 | 0.28 | 4% |
| *Nutrient utilization ratios* | | | | | |
| $\rho C:\rho NO_3$ | 0.27 | 9 | 0.875 | 0.03 | 0% |
| $\rho Si:\rho C$ | 1.69 | 9 | 0.430 | 0.21 | 0% |
| $\rho Si:\rho NO_3$ | 0.36 | 9 | 0.837 | 0.04 | 0% |

**Table F.5.** Statistical summary of Kruskal-Wallis rank sum tests between variables under different pH treatments for post-bloom phase (day 6). Variables tested are listed in the same order as heatmap Fig. 6.7. H ($\chi^2$) is the chi-squared test statistic, n is the sample size, p-value is interpreted with $\alpha = 0.05$. Effect sizes $\varepsilon^2$ and $\eta^2$ are interpreted as described in the methods. "*na*" indicates where data were excluded due to the phase of the experiment, e.g. $NO_3^-$ was depleted so any $\rho NO_3$ measured was not useful and a statistical test was not completed.

| **Variable** | **H ($\chi^2$)** | **n** | **p-value** | **$\varepsilon^2$** | **$\eta^2$** |
|---|---|---|---|---|---|
| *Particulate biomass* | | | | | |
| Chl-*a* | 5.00 | 8 | 0.082 | 0.71 | 60% |
| Chl-*a* > 5 µm | 1.87 | 9 | 0.393 | 0.23 | 0% |
| $bSiO_2$ | 0.71 | 7 | 0.700 | 0.12 | 0% |
| $bSiO_2$ > 5 µm | 0.00 | 9 | 1.000 | 0.00 | 0% |
| PC | 0.47 | 8 | 0.790 | 0.07 | 0% |
| PN | 3.14 | 8 | 0.208 | 0.45 | 23% |
| *Particulate ratios* | | | | | |
| C:N | 0.69 | 8 | 0.707 | 0.10 | 0% |
| Si:C | 0.00 | 6 | 1.000 | 0.00 | 0% |
| Si:N | 1.14 | 6 | 0.565 | 0.23 | 0% |
| C:chl-*a* | 3.93 | 7 | 0.140 | 0.65 | 48% |
| *Nutrient utilization rates* | | | | | |
| $\rho C$ | 2.89 | 8 | 0.236 | 0.41 | 18% |
| $\rho NO_3$ | *na* | *na* | *na* | *na* | *na* |
| $\rho Si$ | *na* | *na* | *na* | *na* | *na* |
| $V_C$ | 2.89 | 8 | 0.236 | 0.41 | 18% |
| $V_{NO3}$ | *na* | *na* | *na* | *na* | *na* |
| $V_{Si}$ | *na* | *na* | *na* | *na* | *na* |
| *Nutrient utilization ratios* | | | | | |
| $\rho C:\rho NO_3$ | *na* | *na* | *na* | *na* | *na* |
| $\rho Si:\rho C$ | *na* | *na* | *na* | *na* | *na* |
| $\rho Si:\rho NO_3$ | *na* | *na* | *na* | *na* | *na* |

**Table F.6.** Relative cell abundances for initial (ambient *in situ*) and exponential growth phases (day 4) of a northern Bering Sea phytoplankton assemblage acclimated to different pH levels. Cell counts come from Lugol's preserved samples. Values are the mean (n = 3) ± standard deviation. Comparisons among LC, MC, and HC treatments were made with a Kruskal-Wallis rank-sum test. Statistical terms are described in Table F.3. Total cell counts are presented in Chapter 6, Table 6.4.

| | **Ambient** | **LC ($pH_T$ 8.26)** | **MC ($pH_T$ 7.90)** | **HC ($pH_T$ 7.70)** | **H ($\chi^2$)** | **n** | **p-value** | **$\varepsilon^2$** | **$\eta^2$** |
|---|---|---|---|---|---|---|---|---|---|
| % of total cells | | | | | | | | | |
| % *Thalassiosira* | 19±8 | 33±9 | 31±3 | 20±9 | 2.49 | 9 | 0.288 | 0.31 | 8% |
| % *Chaetoceros* | 46±3 | 51±7 | 51±2 | 63±10 | 1.87 | 9 | 0.393 | 0.23 | 0% |
| % Other diatoms | 8.8±1.0 | 5.0±0.8 | 6.2±1.8 | 5.7±0.7 | 1.16 | 9 | 0.561 | 0.14 | 0% |
| % Diatoms | 74±10 | 89±1.0 | 88±0.3 | 89±1.1 | 2.76 | 9 | 0.252 | 0.34 | 13% |

# Bibliography

## References for Chapter 1


Alldredge, A.L., Silver, M.W., 1988. Characteristics, dynamics and significance of marine snow. Progress in Oceanography 20, 41–82.

Ardyna, M., Arrigo, K.R., 2020. Phytoplankton dynamics in a changing Arctic Ocean. Nat Clim Change 10, 892–903. https://doi.org/10.1038/s41558-020-0905-y

Armbrust, E.V., 2009. The life of diatoms in the world's oceans. Nature 459, 185–192.

Arrigo, K.R., Dijken, G. van, Pabi, S., 2008. Impact of a shrinking Arctic ice cover on marine primary production. Geophys. Res. Lett. 35. https://doi.org/10.1029/2008gl035028

Bach, L.T., Taucher, J., 2019. CO2 effects on diatoms: a synthesis of more than a decade of ocean acidification experiments with natural communities. Ocean Sci 15, 1159–1175. https://doi.org/10.5194/os-15-1159-2019

Bates, N.R., Hansell, D.A., Moran, S.B., Codispoti, L.A., 2005. Seasonal and spatial distribution of particulate organic matter (POM) in the Chukchi and Beaufort Seas. Deep Sea Research Part II: Topical Studies in Oceanography 52, 3324–3343. https://doi.org/10.1016/j.dsr2.2005.10.003

Bates, N.R., Johnson, R.J., 2020. Acceleration of ocean warming, salinification, deoxygenation and acidification in the surface subtropical North Atlantic Ocean. Commun Earth Environ 33, 33. https://doi.org/10.1038/s43247-020-00030-5

Booth, B.C., Horner, R.A., 1997. Microalgae on the arctic ocean section, 1994: species abundance and biomass. Deep Sea Research Part II: Topical Studies in Oceanography 44, 1607–1622. https://doi.org/10.1016/s0967-0645(97)00057-x

Brzezinski, M.A., 1985. The Si:C:N ratio of marine diatoms: Interspecific variability and the effect of some environmental variables. Journal of Phycology 21, 347–357. https://doi.org/10.1111/j.0022-3646.1985.00347.x

Caldeira, K., Wickett, M., 2003. Anthropogenic carbon and ocean pH. Nature 425, 365.

Cavalieri, D.J., Parkinson, C.L., 2012. Arctic sea ice variability and trends, 1979–2010. Cryosphere 6, 881–889. https://doi.org/10.5194/tc-6-881-2012

Crawford, D.W., Cefarelli, A.O., Wrohan, I.A., Wyatt, S.N., Varela, D.E., 2018. Spatial patterns in abundance, taxonomic composition and carbon biomass of nano- and microphytoplankton in Subarctic and Arctic Seas. Progress in Oceanography 162, 132–159. https://doi.org/10.1016/j.pocean.2018.01.006

Crawford, D.W., Wyatt, S.N., Wrohan, I.A., Cefarelli, A.O., Giesbrecht, K.E., Kelly, B., Varela, D.E., 2015. Low particulate carbon to nitrogen ratios in marine surface waters of the Arctic. Glob. Biogeochem. Cycles 29, 2021–2033. https://doi.org/10.1002/2015gb005200

Daly, K.L., Wallace, D., Smith, W.O., Skoog, A., Lara, R., Gosselin, M., Falck, E., Yager, P.L., 1999. Non-Redfield carbon and nitrogen cycling in the Arctic: Effects of ecosystem structure and dynamics. Journal of Geophysical Research-Oceans 104, 3185–3199. https://doi.org/10.1029/1998jc900071

Davidson, A.T., Bramich, D., Marchant, H.J., McMinn, A., 1994. Effects of UV-B irradiation on growth and survival of Antarctic marine diatoms. Mar. Biol. 119, 507–515. https://doi.org/10.1007/bf00354312

Duarte, C.M., Lenton, T.M., Wadhams, P., Wassmann, P., 2012. Abrupt climate change in the Arctic. Nat. Clim. Chang. 2, 60–62. https://doi.org/10.1038/nclimate1386

Egge, J.K., Thingstad, T.F., Engel, A., Bellerby, R.G.J., Riebesell, U., 2007. Primary production during nutrient-induced blooms at elevated CO2 concentrations. Biogeosciences Discussions 4, 4385–4410.

Field, C.B., Behrenfeld, M.J., Randerson, J.T., Falkowski, P., 1998. Primary production of the biosphere: Integrating terrestrial and oceanic components. Science 281, 237–240. https://doi.org/10.1126/science.281.5374.237

Frey, K.E., Maslanik, J.A., Kinney, J.C., Maslowski, W., 2014. Recent variability in sea ice cover, age, and thickness in the Pacific Arctic Region, in: The Pacific Arctic Region. Springer, Dordrecht, pp. 31–63.

Frey, K.E., Moore, G.W.K., Cooper, L.W., Grebmeier, J.M., 2015. Divergent patterns of recent sea ice cover across the Bering, Chukchi, and Beaufort Seas of the Pacific Arctic Region. Progress in Oceanography 136, 32–49.

Frigstad, H., Andersen, T., Bellerby, R.G.J., Silyakova, A., Hessen, D.O., 2014. Variation in the seston C:N ratio of the Arctic Ocean and pan-Arctic shelves. Journal of Marine Systems 129, 214–223. https://doi.org/10.1016/j.jmarsys.2013.06.004

Gaffey, C.B., Frey, K.E., Cooper, L.W., Grebmeier, J.M., 2022. Phytoplankton bloom stages estimated from chlorophyll pigment proportions suggest delayed summer production in low sea ice years in the northern Bering Sea. Plos One 17, e0267586. https://doi.org/10.1371/journal.pone.0267586

Giesbrecht, K.E., Varela, D.E., 2021. Summertime Biogenic Silica Production and Silicon Limitation in the Pacific Arctic Region From 2006 to 2016. Global Biogeochem Cy 35. https://doi.org/10.1029/2020gb006629

Giesbrecht, K.E., Varela, D.E., Wiktor, J., Grebmeier, J.M., Kelly, B., Long, J.E., 2019. A decade of summertime measurements of phytoplankton biomass, productivity and assemblage composition in the Pacific Arctic Region from 2006 to 2016. Deep Sea Research Part II: Topical Studies in Oceanography 162, 93–113. https://doi.org/10.1016/j.dsr2.2018.06.010

Goldman, J.A.L., Bender, M.L., Morel, F.M.M., 2017. The effects of pH and pCO2 on photosynthesis and respiration in the diatom Thalassiosira weissflogii. Photosynthesis research 132, 83–93. https://doi.org/10.1007/s11120-016-0330-2

Goldman, J.C., 1993. Potential role of large oceanic diatoms in new primary production. Deep Sea Research Part I: Oceanographic Research Papers 40, 159-. https://doi.org/10.1016/0967-0637(93)90059-c

Goni, M.A., Corvi, E.R., Welch, K.A., Buktenica, M., Lebon, K., Alleau, Y., Juranek, L.W., 2019. Particulate organic matter distributions in surface waters of the Pacific Arctic shelf during the late summer and fall season. Marine Chemistry 211, 75–93. https://doi.org/10.1016/j.marchem.2019.03.010

Gradinger, R., 2009. Sea-ice algae: Major contributors to primary production and algal biomass in the Chukchi and Beaufort Seas during May/June 2002. Deep Sea Research Part II: Topical Studies in Oceanography 56, 1201–1212. https://doi.org/10.1016/j.dsr2.2008.10.016

Grebmeier, J., Frey, K., Cooper, L., Kędra, M., 2018. Trends in Benthic Macrofaunal Populations, Seasonal Sea Ice Persistence, and Bottom Water Temperatures in the Bering Strait Region. Oceanography 31. https://doi.org/10.5670/oceanog.2018.224

Grebmeier, J.M., 2012. Shifting patterns of life in the Pacific Arctic and Sub-Arctic seas. Annual Review of Marine Science 4, 63–78. https://doi.org/10.1146/annurev-marine-120710-100926

Grebmeier, J.M., Bluhm, B.A., Cooper, L.W., Danielson, S.L., Arrigo, K.R., Blanchard, A.L., Clarke, J.T., Day, R.H., Frey, K.E., Gradinger, R.R., Kędra, M., Konar, B., Kuletz, K.J., Lee, S.H., Lovvorn, J.R., Norcross, B.L., Okkonen, S.R., 2015. Ecosystem characteristics and processes facilitating persistent macrobenthic biomass hotspots and associated benthivory in the Pacific Arctic. Progress in Oceanography 136, 92–114. https://doi.org/10.1016/j.pocean.2015.05.006

Grebmeier, J.M., McRoy, C.P., 1989. Pelagic-benthic coupling on the shelf of the northern Bering and Chukchi Seas. III. Benthic food supply and carbon cycling. Marine Ecology Progress Series 53, 79–91.

Highsmith, R.C., Coyle, K.O., 1990. High productivity of northern Bering Sea benthic amphipods. Nature 344, 862–864. https://doi.org/10.1038/344862a0

Hoppe, C.J.M., Holtz, L.M., Trimborn, S., Rost, B., 2015. Ocean acidification decreases the light-use efficiency in an Antarctic diatom under dynamic but not constant light. The New Phytologist 207, 159–171. https://doi.org/10.1111/nph.13334

IPCC, 2022. Summary for Policymakers, in: H.-O.Pörtner, D.C.Roberts, E.S.Poloczanska, K.Mintenbeck, M.Tignor, Alegría, A., Craig, M., Langsdorf, S., Löschke, S., Möller, V., Okem, A. (Eds.), Climate Change 2022: Impacts, Adaptation and Vulnerability. Cambridge University Press, Cambridge, UK and New York, NY. https://doi.org/10.1017/9781009325844.001

Jeffries, M.O., Overland, J.E., Perovich, D.K., 2013. The Arctic shifts to a new normal. Phys. Today 66, 35–40. https://doi.org/10.1063/pt.3.2147

Krause, J.W., Brzezinski, M.A., Baines, S.B., Collier, J.L., Twining, B.S., Ohnemus, D.C., 2017. Picoplankton contribution to biogenic silica stocks and production rates in the Sargasso Sea. Global Biogeochemical Cycles 31, 762–774. https://doi.org/10.1002/2017gb005619

Krause, J.W., Nelson, D.M., Lomas, M.W., 2009. Biogeochemical responses to late-winter storms in the Sargasso Sea, II: Increased rates of biogenic silica production and export. Deep Sea Research Part I: Oceanographic Research Papers 56, 861–874. https://doi.org/10.1016/j.dsr.2009.01.002

Kroeker, K.J., Kordas, R.L., Crim, R., Hendriks, I.E., Ramajo, L., Singh, G.S., Duarte, C.M., Gattuso, J.P., 2013. Impacts of ocean acidification on marine organisms: quantifying sensitivities and interaction with warming. Global Change Biology 19, 1884–1896. https://doi.org/10.1111/gcb.12179

Lipschultz, F., 2001. A time-series assessment of the nitrogen cycle at BATS. Deep Sea Res. Part II: Top. Stud. Oceanogr. 48, 1897–1924. https://doi.org/10.1016/s0967-0645(00)00168-5

Lomas, M., Eisner, L., Gann, J., Baer, S., Mordy, C., Stabeno, P., 2020. Time-series of direct primary production and phytoplankton biomass in the southeastern Bering Sea: responses to cold and warm stanzas. Mar Ecol Prog Ser 642, 39–54. https://doi.org/10.3354/meps13317

Lomas, M.W., Bates, N.R., Johnson, R.J., Knap, A.H., Steinberg, D.K., Carlson, C.A., 2013. Two decades and counting: 24-years of sustained open ocean biogeochemical measurements in the Sargasso Sea. Deep Sea Research Part II: Topical Studies in Oceanography 93, 16–32. https://doi.org/10.1016/j.dsr2.2013.01.008

Lomas, M.W., Bates, N.R., Johnson, R.J., Steinberg, D.K., Tanioka, T., 2022. Adaptive carbon export response to warming in the Sargasso Sea. Nat. Commun. 13, 1211. https://doi.org/10.1038/s41467-022-28842-3

Longhurst, A., Sathyendranath, S., Platt, T., 1995. An estimate of global primary production in the ocean from satellite radiometer data. Journal of Plankton Research. https://doi.org/10.1093/plankt/17.6.1245

Martin-Jezequel, V., Hildebrand, M., Brzezinski, M.A., 2000. Silicon metabolism in diatoms: Implications for growth. Journal of Phycology 36, 821–840.

Martiny, A.C., Pham, C.T.A., Primeau, F.W., Vrugt, J.A., Moore, J.K., Levin, S.A., Lomas, M.W., 2013a. Strong latitudinal patterns in the elemental ratios of marine plankton and organic matter. Nat. Geosci. 6, 279–283. https://doi.org/10.1038/ngeo1757

Martiny, A.C., Vrugt, J.A., Primeau, F.W., Lomas, M.W., 2013b. Regional variation in the particulate organic carbon to nitrogen ratio in the surface ocean. Global Biogeochemical Cycles 27, 723–731. https://doi.org/10.1002/gbc.20061

Mathis, J.T., Grebmeier, J.M., Hansell, D.A., Hopcroft, R.R., Kirchman, D.L., Lee, S.H., Moran, S.B., Bates, N.R., VanLaningham, S., Cross, J.N., Cai, W.-J., 2014. Carbon Biogeochemistry of the Western Arctic: Primary Production, Carbon Export and the Controls on Ocean Acidification, in: The Pacific Arctic Region. Springer, Dordrecht, pp. 223–268. https://doi.org/10.1007/978-94-017-8863-2_9

Mongin, M., Nelson, D.M., Pondaven, P., Brzezinski, M.A., Tréguer, P., 2003. Simulation of upper-ocean biogeochemistry with a flexible-composition phytoplankton model: C, N and Si cycling in the western Sargasso Sea. Deep Sea Res. Part : Oceanogr. Res. Pap. 50, 1445–1480. https://doi.org/10.1016/j.dsr.2003.08.003

Moore, C.M., Mills, M.M., Arrigo, K.R., Berman-Frank, I., Bopp, L., Boyd, P.W., Galbraith, E.D., Geider, R.J., Guieu, C., Jaccard, S.L., Jickells, T.D., Roche, J.L., Lenton, T.M., Mahowald, N.M., Maranon, E., Marinov, I., Moore, J.K., Nakatsuka, T., Oschlies, A., Saito, M.A., Thingstad, T.F., Tsuda, A., Ulloa, O., 2013. Processes and patterns of oceanic nutrient limitation. Nature Geoscience 6, 701–710. https://doi.org/10.1038/ngeo1765

Nelson, D.M., Brzezinski, M.A., 1997. Diatom growth and productivity in an oligo-trophic midocean gyre: A 3-yr record from the Sargasso Sea near Bermuda. Limnology and Oceanography 42, 473–486. https://doi.org/10.4319/lo.1997.42.3.0473

Nelson, D.M., Tréguer, P., Brzezinski, M.A., Leynaert, A., Quéguiner, B., 1995. Production and dissolution of biogenic silica in the ocean: Revised global estimates, comparison with regional data and relationship to biogenic sedimentation. Global Biogeochemical Cycles 9, 359–372. https://doi.org/10.1029/95gb01070

Petrou, K., Baker, K.G., Nielsen, D.A., Hancock, A.M., Schulz, K.G., Davidson, A.T., 2019. Acidification diminishes diatom silica production in the Southern Ocean. Nature Climate Change 9, 781–786. https://doi.org/10.1038/s41558-019-0557-y

Raven, J.A., 1983. The transport and function of silicon in plants. Biol. Rev. 58, 179–207. https://doi.org/10.1111/j.1469-185x.1983.tb00385.x

Redfield, A.C., 1958. The Biological Control of Chemical Factors in the Environment. American Scientist 46, 205–221. https://doi.org/10.2307/27827150

Riebesell, U., Gattuso, J.P., Thingstad, T.F., Middelburg, J.J., 2013. Arctic ocean acidification: pelagic ecosystem and biogeochemical responses during a mesocosm study. oceanrep.geomar.de.

Riebesell, U., Zondervan, I., Rost, B., Tortell, P.D., Zeebe, R.E., Morel, F., 2000. Reduced calcification of marine plankton in response to increased atmospheric CO2. Nature 407, 364–367.

Ryther, J.H., 1969. Photosynthesis and fish production in the sea. The production of organic matter and its conversion to higher forms of life vary throughout the world ocean. Science (Washington).

Sherr, E.B., Sherr, B.F., Hartz, A.J., 2009. Microzooplankton grazing impact in the Western Arctic Ocean. Deep Sea Research Part II: Topical Studies in Oceanography 56, 1264–1273. https://doi.org/10.1016/j.dsr2.2008.10.036

Sherr, E.B., Sherr, B.F., Ross, C., 2013. Microzooplankton grazing impact in the Bering Sea during spring sea ice conditions. Deep Sea Research Part II: Topical Studies in Oceanography 94, 57–67. https://doi.org/10.1016/j.dsr2.2013.03.019

SIO, 2024. The Keeling Curve [WWW Document]. URL https://scripps.ucsd.edu/programs/keelingcurve/ (accessed 7.10.24).

Smetacek, V., 1999. Diatoms and the ocean carbon cycle. Protist 150, 25–32. https://doi.org/10.1016/s1434-4610(99)70006-4

Stabeno, P.J., Bond, N.A., Salo, S.A., 2007. On the recent warming of the southeastern Bering Sea shelf. Deep Sea Res. Part II: Top. Stud. Oceanogr. 54, 2599–2618. https://doi.org/10.1016/j.dsr2.2007.08.023

Steinberg, D.K., Carlson, C.A., Bates, N.R., Johnson, R.J., Michaels, A.F., Knap, A.H., 2001. Overview of the US JGOFS Bermuda Atlantic Time-series Study (BATS): a decade-scale look at ocean biology and biogeochemistry. Deep Sea Research Part II: Topical Studies in Oceanography 48, 1405–1447.

Stroeve, J.C., Markus, T., Boisvert, L., Miller, J., Barrett, A., 2014. Changes in Arctic melt season and implications for sea ice loss. Geophysical Research Letters 41, 1216–1225.

Sun, J., Hutchins, D.A., Feng, Y., Seubert, E.L., Caron, D.A., Fu, F.-X., 2011. Effects of changing pCO2 and phosphate availability on domoic acid production and physiology of the marine harmful bloom diatom Pseudo-nitzschia multiseries. Limnology and Oceanography 56, 829–840. https://doi.org/10.4319/lo.2011.56.3.0829

Tatters, A.O., Fu, F.-X., Hutchins, D.A., 2012. High CO2 and silicate limitation synergistically increase the toxicity of Pseudo-nitzschia fraudulenta. PLoS One 7, e32116. https://doi.org/10.1371/journal.pone.0032116

Tatters, A.O., Roleda, M.Y., Schnetzer, A., Fu, F., Hurd, C.L., Boyd, P.W., Caron, D.A., Lie, A.A.Y., Hoffmann, L.J., Hutchins, D.A., 2013. Short- and long-term conditioning of a temperate marine diatom community to acidification and warming. Philosophical Transactions: Biological Sciences 368, 1–14. https://doi.org/10.2307/42569220

Treguer, P., Nelson, D.M., Vanbennekon, A.J., Demaster, D.J., Leynaert, A., Queguiner, B., 1995. The Silica Balance in the World Ocean - a Re-estimate. Science 268, 375–379. https://doi.org/10.1126/science.268.5209.375

Tréguer, P., Pondaven, P., 2000. Silica control of carbon dioxide. Nature 406, 358–359. https://doi.org/10.1038/35019236

Tréguer, P.J., Sutton, J.N., Brzezinski, M., Charette, M.A., Devries, T., Dutkiewicz, S., Ehlert, C., Hawkings, J., Leynaert, A., Liu, S.M., Monferrer, N.L., López-Acosta, M., Maldonado, M., Rahman, S., Ran, L., Rouxel, O., 2021. Reviews and syntheses: The biogeochemical cycle of silicon in the modern ocean. Biogeosciences 18, 1269–1289. https://doi.org/10.5194/bg-18-1269-2021

Varela, D.E., Crawford, D.W., Wrohan, I.A., Wyatt, S.N., Carmack, E.C., 2013. Pelagic primary productivity and upper ocean nutrient dynamics across Subarctic and Arctic Seas. J. Geophys. Res.: Oceans 118, 7132–7152. https://doi.org/10.1002/2013jc009211

Villareal, T.A., 1988. Positive buoyancy in the oceanic diatom Rhizosolenia debyana H. Peragallo. Deep Sea Res. Part A Oceanogr. Res. Pap. 35, 1037–1045. https://doi.org/10.1016/0198-0149(88)90075-1

Volk, T., Hoffert, M.I., 1985. Ocean carbon pumps: Analysis of relative strengths and efficiencies in ocean-driven atmospheric CO2 changes, in: Sundquist, E.T., Broecker, W.S. (Eds.), The Carbon Cycle

and Atmospheric $CO_2$: Natural Variations Archean to Present, Geophysical Monograph Series. American Geophysical Union, Washington, D.C., pp. 99–110. https://doi.org/10.1029/gm032p0099

Winder, M., Sommer, U., 2012. Phytoplankton response to a changing climate. Hydrobiologia 698, 5–16. https://doi.org/10.1007/s10750-012-1149-2

Wood, K.R., Bond, N.A., Danielson, S.L., Overland, J.E., Salo, S.A., Stabeno, P.J., Whitefield, J., 2015. A decade of environmental change in the Pacific Arctic region. Prog. Oceanogr. 136, 12–31. https://doi.org/10.1016/j.pocean.2015.05.005

Woodgate, R.A., Weingartner, T.J., Lindsay, R., 2012. Observed increases in Bering Strait oceanic fluxes from the Pacific to the Arctic from 2001 to 2011 and their impacts on the Arctic Ocean water column. Geophysical Research Letters 39, L24603. https://doi.org/10.1029/2012gl054092

Wyatt, S.N., Crawford, D.W., Wrohan, I.A., Varela, D.E., 2013. Distribution and composition of suspended biogenic particles in surface waters across Subarctic and Arctic Seas. Journal of Geophysical Research-Oceans 118, 6867–6880. https://doi.org/10.1002/2013jc009214

Wyatt, S.N., McNabb, B.J., Varela, D.E., 2024. Morphological and physiological responses of the cosmopolitan marine diatom Thalassiosira rotula to acidification. Diatom Res. 39, 61–74. https://doi.org/10.1080/0269249x.2024.2369049

Zhang, S., Bai, X., Zhao, C., Tan, Q., Luo, G., Wang, J., Li, Q., Wu, L., Chen, F., Li, C., Deng, Y., Yang, Y., Xi, H., 2021. Global CO2 Consumption by Silicate Rock Chemical Weathering: Its Past and Future. Earth's Futur. 9. https://doi.org/10.1029/2020ef001938

## References for Chapter 2 and Appendix A


Amacher, J., Neuer, S., Lomas, M., 2013. DNA-based molecular fingerprinting of eukaryotic protists and cyanobacteria contributing to sinking particle flux at the Bermuda Atlantic time-series study. Deep Sea Res. Part II: Top. Stud. Oceanogr. 93, 71–83. https://doi.org/10.1016/j.dsr2.2013.01.001

Andersen, R.A., Bidigare, R.R., Keller∗, M.D., Latasa, M., 1996. A comparison of HPLC pigment signatures and electron microscopic observations for oligotrophic waters of the North Atlantic and Pacific Oceans. Deep Sea Res. Part II: Top. Stud. Oceanogr. 43, 517–537. https://doi.org/10.1016/0967-0645(95)00095-x

Baer, S.E., Lomas, M.W., Terpis, K.X., Mouginot, C., Martiny, A.C., 2017. Stoichiometry of Prochlorococcus, Synechococcus, and small eukaryotic populations in the western North Atlantic Ocean. Environ. Microbiol. 19, 1568–1583. https://doi.org/10.1111/1462-2920.13672

Barwell-Clarke, J., Whitney, F., 1996. Institute of Ocean Sciences nutrient methods and analysis. Canadian Technical Report of Hydrography and Ocean Sciences 182, 1–49.

Bates, N.R., Johnson, R.J., 2023. Forty years of ocean acidification observations (1983–2023) in the Sargasso Sea at the Bermuda Atlantic Time-series Study site. Front. Mar. Sci. 10, 1289931. https://doi.org/10.3389/fmars.2023.1289931

Bates, N.R., Johnson, R.J., 2020. Acceleration of ocean warming, salinification, deoxygenation and acidification in the surface subtropical North Atlantic Ocean. Commun Earth Environ 33, 33. https://doi.org/10.1038/s43247-020-00030-5

Brzezinski, M.A., 1985. The Si:C:N ratio of marine diatoms: Interspecific variability and the effect of some environmental variables. Journal of Phycology 21, 347–357. https://doi.org/10.1111/j.0022-3646.1985.00347.x

Brzezinski, M.A., Nelson, D.M., 1996. Chronic substrate limitation of silicic acid uptake rates in the western Sargasso Sea. Deep Sea Res. Part II: Top. Stud. Oceanogr. 43, 437–453. https://doi.org/10.1016/0967-0645(95)00099-2

Brzezinski, M.A., Nelson, D.M., 1995. The annual silica cycle in the Sargasso Sea near Bermuda. Deep Sea Research Part I: Oceanographic Research Papers 42, 1215–1237.

Brzezinski, M.A., Nelson, D.M., 1986. A solvent extraction method for the colorimetric determination of nanomolar concentrations of silicic acid in seawater. Marine Chemistry 19, 139–151. https://doi.org/10.1016/0304-4203(86)90045-9

Brzezinski, M.A., Phillips, D.R., 1997. Evaluation of 32Si as a tracer for measuring silica production rates in marine waters. Limnology and Oceanography 42, 856–865. https://doi.org/10.4319/lo.1997.42.5.0856

Casey, J.R., Aucan, J.P., Goldberg, S.R., Lomas, M.W., 2013. Changes in partitioning of carbon amongst photosynthetic pico- and nano-plankton groups in the Sargasso Sea in response to changes in the

North Atlantic Oscillation. Deep Sea Res. Part II: Top. Stud. Oceanogr. 93, 58–70. https://doi.org/10.1016/j.dsr2.2013.02.002

Chisholm, S.W., 1992. Primary Productivity and Biogeochemical Cycles in the Sea 213–237. https://doi.org/10.1007/978-1-4899-0762-2_12

Cotti-Rausch, B.E., Lomas, M.W., Lachenmyer, E.M., Baumann, E.G., Richardson, T.L., 2020. Size-fractionated biomass and primary productivity of Sargasso Sea phytoplankton. Deep Sea Res. Part : Oceanogr. Res. Pap. 156, 103141. https://doi.org/10.1016/j.dsr.2019.103141

Cruz, B.N., Brozak, S., Neuer, S., 2021. Microscopy and DNA-based characterization of sinking particles at the Bermuda Atlantic Time-series Study station point to zooplankton mediation of particle flux. Limnol. Oceanogr. 66, 3697–3713. https://doi.org/10.1002/lno.11910

Dugdale, R.C., Goering, J.J., 1967. Uptake of new and regenerated forms of nitrogen in primary productivity. Limnology and Oceanography 12, 196–206. https://doi.org/10.4319/lo.1967.12.2.0196

Dugdale, R.C., Wilkerson, F.P., 1986. The use of 15N to measure nitrogen uptake in eutrophic oceans; experimental considerations. Limnology and Oceanography 31, 673–689. https://doi.org/10.4319/lo.1986.31.4.0673

Durak, G.M., Taylor, A.R., Walker, C.E., Probert, I., Vargas, C. de, Audic, S., Schroeder, D., Brownlee, C., Wheeler, G.L., 2016. A role for diatom-like silicon transporters in calcifying coccolithophores. Nat. Commun. 7, 10543. https://doi.org/10.1038/ncomms10543

DuRand, M.D., Olson, R.J., Chisholm, S.W., 2001. Phytoplankton population dynamics at the Bermuda Atlantic Time-series station in the Sargasso Sea. Deep Sea Res. Part II: Top. Stud. Oceanogr. 48, 1983–2003. https://doi.org/10.1016/s0967-0645(00)00166-1

Eppley, R.W., Peterson, B.J., 1979. Particulate organic matter flux and planktonic new production in the deep ocean. Nature 282, 677–680. https://doi.org/10.1038/282677a0

Falkowski, P.G., Barber, R.T., Smetacek, V., 1998. Biogeochemical Controls and Feedbacks on Ocean Primary Production. Science 281, 200–206. https://doi.org/10.1126/science.281.5374.200

Fawcett, S.E., Lomas, M.W., Casey, J.R., Ward, B.B., Sigman, D.M., 2011. Assimilation of upwelled nitrate by small eukaryotes in the Sargasso Sea. Nat. Geosci. 4, 717–722. https://doi.org/10.1038/ngeo1265

Fawcett, S.E., Lomas, M.W., Ward, B.B., Sigman, D.M., 2014. The counterintuitive effect of summer-to-fall mixed layer deepening on eukaryotic new production in the Sargasso Sea. Glob. Biogeochem. Cycles 28, 86–102. https://doi.org/10.1002/2013gb004579

Giesbrecht, K.E., Varela, D.E., 2021. Summertime Biogenic Silica Production and Silicon Limitation in the Pacific Arctic Region From 2006 to 2016. Global Biogeochem Cy 35. https://doi.org/10.1029/2020gb006629

Glover, H.E., Prézelin, B.B., Campbell, L., Wyman, M., Garside, C., 1988. A nitrate-dependent Synechococcus bloom in surface Sargasso Sea water. Nature 331, 161–163. https://doi.org/10.1038/331161a0

Goldman, J.C., 1993. Potential role of large oceanic diatoms in new primary production. Deep Sea Research Part I: Oceanographic Research Papers 40, 159-. https://doi.org/10.1016/0967-0637(93)90059-c

Hama, T., Miyazaki, T., Ogawa, Y., Iwakuma, T., Takahashi, M., Otsuki, A., Ichimura, S., 1983. Measurement of photosynthetic production of a marine-phytoplankton population using a stable C-13 isotope. Marine Biology 73, 31–36. https://doi.org/10.1007/bf00396282.pdf

Knap, A.H., Michaels, A.F., Steinberg, D., Bahr, F., N, B., S, B., P, C., A, C., A, D., F, H., K, G., R, J., R, L., K, O., R, P., C, R., M, S., S, S., 1997. BATS methods manual. U.S. JGOFS Planning Office, Woods Hole.

Krause, J.W., Brzezinski, M.A., Baines, S.B., Collier, J.L., Twining, B.S., Ohnemus, D.C., 2017. Picoplankton contribution to biogenic silica stocks and production rates in the Sargasso Sea. Global Biogeochemical Cycles 31, 762–774. https://doi.org/10.1002/2017gb005619

Krause, J.W., Brzezinski, M.A., Jones, J.L., 2011. Application of low-level beta counting of 32Si for the measurement of silica production rates in aquatic environments. Marine Chemistry 127, 40–47. https://doi.org/10.1016/j.marchem.2011.07.001

Krause, J.W., Brzezinski, M.A., Landry, M.R., Baines, S.B., Nelson, D.M., Selph, K.E., Taylor, A.G., Twiningf, B.S., 2010a. The effects of biogenic silica detritus, zooplankton grazing, and diatom size structure on silicon cycling in the euphotic zone of the eastern equatorial Pacific. Limnol. Oceanogr. 55, 2608–2622. https://doi.org/10.4319/lo.2010.55.6.2608

Krause, J.W., Nelson, D.M., Lomas, M.W., 2010b. Production, dissolution, accumulation, and potential export of biogenic silica in a Sargasso Sea mode-water eddy. Limnol. Oceanogr. 55, 569–579. https://doi.org/10.4319/lo.2010.55.2.0569

Krause, J.W., Nelson, D.M., Lomas, M.W., 2009. Biogeochemical responses to late-winter storms in the Sargasso Sea, II: Increased rates of biogenic silica production and export. Deep Sea Research Part I: Oceanographic Research Papers 56, 861–874. https://doi.org/10.1016/j.dsr.2009.01.002

Leblanc, K., Quéguiner, B., Diaz, F., Cornet, V., Michel-Rodriguez, M., Madron, X.D. de, Bowler, C., Malviya, S., Thyssen, M., Grégori, G., Rembauville, M., Grosso, O., Poulain, J., Vargas, C. de, Pujo-Pay, M., Conan, P., 2018. Nanoplanktonic diatoms are globally overlooked but play a role in spring blooms and carbon export. Nat. Commun. 9, 953. https://doi.org/10.1038/s41467-018-03376-9

Letelier, R.M., Bidigare, R.R., Hebel, D.V., Ondrusek, M., Winn, C.D., Karl, D.M., 1993. Temporal variability of phytoplankton community structure based on pigment analysis. Limnol. Oceanogr. 38, 1420–1437. https://doi.org/10.4319/lo.1993.38.7.1420

Likhoshway, Ye.V., Masyukova, Yu.A., Sherbakova, T.A., Petrova, D.P., Grachev, M.A., 2006. Detection of the gene responsible for silicic acid transport in chrysophycean algae. Dokl. Biol. Sci. 408, 256–260. https://doi.org/10.1134/s001249660603015x

Lipschultz, F., 2001. A time-series assessment of the nitrogen cycle at BATS. Deep Sea Res. Part II: Top. Stud. Oceanogr. 48, 1897–1924. https://doi.org/10.1016/s0967-0645(00)00168-5

Lipschultz, F., Bates, N.R., Carlson, C.A., Hansell, D.A., 2002. New production in the Sargasso Sea: History and current status. Glob. Biogeochem. Cycles 16, 1-1-1–17. https://doi.org/10.1029/2000gb001319

Lomas, M.W., Bates, N.R., Johnson, R.J., Knap, A.H., Steinberg, D.K., Carlson, C.A., 2013. Two decades and counting: 24-years of sustained open ocean biogeochemical measurements in the Sargasso Sea. Deep Sea Research Part II: Topical Studies in Oceanography 93, 16–32. https://doi.org/10.1016/j.dsr2.2013.01.008

Lomas, M.W., Bates, N.R., Johnson, R.J., Steinberg, D.K., Tanioka, T., 2022. Adaptive carbon export response to warming in the Sargasso Sea. Nat. Commun. 13, 1211. https://doi.org/10.1038/s41467-022-28842-3

Lomas, M.W., Lipschultz, F., Nelson, D.M., Krause, J.W., Bates, N.R., 2009a. Biogeochemical responses to late-winter storms in the Sargasso Sea, I—Pulses of primary and new production. Deep Sea Res. Part : Oceanogr. Res. Pap. 56, 843–860. https://doi.org/10.1016/j.dsr.2008.09.002

Lomas, M.W., Roberts, N., Lipschultz, F., Krause, J.W., Nelson, D.M., Bates, N.R., 2009b. Biogeochemical responses to late-winter storms in the Sargasso Sea. IV. Rapid succession of major phytoplankton groups. Deep Sea Res. Part : Oceanogr. Res. Pap. 56, 892–908. https://doi.org/10.1016/j.dsr.2009.03.004

Longhurst, A., Sathyendranath, S., Platt, T., 1995. An estimate of global primary production in the ocean from satellite radiometer data. Journal of Plankton Research. https://doi.org/10.1093/plankt/17.6.1245

Lozier, M.S., Dave, A.C., Palter, J.B., Gerber, L.M., Barber, R.T., 2011. On the relationship between stratification and primary productivity in the North Atlantic. Geophys. Res. Lett. 38, n/a-n/a. https://doi.org/10.1029/2011gl049414

Malone, T.C., Pike, S.E., Conley, D.J., 1993. Transient variations in phytoplankton productivity at the JGOFS Bermuda time series station. Deep Sea Res. Part : Oceanogr. Res. Pap. 40, 903–924. https://doi.org/10.1016/0967-0637(93)90080-m

Margalef, R., 1978. Life-forms of phytoplankton as survival alternatives in an unstable environment. Oceanol. Acta 1, 493–509.

Marron, A.O., Ratcliffe, S., Wheeler, G.L., Goldstein, R.E., King, N., Not, F., Vargas, C. de, Richter, D.J., 2016. The Evolution of Silicon Transport in Eukaryotes. Mol Biol Evol 33, 3226–3248. https://doi.org/10.1093/molbev/msw209

Martin, A.P., Pondaven, P., 2006. New primary production and nitrification in the western subtropical North Atlantic: A modeling study. Glob. Biogeochem. Cycles 20. https://doi.org/10.1029/2005gb002608

Martin-Jezequel, V., Hildebrand, M., Brzezinski, M.A., 2000. Silicon metabolism in diatoms: Implications for growth. Journal of Phycology 36, 821–840.

McGillicuddy, D.J., 2014. Mechanisms of Physical-Biological-Biogeochemical Interaction at the Oceanic Mesoscale. Annu. Rev. Mar. Sci. 8, 1–35. https://doi.org/10.1146/annurev-marine-010814-015606

Menzel, D.W., Ryther, J.H., 1960. The annual cycle of primary production in the Sargasso Sea off Bermuda. Deep Sea Res. (1953) 6, 351–367. https://doi.org/10.1016/0146-6313(59)90095-4

Michaels, A.F., Knap, A.H., Dow, R.L., Gundersen, K., Johnson, R.J., Sorensen, J., Close, A., Knauer, G.A., Lohrenz, S.E., Asper, V.A., Tuel, M., Bidigare, R., 1994. Seasonal patterns of ocean biogeochemistry at the U.S. JGOFS Bermuda Atlantic time-series study site. Deep Sea Res. Part : Oceanogr. Res. Pap. 41, 1013–1038. https://doi.org/10.1016/0967-0637(94)90016-7

Moriceau, B., Gehlen, M., Tréguer, P., Baines, S., Livage, J., André, L., 2019. Editorial: Biogeochemistry and Genomics of Silicification and Silicifiers. Front. Mar. Sci. 6, 57. https://doi.org/10.3389/fmars.2019.00057

Nelson, D.M., Brzezinski, M.A., 1997. Diatom growth and productivity in an oligo-trophic midocean gyre: A 3-yr record from the Sargasso Sea near Bermuda. Limnology and Oceanography 42, 473–486. https://doi.org/10.4319/lo.1997.42.3.0473

Nelson, D.M., Tréguer, P., Brzezinski, M.A., Leynaert, A., Quéguiner, B., 1995. Production and dissolution of biogenic silica in the ocean: Revised global estimates, comparison with regional data and relationship to biogenic sedimentation. Global Biogeochemical Cycles 9, 359–372. https://doi.org/10.1029/95gb01070

Ohnemus, D.C., Rauschenberg, S., Krause, J.W., Brzezinski, M.A., Collier, J.L., Geraci-Yee, S., Baines, S.B., Twining, B.S., 2016. Silicon content of individual cells of Synechococcus from the North Atlantic Ocean. Mar. Chem. 187, 16–24. https://doi.org/10.1016/j.marchem.2016.10.003

Oostende, N.V., Fawcett, S.E., Marconi, D., Lueders-Dumont, J., Sabadel, A.J.M., Woodward, E.M.S., Jönsson, B.F., Sigman, D.M., Ward, B.B., 2017. Variation of summer phytoplankton community composition and its relationship to nitrate and regenerated nitrogen assimilation across the North Atlantic Ocean. Deep Sea Res. Part : Oceanogr. Res. Pap. 121, 79–94. https://doi.org/10.1016/j.dsr.2016.12.012

Parsons, T.R., Maita, T., Lalli, C.M., 1984. A Manual of Chemical & Biological Methods for Seawater Analysis, 1st ed, Pergamon Press. Pergamon Press, Oxford.

Ryther, J.H., 1969. Photosynthesis and fish production in the sea. The production of organic matter and its conversion to higher forms of life vary throughout the world ocean. Science (Washington).

Sarmiento, J.L., Slater, R., Barber, R., Bopp, L., Doney, S.C., Hirst, A.C., Kleypas, J., Matear, R., Mikolajewicz, U., Monfray, P., Soldatov, V., Spall, S.A., Stouffer, R., 2004. Response of ocean ecosystems to climate warming. Glob. Biogeochem. Cycles 18. https://doi.org/10.1029/2003gb002134

Slawyk, G., Collos, Y., Auclair, J.C., 1977. The use of the 13C and 15N isotopes for the simultaneous measurement of carbon and nitrogen turnover rates in marine phytoplankton. Limnology and Oceanography 22, 925–932. https://doi.org/10.4319/lo.1977.22.5.0925

Steinberg, D.K., Carlson, C.A., Bates, N.R., Johnson, R.J., Michaels, A.F., Knap, A.H., 2001. Overview of the US JGOFS Bermuda Atlantic Time-series Study (BATS): a decade-scale look at ocean biology and biogeochemistry. Deep Sea Research Part II: Topical Studies in Oceanography 48, 1405–1447.

Sverdrup, H.U., 1953. On conditions for the vernal blooming of phytoplankton. ICES J. Mar. Sci. 18, 287–295. https://doi.org/10.1093/icesjms/18.3.287

Tang, E.P.Y., 1995. The allometry of algal growth rates. J. Plankton Res. 17, 1325–1335. https://doi.org/10.1093/plankt/17.6.1325

Tréguer, P.J., De La Rocha, C.L., 2013. The World Ocean Silica Cycle. Annu Rev Mar Sci 5, 477–501. https://doi.org/10.1146/annurev-marine-121211-172346

Tréguer, P.J., Sutton, J.N., Brzezinski, M., Charette, M.A., Devries, T., Dutkiewicz, S., Ehlert, C., Hawkings, J., Leynaert, A., Liu, S.M., Monferrer, N.L., López-Acosta, M., Maldonado, M., Rahman, S., Ran, L., Rouxel, O., 2021. Reviews and syntheses: The biogeochemical cycle of silicon in the modern ocean. Biogeosciences 18, 1269–1289. https://doi.org/10.5194/bg-18-1269-2021

Treusch, A.H., Demir-Hilton, E., Vergin, K.L., Worden, A.Z., Carlson, C.A., Donatz, M.G., Burton, R.M., Giovannoni, S.J., 2011. Phytoplankton distribution patterns in the northwestern Sargasso Sea revealed by small subunit rRNA genes from plastids. ISME J. 6, 481–492. https://doi.org/10.1038/ismej.2011.117

Twomey, L.J., Waite, A.M., Pez, V., Pattiaratchi, C.B., 2007. Variability in nitrogen uptake and fixation in the oligotrophic waters off the south west coast of Australia. Deep Sea Res. Part II: Top. Stud. Oceanogr. 54, 925–942. https://doi.org/10.1016/j.dsr2.2006.10.001

Wright, S., Jeffrey, S., Mantoura, R., Llewellyn, C., Bjornland, T., Repeta, D., Welschmeyer, N., 1991. Improved HPLC method for the analysis of chlorophylls and carotenoids from marine phytoplankton. Mar. Ecol. Prog. Ser. 77, 183–196. https://doi.org/10.3354/meps077183

Yool, A., Martin, A.P., Fernández, C., Clark, D.R., 2007. The significance of nitrification for oceanic new production. Nature 447, 999–1002. https://doi.org/10.1038/nature05885

## References for Appendix B


Barwell-Clarke, J., Whitney, F., 1996. Institute of Ocean Sciences nutrient methods and analysis. Canadian Technical Report of Hydrography and Ocean Sciences 182, 1–49.

Bates, N.R., Johnson, R.J., 2020. Acceleration of ocean warming, salinification, deoxygenation and acidification in the surface subtropical North Atlantic Ocean. Commun Earth Environ 33, 33. https://doi.org/10.1038/s43247-020-00030-5

Bates, N.R., Knap, A.H., Michaels, A.F., 1998. Contribution of hurricanes to local and global estimates of air–sea exchange of CO2. Nature 395, 58–61. https://doi.org/10.1038/25703

Brzezinski, M.A., Nelson, D.M., 1995. The annual silica cycle in the Sargasso Sea near Bermuda. Deep Sea Research Part I: Oceanographic Research Papers 42, 1215–1237.

Brzezinski, M.A., Nelson, D.M., 1986. A solvent extraction method for the colorimetric determination of nanomolar concentrations of silicic acid in seawater. Marine Chemistry 19, 139–151. https://doi.org/10.1016/0304-4203(86)90045-9

Brzezinski, M.A., Phillips, D.R., 1997. Evaluation of 32Si as a tracer for measuring silica production rates in marine waters. Limnology and Oceanography 42, 856–865. https://doi.org/10.4319/lo.1997.42.5.0856

Costin, J.M., 1968. Direct current measurements in the Antilles Current. J. Geophys. Res. 73, 3341–3344. https://doi.org/10.1029/jb073i010p03341

Dugdale, R.C., Goering, J.J., 1967. Uptake of new and regenerated forms of nitrogen in primary productivity. Limnology and Oceanography 12, 196–206. https://doi.org/10.4319/lo.1967.12.2.0196

Dugdale, R.C., Wilkerson, F.P., 1986. The use of 15N to measure nitrogen uptake in eutrophic oceans; experimental considerations. Limnology and Oceanography 31, 673–689. https://doi.org/10.4319/lo.1986.31.4.0673

Hama, T., Miyazaki, T., Ogawa, Y., Iwakuma, T., Takahashi, M., Otsuki, A., Ichimura, S., 1983. Measurement of photosynthetic production of a marine-phytoplankton population using a stable C-13 isotope. Marine Biology 73, 31–36. https://doi.org/10.1007/bf00396282.pdf

Knap, A.H., Michaels, A.F., Steinberg, D., Bahr, F., N, B., S, B., P, C., A, C., A, D., F, H., K, G., R, J., R, L., K, O., R, P., C, R., M, S., S, S., 1997. BATS methods manual. U.S. JGOFS Planning Office, Woods Hole.

Krause, J.W., Brzezinski, M.A., Jones, J.L., 2011. Application of low-level beta counting of 32Si for the measurement of silica production rates in aquatic environments. Marine Chemistry 127, 40–47. https://doi.org/10.1016/j.marchem.2011.07.001

Krause, J.W., Nelson, D.M., Lomas, M.W., 2009. Biogeochemical responses to late-winter storms in the Sargasso Sea, II: Increased rates of biogenic silica production and export. Deep Sea Research Part I: Oceanographic Research Papers 56, 861–874. https://doi.org/10.1016/j.dsr.2009.01.002

Lomas, M.W., Bates, N.R., Johnson, R.J., Knap, A.H., Steinberg, D.K., Carlson, C.A., 2013. Two decades and counting: 24-years of sustained open ocean biogeochemical measurements in the Sargasso Sea. Deep Sea Research Part II: Topical Studies in Oceanography 93, 16–32. https://doi.org/10.1016/j.dsr2.2013.01.008

Lomas, M.W., Lipschultz, F., Nelson, D.M., Krause, J.W., Bates, N.R., 2009. Biogeochemical responses to late-winter storms in the Sargasso Sea, I—Pulses of primary and new production. Deep Sea Res. Part : Oceanogr. Res. Pap. 56, 843–860. https://doi.org/10.1016/j.dsr.2008.09.002

McClain, C.R., Firestone, J., 1993. An investigation of Ekman upwelling in the North Atlantic. J. Geophys. Res.: Oceans 98, 12327–12339. https://doi.org/10.1029/93jc00868

McGillicuddy, D.J., Robinson, A.R., 1997. Eddy-induced nutrient supply and new production in the Sargasso Sea. Deep Sea Res. Part : Oceanogr. Res. Pap. 44, 1427–1450. https://doi.org/10.1016/s0967-0637(97)00024-1

Meinen, C.S., Johns, W.E., Moat, B.I., Smith, R.H., Johns, E.M., Rayner, D., Frajka-Williams, E., Garcia, R.F., Garzoli, S.L., 2019. Structure and Variability of the Antilles Current at 26.5°N. J. Geophys. Res.: Oceans 124, 3700–3723. https://doi.org/10.1029/2018jc014836

Nelson, N.B., 1998. Spatial and Temporal Extent of Sea Surface Temperature Modifications by Hurricanes in the Sargasso Sea during the 1995 Season. Mon. Weather Rev. 126, 1364–1368. https://doi.org/10.1175/1520-0493(1998)126<1364:sateos>2.0.co;2

Parsons, T.R., Maita, T., Lalli, C.M., 1984. A Manual of Chemical & Biological Methods for Seawater Analysis, 1st ed, Pergamon Press. Pergamon Press, Oxford.

Siegel, D.A., Deuser, W.G., 1997. Trajectories of sinking particles in the Sargasso Sea: modeling of statistical funnels above deep-ocean sediment traps. Deep Sea Res. Part : Oceanogr. Res. Pap. 44, 1519–1541. https://doi.org/10.1016/s0967-0637(97)00028-9

Siegel, D.A., McGillicuddy, D.J., Fields, E.A., 1999. Mesoscale eddies, satellite altimetry, and new production in the Sargasso Sea. J. Geophys. Res.: Oceans 104, 13359–13379. https://doi.org/10.1029/1999jc900051

Slawyk, G., Collos, Y., Auclair, J.C., 1977. The use of the 13C and 15N isotopes for the simultaneous measurement of carbon and nitrogen turnover rates in marine phytoplankton. Limnology and Oceanography 22, 925–932. https://doi.org/10.4319/lo.1977.22.5.0925

Steinberg, D.K., Carlson, C.A., Bates, N.R., Johnson, R.J., Michaels, A.F., Knap, A.H., 2001. Overview of the US JGOFS Bermuda Atlantic Time-series Study (BATS): a decade-scale look at ocean biology and biogeochemistry. Deep Sea Research Part II: Topical Studies in Oceanography 48, 1405–1447.

## References for Chapter 3


Ardyna, M., Arrigo, K.R., 2020. Phytoplankton dynamics in a changing Arctic Ocean. Nat Clim Change 10, 892–903. https://doi.org/10.1038/s41558-020-0905-y

Armstrong, R.A., Lee, C., Hedges, J.I., Honjo, S., Wakeham, S.G., 2001. A new, mechanistic model for organic carbon fluxes in the ocean based on the quantitative association of POC with ballast minerals. Deep Sea Res. Part II: Top. Stud. Oceanogr. 49, 219–236. https://doi.org/10.1016/s0967-0645(01)00101-1

Arrigo, K.R., Dijken, G. van, Pabi, S., 2008. Impact of a shrinking Arctic ice cover on marine primary production. Geophys. Res. Lett. 35. https://doi.org/10.1029/2008gl035028

Baines, S.B., Twining, B.S., Brzezinski, M.A., Nelson, D.M., Fisher, N.S., 2010. Causes and biogeochemical implications of regional differences in silicification of marine diatoms. Global Biogeochem Cy 24, GB4031. https://doi.org/10.1029/2010gb003856

Barkhordarian, A., Nielsen, D.M., Olonscheck, D., Baehr, J., 2024. Arctic marine heatwaves forced by greenhouse gases and triggered by abrupt sea-ice melt. Commun. Earth Environ. 5, 57. https://doi.org/10.1038/s43247-024-01215-y

Barwell-Clarke, J., Whitney, F., 1996. Institute of Ocean Sciences nutrient methods and analysis. Canadian Technical Report of Hydrography and Ocean Sciences 182, 1–49.

Beaird, N.L., Shroyer, E.L., Juranek, L.W., Hales, B., Goñi, M.A., 2020. Nutrient-Rich Gravity Current Formed by Upwelling in Barrow Canyon: High-Resolution Observations. J. Geophys. Res.: Oceans 125. https://doi.org/10.1029/2020jc016160

Bond, N.A., Cronin, M.F., Freeland, H., Mantua, N., 2015. Causes and impacts of the 2014 warm anomaly in the NE Pacific. Geophys. Res. Lett. 42, 3414–3420. https://doi.org/10.1002/2015gl063306

Booth, B.C., Horner, R.A., 1997. Microalgae on the arctic ocean section, 1994: species abundance and biomass. Deep Sea Research Part II: Topical Studies in Oceanography 44, 1607–1622. https://doi.org/10.1016/s0967-0645(97)00057-x

Brown, Z.W., Dijken, G.L. van, Arrigo, K.R., 2011. A reassessment of primary production and environmental change in the Bering Sea. J. Geophys. Res.: Oceans 116. https://doi.org/10.1029/2010jc006766

Brzezinski, M.A., 1985. The Si:C:N ratio of marine diatoms: Interspecific variability and the effect of some environmental variables. Journal of Phycology 21, 347–357. https://doi.org/10.1111/j.0022-3646.1985.00347.x

Brzezinski, M.A., Nelson, D.M., 1995. The annual silica cycle in the Sargasso Sea near Bermuda. Deep Sea Research Part I: Oceanographic Research Papers 42, 1215–1237.

Brzezinski, M.A., Nelson, D.M., 1986. A solvent extraction method for the colorimetric determination of nanomolar concentrations of silicic acid in seawater. Marine Chemistry 19, 139–151. https://doi.org/10.1016/0304-4203(86)90045-9

Brzezinski, M.A., Phillips, D.R., 1997. Evaluation of 32Si as a tracer for measuring silica production rates in marine waters. Limnology and Oceanography 42, 856–865. https://doi.org/10.4319/lo.1997.42.5.0856

Campbell, R.G., Sherr, E.B., J, A.C., S, P., Sherr, B.F., V, H., A, S.D., 2009. Mesozooplankton prey preference and grazing impact in the western Arctic Ocean. Deep Sea Research Part II: Topical Studies in Oceanography 56, 1274–1289. https://doi.org/10.1016/j.dsr2.2008.10.027

Carmack, E., Wassmann, P., 2006. Food webs and physical-biological coupling on pan-Arctic shelves: Unifying concepts and comprehensive perspectives. Progress in Oceanography 71, 446–477. https://doi.org/10.1016/j.pocean.2006.10.004

Carvalho, K.S., Smith, T.E., Wang, S., 2021. Bering Sea marine heatwaves: Patterns, trends and connections with the Arctic. J. Hydrol. 600, 126462. https://doi.org/10.1016/j.jhydrol.2021.126462

Carvalho, K.S., Wang, S., 2020. Sea surface temperature variability in the Arctic Ocean and its marginal seas in a changing climate: Patterns and mechanisms. Glob. Planet. Chang. 193, 103265. https://doi.org/10.1016/j.gloplacha.2020.103265

Cavalieri, D.J., Parkinson, C.L., 2012. Arctic sea ice variability and trends, 1979–2010. Cryosphere 6, 881–889. https://doi.org/10.5194/tc-6-881-2012

Coello-Camba, A., Agustí, S., 2017. Thermal Thresholds of Phytoplankton Growth in Polar Waters and Their Consequences for a Warming Polar Ocean. Front. Mar. Sci. 4, 168. https://doi.org/10.3389/fmars.2017.00168

Coello-Camba, A., Agustí, S., Vaqué, D., Holding, J., Arrieta, J.M., Wassmann, P., Duarte, C.M., 2015. Experimental Assessment of Temperature Thresholds for Arctic Phytoplankton Communities. Estuaries Coasts 38, 873–885. https://doi.org/10.1007/s12237-014-9849-7

Cooper, L.W., Grebmeier, J.M., 2022. A Chlorophyll Biomass Time-Series for the Distributed Biological Observatory in the Context of Seasonal Sea Ice Declines in the Pacific Arctic Region. Geosciences 12, 307. https://doi.org/10.3390/geosciences12080307

Crawford, D.W., Cefarelli, A.O., Wrohan, I.A., Wyatt, S.N., Varela, D.E., 2018. Spatial patterns in abundance, taxonomic composition and carbon biomass of nano- and microphytoplankton in Subarctic and Arctic Seas. Progress in Oceanography 162, 132–159. https://doi.org/10.1016/j.pocean.2018.01.006

Crawford, D.W., Wyatt, S.N., Wrohan, I.A., Cefarelli, A.O., Giesbrecht, K.E., Kelly, B., Varela, D.E., 2015. Low particulate carbon to nitrogen ratios in marine surface waters of the Arctic. Glob. Biogeochem. Cycles 29, 2021–2033. https://doi.org/10.1002/2015gb005200

Dickson, A.G., 1990. Standard potential of the reaction: AgCl(s) + 12H2(g) = Ag(s) + HCl(aq), and the standard acidity constant of the ion HSO4− in synthetic sea water from 273.15 to 318.15 K. J Chem Thermodyn 22, 113–127. https://doi.org/10.1016/0021-9614(90)90074-z

Dickson, A.G., Sabine, C.L., Christian, J.R., 2007. Determination of the pH of seawater using a glass/reference electrode cell, in: Dickson, A.G., Sabine, C.L., Christian, J.R. (Eds.), Guide to Best Practices for Ocean CO2 Measurements. PICES, Sidney, BC, p. SOP6a.

Duarte, C.M., Lenton, T.M., Wadhams, P., Wassmann, P., 2012. Abrupt climate change in the Arctic. Nat. Clim. Chang. 2, 60–62. https://doi.org/10.1038/nclimate1386

Duffy-Anderson, J.T., Stabeno, P., Andrews, A.G., Cieciel, K., Deary, A., Farley, E., Fugate, C., Harpold, C., Heintz, R., Kimmel, D., Kuletz, K., Lamb, J., Paquin, M., Porter, S., Rogers, L., Spear, A., Yasumiishi, E., 2019. Responses of the Northern Bering Sea and Southeastern Bering Sea Pelagic Ecosystems Following Record-Breaking Low Winter Sea Ice. Geophys. Res. Lett. 46, 9833–9842. https://doi.org/10.1029/2019gl083396

Dugdale, R.C., Goering, J.J., 1967. Uptake of new and regenerated forms of nitrogen in primary productivity. Limnology and Oceanography 12, 196–206. https://doi.org/10.4319/lo.1967.12.2.0196

Dugdale, R.C., Wilkerson, F.P., 1986. The use of 15N to measure nitrogen uptake in eutrophic oceans; experimental considerations. Limnology and Oceanography 31, 673–689. https://doi.org/10.4319/lo.1986.31.4.0673

Frey, K.E., Maslanik, J.A., Kinney, J.C., Maslowski, W., 2014. Recent variability in sea ice cover, age, and thickness in the Pacific Arctic Region, in: The Pacific Arctic Region. Springer, Dordrecht, pp. 31–63.

Frey, K.E., Moore, G.W.K., Cooper, L.W., Grebmeier, J.M., 2015. Divergent patterns of recent sea ice cover across the Bering, Chukchi, and Beaufort Seas of the Pacific Arctic Region. Progress in Oceanography 136, 32–49.

Fujiwara, A., Hirawake, T., Suzuki, K., Eisner, L., Imai, I., Nishino, S., Kikuchi, T., Saitoh, S.-I., 2015. Influence of timing of sea ice retreat on phytoplankton size during marginal ice zone bloom period on the Chukchi and Bering shelves. Biogeosciences 13, 115–131. https://doi.org/10.5194/bg-13-115-2016

Geider, R., Roche, J.L., 2002. Redfield revisited: variability of C:N:P in marine microalgae and its biochemical basis. Eur. J. Phycol. 37, 1–17. https://doi.org/10.1017/s0967026201003456

Giesbrecht, K.E., Varela, D.E., 2021. Summertime Biogenic Silica Production and Silicon Limitation in the Pacific Arctic Region From 2006 to 2016. Global Biogeochem Cy 35. https://doi.org/10.1029/2020gb006629

Giesbrecht, K.E., Varela, D.E., Wiktor, J., Grebmeier, J.M., Kelly, B., Long, J.E., 2019. A decade of summertime measurements of phytoplankton biomass, productivity and assemblage composition in the Pacific Arctic Region from 2006 to 2016. Deep Sea Research Part II: Topical Studies in Oceanography 162, 93–113. https://doi.org/10.1016/j.dsr2.2018.06.010

Gradinger, R., 2009. Sea-ice algae: Major contributors to primary production and algal biomass in the Chukchi and Beaufort Seas during May/June 2002. Deep Sea Research Part II: Topical Studies in Oceanography 56, 1201–1212. https://doi.org/10.1016/j.dsr2.2008.10.016

Grebmeier, J., Frey, K., Cooper, L., Kędra, M., 2018. Trends in Benthic Macrofaunal Populations, Seasonal Sea Ice Persistence, and Bottom Water Temperatures in the Bering Strait Region. Oceanography 31. https://doi.org/10.5670/oceanog.2018.224

Grebmeier, J.M., 2012. Shifting patterns of life in the Pacific Arctic and Sub-Arctic seas. Annual Review of Marine Science 4, 63–78. https://doi.org/10.1146/annurev-marine-120710-100926

Grebmeier, J.M., Bluhm, B.A., Cooper, L.W., Danielson, S.L., Arrigo, K.R., Blanchard, A.L., Clarke, J.T., Day, R.H., Frey, K.E., Gradinger, R.R., Kędra, M., Konar, B., Kuletz, K.J., Lee, S.H., Lovvorn, J.R., Norcross, B.L., Okkonen, S.R., 2015. Ecosystem characteristics and processes facilitating persistent macrobenthic biomass hotspots and associated benthivory in the Pacific Arctic. Progress in Oceanography 136, 92–114. https://doi.org/10.1016/j.pocean.2015.05.006

Grebmeier, J.M., Cooper, L.W., Feder, H.M., Sirenko, B.I., 2006. Ecosystem dynamics of the Pacific-influenced Northern Bering and Chukchi Seas in the Amerasian Arctic. Progress in Oceanography 71, 331–361. https://doi.org/10.1016/j.pocean.2006.10.001

Grebmeier, J.M., McRoy, C.P., 1989. Pelagic-benthic coupling on the shelf of the northern Bering and Chukchi Seas. III. Benthic food supply and carbon cycling. Marine Ecology Progress Series 53, 79–91.

Hama, T., Miyazaki, T., Ogawa, Y., Iwakuma, T., Takahashi, M., Otsuki, A., Ichimura, S., 1983. Measurement of photosynthetic production of a marine-phytoplankton population using a stable C-13 isotope. Marine Biology 73, 31–36. https://doi.org/10.1007/bf00396282.pdf

Highsmith, R.C., Coyle, K.O., 1990. High productivity of northern Bering Sea benthic amphipods. Nature 344, 862–864. https://doi.org/10.1038/344862a0

Hill, V., Cota, G., 2005. Spatial patterns of primary production on the shelf, slope and basin of the Western Arctic in 2002. Deep Sea Res. Part II: Top. Stud. Oceanogr. 52, 3344–3354. https://doi.org/10.1016/j.dsr2.2005.10.001

Holding, J.M., Duarte, C.M., Arrieta, J.M., Vaquer-Sunyer, R., Coello-Camba, A., Wassmann, P., Agustí, S., 2013. Experimentally determined temperature thresholds for Arctic plankton community metabolism. Biogeosciences 10, 357–370. https://doi.org/10.5194/bg-10-357-2013

Hunt, G.L., Coyle, K.O., Eisner, L.B., Farley, E.V., Heintz, R.A., Mueter, F., Napp, J.M., Overland, J.E., Ressler, P.H., Salo, S., Stabeno, P.J., 2011. Climate impacts on eastern Bering Sea foodwebs: a synthesis of new data and an assessment of the Oscillating Control Hypothesis. ICES J. Mar. Sci. 68, 1230–1243. https://doi.org/10.1093/icesjms/fsr036

Jeffries, M.O., Overland, J.E., Perovich, D.K., 2013. The Arctic shifts to a new normal. Phys. Today 66, 35–40. https://doi.org/10.1063/pt.3.2147

Krause, J.W., Brzezinski, M.A., Jones, J.L., 2011. Application of low-level beta counting of 32Si for the measurement of silica production rates in aquatic environments. Marine Chemistry 127, 40–47. https://doi.org/10.1016/j.marchem.2011.07.001

Lalande, C., Grebmeier, J.M., McDonnell, A.M.P., Hopcroft, R.R., O'Daly, S., Danielson, S.L., 2021. Impact of a warm anomaly in the Pacific Arctic region derived from time-series export fluxes. PLoS ONE 16, e0255837. https://doi.org/10.1371/journal.pone.0255837

Lomas, M., Eisner, L., Gann, J., Baer, S., Mordy, C., Stabeno, P., 2020. Time-series of direct primary production and phytoplankton biomass in the southeastern Bering Sea: responses to cold and warm stanzas. Mar Ecol Prog Ser 642, 39–54. https://doi.org/10.3354/meps13317

Lomas, M.W., Baer, S.E., Acton, S., Krause, J.W., 2019. Pumped up by the cold: elemental quotas and stoichiometry of cold-water diatoms. Frontiers in Marine Science 6, 286. https://doi.org/10.3389/fmars.2019.00286

Lueker, T.J., Dickson, A.G., Keeling, C.D., 2000. Ocean pCO2 calculated from dissolved inorganic carbon, alkalinity, and equations for K1 and K2: validation based on laboratory measurements of CO2 in gas and seawater at equilibrium. Mar Chem 70, 105–119. https://doi.org/10.1016/s0304-4203(00)00022-0

Martin-Jezequel, V., Hildebrand, M., Brzezinski, M.A., 2000. Silicon metabolism in diatoms: Implications for growth. Journal of Phycology 36, 821–840.

Martiny, A.C., Pham, C.T.A., Primeau, F.W., Vrugt, J.A., Moore, J.K., Levin, S.A., Lomas, M.W., 2013. Strong latitudinal patterns in the elemental ratios of marine plankton and organic matter. Nat. Geosci. 6, 279–283. https://doi.org/10.1038/ngeo1757

Mathis, J.T., Grebmeier, J.M., Hansell, D.A., Hopcroft, R.R., Kirchman, D.L., Lee, S.H., Moran, S.B., Bates, N.R., VanLaningham, S., Cross, J.N., Cai, W.-J., 2014. Carbon Biogeochemistry of the Western Arctic: Primary Production, Carbon Export and the Controls on Ocean Acidification, in: The Pacific Arctic Region. Springer, Dordrecht, pp. 223–268. https://doi.org/10.1007/978-94-017-8863-2_9

Mehrbach, C., Culberson, C.H., Hawley, J.E., Pytkowicx, R.M., 1973. Measurement of the apparent dissociation constants of carbonic acid in seawater at atmospheric pressure. Limnol Oceanogr 18, 897–907. https://doi.org/10.4319/lo.1973.18.6.0897

Moreno, A.R., Martiny, A.C., 2018. Ecological Stoichiometry of Ocean Plankton. Annual review of marine science 10, 43–69. https://doi.org/10.1146/annurev-marine-121916-063126

Neeley, A.R., Harris, L.A., Frey, K.E., 2018. Unraveling Phytoplankton Community Dynamics in the Northern Chukchi Sea Under Sea-Ice-Covered and Sea-Ice-Free Conditions. Geophys. Res. Lett. 45, 7663–7671. https://doi.org/10.1029/2018gl077684

Nelson, D.M., Tréguer, P., Brzezinski, M.A., Leynaert, A., Quéguiner, B., 1995. Production and dissolution of biogenic silica in the ocean: Revised global estimates, comparison with regional data and relationship to biogenic sedimentation. Global Biogeochemical Cycles 9, 359–372. https://doi.org/10.1029/95gb01070

Neukermans, G., Oziel, L., Babin, M., 2018. Increased intrusion of warming Atlantic water leads to rapid expansion of temperate phytoplankton in the Arctic. Glob. Chang. Biol. 24, 2545–2553. https://doi.org/10.1111/gcb.14075

Nielsen, J.M., Sigler, M.F., Eisner, L.B., Watson, J.T., Rogers, L.A., Bell, S.W., Pelland, N., Mordy, C.W., Cheng, W., Kivva, K., Osborne, S., Stabeno, P., 2024. Spring phytoplankton bloom phenology during recent climate warming on the Bering Sea shelf. Prog. Oceanogr. 220, 103176. https://doi.org/10.1016/j.pocean.2023.103176

Nöthig, E.-M., Bracher, A., Engel, A., Metfies, K., Niehoff, B., Peeken, I., Bauerfeind, E., Cherkasheva, A., Gäbler-Schwarz, S., Hardge, K., Kilias, E., Kraft, A., Kidane, Y.M., Lalande, C., Piontek, J., Thomisch, K., Wurst, M., 2015. Summertime plankton ecology in Fram Strait—a compilation of long- and short-term observations. Polar Res. 34, 23349. https://doi.org/10.3402/polar.v34.23349

Orkney, A., Platt, T., Narayanaswamy, B.E., Kostakis, I., Bouman, H.A., 2020. Bio-optical evidence for increasing Phaeocystis dominance in the Barents Sea. Philos. Trans. R. Soc. A 378, 20190357. https://doi.org/10.1098/rsta.2019.0357

Oziel, L., Baudena, A., Ardyna, M., Massicotte, P., Randelhoff, A., Sallée, J.-B., Ingvaldsen, R.B., Devred, E., Babin, M., 2020. Faster Atlantic currents drive poleward expansion of temperate phytoplankton in the Arctic Ocean. Nat. Commun. 11, 1705. https://doi.org/10.1038/s41467-020-15485-5

Palmer, M.A., Saenz, B.T., Arrigo, K.R., 2014. Impacts of sea ice retreat, thinning, and melt-pond proliferation on the summer phytoplankton bloom in the Chukchi Sea, Arctic Ocean. Deep Sea Res. Part II: Top. Stud. Oceanogr. 105, 85–104. https://doi.org/10.1016/j.dsr2.2014.03.016

Park, J., Lee, S., Jo, Y.-H., Kim, H.-C., 2021. Phytoplankton Bloom Changes under Extreme Geophysical Conditions in the Northern Bering Sea and the Southern Chukchi Sea. Remote Sens. 13, 4035. https://doi.org/10.3390/rs13204035

Parsons, T.R., Maita, T., Lalli, C.M., 1984. A Manual of Chemical & Biological Methods for Seawater Analysis, 1st ed, Pergamon Press. Pergamon Press, Oxford.

Pelletier, G., Lewis, E., Wallace, D., 2007. CO2SYS.xls A calculator for the CO2 system in seawater for Microsoft Excel/VBA. Washington State Department of Ecology/Brookhaven National Laboratory, Olympia, WA/Upton, NY.

Rehder, L., Rokitta, S.D., Hoppe, C.J.M., Buschmann, I., Jasper, L., Rost, B., 2024. Different temperature sensitivities of key physiological processes lead to divergent trait response patterns in Arctic phytoplankton. Limnol. Oceanogr. https://doi.org/10.1002/lno.12633

Riebesell, U., Schloss, I., Smetacek, V., 1991. Aggregation of algae released from melting sea ice: implications for seeding and sedimentation. Polar Biol. 11, 239–248. https://doi.org/10.1007/bf00238457

Sakshaug, E., 2004. The Organic Carbon Cycle in the Arctic Ocean 57–81. https://doi.org/10.1007/978-3-642-18912-8_3

Sherr, E.B., Sherr, B.F., Hartz, A.J., 2009. Microzooplankton grazing impact in the Western Arctic Ocean. Deep Sea Research Part II: Topical Studies in Oceanography 56, 1264–1273. https://doi.org/10.1016/j.dsr2.2008.10.036

Sherr, E.B., Sherr, B.F., Ross, C., 2013. Microzooplankton grazing impact in the Bering Sea during spring sea ice conditions. Deep Sea Research Part II: Topical Studies in Oceanography 94, 57–67. https://doi.org/10.1016/j.dsr2.2013.03.019

Slawyk, G., Collos, Y., Auclair, J.C., 1977. The use of the 13C and 15N isotopes for the simultaneous measurement of carbon and nitrogen turnover rates in marine phytoplankton. Limnology and Oceanography 22, 925–932. https://doi.org/10.4319/lo.1977.22.5.0925

Smale, D.A., Wernberg, T., Oliver, E.C.J., Thomsen, M., Harvey, B.P., Straub, S.C., Burrows, M.T., Alexander, L.V., Benthuysen, J.A., Donat, M.G., Feng, M., Hobday, A.J., Holbrook, N.J., Perkins-Kirkpatrick, S.E., Scannell, H.A., Gupta, A.S., Payne, B.L., Moore, P.J., 2019. Marine heatwaves threaten global biodiversity and the provision of ecosystem services. Nat. Clim. Chang. 9, 306–312. https://doi.org/10.1038/s41558-019-0412-1

Smith, K.E., Burrows, M.T., Hobday, A.J., King, N.G., Moore, P.J., Gupta, A.S., Thomsen, M.S., Wernberg, T., Smale, D.A., 2022. Biological Impacts of Marine Heatwaves. Annu. Rev. Mar. Sci. 15, 119–145. https://doi.org/10.1146/annurev-marine-032122-121437

Soltwedel, T., Bauerfeind, E., Bergmann, M., Bracher, A., Budaeva, N., Busch, K., Cherkasheva, A., Fahl, K., Grzelak, K., Hasemann, C., Jacob, M., Kraft, A., Lalande, C., Metfies, K., Nöthig, E.-M., Meyer, K., Quéric, N.-V., Schewe, I., Włodarska-Kowalczuk, M., Klages, M., 2016. Natural variability or anthropogenically-induced variation? Insights from 15 years of multidisciplinary observations at the arctic marine LTER site HAUSGARTEN. Ecol. Indic. 65, 89–102. https://doi.org/10.1016/j.ecolind.2015.10.001

Stabeno, P.J., Bell, S.W., 2019. Extreme Conditions in the Bering Sea (2017–2018): Record-Breaking Low Sea-Ice Extent. Geophys. Res. Lett. 46, 8952–8959. https://doi.org/10.1029/2019gl083816

Stabeno, P.J., Bond, N.A., Salo, S.A., 2007. On the recent warming of the southeastern Bering Sea shelf. Deep Sea Res. Part II: Top. Stud. Oceanogr. 54, 2599–2618. https://doi.org/10.1016/j.dsr2.2007.08.023

Stabeno, P.J., Jr., E.V.F., Kachel, N.B., Moore, S., Mordy, C.W., Napp, J.M., Overland, J.E., Pinchuk, A.I., Sigler, M.F., 2012a. A comparison of the physics of the northern and southern shelves of the eastern Bering Sea and some implications for the ecosystem. Deep Sea Res. Part II: Top. Stud. Oceanogr. 65, 14–30. https://doi.org/10.1016/j.dsr2.2012.02.019

Stabeno, P.J., Kachel, N.B., Moore, S.E., Napp, J.M., Sigler, M., Yamaguchi, A., Zerbini, A.N., 2012b. Comparison of warm and cold years on the southeastern Bering Sea shelf and some implications for the ecosystem. Deep Sea Res. Part II: Top. Stud. Oceanogr. 65, 31–45. https://doi.org/10.1016/j.dsr2.2012.02.020

Stabeno, P.J., Mordy, C.W., Sigler, M.F., 2020. Seasonal patterns of near-bottom chlorophyll fluorescence in the eastern Chukchi Sea: 2010–2019. Deep Sea Res. Part II: Top. Stud. Oceanogr. 177, 104842. https://doi.org/10.1016/j.dsr2.2020.104842

Sterner, R.W., Andersen, T., Elser, J.J., Hessen, D.O., Hood, J.M., McCauley, E., Urabe, J., 2008. Scale-dependent carbon:nitrogen:phosphorus seston stoichiometry in marine and freshwaters. Limnology and Oceanography 53, 1169–1180. https://doi.org/10.4319/lo.2008.53.3.1169

Sterner, R.W., Elser, J.J., 2002. Ecological Stoichiometry.

Stroeve, J.C., Markus, T., Boisvert, L., Miller, J., Barrett, A., 2014. Changes in Arctic melt season and implications for sea ice loss. Geophysical Research Letters 41, 1216–1225.

Tréguer, P., Pondaven, P., 2000. Silica control of carbon dioxide. Nature 406, 358–359. https://doi.org/10.1038/35019236

Tréguer, P.J., De La Rocha, C.L., 2013. The World Ocean Silica Cycle. Annu Rev Mar Sci 5, 477–501. https://doi.org/10.1146/annurev-marine-121211-172346

Ummenhofer, C.C., Meehl, G.A., 2017. Extreme weather and climate events with ecological relevance: a review. Philos. Trans. R. Soc. B: Biol. Sci. 372, 20160135. https://doi.org/10.1098/rstb.2016.0135

Varela, D.E., Crawford, D.W., Wrohan, I.A., Wyatt, S.N., Carmack, E.C., 2013. Pelagic primary productivity and upper ocean nutrient dynamics across Subarctic and Arctic Seas. J. Geophys. Res.: Oceans 118, 7132–7152. https://doi.org/10.1002/2013jc009211

Waga, H., Hirawake, T., 2020. Changing Occurrences of Fall Blooms Associated With Variations in Phytoplankton Size Structure in the Pacific Arctic. Front. Mar. Sci. 7, 209. https://doi.org/10.3389/fmars.2020.00209

Waga, H., Hirawake, T., Grebmeier, J.M., 2020. Recent change in benthic macrofaunal community composition in relation to physical forcing in the Pacific Arctic. Polar Biol. 43, 285–294. https://doi.org/10.1007/s00300-020-02632-3

Walsh, J.E., Ballinger, T.J., Euskirchen, E.S., Hanna, E., Mård, J., Overland, J.E., Tangen, H., Vihma, T., 2020. Extreme weather and climate events in northern areas: A review. Earth-Sci. Rev. 209, 103324. https://doi.org/10.1016/j.earscirev.2020.103324

Wood, K.R., Bond, N.A., Danielson, S.L., Overland, J.E., Salo, S.A., Stabeno, P.J., Whitefield, J., 2015. A decade of environmental change in the Pacific Arctic region. Prog. Oceanogr. 136, 12–31. https://doi.org/10.1016/j.pocean.2015.05.005

Woodgate, R.A., Weingartner, T., Lindsay, R., 2010. The 2007 Bering Strait oceanic heat flux and anomalous Arctic sea-ice retreat. Geophys. Res. Lett. 37, n/a-n/a. https://doi.org/10.1029/2009gl041621

Woodgate, R.A., Weingartner, T.J., Lindsay, R., 2012. Observed increases in Bering Strait oceanic fluxes from the Pacific to the Arctic from 2001 to 2011 and their impacts on the Arctic Ocean water column. Geophysical Research Letters 39, L24603. https://doi.org/10.1029/2012gl054092

Wyatt, S.N., Crawford, D.W., Wrohan, I.A., Varela, D.E., 2013. Distribution and composition of suspended biogenic particles in surface waters across Subarctic and Arctic Seas. Journal of Geophysical Research-Oceans 118, 6867–6880. https://doi.org/10.1002/2013jc009214

Yeo, S.-R., Kim, K.-Y., Yeh, S.-W., Kim, B.-M., Shim, T., Jhun, J.-G., 2014. Recent climate variation in the Bering and Chukchi Seas and its linkages to large-scale circulation in the Pacific. Clim. Dyn. 42, 2423–2437. https://doi.org/10.1007/s00382-013-2042-z

## References for Chapter 4


Alcaraz-Rocha, P., Puig-Fàbregas, J., Garrido, J.L., Sobrino, C., 2023. Ocean acidification affects pigment concentration and photoprotection of marine phytoplankton. Limnol Oceanogr 68, 831–844. https://doi.org/10.1002/lno.12313

Alldredge, A.L., Silver, M.W., 1988. Characteristics, dynamics and significance of marine snow. Progress in Oceanography 20, 41–82.

Bach, L.T., Alvarez-Fernandez, S., Hornick, T., Stuhr, A., Riebesell, U., 2017. Simulated ocean acidification reveals winners and losers in coastal phytoplankton. PLoS One 12, e0188198. https://doi.org/10.1371/journal.pone.0188198

Bach, L.T., Taucher, J., 2019. CO2 effects on diatoms: a synthesis of more than a decade of ocean acidification experiments with natural communities. Ocean Sci 15, 1159–1175. https://doi.org/10.5194/os-15-1159-2019

Baines, S.B., Twining, B.S., Brzezinski, M.A., Nelson, D.M., Fisher, N.S., 2010. Causes and biogeochemical implications of regional differences in silicification of marine diatoms. Global Biogeochem Cy 24, GB4031. https://doi.org/10.1029/2010gb003856

Baines, S.B., Twining, B.S., Vogt, S., Balch, W.M., Fisher, N.S., Nelson, D.M., 2011. Elemental composition of equatorial Pacific diatoms exposed to additions of silicic acid and iron. Deep Sea Research Part II: Topical Studies in Oceanography 58, 512–523. https://doi.org/10.1016/j.dsr2.2010.08.003

Barwell-Clarke, J., Whitney, F., 1996. Institute of Ocean Sciences nutrient methods and analysis. Canadian Technical Report of Hydrography and Ocean Sciences 182, 1–49.

Berges, J.A., Franklin, D.J., Harrison, P.J., 2001. Evolution of an artificial seawater medium: Improvements in enriched seawater, artificial water over the last two decades. Journal of Phycology 37, 1138–1145. https://doi.org/10.1046/j.1529-8817.2001.01052.x

Berges, J.A., Varela, D.E., Harrison, P.J., 2002. Effects of temperature on growth rate, cell composition and nitrogen metabolism in the marine diatom *Thalassiosira pseudonana* (Bacillariophyceae). Marine Ecology Progress Series 225, 139–146.

Brzezinski, M.A., 1985. The Si:C:N ratio of marine diatoms: Interspecific variability and the effect of some environmental variables. Journal of Phycology 21, 347–357. https://doi.org/10.1111/j.0022-3646.1985.00347.x

Brzezinski, M.A., Dickson, M.-L., Nelson, D.M., Sambrotto, R.N., 2003. Ratios of Si, C and N uptake by microplankton in the Southern Ocean. Deep Sea Research Part II: Topical Studies in Oceanography 50, 619–633. https://doi.org/10.1016/s0967-0645(02)00587-8

Brzezinski, M.A., Nelson, D.M., 1995. The annual silica cycle in the Sargasso Sea near Bermuda. Deep Sea Research Part I: Oceanographic Research Papers 42, 1215–1237.

Brzezinski, M.A., Nelson, D.M., 1986. A solvent extraction method for the colorimetric determination of nanomolar concentrations of silicic acid in seawater. Marine Chemistry 19, 139–151. https://doi.org/10.1016/0304-4203(86)90045-9

Brzezinski, M.A., Phillips, D.R., 1997. Evaluation of 32Si as a tracer for measuring silica production rates in marine waters. Limnology and Oceanography 42, 856–865. https://doi.org/10.4319/lo.1997.42.5.0856

Chen, B., Liu, H., 2010. Relationships between phytoplankton growth and cell size in surface oceans: Interactive effects of temperature, nutrients, and grazing. Limnol Oceanogr 55, 965–972. https://doi.org/10.4319/lo.2010.55.3.0965

Clark, D.R., Flynn, K.J., Fabian, H., 2014. Variation in elemental stoichiometry of the marine diatom *Thalassiosira weissflogii* (Bacillariophyceae) in response to combined nutrient stress and changes in carbonate chemistry. J Phycol 50, 640–651. https://doi.org/10.1111/jpy.12208

Conley, D.J., Kilham, S.S., Theriot, E., 1989. Differences in silica content between marine and freshwater diatoms. Limnol Oceanogr 34, 205–212. https://doi.org/10.4319/lo.1989.34.1.0205

Dickson, A.G., 1990. Standard potential of the reaction: AgCl(s) + 12H2(g) = Ag(s) + HCl(aq), and the standard acidity constant of the ion HSO4− in synthetic sea water from 273.15 to 318.15 K. J Chem Thermodyn 22, 113–127. https://doi.org/10.1016/0021-9614(90)90074-z

Dickson, A.G., Sabine, C.L., Christian, J.R., 2007. Determination of the pH of seawater using a glass/reference electrode cell, in: Dickson, A.G., Sabine, C.L., Christian, J.R. (Eds.), Guide to Best Practices for Ocean CO2 Measurements. PICES, Sidney, BC, p. SOP6a.

Dugdale, R.C., Goering, J.J., 1967. Uptake of new and regenerated forms of nitrogen in primary productivity. Limnology and Oceanography 12, 196–206. https://doi.org/10.4319/lo.1967.12.2.0196

Dugdale, R.C., Wilkerson, F.P., 1986. The use of 15N to measure nitrogen uptake in eutrophic oceans; experimental considerations. Limnology and Oceanography 31, 673–689. https://doi.org/10.4319/lo.1986.31.4.0673

Edwards, K.F., Klausmeier, C.A., Litchman, E., 2011. Evidence for a three-way trade-off between nitrogen and phosphorus competitive abilities and cell size in phytoplankton. Ecology 92, 2085–2095. https://doi.org/10.1890/11-0395.1

Fabry, V.J., Seibel, B.A., Feely, R.A., Orr, J.C., 2008. Impacts of ocean acidification on marine fauna and ecosystem processes. Ices J Mar Sci 65, 414–432. https://doi.org/10.1093/icesjms/fsn048

Field, C.B., Behrenfeld, M.J., Randerson, J.T., Falkowski, P., 1998. Primary production of the biosphere: Integrating terrestrial and oceanic components. Science 281, 237–240. https://doi.org/10.1126/science.281.5374.237

Gao, K., Xu, J., Gao, G., Li, Y., Hutchins, D.A., Huang, B., Wang, L., Zheng, Y., Jin, P., Cai, X., Häder, D.-P., Li, W., Xu, K., Liu, N., Riebesell, U., 2012. Rising CO2 and increased light exposure synergistically reduce marine primary productivity. Nat Clim Change 2, 519–523. https://doi.org/10.1038/nclimate1507

Hama, T., Miyazaki, T., Ogawa, Y., Iwakuma, T., Takahashi, M., Otsuki, A., Ichimura, S., 1983. Measurement of photosynthetic production of a marine-phytoplankton population using a stable C-13 isotope. Marine Biology 73, 31–36. https://doi.org/10.1007/bf00396282.pdf

Hasle, G.R., 1976. The biogeography of some marine planktonic diatoms. Deep Sea Res Oceanogr Abstr 23, 319–338. https://doi.org/10.1016/0011-7471(76)90873-1

Hofmann, P., Chatzinotas, A., Harpole, W.S., Dunker, S., 2019. Temperature and stoichiometric dependence of phytoplankton traits. Ecology 100, e02875. https://doi.org/10.1002/ecy.2875

Hoppe, C.J.M., Holtz, L.M., Trimborn, S., Rost, B., 2015. Ocean acidification decreases the light-use efficiency in an Antarctic diatom under dynamic but not constant light. The New Phytologist 207, 159–171. https://doi.org/10.1111/nph.13334

Hoppe, C.J.M., Langer, G., Rokitta, S.D., Wolf-Gladrow, D.A., Rost, B., 2012. Implications of observed inconsistencies in carbonate chemistry measurements for ocean acidification studies. Biogeosciences 9, 2401–2405. https://doi.org/10.5194/bg-9-2401-2012

Hoppe, C.J.M., Schuback, N., Semeniuk, D., Giesbrecht, K., Mol, J., Thomas, H., Maldonado, M.T., Rost, B., Varela, D.E., Tortell, P.D., 2017a. Resistance of Arctic phytoplankton to ocean acidification and enhanced irradiance. Polar Biology 41, 1–15. https://doi.org/10.1007/s00300-017-2186-0

Hoppe, C.J.M., Schuback, N., Semeniuk, D.M., Maldonado, M.T., Rost, B., 2017b. Functional redundancy facilitates resilience of subarctic phytoplankton assemblages toward ocean acidification and high irradiance. Frontiers Mar Sci 4, 229. https://doi.org/10.3389/fmars.2017.00229

Hoppe, C.J.M., Wolf, K.K.E., Schuback, N., Tortell, P.D., Rost, B., 2018. Compensation of ocean acidification effects in Arctic phytoplankton assemblages. Nat Clim Change 8, 529–533. https://doi.org/10.1038/s41558-018-0142-9

Irwin, A.J., Finkel, Z.V., Schofield, O.M.E., Falkowski, P.G., 2006. Scaling-up from nutrient physiology to the size-structure of phytoplankton communities. J. Plankton Res. 28, 459–471. https://doi.org/10.1093/plankt/fbi148

Jewson, D.H., 1992. Size reduction, reproductive strategy and the life cycle of a centric diatom. Philosophical Transactions Royal Soc Lond Ser B Biological Sci 336, 191–213. https://doi.org/10.1098/rstb.1992.0056

Krause, J.W., Brzezinski, M.A., Jones, J.L., 2011. Application of low-level beta counting of 32Si for the measurement of silica production rates in aquatic environments. Marine Chemistry 127, 40–47. https://doi.org/10.1016/j.marchem.2011.07.001

Lakens, D., 2013. Calculating and reporting effect sizes to facilitate cumulative science: a practical primer for t-tests and ANOVAs. Front Psychol 4, 863. https://doi.org/10.3389/fpsyg.2013.00863

Leblanc, K., Arístegui, J., Armand, L., Assmy, P., Beker, B., Bode, A., Breton, E., Cornet, V., Gibson, J., Gosselin, M.-P., Kopczynska, E., Marshall, H., Peloquin, J., Piontkovski, S., Poulton, A.J., Quéguiner, B., Schiebel, R., Shipe, R., Stefels, J., Leeuwe, M.A. van, Varela, M., Widdicombe, C., Yallop, M.,

2012. A global diatom database – abundance, biovolume and biomass in the world ocean. Earth Syst Sci Data 4, 149–165. https://doi.org/10.5194/essd-4-149-2012

Li, H., Xu, T., Ma, J., Li, F., Xu, J., 2021. Physiological responses of *Skeletonema costatum* to the interactions of seawater acidification and the combination of photoperiod and temperature. Biogeosciences 18, 1439–1449. https://doi.org/10.5194/bg-18-1439-2021

Li, W., Gao, K., Beardall, J., 2015. Nitrate limitation and ocean acidification interact with UV-B to reduce photosynthetic performance in the diatom *Phaeodactylum tricornutum*. Biogeosciences 12, 2383–2393. https://doi.org/10.5194/bg-12-2383-2015

Li, W., Gao, K., Beardall, J., 2012. Interactive effects of ocean acidification and nitrogen-limitation on the diatom *Phaeodactylum tricornutum*. Plos One 7, e51590. https://doi.org/10.1371/journal.pone.0051590

Li, W., Wang, T., Campbell, D.A., Gao, K., 2020. Ocean acidification interacts with variable light to decrease growth but increase particulate organic nitrogen production in a diatom. Mar Environ Res 160, 104965. https://doi.org/10.1016/j.marenvres.2020.104965

Lomas, M.W., Baer, S.E., Acton, S., Krause, J.W., 2019. Pumped up by the cold: elemental quotas and stoichiometry of cold-water diatoms. Frontiers in Marine Science 6, 286. https://doi.org/10.3389/fmars.2019.00286

Lueker, T.J., Dickson, A.G., Keeling, C.D., 2000. Ocean *p*CO2 calculated from dissolved inorganic carbon, alkalinity, and equations for K1 and K2: validation based on laboratory measurements of CO2 in gas and seawater at equilibrium. Mar Chem 70, 105–119. https://doi.org/10.1016/s0304-4203(00)00022-0

Marañón, E., 2015. Cell size as a key determinant of phytoplankton metabolism and community structure. Annu Rev Mar Sci 7, 1–24. https://doi.org/10.1146/annurev-marine-010814-015955

Marañón, E., Cermeño, P., López-Sandoval, D.C., Rodríguez-Ramos, T., Sobrino, C., Huete-Ortega, M., Blanco, J.M., Rodríguez, J., 2013. Unimodal size scaling of phytoplankton growth and the size dependence of nutrient uptake and use. Ecol Lett 16, 371–379. https://doi.org/10.1111/ele.12052

Marchetti, A., Varela, D.E., Lance, V.P., Johnson, Z., Palmucci, M., Giordano, M., Armbrust, E.V., 2010. Iron and silicic acid effects on phytoplankton productivity, diversity, and chemical composition in the central equatorial Pacific Ocean. Limnology and Oceanography 55, 11–29. https://doi.org/10.4319/lo.2010.55.1.0011

Martin-Jezequel, V., Hildebrand, M., Brzezinski, M.A., 2000. Silicon metabolism in diatoms: Implications for growth. Journal of Phycology 36, 821–840.

Mathis, J., Cross, J., Evans, W., Doney, S., 2015. Ocean acidification in the surface waters of the Pacific-Arctic boundary regions. Oceanography 25, 122–135. https://doi.org/10.5670/oceanog.2015.36

Mehrbach, C., Culberson, C.H., Hawley, J.E., Pytkowicx, R.M., 1973. Measurement of the apparent dissociation constants of carbonic acid in seawater at atmospheric pressure. Limnol Oceanogr 18, 897–907. https://doi.org/10.4319/lo.1973.18.6.0897

Mejía, L.M., Isensee, K., Méndez-Vicente, A., Pisonero, J., Shimizu, N., González, C., Monteleone, B., Stoll, H., 2013. B content and Si/C ratios from cultured diatoms (*Thalassiosira pseudonana* and *Thalassiosira weissflogii*): Relationship to seawater pH and diatom carbon acquisition. Geochim Cosmochim Ac 123, 322–337. https://doi.org/10.1016/j.gca.2013.06.011

Meyerink, S.W., Ellwood, M.J., Maher, W.A., Price, G.D., Strzepek, R.F., 2017. Effects of iron limitation on silicon uptake kinetics and elemental stoichiometry in two Southern Ocean diatoms, *Eucampia antarctica* and *Proboscia inermis*, and the temperate diatom *Thalassiosira pseudonana*. Limnology and Oceanography 62, 2445–2462. https://doi.org/10.1002/lno.10578

Miklasz, K.A., Denny, M.W., 2010. Diatom sinkings speeds: Improved predictions and insight from a modified Stokes' law. Limnol Oceanogr 55, 2513–2525. https://doi.org/10.4319/lo.2010.55.6.2513

Milligan, A.J., Varela, D.E., Brzezinski, M.A., Morel, F.M.M., 2004. Dynamics of silicon metabolism and silicon isotopic discrimination in a marine diatom as a function of pCO2. Limnology and Oceanography 49, 322–329. https://doi.org/10.4319/lo.2004.49.2.0322

Montagnes, D.J.S., Franklin, M., 2001. Effect of temperature on diatom volume, growth rate, and carbon and nitrogen content: Reconsidering some paradigms. Limnol Oceanogr 46, 2008–2018. https://doi.org/10.4319/lo.2001.46.8.2008

Nakagawa, S., Cuthill, I.C., 2007. Effect size, confidence interval and statistical significance: a practical guide for biologists. Biol. Rev. 82, 591–605. https://doi.org/10.1111/j.1469-185x.2007.00027.x

Nelson, D.M., Tréguer, P., Brzezinski, M.A., Leynaert, A., Quéguiner, B., 1995. Production and dissolution of biogenic silica in the ocean: Revised global estimates, comparison with regional data and relationship to biogenic sedimentation. Global Biogeochemical Cycles 9, 359–372. https://doi.org/10.1029/95gb01070

Parsons, T.R., Maita, T., Lalli, C.M., 1984. A Manual of Chemical & Biological Methods for Seawater Analysis, 1st ed, Pergamon Press. Pergamon Press, Oxford.

Pelletier, G., Lewis, E., Wallace, D., 2007. CO2SYS.xls A calculator for the CO2 system in seawater for Microsoft Excel/VBA. Washington State Department of Ecology/Brookhaven National Laboratory, Olympia, WA/Upton, NY.

Petrou, K., Baker, K.G., Nielsen, D.A., Hancock, A.M., Schulz, K.G., Davidson, A.T., 2019. Acidification diminishes diatom silica production in the Southern Ocean. Nature Climate Change 9, 781–786. https://doi.org/10.1038/s41558-019-0557-y

Pondaven, P., Gallinari, M., Chollet, S., Bucciarelli, E., Sarthou, G., Schultes, S., Jean, F., 2007. Grazing-induced changes in cell wall silicification in a marine diatom. Protist 158, 21–28. https://doi.org/10.1016/j.protis.2006.09.002

Qu, L., Campbell, D.A., Gao, K., 2021. Ocean acidification interacts with growth light to suppress CO2 acquisition efficiency and enhance mitochondrial respiration in a coastal diatom. Mar Pollut Bull 163, 112008. https://doi.org/10.1016/j.marpolbul.2021.112008

Ragueneau, O., Schultes, S., Bidle, K., Claquin, P., Moriceau, B., 2006. Si and C interactions in the world ocean: Importance of ecological processes and implications for the role of diatoms in the biological pump. Glob. Biogeochem. Cycles 20, GB4S02. https://doi.org/10.1029/2006gb002688

Reinfelder, J.R., 2011. Carbon concentrating mechanisms in eukaryotic marine phytoplankton. Annu. Rev. Mar. Sci. 3, 291–315. https://doi.org/10.1146/annurev-marine-120709-142720

Riebesell, U., Schulz, K.G., Bellerby, R.G.J., Botros, M., Fritsche, P., Meyerhöfer, M., Neill, C., Nondal, G., Oschlies, A., Wohlers, J., Zöllner, E., 2007. Enhanced biological carbon consumption in a high CO2 ocean. Nature 450, 545–548. https://doi.org/10.1038/nature06267

Roberts, K., Granum, E., Leegood, R.C., Raven, J.A., 2007. Carbon acquisition by diatoms. Photosynthesis research 93, 79–88. https://doi.org/10.1007/s11120-007-9172-2

Rosenberg, M.S., Rothstein, H.R., Gurevitch, J., 2013. Effect sizes: Conventional choices and calculations, in: Koricheva, J., Gurevitch, Juessica, Mengersen, K. (Eds.), Handbook of Meta-Analysis in Ecology and Evolution. Princeton University Press, Princeton, NJ, pp. 61–71. https://doi.org/10.23943/princeton/9780691137285.003.0006

Rossum, G. van, Drake, F.L., 2009. Python 3 Reference Manual. CreateSpace, Scotts Valley, CA.

Sar, E.A., Sunesen, I., Lavigne, A.S., Lofeudo, S., 2011. *Thalassiosira rotula*, a heterotypic synonym of *Thalassiosira gravida*: morphological evidence. Diatom Res 26, 109–119. https://doi.org/10.1080/0269249x.2011.573691

Schone, H., 1974. Experimental investigations on the ecology of the marine diatom *Thalassiosira rotula*. II. The influence of salinity. Mar Biol 27, 287–298. https://doi.org/10.1007/bf00394364

Schone, H., 1972. Experimental investigations on the ecology of the marine diatom *Thalassiosira rotula*. I. Temperature and light. Mar Biol 13, 284–291. https://doi.org/10.1007/bf00348075

Seebah, S., Fairfield, C., Ullrich, M.S., Passow, U., 2014. Aggregation and sedimentation of *Thalassiosira weissflogii* (diatom) in a warmer and more acidified future ocean. Plos One 9, e112379. https://doi.org/10.1371/journal.pone.0112379

Shi, D., Li, W., Hopkinson, B.M., Hong, H., Li, D., Kao, S., Lin, W., 2015. Interactive effects of light, nitrogen source, and carbon dioxide on energy metabolism in the diatom *Thalassiosira pseudonana*. Limnol Oceanogr 60, 1805–1822. https://doi.org/10.1002/lno.10134

Slawyk, G., Collos, Y., Auclair, J.C., 1977. The use of the 13C and 15N isotopes for the simultaneous measurement of carbon and nitrogen turnover rates in marine phytoplankton. Limnology and Oceanography 22, 925–932. https://doi.org/10.4319/lo.1977.22.5.0925

Smetacek, V., 1999. Diatoms and the ocean carbon cycle. Protist 150, 25–32. https://doi.org/10.1016/s1434-4610(99)70006-4

Spalding, M.H., 2008. Microalgal carbon-dioxide-concentrating mechanisms: *Chlamydomonas* inorganic carbon transporters. J Exp Bot 59, 1463–1473. https://doi.org/10.1093/jxb/erm128

Spilling, K., Ylöstalo, P., Simis, S., Seppälä, J., 2015. Interaction effects of light, temperature and nutrient limitations (N, P and Si) on growth, stoichiometry and photosynthetic parameters of the cold-water diatom *Chaetoceros wighamii*. PLoS One 10, e0126308. https://doi.org/10.1371/journal.pone.0126308

Taylor, A., Geider, R., Gilbert, F., 1997. Seasonal and latitudinal dependencies of phytoplankton carbon-to-chlorophyll a ratios: Results of a modelling study. Mar Ecol Prog Ser 152, 51–66. https://doi.org/10.3354/meps152051

Tréguer, P., Bowler, C., Moriceau, B., Dutkiewicz, S., Gehlen, M., Aumont, O., Bittner, L., Dugdale, R., Finkel, Z., Iudicone, D., Jahn, O., Guidi, L., Lasbleiz, M., Leblanc, K., Levy, M., Pondaven, P., 2018. Influence of diatom diversity on the ocean biological carbon pump. Nat Geosci 11, 27–37. https://doi.org/10.1038/s41561-017-0028-x

Tréguer, P.J., Sutton, J.N., Brzezinski, M., Charette, M.A., Devries, T., Dutkiewicz, S., Ehlert, C., Hawkings, J., Leynaert, A., Liu, S.M., Monferrer, N.L., López-Acosta, M., Maldonado, M., Rahman, S., Ran, L., Rouxel, O., 2021. Reviews and syntheses: The biogeochemical cycle of silicon in the modern ocean. Biogeosciences 18, 1269–1289. https://doi.org/10.5194/bg-18-1269-2021

Valenzuela, J.J., Lomana, A.L.G. de, Lee, A., Armbrust, E.V., Orellana, M.V., Baliga, N.S., 2018. Ocean acidification conditions increase resilience of marine diatoms. Nat Commun 9, 2328. https://doi.org/10.1038/s41467-018-04742-3

Volk, T., Hoffert, M.I., 1985. Ocean carbon pumps: Analysis of relative strengths and efficiencies in ocean-driven atmospheric CO2 changes, in: Sundquist, E.T., Broecker, W.S. (Eds.), The Carbon Cycle and Atmospheric $CO_2$: Natural Variations Archean to Present, Geophysical Monograph Series. American Geophysical Union, Washington, D.C., pp. 99–110. https://doi.org/10.1029/gm032p0099

Wassmann, P., Duarte, C.M., Agustí, S., Sekr, M.J., 2010. Footprints of climate change in the Arctic marine ecosystem. Global Change Biol 17, 1235–1249. https://doi.org/10.1111/j.1365-2486.2010.02311.x

Wu, Y., Campbell, D.A., Irwin, A.J., Suggett, D.J., Finkel, Z.V., 2014. Ocean acidification enhances the growth rate of larger diatoms. Limnology and Oceanography 59, 1027–1034. https://doi.org/10.4319/lo.2014.59.3.1027

Wu, Y., Gao, K., Riebesell, U., 2010. CO2-induced seawater acidification affects physiological performance of the marine diatom *Phaeodactylum tricornutum*. Biogeosciences 7, 2915–2923. https://doi.org/10.5194/bg-7-2915-2010

Yang, G., Gao, K., 2012. Physiological responses of the marine diatom *Thalassiosira pseudonana* to increased pCO2 and seawater acidity. Mar Environ Res 79, 142–151. https://doi.org/10.1016/j.marenvres.2012.06.002

## References for Chapter 5


Amacher, J., Neuer, S., Lomas, M., 2013. DNA-based molecular fingerprinting of eukaryotic protists and cyanobacteria contributing to sinking particle flux at the Bermuda Atlantic time-series study. Deep Sea Res. Part II: Top. Stud. Oceanogr. 93, 71–83. https://doi.org/10.1016/j.dsr2.2013.01.001

Bach, L.T., Taucher, J., 2019. CO2 effects on diatoms: a synthesis of more than a decade of ocean acidification experiments with natural communities. Ocean Sci 15, 1159–1175. https://doi.org/10.5194/os-15-1159-2019

Bach, L.T., Taucher, J., Boxhammer, T., Ludwig, A., Consortium, T.K.K., Achterberg, E.P., Algueró-Muñiz, M., Anderson, L.G., Bellworthy, J., Büdenbender, J., Czerny, J., Ericson, Y., Esposito, M., Fischer, M., Haunost, M., Hellemann, D., Horn, H.G., Hornick, T., Meyer, J., Sswat, M., Zark, M., Riebesell, U., 2016. Influence of Ocean Acidification on a Natural Winter-to-Summer Plankton Succession: First Insights from a Long-Term Mesocosm Study Draw Attention to Periods of Low Nutrient Concentrations. PLoS ONE 11, e0159068. https://doi.org/10.1371/journal.pone.0159068

Bao, N., Gao, K., 2021. Interactive Effects of Elevated CO2 Concentration and Light on the Picophytoplankton Synechococcus. Frontiers Mar Sci 8, 634189. https://doi.org/10.3389/fmars.2021.634189

Barwell-Clarke, J., Whitney, F., 1996. Institute of Ocean Sciences nutrient methods and analysis. Canadian Technical Report of Hydrography and Ocean Sciences 182, 1–49.

Bates, N.R., Johnson, R.J., 2023. Forty years of ocean acidification observations (1983–2023) in the Sargasso Sea at the Bermuda Atlantic Time-series Study site. Front. Mar. Sci. 10, 1289931. https://doi.org/10.3389/fmars.2023.1289931

Bates, N.R., Johnson, R.J., 2020. Acceleration of ocean warming, salinification, deoxygenation and acidification in the surface subtropical North Atlantic Ocean. Commun Earth Environ 33, 33. https://doi.org/10.1038/s43247-020-00030-5

Brzezinski, M.A., 1985. The Si:C:N ratio of marine diatoms: Interspecific variability and the effect of some environmental variables. Journal of Phycology 21, 347–357. https://doi.org/10.1111/j.0022-3646.1985.00347.x

Brzezinski, M.A., Nelson, D.M., 1995. The annual silica cycle in the Sargasso Sea near Bermuda. Deep Sea Research Part I: Oceanographic Research Papers 42, 1215–1237.

Brzezinski, M.A., Nelson, D.M., 1986. A solvent extraction method for the colorimetric determination of nanomolar concentrations of silicic acid in seawater. Marine Chemistry 19, 139–151. https://doi.org/10.1016/0304-4203(86)90045-9

Brzezinski, M.A., Phillips, D.R., 1997. Evaluation of 32Si as a tracer for measuring silica production rates in marine waters. Limnology and Oceanography 42, 856–865. https://doi.org/10.4319/lo.1997.42.5.0856

Caldeira, K., Wickett, M., 2003. Anthropogenic carbon and ocean pH. Nature 425, 365.

Casey, J.R., Aucan, J.P., Goldberg, S.R., Lomas, M.W., 2013. Changes in partitioning of carbon amongst photosynthetic pico- and nano-plankton groups in the Sargasso Sea in response to changes in the North Atlantic Oscillation. Deep Sea Res. Part II: Top. Stud. Oceanogr. 93, 58–70. https://doi.org/10.1016/j.dsr2.2013.02.002

Chisholm, S.W., 1992. Primary Productivity and Biogeochemical Cycles in the Sea 213–237. https://doi.org/10.1007/978-1-4899-0762-2_12

Clark, D.R., Flynn, K.J., Fabian, H., 2014. Variation in elemental stoichiometry of the marine diatom *Thalassiosira weissflogii* (Bacillariophyceae) in response to combined nutrient stress and changes in carbonate chemistry. J Phycol 50, 640–651. https://doi.org/10.1111/jpy.12208

Cotti-Rausch, B.E., Lomas, M.W., Lachenmyer, E.M., Baumann, E.G., Richardson, T.L., 2020. Size-fractionated biomass and primary productivity of Sargasso Sea phytoplankton. Deep Sea Res. Part : Oceanogr. Res. Pap. 156, 103141. https://doi.org/10.1016/j.dsr.2019.103141

Cruz, B.N., Brozak, S., Neuer, S., 2021. Microscopy and DNA-based characterization of sinking particles at the Bermuda Atlantic Time-series Study station point to zooplankton mediation of particle flux. Limnol. Oceanogr. 66, 3697–3713. https://doi.org/10.1002/lno.11910

Deng, W., Cruz, B., Neuer, S., 2016. Effects of nutrient limitation on cell growth, TEP production and aggregate formation of marine Synechococcus. Aquat. Microb. Ecol. 78, 39–49. https://doi.org/10.3354/ame01803

Dickson, A.G., 1990. Standard potential of the reaction: AgCl(s) + 12H2(g) = Ag(s) + HCl(aq), and the standard acidity constant of the ion HSO4− in synthetic sea water from 273.15 to 318.15 K. J Chem Thermodyn 22, 113–127. https://doi.org/10.1016/0021-9614(90)90074-z

Dickson, A.G., Sabine, C.L., Christian, J.R., 2007. Determination of the pH of seawater using a glass/reference electrode cell, in: Dickson, A.G., Sabine, C.L., Christian, J.R. (Eds.), Guide to Best Practices for Ocean CO2 Measurements. PICES, Sidney, BC, p. SOP6a.

Dugdale, R.C., Goering, J.J., 1967. Uptake of new and regenerated forms of nitrogen in primary productivity. Limnology and Oceanography 12, 196–206. https://doi.org/10.4319/lo.1967.12.2.0196

Dugdale, R.C., Wilkerson, F.P., 1986. The use of 15N to measure nitrogen uptake in eutrophic oceans; experimental considerations. Limnology and Oceanography 31, 673–689. https://doi.org/10.4319/lo.1986.31.4.0673

DuRand, M.D., Olson, R.J., Chisholm, S.W., 2001. Phytoplankton population dynamics at the Bermuda Atlantic Time-series station in the Sargasso Sea. Deep Sea Res. Part II: Top. Stud. Oceanogr. 48, 1983–2003. https://doi.org/10.1016/s0967-0645(00)00166-1

Engel, A., Zondervan, I., Aerts, K., Beaufort, L., Benthien, A., Chou, L., Delille, B., Gattuso, J.-P., Harlay, J., Heemann, C., Hoffmann, L., Jacquet, S., Nejstgaard, J., Pizay, M.-D., Rochelle-Newall, E., Schneider, U., Terbrueggen, A., Riebesell, U., 2005. Testing the direct effect of CO2 concentration on a bloom of the coccolithophorid Emiliania huxleyi in mesocosm experiments. Limnol. Oceanogr. 50, 493–507. https://doi.org/10.4319/lo.2005.50.2.0493

Friedlingstein, P., O'Sullivan, M., Jones, M.W., Andrew, R.M., Hauck, J., Olsen, A., Peters, G.P., Peters, W., Pongratz, J., Sitch, S., Quéré, C.L., Canadell, J.G., Ciais, P., Jackson, R.B., Alin, S., Aragão, L.E.O.C., Arneth, A., Arora, V., Bates, N.R., Becker, M., Benoit-Cattin, A., Bittig, H.C., Bopp, L., Bultan, S., Chandra, N., Chevallier, F., Chini, L.P., Evans, W., Florentie, L., Forster, P.M., Gasser, T., Gehlen, M., Gilfillan, D., Gkritzalis, T., Gregor, L., Gruber, N., Harris, I., Hartung, K., Haverd, V., Houghton, R.A., Ilyina, T., Jain, A.K., Joetzjer, E., Kadono, K., Kato, E., Kitidis, V., Korsbakken, J.I., Landschützer, P., Lefèvre, N., Lenton, A., Lienert, S., Liu, Z., Lombardozzi, D., Marland, G., Metzl, N., Munro, D.R., Nabel, J.E.M.S., Nakaoka, S.-I., Niwa, Y., O'Brien, K., Ono, T., Palmer, P.I., Pierrot, D., Poulter, B., Resplandy, L., Robertson, E., Rödenbeck, C., Schwinger, J., Séférian, R., Skjelvan, I., Smith, A.J.P., Sutton, A.J., Tanhua, T., Tans, P.P., Tian, H., Tilbrook, B., Werf, G. van der, Vuichard, N., Walker, A.P., Wanninkhof, R., Watson, A.J., Willis, D., Wiltshire, A.J., Yuan, W., Yue, X., Zaehle, S., 2020. Global Carbon Budget 2020. Earth Syst. Sci. Data 12, 3269–3340. https://doi.org/10.5194/essd-12-3269-2020

Fu, F., Warner, M.E., Zhang, Y., Feng, Y., Hutchins, D.A., 2007. Effects of increased temperature and CO2 on photosynthesis, growth, and elemental ratios, in marine *Synechococcus* and *Prochlorococcus* (cyanobacteria). J. Phycol. 43, 485–496. https://doi.org/10.1111/j.1529-8817.2007.00355.x

Gazeau, F., Sallon, A., Pitta, P., Tsiola, A., Maugendre, L., Giani, M., Celussi, M., Pedrotti, M.L., Marro, S., Guieu, C., 2017. Limited impact of ocean acidification on phytoplankton community structure and carbon export in an oligotrophic environment: Results from two short-term mesocosm studies in the Mediterranean Sea. Estuar., Coast. Shelf Sci. 186, 72–88. https://doi.org/10.1016/j.ecss.2016.11.016

Giesbrecht, K.E., Varela, D.E., 2021. Summertime Biogenic Silica Production and Silicon Limitation in the Pacific Arctic Region From 2006 to 2016. Global Biogeochem Cy 35. https://doi.org/10.1029/2020gb006629

Goericke, R., Repeta, D.J., 1992. The pigments of Prochlorococcus marinus: The presence of divinylchlorophyll a and b in a marine procaryote. Limnol. Oceanogr. 37, 425–433. https://doi.org/10.4319/lo.1992.37.2.0425

Goericke, R., Welschmeyer, N.A., 1993. The marine prochlorophyte Prochlorococcus contributes significantly to phytoplankton biomass and primary production in the Sargasso Sea. Deep Sea Res. Part : Oceanogr. Res. Pap. 40, 2283–2294. https://doi.org/10.1016/0967-0637(93)90104-b

Goldman, J.C., 1993. Potential role of large oceanic diatoms in new primary production. Deep Sea Research Part I: Oceanographic Research Papers 40, 159-. https://doi.org/10.1016/0967-0637(93)90059-c

Gruber, N., Clement, D., Carter, B.R., Feely, R.A., Heuven, S. van, Hoppema, M., Ishii, M., Key, R.M., Kozyr, A., Lauvset, S.K., Monaco, C.L., Mathis, J.T., Murata, A., Olsen, A., Perez, F.F., Sabine, C.L., Tanhua, T., Wanninkhof, R., 2019. The oceanic sink for anthropogenic CO2 from 1994 to 2007. Science 363, 1193–1199. https://doi.org/10.1126/science.aau5153

Hama, T., Miyazaki, T., Ogawa, Y., Iwakuma, T., Takahashi, M., Otsuki, A., Ichimura, S., 1983. Measurement of photosynthetic production of a marine-phytoplankton population using a stable C-13 isotope. Marine Biology 73, 31–36. https://doi.org/10.1007/bf00396282.pdf

Hulburt, E.M., 1990. Description of phytoplankton and nutrient in spring in the western North Atlantic Ocean. J. Plankton Res. 12, 1–28. https://doi.org/10.1093/plankt/12.1.1

Khatiwala, S., Tanhua, T., Fletcher, S.M., Gerber, M., Doney, S.C., Graven, H.D., Gruber, N., McKinley, G.A., Murata, A., Ríos, A.F., Sabine, C.L., 2013. Global ocean storage of anthropogenic carbon. Biogeosciences 10, 2169–2191. https://doi.org/10.5194/bg-10-2169-2013

Knap, A.H., Michaels, A.F., Steinberg, D., Bahr, F., N, B., S, B., P, C., A, C., A, D., F, H., K, G., R, J., R, L., K, O., R, P., C, R., M, S., S, S., 1997. BATS methods manual. U.S. JGOFS Planning Office, Woods Hole.

Krause, J.W., Brzezinski, M.A., Jones, J.L., 2011. Application of low-level beta counting of 32Si for the measurement of silica production rates in aquatic environments. Marine Chemistry 127, 40–47. https://doi.org/10.1016/j.marchem.2011.07.001

Lakens, D., 2013. Calculating and reporting effect sizes to facilitate cumulative science: a practical primer for t-tests and ANOVAs. Front Psychol 4, 863. https://doi.org/10.3389/fpsyg.2013.00863

Leblanc, K., Quéguiner, B., Diaz, F., Cornet, V., Michel-Rodriguez, M., Madron, X.D. de, Bowler, C., Malviya, S., Thyssen, M., Grégori, G., Rembauville, M., Grosso, O., Poulain, J., Vargas, C. de, Pujo-Pay, M., Conan, P., 2018. Nanoplanktonic diatoms are globally overlooked but play a role in spring blooms and carbon export. Nat. Commun. 9, 953. https://doi.org/10.1038/s41467-018-03376-9

Li, W., Gao, K., Beardall, J., 2015. Nitrate limitation and ocean acidification interact with UV-B to reduce photosynthetic performance in the diatom *Phaeodactylum tricornutum*. Biogeosciences 12, 2383–2393. https://doi.org/10.5194/bg-12-2383-2015

Lomas, M., Hopkinson, B., Losh, J., Ryan, D., Shi, D., Xu, Y., Morel, F., 2012. Effect of ocean acidification on cyanobacteria in the subtropical North Atlantic. Aquat. Microb. Ecol. 66, 211–222. https://doi.org/10.3354/ame01576

Lomas, M.W., Bates, N.R., Johnson, R.J., Knap, A.H., Steinberg, D.K., Carlson, C.A., 2013. Two decades and counting: 24-years of sustained open ocean biogeochemical measurements in the Sargasso Sea. Deep Sea Research Part II: Topical Studies in Oceanography 93, 16–32. https://doi.org/10.1016/j.dsr2.2013.01.008

Lomas, M.W., Bates, N.R., Johnson, R.J., Steinberg, D.K., Tanioka, T., 2022. Adaptive carbon export response to warming in the Sargasso Sea. Nat. Commun. 13, 1211. https://doi.org/10.1038/s41467-022-28842-3

Longhurst, A., Sathyendranath, S., Platt, T., 1995. An estimate of global primary production in the ocean from satellite radiometer data. Journal of Plankton Research. https://doi.org/10.1093/plankt/17.6.1245

Lu, Z., Jiao, N., Zhang, H., 2006. Physiological changes in marine picocyanobacterial Synechococcus strains exposed to elevated CO2 partial pressure. Mar. Biol. Res. 2, 424–430. https://doi.org/10.1080/17451000601055419

Lueker, T.J., Dickson, A.G., Keeling, C.D., 2000. Ocean pCO2 calculated from dissolved inorganic carbon, alkalinity, and equations for K1 and K2: validation based on laboratory measurements of CO2 in gas and seawater at equilibrium. Mar Chem 70, 105–119. https://doi.org/10.1016/s0304-4203(00)00022-0

Maugendre, L., Gattuso, J.-P., Poulton, A.J., Dellisanti, W., Gaubert, M., Guieu, C., Gazeau, F., 2017. No detectable effect of ocean acidification on plankton metabolism in the NW oligotrophic Mediterranean Sea: Results from two mesocosm studies. Estuar., Coast. Shelf Sci. 186, 89–99. https://doi.org/10.1016/j.ecss.2015.03.009

Mehrbach, C., Culberson, C.H., Hawley, J.E., Pytkowicx, R.M., 1973. Measurement of the apparent dissociation constants of carbonic acid in seawater at atmospheric pressure. Limnol Oceanogr 18, 897–907. https://doi.org/10.4319/lo.1973.18.6.0897

Nelson, D.M., Brzezinski, M.A., 1997. Diatom growth and productivity in an oligo-trophic midocean gyre: A 3-yr record from the Sargasso Sea near Bermuda. Limnology and Oceanography 42, 473–486. https://doi.org/10.4319/lo.1997.42.3.0473

Orr, J.C., Epitalon, J.-M., Dickson, A.G., Gattuso, J.-P., 2018. Routine uncertainty propagation for the marine carbon dioxide system. Mar. Chem. 207, 84–107. https://doi.org/10.1016/j.marchem.2018.10.006

Parsons, T.R., Maita, T., Lalli, C.M., 1984. A Manual of Chemical & Biological Methods for Seawater Analysis, 1st ed, Pergamon Press. Pergamon Press, Oxford.

Peng, B., Li, J., Zhang, H., Overmans, S., Wang, Y., Xu, L., Jia, Y., Huang, B., Liu, F., Liu, P., Xiao, M., Ye, M., Xia, J., Jin, P., 2024. Interactions between ocean acidification and multiple environmental drivers on the biochemical traits of marine primary producers: A meta-analysis. Mar. Environ. Res. 201, 106707. https://doi.org/10.1016/j.marenvres.2024.106707

Polovina, J.J., Howell, E.A., Abecassis, M., 2008. Ocean's least productive waters are expanding. Geophys. Res. Lett. 35. https://doi.org/10.1029/2007gl031745

Qu, L., Campbell, D.A., Gao, K., 2021. Ocean acidification interacts with growth light to suppress CO2 acquisition efficiency and enhance mitochondrial respiration in a coastal diatom. Mar Pollut Bull 163, 112008. https://doi.org/10.1016/j.marpolbul.2021.112008

Riebesell, U., Fabry, V J, Hansson, L, Gattuso, J.P. (Eds.), 2011. Guide to best practices for ocean acidification research and data reporting, Publications Office of the European Union. Publications Office of the European Union.

Rosenberg, M.S., Rothstein, H.R., Gurevitch, J., 2013. Effect sizes: Conventional choices and calculations, in: Koricheva, J., Gurevitch, Juessica, Mengersen, K. (Eds.), Handbook of Meta-Analysis in Ecology and Evolution. Princeton University Press, Princeton, NJ, pp. 61–71. https://doi.org/10.23943/princeton/9780691137285.003.0006

Ryther, J.H., 1969. Photosynthesis and fish production in the sea. The production of organic matter and its conversion to higher forms of life vary throughout the world ocean. Science (Washington).

Seebah, S., Fairfield, C., Ullrich, M.S., Passow, U., 2014. Aggregation and sedimentation of *Thalassiosira weissflogii* (diatom) in a warmer and more acidified future ocean. Plos One 9, e112379. https://doi.org/10.1371/journal.pone.0112379

Slawyk, G., Collos, Y., Auclair, J.C., 1977. The use of the 13C and 15N isotopes for the simultaneous measurement of carbon and nitrogen turnover rates in marine phytoplankton. Limnology and Oceanography 22, 925–932. https://doi.org/10.4319/lo.1977.22.5.0925

Steinberg, D.K., Carlson, C.A., Bates, N.R., Johnson, R.J., Michaels, A.F., Knap, A.H., 2001. Overview of the US JGOFS Bermuda Atlantic Time-series Study (BATS): a decade-scale look at ocean biology and biogeochemistry. Deep Sea Research Part II: Topical Studies in Oceanography 48, 1405–1447.

Taucher, J., Arístegui, J., Bach, L.T., Guan, W., Montero, M.F., Nauendorf, A., Achterberg, E.P., Riebesell, U., 2018. Response of Subtropical Phytoplankton Communities to Ocean Acidification Under Oligotrophic Conditions and During Nutrient Fertilization. Frontiers Mar Sci 5, 330. https://doi.org/10.3389/fmars.2018.00330

Taylor, A., Geider, R., Gilbert, F., 1997. Seasonal and latitudinal dependencies of phytoplankton carbon-to-chlorophyll a ratios: Results of a modelling study. Mar Ecol Prog Ser 152, 51–66. https://doi.org/10.3354/meps152051

Wyatt, S.N., McNabb, B.J., Varela, D.E., 2024. Morphological and physiological responses of the cosmopolitan marine diatom Thalassiosira rotula to acidification. Diatom Res. 39, 61–74. https://doi.org/10.1080/0269249x.2024.2369049

## References for Chapter 6


Alldredge, A.L., Silver, M.W., 1988. Characteristics, dynamics and significance of marine snow. Progress in Oceanography 20, 41–82.

Armbrust, E.V., 2009. The life of diatoms in the world's oceans. Nature 459, 185–192.

Bach, L.T., Taucher, J., 2019. CO2 effects on diatoms: a synthesis of more than a decade of ocean acidification experiments with natural communities. Ocean Sci 15, 1159–1175. https://doi.org/10.5194/os-15-1159-2019

Barkhordarian, A., Nielsen, D.M., Olonscheck, D., Baehr, J., 2024. Arctic marine heatwaves forced by greenhouse gases and triggered by abrupt sea-ice melt. Commun. Earth Environ. 5, 57. https://doi.org/10.1038/s43247-024-01215-y

Barwell-Clarke, J., Whitney, F., 1996. Institute of Ocean Sciences nutrient methods and analysis. Canadian Technical Report of Hydrography and Ocean Sciences 182, 1–49.

Bates, N.R., Garley, R., Frey, K.E., Shake, K.L., Mathis, J.T., 2014. Sea-ice melt CO2–carbonate chemistry in the western Arctic Ocean: meltwater contributions to air–sea CO2 gas exchange, mixed-layer properties and rates of net community production under sea ice. Biogeosciences 11, 6769–6789. https://doi.org/10.5194/bg-11-6769-2014

Bates, N.R., Johnson, R.J., 2023. Forty years of ocean acidification observations (1983–2023) in the Sargasso Sea at the Bermuda Atlantic Time-series Study site. Front. Mar. Sci. 10, 1289931. https://doi.org/10.3389/fmars.2023.1289931

Bates, N.R., Mathis, J.T., Cooper, L.W., 2009. Ocean acidification and biologically induced seasonality of carbonate mineral saturation states in the western Arctic Ocean. J. Geophys. Res.: Oceans 114. https://doi.org/10.1029/2008jc004862

Behrenfeld, M.J., O'Malley, R.T., Siegel, D.A., McClain, C.R., Sarmiento, J.L., Feldman, G.C., Milligan, A.J., Falkowski, P.G., Letelier, R.M., Boss, E.S., 2006. Climate-driven trends in contemporary ocean productivity. Nature 444, 752–755. https://doi.org/10.1038/nature05317

Biswas, H., 2022. A story of resilience: Arctic diatom Chaetoceros gelidus exhibited high physiological plasticity to changing CO2 and light levels. Front. Plant Sci. 13, 1028544. https://doi.org/10.3389/fpls.2022.1028544

Boyd, P.W., Collins, S., Dupont, S., Fabricius, K., Gattuso, J., Havenhand, J., Hutchins, D.A., Riebesell, U., Rintoul, M.S., Vichi, M., Biswas, H., Ciotti, A., Gao, K., Gehlen, M., Hurd, C.L., Kurihara, H., McGraw, C.M., Navarro, J.M., Nilsson, G.E., Passow, U., Pörtner, H., 2018. Experimental strategies to assess the biological ramifications of multiple drivers of global ocean change—A review. Glob. Chang. Biol. 24, 2239–2261. https://doi.org/10.1111/gcb.14102

Brussaard, C.P.D., Noordeloos, A.A.M., Witte, H., Collenteur, M.C.J., Schulz, K., Ludwig, A., Riebesell, U., 2013. Arctic microbial community dynamics influenced by elevated $CO_2$ levels. Biogeosciences 10, 719–731. https://doi.org/10.5194/bg-10-719-2013

Brzezinski, M.A., Nelson, D.M., 1995. The annual silica cycle in the Sargasso Sea near Bermuda. Deep Sea Research Part I: Oceanographic Research Papers 42, 1215–1237.

Brzezinski, M.A., Nelson, D.M., 1986. A solvent extraction method for the colorimetric determination of nanomolar concentrations of silicic acid in seawater. Marine Chemistry 19, 139–151. https://doi.org/10.1016/0304-4203(86)90045-9

Brzezinski, M.A., Phillips, D.R., 1997. Evaluation of 32Si as a tracer for measuring silica production rates in marine waters. Limnology and Oceanography 42, 856–865. https://doi.org/10.4319/lo.1997.42.5.0856

Coello-Camba, A., Agustí, S., Holding, J., Arrieta, J.M., Duarte, C.M., 2014. Interactive effect of temperature and CO2 increase in Arctic phytoplankton. Frontiers Mar Sci 1, 49. https://doi.org/10.3389/fmars.2014.00049

Crawford, R., 2024. Spatial and Seasonal Variability in Eukaryotic Phytoplankton Composition in the Arctic Ocean Revealed with Metabarcoding Analysis. University of Victoria.

Cross, J.N., Mathis, J.T., Bates, N.R., 2012. Hydrographic controls on net community production and total organic carbon distributions in the eastern Bering Sea. Deep Sea Res. Part II: Top. Stud. Oceanogr. 65, 98–109. https://doi.org/10.1016/j.dsr2.2012.02.003

Dickson, A.G., 1990. Standard potential of the reaction: AgCl(s) + 12H2(g) = Ag(s) + HCl(aq), and the standard acidity constant of the ion HSO4− in synthetic sea water from 273.15 to 318.15 K. J Chem Thermodyn 22, 113–127. https://doi.org/10.1016/0021-9614(90)90074-z

Dickson, A.G., Sabine, C.L., Christian, J.R., 2007. Determination of the pH of seawater using a glass/reference electrode cell, in: Dickson, A.G., Sabine, C.L., Christian, J.R. (Eds.), Guide to Best Practices for Ocean CO2 Measurements. PICES, Sidney, BC, p. SOP6a.

Dugdale, R.C., Goering, J.J., 1967. Uptake of new and regenerated forms of nitrogen in primary productivity. Limnology and Oceanography 12, 196–206. https://doi.org/10.4319/lo.1967.12.2.0196

Dugdale, R.C., Wilkerson, F.P., 1986. The use of 15N to measure nitrogen uptake in eutrophic oceans; experimental considerations. Limnology and Oceanography 31, 673–689. https://doi.org/10.4319/lo.1986.31.4.0673

Engel, A., Borchard, C., Piontek, J., Schulz, K.G., Riebesell, U., Bellerby, R., 2013. $CO_2$ increases $^{14}C$ primary production in an Arctic plankton community. Biogeosciences 10, 1291–1308. https://doi.org/10.5194/bg-10-1291-2013

Engel, A., Zondervan, I., Aerts, K., Beaufort, L., Benthien, A., Chou, L., Delille, B., Gattuso, J.-P., Harlay, J., Heemann, C., Hoffmann, L., Jacquet, S., Nejstgaard, J., Pizay, M.-D., Rochelle-Newall, E., Schneider, U., Terbrueggen, A., Riebesell, U., 2005. Testing the direct effect of CO2 concentration on a bloom of the coccolithophorid Emiliania huxleyi in mesocosm experiments. Limnol. Oceanogr. 50, 493–507. https://doi.org/10.4319/lo.2005.50.2.0493

Fabry, V., McClintock, J., Mathis, J., Grebmeier, J., 2009. Ocean Acidification at High Latitudes: The Bellwether. Oceanography 22, 160–171. https://doi.org/10.5670/oceanog.2009.105

Fabry, V.J., Seibel, B.A., Feely, R.A., Orr, J.C., 2008. Impacts of ocean acidification on marine fauna and ecosystem processes. Ices J Mar Sci 65, 414–432. https://doi.org/10.1093/icesjms/fsn048

Feely, R.A., Sabine, C.L., Lee, K., Berelson, W., Kleypas, J., Fabry, V.J., Millero, F.J., 2004. Impact of anthropogenic CO2 on the CaCO3 system in the oceans. Sci. (N. York, NY) 305, 362–6. https://doi.org/10.1126/science.1097329

Field, C.B., Behrenfeld, M.J., Randerson, J.T., Falkowski, P., 1998. Primary production of the biosphere: Integrating terrestrial and oceanic components. Science 281, 237–240. https://doi.org/10.1126/science.281.5374.237

Frey, K.E., Moore, G.W.K., Cooper, L.W., Grebmeier, J.M., 2015. Divergent patterns of recent sea ice cover across the Bering, Chukchi, and Beaufort Seas of the Pacific Arctic Region. Progress in Oceanography 136, 32–49.

Gao, K., Xu, J., Gao, G., Li, Y., Hutchins, D.A., Huang, B., Wang, L., Zheng, Y., Jin, P., Cai, X., Häder, D.-P., Li, W., Xu, K., Liu, N., Riebesell, U., 2012. Rising CO2 and increased light exposure synergistically reduce marine primary productivity. Nat Clim Change 2, 519–523. https://doi.org/10.1038/nclimate1507

Giesbrecht, K.E., Varela, D.E., 2021. Summertime Biogenic Silica Production and Silicon Limitation in the Pacific Arctic Region From 2006 to 2016. Global Biogeochem Cy 35. https://doi.org/10.1029/2020gb006629

Giesbrecht, K.E., Varela, D.E., Wiktor, J., Grebmeier, J.M., Kelly, B., Long, J.E., 2019. A decade of summertime measurements of phytoplankton biomass, productivity and assemblage composition in the Pacific Arctic Region from 2006 to 2016. Deep Sea Research Part II: Topical Studies in Oceanography 162, 93–113. https://doi.org/10.1016/j.dsr2.2018.06.010

Goethel, C.L., Grebmeier, J.M., Cooper, L.W., Miller, T.J., 2017. Implications of ocean acidification in the Pacific Arctic: Experimental responses of three Arctic bivalves to decreased pH and food availability. Deep Sea Res. Part II: Top. Stud. Oceanogr. 144, 112–124. https://doi.org/10.1016/j.dsr2.2017.08.013

Grebmeier, J.M., 2012. Shifting patterns of life in the Pacific Arctic and Sub-Arctic seas. Annual Review of Marine Science 4, 63–78. https://doi.org/10.1146/annurev-marine-120710-100926

Grebmeier, J.M., Overland, J.E., Moore, S.E., Farley, E.V., Carmack, E.C., Cooper, L.W., Frey, K.E., Helle, J.H., McLaughlin, F.A., McNutt, S.L., 2006. A Major Ecosystem Shift in the Northern Bering Sea. Science 311, 1461–1464. https://doi.org/10.1126/science.1121365

Hama, T., Miyazaki, T., Ogawa, Y., Iwakuma, T., Takahashi, M., Otsuki, A., Ichimura, S., 1983. Measurement of photosynthetic production of a marine-phytoplankton population using a stable C-13 isotope. Marine Biology 73, 31–36. https://doi.org/10.1007/bf00396282.pdf

Hervé, V., Derr, J., Douady, S., Quinet, M., Moisan, L., Lopez, P.J., 2012. Multiparametric analyses reveal the pH-dependence of silicon biomineralization in diatoms. PLoS One 7, e46722. https://doi.org/10.1371/journal.pone.0046722

Hoegh-Guldberg, O., Mumby, P.J., Hooten, A.J., Steneck, R.S., Greenfield, P., Gomez, E., Harvell, C.D., Sale, P.F., Edwards, A.J., Caldeira, K., Knowlton, N., Eakin, C.M., Iglesias-Prieto, R., Muthiga, N., Bradbury, R.H., Dubi, A., Hatziolos, M.E., 2007. Coral Reefs Under Rapid Climate Change and Ocean Acidification. Science 318, 1737–1742. https://doi.org/10.1126/science.1152509

Holding, J.M., Duarte, C.M., Sanz-Martín, M., Mesa, E., Arrieta, J.M., Chierici, M., Hendriks, I.E., García-Corral, L.S., Regaudie-de-Gioux, A., Delgado, A., Reigstad, M., Wassmann, P., Agustí, S., 2015. Temperature dependence of CO2-enhanced primary production in the European Arctic Ocean. Nat. Clim. Chang. 5, 1079–1082. https://doi.org/10.1038/nclimate2768

Hoppe, C.J.M., Holtz, L.M., Trimborn, S., Rost, B., 2015. Ocean acidification decreases the light-use efficiency in an Antarctic diatom under dynamic but not constant light. The New Phytologist 207, 159–171. https://doi.org/10.1111/nph.13334

Hoppe, C.J.M., Schuback, N., Semeniuk, D., Giesbrecht, K., Mol, J., Thomas, H., Maldonado, M.T., Rost, B., Varela, D.E., Tortell, P.D., 2017a. Resistance of Arctic phytoplankton to ocean acidification and enhanced irradiance. Polar Biology 41, 1–15. https://doi.org/10.1007/s00300-017-2186-0

Hoppe, C.J.M., Schuback, N., Semeniuk, D.M., Maldonado, M.T., Rost, B., 2017b. Functional redundancy facilitates resilience of subarctic phytoplankton assemblages toward ocean acidification and high irradiance. Frontiers Mar Sci 4, 229. https://doi.org/10.3389/fmars.2017.00229

Hoppe, C.J.M., Wolf, K.K.E., Schuback, N., Tortell, P.D., Rost, B., 2018. Compensation of ocean acidification effects in Arctic phytoplankton assemblages. Nat Clim Change 8, 529–533. https://doi.org/10.1038/s41558-018-0142-9

Krause, J.W., Brzezinski, M.A., Jones, J.L., 2011. Application of low-level beta counting of 32Si for the measurement of silica production rates in aquatic environments. Marine Chemistry 127, 40–47. https://doi.org/10.1016/j.marchem.2011.07.001

Kvernvik, A.C., Rokitta, S.D., Leu, E., Harms, L., Gabrielsen, T.M., Rost, B., Hoppe, C.J.M., 2020. Higher sensitivity towards light stress and ocean acidification in an Arctic sea-ice-associated diatom compared to a pelagic diatom. N. Phytol. 226, 1708–1724. https://doi.org/10.1111/nph.16501

Langer, G., Nehrke, G., Probert, I., Ly, J., Ziveri, P., 2009. Strain-specific responses of *Emiliania huxleyi* to changing seawater carbonate chemistry. Biogeosciences 6, 2637–2646. https://doi.org/10.5194/bg-6-2637-2009

Leung, J.Y.S., Zhang, S., Connell, S.D., 2022. Is Ocean Acidification Really a Threat to Marine Calcifiers? A Systematic Review and Meta-Analysis of 980+ Studies Spanning Two Decades. Small 18, 2107407. https://doi.org/10.1002/smll.202107407

Loucaides, S., Cappellen, P.V., Roubeix, V., Moriceau, B., Ragueneau, O., 2012. Controls on the Recycling and Preservation of Biogenic Silica from Biomineralization to Burial. Silicon 4, 7–22. https://doi.org/10.1007/s12633-011-9092-9

Lueker, T.J., Dickson, A.G., Keeling, C.D., 2000. Ocean pCO2 calculated from dissolved inorganic carbon, alkalinity, and equations for K1 and K2: validation based on laboratory measurements of CO2 in gas and seawater at equilibrium. Mar Chem 70, 105–119. https://doi.org/10.1016/s0304-4203(00)00022-0

Martin-Jezequel, V., Hildebrand, M., Brzezinski, M.A., 2000. Silicon metabolism in diatoms: Implications for growth. Journal of Phycology 36, 821–840.

Mathis, J., Cross, J., Evans, W., Doney, S., 2015. Ocean acidification in the surface waters of the Pacific-Arctic boundary regions. Oceanography 25, 122–135. https://doi.org/10.5670/oceanog.2015.36

Mathis, J.T., Cross, J.N., Bates, N.R., 2011. Coupling primary production and terrestrial runoff to ocean acidification and carbonate mineral suppression in the eastern Bering Sea. J. Geophys. Res.: Oceans 116. https://doi.org/10.1029/2010jc006453

Mehrbach, C., Culberson, C.H., Hawley, J.E., Pytkowicx, R.M., 1973. Measurement of the apparent dissociation constants of carbonic acid in seawater at atmospheric pressure. Limnol Oceanogr 18, 897–907. https://doi.org/10.4319/lo.1973.18.6.0897

Milligan, A.J., Varela, D.E., Brzezinski, M.A., Morel, F.M.M., 2004. Dynamics of silicon metabolism and silicon isotopic discrimination in a marine diatom as a function of pCO2. Limnology and Oceanography 49, 322–329. https://doi.org/10.4319/lo.2004.49.2.0322

Nagao, R., Ueno, Y., Akimoto, S., Shen, J.-R., 2020. Effects of CO2 and temperature on photosynthetic performance in the diatom Chaetoceros gracilis. Photosynth. Res. 146, 189–195. https://doi.org/10.1007/s11120-020-00729-8

Nakagawa, S., Cuthill, I.C., 2007. Effect size, confidence interval and statistical significance: a practical guide for biologists. Biol. Rev. 82, 591–605. https://doi.org/10.1111/j.1469-185x.2007.00027.x

Nelson, D.M., Tréguer, P., Brzezinski, M.A., Leynaert, A., Quéguiner, B., 1995. Production and dissolution of biogenic silica in the ocean: Revised global estimates, comparison with regional data and relationship to biogenic sedimentation. Global Biogeochemical Cycles 9, 359–372. https://doi.org/10.1029/95gb01070

Newbold, L.K., Oliver, A.E., Booth, T., Tiwari, B., DeSantis, T., Maguire, M., Andersen, G., Gast, C.J. van der, Whiteley, A.S., 2012. The response of marine picoplankton to ocean acidification. Environ. Microbiol. 14, 2293–2307. https://doi.org/10.1111/j.1462-2920.2012.02762.x

Orr, J.C., Epitalon, J.-M., Dickson, A.G., Gattuso, J.-P., 2018. Routine uncertainty propagation for the marine carbon dioxide system. Mar. Chem. 207, 84–107. https://doi.org/10.1016/j.marchem.2018.10.006

Parsons, T.R., Maita, T., Lalli, C.M., 1984. A Manual of Chemical & Biological Methods for Seawater Analysis, 1st ed, Pergamon Press. Pergamon Press, Oxford.

Petrou, K., Baker, K.G., Nielsen, D.A., Hancock, A.M., Schulz, K.G., Davidson, A.T., 2019. Acidification diminishes diatom silica production in the Southern Ocean. Nature Climate Change 9, 781–786. https://doi.org/10.1038/s41558-019-0557-y

Ragueneau, O., Schultes, S., Bidle, K., Claquin, P., Moriceau, B., 2006. Si and C interactions in the world ocean: Importance of ecological processes and implications for the role of diatoms in the biological pump. Glob. Biogeochem. Cycles 20, GB4S02. https://doi.org/10.1029/2006gb002688

Reinfelder, J.R., 2011. Carbon concentrating mechanisms in eukaryotic marine phytoplankton. Annu. Rev. Mar. Sci. 3, 291–315. https://doi.org/10.1146/annurev-marine-120709-142720

Riebesell, U., Zondervan, I., Rost, B., Tortell, P.D., Zeebe, R.E., Morel, F., 2000. Reduced calcification of marine plankton in response to increased atmospheric CO2. Nature 407, 364–367.

Rosenberg, M.S., Rothstein, H.R., Gurevitch, J., 2013. Effect sizes: Conventional choices and calculations, in: Koricheva, J., Gurevitch, Juessica, Mengersen, K. (Eds.), Handbook of Meta-Analysis in Ecology and Evolution. Princeton University Press, Princeton, NJ, pp. 61–71. https://doi.org/10.23943/princeton/9780691137285.003.0006

Seifert, M., Rost, B., Trimborn, S., Hauck, J., 2020. Meta-analysis of multiple driver effects on marine phytoplankton highlights modulating role of pCO2. Global Change Biol 26, 6787–6804. https://doi.org/10.1111/gcb.15341

Slawyk, G., Collos, Y., Auclair, J.C., 1977. The use of the 13C and 15N isotopes for the simultaneous measurement of carbon and nitrogen turnover rates in marine phytoplankton. Limnology and Oceanography 22, 925–932. https://doi.org/10.4319/lo.1977.22.5.0925

Spalding, M.H., 2008. Microalgal carbon-dioxide-concentrating mechanisms: *Chlamydomonas* inorganic carbon transporters. J Exp Bot 59, 1463–1473. https://doi.org/10.1093/jxb/erm128

Taucher, J., Jones, J., James, A., Brzezinski, M.A., Carlson, C.A., Riebesell, U., Passow, U., 2015. Combined effects of CO2 and temperature on carbon uptake and partitioning by the marine diatoms Thalassiosira weissflogii and Dactyliosolen fragilissimus. Limnol Oceanogr 60, 901–919. https://doi.org/10.1002/lno.10063

Tomczak, M., Tomczak, E., 2014. The need to report effect size estimates revisited. An overview of some recommended measures of effect size. Trends in Sport Sciences 1, 19–25.

Torres-Valdés, S., Tsubouchi, T., Bacon, S., Naveira-Garabato, A.C., Sanders, R., McLaughlin, F.A., Petrie, B., Kattner, G., Azetsu-Scott, K., Whitledge, T.E., 2013. Export of nutrients from the Arctic Ocean. J. Geophys. Res.: Oceans 118, 1625–1644. https://doi.org/10.1002/jgrc.20063

Tréguer, P., Bowler, C., Moriceau, B., Dutkiewicz, S., Gehlen, M., Aumont, O., Bittner, L., Dugdale, R., Finkel, Z., Iudicone, D., Jahn, O., Guidi, L., Lasbleiz, M., Leblanc, K., Levy, M., Pondaven, P., 2018. Influence of diatom diversity on the ocean biological carbon pump. Nat Geosci 11, 27–37. https://doi.org/10.1038/s41561-017-0028-x

Tréguer, P.J., Sutton, J.N., Brzezinski, M., Charette, M.A., Devries, T., Dutkiewicz, S., Ehlert, C., Hawkings, J., Leynaert, A., Liu, S.M., Monferrer, N.L., López-Acosta, M., Maldonado, M., Rahman, S., Ran, L., Rouxel, O., 2021. Reviews and syntheses: The biogeochemical cycle of silicon in the modern ocean. Biogeosciences 18, 1269–1289. https://doi.org/10.5194/bg-18-1269-2021

Vrieling, E.G., Gieskes, W.W.C., Beelen, T.P.M., 1999. Silicon Deposition In Diatoms: Control By The pH Inside The Silicon Deposition Vesicle. J Phycol 35, 548–559. https://doi.org/10.1046/j.1529-8817.1999.3530548.x

Walsh, J.E., Ballinger, T.J., Euskirchen, E.S., Hanna, E., Mård, J., Overland, J.E., Tangen, H., Vihma, T., 2020. Extreme weather and climate events in northern areas: A review. Earth-Sci. Rev. 209, 103324. https://doi.org/10.1016/j.earscirev.2020.103324

Wolf, K.K.E., Hoppe, C.J.M., Rost, B., 2018. Resilience by diversity: Large intraspecific differences in climate change responses of an Arctic diatom. Limnol. Oceanogr. 63, 397–411. https://doi.org/10.1002/lno.10639

Wolf-Gladrow, D., Riebesell, U., 1997. Diffusion and reactions in the vicinity of plankton: A refined model for inorganic carbon transport. Mar Chem 59, 17–34. https://doi.org/10.1016/s0304-4203(97)00069-8

Wu, Y., Campbell, D.A., Irwin, A.J., Suggett, D.J., Finkel, Z.V., 2014. Ocean acidification enhances the growth rate of larger diatoms. Limnology and Oceanography 59, 1027–1034. https://doi.org/10.4319/lo.2014.59.3.1027

Wyatt, S.N., McNabb, B.J., Varela, D.E., 2024. Morphological and physiological responses of the cosmopolitan marine diatom Thalassiosira rotula to acidification. Diatom Res. 39, 61–74. https://doi.org/10.1080/0269249x.2024.2369049

## References for Chapter 7


Aumont, O., Maier-Reimer, E., Blain, S., Monfray, P., 2003. An ecosystem model of the global ocean including Fe, Si, P colimitations. Glob. Biogeochem. Cycles 17. https://doi.org/10.1029/2001gb001745

Bopp, L., Aumont, O., Cadule, P., Alvain, S., Gehlen, M., 2005. Response of diatoms distribution to global warming and potential implications: A global model study. Geophys. Res. Lett. 32. https://doi.org/10.1029/2005gl023653

Bopp, L., Resplandy, L., Orr, J.C., Doney, S.C., Dunne, J.P., Gehlen, M., Halloran, P., Heinze, C., Ilyina, T., Séférian, R., Tjiputra, J., Vichi, M., 2013. Multiple stressors of ocean ecosystems in the 21st century: projections with CMIP5 models. Biogeosciences 10, 6225–6245. https://doi.org/10.5194/bg-10-6225-2013

Laufkötter, C., Vogt, M., Gruber, N., Aita-Noguchi, M., Aumont, O., Bopp, L., Buitenhuis, E., Doney, S.C., Dunne, J., Hashioka, T., Hauck, J., Hirata, T., John, J., Quéré, C.L., Lima, I.D., Nakano, H., Seferian, R., Totterdell, I., Vichi, M., Völker, C., 2015. Drivers and uncertainties of future global marine primary production in marine ecosystem models. Biogeosciences 12, 6955–6984. https://doi.org/10.5194/bg-12-6955-2015

Tréguer, P., Bowler, C., Moriceau, B., Dutkiewicz, S., Gehlen, M., Aumont, O., Bittner, L., Dugdale, R., Finkel, Z., Iudicone, D., Jahn, O., Guidi, L., Lasbleiz, M., Leblanc, K., Levy, M., Pondaven, P., 2018. Influence of diatom diversity on the ocean biological carbon pump. Nat Geosci 11, 27–37. https://doi.org/10.1038/s41561-017-0028-x

Tréguer, P.J., Sutton, J.N., Brzezinski, M., Charette, M.A., Devries, T., Dutkiewicz, S., Ehlert, C., Hawkings, J., Leynaert, A., Liu, S.M., Monferrer, N.L., López-Acosta, M., Maldonado, M., Rahman, S., Ran, L., Rouxel, O., 2021. Reviews and syntheses: The biogeochemical cycle of silicon in the modern ocean. Biogeosciences 18, 1269–1289. https://doi.org/10.5194/bg-18-1269-2021